DEVELOPMENT OF A COASTAL PREDICTION SYSTEM THAT INCORPORATES FULL 3D WAVE-CURRENT INTERACTIONS ON THE MEAN FLOW AND THE SCALAR TRANSPORT WITH INITIAL APPLICATION TO THE LAKE MICHIGAN TURBIDITY PLUME

DISSERTATION

Presented in Partial Fulfillment of the Requirements for

the Degree Doctor of Philosophy in the

Graduate School of The Ohio State University

By

Panagiotis Velissariou, B.S., M.S., P.E.

* * * * *

The Ohio State University

2009

Dissertation Committee:

Keith W. Bedford, Adviser

Carolyn J. Merry

Gil Bohrer

Approved by

_____

Adviser

Graduate Program in Civil Engineering

ABSTRACT

The present work focuses on the development of a Modular Multi-Component Coastal Ocean Prediction System (M^2COPS) that incorporates the full 3D wave-current interactions for a better representation of the entrainment and transport mechanics in complex deep and shallow water coastal environments. The system incorporates wind, temperature and atmospheric pressure forcing that drive the circulation, wave, sediment and bottom boundary layer model components.

The effects of the wind generated surface waves on the water column and bottom layer dynamics are parametrized by the inclusion of the Stokes drift, and the wave radiation stress terms that quantify the excess of mass and momentum flux produced by the waves. Coupled wave-hydrodynamic models traditionally incorporate the radiation stress terms only into the vertically integrated momentum. Considering the fact that currents are 3D structures, the vertical variation of the radiation stress should be also considered. In the present work the 3D momentum equations are re-derived to include the full 3D impact of the radiation stresses on the currents.

As a preliminary test, the system is applied to Lake Michigan with a twofold purpose: *(a)* to conduct an initial testing of the model prognostic variables with and without the effect of the waves; and *(b)* to develop a methodology required to answer whether the annually observed Spring turbidity nearshore plume in Southern Lake Michigan is transporting material from its origin in one continuous transport mode or as generated by a series of local deposition, resuspension and transport activities. To this end data collected during the *EEGLE* project are fully analyzed; shoreline erosion rates and texture of the eroded material were collected from various sources and via various methods and are presented for 34 shoreline segments in a uniform format; an Eulerian Particle Tracking formulation that identifies the source and origin of the various particle sizes within the sediment plume is presented; and a conceptual and computational set up of the control volumes or sediment plume sources/origins required for a detailed study of the Spring turbidity plume is developed.

This work is dedicated to my wife *Vasso* for her love, understanding and continuous encouragement.

ACKNOWLEDGMENTS

I would like to thank my academic adviser, Dr. Keith W. Bedford, for the chance to pursue this subject for my dissertation, for the financial support that made this come true and for his guidance throughout this research and during all my years as a graduate student.

I would like to thank Dr. Carolyn J. Merry for enthusiastically serving in my reading and oral defense committees.

I would like to thank Dr. Gil Bohrer for his willingness to serve under only short notice in my oral defense committee.

I would like to thank Dr. James N. Scott for serving in my advisory and candidacy exam committees.

I would like to thank Dr. Dave Schwab, Physical Oceanographer at *GLERL/NOAA* for providing shoreline and shore erosion data of Lake Michigan for my dissertation and for always answering my requests for information and data.

I would like to thank Dan Vehr, senior systems manager at the computer lab in Hitchcock Hall, at the OSU for his continual and enthusiastic help in many computer and system administration related issues.

Finally, I would like to thank my family for their endless love and their continuous encouragement and patience.

VITA

1985	B.S. Agricultural Engineering, Aristotelian University of Thessaloniki, Greece
1991	M.S. Civil & Environmental Engineering and Geodetic Sciences, The Ohio State University, U.S.A
2001	P.E. (Ohio, E-67134)
1992-2007	Graduate Research Associate, Graduate Teaching Associate, Instructor, and Systems Manager at The Ohio State University.

PUBLICATIONS

Research Publications

P. Velissariou, V. Velissariou, Y. Guo, and K. Bedford. "*A Multi-Size, Multi-Source Formulation for Determining Impacts of Sediments on Near-Shore Sensitive Sites*". Estuarine and Coastal Modeling. Proceedings of the Sixth International Conference, pages 59-73, New Orleans, Louisiana, 1999. ASCE.

Keith W. Bedford, Panagiotis Velissariou, Vasilia Velissariou and Yong Guo. "*Integrated Analysis of the Impact of Unconfined Placement Activities on Near-Shore Sensitive Areas*". Technical Report, no 3, US Army Corps of Engineers, Waterways Experiment Station, Vicksburg, MS, 1999.

Keith W. Bedford, Onyx Wai, Robert Van Evra III, Panagiotis Velissariou, Jongook Lee and Charles Libicki. "*The Local Near-Bottom Response of a Dredged Material Placement Site to Wind and Tide Effects*". Technical Report, US Army Corps of Engineers, Washington, D.C, 1990.

Panagiotis Velissariou, Keith W. Bedford. "*The Response of Estuarine Sediment Concentration Profiles to Weak Surface Swell*". Hydraulics and the Environment, Proceedings of Environmental Hydraulics at the IAHR, XXIII Congress, The National Research Council/Canada, 1989.

Panagiotis Velissariou. "*The Response of Bottom Concentration Profiles in Central Long Island Sound to Weak Swell*". Master Thesis, The Ohio State University, 1991.

Presentations/Abstracts

Velissariou Panagiotis and Keith W. Bedford. "*Modeling the Complexities of Near/Off-Shore Entrainment and Transport Mechanisms in Lake-Coastal Environments*". Abstract, 9th International Conference on Estuarine and Coastal Modeling - Charleston, SC, 2005.

Panagiotis Velissariou, Yong Guo, Vasilia Velissariou, and Keith W. Bedford. "*A Multi-Size, Multi-Source Formulation for Determining Impacts of Sediments on Near-Shore Sensitive Sites*". Abstract, IAGLR 99, 42nd Conference on Great Lakes Research, May 24-28, Case Western Reserve University, Cleveland, Ohio, 1999.

Instructional Publications

Panagiotis Velissariou. "*Solutions Manual to accompany the book: Fluid Mechanics, by Streeter, Wylie and Bedford, 9th edition*". Published by McGraw-Hill, pp. 1000, 1998.

AWARDS

American Meteorological Society Special Award, 2001, For Developing the First Coastal Forecasting System to Make Routine Operational Predictions of Currents, Temperature, and Key Trace Constituents.

FIELDS OF STUDY

Major Field: Civil Engineering

Studies in:

Coastal and Ocean Engineering	Prof. Keith W. Bedford
Computational Fluid Dynamics	Prof. James N. Scott, Prof. Richard J. Bodonyi

TABLE OF CONTENTS

Page

LIST OF TABLES

LIST OF FIGURES

CHAPTER 1

INTRODUCTION

Modern expectations from the application of coastal prediction systems require increased accuracy and detailed information of the field being modeled. Therefore, these prediction systems are gradually using more enhanced physics and the locations of interest are more closely monitored. The coastal prediction system developed in this dissertation is a combination of thoroughly tested and approved approaches in hydrodynamic modeling and of newer developments and trends towards a better representation of the physical interactions between waves and currents in the modeled coastal domains.

The most prominent feature of the developed system is the inclusion of a complete three dimensional methodology for incorporating wave contributions to momentum, heat and sediment transport distributions in freshwater lakes and coastal zones. For the better part of 20 years these distributions have been routinely made using widely available models that have essentially the same physics components and structure and differ only in the details of some boundary condition formulations, gridding technology, and minor numerics. Examples of such codes include the venerable Princeton Ocean Model *POM* (Mellor [1998], Blumberg and Mellor [1987]), the Regional Ocean Modeling System *ROMS* (Warner et al. [2008]), and the models by Sheng (Sheng [1990], Sheng et al. [1990]), which the U.S. Army Corps of Engineers has labeled and used as *CH3D* (Chapman et al. [1996]).

The structures of these models are all quite similar, so much that henceforth they will be labeled as the Standard Model Formulation (*SMF*). Shared formulation features include: incompressible flow, full inertia term resolution, Reynolds averaged governing equations, quasi three dimensional equations with hydrostatic pressure assumed, full Boussinesq coupling between heat and momentum distributions and sediments if present, long-wave three dimensional free surface predictions by solution of the continuity equation, a split barotropic/baroclinic formulation for computing time

efficiency, turbulent momentum and flux closures by higher order formulations of at least a κ-ϵ complexity, imposition of sea surface boundary conditions by wind drag and heat flux time histories at the surface, imposition of bottom boundary conditions by imposition of time histories of frictional shear stress and heat and/or sediment fluxes, and the ability to use rectangular z-grids or terrain-following rectangular, curvilinear, orthogonal or nonorthogonal formulations.

The incorporation of surface wave effects cannot be handled by merely imposing a traditional drag coefficient formulation at the free surface of the model tuned by ad hoc coefficient adjustments. Wave effects penetrate to depths below the free surface and in shallower waters or larger wave climates they may impact the bottom directly. Therefore, the *SMF* will not resolve these wave effects and the governing equations must be re-derived to incorporate them. These derivations and the subsequent model reformulation is the central core of this dissertation. Rather than reconstruct a *SMF* and then re-derive it to incorporate the new derivations, an existing model is adopted here, The U.S. Army Corps of Engineers *CH3D* model originally developed by Sheng and used by the Army Corps to perform the first Chesapeake Bay 3D simulations (Johnson et al. [1990]).

Application of the system in coastal areas targets better representation of storm surges, entrainment and resuspension of the bottom sediments in shallow waters, shoreline erosion and longshore and crossshore sediment transport. The developed system is applied to the very well monitored Lake Michigan to examine the resuspension and entrainment of the bottom sediments during the 1998 Spring plume.

1.1 The Modular Multi-Component Ocean Prediction System (M^2COPS)

Several numerical model formulations and physics are employed in the development of the new coastal prediction system that when combined together comprise the Modular Multi-Component Ocean Prediction System *MMCOPS* or better M^2COPS.

The system consists of a core hydrodynamic model (M^2HYD), a sediment erosion/transport model (M^2SED), a deep water wave propagation model (M^2WAM), a shallow water wave prediction model (M^2SWAN) and a combined wave-current bottom boundary layer model (M^2BBL). The above models are all coupled together, either directly by sharing common variables and calculation blocks, or indirectly by passing the required information to each other using the Message Passing Interface (*MPI*). The implementation of *MPI* used here is compatible: *(a)* with the one developed at the

Argonne National Laboratory (*MPICH*: http://www-unix.mcs.anl.gov/mpi/mpich1/ and *MPICH2*: http://www.mcs.anl.gov/research/projects/mpich2/), and *(b)* with *OpenMPI* (http://www.open-mpi.org/).

In M^2HYD, the surface drag coefficients for heat and momentum have been re-formulated to account for both the effects of the stability of the Atmospheric Boundary Layer (*ABL*) and the wind generated surface gravity waves (Section 2.5.1). The heat flux formulation of the original *CH3D* has been completely replaced to use the heat energy balance equation as described in Section 2.6. The equation of state used in M^2HYD is the *UNESCO* equation of state (Fofonoff and Millard [1983]) that replaces the original Eckart's formulation (Eckart [1958]). Special consideration is given in the spatial and the temporal variation of the barometric pressure, as well as the vertical distribution of the pressure in the water column, both of which are included into the calculations of the *UNESCO* equation of state.

The original governing equations of the "standard" hydrodynamic model have been re-derived and re-formulated in (M^2HYD) to account for the variation of the barometric pressure along the solution domain, and for the effects of the propagating surface waves in the water column both near and away from the free surface. The 3D radiation stresses terms have been included into the baroclinic equations of the model and the 2D radiation stress terms have been included into the barotropic equations. Additional terms have been introduced in the governing equations to account for the Stokes drift and the Langmuir circulation patterns. The radiation stress terms are particularly important in the calculation of the near-shore hydrodynamics and, of course, they are of significance for the current application to Lake Michigan.

The two spectral wave models used in M^2COPS, namely *WAM* (The WAMDI Group [1988]) and *SWAN* (Booij et al. [2004]), are slightly modified to account for the effects of the stability of the *ABL* and the enhanced calculation of the bottom friction coefficient as defined in M^2BBL. Both models are renamed as M^2WAM and M^2SWAN to conform with the naming scheme used in M^2COPS. Chapter 3 presents the governing equations of the two models, where the equations of the source terms have been properly modified to include the above effects.

The output of the current spectral wave models, *WAM* and *SWAN*, do not allow the direct calculation of the 3D radiation stress terms, since they only supply the vertically averaged 2D radiation stresses. To accommodate the above limitation, a vertical distribution or shape function, is derived

that relates the 3D to the 2D radiation stresses. The derived radiation stress terms and the accompanying vertical shape functions are given in Chapter 5. Simplifications of the above equations are presented that allow both the shallow and the deep water calculations.

The sediment calculations in M^2SED have been improved by introducing the effects of the surface waves on the entrainment and resuspension of the bottom sediments; the calculation of the bedload transport; and the transport and deposition of the suspended sediments. The radiation stresses are of great importance for the near-shore hydrodynamics and their effect is directly felt by the bottom physics. Radiation stress terms exhibit rather increased magnitudes near the bottom in shallow waters, thus affecting the dynamics of both the bottom boundary layer and the transport of the bottom sediments. The full details and the derived equations for the sediment transport calculations are found in Chapters 2 and 4.

The original bottom boundary layer model used in previous calculations by this author and other members of the Great Lakes Forecasting System (*GLFS*) research group at The Ohio State University employed the version developed by Glenn and Grant (Glenn [1987], Glenn and Grant [1987]). In M^2BBL, the governing equations have been re-derived to include the radiation stress terms and to account for the use of spectral wave models. The elaborate numerical calculations for the determination of the bottom friction coefficient of the original Glenn and Grant's model have been completely replaced by the formulations described in Mathisen and Madsen [1996b], Mathisen and Madsen [1999] and Mellor [2002]. The new approach in calculating the bottom friction coefficient eliminates the convergence problems encountered in Glenn and Grant's model; accounts for the use of spectral waves; and substantially improves the *CPU* and real computing time required for the extensive calculations in M^2COPS. The details of all the derived equations are found in Chapter 6.

Application of a detailed modeling system like M^2COPS is expected to increase *CPU* time and slow down the calculations. Fortunately, modern computer platforms are very powerful as they use very fast single or multi-core *CPU*s and are equipped with significant amounts of system memory. Even home-based computers come with multi-core *CPU*s and system memory of 8 GB or more. To accommodate the requirements of the present and future research studies, M^2COPS is fully parallelized such that it can be run on single or multi-core computer cluster systems. In particular,

for the model application in Lake Michigan *M*^{2}*COPS* ran on a home-built 32-bit multi-core cluster system, such that multiple parallel simulations could take place at the same time.

M^2*COPS* is a hybrid coded system using *Fortran 77*, *Fortran 90/95* and *C*. The *C* and *Fortran* parts in *M*^{2}*COPS* are linked together via an *API*, which was developed using *CFortran* (http://www-zeus.desy.de/~burow/cfortran). The production of the graphics and the data analysis were performed using *IDL* (http://www.ittvis.com/), not directly linked with *M*^{2}*COPS*. An *IDL-C-Fortran* interface has been developed based on *CFortran*, such that certain functionality in *M*^{2}*COPS* can be used within *IDL*. Finally, an extensive number of scripts were written to accommodate the requirements of the various *M*^{2}*COPS* simulations.

The complexity of the developed prediction system gives rise to the following question: "How will the individual model components and the physical processes involved be validated?" Fortunately, the enormous amount of available field data in Lake Michigan collected during the *EEGLE* project (http://www.glerl.noaa.gov/eegle/) accompanied by data collected during previous projects will be used to answer the above question. The *EEGLE* project was a five year collective effort of 40 scientists from a variety of disciplines. Among the measured data collected during this period are wave, current, temperature, sediment trap, phytoplankton and zooplankton concentration data.

The wave data used for the model validation are a combination of tripod deployment data at Benton Harbor (lat: 42.135 ^{o}N, lon: 86.493 ^{o}W, Michigan City (lat: 41.735 ^{o}N, lon: 86.907 ^{o}W) and Milwaukee (lat: 42.958 ^{o}N, lon: 87.813 ^{o}W) collected during the *EEGLE* project and data collected at meteorological stations operated by *NOAA* (buoys 45002 and 45007) on a regular basis. The velocity data were obtained from the *EEGLE* project. The measurements were provided by Acoustic Doppler Current Profiler (*ADCP*), Smart Acoustic Current Meter (*SACM*) and Vector Averaging Current Meter (*VACM*) moorings.

Two sets of temperature data were obtained from the *EEGLE* project: the first set is comprised of temperature data that accompany the wave and velocity data from the same project and have been used for depth averaged temperature comparisons, the second set are additional temperature data taken by *CTD* (Conductivity-Temperature-Depth) profilers, which have been used for comparisons of vertical temperature distributions. The water elevation data are available at various water elevation gage stations around Lake Michigan and were obtained from the Center for Operational Oceanographic Products and Services (*NOAA-COOPS*).

The suspended particle data from the *EEGLE* project are categorized into data of total suspended mass, chlorophyll-a, and zooplankton mass. Measurements of suspended particles mass include: *(a)* collection of water samples at various locations and depths that were analyzed to give total suspended mass and chlorophyll-a concentrations, *(b)* collection of data on light scattering and fluorescence by various instruments moored with *CTD* profilers that were related to total mass and chlorophyll-a concentrations, *(c)* collection of continuous data on zooplankton concentrations, and *(d)* collection of settling suspended particles onto sediment traps.

In addition to data used for the model evaluation a huge amount of data are necessary as model input. Model input requires meteorological, water elevation and sediment data. Meteorological data were obtained from the Great Lakes Forecasting System *MAROBS* (Marine Observation System) database. Bottom sediment grain size distribution data were obtained from the Lake Michigan Mass Balance (*LMMB*) and the Environmental Mapping and Assessment (*EMAP*) projects sponsored by the *EPA*. The shoreline types and their distribution around Lake Michigan and clay, silt and sand mass fractions for 11 counties were obtained from the *EEGLE* database. Soil types for the rest of the counties were decided from the geological map and the soil descriptions in Veach [1953], and from the Web Soil Survey Maps and Soil Descriptions. Erosion rates for Lake Michigan were decided from the work of Armstrong et al. [1976], as cited by Monteith and Sonzogni [1976]. More information on the above data sets and how they are used in the present study is given in Chapters 8, 9, and 10.

1.2 The Lake Michigan System

Lake Michigan is located at the Northern part of the United States and belongs to an interconnecting natural system of large lakes and channels shared by the United States and Canada, known as the Great Lakes. Great lakes reach the Atlantic ocean through the St. Lawrence River in the East and the Gulf of Mexico through the Mississippi River in the South. Lake Michigan extends in the North-South direction from latitude 41.6 ^{o}N to 46.1 ^{o}N and in the East-West direction from longitude 85 ^{o}W to 88 ^{o}W. With a surface area of 57753 km^2 and a volume of 4918 km^3, Lake Michigan is classified as the fourth largest freshwater lake in the world by area and as the fifth largest freshwater lake in the world by volume. The lake is connected at its North-Eastern side to Lake Huron through the straits of Mackinac, the Lake's only outlet. The orientation of the lake is North to South

with a length of 494 km and a maximum width of 190 km at its Northern part (source: http://www.glerl.noaa.gov/pr/ourlakes/lakes.html#michigan).

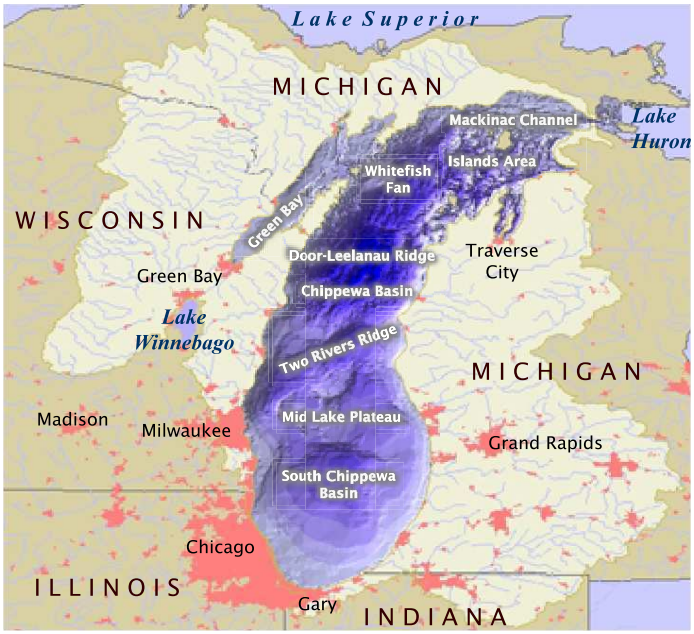

Figure 1.1 Lake Michigan bathymetry (source: http://coastal.lic.wisc.edu/bathyexplorer/lmbathy/lmbathy.html).

Lake Michigan is divided into a Northern basin and a Southern basin by the Two Rivers ridge (Figure 1.1). The Northern basin is characterized by two large bays, one on the West side, the Green Bay, and one on the East side, the Traverse Bay, 11 large and small islands and a basin plain, Chippewa Basin, where the lake depth reaches its maximum at 281 m. The Southern basin is characterized by the Middle Lake Plateau, a shallow water area that is surrounded by four basin plains, the Ludington and Muskegon basins on the East, the Milwaukee basin on the West and the South Chippewa Basin at the Central-South part of the lake. The South Chippewa Basin is the deepest of the four basins with a maxim depth of 164 m (source: http://coastal.lic.wisc.edu/bathyexplorer/welcome.htm). The average depth of the lake is 84.44 m. All depths given in the present study are referenced to the Low Water Datum, or Chart Datum, which for Lake Michigan is 176.022 m above the mean water level at Rimouski, Québec. Benchmark #1250G, located at Rimouski, Québec is the reference zero for the International Great Lakes Datum 1985 (*IGLD85*),

which has been the vertical control reference system used in hydraulic and hydrologic applications in the Great Lakes Basin since January, 1992.

The lake and its watershed cover an area of 173000 km^2 that is shared by 34 counties; 11 of which are in the State of Wisconsin, 2 in Illinois, 3 in Indiana, and 18 in Michigan. According to the *USGS* data about 300 rivers, streams and creeks cross the watershed. Among the larger rivers that drain into the lake are the Fox and the Menominee Rivers in Northeast Wisconsin and the St. Joseph, the Kalamazoo and the Grand River in Southwest Michigan. The amount of sediments from the watershed carried by the rivers into the lake is, however, relatively small consisting only of 5.5 % of its total external sediment loading (Monteith and Sonzogni [1976]). The lake shoreline is about 2670 km. At the Northern part the lake consists mainly of beaches with fine and coarse sand and secondarily of low bluffs, rocky areas and wetlands. At the Southern part the lake consists mainly of high bluffs that may be accompanied by beaches and secondarily of low bluffs with beaches, sandy or silty banks and artificial soils high in silty and clayey material. Lake Michigan is known for the extensive formation of sandy dunes along its shoreline. Seventy per cent of the dune type shoreline is found along the shoreline of the Northern part (source: www.glerl.noaa.gov/eegle/resources/#reg_met).

1.3 Lake Michigan Hydrodynamic Processes

The water at the Northern and Northwestern parts of the lake freezes from late December until early April. During this period the areas around the straits of Mackinac and the Green Bay are usually 80 % to 100 % covered by ice. The water at the Southern part of the lake, except in very cold years like 1994, are usually ice free or covered about 5 % by ice in the deeper waters, but they may freeze as much as 95 % in the near-shore areas of either or both sides of the lake (source: http://www.glerl.noaa.gov/data/ice/atlas/ice_charts/index.html).

Like most large lakes at the temperate zone, Lake Michigan is a dimictic lake. After the melting of the ice and the rising of the water temperature, the conditions are appropriate for the first annual overturn and mixing of the water by the storms and the strong gales of the Spring (wind speeds of 20 – 24 m/s). The Spring overturn is followed by the Summer stratification characterized by lighter warmer water in the epilimnion and colder heavier water in the hypolimnion and by the development of the thermocline in the metalimnion, where temperatures change rapidly. The second

annual overturn of the lake is the combined result of colder air temperatures and strong winds during Autumn. The resulting heavier colder surface water sinks causing the initial mixing that is completed by the strong gales and violent storms of the Autumn (wind speeds of 24 – 28 m/s).

The orientation of the prevailing winds varies with the season, e.g., in Winter, the prevailing winds follow the North to North-West directions, in Spring the North-East to East directions, and in Autumn the South-West to West directions. Winds are the cause for two types of oscillatory movements over the lake, waves and seiches. The wave height, direction and duration depend on the intensity, direction and duration of the winds. Observed maximum wave heights in Lake Michigan are on the order of 3 m to 3.5 m, while monthly average significant wave heights over the 20 year period 1981- 2001 are on the order of 0.7 m during June, and on the order of 2 m during November and December (source: http://www.ndbc.noaa.gov/maps/great_lakes_hist.shtml). Under certain strong winds, whole basin oscillatory motions known as seiches occur and continue until all the energy is consumed and equilibrium is achieved. Water elevation power spectra in Lake Michigan show spectral peaks with a period of 9 h (As-Salek and Schwab [2004] and present study). This observed period is very close to the 9.53 h period of seiches calculated by the Merian's equation (CEM II [2006], pp. II-5-51).

The gravitational attraction of the sun and moon also create tides. As-Salek and Schwab [2004] and Sawicki [1999] claim, the existence of a semi-diurnal tide at the 12.42 h and 12.0 h at the lake. Their findings are also confirmed in the present study via spectral analysis of gage water elevation time series for the years 1996-2001 (Section 8.2). The amplitude of the tides in Lake Michigan are in the order of 5 cm, which can equal the often observed seiche amplitudes.

1.4 Lake Michigan Turbidity Plume

The mechanical action of the winds, waves and currents on Lake Michigan is the mechanism responsible for the erosion of the lake bed and shoreline. The energy of the waves depends on the speed of the wind, its duration and fetch, and the angle at which the wave reaches the shore. This, in turn, determines the size and amount of the material that is eroded and the distance traveled before settling at a new location. Low energy waves move fine sand, silt and clays; high energy waves move coarser material. The suspended material from the eroded areas is carried by the waves until the water velocity slows enough to allow deposition. Such deposition may be permanent or temporary

depending on the size and the nature of the forces that affect the new location. Sediments that move towards the deeper water middle part of the lake and settle on its bottom can be permanently buried there, whereas sediments that move along-shore and settle at shallower waters or at the beaches are more prone to re-suspension during any future storm event that will create the appropriate flow conditions. Whenever the eroded shore material follows the water in a net movement along its shoreline, it becomes part of the lake's long-shore current or littoral drift. Whenever the suspended material follows the water in an on-shore off-shore motion, it becomes part of an erosion accretion process responsible for the shoreline displacement.

Factors that affect the erosion process in Lake Michigan are its water level fluctuations, the seasonal change of the wind direction, the slopes of the various shore segments, the ice formation along the shoreline and the existence of dunes. Low water levels expose new surfaces to erosion, while high water levels enhance the action of the waves and increase erosion rates. Seasonal changes in the wind direction expose different segments of the lake shoreline to the destructive action of the waves and currents. Gently sloping shoreline segments, dunes and ice formation act as natural protective mechanisms in areas where found. Turbidity plumes originating from the introduction of eroded material into the water column occur in Lake Michigan throughout the year. Their intensity is lower in the Summer, when the wind strength is lower and the lake is stratified, and higher in late Winter and early Spring, when the winds are stronger and the lake is unstratified and easily disturbed.

The interest of the present study is focused in the high turbidity plume that occurs every year during the late Winter early Spring months, while the lake is still unstratified. Although various explanations and assumptions have been made about the nature of the suspended material (algal blooms versus increased sediment consentrations) and the mechanisms of the plume's formation, it was soon concluded that shoreline erosion due to wave action was the main cause of the phenomenon. Eadie et al. [2000b] refers to the two assumptions initially proposed by scientists about the main mechanism that causes the late Winter early Spring plume. The first assumption was that the plume event is caused by the first big storm after the ice melted and exposed the lake surface, and the second assumption was that the plume was driven mostly by the strong Northern winds. The first assumption was abandoned in favor of the second one in 1998 when the lake experienced an ice free Winter and a plume bigger than the previous years (source: http://www.glerl.noaa.gov/pubs/brochures/eegleflyer/eegle2).

Wind driven waves and currents that erode the bluffs in the South-Western shore of the lake, especially the area near Milwaukee, Wisconsin, entrain particulate matter from the lake bottom and are consequently thought to be the principal plume forming mechanism. Furthermore, the fate of the eroded and resuspended material is controlled by the physical processes responsible for the exchange of the material between the near-shore and off-shore regions of the lake, by the physical processes responsible for its deposition and resuspension, and finally by the processes responsible for its along-shore movement. The question, however, is whether the nearshore plume is transporting material from its origin in one continuous transport mode or whether the material in the plume consists of material generated by a series of local deposition, resuspension and transport. The proposal of a cellular transport mode is unique and after much study the question still remains. The answer to this essential question might be given by applying an Eulerian Particle Tracking formulation M^2EPT, based on a concept first captured and successfully applied during an unrelated research project in Lake Erie (Bedford et al. [1999], Velissariou et al. [1999]) to identify the paths followed by the various grain sizes of the sediments dumped at a disposal site in the lake.

Monitoring of the Lake Michigan sediment plume has mainly occurred through visible-band satellite imagery (Figure 1.2). Satellite images of suspended particulate material in Lake Michigan obtained during the late 1970's - early 1980's period were analyzed by Mortimer [1988] and revealed for the first time the formation of the early Spring turbidity plume along the Southern shoreline of Lake Michigan. In 1992 satellite images became routinely available through the *NOAA* Coast Watch program and the plume was observed every year around mid-March. The usual Lake Michigan cloudiness for this time of the year was an obstacle in recognizing the full extent of the plume until the unusually clear conditions in 1996. The plume formed that year was approximately 10 km wide and 100 km long and eventually stretched to 350 km along the Southern shoreline of the lake. The development and the dissipation of the 1996 plume from mid-March to late-April was tracked by the scientists at the Great Lakes Environmental Research Laboratory (*GLERL*) using a frame-by-frame analysis of *NOAA* satellite images. The mass of the suspended particulate matter was estimated to be one million tons (source: http://www.glerl.noaa.gov/news/1996/plume.html).

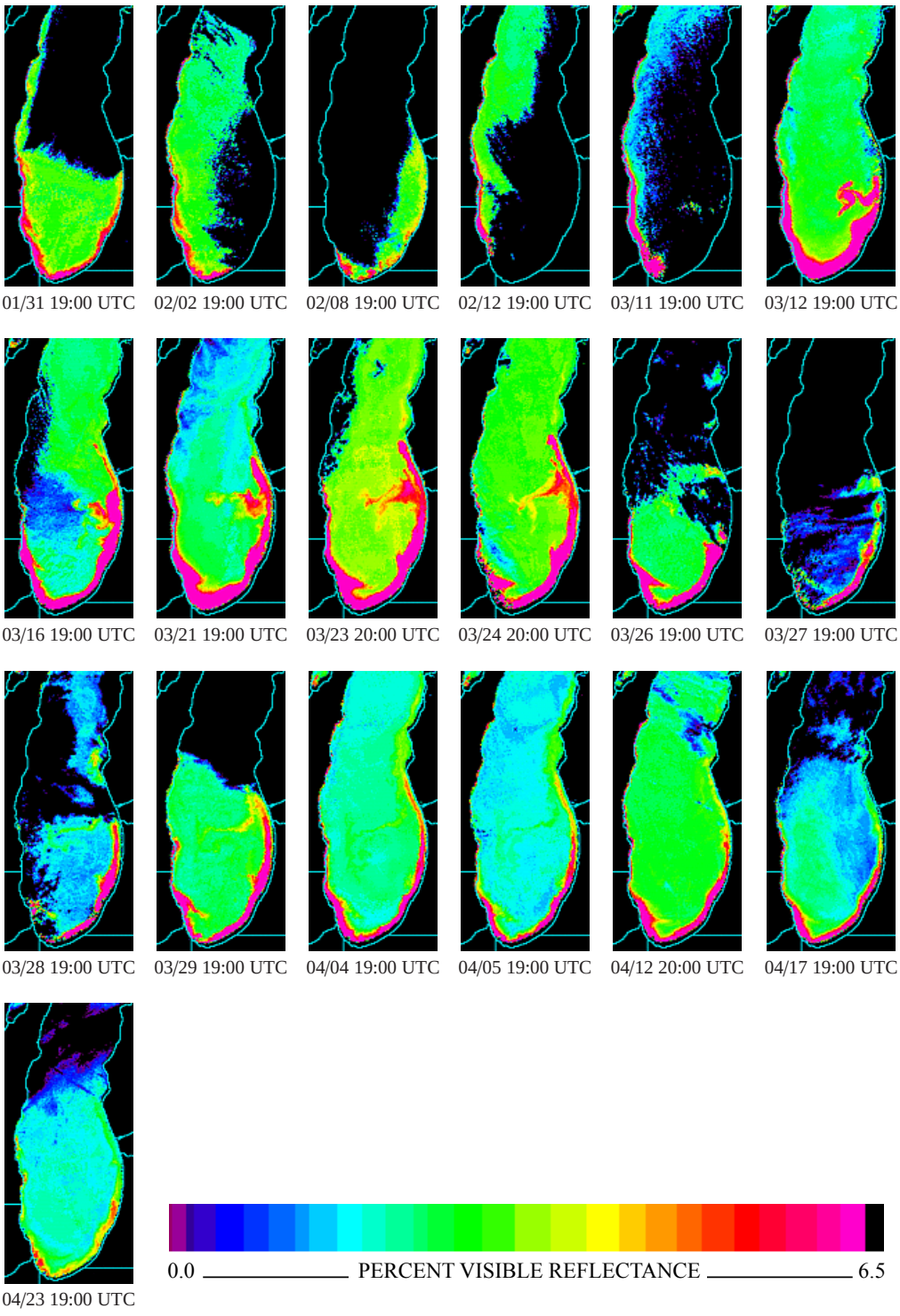

Figure 1.2 Lake Michigan turbidity plume images for the year 1998 (*GLERL/NOAA - EEGLE* project).

CHAPTER 2

THE STANDARD HYDRODYNAMIC AND SEDIMENT MODELS

2.1 Hydrodynamic Model

The equations describing the turbulent motion of water surface flows and transport are well known. Numerous circulation models presently employ these essentially identical equations for a variety of applications that include storm-induced water quality predictions, sediment transport predictions, studies on plume patterns and regularly scheduled operational water forecasts, to mention a few. These equations form the basis of what is called here the Standard Model Equations (*SME*).

The circulation model employed by M^2COPS is a free surface, three-dimensional, primitive equation, shallow water circulation model. The model assumes a hydrostatic pressure distribution and the turbulence mixing is described by the Boussinesq approximation and the eddy viscosity approach. The model solves the time dependent three-dimensional equations of motion for water elevation, the three-dimensional flow velocities and the three-dimensional temperature and salinity fields, while it performs its calculations either on a rectangular Cartesian or on a curvilinear, boundary fitted, orthogonal or non-orthogonal horizontal grid (user's choice). In the vertical direction, the model can accommodate both regular z-coordinates and σ-coordinates (user's choice). For the current research, a rectangular orthogonal horizontal grid and a σ vertical grid have been chosen.

The algorithm for the solution of the governing equations employs a standard mode splitting technique, according to which the vertically averaged equations of motion and continuity equation provide a solution for the free water surface displacement. The vertically averaged flow velocities (*external mode*) and the three-dimensional equations provide a solution for the three-dimensional velocity and scalar fields (*internal mode*). During the *internal mode* calculations, the fluctuations of the 3D velocities from the vertically averaged velocities are computed and then added to the

vertically averaged velocities to produce the full 3D horizontal velocity components (Chapman et al. [1996]).

2.1.1 Model Physics and Dynamics

The system of the turbulent equations of motion are "closed" in the Standard Model (*SM*) by use of a vertical turbulent eddy viscosity model (ASCE Task Committee on Turbulence Models in Hydraulic Computation [1988a], ASCE Task Committee on Turbulence Models in Hydraulic Computation [1988b], Rodi [1994], Chapman et al. [1996]). Here due to the unimportance of stratification a κ-ϵ vertical diffusivity formulation is used that furnishes the vertical eddy viscosities/diffusivities while their horizontal counterparts are held constant (user input).

In the present version of the hydrodynamic model a drag law is used to relate the surface shear stresses with the winds encountered above the water surface. The temperature distribution (and its related flow motions due to resulting temperature/density gradients) in the water column is forced by a newly introduced heat balance equation at the surface (Garnier et al. [2000], Ahsan and Blumberg [1999], Wu et al. [2001], Cole and Wells [2005]). Both replaces an obsolete equilibrium temperature formulation described in Cole and Wells [2005], Mohseni and Stefan [1999] that had its roots in the 1960's.

The older formulation for the surface heat balance used the concept of an equilibrium temperature, defined as the temperature at which the net surface heat flux is null. The concept is simpler to apply by using a bulk formulation for the heat flux, but still the equilibrium temperature and the bulk heat transfer coefficient need to be determined from meteorological data. Since, in principle, the equilibrium temperature and the surface heat transfer coefficient can be derived from the heat balance equation after all its terms have been evaluated, the computational load will be the same as with the direct incorporation of the heat balance equation into the model. The possible use of averaged values for the equilibrium temperature will be unacceptable, if accurate temperature predictions are required.

A new equation of state, based on the International Equation of State (*EOS80*) (Millard [1987], Fofonoff and Millard [1983]), is also introduced in the model for the reasons described in Section 2.2. Relevant thermodynamic and transport fluid properties (e.g., specific heat, viscosity) for both the water and the air are now calculated as functions of temperature, pressure and salinity (where applicable). In the course of the derivation of the governing equations of motion, the atmospheric

pressure terms have been retained to account for the inclusion of possible horizontal atmospheric pressure gradients at the free surface.

The incorporation of the lateral boundary conditions accounts for riverine inputs or tidal boundaries. The tidal conditions are specified by a user supplied, time dependent tidal elevation array, while the riverine flow conditions are supplied by a time dependent flow rate array. In both cases, time dependent temperature and salinity profiles may be furnished by the user.

2.1.2 The *SM* Governing Equations

The *SM* turbulent equations of motion and conservation of mass are derived for an incompressible fluid ($D\rho/Dt = 0$), under the assumptions that: *(a)* the Boussinesq approximation holds and *(b)* the pressure distribution in the water column follows the hydrostatic law. For a right-handed, rectangular Cartesian coordinate system (Figure 2.1) the equations take the form:

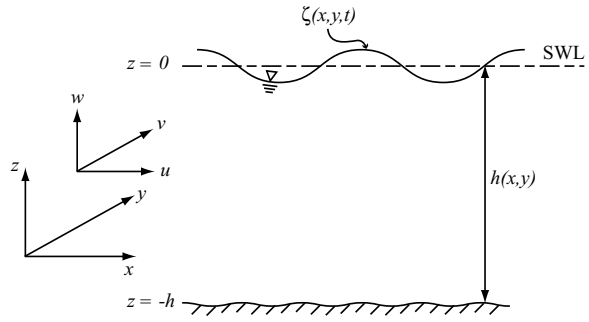

Figure 2.1 Cartesian coordinate notation.

continuity:
$$\frac{\partial u}{\partial x} + \frac{\partial v}{\partial y} + \frac{\partial w}{\partial z} = 0 \tag{2.1.1}$$

x-momentum:
$$\frac{\partial u}{\partial t} + \frac{\partial (u^2)}{\partial x} + \frac{\partial (uv)}{\partial y} + \frac{\partial (uw)}{\partial z} = fv - \frac{1}{\rho_o}\frac{\partial p}{\partial x} + \frac{\partial}{\partial x}\left[\mathcal{A}_h \frac{\partial u}{\partial x}\right] + \frac{\partial}{\partial y}\left[\mathcal{A}_h \frac{\partial u}{\partial y}\right] + \frac{\partial}{\partial z}\left[\mathcal{A}_v \frac{\partial u}{\partial z}\right] \tag{2.1.2}$$

y-momentum:
$$\frac{\partial v}{\partial t} + \frac{\partial (uv)}{\partial x} + \frac{\partial (v^2)}{\partial y} + \frac{\partial (vw)}{\partial z} = -fu - \frac{1}{\rho_o}\frac{\partial p}{\partial y} + \frac{\partial}{\partial x}\left[\mathcal{A}_h \frac{\partial v}{\partial x}\right] + \frac{\partial}{\partial y}\left[\mathcal{A}_h \frac{\partial v}{\partial y}\right] + \frac{\partial}{\partial z}\left[\mathcal{A}_v \frac{\partial v}{\partial z}\right] \tag{2.1.3}$$

z-momentum:
$$\frac{\partial p}{\partial z} = -\rho g \tag{2.1.4}$$

scalar transport:
$$\frac{\partial \Phi}{\partial t} + \frac{\partial (u\Phi)}{\partial x} + \frac{\partial (v\Phi)}{\partial y} + \frac{\partial (w\Phi)}{\partial z} =$$
$$\frac{\partial}{\partial x}\left[\mathcal{B}_h \frac{\partial \Phi}{\partial x}\right] + \frac{\partial}{\partial y}\left[\mathcal{B}_h \frac{\partial \Phi}{\partial y}\right] + \frac{\partial}{\partial z}\left[\mathcal{B}_v \frac{\partial \Phi}{\partial z}\right] + \boldsymbol{S_\Phi} \tag{2.1.5}$$

where: $f = 2\Omega \sin\phi$ is the Coriolis parameter, ϕ is the latitude, Ω is the rotational speed of the earth taken as: $\Omega = \frac{2\pi}{24 \cdot 3600} = 7.27221 \cdot 10^{-5}\ \mathrm{s}^{-1}$, ρ_o is a reference fluid density, Φ represents the scalar field(s) being modeled, $\mathcal{A}_h$ and $\mathcal{B}_h$ are the horizontal turbulent eddy viscosity/diffusivity coefficients and $\mathcal{A}_v$ and $\mathcal{B}_v$ are the vertical turbulent eddy viscosity/diffusivity coefficients. Depending upon the modeled scalar quantity (temperature, salinity, sediments, ...), the coefficient $\mathcal{B}$ is replaced by $\mathcal{K}$ (thermal diffusivity) or $\mathcal{D}$ (mass diffusivity). The term $\boldsymbol{S_\Phi}$ in equation 2.1.5 collectively represents the presence of additional source/sink terms for the scalar Φ in the modeled physical domain.

The assumption of a hydrostatic pressure distribution is the usual assumption made in most shallow water computations and especially in calculating wind driven lake circulation, as well as continental shelf and open coast transport. The Boussinesq approximation assumes that the variations of the density ($\rho = \rho_o + \rho'$) can be neglected, with the exception of the gravity acceleration term that is buoyancy. With this approximation, the density in equations 2.1.2 and 2.1.3 is replaced by ρ_o, while it is retained in equation 2.1.4, where ρ_o is a constant average or a reference density. This reference density can be regarded as the basic density of the homogeneous fluid and in many practical applications can be taken as the depth averaged fluid density:

$$\rho_o = \frac{1}{\zeta + h}\int_{-h}^{\zeta} \rho\, dz = \frac{1}{D}\int_{-h}^{\zeta} \rho\, dz \tag{2.1.6}$$

The shallow water assumption implies weak vertical accelerations in the water column and, therefore, the vertical momentum equation reduces to the hydrostatic law. The vertical integration of equation 2.1.4 yields:

$$p|_\zeta - p|_z = g\int_z^{\zeta} \rho\, dz' \Longrightarrow p = p_{atm} + g\int_z^{\zeta} \rho\, dz' \tag{2.1.7}$$

where: z' is a dummy variable for integration, $p|_z = p = p(x, y, z, t)$ and $p|_\zeta = p_{atm} = p_{atm}(x, y, t)$. Using Leibnitz's rule (equation B.46), the two horizontal pressure gradients in equations 2.1.2 and

2.1.3 are determined from equation 2.1.7 as follows:

$$\frac{\partial p}{\partial x} = \frac{\partial p_{\text{atm}}}{\partial x} + g\left[\rho\frac{\partial \zeta}{\partial x}\right]_{\zeta} + g\int_{z}^{\zeta}\frac{\partial \rho}{\partial x}dz' = \frac{\partial p_{\text{atm}}}{\partial x} + g\rho_{\text{o}}\frac{\partial \zeta}{\partial x} + g\int_{z}^{\zeta}\frac{\partial \rho}{\partial x}dz' \tag{2.1.8}$$

$$\frac{\partial p}{\partial y} = \frac{\partial p_{\text{atm}}}{\partial y} + g\left[\rho\frac{\partial \zeta}{\partial y}\right]_{\zeta} + g\int_{z}^{\zeta}\frac{\partial \rho}{\partial y}dz' = \frac{\partial p_{\text{atm}}}{\partial y} + g\rho_{\text{o}}\frac{\partial \zeta}{\partial y} + g\int_{z}^{\zeta}\frac{\partial \rho}{\partial y}dz' \tag{2.1.9}$$

where the water density at the free surface was approximated by: $\rho|_{\zeta} = \rho(x, y, \zeta, t) = \rho_{\text{o}}$. This approximation is valid as long as $\zeta\Delta\rho/\rho\Delta\zeta \ll 1$, where $\Delta\rho$ and $\Delta\zeta$ represent typical horizontal variations, which is true over the horizontal length scales of a model grid box (Pacanowski and Griffies [2000]). Substitution of the expressions for the horizontal pressure gradients into equations 2.1.2 and 2.1.3 yields the following form of the *SM* horizontal momentum equations:

$$\frac{\partial u}{\partial t} + \frac{\partial (u^2)}{\partial x} + \frac{\partial (uv)}{\partial y} + \frac{\partial (uw)}{\partial z} = fv - \underbrace{\frac{1}{\rho_{\text{o}}}\frac{\partial p_{\text{atm}}}{\partial x} - g\frac{\partial \zeta}{\partial x}}_{\text{barotropic terms}} - \underbrace{\frac{g}{\rho_{\text{o}}}\int_{z}^{\zeta}\frac{\partial \rho}{\partial x}dz'}_{\text{baroclinic term}} +$$

$$\frac{\partial}{\partial x}\left[\mathcal{A}_{\text{h}}\frac{\partial u}{\partial x}\right] + \frac{\partial}{\partial y}\left[\mathcal{A}_{\text{h}}\frac{\partial u}{\partial y}\right] + \frac{\partial}{\partial z}\left[\mathcal{A}_{\text{v}}\frac{\partial u}{\partial z}\right] \tag{2.1.10}$$

$$\frac{\partial v}{\partial t} + \frac{\partial (uv)}{\partial y} + \frac{\partial (v^2)}{\partial y} + \frac{\partial (vw)}{\partial z} = -fu - \underbrace{\frac{1}{\rho_{\text{o}}}\frac{\partial p_{\text{atm}}}{\partial y} - g\frac{\partial \zeta}{\partial y}}_{\text{barotropic terms}} - \underbrace{\frac{g}{\rho_{\text{o}}}\int_{z}^{\zeta}\frac{\partial \rho}{\partial y}dz'}_{\text{baroclinic term}} +$$

$$\frac{\partial}{\partial x}\left[\mathcal{A}_{\text{h}}\frac{\partial v}{\partial x}\right] + \frac{\partial}{\partial y}\left[\mathcal{A}_{\text{h}}\frac{\partial v}{\partial y}\right] + \frac{\partial}{\partial z}\left[\mathcal{A}_{\text{v}}\frac{\partial v}{\partial z}\right] \tag{2.1.11}$$

In the derivation of the two momentum equations, the atmospheric pressure terms were intentionally retained to account for the presence of any horizontal atmospheric pressure gradients. Since only the pressure gradients are present in the momentum equations, the pressure p_{atm} can be either absolute or gage. This fact is worth noting since some formulations for the equation of state and in the equations calculating the various properties of the water and air use mixtures of absolute pressures and some gage pressures.

2.1.3 Boundary Conditions

The solution of the system of the partial differential equations of fluid motion and species transport presented in the previous Chapters are obtained for the problem being solved when boundary conditions are specified for all the involved dependent variables.

The boundary conditions are distinguished as "surface conditions" describing the interaction of the water body with the atmosphere, as "bottom conditions" describing the interaction of the bottom physics with the overlying water column, and finally as "lateral conditions" that describe the material fluxes into or out of the water body (e.g., riverine inputs,shoreline erosion rates). At the surface and bottom boundaries the momentum, continuity and scalar conditions are defined as:

free surface conditions

$$\mathcal{A}_{\mathrm{v}} \begin{pmatrix} \dfrac{\partial u}{\partial z} \\ \dfrac{\partial v}{\partial z} \end{pmatrix}_{\zeta} = \begin{pmatrix} \dfrac{\tau_{sx}}{\rho_{\mathrm{o}}} \\ \dfrac{\tau_{sy}}{\rho_{\mathrm{o}}} \end{pmatrix} \tag{2.1.12}$$

$$\mathcal{B}_{\mathrm{v}} \left. \frac{\partial \Phi}{\partial z} \right|_{\zeta} = \dot{\Phi} \tag{2.1.13}$$

$$w|_{\zeta} = \left[\frac{\partial \zeta}{\partial t} + u \frac{\partial \zeta}{\partial x} + v \frac{\partial \zeta}{\partial y} \right]_{\zeta} \tag{2.1.14}$$

In equation 2.1.13, $\dot{\Phi}$ represents the vertical flux of the scalar quantity at the surface. If salinity is the scalar, then $\dot{\Phi} = 0$. The surface wind stresses are parametrized after G.I.Taylor (Stull [1988]), with the individual stresses given by the following drag laws:

$$\begin{pmatrix} \tau_{sx} \\ \tau_{sy} \end{pmatrix} = \rho_{\mathrm{air}}\, \mathrm{C_M}\, W \begin{pmatrix} W_x \\ W_y \end{pmatrix} ; \qquad \tau_s = \rho_{\mathrm{air}} \mathrm{C_M} W^2 ; \qquad W = \left(W_x^2 + W_y^2 \right)^{1/2} \tag{2.1.15}$$

where, W (m/s) is the wind speed at the reference elevation of 10 m above the mean water surface, W_x and W_y are the two components of the wind speed vector, ρ_{air} (kg/m^3) is the density of the air at standard atmospheric conditions, $\mathrm{C_M}$ is the bulk momentum transfer coefficient calculated by the methods described in Section 2.5.1 with τ_s representing the wind imposed surface stress. When neutral conditions are encountered during the calculations, the drag coefficient is computed using equation 2.5.7. A maximum allowable value of 0.003 is set in the model that corresponds to an approximately 130 km/h wind speed.

In the case of the modeled temperature field, then equation 2.1.13 becomes: $\dot{\Phi} = \mathcal{K}_v \left.\frac{\partial T}{\partial z}\right|_\zeta = \frac{\mathcal{H}_N}{\rho_o c_p}$ where, $\mathcal{H}_N$ is the net surface heat flux (Section 2.6). The only term in the surface heat flux that is a function of depth is the penetrative shortwave solar radiation (Section 2.6.1), therefore, the calculation of $\mathcal{H}_N$ requires that this term is appropriately integrated.

bottom conditions

$$\mathcal{A}_v \begin{pmatrix} \frac{\partial u}{\partial z} \\ \frac{\partial v}{\partial z} \end{pmatrix}_{-h} = \begin{pmatrix} \frac{\tau_{bx}}{\rho_o} \\ \frac{\tau_{by}}{\rho_o} \end{pmatrix} \tag{2.1.16}$$

$$\mathcal{B}_v \left.\frac{\partial \Phi}{\partial z}\right|_{-h} = 0 \tag{2.1.17}$$

$$w|_{-h} = -\left[u \frac{\partial h}{\partial x} + v \frac{\partial h}{\partial y}\right]_{-h} \tag{2.1.18}$$

Similarly with equations 2.1.15 the bottom shear stresses are parametrized as follows:

$$\begin{pmatrix} \tau_{bx} \\ \tau_{by} \end{pmatrix} = \rho_o C_D |u| \begin{pmatrix} u \\ v \end{pmatrix} ; \qquad \tau_b = \rho_o C_D |u|^2 ; \qquad |u| = \left(u^2 + v^2\right)^{1/2} \tag{2.1.19}$$

where C_D is the bottom drag coefficient and (u, v) are the near bottom horizontal flow velocities. When the full 3D calculations are employed, then C_D is determined by the logarithmic law:

$$C_D = \mathbf{k}^2 \left[\ln \frac{z_r}{z_o}\right]^{-2} \tag{2.1.20}$$

where z_o is the bottom roughness height, z_r is defined as one half of the bottom layer thickness and $\mathbf{k} = 0.4$ is the von Kármán's constant. If only the 2D (vertically integrated) equations are employed then, C_D is calculated by the following Manning's formulation:

$$C_D = g\, n^2\, R^{-1/3} \tag{2.1.21}$$

where n is the Manning's coefficient (default value is 0.002), g is the gravitational acceleration and R is the hydraulic radius, which is approximated as $R \approx D$, since the horizontal length scale is much larger than the vertical length scale.

Equations 2.1.14 and 2.1.18 represent the kinematic boundary conditions at the water surface and the bottom. At the free surface, the kinematic boundary condition can be derived considering

the fact that the free surface is a material boundary for which a particle initially on the boundary will remain on the boundary. Assuming that there is no water penetrating the free surface, then the material or total derivative at the free surface $(\zeta - z)$ is zero, therefore:

$$\frac{D(\zeta - z)}{Dt} = \frac{D\zeta}{Dt} - \frac{Dz}{Dt} = 0 \quad \Rightarrow$$

$$\left[\frac{\partial \zeta}{\partial t} + u\frac{\partial \zeta}{\partial x} + v\frac{\partial \zeta}{\partial y} + w\frac{\partial \zeta}{\partial z}\right]_{\zeta} - \left[\frac{\partial z}{\partial t} + u\frac{\partial z}{\partial x} + v\frac{\partial z}{\partial y} + w\frac{\partial z}{\partial z}\right]_{\zeta} = 0 \tag{2.1.22}$$

Since, $\partial\zeta/\partial z = \partial z/\partial t = \partial z/\partial x = \partial z/\partial y = 0$ and $\partial z/\partial z = 1$, equation 2.1.22 reduces to equation 2.1.14. At the bottom, the kinematic boundary condition reflects the fact that there is no flow normal to the boundary. The bottom is a material boundary and, therefore, the material derivative at the bottom $(z + h)$ is zero, yielding:

$$\frac{D(z + h)}{Dt} = \frac{Dz}{Dt} + \frac{Dh}{Dt} = 0 \quad \Rightarrow$$

$$\left[\frac{\partial z}{\partial t} + u\frac{\partial z}{\partial x} + v\frac{\partial z}{\partial y} + w\frac{\partial z}{\partial z}\right]_{-h} + \left[\frac{\partial h}{\partial t} + u\frac{\partial h}{\partial x} + v\frac{\partial h}{\partial y} + w\frac{\partial h}{\partial z}\right]_{-h} = 0 \tag{2.1.23}$$

and since, $\partial z/\partial t = \partial h/\partial t = \partial z/\partial x = \partial z/\partial y = \partial h/\partial z = 0$ and $\partial z/\partial z = 1$, equation 2.1.23 reduces to equation 2.1.18.

The lateral conditions for a wall boundary are specified such that: *(a)* there is no flow normal to the wall $(\partial \boldsymbol{u}_n/\partial n = 0)$, and *(b)* the no slip conditions tangential to the wall are valid $(\boldsymbol{u}_\tau = 0)$, where $\boldsymbol{u}$ represents the velocity vector, and n and τ are the normal and tangential directions respectively. If open lateral conditions (e.g., rivers) are required, then either the normal to the boundary flow velocities or the corresponding flow rates need to be specified.

2.1.4 External Mode Equations

The external mode equations provide the solution for the water surface fluctuation ζ and the water depth D and calculate the vertically averaged field variables. This prognostic calculation allows the simulation of tidal events and surges and dominant horizontal advective processes. The averaged equations are derived from the turbulent continuity, momentum and scalar transport equations (2.1.1 through 2.1.5) by integration in the interval $(-h, \zeta)$. To derive the equations, the definitions for the Leibnitz's rule (equation B.46) and the vertical average of a variable α:

$$A = \overline{\alpha} = \frac{1}{\zeta + h}\int_{-h}^{\zeta} \alpha(z, \ldots)\, dz = \frac{1}{D}\int_{-h}^{\zeta} \alpha(z, \ldots)\, dz = \int_{-1}^{0} \alpha(\sigma, \ldots)\, d\sigma \tag{2.1.24}$$

were employed to evaluate the vertical integral of any partial derivative present. Finally, the surface and bottom kinetic boundary conditions (equations 2.1.14 and 2.1.18) were incorporated into the resulting equations. The presentation of all the intermediate derivation steps for all the equations involved is so very well known that its reproduction here is unnecessary therefore, only the steps needed for clarification and the final equations will be given here. The integration of continuity equation 2.1.1 gives:

$$\int_{-h}^{\zeta}\left(\frac{\partial u}{\partial x}+\frac{\partial v}{\partial y}+\frac{\partial w}{\partial z}\right)dz=\frac{\partial}{\partial x}\int_{-h}^{\zeta}u\,dz+\frac{\partial}{\partial y}\int_{-h}^{\zeta}v\,dz+$$

$$\underbrace{\left[w|_{\zeta}-u|_{\zeta}\frac{\partial\zeta}{\partial x}-v|_{\zeta}\frac{\partial\zeta}{\partial y}\right]}_{\text{apply surface kinematic B.C}}-\underbrace{\left[w|_{-h}+u|_{-h}\frac{\partial h}{\partial x}+v|_{-h}\frac{\partial h}{\partial y}\right]}_{\text{apply bottom kinematic B.C}}\Longrightarrow$$

$$\frac{\partial\zeta}{\partial t}+\frac{\partial(DU)}{\partial x}+\frac{\partial(DV)}{\partial y}=0 \tag{2.1.25}$$

Introducing the two new variables $\tilde{U}$ and $\tilde{V}$ as the volumetric flow rates per unit width (unit flow rates) the above equation becomes:

$$\frac{\partial\zeta}{\partial t}+\frac{\partial(DU)}{\partial x}+\frac{\partial(DV)}{\partial y}=\frac{\partial\zeta}{\partial t}+\frac{\partial\tilde{U}}{\partial x}+\frac{\partial\tilde{V}}{\partial y}=0 \tag{2.1.26a}$$

$$\frac{\partial D}{\partial t}+\frac{\partial(DU)}{\partial x}+\frac{\partial(DV)}{\partial y}=\frac{\partial D}{\partial t}+\frac{\partial\tilde{U}}{\partial x}+\frac{\partial\tilde{V}}{\partial y}=0 \tag{2.1.26b}$$

The integration of the momentum equations is straight forward, but special attention will be given in the evaluation of the integrals of the baroclinic and diffusion terms to outline the approximations used. The integration of the baroclinic terms (e.g., the x-momentum term) proceeds as follows:

$$\int_{-h}^{\zeta}\Big(\frac{g}{\rho_o}\int_{z}^{\zeta}\frac{\partial\rho}{\partial x}dz'\Big)dz=\frac{g}{\rho_o}\int_{-h}^{\zeta}\underbrace{\Big(\frac{\partial}{\partial x}\int_{z}^{\zeta}\rho\,dz'-\rho|_{\zeta}\frac{\partial\zeta}{\partial x}+\rho|_{z}\frac{\partial z}{\partial x}\Big)}_{\text{using Leibnitz's rule}}dz=$$

$$\frac{g}{\rho_o}\int_{-h}^{\zeta}\Big(\frac{\partial(\zeta-z)\,\overline{\rho}^{z}}{\partial x}-\rho|_{\zeta}\frac{\partial\zeta}{\partial x}\Big)dz=\frac{g}{\rho_o}\int_{-h}^{\zeta}\Big(\frac{\partial\zeta}{\partial x}\underbrace{(\overline{\rho}^{z}-\rho|_{\zeta})}_{\approx 0}+(\zeta-z)\frac{\partial\overline{\rho}^{z}}{\partial x}\Big)dz=$$

$$\frac{g}{\rho_o}\frac{\partial\overline{\rho}^{z}}{\partial x}\int_{-h}^{\zeta}(\zeta-z)\,dz=\frac{g}{\rho_o}\frac{\partial\overline{\rho}^{z}}{\partial x}\frac{D^2}{2} \tag{2.1.27}$$

The diffusion terms are integrated in a similar fashion, as shown next:

$$\int_{-h}^{\zeta} \frac{\partial}{\partial x}\left[\mathcal{A}_h \frac{\partial u}{\partial x}\right] dz = \frac{\partial}{\partial x}\int_{-h}^{\zeta} \mathcal{A}_h \frac{\partial u}{\partial x}\, dz - \underbrace{\mathcal{A}_h \frac{\partial u}{\partial x}\Big|_{\zeta} \frac{\partial \zeta}{\partial x} - \mathcal{A}_h \frac{\partial u}{\partial x}\Big|_{-h} \frac{\partial h}{\partial x}}_{\text{neglect these higher order terms}} =$$

$$\frac{\partial}{\partial x}\left[D\,\overline{\mathcal{A}_h \frac{\partial u}{\partial x}}\right] \approx \frac{\partial}{\partial x}\left[D\overline{\mathcal{A}}_h \overline{\frac{\partial u}{\partial x}}\right] = \frac{\partial}{\partial x}\left[\overline{\mathcal{A}}_h \int_{-h}^{\zeta} \frac{\partial u}{\partial x} dz\right] =$$

$$\frac{\partial}{\partial x}\left[\overline{\mathcal{A}}_h \frac{\partial (DU)}{\partial x}\right] - \underbrace{\frac{\partial}{\partial x}\left[\overline{\mathcal{A}}_h u|_{\zeta} \frac{\partial \zeta}{\partial x}\right] - \frac{\partial}{\partial x}\left[\overline{\mathcal{A}}_h u|_{-h} \frac{\partial h}{\partial x}\right]}_{\text{neglect these higher order terms}} = \frac{\partial}{\partial x}\left[\overline{\mathcal{A}}_h \frac{\partial (DU)}{\partial x}\right] \tag{2.1.28}$$

Since the horizontal eddy viscosities/diffusivities are held constant in the current formulation used in *M*^{2}*COPS*, their vertically averaged horizontal counterparts are held constant as well, that is, $\overline{\mathcal{A}}_h = \mathcal{A}_h$ and $\overline{\mathcal{B}}_h = \mathcal{B}_h$.

The two vertically averaged momentum equations in terms of both the averaged flow velocities and the unit flow rates, after dropping the overbars, are written as:

$$\frac{\partial (DU)}{\partial t} + \frac{\partial (DU^2)}{\partial x} + \frac{\partial (DUV)}{\partial y} = fDV - \underbrace{\frac{D}{\rho_o}\frac{\partial p_{atm}}{\partial x} - gD\frac{\partial \zeta}{\partial x}}_{\text{barotropic terms}} - \underbrace{\frac{g}{\rho_o}\frac{D^2}{2}\frac{\partial \rho}{\partial x}}_{\text{baroclinic term}} +$$

$$\frac{\partial}{\partial x}\left[\mathcal{A}_h \frac{\partial (DU)}{\partial x}\right] + \frac{\partial}{\partial y}\left[\mathcal{A}_h \frac{\partial (DU)}{\partial y}\right] + \boldsymbol{S_u} - \underbrace{\frac{\partial (D\overline{u'^2})}{\partial x} - \frac{\partial (D\overline{u'v'})}{\partial y}}_{\text{dispersion terms}} \tag{2.1.29a}$$

$$\frac{\partial \tilde{U}}{\partial t} + \frac{\partial}{\partial x}\left(\frac{\tilde{U}\tilde{U}}{D}\right) + \frac{\partial}{\partial x}\left(\frac{\tilde{U}\tilde{V}}{D}\right) = f\tilde{V} - \frac{D}{\rho_o}\frac{\partial p_{atm}}{\partial x} - gD\frac{\partial \zeta}{\partial x} - \frac{g}{\rho_o}\frac{D^2}{2}\frac{\partial \rho}{\partial x} +$$

$$\frac{\partial}{\partial x}\left[\mathcal{A}_h \frac{\partial \tilde{U}}{\partial x}\right] + \frac{\partial}{\partial y}\left[\mathcal{A}_h \frac{\partial \tilde{U}}{\partial y}\right] + \boldsymbol{S_u} - \frac{\partial (D\overline{u'^2})}{\partial x} - \frac{\partial (D\overline{u'v'})}{\partial y} \tag{2.1.29b}$$

$$\frac{\partial (DV)}{\partial t} + \frac{\partial (DUV)}{\partial x} + \frac{\partial (DV^2)}{\partial y} = -fDU - \underbrace{\frac{D}{\rho_o}\frac{\partial p_{atm}}{\partial y} - gD\frac{\partial \zeta}{\partial y}}_{\text{barotropic terms}} - \underbrace{\frac{g}{\rho_o}\frac{D^2}{2}\frac{\partial \rho}{\partial y}}_{\text{baroclinic term}} +$$

$$\frac{\partial}{\partial x}\left[\mathcal{A}_h \frac{\partial (DV)}{\partial x}\right] + \frac{\partial}{\partial y}\left[\mathcal{A}_h \frac{\partial (DV)}{\partial y}\right] + \boldsymbol{S_v} - \underbrace{\frac{\partial (D\overline{u'v'})}{\partial x} - \frac{\partial (D\overline{v'^2})}{\partial y}}_{\text{dispersion terms}} \tag{2.1.30a}$$

$$\frac{\partial \tilde{V}}{\partial t} + \frac{\partial}{\partial x}\left(\frac{\tilde{U}\tilde{V}}{D}\right) + \frac{\partial}{\partial x}\left(\frac{\tilde{V}\tilde{V}}{D}\right) = -f\tilde{U} - \frac{D}{\rho_o}\frac{\partial p_{atm}}{\partial y} - gD\frac{\partial \zeta}{\partial y} - \frac{g}{\rho_o}\frac{D^2}{2}\frac{\partial \rho}{\partial y} +$$

$$\frac{\partial}{\partial x}\left[\mathcal{A}_h\frac{\partial \tilde{V}}{\partial x}\right] + \frac{\partial}{\partial y}\left[\mathcal{A}_h\frac{\partial \tilde{V}}{\partial y}\right] + \boldsymbol{S_v} - \frac{\partial(D\overline{u'v'})}{\partial x} - \frac{\partial(D\overline{v'^2})}{\partial y} \tag{2.1.30b}$$

The two new terms $\boldsymbol{S_u}$ and $\boldsymbol{S_v}$ in the momentum equations are the results of the integrations $\int_{-h}^{\zeta}\frac{\partial}{\partial z}\left(\mathcal{A}_v\frac{\partial u}{\partial z}\right)dz$ and $\int_{-h}^{\zeta}\frac{\partial}{\partial z}\left(\mathcal{A}_v\frac{\partial v}{\partial z}\right)dz$, respectively. These two terms are evaluated using the momentum boundary conditions (equations 2.1.12 and 2.1.16) as follows:

$$\left.\begin{aligned} \boldsymbol{S_u} &= \int_{-h}^{\zeta}\frac{\partial}{\partial z}\left(\mathcal{A}_v\frac{\partial u}{\partial z}\right)dz = \left[\mathcal{A}_v\frac{\partial u}{\partial z}\right]_{-h}^{\zeta} = \frac{\tau_{sx} - \tau_{bx}}{\rho_o} \\ \boldsymbol{S_v} &= \int_{-h}^{\zeta}\frac{\partial}{\partial z}\left(\mathcal{A}_v\frac{\partial v}{\partial z}\right)dz = \left[\mathcal{A}_v\frac{\partial v}{\partial z}\right]_{-h}^{\zeta} = \frac{\tau_{sy} - \tau_{by}}{\rho_o} \end{aligned}\right\} \tag{2.1.31}$$

2.1.5 Non-Dimensional Equations

The governing equations are modeled using their non-dimensional form that makes it easier to compare the relative importance of one physical process to another. The non-dimensionalization of the governing equations is based upon the normalization of all dependent and independent variables with respect to reference constant values, presumably the largest values encountered in the problem being solved (Streeter et al. [1998]) and, therefore, the newly created variables will have values ranging between -1 and 1.

Substitution of all the relevant variables in equations 2.1.1, 2.1.10, 2.1.11 and 2.1.5 by their non-dimensional counterparts (equations B.36 through B.41), evaluation of all the partial derivatives using equations B.45, division of both sides of: the continuity equation by $\frac{U_r}{X_r}$, the momentum equations by $f\,U_r$ and the scalar equation by $f\,(\Phi_r - \Phi_o)$, taking into account equations B.42 through B.44 and dropping the check accents, then the final forms of the non-dimensional equations are written as:

continuity: $$\frac{\partial u}{\partial x} + \frac{\partial v}{\partial y} + \frac{\partial w}{\partial z} = 0 \tag{2.1.32}$$

x-momentum: $$\frac{\partial u}{\partial t} + \mathbb{R}_o\left[\frac{\partial(u^2)}{\partial x} + \frac{\partial(uv)}{\partial y} + \frac{\partial(uw)}{\partial z}\right] = v - \frac{\partial p_{atm}}{\partial x} - \frac{\partial \zeta}{\partial x} - \frac{\mathbb{R}_o}{\mathbb{F}_{rd}^2}\int_z^\zeta \frac{\partial \rho}{\partial x}\,dz' +$$

$$\mathbb{E}_{kh}\frac{\partial}{\partial x}\left[\mathcal{A}_h\frac{\partial u}{\partial x}\right] + \mathbb{E}_{kh}\frac{\partial}{\partial y}\left[\mathcal{A}_h\frac{\partial u}{\partial y}\right] + \mathbb{E}_{kv}\frac{\partial}{\partial z}\left[\mathcal{A}_v\frac{\partial u}{\partial z}\right] \qquad (2.1.33)$$

y-momentum: $$\frac{\partial v}{\partial t} + \mathbb{R}_o\left[\frac{\partial(uv)}{\partial y} + \frac{\partial(v^2)}{\partial y} + \frac{\partial(vw)}{\partial z}\right] = -u - \frac{\partial p_{atm}}{\partial y} - \frac{\partial \zeta}{\partial y} - \frac{\mathbb{R}_o}{\mathbb{F}_{rd}^2}\int_z^\zeta \frac{\partial \rho}{\partial y}\,dz' +$$

$$\mathbb{E}_{kh}\frac{\partial}{\partial x}\left[\mathcal{A}_h\frac{\partial v}{\partial x}\right] + \mathbb{E}_{kh}\frac{\partial}{\partial y}\left[\mathcal{A}_h\frac{\partial v}{\partial y}\right] + \mathbb{E}_{kv}\frac{\partial}{\partial z}\left[\mathcal{A}_v\frac{\partial v}{\partial z}\right] \qquad (2.1.34)$$

scalar: $$\frac{\partial \Phi}{\partial t} + \mathbb{R}_o\left[\frac{\partial(u\Phi)}{\partial x} + \frac{\partial(v\Phi)}{\partial y} + \frac{\partial(w\Phi)}{\partial z}\right] =$$

$$\frac{\mathbb{E}_{kh}}{\mathbb{S}_{ch}}\frac{\partial}{\partial x}\left[\mathcal{B}_h\frac{\partial \Phi}{\partial x}\right] + \frac{\mathbb{E}_{kh}}{\mathbb{S}_{ch}}\frac{\partial}{\partial y}\left[\mathcal{B}_h\frac{\partial \Phi}{\partial y}\right] + \frac{\mathbb{E}_{kv}}{\mathbb{S}_{cv}}\frac{\partial}{\partial z}\left[\mathcal{B}_v\frac{\partial \Phi}{\partial z}\right] + \boldsymbol{S_\Phi} \qquad (2.1.35)$$

The vertical momentum equation has been eliminated, since it is already incorporated into the equations 2.1.33 and 2.1.34. In the derivation of the scalar equation 2.1.35 the continuity equation 2.1.32 was used to eliminate all relevant terms. The corresponding non-dimensional, vertically averaged equations of motion are derived in a similar fashion from the equations 2.1.26a, 2.1.29a and 2.1.30a. After dropping the check accents the equations resume their final form:

$$\frac{\partial \zeta}{\partial t} + \left(\frac{\mathbb{R}_o}{\mathbb{F}_r}\right)^2\left[\frac{\partial(DU)}{\partial x} + \frac{\partial(DV)}{\partial y}\right] = \frac{\partial \zeta}{\partial t} + \left(\frac{\mathbb{R}_o}{\mathbb{F}_r}\right)^2\left[\frac{\partial \tilde{U}}{\partial x} + \frac{\partial \tilde{V}}{\partial y}\right] = 0 \qquad (2.1.36a)$$

$$\frac{\partial D}{\partial t} + \mathbb{R}_o\left[\frac{\partial(DU)}{\partial x} + \frac{\partial(DV)}{\partial y}\right] = \frac{\partial D}{\partial t} + \mathbb{R}_o\left[\frac{\partial \tilde{U}}{\partial x} + \frac{\partial \tilde{V}}{\partial y}\right] = 0 \qquad (2.1.36b)$$

$$\frac{\partial(DU)}{\partial t} + \mathbb{R}_o\left[\frac{\partial(DU^2)}{\partial x} + \frac{\partial(DUV)}{\partial y}\right] = DV - D\frac{\partial p_{atm}}{\partial x} - D\frac{\partial \zeta}{\partial x} -$$

$$\frac{D^2\,\mathbb{R}_o}{2\,\mathbb{F}_{rd}^2}\frac{\partial \rho}{\partial x} + \mathbb{E}_{kh}\frac{\partial}{\partial x}\left[\mathcal{A}_h\frac{\partial(DU)}{\partial x}\right] + \mathbb{E}_{kh}\frac{\partial}{\partial y}\left[\mathcal{A}_h\frac{\partial(DU)}{\partial y}\right] + \tau_{sx} - \tau_{bx} \qquad (2.1.37a)$$

$$\frac{\partial \underset{\sim}{U}}{\partial t}+\mathbb{R}_{o}\left[\frac{\partial}{\partial x}\left(\frac{\underset{\sim}{U}\underset{\sim}{U}}{D}\right)+\frac{\partial}{\partial y}\left(\frac{\underset{\sim}{U}\underset{\sim}{V}}{D}\right)\right]=\underset{\sim}{V}-D\frac{\partial p_{\text{atm}}}{\partial x}-D\frac{\partial \zeta}{\partial x}-$$

$$\frac{D^2\,\mathbb{R}_{o}}{2\,\mathbb{F}_{\text{rd}}^2}\frac{\partial \rho}{\partial x}+\mathbb{E}_{\text{kh}}\frac{\partial}{\partial x}\left[\mathcal{A}_{\text{h}}\frac{\partial \underset{\sim}{U}}{\partial x}\right]+\mathbb{E}_{\text{kh}}\frac{\partial}{\partial y}\left[\mathcal{A}_{\text{h}}\frac{\partial \underset{\sim}{U}}{\partial y}\right]+\tau_{sx}-\tau_{bx} \tag{2.1.37b}$$

$$\frac{\partial (DV)}{\partial t}+\mathbb{R}_{o}\left[\frac{\partial (DUV)}{\partial x}+\frac{\partial (DV^2)}{\partial y}\right]=-DU-D\frac{\partial p_{\text{atm}}}{\partial y}-D\frac{\partial \zeta}{\partial y}-$$

$$\frac{D^2\,\mathbb{R}_{o}}{2\,\mathbb{F}_{\text{rd}}^2}\frac{\partial \rho}{\partial y}+\mathbb{E}_{\text{kh}}\frac{\partial}{\partial x}\left[\mathcal{A}_{\text{h}}\frac{\partial (DV)}{\partial x}\right]+\mathbb{E}_{\text{kh}}\frac{\partial}{\partial y}\left[\mathcal{A}_{\text{h}}\frac{\partial (DV)}{\partial y}\right]+\tau_{sy}-\tau_{by} \tag{2.1.38a}$$

$$\frac{\partial \underset{\sim}{V}}{\partial t}+\mathbb{R}_{o}\left[\frac{\partial}{\partial x}\left(\frac{\underset{\sim}{U}\underset{\sim}{V}}{D}\right)+\frac{\partial}{\partial y}\left(\frac{\underset{\sim}{V}\underset{\sim}{V}}{D}\right)\right]=-\underset{\sim}{U}-D\frac{\partial p_{\text{atm}}}{\partial y}-D\frac{\partial \zeta}{\partial y}-$$

$$\frac{D^2\,\mathbb{R}_{o}}{2\,\mathbb{F}_{\text{rd}}^2}\frac{\partial \rho}{\partial y}+\mathbb{E}_{\text{kh}}\frac{\partial}{\partial x}\left[\mathcal{A}_{\text{h}}\frac{\partial \underset{\sim}{V}}{\partial x}\right]+\mathbb{E}_{\text{kh}}\frac{\partial}{\partial y}\left[\mathcal{A}_{\text{h}}\frac{\partial \underset{\sim}{V}}{\partial y}\right]+\tau_{sy}-\tau_{by} \tag{2.1.38b}$$

2.2 The Equation of State for Water

The continuity equation along with the equations of motion do not form a closed set of equations regarding the dependent variables u, v, w, p and ρ, therefore, an equation of state for the water is employed in order to close the set. The equation of state, which is a diagnostic equation, relates the density with the thermodynamic properties of the water (temperature, pressure) and in the case of seawater with the salinity as well.

There is a wide spectrum of such equations, some of empirical nature, some based on theoretical statistical thermodynamic considerations and some semi-empirical that combine features from both the theoretical and the empirical equations. Due to present limitations in theory the theoretical equations tend to be less accurate (Deiters and Reuck [1997]), although significant efforts are under way for the improvement of these equations (Feistel [2003], McDougall and Jackett [2003]).

2.2.1 Eckart's Equation of State and its Limitations

CH3D, the original code for M^2COPS, uses a semi-empirical equation of state developed by Eckart [1958]. The full Eckart's equation gives density as a function of both temperature and pressure as:

$$\rho=\frac{P}{\text{a}+0.698P}\cdot 10^3 \tag{2.2.1}$$

where, a and P are both functions of T (^{o}C), S (ppt) and absolute pressure p (atm), and ρ is in kg/m^3. The functions a, P are defined as follows:

$$P = p + 5890 + 38T - 0.375T^2 + 3S \tag{2.2.2}$$

$$\alpha = 1779.5 + 11.25T - 0.0745T^2 - (3.8 + 0.01T)S \tag{2.2.3}$$

The equations 2.2.1, 2.2.2 and 2.2.3 are valid for the range of values: $0\,\text{ppt} \leq S \leq 40\,\text{ppt}$, $0\,^{o}\text{C} \leq T \leq 40\,^{o}\text{C}$ and $1\,\text{atm} \leq p \leq 1000\,\text{atm}$ ($1\,\text{atm} = 1.01325\,\text{bar} = 101.325\,\text{kPa}$), with an error not less than $\pm 0.2\,\text{kg/m}^3$ (Eckart [1958]).

Some drawbacks in the use of the Eckart's equation are: *(a)* its application is suitable only in shallow water environments, since in higher pressure environments it exhibits large deviations due to systematic errors (Eckart [1958]); *(b)* the accuracy of the density values produced by this equation, tested at the time of its development only by limited available pure water experimental data, is not judged as satisfactory by the present standards (Wright [1997], Bryan and Cox [1972]); and *(c)* the equation is based on the definition of salinity and its scale prior to 1978 while current salinity data for sea or fresh water are referred in psu (practical salinity units) in accordance with the definition for the practical salinity, making the use of the above equation inappropriate (Millard [1987]). Eliminating the pressure from equation 2.2.2 (as it has been done in *CH3D*) produces a reduced version of Eckart's equation. This version, while it increases the computational efficiency of the model, introduces additional errors in the calculation of the water density, even in shallow waters ($< 1000\,\text{m}$).

Justification for the use of a more appropriate equation of state in *M*^{2}*COPS* is drawn from Table 2.1 that lists the density values obtained from Eckart's equation (ρ_E) and from the *UNESCO* international equation of state ($\rho_{EOS\,80}$) at various temperature, salinity and pressure values. The salinity and temperature ranges were chosen to approximately reflect the values that are most likely to occur in fresh waters.

The maximum absolute difference of the calculated densities by the two equations is $\sim 1.5\,\text{kg/m}^3$ ($\sim 0.11\,\text{kg/m}^3$ if pressure is included) and the rms difference is $\sim 0.9\,\text{kg/m}^3$ ($\sim 0.08\,\text{kg/m}^3$ if pressure is included). In both cases the differences in the computed density values are significant and greater than the maximum difference of no more than $0.001\,\text{kg/m}^3$ between density values calculated by the international equation of state and experimental data (McDougall and Jackett [2003]).

p (dbars)	S (psu)	T (^{o}C)	ρ_{EOS80} (kg/m^3)	ρ_E (kg/m^3)	$\rho_{EOS80} - \rho_E$ (kg/m^3)	p included $\rho_{EOS80} - \rho_E$ (kg/m^3)
0.00	0.00	0.00	999.842594	999.877774	-0.035180	-0.086455
0.00	0.00	15.00	999.101575	999.052169	0.049406	0.001984
0.00	0.00	30.00	995.651134	995.712892	-0.061759	-0.107131
0.00	0.10	0.00	999.924867	999.957661	-0.032794	-0.084061
0.00	0.10	15.00	999.179218	999.128236	0.050982	0.003568
0.00	0.10	30.00	995.726276	995.787246	-0.060970	-0.106336
0.00	0.20	0.00	1000.007000	1000.037553	-0.030553	-0.081812
0.00	0.20	15.00	999.256752	999.204308	0.052444	0.005036
0.00	0.20	30.00	995.801320	995.861604	-0.060285	-0.105644
150.00	0.00	0.00	1000.604444	999.877774	0.726670	-0.082262
150.00	0.00	15.00	999.800817	999.052169	0.748648	0.000418
150.00	0.00	30.00	996.318712	995.712892	0.605819	-0.110135
150.00	0.10	0.00	1000.686568	999.957661	0.728907	-0.079899
150.00	0.10	15.00	999.878359	999.128236	0.750122	0.002001
150.00	0.10	30.00	996.393771	995.787246	0.606525	-0.109330
150.00	0.20	0.00	1000.768551	1000.037553	0.730998	-0.077681
150.00	0.20	15.00	999.955790	999.204308	0.751482	0.003470
150.00	0.20	30.00	996.468731	995.861604	0.607126	-0.108627
300.00	0.00	0.00	1001.363693	999.877774	1.485919	-0.078020
300.00	0.00	15.00	1000.497826	999.052169	1.445657	-0.001121
300.00	0.00	30.00	996.984172	995.712892	1.271279	-0.113202
300.00	0.10	0.00	1001.445668	999.957661	1.488007	-0.075688
300.00	0.10	15.00	1000.575266	999.128236	1.447030	0.000464
300.00	0.10	30.00	997.059148	995.787246	1.271902	-0.112385
300.00	0.20	0.00	1001.527504	1000.037553	1.489951	-0.073500
300.00	0.20	15.00	1000.652596	999.204308	1.448287	0.001933
300.00	0.20	30.00	997.134025	995.861604	1.272421	-0.111672
			Check Values			
0.00	0.00	5.00	999.966751	999.907967	0.058784	0.009036
10000.00	0.00	5.00	1044.128016	999.907967	44.220049	0.080552
0.00	0.00	25.00	997.047958	997.088453	-0.040495	-0.086383
10000.00	0.00	25.00	1037.902044	997.088453	40.813592	-0.250212
0.00	35.00	5.00	1027.675465	1027.605470	0.069995	0.022955
10000.00	35.00	5.00	1069.489138	1027.605470	41.883668	0.190184
0.00	35.00	25.00	1023.343058	1023.514427	-0.171368	-0.214922
10000.00	35.00	25.00	1062.538172	1023.514427	39.023745	0.086810

Table 2.1 Comparison between the international and Eckart's equation of state for seawater. The last column differences are computed by including the pressure term in Eckart's equation.

2.2.2 *UNESCO* Equation of State

Because of the limitations of Eckart's equation, the formulation used in M^2COPS parametrizes the water density using the *UNESCO* international equation of state, which is considered to be the standard equation of state for seawater (Millard [1987], Fofonoff and Millard [1983], Fofonoff and Millard, Jr. [1990]) and it is referenced from here on as *EOS80*. The full *EOS80* involves 42 coefficients of the fitted polynomials and is computationally intensive. Since the equation of state is evaluated at each grid point and every time step in the hydrodynamic models, the computational requirements of the full *EOS80* could increase the *CPU* time requirements significantly (reported values range between 10% and 50% increase in *CPU* time, Kruger et al. [2005], Wright [1997]).

Mellor [1991] introduced an approximation for the pressure terms in *EOS80* that decreases the computational time by a factor of 3. The difference in the computed density values between the full *EOS80* and the Mellor's approximation (*MEOS80*) is about 1% and this difference decreases with increasing water depths (Mellor [1991]). The equation of state proposed by Mellor is used in M^2COPS and is defined as:

$$\rho(S,\theta,p) = \rho(S,\theta,0) + \frac{p}{c^2}(1 - 0.20\,\frac{p}{c^2}) \cdot 10^4 \tag{2.2.4}$$

$$c(S,\theta,p) = 1449.2 + 1.34(S-35) + 4.55\theta - 0.045\theta^2 + 0.00821p + 15.0 \cdot 10^{-9}p^2 \tag{2.2.5}$$

where, θ is the potential temperature (^{o}C), p is the applied or gage pressure (dbar), S is the salinity (psu) and c is the speed of sound (m/s). The potential temperature is defined as the temperature of a parcel of water at the sea surface, after it has been raised adiabatically from some depth in the ocean (Stewart [2005]).

The use of θ in equations 2.2.4 and 2.2.5 is consistent with the ocean hydrodynamic models that use θ as the conservative variable for the temperature distribution in the ocean. Relationships between T and θ do exist (Bryden [1973], McDougall and Jackett [2003]) and are usually functional relationships among p, S, T and θ. An approximate equation for θ is (McDougall and Jackett [2003]):

$$\theta(S,T,p) = T + p(a_1 + a_2S + a_3p + a_4T + a_5ST + a_6T^2 + a_7pT) \tag{2.2.6}$$

where, S is in psu, T is in ^{o}C and p is in dbar. For shallow waters θ is approximately equal to T (Fofonoff and Millard [1983]) therefore, for lake, coastal and estuary waters, θ can be replaced by

T in equations 2.2.4 and 2.2.5. The coefficients a_i in equation 2.2.6 are given by:

$$\left.\begin{aligned} a_1 &= 1.067610 \cdot 10^{-5} & a_5 &= 3.074672 \cdot 10^{-8} \\ a_2 &= -1.434297 \cdot 10^{-6} & a_6 &= 1.918639 \cdot 10^{-8} \\ a_3 &= -7.566349 \cdot 10^{-9} & a_7 &= 1.788718 \cdot 10^{-10} \\ a_4 &= -8.535585 \cdot 10^{-6} \end{aligned}\right\} \tag{2.2.7}$$

The *EOS80* for $p = 0$ is given as (Millard [1987]):

$$\rho(S,\theta,0) \approx \rho(S,T,0) = \rho_w + (b_0 + b_1 T + b_2 T^2 + b_3 T^3 + b_4 T^4)S + (c_0 + c_1 T + c_2 T^2)S^{3/2} + d_0 S^2 \tag{2.2.8}$$

while the density of the reference pure water (ρ_w) is given by:

$$\rho_w = e_0 + e_1 T + e_2 T^2 + e_3 T^3 + e_4 T^4 + e_5 T^5 \tag{2.2.9}$$

where, S is in psu, T is in ^{o}C, p is in dbar and ρ is in kg/m^3. All the above equations are valid for the range of values: $0\,\text{psu} \le S \le 40\,\text{psu}$, $-2\,^{o}\text{C} \le T \le 40\,^{o}\text{C}$ and $0\,\text{dbar} \le p \le 10000\,\text{dbar}$ (Millard [1987]).

The leading coefficients of the polynomials in equations 2.2.8 and 2.2.9 are given by:

$$\left.\begin{aligned} b_0 &= 8.24493 \cdot 10^{-1} & c_0 &= -5.72466 \cdot 10^{-3} \\ b_1 &= -4.08990 \cdot 10^{-3} & c_1 &= 1.02270 \cdot 10^{-4} \\ b_2 &= 7.64380 \cdot 10^{-5} & c_2 &= -1.65460 \cdot 10^{-6} \\ b_3 &= -8.24670 \cdot 10^{-7} & d_0 &= 4.83140 \cdot 10^{-4} \\ b_4 &= 5.38750 \cdot 10^{-9} \\ \\ e_0 &= 999.842594 & e_3 &= 1.001685 \cdot 10^{-4} \\ e_1 &= 6.793952 \cdot 10^{-2} & e_4 &= -1.120083 \cdot 10^{-6} \\ e_2 &= -9.095290 \cdot 10^{-3} & e_5 &= 6.536332 \cdot 10^{-9} \end{aligned}\right\} \tag{2.2.10}$$

As previously mentioned, Mellor's approximation reduces the computational time for the equation of state by a factor of 3. A further reduction in the computational time by a factor of 2-16 (computer platform and compiler dependent, Kruger et al. [2005]) can be achieved by using Horner's rule. According to this rule, given an nth degree polynomial of x and factoring out powers of x, the number of calculations required to evaluate the polynomial at a value $x = x_0$ is reduced to n additions and n multiplications, resulting in less numerical instability (due to potential subtraction of one large number from another) and faster evaluation of the polynomial. The nth degree polynomial is written as:

$$\begin{aligned} f(x) &= a_0 + a_1 x + a_2 x^2 + a_3 x^3 + \cdots + a_n x^n \\ &= a_0 + x(a_1 + x(a_2 + x(a_3 + \cdots + x a_n))\cdots) \end{aligned} \tag{2.2.11}$$

Regarding the power of 3/2 in equation 2.2.8, it can be written as $x^{3/2} = x\sqrt{x}$, which is computationally less demanding.

2.3 Thermodynamic and Transport Properties of Water

The thermodynamic and transport properties of the water considered in this Section are the specific heat (c_p) and the dynamic viscosity (μ). Traditionally in the hydrodynamic models, both properties are treated as constants, therefore, introducing bias in the model calculations. The equations of these properties presented in this Section complement the equation of state and are consistent with the derivation of *EOS80*, based on thermodynamic properties of the fluid and extensive experimental data.

2.3.1 Specific Heat

The specific heat of seawater is defined as the heat in Joules required to raise the temperature of 1 kg of seawater by 1 ^{o}C at constant pressure. The specific heat is a function of salinity, temperature and pressure. Fofonoff and Millard [1983] introduced polynomial expansions for the calculation of c_p that are computationally intensive, but validated and endorsed by *UNESCO*. The specific heat for seawater, as a function of S, T and p is defined as:

$$c_p(S,T,p) = c_p(S,T,0) + \Delta_1 c_p(0,T,p) + \Delta_2 c_p(S,T,p) \tag{2.3.1}$$

where all the terms in the r.h.s side of equation 2.3.1 are polynomial expansions of S, T and p:

$$\begin{aligned}\Delta_1 c_p(0,T,p) =& (a_0 + a_1 T + a_2 T^2 + a_3 T^3 + a_4 T^4)p + \\ & (b_0 + b_1 T + b_2 T^2 + b_3 T^3 + b_4 T^4)p^2 + \\ & (c_0 + c_1 T + c_2 T^2 + c_3 T^3)p^3\end{aligned} \tag{2.3.2}$$

$$\begin{aligned}\Delta_2 c_p(S,T,p) =& \left[(d_0 + d_1 T + d_2 T^2 + d_3 T^3 + d_4 T^4)S + (e_0 + e_1 T + e_2 T^2)S^{3/2}\right] p \\ & + \left[(f_0 + f_1 T + f_2 T^2 + f_3 T^3)S + g_0 S^{3/2}\right] p^2 + \\ & + \left[(h_0 + h_1 T + h_2 T^2)S + j_0 T S^{3/2}\right] p^3\end{aligned} \tag{2.3.3}$$

The value of $c_p\,(S,\,T,\,0)$ in equation 2.3.1 is calculated by the polynomials:

$$c_p(S,T,0) = c_p(0,T,0) + AS + BS^{3/2} \tag{2.3.4}$$

$$c_p(0,T,0) = m_0 + m_1 T + m_2 T^2 + m_3 T^3 + m_4 T^4 \tag{2.3.5}$$

$$A = p_0 + p_1 T + p_2 T^2 \qquad \text{and} \qquad B = q_0 + q_1 T + q_2 T^2 \tag{2.3.6}$$

In accordance with the equation of state, equations 2.3.1 through 2.3.6 are valid for the range of values: 0 psu $\le S \le$ 40 psu, $-2\,^{o}$C $\le T \le 40\,^{o}$C and 0 dbar $\le p \le$ 10000 dbar (Fofonoff and Millard [1983]). The resulting c_p has units of: J/kg·^{o}C. The leading coefficients of the polynomials in the above equations are defined as:

$$\left.\begin{array}{lll} a_0 = -4.95920 \cdot 10^{-1} & b_0 = 2.49310 \cdot 10^{-4} & c_0 = -5.42200 \cdot 10^{-8} \\ a_1 = 1.45747 \cdot 10^{-2} & b_1 = -1.08645 \cdot 10^{-5} & c_1 = 2.63800 \cdot 10^{-9} \\ a_2 = -3.13885 \cdot 10^{-4} & b_2 = 2.87533 \cdot 10^{-7} & c_2 = -6.56370 \cdot 10^{-11} \\ a_3 = 2.03570 \cdot 10^{-6} & b_3 = -4.00270 \cdot 10^{-9} & c_3 = 6.13600 \cdot 10^{-13} \\ a_4 = 1.71680 \cdot 10^{-8} & b_4 = 2.29560 \cdot 10^{-11} & \end{array}\right\} \tag{2.3.7a}$$

$$\left.\begin{array}{lll} d_0 = 4.92470 \cdot 10^{-3} & e_0 = -1.23310 \cdot 10^{-4} & f_0 = -2.95580 \cdot 10^{-6} \\ d_1 = -1.28315 \cdot 10^{-4} & e_1 = -1.51700 \cdot 10^{-6} & f_1 = 1.17054 \cdot 10^{-7} \\ d_2 = 9.80200 \cdot 10^{-7} & e_2 = 3.12200 \cdot 10^{-8} & f_2 = -2.39050 \cdot 10^{-9} \\ d_3 = 2.59410 \cdot 10^{-8} & & f_3 = 1.84480 \cdot 10^{-11} \\ d_4 = -2.91790 \cdot 10^{-10} & & \end{array}\right\} \tag{2.3.7b}$$

$$\left.\begin{array}{lll} h_0 = 5.54000 \cdot 10^{-10} & j_0 = -1.43000 \cdot 10^{-12} & g_0 = 9.97100 \cdot 10^{-8} \\ h_1 = -1.76820 \cdot 10^{-11} & & \\ h_2 = 3.51300 \cdot 10^{-13} & & \end{array}\right\} \tag{2.3.7c}$$

$$\left.\begin{array}{lll} m_0 = 4217.0 & p_0 = -7.64358 & q_0 = 0.17704 \\ m_1 = -3.72028 & p_1 = 0.10728 & q_1 = -4.07718 \cdot 10^{-3} \\ m_2 = 0.14129 & p_2 = -1.38385 \cdot 10^{-3} & q_2 = 5.14800 \cdot 10^{-5} \\ m_3 = -2.65439 \cdot 10^{-3} & & \\ m_4 = 2.09324 \cdot 10^{-5} & & \end{array}\right\} \tag{2.3.7d}$$

2.3.2 Viscosity

According to the equation developed by Millero [1974], the viscosity of pure water μ_w (N·s/m^2) at temperature T (^{o}C) is given in terms of the viscosity of the distilled water at 20 ^{o}C temperature ($\mu_{w20} = 1.002 \cdot 10^{-3}$ N·s/m^2) as:

$$\mu_w = \mu_{w20} \cdot 10^{\Lambda} \quad \text{with:} \quad \Lambda = -\frac{1.1709(T-20) + 0.001827(T-20)^2}{T + 89.93} \tag{2.3.8}$$

and the viscosity of seawater (μ) is calculated as follows:

$$\mu = \mu_w \left[1.0 + A(\rho S)^{1/2} + B(\rho S)\right] \tag{2.3.9}$$

where $A = 2.204 \cdot 10^{-3}\, T + 4.537 \cdot 10^{-3}$, $B = 1.800 \cdot 10^{-8}\, T + 1.434 \cdot 10^{-6}$ and S is the practical salinity.

The pressure change at temperature T affects the viscosity of the fluid, and the change in viscosity $\Delta\mu_p$ due to pressure is given by Matthäus (referenced by Riley and Skirrow [1974]) from the equation:

$$\Delta\mu_p = \left(-1.7913 \cdot 10^{-5} + 1.3550 \cdot 10^{-6} T - 2.5853 \cdot 10^{-8} T^2\right) p$$

$$\left(9.5182 \cdot 10^{-9} - 6.0833 \cdot 10^{-10} T - 1.1652 \cdot 10^{-11} T^2\right) p^2 \tag{2.3.10}$$

where p ($\mathrm{kg_f/m^2}$ = 0.967841 atm) is the applied or gage pressure. The kinematic viscosity ν is then calculated by: $\nu = \mu/\rho$, and ρ is calculated from the equation of state.

2.4 Thermodynamic and Transport Properties of Air

Properties of the air above the water surface, such as density and specific heat, are directly involved in the calculation of surface wind stresses and heat fluxes, the chief forcing functions in the hydrodynamic models. Traditionally, constant values for both the density and the specific heat of the air are used with the possible introduction of errors in the calculation of the surface stresses and fluxes. In M^2COPS functional relationships are introduced for both of these properties in terms of p and T.

2.4.1 Specific Heat

The specific heat of the moist air above the water surface is approximated by the following equation (Miller et al. [1999]):

$$c_p^a = c_{p0}^a \frac{1 + w(c_{p_v}^a / c_{p0}^a)}{1 + w} \tag{2.4.1}$$

where c_{p0}^a is the value of c_p^a when the relative humidity is zero and is taken equal to 1004.6 J/kg·K, c_{pv}^a is the specific heat of water vapor, taken equal to 1870 J/kg·K, and w is the mixing ratio defined as:

$$w = \frac{0.62197 p_\mathrm{v}}{p_\mathrm{atm} - p_\mathrm{v}} \tag{2.4.2}$$

where p_v is the vapor pressure. The vapor pressure is calculated in terms of the relative humidity f and the saturation vapor pressure p_s (N/m^2) as:

$$p_v = f p_s \tag{2.4.3}$$

An equation for approximating the relative humidity developed by Bosen (Linsley, Jr. et al. [1982]) with a 0.6% accuracy for the temperature range $-25\,^{o}$C to $45\,^{o}$C is:

$$f = \left(\frac{112 - 0.1T_{air} + T_d}{112 + 0.9T_{air}} \right)^8 \tag{2.4.4}$$

where, T_{air} and T_d are the air and dewpoint temperatures, respectively (^{o}C). The saturation vapor pressure (N/m^2) as a function of the air temperature (^{o}C) is approximated with the polynomial:

$$p_s = 3386.39 \left[(0.00738T_{air} + 0.8072)^8 - 0.000019|1.8T_{air} + 48| + 0.001316 \right] \tag{2.4.5}$$

As stated in Miller et al. [1999], equation 2.4.5 is accurate to within 1% and it is valid for the temperature range $-50\,^{o}$C to $55\,^{o}$C.

The specific humidity h_q is calculated (Linsley, Jr. et al. [1982]) as:

$$h_q = \frac{0.62197 p_v}{p_{atm} - 0.37803 p_v} \tag{2.4.6}$$

2.4.2 Air Density

The density of the air above the water surface is calculated as the sum of the densities of dry air and water vapor:

$$\rho_{air} = \left(\frac{p_d}{R_d} + \frac{p_v}{R_v} \right) \frac{1}{T_{air}} \tag{2.4.7}$$

where ρ_{air} (kg/m^3) is the density of the moist air, p_d (N/m^2) is the absolute pressure of the dry air, p_v (N/m^2) is the absolute pressure of the water vapor, T_{air} (K) is the air temperature, R_d is the gas constant of dry air taken as: 287.05 J/kg·K, and R_v is the gas constant of water vapor taken as: 461.495 J/kg·K.

The local atmospheric pressure is equal to the sum of the dry air pressure and the pressure of the water vapors, that is $p_{atm} = p_d + p_v$. Introduction of this expression into equation 2.4.7 yields:

$$\rho_{air} = \frac{p_{atm}}{R_d T_v} \qquad \text{with:} \qquad T_v = \frac{T_{air}}{1 - 0.37803(p_v / p_{atm})} \tag{2.4.8}$$

where T_v (K) is the virtual temperature (Miller et al. [1999]).

2.5 Wind Induced Shear Stresses

The basic driving force for the water body hydrodynamics and the growth and propagation of the surface waves is the wind, which is usually incorporated into the models via the surface stress or the friction velocity. Since these parameters are not directly measured, they are estimated from available wind measurements using bulk formulations. The evaluation of the shear stresses (2.1.15) and the heat transfer fluxes (Sections 2.6.2 and 2.6.3) using bulk equations requires a priori knowledge of the bulk drag coefficients for momentum (C_M) and heat (C_H). Both coefficients are functions of the wind speed (W) at a height z above the mean water surface (usually 10 m), the turbulent surface roughness height (z_o) and the state of the wind generated surface waves (Stull [1988], WMO-No. 702 [1998] and others).

The effect of the water surface friction on the wind is its magnitude reduction and as one approaches the surface, the wind speed tends to zero. As described in Stull [1988], WMO-No. 702 [1998], the effects of friction are represented by relating the free atmospheric wind to a stress at the water surface, using the concept of a two regime atmospheric boundary layer (*ABL*).

The portion of the *ABL* close to the surface is called the constant flux or constant stress layer and extends up to ~ 50 m above the mean water surface. Within this layer, it is assumed that the frictional forces are constant with height and that the Coriolis and pressure gradient forces, as well as the the horizontal gradients of the turbulent fluxes, are negligible (WMO-No. 702 [1998]). As a consequence of these assumptions, the wind direction is constant with height. Using Prandtl's mixing layer theory, it can be shown that the horizontal flow velocity of the air follows a logarithmic profile in the vertical direction (Stull [1988], WMO-No. 702 [1998]). Above the constant stress layer and extending up to ~ 1000 m above the mean water surface, is the so called Ekman layer or spiral. Within the Ekman layer, the geostrophic winds dominate and the principal force balance is between the Coriolis, friction and pressure gradient forces. As noted in Stull [1988], the tip of the flow velocity vectors trace out a spiral, thus the name Ekman spiral.

The stability of the *ABL* (difference between the air and water temperatures at the surface) is important in determining the wind speed near the water surface, especially over waters near large land masses (e.g., lakes), while over much of the oceans there is an equilibrium between the air and the water temperatures, so that the neutral conditions dominate. Stable conditions in the *ABL* (warm air over colder waters) increase the friction, resulting in weaker winds and, therefore, weaker

shear stresses, while the unstable conditions (cold air over warmer waters) reduces the dissipation by friction, thus increasing the stress over the water surface (WMO-No. 702 [1998]).

In the current formulation of M^2COPS, the hydrodynamic model is coupled with two wave models, all of which should share common surface drag coefficients. To avoid duplicate calculations, a unified approach shared among these models is used for the determination of the surface drag coefficients as presented in the next Section.

2.5.1 Determination of the Surface Drag Coefficients

In the following discussion, a constant stress *ABL* is assumed and, therefore, the velocity and temperature profiles above the water surface can be described by the following general logarithmic laws (Brutsaert [1982]):

$$\frac{du}{dz} = \frac{u_{\#}}{\mathbf{k}\, z} \qquad \text{and} \qquad \frac{d\theta}{dz} = \frac{\theta_{\#}}{\mathbf{k}\, z} \tag{2.5.1}$$

such that: $u(z = z_o) = 0$ and $\theta(z = z_o) = \theta_w$. In equations 2.5.1, $u\,(z)$ is the wind speed at an elevation z above the mean free surface, $u_{\#}$ is the friction velocity at the atmospheric side of the free surface ($u_{\#}^2 = \tau/\rho_{air}$), $\mathbf{k}$ is the von Kármán's constant, z_o is the aerodynamic friction roughness height, $\theta\,(z)$ is the potential temperature ($\theta(z) = T(z) + \frac{gz}{c_p^a}$), c_p^a is the specific heat coefficient of air, $\theta_{\#}$ is the scaling potential temperature and θ_w is the potential temperature at the water surface.

Janssen, as referenced by Mastenbroek et al. [1993], introduced the idea of a displacement height z_e to account for the effects of the surface waves on the wind by adjusting the profiles (equations 2.5.1) as follows:

$$\frac{du}{dz} = \frac{u_{\#}}{\mathbf{k}\,(z + z_e - z_o)} \qquad \text{and} \qquad \frac{d\theta}{dz} = \frac{\theta_{\#}}{\mathbf{k}\,(z + z_e - z_o)} \tag{2.5.2}$$

and defined the displacement or effective roughness height z_e as:

$$z_e = \frac{z_o}{\left[1 - \frac{\tau_w}{\tau_{tot}}\right]^{1/2}}\,; \qquad \tau_{tot} = \tau_t + \tau_w \tag{2.5.3}$$

where, τ_w is the wave-induced surface shear stress defined in Chapter 3, τ_t is the turbulent surface shear stress (reflecting the direct wind momentum input to the mean flow-currents) defined as: $\tau_t = \rho_{air} u_{\#}^2 = \rho_w u_*^2$ and τ_{tot} is the total shear stress. For a young wind sea, most of the wind momentum is absorbed by the water and the ratio τ_w/τ_{tot} approaches one, thus significantly enhancing the surface shear stresses as can be deducted from equations 2.5.2 and 2.5.3 (Mastenbroek et al.

[1993]). In the absence of waves or as $\tau_w \to 0$, the effective roughness height approaches z_o, therefore, equations 2.5.1 are recovered from equations 2.5.2 as they should. For an old wind sea the ratio τ_w/τ_{tot} is approximately equal to 0.5 (Mastenbroek et al. [1993]).

The effects of the stability of the *ABL* are accounted in the above equations by introducing appropriate stability functions into equations 2.5.2, as described in Liu and Schwab [1987], Stull [1988], Brutsaert [1982] and Paulson [1970]. The integration of equations 2.5.2 after the introduction of the stability functions gives:

$$u(z) = \frac{u_\#}{\mathbf{k}}\,\Phi_m = \frac{u_\#}{\mathbf{k}}\Big[\ln\big(\frac{z + z_e - z_o}{z_e}\big) - \Psi_m\Big] \tag{2.5.4}$$

$$\Delta\theta(z) = \theta(z) - \theta_w = \frac{\theta_\#}{\mathbf{k}}\,\Phi_h = \frac{\theta_\#}{\mathbf{k}}\Big[\ln\big(\frac{z + z_e - z_o}{z_e}\big) - \Psi_h\Big] \tag{2.5.5}$$

where, $u(z \to z_o) = 0$, $\Psi_m(z \to z_o) = 0$, $\theta(z \to z_o) = \theta_w$ and $\Psi_h(z \to z_o) = 0$. The stability functions for momentum Ψ_m and Φ_m are both functions of z, z_o, z_e and the dimensionless stability parameter ϑ for momentum. The stability functions for heat Ψ_h, Φ_h are both functions of z, z_o, z_e and the dimensionless stability parameter ϑ for temperature. The stability parameter ϑ is defined in terms of the Monin-Obukhov length L as: $\vartheta = \dfrac{z}{L}$. Equations 2.5.4 and 2.5.4 are the enhanced versions described in Liu and Schwab [1987], accounting for the effects of both the waves and the atmospheric stability on the winds.

The roughness height z_o and subsequently z_e appearing in equations 2.5.4 and 2.5.5, are related to the friction velocity by the Charnock's relations (Charnock [1955], The WAMDI Group [1988] and Booij et al. [2004]):

$$z_o = \alpha_c \frac{u_\#^2}{g}\;; \qquad z_e = \alpha_{cw} \frac{u_\#^2}{g} = \frac{z_o}{\Big[1 - \dfrac{\tau_w}{\tau_{tot}}\Big]^{1/2}}\;; \qquad \alpha_{cw} = \frac{\alpha_c}{\Big[1 - \dfrac{\tau_w}{\tau_{tot}}\Big]^{1/2}} \tag{2.5.6}$$

where, α_c is the well known Charnock's constant (not really a constant since it is a function of the wind speed and the state of the surface waves) and α_{cw} is the adjusted or effective Charnock's constant that accounts for the effects of the waves (The WAMDI Group [1988], Booij et al. [2004]). The difficulty with equations 2.5.6 lies in the determination of the constant α_c, since the reported values have a wide range, depending upon the wind speed at 10 m above the water surface and the state of the waves. The constant α_c can be viewed as the base or background Charnock's constant, while α_{cw} can be viewed as the enhanced or wave-induced Charnock's constant.

The constant α_c and the surface drag coefficients C_M and C_H are determined in M^2COPS using a variation of the *GLERL* (Great Lakes Environmental Research Laboratory) approach described in Liu and Schwab [1987], with the appropriate replacements $z \rightarrow z + z_e - z_o$ and $z_o \rightarrow z_e$ as described by Janssen's approach to account for the wave effects. First a neutral drag coefficient at $z = 10\,\text{m}$ is determined using the relation of Smith and Banke [1975]:

$$10^3 \cdot C_{NM} = 0.63 + 0.066 \cdot u_{10} = 0.63 + 0.066 \cdot W \tag{2.5.7}$$

with the neutral drag coefficient for momentum (C_{NM}) defined as:

$$C_{NM} = \left[\frac{u_\#}{u(z)}\right]_N^2 = \mathbf{k}^2 \left[\ln\left(\frac{z + z_e - z_o}{z_e}\right)\right]^{-2} \tag{2.5.8}$$

Using a wind speed of $W = 15\,\text{m/s}$ as suggested from the data of Smith and Banke, equation 2.5.7 yields a drag coefficient of 0.00162 and equation 2.5.8 gives a friction velocity equal to: $u_\# = 0.04025 \cdot W = 0.60375\,\text{m/s}$. In the *GLERL* approach, the von Kármán's constant in the calculation of the surface drag coefficients is taken equal to 0.35 following the suggestion of Businger et al. [1971] and, therefore, the value of the roughness height as obtained from equation 2.5.8 (for $z_e = z_o$) is: $z_o = 0.001673\,\text{m}$. Substitution of the values for z_o and $u_\#$ into the first of equations 2.5.6 and using the standard value of $9.806\,\text{m/s}^2$ for the gravitational acceleration, the Charnock's constant is found to be equal to: $\alpha_c = 0.045$.

Using the usual value for the von Kármán's constant ($\mathbf{k} = 0.4$), the corresponding values for z_o and α_c are 0.000483 m and 0.013, respectively. Since all the M^2COPS models are using $\mathbf{k} = 0.4$, the same value for $\mathbf{k}$ will be used for the determination of the drag coefficients as well. As stated in Brutsaert [1982], there is no compelling reason to abandon the consensus value $\mathbf{k} = 0.4$. This choice is also justified from the computation of the drag coefficients using both values of $\mathbf{k}$ that showed no significant difference for wind speeds less than 30 m/s.

The stability functions Ψ and Φ in equations 2.5.4 and 2.5.5 are computed by the methods presented in Long, Jr. and Shaffer [1975], Long, Jr. [1984, 1990] and Liu and Schwab [1987]. The resulting expressions for the stability functions were derived assuming that the velocity and the temperature distributions follow the profiles described in Businger et al. [1971] and Dyer [1974]. The stability of the surface atmospheric layer is classified using the dimensionless stability parameter ϑ as follows: *(a)* for $\vartheta < 0$ ($L < 0$ or $\Delta\theta < 0$), where the conditions are unstable, and *(b)* and for $\vartheta > 0$ ($L > 0$ or $\Delta\theta > 0$) the surface atmospheric layer is stable. Long, Jr. and Shaffer further subdivide

the stable conditions as "mildly stable" when $0 < \vartheta < 1$ and as "strongly stable" when $\vartheta \geq 1$. The neutral conditions are defined by the limiting case: $\lim_{L \to \pm\infty} \vartheta = 0$ ($\Delta\theta \to 0$).

The consideration of a neutral atmospheric surface layer implies that the dominant turbulent kinetic energy generation mechanisms are mechanical and are associated with strong winds and overcast skies (Stull [1988]), situations that are also common over lake and ocean waters. The expressions for the stability functions as presented in Long, Jr. and Shaffer [1975] and Long, Jr. [1984] are:

unstable case: $\vartheta < 0$ ($L < 0$ or $\Delta\theta < 0$)

$$\Phi_m = \ln \frac{(x-1)(x_0+1)}{(x+1)(x_0-1)} + 2\left[\arctan(x) - \arctan(x_0)\right] =$$

$$\ln\left(\frac{\vartheta}{\vartheta_0}\right) + \ln \frac{(1+x_0)^2(1+x_0^2)}{(1+x)^2(1+x^2)} + 2\left[\arctan(x) - \arctan(x_0)\right] \tag{2.5.9}$$

$$\Phi_h = 0.74 \ln \frac{(y-1)(y_0+1)}{(y+1)(y_0-1)} = 0.74 \ln\left(\frac{\vartheta}{\vartheta_0}\right) + 1.48 \ln \frac{1+y_0}{1+y} \tag{2.5.10}$$

with:

$$x = (1 - 15\,\vartheta)^{1/4}\ ; \quad x_0 = (1 - 15\,\vartheta_0)^{1/4}\ ; \quad y = (1 - 9\,\vartheta)^{1/2}\ ; \quad y_0 = (1 - 9\,\vartheta_0)^{1/2} \tag{2.5.11}$$

mildly stable case: $0 < \vartheta < 1$ ($L > z$, $\Delta\theta > 0$)

$$\Phi_m = \ln\left(\frac{\vartheta}{\vartheta_0}\right) + 4.7\,(\vartheta - \vartheta_0)\ ; \qquad \Phi_h = 0.74 \ln\left(\frac{\vartheta}{\vartheta_0}\right) + 4.7\,(\vartheta - \vartheta_0) \tag{2.5.12}$$

strongly stable case: $\vartheta \geq 1$ ($L \leq z$, $\Delta\theta > 0$)

$$\Phi_m = \ln\left(\frac{\vartheta}{\vartheta_0}\right) + 4.7\,(1 - \vartheta_0 + \ln\vartheta)\ ; \qquad \Phi_h = 0.74 \ln\left(\frac{\vartheta}{\vartheta_0}\right) + 4.7\,(1 - \vartheta_0 + \ln\vartheta) \tag{2.5.13}$$

neutral case: $\vartheta = 0$ as $L \to \pm\infty$

$$\Phi_m = \Phi_h = \ln\left(\frac{\vartheta}{\vartheta_0}\right) \qquad \text{as:} \qquad \Psi_m \to 0 \qquad \text{and} \qquad \Psi_h \to 0 \tag{2.5.14}$$

where, $\vartheta = \dfrac{z + z_e - z_o}{L}$ and $\vartheta_0 = \dfrac{z_e}{L}$. The Monin-Obukhov height L is defined (Paulson [1970], Stull [1988]) as:

$$L = -\frac{u_\#^3\, \rho_{air}\, c_p^a\, \bar{\theta}}{\mathbf{k}\, g\, \mathcal{H}} = \frac{u_\#^2\, \bar{\theta}}{\mathbf{k}\, g\, \theta_\#}\ ; \qquad \text{with:} \qquad \theta_\# = -\frac{1}{\mathbf{k}\, u_\#}\, \frac{\mathcal{H}}{\rho_{air}\, c_p^a} \tag{2.5.15}$$

where, $\bar{\theta}$ is a representative or the vertically averaged potential temperature for the surface layer, $\theta_\#$ is the scaling potential temperature, c_p^a is the specific heat of air at constant pressure and $\mathcal{H} =$

$\rho_{air}\, c_p^a\, \overline{w'\theta'}$ is the turbulent heat flux. Defining the bulk Richardson's number between the two elevations z_1 and z_2, such that $z = z_2 - z_1 = z_2 - z_o \approx z_2$, as:

$$\mathbb{R}_{iB} = \frac{g}{\overline{\theta}} \frac{z\,\Delta\theta}{u^2(z)} \tag{2.5.16}$$

the following relations for ϑ and L are obtained (Long, Jr. [1984, 1990]):

$$\vartheta = \frac{z}{L} = \frac{\Phi_m^2}{\Phi_h}\,\mathbb{R}_{iB}\;; \qquad L = \frac{\Phi_h}{\Phi_m^2}\,\frac{u^2(z)\,\overline{\theta}}{g\,\Delta\theta}\;; \qquad L_N = \frac{u^2(z)\,\overline{\theta}}{g\,\Delta\theta}\left[\ln\left(\frac{z + z_e - z_o}{z_e}\right)\right]^{-1} \tag{2.5.17}$$

where, L_N is Monin-Obukhov length for neutral conditions, $\Delta\theta = \theta_{air} - \theta_w$ and $u\,(z)$ is the wind speed at the elevation z (usually 10 m). The two drag coefficients are evaluated using the following relationships (Long, Jr. [1984, 1990]):

$$C_M = \frac{u_\#^2}{u^2(z)} = \frac{\mathbf{k}^2}{\Phi_m^2}\;; \qquad C_H = \frac{u_\#\,\theta_\#}{u(z)\,\Delta\theta} = \frac{\mathbf{k}^2}{\Phi_m\,\Phi_h} \tag{2.5.18}$$

The equations 2.5.4, 2.5.5, 2.5.6, 2.5.9, 2.5.10, 2.5.12, 2.5.13, 2.5.14, 2.5.17 and 2.5.18 are solved iteratively to obtain the solution for z_o, $u_\#$, L, C_M and C_H. This iterative procedure is similar to the one presented in Long, Jr. [1984] and Long, Jr. [1990] and it is outlined as follows:

iterative solution for C_M and C_H:

(a) Estimate the initial guess for z_o from equation 2.5.6, with τ_w supplied from the wave model, and assuming neutral atmospheric conditions ($u_\# = 0.04025\,W$).

(b) Estimate the initial guess for the neutral Monin-Obukhov length L_N (equation 2.5.17).

(c) Calculate the stability functions Φ_m and Φ_h from equations 2.5.9 through 2.5.14, depending upon the stability conditions of the surface layer.

(d) Calculate the updated value of the Monin-Obukhov length L from equation 2.5.17. Repeat the steps *(c)* and *(d)* until $L^{new} \approx L^{old}$ (inner iteration loop).

(e) Calculate the updated values of $u_\#$, $\theta_\#$ and z_o using equations 2.5.4, 2.5.5 and 2.5.6, respectively. Repeat the steps *(c)* through *(e)* until $u_\#^{new} \approx u_\#^{old}$ (outer iteration loop).

(f) Calculate the values of C_M and C_H from equations 2.5.18.

2.6 Surface Heat Balance

The vertical heat transfer is a very important component that affects the thermodynamics of the water body and the circulation dynamics due to forces resulting from heating and cooling (McCormick and Lam [1999]). Water properties, such as density, viscosity and specific heat, are directly

affected by temperature changes and part of the accuracy of the model depends upon the correct determination of these properties. The net water surface heat flux into (positive) or out (negative) of the water is incorporated as the surface boundary condition (equation 2.1.13, $\Phi = T$):

$$\mathcal{B}_v \left.\frac{\partial \Phi}{\partial z}\right|_\zeta = \mathcal{K}_v \left.\frac{\partial T}{\partial z}\right|_\zeta = \frac{\mathcal{H}_N}{\rho_o \, c_p} \tag{2.6.1}$$

where, $\mathcal{H}_N$ (W/m^2) is the net surface heat flux, ρ_o (kg/m^3) is the reference density of the water and c_p (J/kg·^{o}C) is the specific heat of the water. In the current formulation of *M*^{2}*COPS*, the surface heat flux is directly calculated from the heat balance equation:

$$\mathcal{H}_N = \mathcal{H}_S + \mathcal{H}_L + \mathcal{H}_{LR} + \mathcal{H}_{SR} \tag{2.6.2}$$

where, $\mathcal{H}_S$ is the sensible heat transfer, $\mathcal{H}_L$ is the latent heat transfer, $\mathcal{H}_{LR}$ is the long wave radiation from the sun and $\mathcal{H}_{SR}$ is the short wave radiation from the sun (Cole and Wells [2005], Wu et al. [2001], Ahsan and Blumberg [1999], Beletsky and Schwab [2001]). The decision to incorporate the heat balance equation into the model simplifies the heat flux calculations: *(a)* by avoiding the creation of extraneous input files for the spatially and temporally varied heat flux field, and *(b)* by directly controlling the relations and the variables used in the calculation of the heat flux terms, as they explicitly depend from other flow variables calculated by the hydrodynamic model. The procedure for the calculation of $\mathcal{H}_N$ is described in detail in McCormick and Meadows [1988] and Chu et al. [1994], for a mixed upper layer in lakes and it is outlined here.

2.6.1 Shortwave Radiation Transfer

The short wave radiation is calculated as a function of the location (latitude, longitude), the day of the year, the time of the day and the cloud cover of the sky for the particular day and time:

$$\mathcal{H}_{SR} = \mathcal{H}_{CSR} \, f(\chi) \tag{2.6.3}$$

where, $\mathcal{H}_{CSR}$ is the clear sky value of $\mathcal{H}_{SR}$, χ is the cloud cover (for clear sky: $\chi = 0$ and for full coverage: $\chi = 1$) and $f(\chi)$ is a cubic function of χ defined as (Beletsky and Schwab [2001]):

$$f(\chi) = 0.999 - 0.425\chi + 0.922\chi^2 - 1.14\chi^3 \quad ; \qquad 0 \le \chi \le 1 \tag{2.6.4}$$

The values of $f(\chi)$ vary between a minimum value of 0.356 (full cloud coverage) and a maximum value of 1.0 (clear sky). The clear sky value of $\mathcal{H}_{CSR}$ is determined as (Gupta et al. [2001],

McCormick and Meadows [1988]):

$$\mathcal{H}_{\mathrm{CSR}} = (1-\alpha)\,\mathbf{I}(z)\left(\frac{\overline{d}_{sun}}{d_{sun}}\right)^2 \cos \mathrm{Z} \tag{2.6.5}$$

where Z is the solar zenith angle (radians), $\overline{d}_{sun}$ is the average distance between the sun and the earth (also known as astronomical unit (AU) with $1\,\mathrm{AU} = 1.49598 \cdot 10^{11}$ m), d_{sun} is the instantaneous distance between the sun and the earth (varies between a maximum value of $1.521 \cdot 10^{11}$ m in early July and a minimum value of $1.471 \cdot 10^{11}$ m in early January), $\mathbf{I}(z)\,(\mathrm{W/m^2})$ is a function of depth, representing the penetrative nature of the shortwave radiation and α is the surface albedo. The variables $\mathbf{I}(z)$ and α are defined after McCormick and Meadows [1988], as:

$$\mathbf{I}(z) = \mathbf{I}_{\mathrm{o}}\,(0.45 \cdot e^{\varepsilon_1 z} + 0.55 \cdot e^{\varepsilon_2 z}) \quad ; \qquad \alpha = \frac{0.045}{\cos \mathrm{Z}} \tag{2.6.6}$$

where, $\mathbf{I}_{\mathrm{o}}$ is the average solar constant taken equal to $1373\,\mathrm{W/m^2}$ (Frohlich 1977 as referenced in Duffie and Beckman [1980]) and (ε_1, ε_2) are the two extinction coefficients: $\varepsilon_1 = 0.28\,\mathrm{m^{-1}}$ and $\varepsilon_2 = 2.85\,\mathrm{m^{-1}}$.

The leading coefficients in equation 2.6.6, reflect the relative contribution of the visible and the infrared portions of the solar radiation (McCormick and Meadows [1988], Ivanoff [1977]). In the heat balance equation, $\mathcal{H}_{\mathrm{SR}}$ is the only penetrative heat flux, and according to Ivanoff and McCormick and Meadows it can penetrate up to $8-10$ m into the water column. Because of this nature of the short wave radiation, $\mathcal{H}_{\mathrm{SR}}$ is incorporated in M^2COPS either as a source term in the temperature equation (penetrative mode) or as part of the surface temperature boundary condition with $\mathbf{I}(z) = \mathbf{I}(0) = \mathbf{I}_{\mathrm{o}}$ (non-penetrative mode).

The amount of the solar radiation reaching the surface of the water depends upon the position of the sun in the sky. The methodology on determining the sun's position is described extensively in Reda and Andreas [2004], Gupta et al. [2001], Paltridge and Platt [1976] and Michalsky [1988]. The eccentricity correction factor $\overline{d}_{sun}/d_{sun}$ is determined using Spencer's approximation equation (Gupta et al. [2001], Paltridge and Platt [1976]) as:

$$\left(\frac{\overline{d}_{sun}}{d_{sun}}\right)^2 = 1.000110 + 0.034221\,\cos B + 0.001280\,\sin B$$
$$+ 0.000719\,\cos 2B + 0.000077\,\sin 2B \tag{2.6.7}$$

$$B = \frac{2\pi}{365.24219}\,(\mathrm{J_n} - 1) \tag{2.6.8}$$

where, B is the day angle (radians) and J_n is the day of the year (e.g., January 1 is day 1). The factor 365.24219 in equation 2.6.8 represents the average time length of the solar year. The maximum error in $(\overline{d}_{sun}/d_{sun})^2$ is 0.0001 (Gupta et al. [2001]). The cosine of the solar zenith angle for any location and time on earth is calculated as (Gupta et al. [2001], Paltridge and Platt [1976], Duffie and Beckman [1980]):

$$\cos Z = \sin\phi \, \sin\delta + \cos\phi \, \cos\delta \, \cos\theta_h \tag{2.6.9}$$

where ϕ is the latitude of the location, δ is the daily average value of the solar declination (the sun's angular position at solar noon with respect to the plane of equator, $-23.45^o \leq \delta \leq 23.45^o$, and θ_h is the hour angle representing the angular displacement of the sun from the local meridian (east or west) due to the rotation of the earth on its axis at a rate of 15^o per hour.

The declination angle (radians) is calculated using Spencer's approximation (Gupta et al. [2001], Paltridge and Platt [1976]) as:

$$\begin{aligned}\delta = {} & 0.006918 - 0.399912 \, \cos B + 0.070257 \, \sin B \\ & - 0.006758 \, \cos 2B + 0.000907 \, \sin 2B \\ & - 0.002697 \, \cos 3B + 0.001480 \, \sin 3B\end{aligned} \tag{2.6.10}$$

As stated in Paltridge and Platt, equation 2.6.10 approximates δ with a maximum error of 0.0006 radians. The hour angle θ_h is measured in terms of the local solar time with the solar noon defined at 12:00. Since the hour angle represents the angular displacement of the sun with respect to the local meridian due to the earth's spinning about its axis at a rate of Ω, the equation of the hour angle is:

$$\frac{d\theta_h}{dt} = \Omega \quad \Rightarrow \quad \int_0^{\theta_h} d\theta_h = \Omega \int_0^{t_{sol}} dt \quad \Rightarrow \quad \theta_h = \frac{2\pi}{24}(t_{sol} - 12) \tag{2.6.11}$$

The local solar time t_{sol} is not equal with the local clock time and the difference between the two is a function of the longitude and the daylight savings time:

$$t_{sol} = t + \frac{1\,\text{hr}}{15^o}(L_{std} - L_{loc}) + E - DT \tag{2.6.12}$$

where, t (hr) is the local time, L_{std} is the longitude (degrees) of the standard meridian used by the local time zone, L_{loc} is the local longitude (degrees), DT is equal to 1 if daylight savings time is in

effect, otherwise is 0, and E is the time correction (also known as equation of time) that accounts for the perturbations in the earth's rotation rate.

Since the M^2COPS uses the Greenwich mean time (GMT or UTC) in its calculations, then $L_{std} = 0$ and $DT = 0$ and, therefore, equation 2.6.11 becomes:

$$\theta_{\mathrm{h}} = \frac{2\pi}{24}(t_{sol} - 12) - L_{loc} + E \tag{2.6.13}$$

In equation 2.6.11 L_{loc} and E are in radians. Spencer (Paltridge and Platt [1976]) gives the following approximation for the equation of time in radians:

$$\begin{aligned} E = {} & 0.000075 + 0.001868\ \cos B - 0.032077\ \sin B \\ & - 0.014615\ \cos 2B - 0.040849\ \sin 2B \end{aligned} \tag{2.6.14}$$

that has a maximum error of 0.0025 radians (Paltridge and Platt [1976]). If a better accuracy is required for the equation of time, a more sophisticated equation can be used (e.g., Michalsky [1988]).

The temporal average of $\mathcal{H}_{\mathrm{CSR}}$ is calculated by determining the temporal average of $\cos \mathrm{Z}$ (the only time dependent variable). If Δt is the averaging time period, from equation 2.6.13 it is seen that $\Delta\theta_{\mathrm{h}} = \theta_{\mathrm{h2}} - \theta_{\mathrm{h1}} = \frac{2\pi}{24}\Delta t$ and:

$$\overline{\cos \mathrm{Z}} = \frac{1}{\Delta\theta_{\mathrm{h}}}\int_{\theta_{\mathrm{h1}}}^{\theta_{\mathrm{h2}}} \cos \mathrm{Z}\, d\theta_{\mathrm{h}} = \frac{\sin\phi\ \sin\delta}{\Delta\theta_{\mathrm{h}}}\int_{\theta_{\mathrm{h1}}}^{\theta_{\mathrm{h2}}} d\theta_{\mathrm{h}} + \frac{\cos\phi\ \cos\delta}{\Delta\theta_{\mathrm{h}}}\int_{\theta_{\mathrm{h1}}}^{\theta_{\mathrm{h2}}} \cos\theta_{\mathrm{h}}\, d\theta_{\mathrm{h}} =$$

$$\sin\phi\ \sin\delta + \cos\phi\ \cos\delta\ \frac{\sin\theta_{\mathrm{h2}} - \sin\theta_{\mathrm{h1}}}{\Delta\theta_{\mathrm{h}}} \tag{2.6.15}$$

The limiting value of $(\sin\theta_{\mathrm{h2}} - \sin\theta_{\mathrm{h1}})/\Delta\theta_{\mathrm{h}}$ is approximately equal to:

$$\frac{\sin\theta_{\mathrm{h2}} - \sin\theta_{\mathrm{h1}}}{\Delta\theta_{\mathrm{h}}} = \frac{\sin\theta_{\mathrm{h2}} - \sin\theta_{\mathrm{h2}} - \Delta\theta_{\mathrm{h}}}{\Delta\theta_{\mathrm{h}}} =$$

$$\sin\theta_{\mathrm{h2}}\ \frac{1 - \cos\Delta\theta_{\mathrm{h}}}{\Delta\theta_{\mathrm{h}}} + \cos\theta_{\mathrm{h2}}\ \frac{\sin\Delta\theta_{\mathrm{h}}}{\Delta\theta_{\mathrm{h}}} = \sin\theta_{\mathrm{h2}}\cdot 0 + \cos\theta_{\mathrm{h2}}\cdot 1 = \cos\theta_{\mathrm{h2}} \tag{2.6.16}$$

Therefore, the calculation of $\mathcal{H}_{\mathrm{CSR}}$ at $t + \Delta t$ is approximately equal to the average value of $\mathcal{H}_{\mathrm{CSR}}$ for the time period Δt. In the model the value of $\mathcal{H}_{\mathrm{CSR}}$ at $t + \Delta t$ is found by linear interpolation in time between the previous time (hour) and the next time (hour).

2.6.2 Latent Heat Transfer

The latent heat of vaporization represents the energy per unit mass required for the change of the water from the liquid phase to its gas phase (vapor) and it is an energy loss (Streeter et al. [1998]).

The corresponding latent heat flux $\mathcal{H}_{\mathrm{L}}$ is calculated by the bulk aerodynamic equation (Beletsky and Schwab [2001]) as:

$$\mathcal{H}_{\mathrm{L}} = -\rho_{\mathrm{air}}\, C_{\mathrm{M}}\, q_{\mathrm{L}}\, W\, (h_q^w - h_q^a) \tag{2.6.17}$$

where C_{M} is the surface drag coefficient, $\rho_{\mathrm{air}}\,(\mathrm{kg/m^3})$ is the density of the moist air, $W\,(\mathrm{m/s})$ is the wind speed at 10 m above the surface, $q_{\mathrm{L}}\,(\mathrm{J/kg})$ is the latent heat of vaporization of the water, h_q^a is the specific humidity evaluated at the instrument height (usually 10 m above the surface and $T = T_{air}$) and h_q^w is the specific humidity at the surface ($T = T_w$). The latent heat of vaporization is calculated (Miller et al. [1999]) by:

$$q_{\mathrm{L}} = q_{\mathrm{L0}} - 2369\, T \tag{2.6.18}$$

where q_{L0} is the value of q_{L} at $0\,^{\mathrm{o}}\mathrm{C}$, taken as 2500297.8 J/kg and T is the temperature in $^{\mathrm{o}}\mathrm{C}$.

2.6.3 Sensible Heat Transfer

The sensible heat flux out of the water is due to conduction when a temperature gradient exists between the water surface and the air above it. The formulation for the sensible heat flux is similar to the one used for the latent heat flux calculation and takes the following form (Wyrtki [1965], Beletsky and Schwab [2001], Josey et al. [1999]):

$$\mathcal{H}_{\mathrm{S}} = -\rho_{\mathrm{air}}\, C_{\mathrm{H}}\, c_p^a\, W\, (T_w - T_{air}) \tag{2.6.19}$$

where C_{H} is the bulk heat transfer coefficient, $\rho_{\mathrm{air}}\,(\mathrm{kg/m^3})$ is the density of the moist air, $c_p^a\,(\mathrm{J/kg{\cdot}K})$ is the specific heat of the moist air, $T_w\,(\mathrm{K})$ and $T_{air}\,(\mathrm{K})$ are the temperatures of the water surface and the air measured at the instrument height, respectively, and $W\,(\mathrm{m/s})$ is the wind speed at the instrument height (usually 10 m above the surface).

2.6.4 Longwave Heat Transfer

The longwave radiation or back radiation represents the portion of the net incoming solar radiation that is reflected back into space from the surface of the water. The bulk equation introduced by Wyrtki [1965] for the longwave radiation flux calculation is used here and has the form:

$$\mathcal{H}_{\mathrm{LR}} = -\varepsilon\, \sigma_{\mathrm{SB}}\, T_w^4\, (0.39 - 0.05\, p_{\mathrm{v}}^{1/2})\, (1 - \alpha\, \chi^2) + 4\, \varepsilon\, \sigma_{\mathrm{SB}}\, T_w^3\, (T_w - T_{air}) \tag{2.6.20}$$

where, ε is the emittance ($0 \le \varepsilon \le 1$) of the water surface taken as 0.98 (Josey et al. [1999], Suarez et al. [1997]), σ_{SB} is the Stefan-Boltzmann constant that is taken equal to $5.673 \cdot 10^{-8}\,\mathrm{W/m^2{\cdot}K^4}$,

p_v (mbar) is the water vapor pressure, χ is the cloud cover fraction, α is a parameter that increases linearly with latitude from a value of 0.5 (at equator) to a value of 0.8 (at 70^o latitude) taken to be equal to 0.67 for the Great Lakes region, and T_w (K), T_{air} (K) are the temperatures of the water surface and the air above it. According to Josey et al. [1999], equation 2.6.20 is accurate to within $5\,\mathrm{W/m^2}$ and is giving the best estimates from all the equations examined.

2.7 *M*^{2}SED Sediment Transport and Mobile Bed Model

The entrainment and transport of the sediments has long been recognized as an important contributor of the distribution and fate of many contaminants present in local ecosystems. In addition to the chemical and/or biological characteristics, the physical characteristics of the ecosystems are affected by the sediments as well. Stratification due to vertical concentration gradients and flow velocity adjustments are some of the physical effects resulting from the presence of the sediments in the water column. The above reasons establish the necessity for the use of a sediment model coupled with a hydrodynamic model when coastal water calculations are performed.

M^2*COPS* attempts to model entrainment and transport of the sediments considering the following mechanisms: *(a)* the transport of the suspended sediments, *(b)* the transport of the bottom sediments as bedload movement and entrainment, and *(c)* the interaction between the suspended and bottom sediments. The resulting sediment model, referenced as *M*^{2}*SED* from now on, is described in detail in Spasojevic and Holly, Jr [1994] and is simply outlined here with emphasis on the various enhancements that have been incorporated.

2.7.1 Model Physics and Dynamics

The sediment formulation includes a mobile bed model that describes the 2D evolution of the bed and a 3D suspended sediment transport component that uses the scalar equation with the appropriate additions of all relevant source/sink terms. The model takes into account the inhomogeneity of the sediment sizes and classes present in the water column and at the bottom, and considers the fact that, depending upon the local flow conditions, the same sediment particle can either move in suspension or as bedload. The distinction between the suspended sediment and bedload movement is based upon criteria derived from semi-empirical formulations.

The sediment model exchanges information with the underlying hydrodynamic model and relevant parameters, such as water density and bottom friction, which are adjusted based upon the

amount of the suspended material. The solution of the governing equations for each sediment size class addresses the problem of the nonuniformity of the distributions of the sediments in suspension or at the bottom. The total number n_s of the sediment class sizes and their fractional distribution are supplied by the user and they are dependant upon the local resolution required for the solution.

2.7.2 Suspended Sediment Model

The governing equations, either in dimensional or in non-dimensional form, can be obtained from the general scalar equations 2.1.5 and 2.1.35. Let, C_i $(i = 1, n_s)$ be the volumetric (dimensionless) concentration of the "i-th" sediment class, $C = \sum_{i=1}^{n_s} C_i$ be the total volumetric concentration and ρ be the average density of the mixture of water and suspended sediments (all sizes). Replacing Φ by ρC_i, $\mathcal{B}$ by $\mathcal{D}$ and w by $w - w_{s_i}$ in equations 2.1.5 and 2.1.35, the governing equations for the suspended sediment transport are written as:

$$\frac{\partial(\rho C_i)}{\partial t} + \frac{\partial(\rho C_i\, u)}{\partial x} + \frac{\partial(\rho C_i\, v)}{\partial y} + \frac{\partial(\rho C_i\, w)}{\partial z} - \frac{\partial(\rho C_i\, w_{s_i})}{\partial z} = \frac{\partial}{\partial x}\Big[\mathcal{D}_h \frac{\partial(\rho C_i)}{\partial x}\Big] + \frac{\partial}{\partial y}\Big[\mathcal{D}_h \frac{\partial(\rho C_i)}{\partial y}\Big] + \frac{\partial}{\partial z}\Big[\mathcal{D}_v \frac{\partial(\rho C_i)}{\partial z}\Big] \tag{2.7.1}$$

$$\frac{\partial(\rho C_i)}{\partial t} + \mathbb{R}_o\Big[\frac{\partial(\rho C_i\, u)}{\partial x} + \frac{\partial(\rho C_i\, v)}{\partial y} + \frac{\partial(\rho C_i\, w)}{\partial z}\Big] - \mathbb{R}_{op}\Big[\frac{\partial(\rho C_i\, w_{s_i})}{\partial z}\Big] = \frac{\mathbb{E}_{kh}}{\mathbb{S}_{ch}}\frac{\partial}{\partial x}\Big[\mathcal{D}_h \frac{\partial(\rho C_i)}{\partial x}\Big] + \frac{\mathbb{E}_{kh}}{\mathbb{S}_{ch}}\frac{\partial}{\partial y}\Big[\mathcal{D}_h \frac{\partial(\rho C_i)}{\partial y}\Big] + \frac{\mathbb{E}_{kv}}{\mathbb{S}_{cv}}\frac{\partial}{\partial z}\Big[\mathcal{D}_v \frac{\partial(\rho C_i)}{\partial z}\Big] \tag{2.7.2}$$

where: w_{s_i} is the gravitational settling velocity of the particular sediment particle, $\mathbb{R}_{op}$ is the particle Rossby number that is equal to w_{sr}/fZ_r, w_{sr} is a reference gravitational settling velocity, and $\mathcal{D}_h$ and $\mathcal{D}_v$ are the horizontal and vertical turbulent mass diffusivities. The volumetric concentration is defined as the ratio of the mass of the "i-th" sediment class contained within the differential volume $d\forall$ $(\rho C_i\, d\forall)$ to the total mass $(\rho\, d\forall)$ of the differential volume. The mixture density of the water and the suspended sediments is determined according to Zhou and McCorquodale [1992]:

$$\rho = \rho_m = \rho_w + C\,(1 - \frac{1}{S_p - 1}) \tag{2.7.3}$$

The vertical and lateral boundary conditions for equation 2.7.1 represent the rates at which the sediments enter or leave the water column. They are similar to those defined for the general scalar

transport (Section 2.1.3):

$$\left.\begin{array}{ll} \underline{\text{vertical boundary conditions}} & \underline{\text{lateral boundary conditions}} \\ \mathcal{D}_{\text{v}}\Big[\dfrac{\partial(\rho C_i)}{\partial z}\Big]_{\zeta} = 0 & \mathcal{D}_{\text{h}}\,\dfrac{\partial(\rho C_i)}{\partial n} = \boldsymbol{S_{s_i}} + \boldsymbol{S_{ri}} \\ \mathcal{D}_{\text{v}}\Big[\dfrac{\partial(\rho C_i)}{\partial z}\Big]_{-h} = \boldsymbol{S_{e_i}} - \boldsymbol{S_{d_i}} & \end{array}\right\} \tag{2.7.4}$$

The source terms $\boldsymbol{S_{e_i}}$ and $\boldsymbol{S_{d_i}}$ (defined for a particular size class) represent the entrainment of the bottom sediments into suspension and the differential settling of the sediments into the bottom, respectively. Both of these terms are evaluated at a near-bed point some small distance α above the bottom (Section 2.7.3) and are null elsewhere. The lateral source term $\boldsymbol{S_{s_i}}$ represents the rate at which the eroded shoreline sediments enter the water column and the term $\boldsymbol{S_{ri}}$ defines the sediment riverine inputs. Both terms are evaluated at the cell points neighboring the lateral boundaries (shoreline) and they are null elsewhere.

The vertical source terms are defined (Spasojevic and Holly, Jr [1994]) as:

$$\boldsymbol{S_{e_i}} = -\beta_i\Big[\mathcal{D}_{\text{v}}\frac{\partial(\rho C_i)}{\partial z}\Big]_{\alpha} = -\beta_i\,\mathcal{D}_{\text{v}}|_{\alpha}\,\frac{(\rho C_i)_{\alpha+\Delta\alpha} - (\rho C_i)_{\alpha}}{\Delta\alpha} \tag{2.7.5}$$

$$\boldsymbol{S_{d_i}} = \Big[\rho C_i\, w_{s_i}\Big]_{\alpha+\Delta\alpha} \tag{2.7.6}$$

where, $(\rho C_i)_{\alpha} \geq (\rho C_i)_{\alpha+\Delta\alpha}$, β_i is the size fraction of the "i-th" sediment class size currently present in the bed material ($\sum_{i=1}^{N}\beta_i = \sum_{i=1}^{n_s}\beta_i = 1$) and N is the total number of the sediment class sizes in the bed material. The concentration $(\rho C_i)_{\alpha+\Delta\alpha}$ is evaluated using a simple linear extrapolation from the two vertical cell points nearest to the bed surface, while the near-bed concentration $(\rho C_i)_{\alpha}$ is calculated in a way to reflect the near-bed flow conditions and the bedload particles at the specified bed surface location as described in Section 2.7.3.

2.7.3 Mobile Bed Model

The mobile bed model is an essential component of M^2SED and it is used to: *(a)* estimate the entrainment rates of the bottom sediments from the elemental control volume ($\Delta\forall$) via an excess shear stress formulation (Figure 2.2), and *(b)* quantitatively describe the bottom topography as the bed level and its composition change through differential settling, hydraulic sorting and armoring.

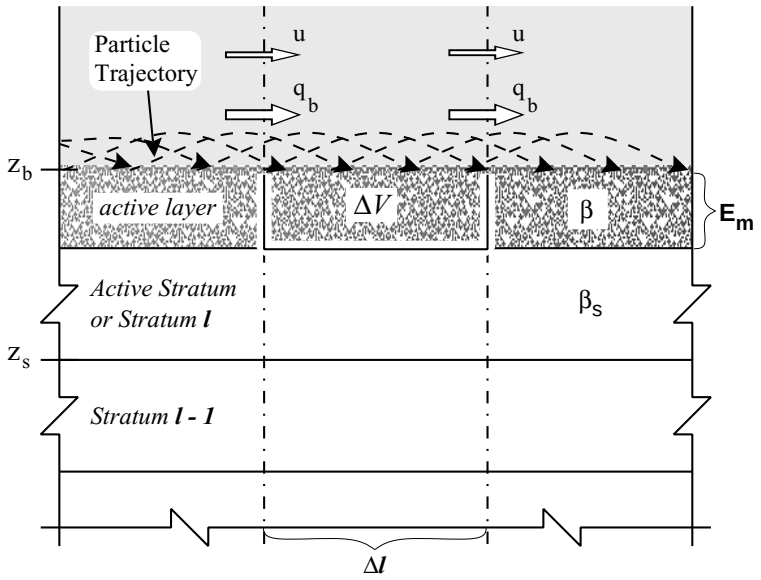

Figure 2.2 Definition of the bed material elemental control volume used in the mobile bed model.

The horizontal dimensions (Δl) of the elemental control volume must satisfy the condition that Δl is greater than the average saltation length and, therefore, in this case the bedload flux simply represents the bedload exchange between two adjacent elemental volumes (Spasojevic and Holly, Jr [1994]). Given the horizontal resolution of the hydrodynamic models, this condition is easily fullfilled. As shown in Figure 2.2, the soil below the bed surface is defined to consist of a series of layers or elemental control volumes of variable thicknesses (user input).

The first layer (next to the bed surface) is called the “active layer”, while the rest of the layers follow the naming convention “stratum 1”, “stratum 2”, and so on. The active layer is the one that exchanges sediment particles with the water column, while stratum 1 or “active stratum” exchanges sediment particles with the active layer. The exchange of the sediment material continues as long as there are strata. As the thickness of the active layer reduces, part of the active stratum becomes part of the active layer and, therefore, the sediment composition of the active layer sediments changes. In the case that the active stratum material is exhausted, its role is assumed by the next stratum.

The exchange of the sediments between the active layer and the active stratum is parametrized by the source term $\boldsymbol{S_f}$ that can be defined by writing the conservation of mass for each sediment size class currently in the active stratum (Spasojevic and Holly, Jr [1994]):

$$\boldsymbol{S}_{f_i} = -\rho_s (1 - p) \frac{\partial}{\partial t} [\beta_{s_i} (z_b - E_m)] \tag{2.7.7}$$

where: β_{s_i} is the sediment class size fraction currently present in the active stratum ($\sum_{i=1}^{M} \beta_{s_i} = \sum_{i=1}^{n_s} \beta_{s_i} = 1$), M is the total number of the sediment class sizes currently present in the active stratum, z_b is the bed elevation and E_m is the thickness of the active layer. The summation of equation 2.7.7 over the total number of the size fractions n_s yields:

$$\boldsymbol{S_f} = \sum_{i=1}^{n_s} \boldsymbol{S_{f_i}} = -\rho_s (1-p) \frac{\partial (z_b - E_m)}{\partial t} \tag{2.7.8}$$

The distribution of the bottom sediments can be determined by writing the governing equation for the conservation of mass for a particular sediment size class currently at the bottom. Let $\vec{U}_b = U_{bx} \cdot \vec{\imath} + U_{by} \cdot \vec{\jmath}$ be the velocity vector that describes the horizontal movement of the bedload (vertically averaged velocity over E_m), $Q_b = \rho_s (1-p) \beta E_m$ be the bottom sediment mass per unit horizontal area and $\vec{q}_b = Q_b \cdot \vec{U}_b$ be the vector describing the horizontal bedload flux. Neglecting the diffusion terms (there is no diffusion for the bottom sediments), the equation for the conservation of mass of the "i-th" sediment class currently present in the active layer is written as (Spasojevic and Holly, Jr [1994]):

$$\rho_s (1-p) \frac{\partial (\beta_i E_m)}{\partial t} + \frac{\partial q_{b_i x}}{\partial x} + \frac{\partial q_{b_i y}}{\partial y} = -\boldsymbol{S_{e_i}} + \boldsymbol{S_{d_i}} + \boldsymbol{S_{f_i}} \tag{2.7.9}$$

where: ρ_s is the density of the sediments and p is the porosity of the bed material. The summation of equation 2.7.9 over the total number of the size fractions gives the following equation:

$$\rho_s (1-p) \frac{\partial E_m}{\partial t} + \sum_{i=1}^{n_s} \left(\frac{\partial q_{b_i x}}{\partial x} + \frac{\partial q_{b_i y}}{\partial y} + \boldsymbol{S_{e_i}} - \boldsymbol{S_{d_i}} \right) = \boldsymbol{S_f} \tag{2.7.10}$$

Combining equations 2.7.8 and 2.7.10, the global equation (all sizes) for the change of the bed elevation is derived:

$$\rho_s (1-p) \frac{\partial z_b}{\partial t} + \sum_{i=1}^{n_s} \left(\frac{\partial q_{b_i x}}{\partial x} + \frac{\partial q_{b_i y}}{\partial y} + \boldsymbol{S_{e_i}} - \boldsymbol{S_{d_i}} \right) = 0 \tag{2.7.11}$$

The active layer thickness is calculated during the current time step computations using the conceptual equation:

$$E_m = -c \left(z_b^{n+1} - z_b^n \right) \tag{2.7.12}$$

where, c is a proportionality constant and z_b^n is the bed elevation at time n. In the case that the bed elevation difference over the current time step approaches zero, the following armor layer thickness

equation is used (Spasojevic and Holly, Jr [1994]):

$$E_{\mathrm{m}} = -c\,(z_{\mathrm{b}}^{n+1} - z_{\mathrm{b}}^{n}) + \frac{1}{\sum_{i=m}^{n_s} \beta_{s_i}} \frac{d_{sm}}{1-\mathrm{p}} \tag{2.7.13}$$

with d_{sm} being the smallest non-moving size class.

The net bedload flux for the particular size class q_{b_i} is calculated as a function of the theoretical net bedload flux q_{tb_i}, adjusted by: *(a)* a hiding factor ζ_{h_i} that accounts for the change of the transport rate of the particular size class when it is a part of a mixture, *(b)* a transport mode allocation parameter γ_{t_i} that accounts for the fact that some fraction of the particular size class particles is transported as suspended load, and *(c)* the particular size class fraction that denotes the availability of that class in the active layer (van Rijn [1984b]):

$$q_{\mathrm{b}_i} = (1-\gamma_{\mathrm{t}_i})\,\zeta_{\mathrm{h}_i}\,\beta_i\,q_{\mathrm{tb}_i} \tag{2.7.14}$$

In the above equation, the parameter γ_{t_i} is calculated from equation 2.8.6

2.8 Definition of the Sediment Transport Related Parameters

The bottom shear stress u_* is calculated in M^2COPS using the combined effects of the waves and the currents, as described in Chapter 6, and the same is true for all the significant M^2SED parameters. For example, in equation 2.1.16, the shear stress τ_b is calculated using a drag law where the coefficient $\mathrm{C_D}$ is a function of the bottom roughness height z_{o}, which is calculated as a function of the wave induced bottom physical roughness k_{b}.

2.8.1 Bottom Roughness Height

The bottom roughness height within the modeling framework of the Standard Model is a user input variable. In M^2COPS the term is evaluated based on the newest formulations of the bottom roughness height by van Rijn [2007a]. The roughness height is defined in terms of the bottom physical roughness k_{b} as:

$$z_{\mathrm{o}} = \frac{k_{\mathrm{b}}}{30} \tag{2.8.1}$$

where, the roughness k_{b} is calculated using the van Rijn [2007a] formulation as a function of the local flow conditions and the bed material.

The formulation detailed next assumes a general bottom profile that consists from: *(a)* small scale ripples, *(b)* ripples with length scales in the order of the water depth (also known as mega ripples), and *(c)* dunes that have length scales larger than the water depth. Mega ripples and dunes are assumed to be present in water depths $D > 1$ m (van Rijn [2007a]). It is also assumed that mega ripples and dunes are absent in the case that the bed consists only from silt and clay size sediments. The definition of the bottom physical roughness is given separately for "current only" and "wave only" conditions, according to the formulations suggested by van Rijn. The "current only" related physical roughness k_{bc} is given as:

$$k_{bc} = \left(k_{bcr}^2 + k_{bcmr}^2 + k_{bcd}^2\right)^{1/2} \tag{2.8.2}$$

where k_{bcr} is the contribution to k_{bc} due to small scale ripples, k_{bcmr} is the contribution due to mega ripples and k_{bcd} is the dune related bottom physical roughness. Following van Rijn, the three physical roughnesses are defined by empirical equations as follows:

$$k_{bcr} = f_{cs}\, d_{50} \left\{85 - 65 \tanh\left[0.015\,(\Psi - 150)\right]\right\} \qquad d_{50} \geq d_{silt} \tag{2.8.3a}$$

$$k_{bcr} = 20\, d_{silt} \qquad d_{50} < d_{silt} \tag{2.8.3b}$$

$$\Psi \leq 550: \qquad k_{bcmr} = 0.00002\, f_{fs}\, D \left\{1 - \exp\left(-0.05\,\Psi\right)\right\} (550 - \Psi) \tag{2.8.4a}$$

$$\Psi > 550: \qquad k_{bcmr} = 0.02\,; \qquad d_{50} \geq 1.5\, d_{sand} \tag{2.8.4b}$$

$$\Psi > 550: \qquad k_{bcmr} = 200\, d_{50}\,; \qquad d_{50} < 1.5\, d_{sand} \tag{2.8.4c}$$

$$k_{bcmr} = 0\,; \qquad d_{50} < d_{silt} \tag{2.8.4d}$$

$$\Psi \leq 600: \qquad k_{bcd} = 0.00008\, f_{fs}\, D \left\{1 - \exp\left(-0.02\,\Psi\right)\right\} (600 - \Psi) \tag{2.8.5a}$$

$$\Psi > 600: \qquad k_{bcd} = 0 \tag{2.8.5b}$$

$$k_{bcd} = 0\,; \qquad d_{50} < d_{silt} \tag{2.8.5c}$$

$$f_{cs} = \begin{cases} \left(0.25\, \dfrac{d_{gravel}}{d_{50}}\right)^{3/2} & d_{50} > 0.25\, d_{gravel} \\ 1 & d_{50} \leq 0.25\, d_{gravel} \end{cases} \qquad f_{fs} = \begin{cases} \dfrac{d_{50}}{1.5\, d_{sand}} & d_{50} < 1.5\, d_{sand} \\ 1 & d_{50} \geq 1.5\, d_{sand} \end{cases} \tag{2.8.6}$$

$$\Psi = \frac{U_{cw}^2}{g\,(S_p - 1)\,d_{50}}\ ; \qquad U_{cw}^2 = U_c^2 + U_{wb}^2 \tag{2.8.7}$$

where, D is the water depth, $d_{silt} = 0.000032$ m, $d_{sand} = 0.000062$ m, $d_{gravel} = 0.002$ m, d_{50} is the median diameter of the bed material, Ψ is the current-wave mobility parameter, U_c is the vertically averaged current velocity and U_{wb} is the near bottom peak wave orbital velocity. The definition of k_{bc} by equations 2.8.3a through 2.8.7 assumes a horizontal dependence on the local flow conditions, an approach that is physically more sound since the bed profile evolution is a function of the local flow conditions in addition to the bed composition.

The wave induced bottom physical roughness is related to the flow separation and vortex shedding due to the wave motion (van Rijn [2007a]), therefore, it is related to the small scale ripples only. It is suggested by van Rijn that the wave induced bottom physical roughness (k_{bw}) can be estimated by:

$$k_{bw} = k_{bcr} \tag{2.8.8}$$

Combining the results of the above discussion, the current friction coefficient f_c is calculated using k_{bc}, while the wave related friction coefficient f_w is calculated using $k_{bw} = k_{bcr}$.

2.8.2 Bottom Sediments – Initiation of Motion

The shear stresses that the flow field above the bed experiences are highly correlated to the bed formations (form drag) (Grant and Madsen [1982], Glenn and Grant [1987], Styles and Glenn [2002]), rather than the skin friction produced by the sediment particles. The calculation of k_b described in the previous Section is, therefore, only used in the determination of z_o and subsequently in the calculation of the shear stresses relevant to the overlying flow field.

The shear stresses required for the initiation of the motion of the bottom sediments and the calculation of the bed load transport and the near bed reference sediment concentration are related to the skin friction, which depend upon the local flow conditions and the type of material comprising the bed sediments. All the subsequent calculations are based on the Shields parameter (dimensionless particle size):

$$D_{*i} = d_{si}\left[\frac{g\,(S_p - 1)}{\nu^2}\right]^{1/3} \tag{2.8.9}$$

where d_{s_i} is a designated sediment particle diameter representing a particular sediment class, ν is the water viscosity and $S_p = \rho_s/\rho$ is the specific gravity of the sediments. The critical Shields shear stress $\tau_{cr,s}$ depicting the initiation of the motion of the sediment particles d_{s_i} is defined and is given by:

$$\tau_{cr,s} = \theta_{cr,s}\,\rho_w\,g\,(S_p - 1)\,d_{s_i} \tag{2.8.10}$$

where $\theta_{cr,s}$ is the Shields parameter determined from the Shields diagram (Vanoni [1977]) and computationally can be estimated using either the Soulsby-Whitehouse equation (Soulsby [1997]) or the van Rijn equations (van Rijn [1984a, 2007a]):

Soulsby equation:
$$\theta_{cr,s} = \frac{0.30}{1 + 1.2\,D_{*_i}} + 0.55\left[1 - \exp\left(-0.020\,D_{*_i}\right)\right] \tag{2.8.11}$$

van Rijn equations:
$$\theta_{cr,s} = 0.115\,D_{*_i}^{-0.5}\ ; \qquad D_{*_i} < 4 \tag{2.8.12a}$$
$$\theta_{cr,s} = 0.14\,D_{*_i}^{-0.64}\ ; \qquad 4 \le D_{*_i} < 10 \tag{2.8.12b}$$
$$\theta_{cr,s} = 0.04\,D_{*_i}^{-0.10}\ ; \qquad 10 \le D_{*_i} < 20 \tag{2.8.12c}$$
$$\theta_{cr,s} = 0.013\,D_{*_i}^{0.29}\ ; \qquad 20 \le D_{*_i} < 150 \tag{2.8.12d}$$
$$\theta_{cr,s} = 0.055\ ; \qquad D_{*_i} \ge 150 \tag{2.8.12e}$$

where both the Soulsby and van Rijn equations give $\theta_{cr,s} = 0.055$ for $D_{*_i} = 200$. Equations 2.8.11 through 2.8.12e assume a flat bed therefore, their application over rippled beds can only be used for the calculation of the grain related, skin friction coefficients. Both options are available in M^2COPS. To account for the effects of the cohesive forces and the packing effects on τ_{cr}, van Rijn [2007a] suggests that the Shields critical stress should be adjusted as follows:

$$\tau_{cr} = \left(\frac{d_{sand}}{d_{50}}\right)^{0.5}\tau_{cr,s} \quad \text{for:} \quad d_{50} < 62\,\mu\text{m}\ ; \qquad \tau_{cr} = \left(1 + P_{cs}\right)\tau_{cr,s} \quad \text{for:} \quad d_{50} \ge 62\,\mu\text{m} \tag{2.8.13}$$

The parameter P_{cs} is defined as the portion of clay ($d_{s_i} < 8\,\mu$m) fraction of the bed material, which for $P_{cs} \approx 0$ and $d_{50} \ge 62\,\mu$m gives: $\tau_{cr} = \tau_{cr,s}$. It is noted here that ρ_w in equation 2.8.10 is the water reference density, possibly affected by the variations of temperature and salinity, and it is calculated from the equation of state (Section 2.2). The initiation of the motion of the bottom sediments is computationally controlled by the dimensionless shear parameter, also known as the

transport stage parameter (van Rijn [2007b], Soulsby [1997], Chapman et al. [1996]):

$$T_i = \frac{u^2_{*cw_i} - u^2_{*\mathrm{cr}_i}}{u^2_{*\mathrm{cr}_i}} = \frac{\tau_{cw_i} - \tau_{\mathrm{cr}_i}}{\tau_{\mathrm{cr}_i}} \tag{2.8.14}$$

where the subscript i refers to the sediment class "i" designated with the particle diameter d_{s_i} and τ_{cw_i}, τ_{cr_i} are the grain related wave-current enhanced, and Shields critical shear stresses respectively. The motion of the sediment particle d_{s_i} commences when $T_i > 0$, while it remains immobile for $T_i \leq 0$. Equation 2.8.14 is suggested in van Rijn [2007b] and van Rijn [2007c] and it is adopted in *M*^{2}*COPS* as well. Both τ_{cw_i} and τ_{cr_i} are defined as time averaged shear stresses with the magnitude of τ_{cw_i} determined by assuming co-linear and co-directional current and wave only shear stress components (maximum effect). The wave-current shear stress is calculated as:

$$\tau_{cw_i} = \frac{1}{2}\, f_{cw_i}\, \rho_{\mathrm{w}}\, U^2_{wb} \tag{2.8.15a}$$

where U_{wb} is the near bottom wave orbital velocity and the friction factor f_{cw_i} is calculated as suggested in van Rijn [2007a] and Madsen [1994]:

$$f_{cw_i} = (1 - \alpha)\, f_{w_i} + \alpha\, f_{c_i} \tag{2.8.15b}$$

where α is defined as the relative strength of the currents and the waves and it is calculated as:

$$\alpha = \frac{|\mathcal{u}|}{|\mathcal{u}| + U_{wb}} \tag{2.8.15c}$$

The inclusion of the Lagrangian velocity $|\mathcal{u}|$ instead of the flow velocity $|\boldsymbol{u}|$ is a consequence of the present work. It is suggested here, that since all bottom shear stress calculations are performed by matching the flow velocities at the top of the bottom wave-current boundary layer, the same approach can be used for the calculation of α as well. This approach will include the effects of Eulerian streaming (as defined at the top of the *WCBBL*), see Davies and Villaret [1999], Marin [2004] and Mellor [2002]. Therefore, the proposed expression for α is:

$$\alpha = \frac{|\mathcal{u}|_\delta}{|\mathcal{u}|_\delta + U_{wb}} \tag{2.8.15d}$$

where $\mathcal{u}_\delta$ is the magnitude of the Lagrangian flow velocity at the top of the *WCBBL* (practically is calculated at the half grid point above the bottom) and U_{wb} is the near bottom wave peak orbital velocity. In the absence of waves, it is $\alpha = 1$. The f_{w_i} coefficient in equation 2.8.15b is calculated using equations 6.7.12 and 6.7.13, by using $k_{\mathrm{b}} = d_{90}$ (van Rijn [2007a]).

The current related friction coefficient f_{c_i} is calculated as:

$$f_{c_i} = \frac{8g}{\mathbb{C}_{\mathbb{Z}}^2} \; ; \qquad \mathbb{C}_{\mathbb{Z}} = 18 \log_{10}\left(\frac{12D}{d_{90}}\right) \tag{2.8.16}$$

The second of equations 2.8.16 is the result of the recent work of van Rijn [2007a], that introduces a slightly different definition of the Chezy coefficient $\mathbb{C}_{\mathbb{Z}}$ than the one defined in van Rijn [1984b].

2.8.3 Bottom Reference Sediment Concentration

The near bed reference concentration is formulated to also account for the wave-current interactions, such that the resulting concentration profiles fully include the wave induced effects. The near bed reference concentration for the sediment class "i", C_{α_i} is defined as (van Rijn [2007c]):

$$C_{\alpha_i} = 0.015 \, f_{s_i} \frac{d_{s_i}}{\alpha} \frac{T_i^{1.5}}{D_{*i}^{0.3}} \; ; \qquad C_{\alpha_i} \leq 0.05 \;\; (\sim 130\,\mathrm{kg/m^3}) \tag{2.8.17a}$$

$$f_{s_i} = \frac{d_{sand}}{d_{s_i}} \qquad \text{and:} \qquad f_{s_i} = 1 \quad \text{for} \quad d_{s_i} \geq d_{sand} \tag{2.8.17b}$$

where α is the height above the bed where the near bed sediment concentration is evaluated and it is given by:

$$\alpha = \max\left[0.01\,\mathrm{m}, \; \frac{1}{2} k_{bcr}, \; \frac{1}{2} k_{bw}\right] \tag{2.8.18}$$

and f_{s_i} is a silt factor that accounts for the increased C_{α_i} of the small sediment particles ($d_{s_i} < d_{sand}$). The difference between the original equation of van Rijn [1984b] and equation 2.8.17a is just the silt factor f_{s_i}. Equation 2.8.17a is the one adopted in M^2COPS, since it has been more thoroughly evaluated (van Rijn [2007b] and van Rijn [2007c]) using additional datasets.

2.8.4 Suspended Sediment Parameters

The suspended sediment calculations in M^2COPS are controlled by: *(a)* the mass diffusivity $\mathcal{D}_v$, and *(b)* the sediment particle settling velocity w_{s_i}. The mass diffusivity is defined in van Rijn [1984b] and van Rijn [2007b] as:

$$\mathcal{D}_v = \Phi_d \, \beta_d \, \mathcal{A}_v \tag{2.8.19}$$

where in van Rijn [2007b], $\mathcal{A}_v$ is calculated using empirical functions. In M^2COPS, the vertical diffusion coefficient $\mathcal{A}_v$ is directly calculated from the turbulence model (Chapter 7), while the horizontal mass diffusivity $\mathcal{D}_h$ is held constant (a user supplied value). The effects of the sediments

on the mass diffusion coefficient are expressed by: *(a)* the factor Φ_{d}, which accounts for the sediment stratification, and *(b)* the factor β_{d}, which accounts for the difference in diffusion between a discrete sediment particle and a fluid particle. These two factors are calculated using the van Rijn empirical equations (van Rijn [1984b], van Rijn [2007b]) as follows:

$$\beta_{\mathrm{d}} = \beta_{cw_i} = 1 + 2\left(\frac{w_{\mathrm{s}_i}}{u_{*cw}}\right)^2 \tag{2.8.20a}$$

$$\left.\begin{aligned} \Phi_{\mathrm{d}} &= \Phi_{\mathrm{fs}}\left[1 + \left(\frac{C}{C_{\mathrm{o}}}\right)^{0.8} - 2\left(\frac{C}{C_{\mathrm{o}}}\right)^{0.4}\right] \\ \Phi_{\mathrm{fs}} &= 1 \quad \text{for} \quad d_{50} \geq 1.5 d_{sand} \\ \Phi_{\mathrm{fs}} &= \frac{d_{50}}{d_{sand}} \quad \text{for} \quad d_{50} < 1.5 d_{sand} \end{aligned}\right\} \tag{2.8.20b}$$

where C is the total volumetric concentration of the suspended sediments and C_{o} is the maximum volumetric concentration set in M^2COPS equal to: $C_{\mathrm{o}} = 0.65$. Equations 2.8.20b are the van Rijn [2007b] empirical equations that account for the turbulence damping by the sediments, while the factor Φ_{fs} accounts for the presence of wash load (very fine sediments).

The functional form of β_{cw_i} is similar to the expressions used in van Rijn [2007b], for "current-only" and "wave-only" conditions and the same form has been adopted in M^2COPS to account for the combined effects of the currents and the waves. In the absence of waves, $u_{*cw} = u_{*c}$ and in the absence of currents, $u_{*cw} = u_{*w}$, that is, in any case the effects of the flow field are reflected in β_{d} through the model calculated total bottom shear stress (see Chapter 6).

2.8.5 Settling Velocity

The particle settling velocities w_{s_i} are calculated as functions of their respective particle diameters as follows:

$$w_{\mathrm{s}_i} = \frac{1}{18}\frac{g\,(\mathrm{S_p} - 1)\,d_{\mathrm{s}_i}^2}{\nu} \quad \text{for} \quad d_{\mathrm{s}_i} < 100\,\mu\mathrm{m} \tag{2.8.21}$$

$$w_{\mathrm{s}_i} = 10\frac{\nu}{d_{\mathrm{s}_i}}\left[\sqrt{1 + \frac{0.01\,g\,(\mathrm{S_p} - 1)\,d_{\mathrm{s}_i}^3}{\nu^2}} - 1\right] \quad \text{for} \quad 100\,\mu\mathrm{m} \leq d_{\mathrm{s}_i} \leq 1000\,\mu\mathrm{m} \tag{2.8.22}$$

$$w_{\mathrm{s}_i} = 1.1\sqrt{g\,(\mathrm{S_p} - 1)\,d_{\mathrm{s}_i}} \quad \text{for} \quad d_{\mathrm{s}_i} > 1000\,\mu\mathrm{m} \tag{2.8.23}$$

where d_{s_i} is the sediment particle diameter, ν is the kinematic viscosity of the clear water and S_p is the specific gravity of the sediments taken equal to 2.65 (quartz sediments). The kinematic viscosity in M^2COPS is considered to be a function of T, S and p and is determined by the methods described in Section 2.3.2 or it can be held constant (user input). The settling velocities of the sediment particles are further adjusted (van Rijn [2007b]) to account for: *(a)* the flocculation effects represented by the factor Φ_{floc}, and *(b)* the effects of hindered settling in high sediment concentrations represented by the factor Φ_{hs}:

$$w_{s_i} = \Phi_{floc}\, \Phi_{hs}\, w_{s_i,o} \tag{2.8.24}$$

where $w_{s_i,o}$ is the sediment particle settling velocity, as calculated from equations 2.8.21, 2.8.22 and 2.8.23. The two factors are estimated as:

$$\left.\begin{aligned} \Phi_{floc} &= \left[4 + \log_{10}\left(2\,\frac{d_{sand}}{d_{50}}\,\frac{C}{C_o}\right)\right]^{\alpha} \\ \alpha &= \frac{d_{sand}}{d_{50}} - 1 \qquad \begin{cases} \alpha_{min} = 0 \\ \alpha_{max} = 3 \end{cases} \\ \Phi_{floc}^{min} &= 1 \quad \text{and} \quad \Phi_{floc}^{max} = 10 \end{aligned}\right\} \tag{2.8.25}$$

$$\Phi_{hs} = (1 - \frac{d_{sand}}{d_{50}\, C})^5 \tag{2.8.26}$$

2.8.6 Bed Load Parameters

The theoretical bed load sediment flux q_{tb_i} is calculated using the van Rijn [1984b] empirical equation, slightly adjusted to include the silt factor f_{s_i} to be consistent with equation 2.8.17a:

$$q_{tb_i} = 0.053\, f_{s_i}\, \rho_s\, [g\,(S_p - 1)\,]^{1/2}\, \frac{d_{s_i}^{3/2}}{D_{*i}^{0.3}}\, T_i^{2.1} \tag{2.8.27}$$

where f_{s_i} is calculated from equation 2.8.17b and the transport stage parameter T_i is determined from equation 2.8.14. The remaining parameters appearing in equation 2.7.14 are calculated using the empirical equations presented in van Rijn [1984b]:

$$\zeta_{h_i} = \left(\frac{d_{s_i}}{d_{s50}}\right)^{0.85} \tag{2.8.28}$$

$$\gamma_{t_i} = 0.25 + 0.325 \ln\left(\frac{u_*}{w_{s_i}}\right); \qquad 0.4 < \frac{u_*}{w_{s_i}} < 10 \tag{2.8.29}$$

The two horizontal components $q_{b_i x}$ and $q_{b_i y}$ are calculated using the two components of the total bottom shear stress as follows:

$$q_{b_i x} = q_{b_i} \frac{\tau_{bx}}{\left[\tau_{bx}^2 + (\tau_{by}^2\right]^{1/2}}; \qquad q_{b_i y} = q_{b_i} \frac{\tau_{by}}{\left[(\tau_{bx}^2 + (\tau_{by}^2\right]^{1/2}} \tag{2.8.30}$$

where the wave-current induced bottom shear stress is calculated by the methods described in Chapter 6.

2.9 Standard Numerical Algorithms and Model Stability

Regarding the advective terms in the momentum equations, Roache's second order upwind differencing scheme (Roache [1972]) is used for the discretization of these terms. The advective terms in the temperature, salinity and sediment concentration equations are discretized using Leonard's QUICKEST scheme, generalized for the 3D curvilinear coordinates. QUICKEST is a spatially third order scheme and conditionally stable for Courant numbers, $C_r = \frac{|\boldsymbol{u}|\Delta t}{\Delta x}$, less than one (Leonard [1979]).

Roache's upwind scheme, used in the discretization of the advection terms, is conditionally stable for $C_r \leq 1$ (Roache [1972]). The discretization of the diffusion terms uses the Crank-Nicholson fully explicit scheme, which is conditionally stable for: $\mathcal{B}\frac{\Delta t}{(\Delta x)^2} \leq \frac{1}{2}$. This condition is much less restrictive than the one related with the advective terms and, therefore, the overall stability of the hydrodynamic and sediment models is controlled by the Courant-Friedrich's-Lewy (*CFL*) condition:

$$C_r = \frac{|\boldsymbol{u}|\Delta t}{\Delta x} \leq 1 \tag{2.9.1}$$

There are situations where the model calculates unstable free water surface elevations, usually attributed to Courant numbers reaching values close or even greater than unity. Whenever higher time steps are chosen, to avoid demanding *CPU* times, along with more refined horizontal grid resolution, the *CFL* condition (equation 2.9.1) is often violated.

Another important reason for model instability may be the development of supercritical or transitional flows ($\mathbb{F}_r \geq 1$), usually in bounded regions of the computational domain, since the model

is only capable in calculating slowly varying or subcritical flows. If this situation appears sporadically in the computational domain, major problems in the calculations do not appear, but if this is a consistent situation throughout the domain, then the model becomes unstable.

Situations where supercritical flows can appear during the calculation of subcritical flows are largely related to poorly incorporated data for either the initial conditions or for the calculation of the bottom friction coefficient. It is common to have supercritical regions in the computational domain during the initial "spin-up" or stabilization period for the model, when realistic boundary conditions are combined with exact, but unrealistic initial conditions (e.g., $u = 0, \zeta = 0$).

The appearance of regions with high Froude numbers, possibly responsible for the violation of the *CFL* condition, can be caused by the calculation of artificially small bottom friction coefficients, especially in the shallow water areas. The bottom friction coefficient is calculated in the model using the maximum value between a user supplied constant friction coefficient value (C_D^u), typically equal to 0.003, and the one calculated from equation 2.1.20, that is $C_D = \max(C_D^u, C_D)$. If C_D^u is suitable for shallow water areas, then the model will overestimate the friction term in deeper waters and the opposite if so happens that the C_D^u supplied value is suitable for the deep water regions. To avoid these problems, it was decided to consistently use the spatially varying C_D as calculated by equation 2.1.20 by setting $C_D^u = 0$.

D (m)	$\Delta\sigma$	n_σ
5.0	0.0204	49
4.0	0.0255	39
3.0	0.0340	29
2.0	0.0510	20
1.0	0.1020	10
0.5	0.2040	5

Δx (m)	Δt (min)
2000	33
1000	17
500	8
100	2
50	0.8
10	0.2

Table 2.2 Suggested limiting values of the time step and the vertical grid resolution for the hydrodynamic model computations.

To ensure that the model stability criteria are not violated, various values of the vertical grid resolution and the time step are calculated as shown in Table 2.2. The vertical grid resolution is controlled by the cell Froude number, defined as: $\mathbb{F}_{rc} = \dfrac{U_{curr}^{max}}{(g\,\Delta z)^{1/2}} = \dfrac{U_{curr}^{max}}{(g\,\Delta\sigma\,D)^{1/2}} \leq 1$, and the time step should satisfy the *CFL* condition: $\Delta t \leq \Delta x / U_{curr}^{max}$. The expected maximum current velocity

U_{curr}^{max} is a design velocity taken equal to $1\,\mathrm{m/s}$, as it was decided after viewing the values of the surface currents for Lake Michigan reported at the GLCFS web site (http://www.glerl.noaa.gov/res/glcfs/).

The vertical grid resolution (in σ-coordinates) that is, $\Delta\sigma$ or n_σ (the total number of the σ vertical layers) is determined as: $\Delta\sigma \geq (U_{curr}^{max})^2/gD$ or $n_\sigma \leq g\,D/(U_{curr}^{max})^2$. The gravitational acceleration is set equal to: $g = 9.806119\,\mathrm{m/s^2}$.

CHAPTER 3

WIND WAVE MODELS

3.1 Surface Waves

Accurate prediction of near-shore and off-shore wind waves is essential for the correct modeling of the sediment transport. Correct examination of the near-shore plume must also include wave modeling that predicts the spectrum of wave magnitudes and directions in response to the passage of storms across the lake.

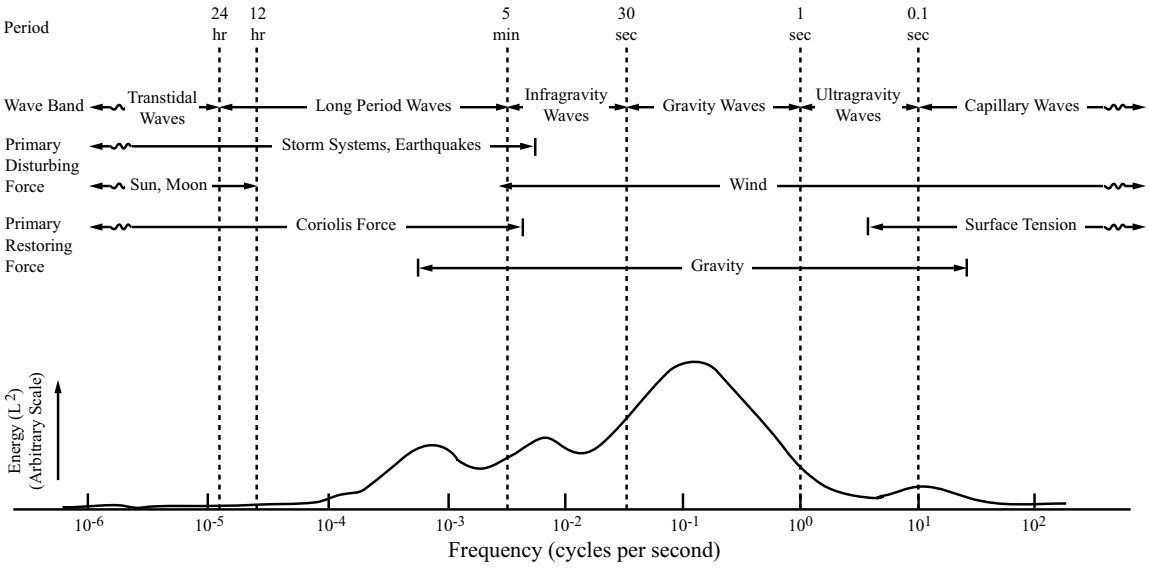

Figure 3.1 Schematic representation of the classification of the ocean waves (Kinsman [1984]).

A classification of the variety of the surface waves generated from the various physical mechanisms, as well as their restoring forces, is shown in Figure 3.1. In this Chapter the two wave models used in the present research are reviewed including, their governing equations, limitations and interactions with the hydrodynamic models.

3.2 Model Physics and Dynamics

The propagation of the wind generated, surface gravity waves is described in the newest, third-generation wave models, using the empirically validated statistical description of the waves. The statistical description of the waves is used as opposed to the traditional ray tracing techniques of the conventional wave models, because chaotic ray patterns cannot be evaluated on a time step by time step basis required here.

Let $\mathcal{E}(\vec{x},\vec{k},t)$ be the spectral wave energy (wave variance spectrum, m^2), $\mathring{\mathcal{E}}(\vec{x},\vec{k},t)$ be the wave variance density spectrum ($\mathrm{m}^2\mathrm{s}$), where $\vec{x}=(x_1,x_2)$ is the position vector either in plain Cartesian (x,y) or in geographical coordinates (λ,ϕ) and $\vec{k}=(k_1,k_2)$ is the wavenumber vector. The wavenumber k is the magnitude of $\vec{k}$ defined as: $k=\sqrt{k_1^2+k_2^2}=2\pi/L$ where, L (m) is the wavelength. Let f (s^{-1}) be the wave frequency defined as $f=1/T$, where T (s) is the wave period, ω (s^{-1}) be the wave angular or absolute frequency and $\mathring{\sigma}$ (s^{-1}) be the relative or intrinsic or Doppler shifted frequency, defined as a function of the wavenumber and the water depth D:

$$\mathring{\sigma}^2 = gk\tanh(kD) \tag{3.2.1}$$

The wave frequency f is related with $\mathring{\sigma}$ by the expression $\mathring{\sigma}=2\pi f$, while the two frequencies ω and $\mathring{\sigma}$ are related with the following dispersion relation $\mathbf{\Omega}$:

$$\omega=\mathbf{\Omega}(\vec{x},\vec{k},t)=\mathring{\sigma}+\vec{k}\cdot\hat{u}_{Av}\;;\qquad \hat{u}_A=\frac{1}{D}\int_{-h}^{\zeta}u(z)\zeta_s(z)\,dz=\int_{-1}^{0}u(\sigma)\zeta_s(\sigma)\,d\sigma \tag{3.2.2}$$

where, $\hat{u}_A$ is the Doppler velocity, u is the flow velocity and ζ_s is a vertical shape function defined as (Kirby and Chen [1989]): $\zeta_s(\sigma)=2kD\cosh\left[2kD\left(1+\sigma\right)\right]/\sinh 2kD$.

The Doppler velocity can be related to the vertically averaged flow velocity $\vec{U}=\bar{u}\,\vec{\imath}+\bar{v}\,\vec{\jmath}$, using the first mean value theorem of integral calculus (equation B.47). Choosing the two functions f and g to be equal to u and ζ_s, respectively, with the observation that: $\int_{-1}^{0}\zeta_s(\sigma)\,d\sigma=1$, the second of

equations 3.2.2 gives:

$$U = \int_{-1}^{0} u(\sigma)\,d\sigma = \frac{\int_{-1}^{0} u(\sigma)\zeta_s(\sigma)\,d\sigma}{\int_{-1}^{0} \zeta_s(\sigma)\,d\sigma} \approx \hat{u}_A = \int_{-1}^{0} u(\sigma)\zeta_s(\sigma)\,d\sigma \tag{3.2.3}$$

therefore, the dispersion relation 3.2.2 becomes:

$$\omega = \mathbf{\Omega}(\vec{x}, \vec{k}, t) = \mathring{\sigma} + \vec{k}\cdot\hat{u}_{Av} \approx \mathring{\sigma} + \vec{k}\cdot\vec{U} \tag{3.2.4}$$

which is the same expression for $\mathbf{\Omega}$ given in Komen et al. [1996] and is used here as well. In the absence of currents these two frequencies are equal (equation 3.2.4). As noted in Kirby and Chen, $\hat{u}_A = U + O((kD)^2)$ therefore, the error of the above approximation becomes significant as $kD \to \infty$.

Using the definitions of the wave frequencies and the dispersion relation 3.2.4, the spectral wave energy is described in wavenumber space as well as in phase space (ω, θ) or $(\mathring{\sigma}, \theta)$, where θ is the direction of the propagation ray measured clockwise from the true North (Figure 3.2). The two wave models considered here, calculate the wave spectra in the spectral space $(\mathring{\sigma}, \theta)$.

As noted in LeBlond and Mysak [1978], Komen et al. [1996], Mei [1983], the propagation speeds in the spatial and the spectral directions are connected with the dispersion relation as follows:

$$\frac{dx_i}{dt} = \frac{\partial \mathbf{\Omega}}{\partial k_i} \qquad \text{and} \qquad \frac{dk_i}{dt} = -\frac{\partial \mathbf{\Omega}}{\partial x_i}\,; \qquad i = 1, 2 \tag{3.2.5}$$

while the wave group velocity $\vec{c}_g$, and the average velocity of a travelling wave group are defined (Komen et al. [1996], Rogers et al. [1999]) as:

$$\vec{c}_g = \nabla_k \mathring{\sigma} = \frac{1}{k}\frac{\partial \mathring{\sigma}}{\partial k}\vec{k} = \frac{c_g}{k}\vec{k}\,; \qquad c_g = \frac{1}{2}\Big[1 + \frac{2kh}{\sinh 2kh}\Big]c\,; \qquad c = \frac{\mathring{\sigma}}{k} \tag{3.2.6}$$

$$\vec{k} = (k_1, k_2) = k\,(\sin\theta, \cos\theta) \tag{3.2.7}$$

where c is the wave phase speed.

3.3 Governing Equations

The propagation of the waves in the two third-generation wave action models employed in this research is governed by a 2D hyperbolic wave equation. The equation describes the conservation of

the wave action density along the path of the travelling waves and applies to both moving systems (e.g., presence of currents) and to stationary ones. The spectral wave action density $\mathcal{N}$ (m^2s), defined as $\mathcal{N}(x, y, \mathring{\sigma}, \theta, t) = \mathcal{E}(x, y, \mathring{\sigma}, \theta, t)/\mathring{\sigma}$, was chosen to represent the waves (instead of $\mathcal{E}$) since it is conserved in the presence of currents, while the spectral wave energy $\mathcal{E}$ is not (LeBlond and Mysak [1978], Whitham F. R. S. [1974]). As noted in Mei [1983], $\mathcal{N}$ is conserved either in the $(\mathring{\sigma}, \theta)$ phase space or in the (ω, θ) space and, therefore, in both cases the governing equation assumes a similar form. It is noted here that $\mathcal{N}$ and $\mathcal{E}$ represent the vertically averaged spectral wave action density and wave energy, respectively, both of which are defined in Chapter 4.

The models are designed to work on small to large geographic scale problems and to accommodate this fact, either the Cartesian or the spherical coordinate system can be used in the model calculations (the user can choose either one depending upon the problem scale). To be consistent with the formulation of the equations in the models, the governing and all relevant equations are presented in this Section in both coordinate systems. The conservation of the wave action density in Cartesian coordinates, as defined in Komen et al. [1996], The WAMDI Group [1988] and Booij et al. [2004] has the form:

$$\frac{\partial \mathcal{N}}{\partial t} + \frac{\partial (c_x \mathcal{N})}{\partial x} + \frac{\partial (c_y \mathcal{N})}{\partial y} + \frac{\partial (c_{\mathring{\sigma}} \mathcal{N})}{\partial \mathring{\sigma}} + \frac{\partial (c_\theta \mathcal{N})}{\partial \theta} = \frac{\boldsymbol{S}(x, y, \mathring{\sigma}, \theta)}{\mathring{\sigma}} \tag{3.3.1}$$

and its counterpart in spherical coordinates assumes the forms:

$$\frac{\partial \hat{\mathcal{N}}}{\partial t} + \frac{\partial (c_\lambda \hat{\mathcal{N}})}{\partial \lambda} + \frac{\partial (c_\phi \hat{\mathcal{N}})}{\partial \phi} + \frac{\partial (c_{\mathring{\sigma}} \hat{\mathcal{N}})}{\partial \mathring{\sigma}} + \frac{\partial (c_\theta \hat{\mathcal{N}})}{\partial \theta} = \frac{\boldsymbol{S}(\lambda, \phi, \mathring{\sigma}, \theta)}{\mathring{\sigma}} \tag{3.3.2a}$$

$$\frac{\partial \mathcal{N}}{\partial t} + \frac{\partial (c_\lambda \mathcal{N})}{\partial \lambda} + \frac{1}{\cos\phi} \frac{\partial (c_\phi \cos\phi\, \mathcal{N})}{\partial \phi} + \frac{\partial (c_{\mathring{\sigma}} \mathcal{N})}{\partial \mathring{\sigma}} + \frac{\partial (c_\theta \mathcal{N})}{\partial \theta} = \frac{\boldsymbol{S}(\lambda, \phi, \mathring{\sigma}, \theta)}{\mathring{\sigma}} \tag{3.3.2b}$$

where, $\hat{\mathcal{N}}(\lambda, \phi, \mathring{\sigma}, \theta, t)$ is the wave action density as expressed in spherical coordinates and it is related to $\mathcal{N}$ by the equation $\hat{\mathcal{N}} = \mathcal{N} R^2 \cos\phi$ (Komen et al. [1996]).

In equation 3.3.1 the variables c_x, c_y, $c_{\mathring{\sigma}}$ and c_θ represent the propagation speeds in the 4D space $(x, y, \mathring{\sigma}, \theta)$, while c_λ, c_ϕ, $c_{\mathring{\sigma}}$ and c_θ are their counterparts in spherical coordinates. The first term in the governing equations represents the local rate of change of wave action density, while the second and third terms represent the spatial propagation of the wave spectrum. The fourth term represents the changes of $\mathcal{N}$ as the relative frequency $\mathring{\sigma}$ changes, for example by unsteady water depths or currents. The last term represents the refraction of the waves by depth and currents. Figure 3.2

shows a conceptual visualization of the propagating waves in a Cartesian system and on the globe. As noted in Komen et al. [1996], on the globe the waves travel along a great circle path.

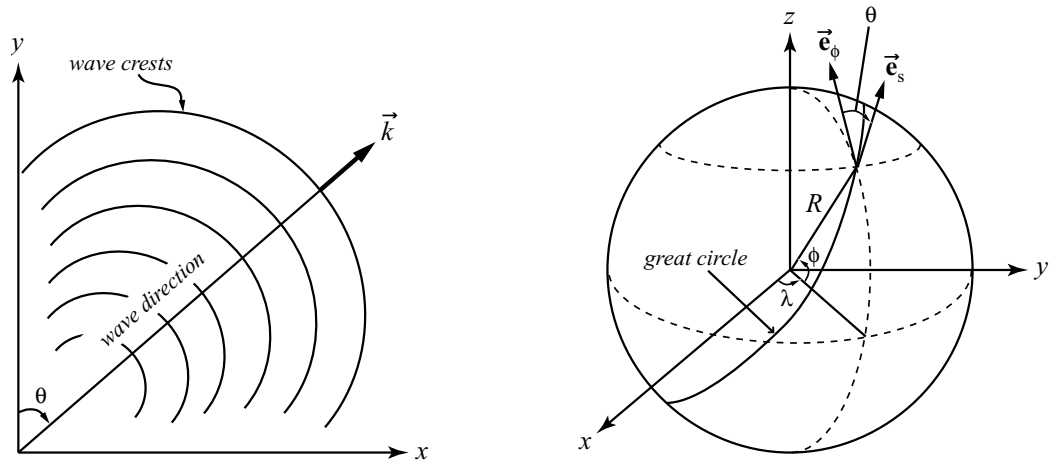

Figure 3.2 Conceptual representation of the propagation of a wave group in Cartesian coordinates.

The refraction of the waves, that is the change in direction due to depth changes or to the presence of currents or combination of both, is a phenomenon that occurs when waves are approaching shallow waters. When spherical coordinates are used for the calculation of the wave spectra, refraction terms also arise in deep water depths due to the wave propagation direction on the globe (Komen et al. [1996]). The term $\boldsymbol{S}$ in the r.h.s side of equation 3.3.1 represents all the sources or sinks considered in the formulation and they are discussed in Sections 3.4.1 and 3.5.1.

To complete the definitions of all the variables present in the governing equations, the relations for the propagation velocities need to be defined. First, two expressions for the total derivative operator are introduced, one for the 4-D space $(x_1, x_2, \mathring{\sigma}, \theta)$ and one for the 2D space (x_1, x_2) as defined in LeBlond and Mysak [1978]:

$$\frac{d}{dt} = \frac{\partial}{\partial t} + \frac{dx_1}{dt}\frac{\partial}{\partial x_1} + \frac{dx_2}{dt}\frac{\partial}{\partial x_2} + \frac{dk_1}{dt}\frac{\partial}{\partial k_1} + \frac{dk_2}{dt}\frac{\partial}{\partial k_2} \tag{3.3.3}$$

$$\frac{d}{dt} = \frac{\partial}{\partial t} + (\vec{c}_g + \vec{U})\cdot\nabla_{x_1,x_2} \tag{3.3.4}$$

so that the wave propagation velocities can be derived in the subsequent Sections.

3.3.1 Propagation Velocities in Cartesian Coordinates

The spatial propagation velocities c_x and c_y that are using either equation 3.2.5 or equation 3.3.4, are given as:

$$c_x = \frac{dx}{dt} = c_g \sin\theta + \bar{u}\,; \qquad c_y = \frac{dy}{dt} = c_g \cos\theta + \bar{v} \tag{3.3.5}$$

The spectral propagation speeds $c_{\mathring{\sigma}}$ and c_θ are derived using equation 3.3.3, along with the equations in 3.2.5; the derivations proceed as follows:

$$c_\theta = \frac{d\theta}{dt} = \frac{dk_1}{dt}\frac{\partial\theta}{\partial k_1} + \frac{dk_2}{dt}\frac{\partial\theta}{\partial k_2} = -\frac{\partial\mathbf{\Omega}}{\partial x}\frac{\partial\theta}{\partial k_1} - \frac{\partial\mathbf{\Omega}}{\partial y}\frac{\partial\theta}{\partial k_2}$$

$$= -\Big\{\frac{\partial\mathring{\sigma}}{\partial h}\frac{\partial h}{\partial x} + \frac{\partial(\vec{k}\cdot\vec{U})}{\partial x}\Big\}\frac{\cos\theta}{k} + \Big\{\frac{\partial\mathring{\sigma}}{\partial h}\frac{\partial h}{\partial y} + \frac{\partial(\vec{k}\cdot\vec{U})}{\partial y}\Big\}\frac{\sin\theta}{k} = \frac{1}{k}\Big\{\frac{\partial\mathring{\sigma}}{\partial h}\frac{\partial h}{\partial m} + \vec{k}\cdot\frac{\partial\vec{U}}{\partial m}\Big\} \tag{3.3.6}$$

$$c_{\mathring{\sigma}} = \frac{d\mathring{\sigma}}{dt} = \frac{\partial\mathring{\sigma}}{\partial t} + \frac{dx}{dt}\frac{\partial\mathring{\sigma}}{\partial x} + \frac{dy}{dt}\frac{\partial\mathring{\sigma}}{\partial y} + \frac{dk_1}{dt}\frac{\partial\mathring{\sigma}}{\partial k_1} + \frac{dk_2}{dt}\frac{\partial\mathring{\sigma}}{\partial k_2}$$

$$= \frac{\partial\mathring{\sigma}}{\partial h}\frac{\partial h}{\partial t} + c_x\frac{\partial\mathring{\sigma}}{\partial h}\frac{\partial h}{\partial x} + c_y\frac{\partial\mathring{\sigma}}{\partial h}\frac{\partial h}{\partial y} - \frac{\partial\mathbf{\Omega}}{\partial x}\frac{\partial\mathring{\sigma}}{\partial k_1} - \frac{\partial\mathbf{\Omega}}{\partial y}\frac{\partial\mathring{\sigma}}{\partial k_2}$$

$$= \frac{\partial\mathring{\sigma}}{\partial h}\frac{\partial h}{\partial t} + \bar{u}\frac{\partial\mathring{\sigma}}{\partial h}\frac{\partial h}{\partial x} + \bar{v}\frac{\partial\mathring{\sigma}}{\partial h}\frac{\partial h}{\partial y} - c_g\Big\{\frac{\partial(\vec{k}\cdot\vec{U})}{\partial x}\sin\theta + \frac{\partial(\vec{k}\cdot\vec{U})}{\partial y}\cos\theta\Big\}$$

$$= \frac{\partial\mathring{\sigma}}{\partial h}\Big\{\frac{\partial h}{\partial t} + (\vec{U}\cdot\nabla_{x,y})\,h\Big\} - c_g\,\vec{k}\cdot\frac{\partial\vec{U}}{\partial s} \tag{3.3.7}$$

In equation 3.3.7, $\dfrac{\partial}{\partial s}$ represents the directional derivative along the propagation path where s is the space coordinate in the direction θ. In equation 3.3.6 $\dfrac{\partial}{\partial m}$ is the directional derivative for the direction m, the normal direction to s (Rogers et al. [1999]). The two directional derivatives are defined as:

$$\frac{\partial}{\partial s} = \sin\theta\frac{\partial}{\partial x_1} + \cos\theta\frac{\partial}{\partial x_2} \qquad \text{and} \qquad \frac{\partial}{\partial m} = -\cos\theta\frac{\partial}{\partial x_1} + \sin\theta\frac{\partial}{\partial x_2} \tag{3.3.8}$$

and can be easily derived considering a rotation of the coordinates (x_1, x_2) by an angle counter-clockwise of $-\dfrac{\pi}{2} + \theta$.

3.3.2 Propagation Velocities in Spherical Coordinates

The derivation of the equations for the propagation velocities follows a similar approach as in the Cartesian system, and they are just summarized here (Komen et al. [1996], Rogers et al. [1999]):

$$c_\lambda = \frac{d\lambda}{dt} = \frac{c_g \sin\theta + \bar{u}_\lambda}{R\cos\phi} = \frac{1}{R\cos\phi}\left(c_g \frac{k_1}{k} + \bar{u}_\lambda\right) \tag{3.3.9}$$

$$c_\phi = \frac{d\phi}{dt} = \frac{c_g \cos\theta + \bar{u}_\phi}{R} = \frac{1}{R}\left(c_g \frac{k_2}{k} + \bar{u}_\phi\right) \tag{3.3.10}$$

$$c_\theta = \frac{d\theta}{dt} = \frac{c_g \sin\theta \tan\phi}{R} + \frac{1}{k}\left\{\frac{\partial \mathring{\sigma}}{\partial h}\frac{\partial h}{\partial m} + \vec{k}\cdot\frac{\partial \vec{U}}{\partial m}\right\} \tag{3.3.11}$$

$$c_{\mathring{\sigma}} = \frac{d\mathring{\sigma}}{dt} = \frac{\partial \mathring{\sigma}}{\partial h}\left\{\frac{\partial h}{\partial t} + (\vec{U}\cdot\nabla_{x,y})\,h\right\} - c_g\,\vec{k}\cdot\frac{\partial \vec{U}}{\partial s} \tag{3.3.12}$$

where, u_λ and u_ϕ are the velocities in the spherical coordinates with directions defined by the unit vectors $\boldsymbol{e}_\lambda$ and $\boldsymbol{e}_\phi$, respectively, as shown in Figure 3.2.

3.4 The Wave Action Cycle 4 Model (*WAM*)

The last open source version of the wave action model is *WAM*, cycle 4 (Komen et al. [1996], The WAMDI Group [1988]) and a version of this release can be obtained upon request from the various wave forecasting centers around the world. This model has been extensively verified from researchers around the world and is heavily used in regularly scheduled global or regional wave forecasts (e.g., Naval Oceanographic Office at: http://www.navo.navy.mil/, European Centre for Medium-Range Weather Forecasts at: http://www.ecmwf.int/). A publicly available version of *WAM* (Norwegian version: *NMI-WAM*) can be obtained from the *UNESCO* web site at: http://ioc.unesco.org/oceanteacher/OpModWorkshop/WAM/wam.htm.

The *WAM* model was developed at the Max Planck Institut für Meteorologie, Hamburg, Germany by S. and K. Hasselmann (The WAMDI Group [1988], Komen et al. [1996]) and it is a third generation, phase averaging, spectral wave model solving the wave transport equation 3.3.1 or 3.3.2b explicitly, without any presumptions on the shape of the wave spectrum (Günther et al. [1992]). The model can run on any regional or global grid, arbitrary in space and time, while the wave propagation can be done in both geographical or Cartesian domains. The description of the Cartesian grid is done using equally spaced latitude/longitude pairs, which makes the coupling of *WAM* with other models run in a regular rectangular Cartesian grid a more complicated task.

According to the *WAM* documentation (Günther et al. [1992]), the model can perform both deep and shallow water wave calculations, but as noted in Rogers and O'Reilly [2002], *WAM* is not

particularly skillful on the prediction of the frequency distribution of the wave energy spectra near its wind source. The use of higher resolution grids can improve the wave predictions by *WAM* in near-shore regions, but because of its explicit numerical algorithms a fine time step resolution is required, making its use in such cases computationally very expensive and, therefore, practically unusable for long scale wave simulations.

Usually, *WAM* is run on a coarse grid, to resolve the deep water wave field, nested with a shallow water wave model (e.g., *SWAN*, Booij et al. [2004]) that runs on finer grid resolutions so that the wave field is adequately resolved in the whole computational domain. The shallow water wave models use implicit numerical schemes and their use is recommended on horizontal grid resolutions of $\sim 1000\,\mathrm{m}$ or less.

More recent global wave models like *NOAA*'s wave model *WAVEWATCH III* (publicly available at: http://polar.ncep.noaa.gov/waves/wavewatch/) are viewed as extensions of the basic *WAM* with some functionality added, like prescription of curvilinear grids, better description of the wave field near or around islands and improved numerical schemes.

All the models mentioned in this Section, solve exactly the same set of governing equations described in Section 3.3 with variations contained in the source terms. In the present research it was chosen to use *WAM* as the deep water wave model and *SWAN* as the shallow water wave model for the reasons explained above. The parametrization of the source terms appearing in equations 3.3.1 and 3.3.2b are presented in different Sections for the two wave models, so that the differences can be exploited more clearly.

3.4.1 Description of the Source Terms

The source term $\boldsymbol{S}$ in the wave action balance equation is expanded to include the effects of winds, wave interactions and the dissipation of the wave energy due to whitecapping and bottom friction as follows:

$$\boldsymbol{S} = \boldsymbol{S}_{in} + \boldsymbol{S}_{nl} + \boldsymbol{S}_{ds}^{w} + \boldsymbol{S}_{ds}^{bot} \tag{3.4.1}$$

where, $\boldsymbol{S}_{in}(\mathring{\sigma}, \theta)$ represents the transfer of the wind energy to the waves, $\boldsymbol{S}_{nl}(\mathring{\sigma}, \theta)$ represents the nonlinear energy transfer between the waves, $\boldsymbol{S}_{ds}^{w}(\mathring{\sigma}, \theta)$ represents the rate at which energy is lost from the wave field due to whitecapping and $\boldsymbol{S}_{ds}^{bot}(\mathring{\sigma}, \theta)$ represents the rate at which energy is lost due to bottom friction.

Wind Input ($\boldsymbol{S}_{in}$):

The wind input term describes the most important element in wave modeling, the interaction of the waves with the atmosphere and specifically the only energy input in the wave field that comes from the winds. The complex interaction between the waves and the atmosphere is represented by the following exponential growth equation:

$$\boldsymbol{S}_{in} = B\,\mathcal{E}(\mathring{\sigma}, \theta) \tag{3.4.2}$$

where, B is a function of the wave frequency $\mathring{\sigma}$, the wave propagation angle θ and the wind speed W and direction θ_W. B is defined as:

$$B = \beta\,\frac{\rho_{\text{air}}}{\rho_{\text{w}}}\,\frac{u_{\#}^2}{c^2}\,\max[0, \cos(\theta - \theta_W)]^2\,\mathring{\sigma}\;; \qquad \beta = \frac{1.2}{\mathbf{k}^2}\,\lambda\,\ln^4\lambda \tag{3.4.3}$$

$$\lambda = \frac{g z_{\text{e}}}{c^2}\,e^r \quad (\lambda \leq 1) \qquad \text{and} \qquad r = \frac{\mathbf{k}c}{|u_{\#}\cos(\theta - \theta_W)|} \tag{3.4.4}$$

in which β is the so called Miles constant, λ is a non-dimensional critical height (for $\lambda > 1$ taken as $\beta = 0$), z_{e} is the effective surface roughness (Section 2.5.1), $\mathbf{k}$ is von Kármán's constant ($\mathbf{k} = 0.4$), c is the phase speed and $u_{\#}$ is the friction velocity determined by: $u_{\#}^2 = \text{C}_{\text{M}} W^2$. The drag coefficient C_{M} is calculated in M^2COPS by the methods described in Section 2.5.1.

The wind source term represents the feedback between the growing waves and the induced turbulent pressure patterns as has been suggested by Miles [1957]. The mathematical formulation of the term is based upon the quasi-linear wind wave generation theory suggested by Janssen [1991].

Dissipation due to Whitecapping ($\boldsymbol{S}_{ds}^{w}$):

Whitecapping describes the phenomenon of the breaking of waves. As the waves grow, their steepness (s) increases until a critical point when they break. This is a nonlinear process that limits the wave growth with the lost energy being transferred into the underlying currents. This energy dissipation term depends upon the wave steepness and it is represented by the pulse based model of Hasselmann (Komen et al. [1996]) reformulated in terms of the wavenumber so it is applicable in shallower water depths (Booij et al. [2004]):

$$\boldsymbol{S}_{ds}^{w} = -C_{ds}\,\tilde{\bar{\sigma}}\,\tilde{\text{s}}^4\left[(1-\delta)\,\frac{k}{\tilde{\bar{k}}} + \delta\left(\frac{k}{\tilde{\bar{k}}}\right)^2\right]\mathcal{E}(\mathring{\sigma}, \theta)\;; \qquad \tilde{\text{s}} = \tilde{k}\,\sqrt{\mathcal{E}_T} \tag{3.4.5}$$

in which, $\tilde{k}$ is the spectrally averaged wavenumber (first of equations 5.4.10) and $\mathcal{E}_T$ is the total spectral wave energy (equation 5.4.5). The spectrally averaged intrinsic frequency is defined as

(The WAMDI Group [1988]):

$$\tilde{\mathring{\sigma}} = \left[\frac{1}{\mathcal{E}_T} \int_0^{2\pi} \int_0^{\infty} \frac{1}{\mathring{\sigma}} \mathring{\mathcal{E}}(\mathring{\sigma}, \theta) \, d\mathring{\sigma} \, d\theta \right]^{-1} \tag{3.4.6}$$

The values of the tunable coefficients C_{ds} and δ are taken from Komen et al. [1996] and are: $C_{ds} = 4.5$ and $\delta = 0.5$

Depth Induced Friction ($\boldsymbol{S}_{ds}^{bot}$):

The interaction between the surface waves and the bottom is significant in shallow water as the orbital motions of the water particles, induced by the waves, extend to the bottom. Wave energy is lost by dissipative wave-bottom interaction mechanisms, such as bottom movement, percolation into a porous bottom and friction in the turbulent bottom boundary layer. The wave energy losses due to bottom friction and percolation are collected into the $\boldsymbol{S}_{ds}^{bot}$ term, which is evaluated by the following equation (The WAMDI Group [1988], Komen et al. [1996]):

$$\boldsymbol{S}_{ds}^{bot} = -\mathrm{C_D} \frac{\mathring{\sigma}^2}{g^2 \sinh^2 kh} \mathcal{E}(\mathring{\sigma}, \theta) \tag{3.4.7}$$

The friction coefficient $\mathrm{C_D}$ depends upon the wave and bottom conditions, generally a function of the bottom roughness height, the near-bottom orbital velocity U_{wb} and excursion wave amplitude A_{wb} defined as:

$$U_{wb}^2 = \int_0^{2\pi} \int_0^{\infty} \frac{\mathring{\sigma}^2 \, \mathring{\mathcal{E}}(\mathring{\sigma}, \theta)}{\sinh^2 kh} \, d\mathring{\sigma} \, d\theta \qquad \text{and} \qquad A_{wb}^2 = 2 \int_0^{2\pi} \int_0^{\infty} \frac{\mathring{\mathcal{E}}(\mathring{\sigma}, \theta)}{\sinh^2 kh} \, d\mathring{\sigma} \, d\theta \tag{3.4.8}$$

When *WAM* is used as a standalone model, the coefficient $\mathrm{C_D}$ is taken from the results of the *JONSWAP* experiment, as described in Komen et al. [1996] and The WAMDI Group [1988] to be equal to: $\mathrm{C_D} = 0.038$. In M^2COPS the value of $\mathrm{C_D}$ is supplied by the wave-current boundary layer model (Chapter 6), where it is calculated during the hydrodynamic computations.

Wave-Wave Interactions ($\boldsymbol{S}_{nl}$):

The wave-wave interactions term describes the weakly nonlinear resonant wave-wave interactions between waves of different frequencies. The resonant interactions are responsible for the energy transfer between the waves, redistributing the energy within the spectrum. The process is internal to the wave spectrum and does not result in changes in the overall energy budget of the wave field.

The lowest order resonance in the case of the gravity waves occurs for four-wave interactions (known as quadruplet wave-wave interactions), while the three wave or triad interactions occur in the capillary region of the spectrum (Komen et al. [1996]). *WAM* considers only the quadruplet wave-wave interactions, with the 2D resonant conditions defined as:

$$k_1 + k_2 - k_3 = k_4 \qquad \text{and} \qquad \mathring{\sigma}_1 + \mathring{\sigma}_2 - \mathring{\sigma}_3 = \mathring{\sigma}_4 \tag{3.4.9}$$

$$\text{with:} \quad \mathring{\sigma}_1 = \mathring{\sigma}_2 = \mathring{\sigma}\,; \quad \mathring{\sigma}_3 = \mathring{\sigma}^+ = \mathring{\sigma}(1+\lambda)\,; \quad \mathring{\sigma}_4 = \mathring{\sigma}^- = \mathring{\sigma}(1-\lambda)\,; \quad \lambda = 0.25 \tag{3.4.10}$$

The nonlinear source term $\boldsymbol{S}_{nl}$ is then formulated as:

$$\boldsymbol{S}_{nl}(\mathring{\sigma},\theta) = 2\,\delta\,\boldsymbol{S}^*_{nl}(a_1\,\mathring{\sigma},\theta) - \delta\,\boldsymbol{S}^*_{nl}(a_2\,\mathring{\sigma},\theta) - \delta\,\boldsymbol{S}^*_{nl}(a_3\,\mathring{\sigma},\theta) \tag{3.4.11}$$

where, $a_1 = 1$, $a_2 = 1+\lambda$ and $a_3 = 1-\lambda$. Each of the contributions $\boldsymbol{S}^*_{nl}$ in equation 3.4.11 is determined for deep water conditions by the following equation:

$$\begin{aligned}\delta\,\boldsymbol{S}^*_{nl}(a_i\,\mathring{\sigma},\theta) =& 3\cdot 10^7\Big(\frac{2\pi}{g^2}\Big)^2\Big(\frac{\mathring{\sigma}}{2\pi}\Big)^{11}\left\{\left[\mathcal{E}^2(a_i\,\mathring{\sigma},\theta)\,\frac{\mathcal{E}(a_i\,\mathring{\sigma}^+,\theta)}{(1+\lambda)^4} + \frac{\mathcal{E}(a_i\,\mathring{\sigma}^-,\theta)}{(1-\lambda)^4}\right] - \right.\\ & \left. 2\,\frac{\mathcal{E}(a_i\,\mathring{\sigma},\theta)\,\mathcal{E}(a_i\,\mathring{\sigma}^+,\theta)\,\mathcal{E}(a_i\,\mathring{\sigma}^-,\theta)}{(1-\lambda^2)^4}\right\}; \qquad i = 1,2,3\end{aligned} \tag{3.4.12}$$

Since equation 3.4.12 is valid for deep waters, the quadruplet interaction in finite water depths is determined from equation 3.4.12 by multiplying the equation with a scaling factor R defined in Komen et al. [1996] as:

$$R(x) = 1 + \frac{5.5}{x}\,(1 - \frac{5x}{6})\,\exp\,(-\frac{5x}{4})\,; \qquad x = \frac{3\,\tilde{k}D}{4} \tag{3.4.13}$$

In shallow waters, $\tilde{k}D \to 0$, the nonlinear transfer approaches infinity therefore, a lower limit of $\tilde{k}D = 0.5$ is applied (Komen et al. [1996], Günther et al. [1992]), which gives a maximum value for the scaling factor of $R_{max} = 4.43$.

3.4.2 Description of the Numerical Algorithms

The source terms are treated implicitly to allow the use of a greater time step than the time adjustment of the dynamic high frequency cut-off used in the model. A dynamic high frequency cut-off, instead of a fixed high frequency cut-off, is implemented in *WAM* to avoid any excessive disparities in the response time scales within the spectrum (Komen et al. [1996]).

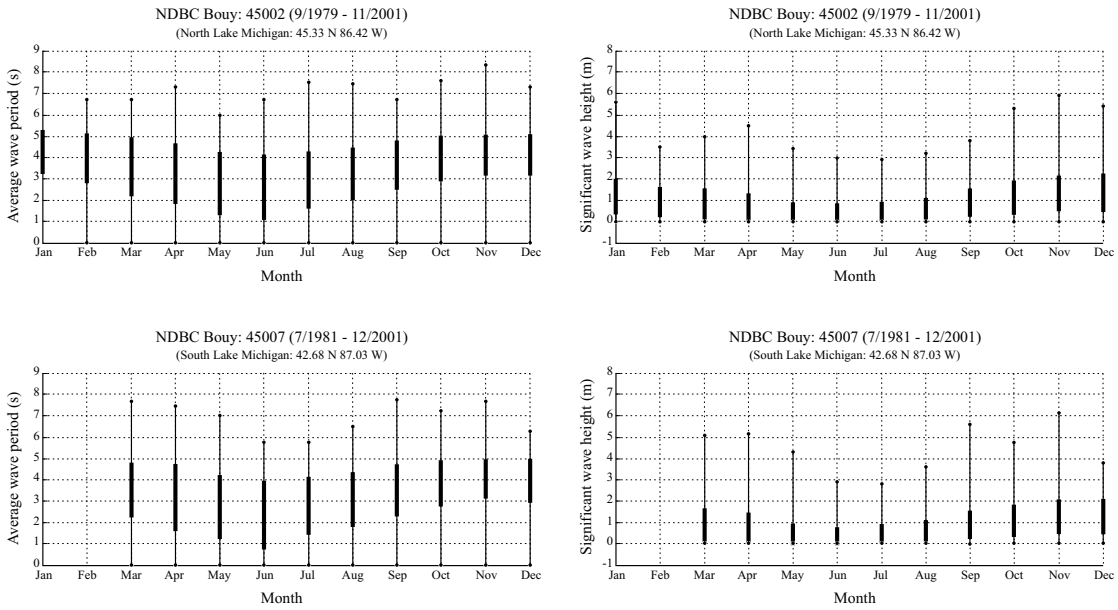

Figure 3.3 Historical significant wave heights and periods recorded at two NDBC buoys in Lake Michigan (National Data Buoy Center, http://www.ndbc.noaa.gov/Maps/WestGL.shtml).

Since the model is to be applied in the deeper ($\geq$ 100 m) Lake Michigan waters, using a 2000 m horizontal resolution, we can estimate an appropriate time step for stable calculations considering the following deep water approximations for a fully developed sea (SPM [1984]):

$$H_s = 0.2433\,\frac{U_A^2}{g}\,; \qquad T_s = 0.95{\cdot}8.134\,\frac{U_A}{g}\,; \qquad c_g = \frac{g\,T}{4\,\pi} \tag{3.4.14}$$

where, H_s and T_s are the significant wave height and period respectively, $U_A = 0.71\,W^{1.23}$ is the wind stress factor calculated from the 10 m wind speed W (m/s) and $g = 9.806\,\mathrm{m/s^2}$.

Using mild to moderately strong winds, different wave conditions can be estimated from equations 3.4.14, as shown in Table 3.1. The results represent the highest possibly expected waves in the lake for the given weather conditions and, therefore, the calculated values of Δt are conservative estimates of the time step required for the stability of the model calculations. Comparing the plots in Figure 3.3 with the values of H_s and T_s reported in Table 3.1, it seems that a time step of $\Delta t = 5$ min is sufficient for the stability of the model calculations.

W (m/s)	H_s (m)	T_s (s)	c_g (m/s)	Δt (min)
15.0	9.52	15.5	12.1	2.75
12.5	6.25	12.5	9.8	3.40
10.0	3.61	9.5	7.5	4.40
7.5	1.78	6.7	5.3	6.30
5.0	0.66	4.1	3.2	10.40
2.5	0.12	1.8	1.4	24.00

Table 3.1 Suggested limiting values of the time step for the *WAM* computations.

3.5 The Simulating Waves Nearshore Cycle 3 Model (*SWAN*)

SWAN is an open source, shallow water wave model and the latest version (*SWAN* cycle 3, ver. 40.41) can be obtained from the model's web site at: http://fluidmechanics.tudelft.nl/swan/. From the same site, patches to the model can be downloaded and applied to bring the code up to date. This model is actively maintained, well documented (Booij et al. [2004]), with a growing user base worldwide.

The *SWAN* model was developed at the Delft University of Technology, Delft, The Netherlands and it is based on the wave action balance equation (Section 3.3) when currents are present or the energy balance equation otherwise. Quoting the model's manual: "*SWAN* is a numerical wave model for obtaining realistic estimates of wave parameters in coastal areas, lakes and estuaries from given wind, bottom, and current conditions".

According to the *SWAN* documentation (Booij et al. [2004]), the model can perform its calculations either in the Cartesian or the spherical coordinate system. Since it is designed for a regional or small scale simulations ($\leq \sim 1000$ m horizontal resolution), the principal purpose of the spherical grid representation is to ease the nesting of the model with global wave models like *WAM* or *WAVEWATCH III*.

3.5.1 Description of the Source Terms

The source term $\boldsymbol{S}$ is an extension to the one defined in *WAM* (equation 3.4.1) to include the dissipation of the wave energy due to the wave breaking (an important term for shallow water calculations):

$$\boldsymbol{S} = \boldsymbol{S}_{in} + \boldsymbol{S}_{nl} + \boldsymbol{S}^{w}_{ds} + \boldsymbol{S}^{bot}_{ds} + \boldsymbol{S}^{br}_{ds} \tag{3.5.1}$$

For the calculation of the source terms, *SWAN* can simulate the behavior of both the *WAM* cycle 3 (The WAMDI Group [1988]) and the *WAM* cycle 4 (Komen et al. [1996], Günther et al. [1992]) models (a user defined choice). Here are only presented the equations relevant to *WAM* cycle 4, since this is the model used in M^2COPS. For the full description of the formulations for the source terms used in *SWAN*, one can refer to the model's manual.

Wind Input ($\boldsymbol{S}_{in}$): The wind input in *SWAN* is an extension of equation 3.4.2 defined as:

$$\boldsymbol{S}_{in} = A + B\,\mathcal{E}(\mathring{\sigma}, \theta) \tag{3.5.2}$$

where, $A(\mathring{\sigma}, \theta)$ represents the reasonant interaction between the waves and turbulent pressure patterns in the air as suggested by Phillips [1957]. The term B is defined identically as in *WAM* (equations 3.4.3 and 3.4.4). The linear growth term A is due to Cavaleri and Malonette-Rizzoli, as referenced in the *SWAN* user's manual (Booij et al. [2004]) and it is filtered to eliminate wave growth at frequencies lower than the Pierson-Moskowitz frequency (equations 3.5.4):

$$A = \mathcal{F}\,\frac{1.5\cdot 10^{-3}}{2\,\pi\,g^2}\left\{u_*\,\max[0, \cos(\theta - \theta_W)]\right\}^4 \tag{3.5.3}$$

$$\mathcal{F} = \exp\left[-\left(\frac{\mathring{\sigma}}{\mathring{\sigma}_{PM}}\right)^{-4}\right]\;; \qquad \mathring{\sigma}_{PM} = 2\,\pi\,\frac{0.13\,g}{28\,u_*} \tag{3.5.4}$$

where, $\mathcal{F}$ is the filter and $\mathring{\sigma}_{PM}$ is the peak frequency of the fully developed sea state according to Pierson and Moskowitz [1964].

Dissipation due to Whitecapping ($\boldsymbol{S}^{w}_{ds}$):

The dissipation term due to whitecapping is the same as the one defined for *WAM* (equation 3.4.5) formulated though in a slightly different way:

$$\boldsymbol{S}^{w}_{ds} = -C_{ds}\,\tilde{\mathring{\sigma}}\left[(1-\delta)\,\frac{k}{\tilde{k}} + \delta\left(\frac{k}{\tilde{k}}\right)^2\right]\left(\frac{\tilde{s}}{\tilde{s}_{PM}}\right)^4 \mathcal{E}(\mathring{\sigma}, \theta) \tag{3.5.5}$$

with, $C_{ds} = 4.10\cdot 10^{-5}$, $\delta = 0.5$ and $\tilde{s}_{PM} = (3.02\cdot 10^{-3})^{1/2}$.

Depth Induced Friction ($\boldsymbol{S}^{bot}_{ds}$):

SWAN uses three friction models (user's choice), all of which are represented by equation 3.4.7 and they are only differentiated by the way the friction coefficient C_D is being calculated. The first is the *JONSWAP* empirical model used in *WAM*, the second is a drag law model and the more important third one is the eddy-viscosity model of Madsen et al. [1988]. In Madsen's model, the

friction coefficient is calculated in terms of the friction factor f_w by:

$$C_D = f_w \frac{g}{\sqrt{2}} U_{wb} \; ; \qquad \frac{1}{4\sqrt{f_w}} + \log\Big[\frac{1}{4\sqrt{f_w}}\Big] = -0.08 + \log\Big[\frac{A_{wb}}{z_o}\Big] \tag{3.5.6}$$

For values of A_{wb}/z_o less than 1.57, the friction factor is taken equal to 0.30. In M^2COPS the value of C_D, as in the case of *WAM*, is supplied by the hydrodynamic calculations.

Dissipation due to Wave Breaking ($\boldsymbol{S}_{ds}^{br}$):

Wave breaking occurs in shallow waters, where depth and water heights are of the same order of magnitude, while in deep water wave calculations this dissipation mechanism is irrelevant. The term $\boldsymbol{S}_{ds}^{br}$ is calculated using the fraction of the breaking waves as:

$$\boldsymbol{S}_{ds}^{br} = -\frac{Q_b \,\bar{\mathring{\sigma}}\, H_m^2}{8\pi} \frac{\mathcal{E}(\mathring{\sigma},\theta)}{\mathcal{E}_T} \qquad \text{with:} \qquad \frac{1-Q_b}{\ln Q_b} = -8\frac{\mathcal{E}_T}{H_m^2} \tag{3.5.7}$$

where, H_m is the maximum wave height that can exist at the given depth and $\bar{\mathring{\sigma}}$ is the mean intrinsic frequency defined as:

$$\bar{\mathring{\sigma}} = \frac{1}{\mathcal{E}_T} \int_0^{2\pi} \int_0^{\infty} \mathring{\sigma}\, \mathring{\mathcal{E}}(\mathring{\sigma},\theta)\, d\mathring{\sigma}\, d\theta \tag{3.5.8}$$

Defining $\beta = \dfrac{H_{rms}}{H_m}$, the fraction of the breaking waves is given in *SWAN* by:

$$Q_b = 0 \quad \text{for:} \quad \beta \le 0.2 \; ; \qquad Q_b = 1 \quad \text{for:} \quad \beta \ge 1$$

$$Q_b = Q_0 - \beta^2 \frac{Q_0 - \exp\left(\dfrac{Q_0 - 1}{\beta^2}\right)}{\beta^2 - \exp\left(\dfrac{Q_0 - 1}{\beta^2}\right)} \quad \text{for:} \quad 0.2 < \beta < 1 \tag{3.5.9}$$

Wave-Wave Interaction ($\boldsymbol{S}_{nl}$):

In *SWAN* the wave-wave interactions consist from the contributions of both the quadruplet ($\boldsymbol{S}_{nl4}$) as well as the triad ($\boldsymbol{S}_{nl3}$) wave-wave interactions. The quadruplet interactions are modeled in the same way as in the case of *WAM*, while the triad interactions are described by the following equations (Booij et al. [2004]):

$$\boldsymbol{S}_{nl}(\mathring{\sigma},\theta) = \boldsymbol{S}_{nl4}(\mathring{\sigma},\theta) + \boldsymbol{S}_{nl3}(\mathring{\sigma},\theta) \; ; \qquad \boldsymbol{S}_{nl3}(\mathring{\sigma},\theta) = \boldsymbol{S}_{nl3}^{-}(\mathring{\sigma},\theta) + \boldsymbol{S}_{nl3}^{+}(\mathring{\sigma},\theta) \tag{3.5.10}$$

$$\boldsymbol{S}_{nl3}^{+}(\mathring{\sigma},\theta) = \max\Big\{0,\; \alpha_{EB}\, 2\pi\, c\, c_g J^2 \,|\sin\beta|\, \{\mathcal{E}^2(\mathring{\sigma}/2,\theta) - 2\,\mathcal{E}(\mathring{\sigma}/2,\theta)\,\mathcal{E}(\mathring{\sigma},\theta)\}\Big\} \tag{3.5.11}$$

$$\boldsymbol{S}^{-}_{nl3}(\mathring{\sigma},\theta) = -2\,\boldsymbol{S}^{+}_{nl3}(2\mathring{\sigma},\theta) \tag{3.5.12}$$

where, α_{EB} is a tunable coefficient, c and c_g are the phase speed and group velocity, respectively and β, J are given in terms of the Ursell number ($\mathbb{U}_r$), the significant wave height (H_s) and the average wave period ($\bar{T}$):

$$\beta = -\frac{\pi}{2} + \frac{\pi}{2}\,\tanh\Big(\frac{0.2}{\mathbb{U}_r}\Big)\,; \qquad \mathbb{U}_r = \frac{g}{8\sqrt{2}\pi^2}\,\frac{H_s\bar{T}^2}{h^2}\,; \qquad \bar{T} = \frac{2\pi}{\mathring{\sigma}} \tag{3.5.13}$$

$$J = -\frac{k^2_{\mathring{\sigma}/2}\,(gh + 2c^2_{\mathring{\sigma}/2})}{k_{\mathring{\sigma}}\,h\,(gh + \frac{2}{15}\,gh^3k^2_{\mathring{\sigma}} - \frac{2}{5}\,\mathring{\sigma}^2h^2)} \tag{3.5.14}$$

The triad interactions are calculated for the range $0.1 \le \mathbb{U}_r \le 10$, but as noted in the *SWAN* manual, for stability reasons are calculated in the range $0 \le \mathbb{U}_r \le 10$, so both the quadruplet and the triad interactions are calculated at the same time.

3.5.2 Description of the Numerical Algorithms

SWAN uses one of the following numerical schemes (user's choice): *(a)* the first order backward in space, backward in time scheme (BSBT), *(b)* the second order upwind scheme with the optional second order diffusion (SORDUP), and *(c)* the second order upwind scheme with the optional third order diffusion (S&L) as proposed in Stelling and Leendertse [1992]. All the above schemes are unconditionally stable and more suitable for fine resolution (near-shore) applications than the one supplied in *WAM*. The BSBT scheme is more diffusive than the *WAM*'s upwind scheme or the SORDUP and S&L schemes, thus the recommendation for the use of *SWAN* in horizontal resolutions less than ~ 1000 m.

The second order schemes exhibit very small diffusive properties, in fact so small that the so called garden-sprinkler effect (GSE) can possibly show up when wave propagation calculations are performed over large distances (Booij et al. [2004]). The errors in the propagation speed are usually larger for the shorter waves and numerical schemes like SORDUP and S&L, that do not dump these short components that exhibit the GSE behavior. The consistent presence of short waves in the field becomes visible as "wiggles" when the above schemes are used (Rogers et al. [2002]). The remedy to the GSE problem is the introduction of extra diffusion terms (a second order term in SORDUP and a third order term in S&L) as described in *SWAN*'s manual (not used in M^2*COPS*). The introduced diffusion terms are discretized explicitly and as a result the overall scheme becomes

conditionally stable, requiring Courant numbers $C_r \leq 0.5$ for oceanic applications and $C_r \leq 1$ for regional applications for stability. In the current application of *SWAN* the BSBT is used since it is computationally less demanding and gives almost identical results with the other two schemes for the spatial resolution used.

3.6 Relation between *WAM* and *SWAN*

The two wave models examined in this Chapter are closely tied, regarding the modeled physics, implementing though different numerical schemes. The basic structure of *SWAN* resembles that of *WAM* (either cycle 4 or cycle 3) with emphasis in the shallow water wave physics. The introduction of the additional shallow water formulations in *SWAN*, along with its implicit numerical schemes, define this model as being a "shallow water wave model".

The different approaches used in the two models for the determination of the wind input are reconciled by the modifications applied to both *WAM* and *SWAN*, such that the surface drag coefficient and shear stress are calculated using the same formulations defined for the hydrodynamic model.

SWAN is designed to work with both *WAM* and *WAVEWATCH III*, therefore, it can be readily nested with both models. The nested grids consist from a coarse grid and a fine grid. The fine grid can be the coarse grid for a next level fine grid and in this sense, infinite levels of model nesting can be done. The coarse grid spectra are saved at every time step so that the fine grid model can interpolate the spectra to use then as input boundary values.

The spectral domain is discretized with a constant directional resolution $\Delta\theta$ and a constant frequency resolution $\Delta\mathring{\sigma}$. The frequency space is described by a low and a high frequency cut-off. In both the models the low frequency cut-off is fixed (user input), but the high frequency cut-off is dynamic in *WAM* and fixed in *SWAN*. The fixed high frequency cut-off is used in *SWAN* because in near-shore regions mixed wave states with different characteristic frequencies may occur, as opposed to the single characteristic frequency calculated by *WAM* for deep waters.

The boundary conditions in both models are fully absorbing for wave energy that is leaving the computational domain or crossing the shoreline. At the open boundaries the energy spectra are defined by the user and are usually calculated by a coarse grid model.

CHAPTER 4

THREE DIMENSIONAL WAVE CURRENT INTERACTIONS

4.1 The Concept of the Wave Radiation Stress

As water waves advance on the free surface, they carry momentum with them thus producing a net momentum flux distributed within the water. This momentum flux excess is quantified and then incorporated into the momentum equations for the moving water as an extra term, traditionally called the "radiation stress" after the work of Longuet-Higgins and Stewart [1964]. The radiation stress $R_{\alpha\beta}$, as defined by Longuet-Higgins and Stewart, is actually not a stress strictly speaking e.g., a force per unit area, but it is rather a vertically integrated stress:

$$R_{\alpha\beta} = \overline{\int_{-h}^{\zeta} (\delta_{\alpha\beta} p + \rho \tilde{u}_\alpha \tilde{u}_\beta) dz}^{t} - \int_{-h}^{0} \delta_{\alpha\beta}\, \overline{p}^{t}\, dz\,, \quad \overline{p}^{t} = -\rho g z\,; \qquad \alpha,\beta = (1,2) \tag{4.1.1}$$

where p is the fluid pressure ($p = \overline{p}^{t} + \tilde{p}$), $\overline{p}^{t}$ is the hydrostatic pressure and $\tilde{u}$, $\tilde{p}$ represent the wave contributions to the flow velocities and pressure, respectively. The evaluation of the terms in the r.h.s of the first of equations 4.1.1 (to the second order in the wave slope $\epsilon_1 = ka$ and assuming a locally flat bottom) gives the following expression for $R_{\alpha\beta}$ (Longuet-Higgins and Stewart [1964], Phillips [1977], Smith [2006]):

$$R_{\alpha\beta} = E\left[\frac{k_\alpha k_\beta}{k^2}\,\frac{c_g}{c} + \delta_{\alpha\beta}\left(\frac{c_g}{c} - \frac{1}{2}\right)\right] \tag{4.1.2}$$

The concept of the radiation stress has been used *(a)* in analyses of near-shore current systems that is, wave-setup (Longuet-Higgins and Stewart [1964]), *(b)* for coastal and rip currents analyses (Longuet-Higgins [1970a,b], Zikanov and Slinn [2001]), *(c)* in surf-zone wave modeling (Veeramony and Svendsen [2000], Feddersen [2004]), *(d)* in the 2D modeling of tides and surges (Osuna

and Monbaliu [2004], Zhang and Li [1996]), and *(e)* lately in coupled 3D wave-hydrodynamic models (Zhang and Li [1997], Welsh et al. [2000], Warner et al. [2008] and others).

The radiation stress as defined by Longuet-Higgins and Stewart is a two-dimensional horizontal tensor and it was derived assuming a 2D structure for the underlying current. To determine the additional forces exerted by the waves on the current, the wave mean momentum equation (e.g., equation 3.3.1) is subtracted from the full mean momentum equation that combines waves and currents. Details of this procedure and the derivations of the terms can be found in the excellent texts of LeBlond and Mysak [1978] and Mei [1983]. Let $\mathcal{M}$ be a differential operator that represents the vertically averaged momentum equations 2.1.29a and 2.1.30a, such that the equations can conceptually be written as:

$$\mathcal{M}_\alpha = 0 \; ; \qquad (\alpha = 1, 2) \tag{4.1.3}$$

The presence of the surface waves introduces an additional force per unit area on the current and modifies the above equations as follows (LeBlond and Mysak [1978]):

$$\mathcal{M}_\alpha = -\frac{1}{\rho_o} \frac{\partial R_{\alpha\beta}}{\partial x_\beta} \; ; \qquad \alpha, \beta = (1, 2) \; ; \quad \text{summation over } \beta \tag{4.1.4}$$

Considering the fact that the currents are 3D structures, especially in near-shore dynamics, the vertical variation of the radiation stress should be considered as well,when studying the interactions between waves and currents. Traditionally, in wave-hydrodynamic model couplings, the radiation stress terms are incorporated only into the vertically integrated momentum equations, thus only enhancing the calculations of the 2D velocities with the 3D velocities remaining greatly unaffected by the waves.

The above approach, physically incorrect, affects the calculations for the total water depth (equations 2.1.26a, 2.1.29a and 2.1.30a), therefore, in this sense, the 3D velocities are indirectly and partially affected by the presence of the surface waves. The more physically correct coupling between the wave dynamics and hydrodynamics requires that the 3D momentum equations should include the appropriate terms for the radiation stresses as well. Upon vertical integration of the 3D momentum equations, the integrated radiation stress should be equal to the one supplied by the wave model. Thus to repeat, the major objective of this dissertation is to represent the full 3D impacts of the radiation stresses on the currents.

In the following Sections, an approach for including the vertical structure of the radiation stress into the hydrodynamic model is introduced as extended from the works of Mellor [2003, 2005,

2008], Ardhuin and Jenkins [2006a] and Xia et al. [2004]. Since, the vertically integrated radiation stress is a standard output of the spectral wave models, the task at hand is to develop a methodology for estimating vertical distribution of the stress and then incorporating the resulting terms into the 3D momentum equations.

4.2 Wave Stokes Drift and Langmuir Circulations: The Upper Water Column and Currents

Water particles in the presence of the surface waves do not follow the closed paths described by the linear wave theory. Rather their paths are open contours described by higher order wave theories and produced by a net flow velocity (drift) in the direction of the propagating waves that diminishes with depth. This phenomenon was first examined by Stokes, thus the name Stokes drift.

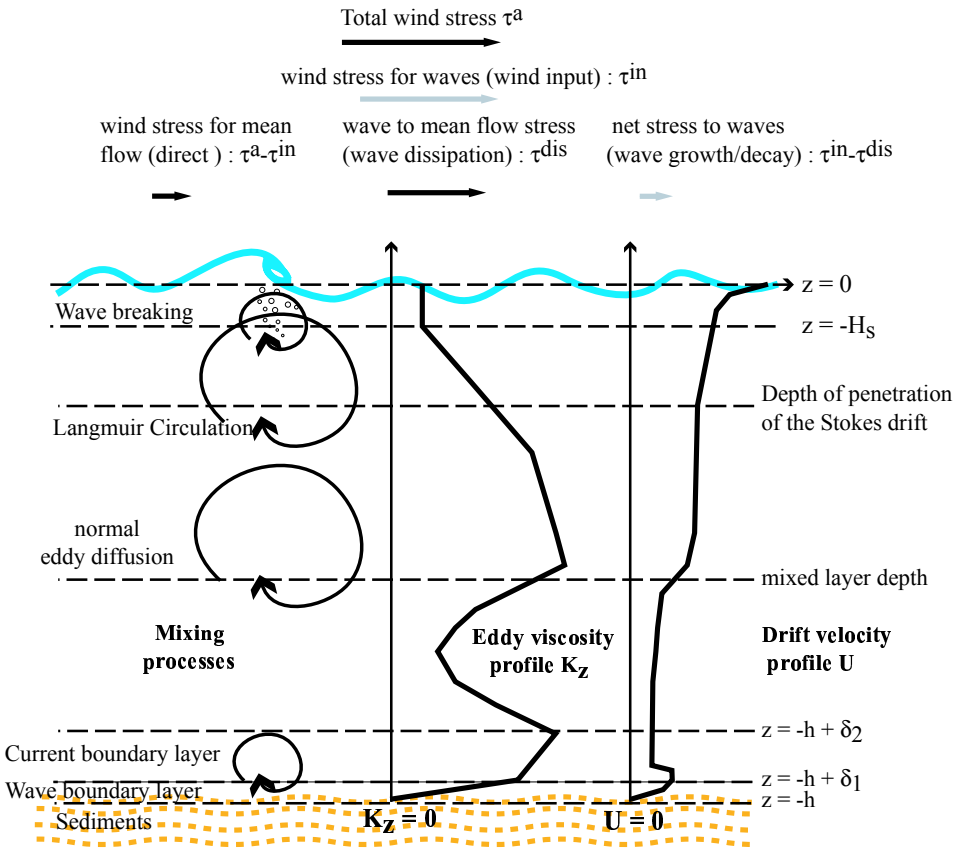

Figure 4.1 Surface waves and current interactions in the ocean for horizontally uniform conditions. Approximate eddy viscosity and Stokes drift vertical profiles (source: Ardhuin et al. [2005]).

The interaction of the Stokes drift with the wind-driven surface shear produces additional circulations in the upper portion (near the surface) of the water column (as shown in Figure 4.1) known as Langmuir circulations. If the effect of the Langmuir circulations is to be modeled, equation 4.4.2 is modified by the inclusion of additional terms that are functions of the Stokes drift (Ardhuin and Jenkins [2006a], Mellor [2003], Moon [2005]). Mathematically, the Stokes drift as deducted from the previous statements, corresponds to a second order accurate correction term of the linear wave theory. With this in mind, Mellor's equations can be described as being accurate to the first order in the wavenumber (k) space and to the second order in the flow variables (Ardhuin and Jenkins [2006a]).

4.3 The Significance of the Wave Effects on the General Mean Flow

The traditional Reynolds averaged equations of motion describe the evolution of a 3D flow-field where the dynamics are driven by winds, tides and density changes. In the absence of wind driven oscillatory motions a flow variable (say velocity) is written as:

$$u = \bar{u} + u' \tag{4.3.1}$$

where, u is the total flow velocity, $\bar{u}$ is the temporally averaged (mean) velocity and u' represents the fluctuating part of u in relation to $\bar{u}$ and describes the background turbulence in the field. The averaging of equation 4.3.1 eliminates u' since by definition $\overline{u'} = 0$. The averaging just filters out the higher frequency turbulent motions, therefore, their effects need to be included in the equations calculating $\bar{u}$ and this is normally done by the use of a turbulence model.

For a model based on *RANS*, as the temporal time step (averaging interval) Δt becomes smaller ($\Delta t \to 0$), the spatial resolution must go to zero as well ($\Delta s \to 0$; $\Delta s = (\Delta x, \Delta y)$), since the *CFL* stability criterion in any hydrodynamic model relates Δt and Δs at any point and at any time.

As $\Delta t \to 0$, the sub grid parametrization used to describe the turbulence effects on $\bar{u}$ becomes less important up to the point where the calculations are performed in the neighborhood ($\Delta t \to 0$, $\Delta s \to 0$) where the turbulence terms appearing in the equations of motion are fully resolved by the model grid. In practice the above approach is not applicable, especially when calculations are performed in global and regional scales, due to the high demands of *CPU* times and storage requirements. In the presence of wind generated waves, additional oscillatory motions are introduced in

the main fluid motion that have significantly different time and space scales compared to those of the background mean fluid flow and associated turbulence.

The above separation of the time and space scales between the fast wave motions (of the order of ω^{-1} and k^{-1}, respectively) and the slow mean flow motions does not allow the Reynolds averaged equations to resolve the wave-mean flow interactions unless a highly empirical sub grid model parametrization is used. Therefore, new equations are required. In other words, a Reynolds averaged and a wave phase (or period) averaged process is required, since a Reynolds averaging operation filters all the higher frequency oscillatory motions, thus filtering out important pieces of physical processes and subsequently introduces errors in the calculation of the Eulerian parameters by the hydrodynamic models.

In the presence of surface waves the velocity field can be represented (Hussain and Reynolds [1970], Finnigan and Einaudi [1981], Finnigan et al. [1984]) as:

$$u = \bar{u} + \tilde{u} + u' \tag{4.3.2}$$

where $\tilde{u}$ represents the oscillatory contributions to the flow field. By the earlier definition given in Hussain and Reynolds, the Reynolds or time averaged $\tilde{u}$ was simply nil. This implies that the higher frequency (higher relative to $1/2\Delta t$) oscillatory motions are simply filtered or averaged out and a hydrodynamic model that calculates $\bar{u}$ would account for the effects of the filtered oscillatory motions via subgrid scale parametrizations.Therefore, only the lower frequency oscillatory motions (as related to Δt) are still resolved, as they are part of $\bar{u}$:

$$\bar{u} = u_E + \tilde{u}_L \tag{4.3.3}$$

where $\tilde{u}_L$ represents the lower frequency oscillatory effects resolved in the average flow field, and u_E represents the "pure Eulerian" portion of the flow velocity. Many researchers label $\bar{u}$ as the "quasi Eulerian" flow velocity (Ardhuin and Jenkins [2006a],Ardhuin et al. [2008b] and others).

Writting the equations of motion in terms of $\bar{u}$ (equation 4.3.3), without including any sub scale parametrization of the wave-current interactions clearly violates the proper calculation of the dynamics of the physical processes involved.

Gravity wave activity exhibits a variety of time scales on order of $T_1 \approx 1 - 10\,\text{s}$, $T_2 \approx 100\,\text{s}$, $T_3 \approx 10^3\,\text{s}$, $T_4 > 10^4\,\text{s}$ (e.g., tides, tsunamis, seiches). To complete the above scale $T_0 \approx 0.1\,\text{s} < T_1$ is added, which refers to the ultra gravity-capillary portion of the spectrum.

Lavrenov [2003] refers to the oscillations of order T_3, T_4 as quasi-oscillations that affect the development of the wave spectrum. Clearly based on the above scaling, within the range of the Reynolds averaging ($\Delta t < 30$ min) the time scales of interest here are T_0, T_1 and T_2. Wave groups repeat themselves every 10-15 average wave periods Lavrenov [2003]. Therefore, for a model $\Delta t = 10$ min T_0, T_1 and T_2 wave classes are not resolved by a hydrodynamic model unless the wave-current interactions are included.

Additionally, gravity waves feed both the low and the high frequencies of the T_0-T_2 bands through non-linear wave interactions (e.g., triad wave interactions), thus creating secondary waves in both the low and high side of the spectrum. The generation and resolution of these low frequency waves near shore is especially crucial, as they affect the sediment transport (Reniers et al. [2004, 2002], MacMahan et al. [2004a,b]).

The problem of the interaction between long and short wave motions has been discussed extensively in the literature by Garrett and Smith [1976], Elgar et al. [1995], Herbers and Burton [1997], Aranha and Martins [2001], Reniers et al. [2002], Uchiyama and McWilliams [2008] and others. All these works clearly show that in near shore calculations, the long-short wave interactions are essential in sediment transport, therefore, wave-current interactions should be resolved as accurately as possible within the model to avoid misleading calculations.

4.4 Reynolds Averaged Equations in σ-Coordinates

The calculations presented here and in the subsequent Sections will be mostly performed in the σ-stretched vertical coordinate system as has been done in Mellor [2003, 2005]. The three-dimensional continuity and momentum equations, in (x, y, σ) coordinates, are obtained from equations C.9, C.13 and C.14 using the expressions shown in equations C.7 and Table C.1. The resulting equations are subsequently written in tensor form as follows:

Continuity:

$$\frac{\partial \zeta}{\partial t} + \frac{\partial (D u_\alpha)}{\partial x_\alpha} + \frac{\partial (D \overset{\star}{\omega})}{\partial \sigma} = 0 \qquad \text{and:} \qquad \frac{\partial D}{\partial t} + \frac{\partial (D u_\alpha)}{\partial x_\alpha} + \frac{\partial (D \overset{\star}{\omega})}{\partial \sigma} = 0 \tag{4.4.1}$$

Momentum:

$$\mathcal{M}_\alpha = \mathrm{C}_\alpha + \mathrm{P}_\alpha + \mathrm{T}_\alpha^{turb} \tag{4.4.2}$$

$$\mathcal{M}_\alpha = \frac{\partial(Du_\alpha)}{\partial t} + \frac{\partial(Du_\alpha u_\beta)}{\partial x_\beta} + \frac{\partial(Du_\alpha \overset{\star}{\omega})}{\partial \sigma} \; ; \qquad \mathrm{C}_\alpha = -\epsilon_{\alpha 3\beta} f_3 D u_\beta \tag{4.4.3}$$

$$\mathrm{P}_\alpha = -D\Big(\frac{1}{\rho_o}\frac{\partial p_{\mathrm{atm}}}{\partial x_\alpha} + g\frac{\partial \zeta}{\partial x_\alpha}\Big) - \frac{gD}{\rho_o}\Big\{D\int_\sigma^0 \frac{\partial \rho}{\partial x_\alpha}\, d\sigma' + \frac{\partial D}{\partial x_\alpha}\Big(\int_\sigma^0 \rho\, d\sigma' + \sigma\rho\Big)\Big\} \tag{4.4.4}$$

The Reynolds turbulent fluxes T_α^{turb} are decomposed in horizontal ($\mathrm{T}_{\mathrm{h}\alpha}^{turb}$) and vertical components ($\mathrm{T}_{\mathrm{v}\alpha}^{turb}$) such that, $\mathrm{T}_\alpha^{turb} = \mathrm{T}_{\mathrm{h}\alpha}^{turb} + \mathrm{T}_{\mathrm{v}\alpha}^{turb}$:

$$\mathrm{T}_{\mathrm{h}\alpha}^{turb} = \frac{\partial}{\partial x_\beta}\Big[\mathcal{A}_{\mathrm{h}}\frac{\partial(Du_\alpha)}{\partial x_\beta}\Big] \; ; \qquad \mathrm{T}_{\mathrm{v}\alpha}^{turb} = \frac{1}{D^2}\frac{\partial}{\partial \sigma}\Big[\mathcal{A}_{\mathrm{v}}\frac{\partial(Du_\alpha)}{\partial \sigma}\Big] \tag{4.4.5}$$

Scalar:

$$\frac{\partial(D\Phi)}{\partial t} + \frac{\partial(Du_\alpha \Phi)}{\partial x_\alpha} + \frac{\partial(\overset{\star}{\omega}\Phi)}{\partial \sigma} = \mathrm{T}_\Phi + \boldsymbol{S_\Phi} \tag{4.4.6}$$

$$\mathrm{T}_\Phi = \frac{\partial}{\partial x_\beta}\Big[\mathcal{B}_{\mathrm{h}}\frac{\partial(D\Phi)}{\partial x_\beta}\Big] + \frac{1}{D^2}\frac{\partial}{\partial \sigma}\Big[\mathcal{B}_{\mathrm{v}}\frac{\partial(D\Phi)}{\partial \sigma}\Big] \tag{4.4.7}$$

where $D\overset{\star}{\omega}$ is the nearly vertical σ flow velocity defined by equation B.26, C_α is the Coriolis vortex term, P_α is the pressure term that includes both the barotropic and the baroclinic terms and $\alpha, \beta = (1, 2)$, summation over β. As it has been shown by Mellor [2003], in the presence of the wind generated surface waves, equation 4.4.2 is modified by the inclusion of additional terms to account for the wave induced effects. In his paper, Mellor introduced a derivation of the three-dimensional, phase averaged equations for monochromatic (single frequency) and uni-directional (single propagation angle) waves from basic principles, using the linear wave theory.

4.5 Wave σ-Coordinate Transformations and Auxiliary Functions

For the derivation of the wave transformed equations it is assumed that:

$$\epsilon_1 = \max\{ka\} \qquad \text{and} \qquad \epsilon_2 = \max\Big\{\frac{\partial h}{\partial x_\alpha}\Big\} \tag{4.5.1}$$

are small quantities where, ϵ_1 is related to the wave slope ka, and ϵ_2 is related to the bottom slope $\partial h/\partial x_\alpha$. The following auxiliary functions are defined here:

$$\lambda_\alpha = \frac{\partial \lambda}{\partial x_\alpha} = \frac{\partial \zeta}{\partial x_\alpha} + \sigma\frac{\partial D}{\partial x_\alpha} \; ; \qquad \lambda_\sigma = \frac{\partial \lambda}{\partial \sigma} = D \; ; \qquad \lambda_t = \frac{\partial \lambda}{\partial t} = (1+\sigma)\frac{\partial D}{\partial t} \tag{4.5.2a}$$

and: $$\frac{\partial \lambda_\alpha}{\partial \sigma} = \frac{\partial^2 \lambda}{\partial \sigma \partial x_\alpha} = \frac{\partial \lambda_\sigma}{\partial x_\alpha} = \frac{\partial D}{\partial x_\alpha} \; ; \qquad \frac{\partial \lambda_t}{\partial \sigma} = \frac{\partial^2 \lambda}{\partial \sigma \partial t} = \frac{\partial \lambda_\sigma}{\partial t} = \frac{\partial D}{\partial t} = \frac{\partial \zeta}{\partial t} \tag{4.5.2b}$$

The wave σ coordinates denoted by s, are defined in Mellor [2003] as:

$$z = s(x^*_\alpha, \sigma, t^*) = \zeta + \sigma D + \tilde{s} \; ; \qquad \tilde{s} = \alpha \frac{\sinh kD(1+\sigma)}{\sinh kD} \cos\psi \tag{4.5.3}$$

Re-arrangement of the first of equations 4.5.3 gives:

$$\frac{z-\zeta}{D} = \bar{\sigma} + \frac{\tilde{s}}{D} \tag{4.5.4}$$

that is, the σ coordinate is slightly perturbed by the quantity $\frac{\tilde{s}}{D}$ to reflect the wave contributions in the water elevation. The transformed coordinates are defined as:

$$x_\alpha = (x, y) \; ; \quad x_\alpha = x^*_\alpha \; ; \quad t = t^* \; ; \quad s_\alpha = \frac{\partial s}{\partial x^*_\alpha} \; ; \quad s_\sigma = \frac{\partial s}{\partial \sigma} \; ; \quad s_t = \frac{\partial s}{\partial t^*} \tag{4.5.5a}$$

with: $$\frac{s_\alpha}{s_\sigma} = -\frac{\partial \sigma}{\partial x_\alpha} \; ; \qquad \frac{s_t}{s_\sigma} = -\frac{\partial \sigma}{\partial t} \; ; \qquad \frac{1}{s_\sigma} = \frac{\partial \sigma}{\partial z} \tag{4.5.5b}$$

and from equations 4.5.3:

$$s_\sigma = \lambda_\sigma + \tilde{s}_\sigma \; ; \qquad \tilde{s}_\sigma = kDa \frac{\cosh kD(1+\sigma)}{\sinh kD} \cos\psi \tag{4.5.5c}$$

$$s_t = \lambda_t + \tilde{s}_t \; ; \qquad \tilde{s}_t = \frac{\lambda_t}{\lambda_\sigma} \tilde{s}_\sigma \tag{4.5.5d}$$

$$s_\alpha = \lambda_\alpha + \tilde{s}_\alpha \; ; \qquad \tilde{s}_\alpha = \frac{\lambda_\alpha}{\lambda_\sigma} \tilde{s}_\sigma \tag{4.5.5e}$$

When phase averaging (equation B.6), the "s" coordinates revert back to the ordinary "σ" co-ordinates (Mellor [2003]) and phase averaged variables, equations, are simply referred to ordinary "σ" coordinates. Using equations 4.5.5b through 4.5.5e, the following phase averaged quantities can be derived:

$$\overline{s}^\psi_\alpha = \lambda_\alpha \; ; \quad \overline{s}^\psi_\sigma = \lambda_\sigma \; ; \quad \overline{s}^\psi_t = \lambda_t \; ; \quad \overline{\left(\frac{s_\alpha}{s_\sigma}\right)}^\psi = \frac{\lambda_\alpha}{\lambda_\sigma} \; ; \quad \overline{\left(\frac{s_t}{s_\sigma}\right)}^\psi = \frac{\lambda_t}{\lambda_\sigma} \; ; \quad \overline{\left(\frac{1}{s_\sigma}\right)}^\psi = \frac{1}{\lambda_\sigma} \tag{4.5.6}$$

Let $\Phi(x_\alpha, z, t) = \Phi^*(x^*_\alpha, \sigma, t)$ be a phase averaged general function. The gradients of Φ are transformed in "s" coordinates as follows (Mellor [2003]):

$$\frac{\partial \Phi}{\partial x_\alpha} = \frac{\partial \Phi^*}{\partial x^*_\alpha} - \frac{s_\alpha}{s_\sigma}\frac{\partial \Phi^*}{\partial \sigma} = \frac{\partial \Phi^*}{\partial x^*_\alpha} - \frac{\lambda_\alpha}{\lambda_\sigma}\frac{\partial \Phi^*}{\partial \sigma}$$

$$\frac{\partial \Phi}{\partial z} = \frac{1}{s_\sigma}\frac{\partial \Phi^*}{\partial \sigma} = \frac{1}{\lambda_\sigma}\frac{\partial \Phi^*}{\partial \sigma} \tag{4.5.7}$$

$$\frac{\partial \Phi}{\partial t} = \frac{\partial \Phi^*}{\partial t^*} - \frac{s_t}{s_\sigma}\frac{\partial \Phi^*}{\partial \sigma} = \frac{\partial \Phi^*}{\partial t^*} - \frac{\lambda_t}{\lambda_\sigma}\frac{\partial \Phi^*}{\partial \sigma}$$

Using the equations 4.5.2a and 4.5.2b it can be shown that the transformation of $\partial\Phi/\partial x_\alpha$ (or $\partial\Phi/\partial t$) is represented using the following two equivalent expressions:

$$\frac{\partial \Phi}{\partial x_\alpha} = \frac{\partial \Phi^*}{\partial x^*_\alpha} - \frac{\lambda_\alpha}{\lambda_\sigma}\frac{\partial \Phi^*}{\partial \sigma} = \frac{1}{\lambda_\sigma}\left[\frac{\partial(\lambda_\sigma \Phi^*)}{\partial x^*_\alpha} - \frac{\partial(\lambda_\alpha \Phi^*)}{\partial \sigma}\right] \tag{4.5.8}$$

where the temporal gradient is obtained from the above equation by simply replacing λ_α with λ_t and x^*_α with t^*.

Before proceeding with more equations, it is useful to define at this point the following hyperbolic functions used in Mellor's papers (Mellor [2003], Mellor et al. [2008]):

$$F_{CS} = \frac{\cosh k(z+h)}{\sinh kD} = \frac{\cosh kD(1+\sigma)}{\sinh kD}\,; \qquad F_{CC} = \frac{\cosh k(z+h)}{\cosh kD} = \frac{\cosh kD(1+\sigma)}{\cosh kD} \tag{4.5.9a}$$

$$F_{SC} = \frac{\sinh k(z+h)}{\cosh kD} = \frac{\sinh kD(1+\sigma)}{\cosh kD}\,; \qquad F_{SS} = \frac{\sinh k(z+h)}{\sinh kD} = \frac{\sinh kD(1+\sigma)}{\sinh kD} \tag{4.5.9b}$$

$$\zeta_s = \frac{\partial(F_{SS}F_{CC})}{\partial z} = \frac{2k\cosh 2k(z+h)}{\sinh 2kD}\,; \qquad \zeta_s = \frac{\partial(F_{SS}F_{CC})}{\partial \sigma} = \frac{2kD\cosh 2kD(1+\sigma)}{\sinh 2kD} \tag{4.5.9c}$$

The plots of the above functions are given in Figures 4.2, 4.3 and 4.4 for both deep and shallow water conditions. The functions F_{CS}, F_{CC}, F_{SC}, F_{SS} and ζ_s approach the limiting function $e^{kD\sigma}$ in deep waters ($kD \to \infty$), while in shallow waters ($kD \to 0$) they asymptotically assume the values: $kDF_{CS} \to 1$, $F_{CC} \to 1$, $F_{SC} \to 0$, $F_{SS} \to 1+\sigma$ and $\zeta_s \to 1$.

The wave induced flow parameters (e.g., fluid particle displacements, fluid velocities, pressure) are given by the following relationships:

$$\tilde{\xi}_\alpha = \tilde{x}_\alpha = -a\frac{k_\alpha}{k}F_{CS}\sin\psi\,; \qquad \tilde{\xi}_3 = \tilde{z} = \tilde{s} = aF_{SS}\cos\psi \tag{4.5.10a}$$

$$\tilde{u}_\alpha = a\mathring{\sigma}\frac{k_\alpha}{k}F_{CS}\cos\psi\,; \qquad \tilde{w} = a\mathring{\sigma}F_{SS}\sin\psi \tag{4.5.10b}$$

$$\tilde{p} = gaF_{CC}\cos\psi \tag{4.5.10c}$$

The depth D that appears in the above equations is defined as the sum of the bathymetric water depth h and the mean free surface fluctuation $\zeta(x,y,t)$, therefore, D is regarded as a function of space and time as well. The distribution function ζ_s vertically integrates to one (equation 4.5.13). Next, the following wave functions are defined and used throughout the present work:

$$\psi = k_\alpha x_\alpha - \omega t \; ; \qquad \omega = \mathring{\sigma} + k_\alpha \hat{u}_{A\alpha} \; ; \qquad \mathring{\sigma}^2 = gk \tanh kD \tag{4.5.11}$$

$$c = \frac{\mathring{\sigma}}{k} = \left(\frac{g}{k}\tanh kD\right)^{1/2} \; ; \qquad c_g = \frac{d\mathring{\sigma}}{dk} = \frac{c}{2}\left(1 + \frac{2kD}{\sinh kD}\right) \tag{4.5.12}$$

$$\hat{u}_{A\alpha} = \int_{-1}^{0} u_\alpha \zeta_s \, d\sigma \; ; \qquad \int_{-1}^{0} \zeta_s \, d\sigma = F_{SS} F_{CC}\Big|_{-1}^{0} = 1 \tag{4.5.13}$$

where ψ is the wave phase, $\mathring{\sigma}$ is the intrinsic frequency, ω is the radial frequency, k_α is the wave number component, c is the wave phase speed, c_g is the wave group speed and $\hat{u}_{A\alpha}$ represents the so called Doppler velocity.

From the first of equations 4.5.11 it is derived that:

$$k_\alpha = \frac{\partial \psi}{\partial x_\alpha} \; ; \qquad \omega = -\frac{\partial \psi}{\partial t} \; ; \qquad \frac{\partial k_\alpha}{\partial t} + \frac{\partial \omega}{\partial x_\alpha} = 0 \; ; \qquad \frac{\partial k_\alpha}{\partial x_\beta} = \frac{\partial k_\beta}{\partial x_\alpha} = \frac{\partial^2 \psi}{\partial x_\alpha \partial x_\beta} \tag{4.5.14}$$

that is, the wave number vector is irrotational. Using the first of equations 4.5.12 the following relationships can be derived:

$$\frac{\partial \mathring{\sigma}}{\partial x_\alpha} = \frac{\partial \mathring{\sigma}}{\partial k}\frac{\partial k}{\partial x_\alpha} + \left(\frac{\partial \mathring{\sigma}}{\partial x_\alpha}\right)_k \; ; \qquad \left(\frac{\partial \mathring{\sigma}}{\partial x_\alpha}\right)_k = \frac{k\mathring{\sigma}}{\sinh 2kD}\frac{\partial D}{\partial x_\alpha} \tag{4.5.15}$$

while using the second of equations 4.5.11 and the first of equations 4.5.15, it is obtained that:

$$\frac{\partial \omega}{\partial x_\alpha} = \frac{\partial \mathring{\sigma}}{\partial k}\frac{\partial k}{\partial x_\alpha} + \hat{u}_{A\beta}\frac{\partial k_\beta}{\partial x_\alpha} + k_\beta \frac{\partial \hat{u}_{A\beta}}{\partial x_\alpha} + \left(\frac{\partial \mathring{\sigma}}{\partial x_\alpha}\right)_k \tag{4.5.16}$$

Substituting equation 4.5.16 into the third of equations 4.5.14, the following well known equation for the conservation of the wave crests is derived:

$$\frac{\partial k_\alpha}{\partial t} + (c_{g\beta} + \hat{u}_{A\beta})\frac{\partial k_\alpha}{\partial x_\beta} = -\left(\frac{\partial \mathring{\sigma}}{\partial x_\alpha}\right)_k - k_\beta \frac{\partial \hat{u}_{A\beta}}{\partial x_\alpha} \tag{4.5.17}$$

where $c_{g\beta}$ is the β-th component of the wave group velocity. For the derivation of equation 4.5.17 the following relationship was applied: $\partial k/\partial x_\alpha = (k_\beta/k)(\partial k_\beta/\partial x_\alpha)$; $k^2 = k_\beta k_\beta$, summation over β.

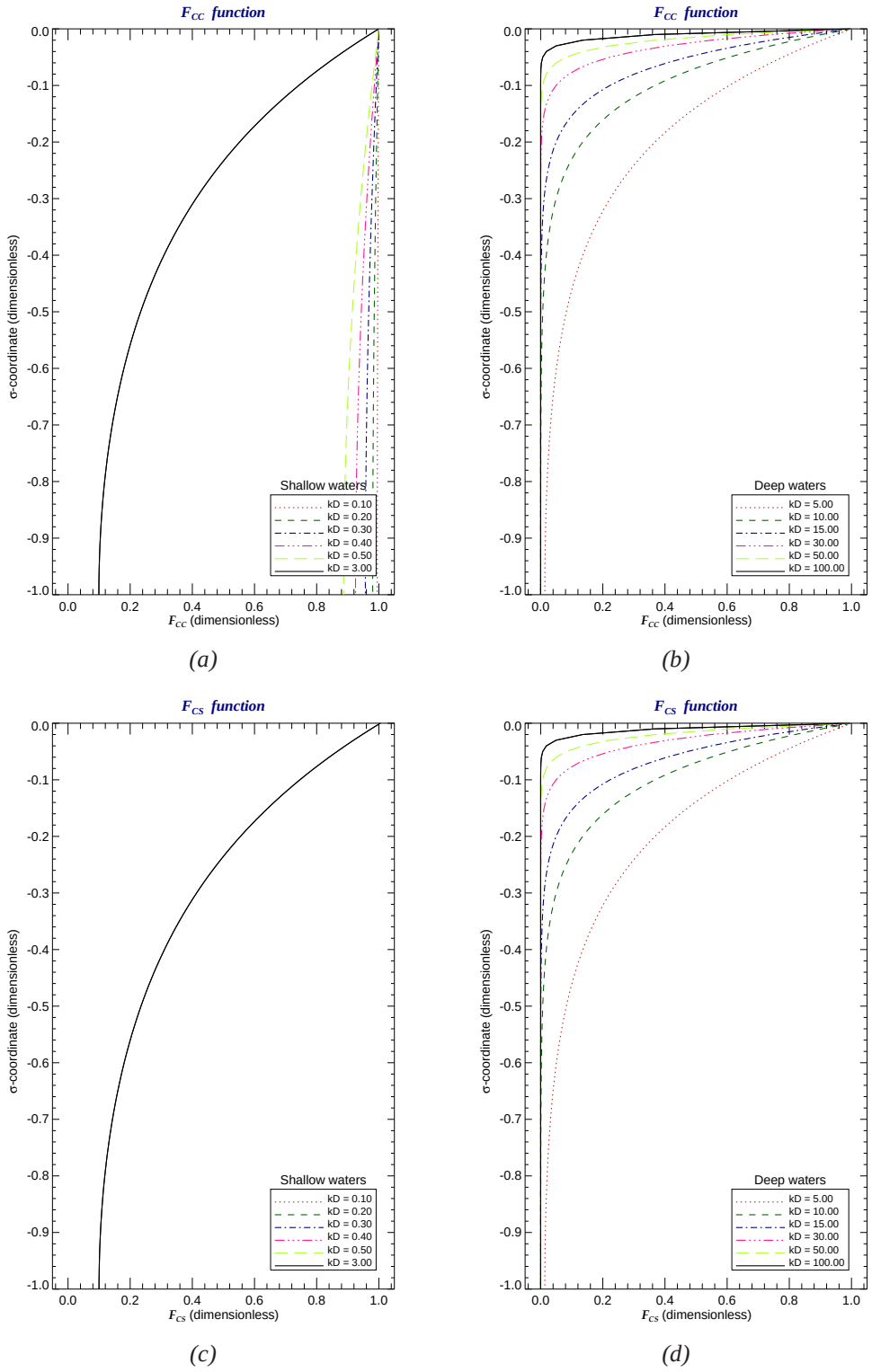

Figure 4.2 Plots of the exponential functions F_{CC} and F_{CS} for shallow and deep water conditions.

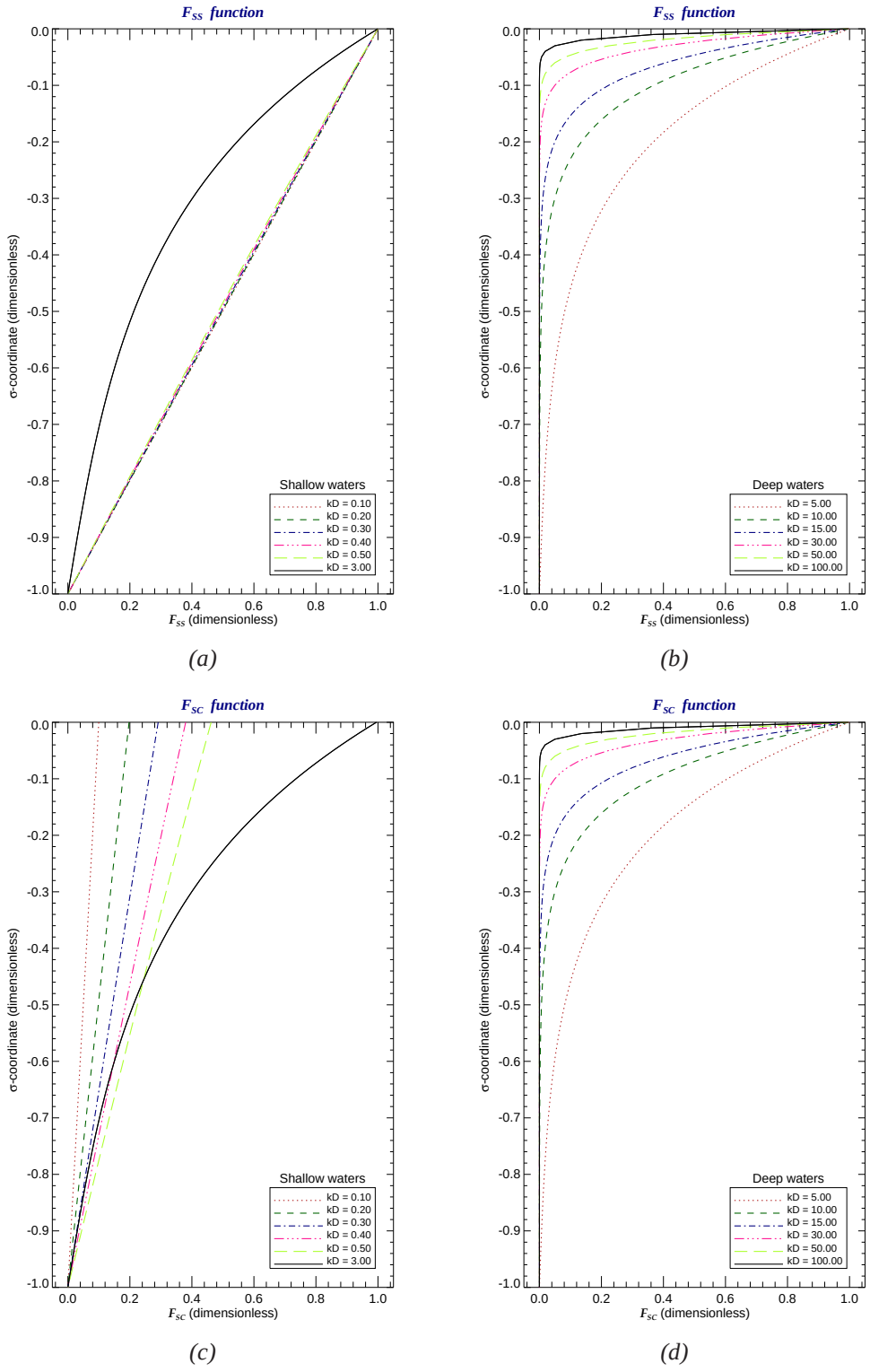

Figure 4.3 Plots of the exponential functions F_{SS} and F_{SC} for shallow and deep water conditions.

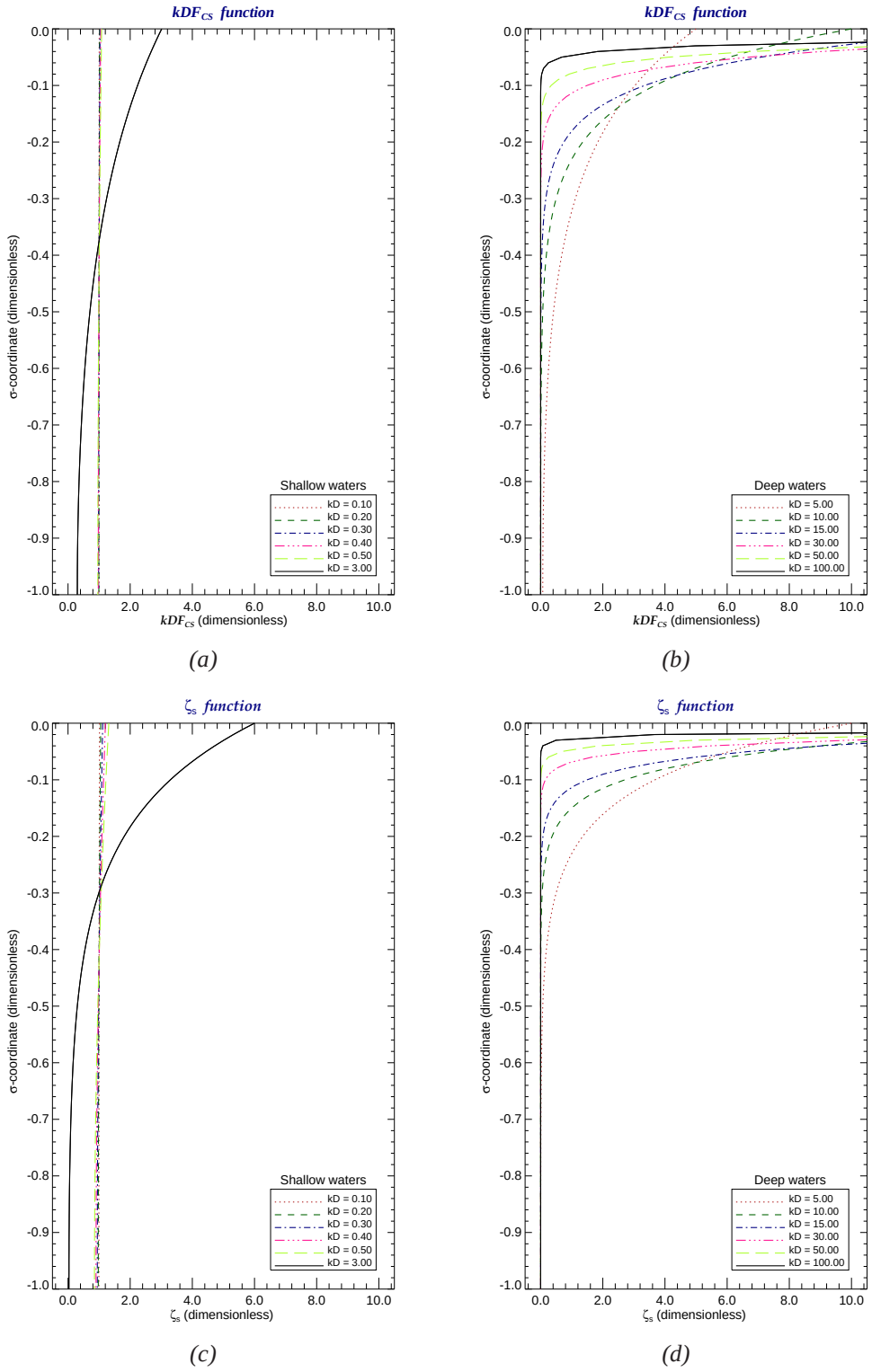

Figure 4.4 Plots of the exponential functions kDF_{CS} and ζ_s for shallow and deep water conditions.

4.6 Generalized Lagrangian Mean (*GLM*) Formulation

Andrews and McIntyre [1978a] derived the exact equations for Lagrangian mean flows based on the definition of their Generalized Lagrangian Mean (*GLM*) averaging, such that the Lagrangian mean operator $\overline{(\cdot)}^L$ corresponds to any given Eulerian mean operator $\overline{(\cdot)}$. The resulting *GLM* equations of motion are hybrid Eulerian-Lagrangian equations, where the independent variables are $\vec{x}$ and t, instead of the initial position and time (Lagrangian formulation), thus allowing the use of Eulerian models in the prediction of Lagrangian flow characteristics (Craik [1988]).

Let $(\vec{x}, t)$ represent a flow particle position in Eulerian representation. Waves introduce particle displacements $\tilde{\xi}$ from their Eulerian positions thus defining the position of a particle in Lagrangian representation as $(\vec{x} + \vec{\tilde{\xi}}, t)$. The introduction of the wave particle displacement $\tilde{\xi}$ simply maps the Eulerian domain to the Lagrangian domain by the coordinate transformation: $\vec{x} \rightarrow \vec{x} + \vec{\tilde{\xi}}$. Mellor's wave induced equations of motion discussed in Section 4.7, were derived using a "wave following" vertical coordinate definition and, as such, fall within the *GLM* formulation.

Averaging all particle positions within $\tilde{\xi}$ defines a *GLM* averaging operation, such that for a function Φ the following is true:

$$\overline{\Phi(\vec{x},t)}^L = \overline{\Phi^{\xi}(\vec{x},t)}\,; \qquad \Phi^{\xi}(\vec{x},t) = \Phi(\vec{x}+\vec{\tilde{\xi}},t)\,; \qquad \overline{\tilde{\xi}}^L = 0 \tag{4.6.1}$$

Assuming small amplitude oscillatory motions and a continuously differentiable function Φ, a Taylor series expansion of the second of equations 4.6.1 and a subsequent Reynolds averaging of the resulting equation, yields:

$$\overline{\Phi}^L = \overline{\Phi} + \overline{\Phi}^S = \overline{\Phi} + \overline{\tilde{\xi}_j \frac{\partial \tilde{\Phi}}{\partial x_j}}^{\psi} + O(\epsilon_1^2) \tag{4.6.2}$$

For the two wave functions $\Phi(\vec{x},\, t;\, \alpha)$ and $\Theta(\vec{x},\, t;\, \alpha)$ the following two properties are true (Andrews and McIntyre [1978b]):

$$\overline{\frac{\partial \Phi}{\partial \alpha}}^{\alpha} = \frac{\partial \overline{\Phi}^{\alpha}}{\partial \alpha} = 0\,; \qquad \overline{\frac{\partial \Phi}{\partial \alpha}\Theta}^{\alpha} = -\overline{\frac{\partial \Theta}{\partial \alpha}\Phi}^{\alpha} \tag{4.6.3}$$

The term $\overline{\Phi}^S$ in equation 4.6.2 is the so called "Stokes correction" to the Eulerian mean variable $\overline{\Phi}$. Let $\overline{u}_\alpha = u_\alpha$ be the temporally, Reynolds averaged Eulerian flow velocity and $\overline{u}_\alpha^L = \mathcal{U}_\alpha$ be the Lagrangian averaged flow velocity, then from equation 4.6.2:

$$\mathcal{U}_\alpha = u_\alpha + \mathrm{u}_{\mathrm{st}\alpha}\,; \qquad \mathrm{u}_{\mathrm{st}\alpha} = \overline{\tilde{\xi}_j \frac{\partial \tilde{u}_\alpha}{\partial x_j}}^{\psi} + O(\epsilon_1^2) \tag{4.6.4}$$

where $u_{st\alpha}$ is the Stokes correction to u_α and $u_{st\alpha}$ is of the second order in wave slope by its definition. Finally, $\mathcal{J}$ is the Jacobian of the transformation between Eulerian and Lagrangian spaces is defined in Andrews and McIntyre [1978b] as:

$$\mathcal{J} = \det\left(\delta_{ij} + \frac{\partial\tilde{\xi}_i}{\partial x_j}\right) = 1 + \frac{\partial\tilde{\xi}_k}{\partial x_k} + \frac{1}{2}\frac{\partial\tilde{\xi}_k}{\partial x_k}\frac{\partial\tilde{\xi}_l}{\partial x_l} + \frac{1}{6}\epsilon_{ijk}\,\epsilon_{\alpha\beta\gamma}\frac{\partial\tilde{\xi}_i}{\partial x_\alpha}\frac{\partial\tilde{\xi}_j}{\partial x_\beta}\frac{\partial\tilde{\xi}_k}{\partial x_\gamma} \tag{4.6.5}$$

$i, j, k, \alpha, \beta, \gamma = (1, 2, 3)$, summation over the repeated indexes.

4.7 Wave Transformed Equations of Motion

The equations presented in this Section are the result of the work of Mellor (Mellor [2003, 2005], Mellor et al. [2008]). The equations were derived using the phase averaged flow variables, but as stated in Lane et al. [2005], Ardhuin and Jenkins [2006a], the mean variables obtained this way correspond to Generalized Lagrangian Means (*GLM*) of these variables as well. In his papers, Mellor [2003, 2005] introduced the coordinate transformation outlined in Section 4.5 to describe the effects of the higher frequency waves on the mean flow and derived the continuity and momentum equations in terms of the Lagrangian flow velocity $\mathcal{U}$ (equation 4.6.4):

Continuity:

$$\frac{\partial\zeta}{\partial t} + \frac{\partial(D\mathcal{U}_\alpha)}{\partial x_\alpha} + \frac{\partial\Omega}{\partial\sigma} = 0 \qquad \text{and:} \qquad \frac{\partial D}{\partial t} + \frac{\partial(D\mathcal{U}_\alpha)}{\partial x_\alpha} + \frac{\partial\Omega}{\partial\sigma} = 0 \tag{4.7.1}$$

Momentum:

$$\frac{\partial(D\mathcal{U}_\alpha)}{\partial t} + \frac{\partial(D\mathcal{U}_\alpha\mathcal{U}_\beta)}{\partial x_\beta} + \frac{\partial(\mathcal{U}_\alpha\Omega)}{\partial\sigma} = -\epsilon_{\alpha 3\beta}\,f_3 D\,\mathcal{U}_\beta + \mathrm{P}_\alpha + \mathrm{T}^{turb} + \mathrm{S}_w^{(1)} + \mathrm{S}_w^{(2)} + \mathrm{T}_w^{in} \tag{4.7.2}$$

Scalar:

$$\frac{\partial(D\Phi)}{\partial t} + \frac{\partial(D\mathcal{U}_\alpha\Phi)}{\partial x_\alpha} + \frac{\partial(\Omega\Phi)}{\partial\sigma} = \mathrm{T}_\Phi + \boldsymbol{S_\Phi} \tag{4.7.3}$$

where the dummy indexes $\alpha, \beta = (1, 2)$ represent the horizontal coordinates (summation over the repeated indexes).

The various terms and variables in equations 4.7.1, 4.7.2 and 4.7.3 are defined as follows: Ω represents the Stokes adjusted sigma vertical velocity, $\epsilon_{\alpha 3\beta}$ represents the well known Levy-Civita symbol, f_3 is the Coriolis parameter, P_α is the pressure term defined by equation 4.4.4, T^{turb} represents the usual Reynolds flux terms expressed as the sum of their horizontal ($\mathrm{T}^{turb}_{\mathrm{h}\alpha}$), and vertical ($\mathrm{T}^{turb}_{\mathrm{v}\alpha}$) components (equations 4.4.5), $\mathrm{S}_w^{(1)}$ represents the wave induced radiation stress per unit mass, $\mathrm{S}_w^{(2)}$

represents another wave radiation stress term (vertical), T_w^{in} represents a kinematic stress term reflecting the wave/stokes growth due to wind pressure fluctuations, T_Φ represents the Reynolds flux terms for the scalar (equation 4.4.7) and $\boldsymbol{S_\Phi}$ represents the various sources being modeled for the scalar Φ. The ζ represents the wave averaged Eulerian mean surface fluctuation, such that the total water depth D is defined as $h + \zeta$.

In equation 4.7.3, it is assumed that the wave and the scalar interactions are uncorrelated ($\overline{\tilde{\Phi}\tilde{u}} = 0$), therefore, the term T_Φ is not modified by the waves (still calculated from equation 4.4.7). In the case of the momentum equation 4.7.2 though, the Reynolds fluxes are modified by including terms that account for the wave induced turbulence. This matter along with the related modifications of the turbulence closure model will be discussed later.

Using the notation outlined in Section 4.5 the terms Ω, $\mathrm{S}_w^{(1)}$, $\mathrm{S}_w^{(2)}$ and T_w^{in}, are expressed mathematically as follows:

$$\Omega = w - \lambda_\alpha u_\alpha - \lambda_t = w - \lambda_\alpha u_\alpha - \lambda_\alpha \mathrm{u}_{\mathrm{st}\alpha} - \lambda_t = D\overset{\star}{\omega} - \lambda_\alpha \mathrm{u}_{\mathrm{st}\alpha} \tag{4.7.4}$$

$$\mathrm{S}_w^{(1)} = -\frac{\partial S_{\alpha\beta}}{\partial x_\beta}\ ; \qquad \mathrm{S}_w^{(2)} = \frac{\partial(\overline{\tilde{p}\tilde{s}}_\alpha^{\psi})}{\partial\sigma}\ ; \qquad S_{\alpha\beta} = D\,\overline{\tilde{u}_\alpha\tilde{u}_\beta}^{\psi} + \delta_{\alpha\beta}\,\overline{\tilde{p}\tilde{s}}_\sigma^{\psi}\ ; \qquad \mathrm{T}_w^{in} = \zeta_\mathrm{s}\cdot\overline{\tilde{p}_{wn}\frac{\partial\tilde{\zeta}}{\partial x_\alpha}}^{\psi} \tag{4.7.5}$$

$$S_{\alpha\beta} = kDE\left[\frac{k_\alpha k_\beta}{k^2}F_{CS}F_{CC} + \delta_{\alpha\beta}\left(F_{CS}F_{CC} - F_{SS}F_{CS}\right)\right] \tag{4.7.6}$$

$$\overline{\tilde{p}\tilde{s}}_\alpha^{\psi} = \left(F_{CC} - F_{SS}\right)E^{1/2}\,\frac{\partial}{\partial x_\alpha}(E^{1/2}F_{SS}) \tag{4.7.7}$$

The Stokes drift in "σ" coordinates is defined in Mellor [2003] as:

$$\mathrm{u}_{\mathrm{st}\alpha} = \frac{1}{D}\frac{\partial(\overline{\tilde{s}\tilde{u}}_\alpha^{\psi})}{\partial\sigma}\ ; \qquad \mathrm{u}_{\mathrm{st}\alpha} = \frac{E}{cD}\frac{k_\alpha}{k}\frac{\partial(F_{SS}F_{CC})}{\partial\sigma} = \frac{E}{cD}\frac{k_\alpha}{k}\zeta_\mathrm{s} \tag{4.7.8}$$

and it is related to the wave action density per unit mass $\mathcal{A}$ by the following equation:

$$\mathrm{u}_{\mathrm{st}\alpha} = k_\alpha\mathcal{A} \tag{4.7.9}$$

The derivation of Mellor's wave induced equations of motion is general in the sense the exact functional forms of the wave terms present in the equations have not been introduced, except for the radiation stress term $S_{\alpha\beta}$. The vertical coordinate is divided in σ layers, or surfaces, accompanied by wave disturbed $\tilde{s}$ surfaces. The $\tilde{s}$ surfaces simulate the oscillatory vertical displacements of the fluid

particles due to the wind generated surface waves. The wave action (or wave pseudo-momentum) is introduced into the core water column through these disturbed surfaces, thus defining the 3D effects of the waves on the currents. Mathematically, this process is described by the term $S_w^{(2)}$ in equation 4.7.2. The above perturbations of the free surface need a reason for their existence. The forcing function responsible for the generation of the wave induced disturbances is the term T_w^{in} in equation 4.7.2. The same term is responsible for the growth of the wave action or the Stokes drift (Mellor [2003]) and it is also a forcing function in the wave models describing the interactions between the wind and the free surface (Mellor [2005], Mellor et al. [2008]).

The 3D radiation stresses vanish in deep waters ($kD \gg 3$), except in the vicinity of the free surface, but they do reveal their full 3D status in shallow waters ($kD < 1$) making them an extremely important factor for the calculations of the wave set-up and the sediment transport. McWilliams et al. [2004], have derived a similar set of the wave induced equations of motion where the concept of the wave radiation stresses has been replaced by the combination of additional Stokes vorticity terms and a Stokes Bernoulli head. As noted in Lane et al. [2005], these equations are applicable from the surf zone and beyond ($kD > 1$), while Mellor's equations can be applied all the way to the shoreline (though their exact accuracy and missing physics are still under investigation). Furthermore, the equations of McWilliams et al. [2004] represent a complicated construct to model within the framework of the existing hydrodynamic models and they do not include turbulence in a realistic way (Ardhuin and Jenkins [2006a]).

Thus far, the physics of the wave induced effects on the mean flow are very well described by equation 4.7.2. The problems arise when the terms $S_w^{(1)}$, $S_w^{(2)}$ and T_w^{in} are finally determined using linear wave theory, making the direct inclusion of equations 4.7.1, 4.7.2 and 4.7.3 in the existing hydrodynamic models problematic and prone to errors. The following Section provides a discussion of the problem.

(a) The modeling of the equations in terms of the Lagrangian velocity $\mathcal{U}$ instead of the Eulerian velocity u, requires higher resolution (temporal and spatial) at regions where the Stokes drift u_{st} is of the same order (or larger) as the Eulerian velocity u. The reasoning for that is the possibility of *CFL* violations in those regions (u_{st} attains its higher values at the free surface).

(b) In shoaling waters the term $S_w^{(2)}$ is asymptotically of order $O(\epsilon_1^2)$ instead of $O(\epsilon_1^2\epsilon_2)$, as are the rest of the wave terms in equation 4.7.2. ϵ_1 is defined as a maximum wave slope, ϵ_2 is

defined as a maximum bottom slope (equations 4.5.1) and both are considered small quantities in the present derivation. This problematic behavior of the term $S_w^{(2)}$ has been recently explored by Ardhuin et al. [2008a,b] and has also been acknowledged by Mellor [2008]. Furthermore, Mellor [2008] discovered that in deep waters ($kD > 3$) the use of the proposed analytical expressions for the combined wave radiation stress terms (equations 4.7.6 and 4.7.7) possibly introduces mean currents in the case of unforced waves over bottom variations, which clearly is physically incorrect.

(c) Regarding the horizontal radiation stress term $S_{\alpha\beta}$, there are many different expressions derived by various researchers according to the point of view used (e.g., Mellor [2003], Xia et al. [2004], Groeneweg and Klopman [1998], Lin and Zhang [2005], to just name a few). Mellor [2008], introduces yet another expression for $S_{\alpha\beta}$ to correct the problems described in item (*b*). Therefore, it is clear that the exact form of the 3D radiation stresses is still not fully established and further research on this subject is required. All the $S_{\alpha\beta}$ proposed expressions vertically integrate to the 2D radiation stresses $R_{\alpha\beta}$ derived by Longuet-Higgins and Stewart [1964], Phillips [1977](equation 4.1.2) a condition referenced by all developers as the minimal basis for the correctness of the derived 3D expressions for $S_{\alpha\beta}$. In that respect, any wave function that vertically integrates to $R_{\alpha\beta}$ can be claimed to be the three-dimensional counterpart of $R_{\alpha\beta}$ whether correct or not.

(d) The analytical form of the term T_w^{in} is not well established, pending further research developments (Mellor [2003]). As it has been shown in Mellor [2005] and in Mellor et al. [2008], $T_w^{in}\big|_{\sigma=0}$ is a wind input term ($\boldsymbol{S}_{in}$) of a wave model and, furthermore, it is the term responsible for the growth of the pseudo-momentum (Mellor [2003]). In any case $T_w^{in}\big|_{\sigma=0}$ is being modeled using empirical parametrizations in the wave model and should be a wave input to the hydrodynamic model and then be distributed vertically in the water column. To account for spectral wave distribution T_w^{in} has to be evaluated first by using a sufficient number of frequencies and wave directions, to accurately resolve the wave spectrum, and then to phase average the resulting term so it can be used by a hydrodynamic model. Assuming that an analytical (approximate or exact) expression for T_w^{in} does exist and that it is well established, the evaluation of T_w^{in} at each grid point (horizontal and vertical) at each time step, imposes significant computational burdens on the model, which is not a desired effect. The same reasoning is true for all the wave terms in equation 4.7.2, except the vertically integrated radiation stress that is an output parameter of the wave model. In any case, the calculation of all the wave related parameters is a job that should be performed by the wave model and not by the hydrodynamic model.

It is believed that the reasons described above give a strong explanation why the direct use of equations 4.7.1, 4.7.2 and 4.7.3 in a hydrodynamic model is impractical, while at the same time, it possibly introduces errors and uncertainties in the calculations of the hydrodynamic model. It is the intention here to derive the wave induced equations of motion in terms of the Eulerian velocity u only and to account for the wave induced effects by the introduction of additional wave dependent forcing terms. The reformulation of the momentum and continuity equations in terms of u, will eliminate the vertical radiation stress gradient $S_w^{(2)}$ and the T_w^{in} terms from equation 4.7.2, thus eliminating all the problems discussed so far.

In the next Sections, the equations of motion that account for the wave current interactions are derived using monochromatic waves and later the results are extended to spectral waves (Chapter 5). After all the equations are derived, the equations are cast in dimensional and non-dimensional form, and their representations in σ and curvilinear coordinates is given in Appendix C.

4.8 Stokes Drift Separation and Conservation of Mass

The objective of this and the subsequent Sections is to separate the Stokes drift from the l.h.s of equations 4.7.1, 4.7.2 and 4.7.3, such that the l.h.s of the resulting equations assumes a similar format as the original equations in the *SMF* (equations 4.4.1, 4.4.2 and 4.4.6), while the additional forcing terms that account for the wave-current interactions are gathered in the r.h.s of the equations.

The reasons for doing this are: *(a)* to write the equations in such a way that they can be easily incorporated into the existing hydrodynamic models, *(b)* to simplify the equations so that they can easily be extended to the spectral waves, *(c)* to relate the wave terms with the vertically averaged parameters of the wave model, *(d)* to derive the appropriate *WCBBL* equations, *(e)* to maintain numerical stability, and *(f)* to better understand the physics involved. The issues addressed in Section 4.7 impose additional reasoning for the necessity of the Stokes drift separation approach discussed here.

The Stokes drift separation involves the derivation of the wave pseudo-momentum equation (Section 4.9), which afterwards will be subtracted from the momentum equation 4.7.2. To achieve this, the momentum equation needs first to be re-formulated. Using the expressions for $\mathcal{U}_\alpha = u_\alpha + u_{st\alpha}$ (the first of equations 4.6.4) and $\Omega = D\overset{\star}{\omega} - \lambda_\alpha u_{st\alpha}$ (the last of equations 4.7.4), equation 4.7.2 is re-written as follows:

$$\underbrace{\frac{\partial(Du_\alpha)}{\partial t}+\frac{\partial(Du_\alpha u_\beta)}{\partial x_\beta}+\frac{\partial(D\overset{\star}{\omega}u_\alpha)}{\partial\sigma}}_{(1)}=-\epsilon_{\alpha 3\beta}f_3 D\,(u_\beta+\mathrm{u}_{st\beta})+\mathrm{P}_\alpha+\mathrm{T}^{turb}+\mathrm{S}_w^{(1)}+\mathrm{S}_w^{(2)}+\mathrm{T}_w^{in}$$

$$-\underbrace{\left\{\frac{\partial(D\mathrm{u}_{st\alpha})}{\partial t}+\frac{\partial(D\mathrm{u}_{st\alpha}\mathrm{u}_{st\beta})}{\partial x_\beta}+\frac{\partial(\mathrm{u}_{st\alpha}\Omega)}{\partial\sigma}\right\}}_{(2)}-\underbrace{\frac{\partial}{\partial x_\beta}\Big[D(u_\alpha\mathrm{u}_{st\beta}+u_\beta\mathrm{u}_{st\alpha})\Big]}_{(3)}+\underbrace{\frac{\partial}{\partial\sigma}(\lambda_\beta u_\alpha\mathrm{u}_{st\beta})}_{(4)}\qquad(4.8.1)$$

The next step is to derive a suitable conservation of mass equation. Using the expression for Ω (equation 4.7.4) and the inverse equations for the σ transformation (Appendix B), equation 4.7.1 is transformed from "σ" coordinates into "z" coordinates as follows:

$$\frac{\partial u_\alpha}{\partial x_\alpha}+\frac{\partial \mathrm{u}_{st\alpha}}{\partial x_\alpha}+\frac{\partial w}{\partial z}\,;\qquad \alpha=(1,2)\qquad(4.8.2)$$

which is the conservation of mass equation. From equation 4.8.2 it is clear that up to this point in the presence of the Stokes drift velocity, the velocity field (u,v,w) is divergent. The re-arrangement of the terms in equation 4.8.2 gives:

$$\frac{\partial u_\alpha}{\partial x_\alpha}+\frac{\partial w}{\partial z}=-\frac{\partial \mathrm{u}_{st\alpha}}{\partial x_\alpha}\qquad(4.8.3)$$

Defining a Stokes vertical pseudo-velocity w_{st} such that:

$$\frac{\partial \mathrm{u}_{st\alpha}}{\partial x_\alpha}+\frac{\partial \mathrm{w}_{st}}{\partial z}=0\qquad(4.8.4)$$

equation 4.8.3 is written as:

$$\frac{\partial u_\alpha}{\partial x_\alpha}+\frac{\partial(w-\mathrm{w}_{st})}{\partial z}=0\qquad(4.8.5)$$

which now represents the continuity equation written in a divergent free form. The surface and bottom kinematic boundary conditions (equations 2.1.14 and 2.1.18) in the presence of the Stokes drift are modified as follows:

$$\underline{\text{surface } (z=\zeta)}:\qquad w|_\zeta=\left[\frac{\partial\zeta}{\partial t}+u_\alpha\frac{\partial\zeta}{\partial x_\alpha}+\mathrm{u}_{st\alpha}\frac{\partial\zeta}{\partial x_\alpha}\right]_{z=\zeta}\,;\qquad \alpha=(1,2)\qquad(4.8.6a)$$

$$\underline{\text{bottom } (z=-h)}:\qquad w|_{-h}=-\left[u_\alpha\frac{\partial h}{\partial x_\alpha}+\mathrm{u}_{st\alpha}\frac{\partial h}{\partial x_\alpha}\right]_{z=-h}\,;\qquad \alpha=(1,2)\qquad(4.8.6b)$$

The definition of equation 4.8.5 implies that equations 4.8.6a and 4.8.6b can be written in the following alternative forms:

$$(w - \mathrm{w_{st}})\big|_{\zeta} = \left[\frac{\partial \zeta}{\partial t} + u_\alpha \frac{\partial \zeta}{\partial x_\alpha}\right]_{z=\zeta} \; ; \qquad \alpha = (1,2) \tag{4.8.7a}$$

$$(w - \mathrm{w_{st}})\big|_{-h} = -\left[u_\alpha \frac{\partial h}{\partial x_\alpha}\right]_{z=-h} \; ; \qquad \alpha = (1,2) \tag{4.8.7b}$$

where:

$$\mathrm{w_{st}}|_{\zeta} = \left[\mathrm{u_{st\alpha}} \frac{\partial \zeta}{\partial x_\alpha}\right]_{z=\zeta} \; ; \qquad \mathrm{w_{st}}|_{-h} = -\left[\mathrm{u_{st\alpha}} \frac{\partial h}{\partial x_\alpha}\right]_{z=-h} \; ; \qquad \alpha = (1,2) \tag{4.8.8}$$

Integrating equation 4.8.4 over the vertical direction gives:

$$\mathrm{w_{st}} = \mathrm{w_{st}}|_{\zeta} + \int_z^{\zeta} \frac{\partial \mathrm{u_{st\alpha}}}{\partial x_\alpha} dz' \tag{4.8.9}$$

Using the Leibniz's rule for the differentiation of the integrals (equation B.46) and the first of equations 4.8.8, equation 4.8.9 is written as:

$$\mathrm{w_{st}} = \frac{\partial}{\partial x_\alpha} \int_z^{\zeta} \mathrm{u_{st\alpha}} \, dz' \tag{4.8.10}$$

and this is the formal definition of the Stokes vertical pseudo-velocity $\mathrm{w_{st}}$. From the definition of $\mathrm{u_{st\alpha}}$ (the second of equations 4.7.8) the Stokes drift can be written as a function of the vertically averaged Stokes drift in Cartesian coordinates as follows:

$$\mathrm{u_{st\alpha}} = D\mathrm{U_{st\alpha}} \frac{\partial (F_{SS} F_{CC})}{\partial z} = D\mathrm{U_{st\alpha}} \frac{2k \cosh 2k(z+h)}{\sinh 2kD} = D\mathrm{U_{st\alpha}} \zeta_{\mathrm{ss}} \tag{4.8.11}$$

Evaluation of equation 4.8.11 at the free surface and the bottom gives the following expressions for $\mathrm{u_{st\alpha}}$:

$$\mathrm{u_{st\alpha}}|_{\zeta} = \mathrm{U_{st\alpha}} \frac{2kD}{\tanh 2kD} \; ; \qquad \mathrm{u_{st\alpha}}|_{-h} = \mathrm{U_{st\alpha}} \frac{2kD}{\sinh 2kD} \tag{4.8.12}$$

The vertical integration of equation 4.8.4 and the use of Leibnitz's rule gives:

$$\int_{-h}^{\zeta} \left[\frac{\partial \mathrm{u_{st\alpha}}}{\partial x_\alpha} + \frac{\partial \mathrm{w_{st\alpha}}}{\partial z}\right] dz = 0 \Rightarrow$$

$$\frac{\partial (D\mathrm{U_{st\alpha}})}{\partial x_\alpha} + \underbrace{\left(\mathrm{w_{st}}|_{\zeta} - \mathrm{u_{st\alpha}}|_{\zeta} \frac{\partial \zeta}{\partial x_\alpha}\right)}_{=0 \text{ (equation 4.8.8)}} - \underbrace{\left(\mathrm{w_{st}}|_{-h} + \mathrm{u_{st\alpha}}|_{-h} \frac{\partial h}{\partial x_\alpha}\right)}_{=0 \text{ (equation 4.8.8)}} = 0 \Rightarrow \qquad \frac{\partial (D\mathrm{U_{st\alpha}})}{\partial x_\alpha} = 0 \tag{4.8.13}$$

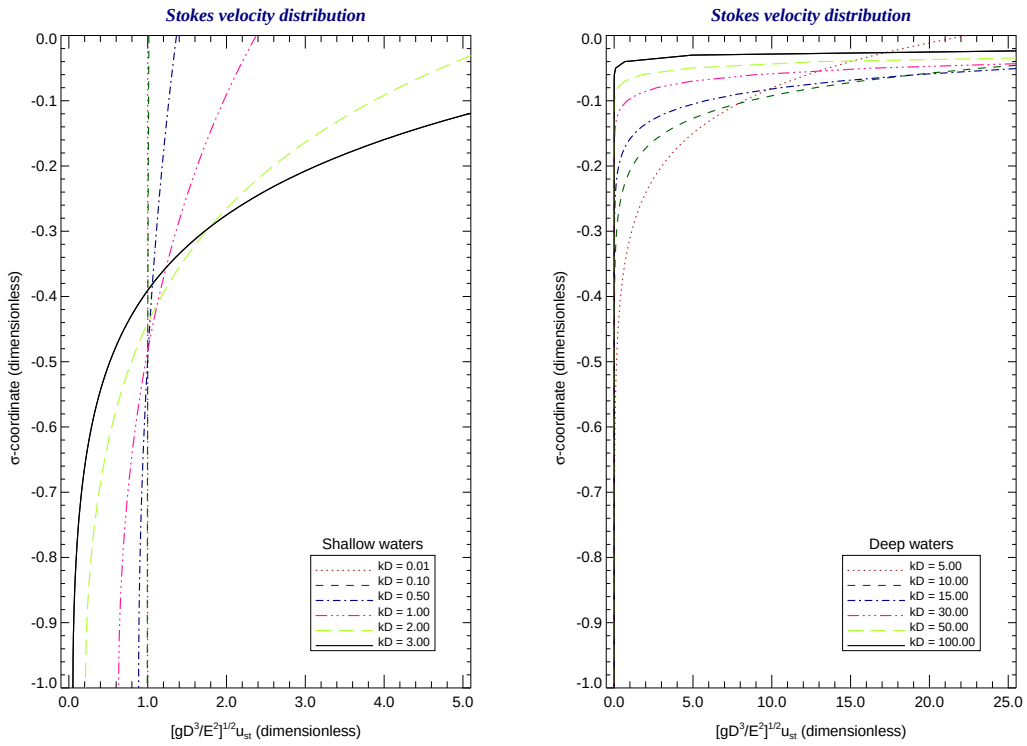

Figure 4.5 Vertical distribution of the Stokes drift in shallow and deep water conditions.

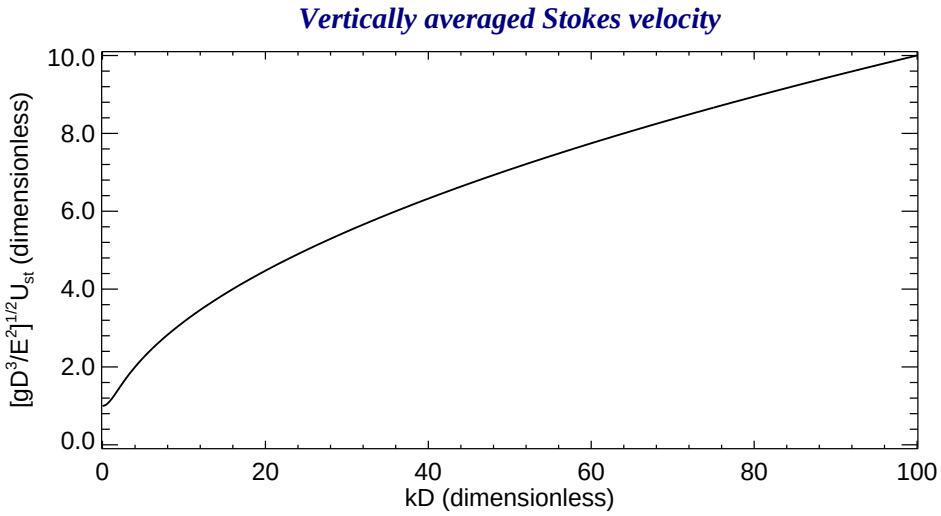

Figure 4.6 Vertically averaged Stokes drift vs. *kD*.

Substituting the second of equations 4.8.11 into equation 4.8.10 and performing the integration, the following analytical expression for w_{st} in "z" coordinates is obtained:

$$w_{st} = -D U_{st\alpha} \frac{\partial(F_{SS} F_{CC})}{\partial x_\alpha} \tag{4.8.14a}$$

where for the derivation of 4.8.14a, the continuity equation for the vertically averaged Stokes drift (equation 4.8.13) has been applied. The expression of w_{st} in "σ" coordinates is:

$$w_{st} = -D U_{st\alpha} \frac{\partial(F_{SS} F_{CC})}{\partial x_\alpha} + \lambda_\alpha u_{st\alpha} \tag{4.8.14b}$$

while the continuity equation 4.8.5 becomes in "σ" coordinates:

$$\frac{\partial \zeta}{\partial t} + \frac{\partial (D u_\alpha)}{\partial x_\alpha} + \frac{\partial (D \overset{\star}{\Omega})}{\partial \sigma} = 0 \qquad \text{and:} \qquad \frac{\partial D}{\partial t} + \frac{\partial (D u_\alpha)}{\partial x_\alpha} + \frac{\partial (D \overset{\star}{\Omega})}{\partial \sigma} = 0 \tag{4.8.15}$$

with:
$$D \overset{\star}{\Omega} = w - w_{st} - \lambda_\alpha u_\alpha - \lambda_t \tag{4.8.16}$$

where λ_α, λ_t are given by equations 4.5.2a. Comparing equations 4.8.15 and 4.7.4 it is seen that Mellor's definition of $w_{st} = \lambda_\alpha u_{st\alpha}$ is slightly different from the present definition given by equation 4.8.14b. In both cases though, the surface and bottom kinematic boundary conditions (equations 4.8.6a and 4.8.6b) remain the same.

Equations 4.8.14a and 4.8.14b are in a form that can be used in a hydrodynamic model. To avoid calculations of the spatial gradients of the term $F_{SS} F_{CC}$ an equation is derived that approximates equations 4.8.14a and 4.8.14b:

$$\frac{\partial F_{SS} F_{CC}}{\partial x_\alpha} = \left[\frac{\partial (2kz)}{\partial x_\alpha} + \frac{\partial (2kh)}{\partial x_\alpha} \right] \frac{F_{CS} F_{CC} + F_{SC} F_{SS}}{2} - 2 \frac{\partial (kD)}{\partial x_\alpha} \frac{F_{CC} F_{SS}}{\tanh 2kD} \tag{4.8.17}$$

The above equation is valid in both the Cartesian and the σ coordinate systems. Equation 4.8.17 can be simplified assuming a slowly spatially varying wavenumber (following LeBlond and Mysak [1978], Mei [1983] and others), so that:

$$\frac{\partial (2kz)}{\partial x_\alpha} + \frac{\partial (2kh)}{\partial x_\alpha} \approx 2k \frac{\partial h}{\partial x_\alpha} \; ; \qquad 2 \frac{\partial (kD)}{\partial x_\alpha} \approx 2k \left(\frac{\partial \zeta}{\partial x_\alpha} + \frac{\partial h}{\partial x_\alpha} \right) \tag{4.8.18}$$

Substituting equations 4.8.18 into equation 4.8.17 we obtain:

$$\frac{w_{st}}{U_{st\alpha}} = F_{SB} \frac{\partial \zeta}{\partial x_\alpha} + (F_{SB} - F_{SA}) \frac{\partial h}{\partial x_\alpha} \tag{4.8.19}$$

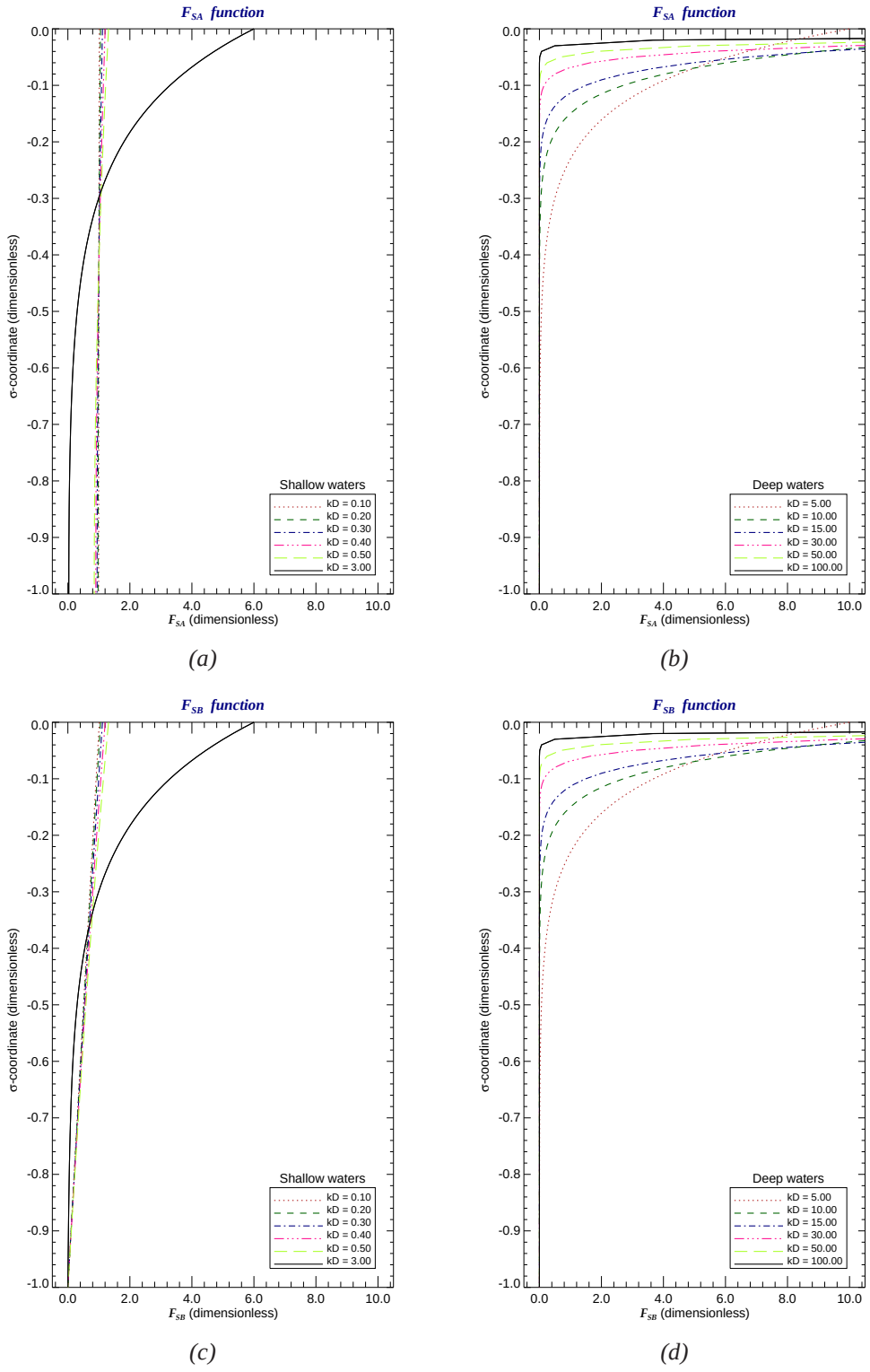

Figure 4.7 Plots of the exponential functions F_{SA} and F_{SB} for shallow and deep water conditions.

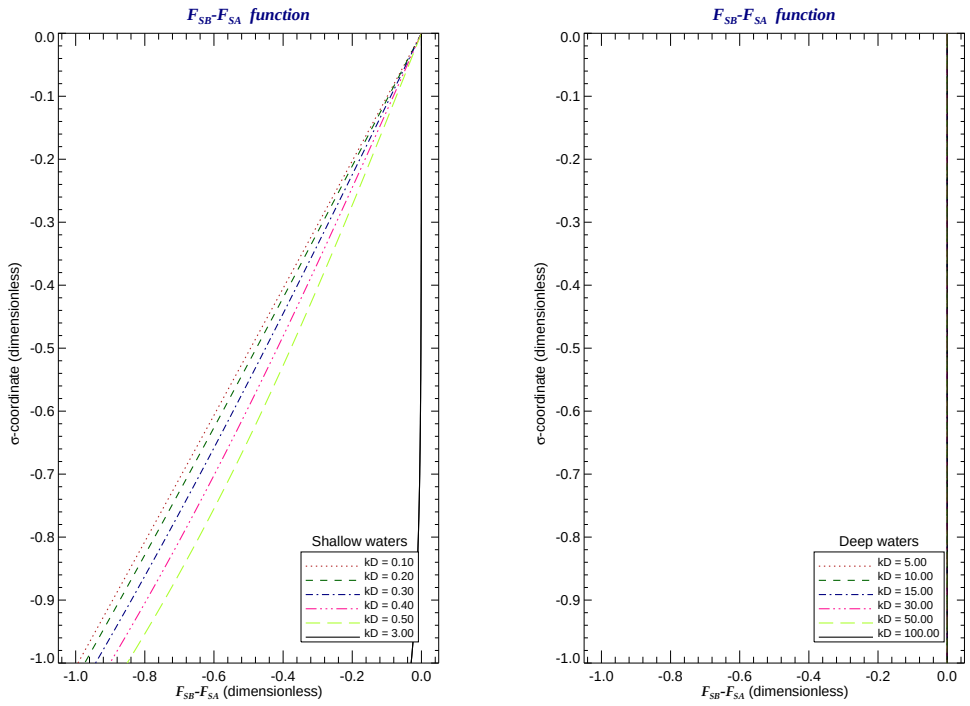

(a) *(b)*

Figure 4.8 Plots of the exponential function $F_{SB} - F_{SA}$ for shallow and deep water conditions.

$$\frac{w_{st}}{U_{st\alpha}} = F_{SA}\frac{\partial \zeta}{\partial x_\alpha} + (F_{SB} - F_{SA})\frac{\partial D}{\partial x_\alpha} \tag{4.8.20}$$

with:
$$F_{SA} = \frac{2kD\,(F_{CS}F_{CC} + F_{SC}F_{SS})}{2}\;; \qquad F_{SB} = \frac{2kD\,F_{CC}F_{SS}}{\tanh 2kD} \tag{4.8.21}$$

The plots of the vertical distribution functions F_{SA} and F_{SB} are given in Figure 4.7 and their difference in Figure 4.8.

4.9 Wave Pseudo-Momentum

Let $\mathcal{A} = \mathcal{A}(x, y, z, t)\,(\mathrm{m^3 s^{-1}})$ be the wave action density per unit mass and $\boldsymbol{u} = (u, v, w)$ be the Lagrangian averaged flow velocity. Andrews and McIntyre [1978b] have derived the following equation for the conservation of the wave action (their equation 2.15):

$$\frac{\partial}{\partial t}(\mathcal{J}\mathcal{A}) + \frac{\partial}{\partial x_\beta}\Big[(u_\beta + c_{g\beta})\,\mathcal{J}\mathcal{A}\Big] + \frac{\partial}{\partial z}(w\mathcal{J}\mathcal{A}) = \mathcal{J}F = \mathcal{J}(\mathcal{G}_w - \mathcal{D}_w) \tag{4.9.1}$$

where $\beta = (1, 2)$, summation over β, $(\mathcal{u}_1, \mathcal{u}_2) = (\mathcal{u}, \mathcal{v})$, $c_{g\beta}$ is the β-th component of the wave group velocity and $\mathcal{J}$ is the Jacobian of the transformation between the Eulerian and the Lagrangian spaces (equation 4.6.3). In the above equation, the incompressibility condition has been applied, while $\mathcal{A}$ represents a wave phased averaged quantity. The Lagrangian vertical velocity is defined as $\mathcal{w} = w + \cancelto{0}{w_{st}} \approx w$.

The variable F represents the source/sink terms for the wave evolution, where $\mathcal{G}_w$ is the collective representation of the source terms responsible for the growth and evolution of the wave action and $\mathcal{D}_w$ is the dissipation term representing the losses of the wave energy due to viscous dissipation (at the free surface), the wave breaking, the production of turbulence in the water column, and the interaction with the bottom sediments. The variables $\mathcal{A}$ and F appearing in equation 4.9.1 are both of order $O(\epsilon_1^2)$ (Andrews and McIntyre [1978b]).

From equation 4.6.3 it is seen that $\mathcal{J} = 1 + O(\epsilon_1) + \cdots$ since $\tilde{\xi}$ is a quantity of the first order in the wave slope ϵ_1, and its phase averaged counterpart is:

$$\overline{\mathcal{J}}^{\psi} = 1 + \frac{1}{2}\overline{\frac{\partial \tilde{\xi}_k}{\partial x_k}\frac{\partial \tilde{\xi}_m}{\partial x_m}}^{\psi} + \cdots = 1 + O(\epsilon_1^2) + \cdots \tag{4.9.2}$$

The calculations here, as in Section 4.7, are $O(\epsilon_1^2)$ accurate, therefore, terms of order higher than $O(\epsilon_1^2)$ are neglected. In equation 4.9.1 the terms $\mathcal{J}\,\mathcal{A}$ are evaluated as follows:

$$\mathcal{J}\mathcal{A} = [1 + O(\epsilon_1) + \cdots]\,\mathcal{A} = \mathcal{A} + \mathcal{A} \cdot O(\epsilon_1) + \cdots = \mathcal{A} + O(\epsilon_1^3) + \cdots \approx \mathcal{A} \tag{4.9.3}$$

Similarly, $\mathcal{J}F \approx F = \mathcal{G}_w - \mathcal{D}_w$, therefore, equation 4.9.1 becomes:

$$\frac{\partial \mathcal{A}}{\partial t} + \frac{\partial}{\partial x_\beta}\Big[(\mathcal{u}_\beta + c_{g\beta})\,\mathcal{A}\Big] + \frac{\partial (w\mathcal{A})}{\partial z} = F = \mathcal{G}_w - \mathcal{D}_w \tag{4.9.4}$$

which is second order accurate in the wave slope ϵ_1.

The objective here is to derive the Stokes pseudo-momentum (u_{st}) equation to be subtracted from equation 4.7.2 to produce the momentum equation for the current velocity (u) that includes the net effects of the waves on the current. First, equation 4.9.4 is transformed in "s" coordinates (Section 4.5) and then $\mathcal{A}$ is expressed in terms of u_{st} (equation 4.7.9) to produce the final pseudo-momentum equation. Equation 4.9.4 is written in (x_α^*, s, t^*) coordinates as follows:

$$\left\{\frac{\partial \mathcal{A}^*}{\partial t^*} - \frac{s_t}{s_\sigma}\frac{\partial \mathcal{A}^*}{\partial \sigma}\right\} + \left\{\frac{\partial}{\partial x_{\beta^*}}\Big[(\mathcal{u}_\beta + c_{g\beta})\mathcal{A}\Big]^* - \frac{s_\beta}{s_\sigma}\frac{\partial}{\partial \sigma}\Big[(\mathcal{u}_\beta + c_{g\beta})\,\mathcal{A}\Big]^*\right\} + \frac{1}{s_\sigma}\frac{\partial}{\partial \sigma}(w\mathcal{A})^* = F^* \tag{4.9.5}$$

The phase averaging of equation 4.9.5 in combination with equations 4.5.6 produces the following equation:

$$\left\{\frac{\partial(\lambda_\sigma \mathcal{A}^*)}{\partial t^*} - \frac{\partial(\lambda_t \mathcal{A}^*)}{\partial \sigma}\right\} + \left\{\frac{\partial}{\partial x_{\beta^*}}\Big[(u_\beta + c_{g\beta})\lambda_\sigma \mathcal{A}\Big]^* - \frac{\partial}{\partial \sigma}\Big[(u_\beta + c_{g\beta})\lambda_\beta \mathcal{A}\Big]^*\right\}$$

$$+\frac{\partial}{\partial \sigma}(w\mathcal{A})^* = \lambda_\sigma F^* \tag{4.9.6}$$

Dropping the asterisks, replacing λ_σ by D and re-arranging the resulting terms, equation 4.9.6 can be written as follows:

$$\frac{\partial(D\mathcal{A})}{\partial t} + \frac{\partial}{\partial x_\beta}\Big[(u_\beta + c_{g\beta})D\mathcal{A}\Big] + \frac{\partial(\Omega\mathcal{A})}{\partial \sigma} = DF + \frac{\partial}{\partial \sigma}(\lambda_\beta c_{g\beta}\mathcal{A}) \tag{4.9.7}$$

where, $\Omega = w - \lambda_\beta u_\beta - \lambda_t$ is the almost vertical flow velocity in "σ" coordinates and it is the same velocity as that defined by equation 4.7.4. Now, let us multiply equation 4.9.7 by the wavenumber component k_α:

$$\underbrace{k_\alpha \frac{\partial(D\mathcal{A})}{\partial t}}_{(1)} + \underbrace{k_\alpha \frac{\partial}{\partial x_\beta}\Big[(u_\beta + c_{g\beta})D\mathcal{A}\Big]}_{(2)} + \underbrace{k_\alpha \frac{\partial(\Omega\mathcal{A})}{\partial \sigma}}_{(3)} = Dk_\alpha F + \underbrace{k_\alpha \frac{\partial}{\partial \sigma}(\lambda_\beta c_{g\beta}\mathcal{A})}_{(4)} \tag{4.9.8}$$

Using the definition $u_{st\alpha} = k_\alpha \mathcal{A}$, the irrotationality condition for the wavenumber k and introducing the Doppler velocity $\hat{u}_{A\beta}$ into the calculations, and after substantial mathematical manipulations based on the chain rule of differentiation, the terms (1), (2), (3) and (4) in equation 4.9.8 are written as follows:

$$(1): \qquad k_\alpha \frac{\partial(D\mathcal{A})}{\partial t} = \frac{\partial(D\,u_{st\alpha})}{\partial t} - D\mathcal{A}\frac{\partial k_\alpha}{\partial t} \tag{4.9.9}$$

$$(2): \qquad k_\alpha \frac{\partial}{\partial x_\beta}\Big[(u_\beta + c_{g\beta})D\mathcal{A}\Big] = \frac{\partial(D\,u_{st\alpha}u_{st\beta})}{\partial x_\beta} - D\mathcal{A}\Big[(\hat{u}_{A\beta} + c_{g\beta})\frac{\partial k_\alpha}{\partial x_\beta} + k_\beta \frac{\partial \hat{u}_{A\beta}}{\partial x_\alpha}\Big] +$$

$$D\mathcal{A}\frac{\partial(k_\beta \hat{u}_{A\beta})}{\partial x_\alpha} - D\mathcal{A}u_\beta \frac{\partial k_\alpha}{\partial x_\beta} + \frac{\partial}{\partial x_\beta}\Big[(u_\beta + c_{g\beta})\,D u_{st\alpha}\Big] \tag{4.9.10}$$

$$(3): \qquad k_\alpha \frac{\partial(\Omega\,\mathcal{A})}{\partial \sigma} = \frac{\partial(\Omega\,u_{st\alpha})}{\partial \sigma} \tag{4.9.11}$$

$$(4): \qquad k_\alpha \frac{\partial}{\partial \sigma}(\lambda_\beta c_{g\beta}\mathcal{A}) = \frac{\partial}{\partial \sigma}(\lambda_\beta c_{g\beta}u_{st\alpha}) \tag{4.9.12}$$

Substituting the derived expressions for the four terms into equation 4.9.8 in combination with equation 4.5.17 and neglecting the terms of order higher than $O(\epsilon_1^2)$, the following equation for the Stokes drift $\mathrm{u_{st}}$ (pseudo momentum) is derived:

$$\frac{\partial(D\,\mathrm{u_{st\alpha}})}{\partial t}+\frac{\partial(D\,\mathrm{u_{st\alpha}u_{st\beta}})}{\partial x_\beta}+\frac{\partial(\Omega\,\mathrm{u_{st\alpha}})}{\partial\sigma}=Dk_\alpha\mathcal{G}_w-Dk_\alpha\mathcal{D}_w-D\mathcal{A}\Big(\frac{\partial\mathring{\sigma}}{\partial x_\alpha}\Big)_k+$$

$$\frac{\partial}{\partial\sigma}(\lambda_\beta c_{g\beta}\mathrm{u_{st\alpha}})-D\mathcal{A}\frac{\partial(k_\beta\hat{u}_{A\beta})}{\partial x_\alpha}+D\mathcal{A}u_\beta\frac{\partial k_\alpha}{\partial x_\beta}-\frac{\partial}{\partial x_\beta}\Big[(u_\beta+c_{g\beta})D\mathrm{u_{st\alpha}}\Big] \tag{4.9.13}$$

Equation 4.9.13 is the $O(\epsilon_1^2)$ pseudo-momentum equation that describes the growth and evolution of the Stokes drift under the action of the forcing $F=\mathcal{G}_w-\mathcal{D}_w$. The above equation assumes an inhomogeneous current interacting with the waves over a non flat bottom.

4.9.1 Conservation of the Non-Advective Wave Action

The 3D wave action equation 4.9.1 used for the derivation of the wave pseudo-momentum in the previous Section, is written in a more general form (Andrews and McIntyre [1978b]) as follows:

$$\frac{\partial}{\partial t}(\mathcal{J}\mathcal{A})+\nabla\cdot(\mathcal{J}\mathcal{B}_{tot})=\mathcal{J}F \tag{4.9.14}$$

where $\mathcal{B}_{tot}$ is the total wave action flux per unit mass written as the sum of a mean flow advective term and a non-advective flux per unit mass term as follows:

$$\mathcal{B}_{tot}=\boldsymbol{u}\mathcal{A}+\mathcal{B} \tag{4.9.15}$$

Two equivalent expressions for the term $\mathcal{B}$ in equation 4.9.15 are given in Andrews and McIntyre [1978b]:

$$\mathcal{B}_i=c_{gi}\mathcal{A}=-\overline{p'\frac{\partial\tilde{\xi}_i}{\partial\psi}}^{\psi}\quad;\qquad i=(1,3) \tag{4.9.16}$$

where $\tilde{\xi}_i$ is the wave induced displacement of the fluid particle, c_{gi} is the i-th component of the wave group velocity, ψ is the wave phase and $p'=p-\bar{p}$ is the Eulerian disturbance of the kinematic pressure. Separating the background turbulence, as prescribed by equation B.3, the pressure p is re-defined such that $p-\bar{p}=\tilde{p}+p'$, where now the wave contributions to the pressure are represented by the term $\tilde{p}$, therefore, equation 4.9.16 becomes:

$$\mathcal{B}_i=c_{gi}\mathcal{A}=-\overline{p'\frac{\partial\tilde{\xi}_i}{\partial\psi}}^{\psi}-\overline{\tilde{p}\frac{\partial\tilde{\xi}_i}{\partial\psi}}^{\psi}\quad;\qquad i=(1,3) \tag{4.9.17}$$

The first term on the r.h.s of the second of equations 4.9.17 is zero because of the definition of the phase averaging operation and the equation reduces to:

$$\mathcal{B}_i = c_{gi}\mathcal{A} = -\overline{\tilde{p}\frac{\partial\tilde{\xi}_i}{\partial\psi}}^{\psi} \quad ; \qquad i = (1,3) \tag{4.9.18}$$

Equation 4.9.18 states that the pressure disturbance $\tilde{p}$ is responsible for the introduction of the wave action into the main flow through disturbed surfaces, which subsequently is transported by the wave group velocity. Using the second alternative expression for $\mathcal{B}$, equation 4.9.14 is transformed as:

$$\frac{\partial\mathcal{A}}{\partial t} + \frac{\partial}{\partial x_\beta}\Big[u_\beta - \overline{\tilde{p}\frac{\partial\tilde{\xi}_\beta}{\partial\psi}}^{\psi}\Big] + \frac{\partial}{\partial z}\Big[w\mathcal{A} - \overline{\tilde{p}\frac{\partial\tilde{\xi}_z}{\partial\psi}}^{\psi}\Big] = F \tag{4.9.19}$$

In the derivation of the above equation, the expressions $\mathcal{J}\mathcal{A} \approx \mathcal{A}$ and $\mathcal{J}F \approx F$ were applied, while the term $\partial\tilde{\xi}_i/\partial\psi$ has been split into its horizontal ($\partial\tilde{\xi}_\beta/\partial\psi$) and its vertical components ($\partial\tilde{\xi}_z/\partial\psi$) with the dummy index β taking the values 1, 2.

Equating the l.h.s sides of equations 4.9.4 and 4.9.19 and deleting the common terms:

$$-\frac{\partial}{\partial x_\beta}\overline{\Big(\tilde{p}\frac{\partial\tilde{\xi}_\beta}{\partial\psi}\Big)}^{\psi} - \frac{\partial}{\partial z}\overline{\Big(\tilde{p}\frac{\partial\tilde{\xi}_z}{\partial\psi}\Big)}^{\psi} = \frac{\partial}{\partial x_\beta}(c_{g\beta}\mathcal{A}) \tag{4.9.20}$$

Using the fact that the odd powers of $\sin\psi, \cos\psi$ as well as their products when they are phase averaged produce terms that are nil, it can be easily shown that the second term in the l.h.s of equation 4.9.20 is zero, but it is kept in place for later use.

Equation 4.9.20 states that non-advective wave action flux is produced by the pressure disturbances associated with the corresponding wave induced particle displacements ($\tilde{\xi}$) and that the wave action is transported by the wave group velocity. In other words, wave action penetrates into the water column only through disturbed surfaces. The term on the r.h.s of equation 4.9.20 describes the horizontal transport of the wave action by c_g, while it is introduced in an elemental control volume $\mathcal{CV}$ bounded by disturbed surfaces, by a vertical flux of horizontal momentum not present at the moment on the r.h.s of the equation. Using equation 4.9.18 and the expressions: $k_\alpha\partial/\partial\psi = \partial/\partial x_\alpha$ and $\psi = k_\alpha x_\alpha - \omega t$, equation 4.9.20 is transformed as follows:

$$-\frac{\partial}{\partial x_\beta}\Big(\overline{\tilde{p}\frac{\partial\tilde{\xi}_\beta}{\partial x_\alpha}}^{\psi}\Big) - \frac{\partial}{\partial z}\Big(\overline{\tilde{p}\frac{\partial\tilde{\xi}_z}{\partial x_\alpha}}^{\psi}\Big) = \frac{\partial}{\partial x_\beta}(c_{g\beta}u_{st\alpha}) \tag{4.9.21}$$

and in σ coordinates:

$$\underbrace{\frac{\partial(\overline{\tilde{p}\tilde{s}_\alpha}^{\psi})}{\partial\sigma}}_{(1)}+\underbrace{\frac{\partial}{\partial x_\beta}(Dc_{g\beta}u_{st\alpha})}_{(2)}-\underbrace{\frac{\partial}{\partial\sigma}(\lambda_\beta c_{g\beta}u_{st\alpha})}_{(3)}=$$

$$\frac{\partial}{\partial x_\beta}\left[\lambda_\sigma\Big(\overline{\tilde{p}\frac{\partial\tilde{\xi}_\beta}{\partial x_\alpha}}^{\psi}\Big)-\lambda_\alpha\Big(\overline{\tilde{p}\frac{\partial\tilde{\xi}_\beta}{\partial\sigma}}^{\psi}\Big)\right]-\frac{\partial}{\partial\sigma}\left[\lambda_\beta\Big(\overline{\tilde{p}\frac{\partial\tilde{\xi}_\beta}{\partial x_\alpha}}^{\psi}\Big)-\frac{\lambda_\alpha\lambda_\beta}{\lambda_\sigma}\Big(\overline{\tilde{p}\frac{\partial\tilde{\xi}_\beta}{\partial\sigma}}^{\psi}\Big)\right]+\frac{\partial}{\partial\sigma}\left[\frac{\lambda_\alpha}{\lambda_\sigma}\Big(\overline{\tilde{p}\tilde{s}_\sigma}^{\psi}\Big)\right]=$$

$$\underbrace{\frac{\partial}{\partial x_\beta}\Big(D\,\overline{\tilde{p}\frac{\partial\tilde{\xi}_\beta}{\partial x_\alpha}}^{\psi}\Big)}_{(4)}-\underbrace{\frac{\partial}{\partial\sigma}\Big(\lambda_\beta\,\overline{\tilde{p}\frac{\partial\tilde{\xi}_\beta}{\partial x_\alpha}}^{\psi}\Big)}_{(5)}+\underbrace{\frac{\partial}{\partial\sigma}\Big(\frac{\lambda_\alpha}{D}\,\overline{\tilde{p}\tilde{s}_\sigma}^{\psi}\Big)}_{(6)}\tag{4.9.22}$$

Equations 4.9.21 and 4.9.22 describe the conservation of the non-advective wave action (wave pseudo-momentum) in (x, y, z) and in (x, y, σ) coordinates, respectively, using the two alternate definitions of the wave action flux $\mathcal{B}$, as described in Andrews and McIntyre [1978b]. For the derivation of the second of equations 4.9.22, the expression: $\overline{\tilde{p}\,(\partial\tilde{\xi}_\beta/\partial\sigma)}^{\psi}=0$ has been applied. Term (1) represents the vertical flux of the horizontal pseudo-momentum entering the elemental control volume $C\mathcal{V}$ bounded by material wave surfaces. This momentum flux is subsequently transported by the wave group velocity, as represented by the terms (2) and (3). Furthermore, term (1) is exactly Mellor's vertical radiation stress term $S_w^{(2)}$ (the second of equations 4.7.5). The terms (4), (5) and (6) describe the fact that the wave action is introduced into the system through the interactions of the pressure and the surface disturbances.

The conservation of non-advective pseudo-momentum is connected with invariance to a translation of the disturbance pattern, while mean particle positions are kept fixed (Andrews and McIntyre [1978b]). The non-advective wave action flux $\mathcal{B}$ penetrates through the wave disturbed iso-s surfaces and, thus is introduced into the water column (Figure 4.9). Upon its introduction into the water column, the non-advective action flux is transported horizontally by the group velocity c_g (a fast motion compared to the slow Eulerian motions). It is emphasized here that this process takes place only through disturbed surfaces (Andrews and McIntyre [1978b]). Figure 4.9 shows an elemental control volume ($C\mathcal{V}$) bounded by an un-disturbed control surface (CS) that defines the regions where the various processes take place.

Using the linear wave theory and assuming nearly plane surface waves (waves with small amplitude), Andrews and McIntyre [1978b] have shown that over undisturbed surfaces the non-advective

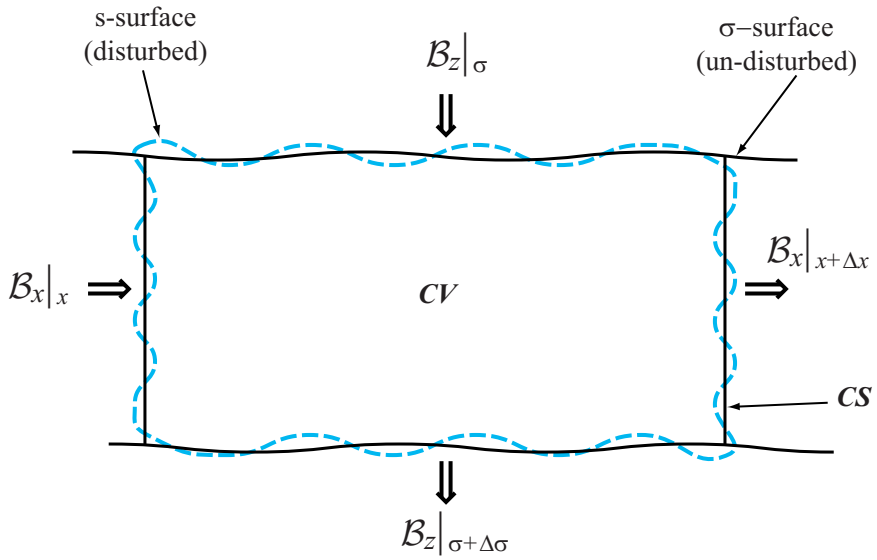

Figure 4.9 Schematic representation of the conservation of the non-advective wave action.

wave action flux is conserved (their equation 3.3), that is: $\vec{\mathcal{B}} \cdot \vec{n} = 0$, where $\vec{n}$ is the unit vector normal to the undisturbed surface. This statement along with the divergence theorem gives:

$$\int_{CV} \vec{u} \cdot \vec{\mathcal{B}}\, d\forall = \int_{CS} \vec{\mathcal{B}} \cdot \vec{n}\, dA = 0 \tag{4.9.23}$$

where the control volume CV is bounded by the control surface CS, which is defined by undisturbed surfaces. Letting $CV \to 0$, it can be seen from equation 4.9.23 that the divergence of the non-advective wave action flux is zero. The above arguments immediately imply that the l.h.s of the first of equations 4.9.22 vanishes. Using the above arguments, equations 4.9.22 are written as follows:

$$\frac{\partial(\overline{\tilde{p}\tilde{s}}^{\psi}_{\alpha})}{\partial\sigma} + \frac{\partial}{\partial x_\beta}(Dc_{g\beta}u_{st\alpha}) - \frac{\partial}{\partial\sigma}(\lambda_\beta c_{g\beta}u_{st\alpha}) = 0 \tag{4.9.24a}$$

$$\frac{\partial}{\partial x_\beta}\Big(D\,\overline{\tilde{p}\frac{\partial\tilde{\xi}_\beta}{\partial x_\alpha}}^{\psi}\Big) - \frac{\partial}{\partial\sigma}\Big(\lambda_\beta\,\overline{\tilde{p}\frac{\partial\tilde{\xi}_\beta}{\partial x_\alpha}}^{\psi}\Big) + \frac{\partial}{\partial\sigma}\Big(\frac{\lambda_\alpha}{D}\,\overline{\tilde{p}\tilde{s}_\sigma}^{\psi}\Big) = 0 \tag{4.9.24b}$$

The above conclusions are possible because the iso-s surfaces are material surfaces for the wave motion, therefore, there is no wave induced vertical velocity Ω or it is negligible. Equation 4.9.24a along with equation 4.9.13 will be used in the derivation of the final wave induced momentum equation for the Eulerian flow velocity u.

4.9.2 Dissipation of the Wave Energy by the Mean Flow

The wave energy dissipation term $\mathcal{D}_w$ in equation 4.9.13 is now regarded as an input (source term) in the wave induced momentum equation, such that any energy loss by the waves will be gained by the mean flow. This term is further decomposed as:

$$\mathcal{D}_w = \mathrm{T}_w^{visc} + \mathrm{T}_w^{break} + \mathrm{T}_w^{turb} + \mathrm{T}_w^{bfric} \tag{4.9.25}$$

to represent the various wave energy dissipation processes being modeled in M^2COPS, where: *(a)* T_w^{visc} represents the viscous dissipation of the wave energy (active at the surface thin viscous sublayer), *(b)* T_w^{break} represents the wave energy dissipation due to the wave breaking/whitecapping, *(c)* T_w^{turb} represents the wave energy losses due to the interactions with the mean flow, and *(d)* T_w^{bfric} represents the wave energy losses due to bottom friction (wave interactions with the bottom sediments and topography).

From the above terms, T_w^{break} is modeled as a modification of the surface boundary condition in the turbulence model (Section 7.4.1). Wave breaking is a source of turbulent kinetic energy (*TKE*) that is introduced at the free surface and distributed in the mean field via the turbulence model. T_w^{bfric} represents the wave energy losses due to the interactions with the sediments at the vicinity of the bottom and it is modeled within the bottom boundary layer framework (Chapter 6) by re-defining the bottom shear stresses.

The viscous term T_w^{visc} is written (Mellor [2005], Ardhuin et al. [2008b]) as:

$$\mathrm{T}_w^{visc} = \nu \frac{\partial \mathrm{u_{st}}_\alpha}{\partial z} \tag{4.9.26}$$

where, ν is the viscosity of the water. Since this term is generally small compared to its turbulent counterpart, it is lumped together with the turbulent Reynolds stresses. The vertical profile of the term T_w^{turb} is generally unknown, but as noted in Ardhuin et al. [2008b] and Mellor [2008], its vertical profile is assumed to be similar to that in equation 4.9.26, therefore, this term can be written as:

$$\mathrm{T}_w^{turb} = \mathcal{A}_\mathrm{v} \frac{\partial \mathrm{u_{st}}_\alpha}{\partial z} \tag{4.9.27}$$

and the vertical Reynolds flux term is modified according to:

$$\mathrm{T}_{\mathrm{v}\alpha}^{turb} = \mathrm{T}_{\mathrm{cv}\alpha}^{turb} + \mathrm{T}_{\mathrm{w}\alpha}^{turb} = \mathcal{A}_\mathrm{v} \frac{\partial u_\alpha}{\partial z} + \mathcal{A}_\mathrm{v} \frac{\partial \mathrm{u_{st}}_\alpha}{\partial z} = \mathcal{A}_\mathrm{v} \frac{\partial \mathcal{U}_\alpha}{\partial z} \tag{4.9.28}$$

where, equation 4.9.28 accounts for the wave energy dissipation in the water column (away from the boundaries), due to the interactions of the Reynolds stresses with the waves.

4.10 Wave Induced Momentum

Using the expression: $D\overset{\star}{\omega} = D\overset{\star}{\Omega} + \mathrm{u_{st}}$ the momentum equation 4.8.1 is written in terms of $\overset{\star}{\Omega}$ as:

$$\frac{\partial(Du_\alpha)}{\partial t} + \frac{\partial(Du_\alpha u_\beta)}{\partial x_\beta} + \frac{\partial(D\overset{\star}{\Omega}u_\alpha)}{\partial \sigma} + \underbrace{\frac{\partial(D\mathrm{u_{st\alpha}})}{\partial t} + \frac{\partial(D\mathrm{u_{st\alpha}u_{st\beta}})}{\partial x_\beta} + \frac{\partial(\mathrm{u_{st\alpha}}\Omega)}{\partial \sigma}}_{\text{Stokes terms}} =$$

$$-\epsilon_{\alpha 3\beta} f_3 D\,(u_\beta + \mathrm{u_{st\beta}}) + \mathrm{P}_\alpha + \mathrm{T}^{turb} + \mathrm{S}_w^{(1)} + \mathrm{S}_w^{(2)} + \mathrm{T}_w^{in}$$

$$-\frac{\partial}{\partial x_\beta}\left[D\,(u_\alpha \mathrm{u_{st\beta}} + u_\beta \mathrm{u_{st\alpha}})\right] + \frac{\partial}{\partial \sigma}(\lambda_\beta u_\alpha \mathrm{u_{st\beta}}) - \frac{\partial(u_\alpha \mathrm{w_{st}})}{\partial \sigma} \qquad (4.10.1)$$

Subtracting equation 4.9.13 from equation 4.10.1 we have:

$$\frac{\partial(Du_\alpha)}{\partial t} + \frac{\partial(Du_\alpha u_\beta)}{\partial x_\beta} + \frac{\partial(D\overset{\star}{\Omega}u_\alpha)}{\partial \sigma} = -\epsilon_{\alpha 3\beta} f_3 D\,(u_\beta + \mathrm{u_{st\beta}}) + \mathrm{P}_\alpha + \underbrace{\left(\mathrm{T}^{turb} + Dk_\alpha \mathcal{D}_w\right)}_{(1)} + \mathrm{S}_w^{(1)}$$

$$+ \underbrace{\left(\mathrm{T}_w^{in} - Dk_\alpha \mathcal{G}_w\right)}_{(2)} + \underbrace{\left[\mathrm{S}_w^{(2)} + \frac{\partial}{\partial x_\beta}(D\,c_{g\beta}\,\mathrm{u_{st\alpha}}) - \frac{\partial}{\partial \sigma}(\lambda_\beta\, c_{g\beta}\,\mathrm{u_{st\alpha}})\right]}_{(3)}$$

$$+ \underbrace{\left\{-\frac{\partial}{\partial x_\beta}\left[D(u_\alpha \mathrm{u_{st\beta}} + u_\beta \mathrm{u_{st\alpha}})\right] - \frac{\partial(u_\alpha \mathrm{w_{st}})}{\partial \sigma} + \frac{\partial}{\partial \sigma}(\lambda_\beta u_\alpha \mathrm{u_{st\alpha}}) + \frac{\partial}{\partial x_\beta}(Du_\beta \mathrm{u_{st\alpha}})\right\}}_{(4)}$$

$$+ D\mathcal{A}\left(\frac{\partial \mathring{\sigma}}{\partial x_\alpha}\right)_k + D\mathcal{A}\,\frac{\partial(k_\beta \hat{u}_{A\beta})}{\partial x_\alpha} - D\mathcal{A}\,u_\beta \frac{\partial k_\alpha}{x_\beta} \qquad (4.10.2)$$

Term (2) in equation 4.10.2 is identically zero, since $Dk_\alpha \mathcal{G}_w$ represents the source terms for the growth and evolution of the wave action and subsequently of the Stokes pseudo-momentum and therefore cancels out the wave growth term T_w^{in}. Term (3) is also zero because of equation 4.9.24a. Using the equation for the Stokes vertical pseudo velocity (equation 4.8.4) transformed in "σ" coordinates as:

$$\frac{\partial \mathrm{w_{st}}}{\partial \sigma} = -D\frac{\partial \mathrm{u_{st\alpha}}}{\partial x_\alpha} + \lambda_\alpha \frac{\partial \mathrm{u_{st\alpha}}}{\partial \sigma} \qquad (4.10.3)$$

the term (4) in equation 4.10.2 is written as follows:

$$(4): \quad u_{st\beta}\left\{\frac{\partial(Du_\beta)}{\partial x_\alpha}-\frac{\partial(Du_\alpha)}{\partial x_\beta}-\frac{\partial(\lambda_\alpha u_\beta)}{\partial\sigma}+\frac{\partial(\lambda_\beta u_\alpha)}{\partial\sigma}\right\}-w_{st}\frac{\partial u_\alpha}{\partial\sigma}-u_{st\beta}\frac{\partial(Du_\beta)}{\partial x_\alpha}+u_{st\beta}\frac{\partial(\lambda_\alpha u_\beta)}{\partial\sigma} \tag{4.10.4}$$

Substituting the expressions/values of the terms (2), (3) and (4) into equation 4.10.2 we obtain:

$$\frac{\partial(Du_\alpha)}{\partial t}+\frac{\partial(Du_\alpha u_\beta)}{\partial x_\beta}+\frac{\partial(D\overset{\star}{\Omega}u_\alpha)}{\partial\sigma}=-\epsilon_{\alpha 3\beta}f_3 D(u_\beta+u_{st\beta})+P_\alpha+\underbrace{\left(T^{turb}+Dk_\alpha\mathcal{D}_w\right)}_{(1)}+S_w^{(1)}$$

$$+u_{st\beta}\left\{\frac{\partial(Du_\beta)}{\partial x_\alpha}-\frac{\partial(Du_\alpha)}{\partial x_\beta}-\frac{\partial(\lambda_\alpha u_\beta)}{\partial\sigma}+\frac{\partial(\lambda_\beta u_\alpha)}{\partial\sigma}\right\}-w_{st}\frac{\partial u_\alpha}{\partial\sigma}$$

$$\underbrace{-u_{st\beta}\frac{\partial(Du_\beta)}{\partial x_\alpha}+u_{st\beta}\frac{\partial(\lambda_\alpha u_\beta)}{\partial\sigma}+D\mathcal{A}\left(\frac{\partial\mathring{\sigma}}{\partial x_\alpha}\right)_k+D\mathcal{A}\frac{\partial(k_\beta\hat{u}_{A\beta})}{\partial x_\alpha}-D\mathcal{A}u_\beta\frac{\partial k_\alpha}{x_\beta}}_{(2)} \tag{4.10.5}$$

Setting:

$$\epsilon_\beta=u_\beta-\hat{u}_{A\beta}\ ; \qquad \int_{-1}^{0}\epsilon_\beta\,\zeta_s\,d\sigma=0 \tag{4.10.6}$$

the term $\partial(k_\beta u_\beta)/\partial x_\alpha$ can be expressed in Cartesian and "σ" coordinates as follows:

$$\frac{\partial(k_\beta u_\beta)}{\partial x_\alpha}=\frac{\partial(k_\beta\hat{u}_{A\beta})}{\partial x_\alpha}+\frac{\partial(k_\beta\epsilon_\beta)}{\partial x_\alpha} \tag{4.10.7a}$$

$$\frac{\partial(k_\beta u_\beta)}{\partial x_\alpha}=\frac{\partial(k_\beta\hat{u}_{A\beta})}{\partial x_\alpha}+\frac{\partial(k_\beta\epsilon_\beta)}{\partial x_\alpha}+\lambda_\alpha\left[\frac{\partial(k_\beta u_\beta)}{\partial\sigma}-\frac{\partial(k_\beta\epsilon_\beta)}{\partial\sigma}\right] \tag{4.10.7b}$$

Using the fourth of equations 4.5.14, which indicates that the wavenumber vector is irrotational, and equation 4.7.9, which relates the Stokes velocity to the wave action density per unit mass $\mathcal{A}$, the terms in equation 4.10.7b are arranged as follows:

$$D\mathcal{A}\frac{\partial(k_\beta\hat{u}_{A\beta})}{\partial x_\alpha}-D\mathcal{A}u_\beta\frac{\partial k_\alpha}{\partial x_\beta}-u_{st\beta}\frac{\partial(Du_\beta)}{\partial x_\alpha}+u_{st\beta}\frac{\partial(\lambda_\alpha u_\beta)}{\partial\sigma}=-\mathcal{A}\frac{\partial(Dk_\beta\epsilon_\beta)}{\partial x_\alpha}+\mathcal{A}\frac{\partial(\lambda_\alpha k_\beta\epsilon_\beta)}{\partial\sigma} \tag{4.10.8}$$

Based on equation 4.10.8, term (2) of equation 4.10.5 reduces to:

$$(2): \qquad D\mathcal{A}\left(\frac{\partial\mathring{\sigma}}{\partial x_\alpha}\right)_k-u_{st\beta}\left\{\frac{\partial(D\epsilon_\beta)}{\partial x_\alpha}-\frac{\partial(\lambda_\alpha\epsilon_\beta)}{\partial\sigma}\right\} \tag{4.10.9}$$

In the derivation of the above equation the assumption that the wavenumber k is a spatially slow varying variable has been applied. The first term in the r.h.s of equation 4.10.9 represents the effects of the sloping bottom on the waves and the second term represents the effects of the vertically

inhomogeneous current on the waves. Substituting the expression for term (2) and using the second of equations 4.5.15, the momentum equation in σ coordinates becomes:

$$\frac{\partial(Du_\alpha)}{\partial t}+\frac{\partial(Du_\alpha u_\beta)}{\partial x_\beta}+\frac{\partial(D\overset{\star}{\Omega}u_\alpha)}{\partial\sigma}=-\underbrace{\epsilon_{\alpha 3\beta}f_3 D\,(u_\beta+\mathrm{u}_{st\beta})}_{(2)}+\mathrm{P}_\alpha+\underbrace{\left(\mathrm{T}^{turb}+Dk_\alpha\mathcal{D}_w\right)}_{(1)}+\mathrm{S}_w^{(1)}$$

$$+\underbrace{\mathrm{u}_{st\beta}\left\{\frac{\partial(Du_\beta)}{\partial x_\alpha}-\frac{\partial(Du_\alpha)}{\partial x_\beta}-\frac{\partial(\lambda_\alpha u_\beta)}{\partial\sigma}+\frac{\partial(\lambda_\beta u_\alpha)}{\partial\sigma}\right\}-\mathrm{w}_{st}\frac{\partial u_\alpha}{\partial\sigma}}_{(3a)}$$

$$+\underbrace{\frac{D\,\mathring{\sigma}\,|\mathbf{u_{st}}|}{\sinh 2kD}\frac{\partial D}{\partial x_\alpha}}_{(4)}-\underbrace{\mathrm{u}_{st\beta}\left\{\frac{\partial[D(u_\beta-\hat{u}_{A\beta})]}{\partial x_\alpha}-\frac{\partial\left[\lambda_\alpha(u_\beta-\hat{u}_{A\beta})\right]}{\partial\sigma}\right\}}_{(3b)} \tag{4.10.10}$$

and in Cartesian coordinates:

$$\frac{\partial u_\alpha}{\partial t}+\frac{\partial(u_\alpha u_\beta)}{\partial x_\beta}+\frac{\partial[u_\alpha\,(w-\mathrm{w}_{st})]}{\partial z}=-\underbrace{\epsilon_{\alpha 3\beta}f_3\,(u_\beta+\mathrm{u}_{st\beta})}_{(2)}+\mathrm{P}_\alpha+\underbrace{\left(\mathrm{T}^{turb}+Dk_\alpha\mathcal{D}_w\right)}_{(1)}+\mathrm{S}_w^{(1)}$$

$$+\underbrace{\mathrm{u}_{st\beta}\left\{\frac{\partial u_\beta}{\partial x_\alpha}-\frac{\partial u_\alpha}{\partial x_\beta}\right\}-\mathrm{w}_{st}\frac{\partial u_\alpha}{\partial z}}_{(3a)}+\underbrace{\frac{\mathring{\sigma}\,|\mathbf{u_{st}}|}{\sinh 2kD}\frac{\partial D}{\partial x_\alpha}}_{4}-\underbrace{\mathrm{u}_{st\beta}\frac{\partial(u_\beta-\hat{u}_{A\beta})}{\partial x_\alpha}}_{(3b)} \tag{4.10.11}$$

Term (1) in equations 4.10.10 and 4.10.11 is evaluated using equations 4.4.5 and the results of Section 4.9.2:

$$\mathrm{T}^{turb}\equiv(\,\mathrm{T}^{turb}+Dk_\alpha\mathcal{D}_w)=\,\mathrm{T}_{\mathrm{h}\alpha}^{turb}+\mathrm{T}_{\mathrm{v}\alpha}^{turb}=\frac{\partial}{\partial x_\beta}\Big[\mathcal{A}_\mathrm{h}\frac{\partial(Du_\alpha)}{\partial x_\beta}\Big]+\frac{1}{D^2}\frac{\partial}{\partial\sigma}\Big[\mathcal{A}_\mathrm{v}\frac{\partial(D\mathcal{u}_\alpha)}{\partial\sigma}\Big] \tag{4.10.12}$$

that is, the vertical Reynolds flux term is adjusted by the inclusion of the Lagrangian velocity $\mathcal{u}$. The corresponding term in "z" coordinates is adjusted accordingly. The radiation stress term in Cartesian coordinates is written as follows:

$$\mathrm{S}_w^{(1)}=-\frac{1}{D}\frac{\partial S_{\alpha\beta}}{\partial x_\beta}-\frac{1}{D}\Big(\frac{\partial\zeta}{\partial x_\beta}+\frac{z-\zeta}{D}\frac{\partial D}{\partial x_\beta}\Big)\frac{\partial S_{\alpha\beta}}{\partial z} \tag{4.10.13}$$

Comparing equation 4.10.13 with the first of equations 4.7.5, it is seen that the radiation stress term $\mathrm{S}_w^{(1)}$ is simpler in "σ" than in Cartesian coordinates, but still is a very complicated construct. The remaining wave terms are simpler in Cartesian coordinates. Equation 4.10.11 is directly comparable with the results of McWilliams et al. [2004], Lane et al. [2005]. Their Stokes vorticity term

appears in the present results as well (term (3a) of equation 4.10.11). The gradient of the Stokes Bernoulli head that appears in the equations of McWilliams et al., Craik and Leibovich [1976] and others is part of term (3b) as shown below:

$$u_{st\beta}\frac{\partial(u_\beta-\hat{u}_{A\beta})}{\partial x_\alpha} = -\underbrace{\frac{\partial(u_\beta u_{st\beta})}{\partial x_\alpha}}_{\text{Bernoulli head}} + \frac{\partial(\hat{u}_{A\beta}u_{st\beta})}{\partial x_\alpha} + (u_\beta-\hat{u}_{A\beta})\frac{\partial u_{st\beta}}{\partial x_\alpha} \tag{4.10.14}$$

4.10.1 Wave Induced Scalar Transport

In the case of a scalar, e.g., temperature, salinity and sediment, it is assumed that there is no interaction between the scalar and the waves, that is, only the Stokes advection term appears in the equation. Separating and moving the Stokes related terms on the r.h.s of the scalar transport equation 4.7.3, the equation is written as:

$$\frac{\partial(D\Phi)}{\partial t}+\frac{\partial(Du_\alpha\Phi)}{\partial x_\alpha}+\frac{\partial(D\overset{\star}{\omega}\Phi)}{\partial\sigma} = -\frac{\partial(Du_{st\alpha}\Phi)}{\partial x_\alpha}+\frac{\partial}{\partial\sigma}\Big[u_{st\alpha}\Big(\frac{\partial\zeta}{\partial x_\alpha}+\sigma\frac{\partial D}{\partial x_\alpha}\Big)\Big]+T_\Phi+\boldsymbol{S_\Phi} \tag{4.10.15}$$

The equations of continuity, momentum and scalar are all written in such a way that the Stokes terms are on the r.h.s acting as forcing terms. Equation 4.10.15 represents the transport of the scalar quantity Φ under the action of currents and waves. The extension to spectral waves is easier this way and the procedure is common for all equations. Using the continuity equation for the Stokes drift velocity (equation 4.8.4) and the results in the previous Sections, equation 4.10.15 is written in "z" coordinates as follows:

$$\frac{\partial(\Phi)}{\partial t}+\frac{\partial(u_\alpha\Phi)}{\partial x_\alpha}+\frac{\partial[(w-w_{st})\Phi]}{\partial z} = \frac{\partial}{\partial x_\alpha}\Big[\mathcal{B}_h\frac{\partial\Phi}{\partial x_\alpha}\Big]+\frac{\partial}{\partial z}\Big[\mathcal{B}_v\frac{\partial\Phi}{\partial z}\Big]-u_{st\alpha}\frac{\partial\Phi}{\partial x_\alpha}-w_{st}\frac{\partial\Phi}{\partial z}+\boldsymbol{S_\Phi} \tag{4.10.16}$$

and in "σ" coordinates:

$$\begin{aligned}\frac{\partial(D\Phi)}{\partial t}+\frac{\partial(Du_\alpha\Phi)}{\partial x_\alpha}+\frac{\partial(D\overset{\star}{\Omega}\Phi)}{\partial\sigma} &= \frac{\partial}{\partial x_\alpha}\Big[\mathcal{B}_h\frac{\partial(D\Phi)}{\partial x_\alpha}\Big]+\frac{1}{D^2}\frac{\partial}{\partial\sigma}\Big[\mathcal{B}_v\frac{\partial(D\Phi)}{\partial\sigma}\Big]\\ &\quad -u_{st\alpha}\Big[\frac{\partial(D\Phi)}{\partial x_\alpha}-\frac{\partial(\lambda_\alpha\Phi)}{\partial\sigma}\Big]-w_{st}\frac{\partial\Phi}{\partial\sigma}+\boldsymbol{S_\Phi}\end{aligned} \tag{4.10.17}$$

4.10.2 External Equations of Motion

The vertical integration of equation 4.8.5 and the incorporation of the boundary conditions (equations 4.8.6a and 4.8.6b) produce the vertically integrated continuity equation for the Eulerian

velocity U_α, which is identical to equation 2.1.25. The corresponding equation for the vertically integrated Stokes drift is given by equation 4.8.13.

For the derivation of the vertically integrated momentum equation the calculations are performed on equation 4.10.11, which is the momentum equation in Cartesian coordinates. Only the wave terms represented by the terms $S_w^{(1)}$, (2), (3a), (3b) and (4) of the equation, are being vertically integrated below, while the remaining portion of the vertically integrated momentum is given by equations 2.1.29a and 2.1.30a. As noted earlier some terms in the equations are simpler in "σ" coordinates (e.g., radiation stresses) and other terms are simpler in Cartesian coordinates. The vertical integration: $\int_{-h}^{\zeta}$ however, does not distinguish between Cartesian and σ coordinates since:

$$\int_{-h}^{\zeta}(\cdot)\,dz = \frac{1}{D}\int_{-1}^{0}(\cdot)\,D\,d\sigma = \int_{-1}^{0}(\cdot)\,d\sigma \tag{4.10.18}$$

The advantage of this fact is that the integration(s) are carried out using the simpler forms of the terms. Consequently, the term $S_w^{(1)}$ has been evaluated in "σ" coordinates and the rest of the terms in Cartesian coordinates e.g.,:

$$S_w^{(1)}: \qquad \int_{-1}^{0} S_w^{(1)}\,d\sigma = -\frac{\partial R_{\alpha\beta}}{\partial x_\beta} \tag{4.10.19}$$

where $R_{\alpha\beta}$ represents Phillips' 2D radiation stress definition (equation 4.1.2).

$$(2): \qquad \int_{-h}^{\zeta}\epsilon_{\alpha 3\beta} f_3 (u_\beta + u_{st\beta})\,dz = \epsilon_{\alpha 3\beta} f_3 D (U_\beta + U_{st\beta}) \tag{4.10.20}$$

$$(4): \qquad \int_{-h}^{\zeta}\frac{\mathring{\sigma}\,|\mathbf{u_{st}}|}{\sinh 2kD}\frac{\partial D}{\partial x_\alpha}\,dz = \frac{\mathring{\sigma}\,D\,|\mathbf{U_{st}}|}{\sinh 2kD}\frac{\partial D}{\partial x_\alpha} \tag{4.10.21}$$

Before the original terms (3a) and (3b) in equation 4.10.11 can be integrated they are mathematically manipulated to yield the following expression:

$$\underbrace{u_{st\beta}\left\{\frac{\partial u_\beta}{\partial x_\alpha} - \frac{\partial u_\alpha}{\partial x_\beta}\right\} - w_{st}\frac{\partial u_\alpha}{\partial z} - u_{st\beta}\frac{\partial(u_\beta - \hat{u}_{A\beta})}{\partial x_\alpha}}_{(3)} = -\frac{\partial(u_\alpha u_{st\beta})}{\partial x_\beta} - \frac{\partial(u_\alpha w_{st})}{\partial z} + u_{st\beta}\frac{\partial \hat{u}_{A\beta}}{\partial x_\alpha} \tag{4.10.22}$$

For the derivation of the above expression, the chain rule differentiation has been applied and the continuity equation for the Stokes drift (equation 4.8.4) has been employed. Equation 4.10.22

in combination with the boundary conditions 4.8.8 is vertically integrated:

$$(3): \qquad -\int_{-h}^{\zeta}\frac{\partial(u_\alpha \mathrm{u_{st\beta}})}{\partial x_\beta}dz-\int_{-h}^{\zeta}\frac{\partial(u_\alpha \mathrm{w_{st}})}{\partial z}dz+\int_{-h}^{\zeta}\mathrm{u_{st\beta}}\frac{\partial \hat{u}_{A\beta}}{\partial x_\alpha}dz=D\,\mathrm{U_{st\beta}}\Big(\frac{\partial \hat{u}_{A\beta}}{\partial x_\alpha}-\frac{\partial \hat{u}_{A\alpha}}{\partial x_\beta}\Big) \tag{4.10.23}$$

Using the previously derived expressions for the terms $\mathrm{S}_w^{(1)}$, (2), (3) and (4) the vertically integrated momentum equations are written as follows:

$$\begin{aligned}\frac{\partial(DU_\alpha)}{\partial t}+\frac{\partial(DU_\alpha U_\beta)}{\partial x_\beta} &= -\epsilon_{\alpha 3\beta} f_3 D\,(U_\beta+\mathrm{U_{st\beta}})\\ &+\underbrace{\Big[-\frac{D}{\rho_o}\frac{\partial p_{\mathrm{atm}}}{\partial x_\alpha}-gD\frac{\partial \zeta}{\partial x_\alpha}-\frac{g}{\rho_o}\frac{D^2}{2}\frac{\partial \rho}{\partial x_\alpha}\Big]}_{\mathrm{P}_\alpha}+\underbrace{\frac{\partial}{\partial x_\beta}\Big[\mathcal{A}_h\frac{\partial(DU_\alpha)}{\partial x_\beta}\Big]+\frac{\tau_{sx_\alpha}-\tau_{bx_\alpha}}{\rho_o}}_{\mathrm{T}_\alpha^{turb}}\\ &-\frac{\partial R_{\alpha\beta}}{\partial x_\beta}+\underbrace{D\,\mathrm{U_{st\beta}}\Big(\frac{\partial \hat{u}_{A\beta}}{\partial x_\alpha}-\frac{\partial \hat{u}_{A\alpha}}{\partial x_\beta}\Big)}_{(1)}+\underbrace{\frac{\mathring{\sigma}\,D\,|\mathbf{U_{st}}|}{\sinh 2kD}\frac{\partial D}{\partial x_\alpha}}_{(2)}\end{aligned} \tag{4.10.24}$$

Equation 4.10.24 is the final vertically integrated momentum equation that adds the wave effects to the original external momentum equations 2.1.29a and 2.1.30a presented in Chapter 2. It is interesting to note that term (3) (equation 4.10.22), has been collapsed into term (1) in equation 4.10.24. The terms (3*a*) and (3*b*) in equation 4.10.11, show the full 3D behavior of the waves represented by the two vertical Stokes vorticity terms. In equation 4.10.24 the Stokes vorticity term is represented by term (1) and all other 3D effects have been filtered out. In shallow waters, $\hat{u}_{A\alpha}\approx U_\alpha$.This comes as a result of the analysis in Kirby and Chen [1989], which states that: $\hat{u}_{A\alpha}=U_\alpha+O((kD)^2)$ and consequently, as $kD\to 0\Rightarrow \hat{u}_{A\alpha}\approx U_\alpha$.

As it is shown in Figure 4.5, the Stokes drift, $\mathrm{u_{st}}$, in shallow waters exhibits a rather uniform vertical distribution, while in deep waters its effects are limited in the upper part of the water column. The results presented here (equations 4.10.10, 4.10.11 and 4.10.24), once more signify the importance of the Stokes drift in the near-shore hydrodynamics and the transport of the sediments found in suspension and at the bottom. Furthermore, term (2) in equation 4.10.24 and its counterpart term (4) in equation 4.10.11 denote the significance of the bottom slope variations especially in shallow waters.

4.10.3 The Non-Dimensional Form of the Equations

The non-dimensional form of the 3D and the 2D equations of motion and scalar transport are derived in this Section using the definitions in Appendix B. The definitions of the non-dimensional variables are expanded to include the wave variables as well. Only the non-dimensional representations of the wave terms are derived here, since the remaining terms have been derived in Section 2.1.5.

Continuity:

The non-dimensional equation for the 3D continuity equation assumes a similar form as in equation 2.1.32, where the non-dimensional vertical velocity w is simply replaced by $w - \mathrm{w_{st}}$. For the two-dimensional case, the equations assume exactly the same form as in equations 2.1.36a and 2.1.36b (Section 2.1.5).

Momentum:

The procedure for deriving the non-dimensional wave terms in both the 3D and the 2D momentum equations is the same for all terms, therefore, only an example of their derivation will be presented here that is, the derivation for the term $\mathrm{S}_w^{(1)}$ in equation 4.10.11. The dimensional form of this term is defined by equation 4.10.13 and the analytical expression for $S_{\alpha\beta}$ is given by equation 4.7.6. All variables in $S_{\alpha\beta}$ are dimensionless, except for the wave energy E.

Using the expression $k = \check{k}/\mathrm{Z_r}$ and the definition for $\check{E}$ (the last of equations B.38), $S_{\alpha\beta}$ is transformed as follows:

$$S_{\alpha\beta} = \frac{f^2 \mathrm{U_r^2 X_r}^2}{g} \check{S}_{\alpha\beta} \tag{4.10.25}$$

The derivation proceeds by first substituting all the dimensional variables in equation 4.10.13 by their non-dimensional representations (Section B.2.4) and then, by dividing the resulting expressions by $f\mathrm{U_r}$, for the 3D equation, and by $f\mathrm{U_r Z_r}$ for the 2D equation, as was done earlier during the derivation for the of the rest non-dimensional terms of equations 2.1.33, 2.1.34, 2.1.37b and 2.1.38b in Section 2.1.5.

The term $\mathrm{S}_w^{(1)}$ is split into four sub-terms, so that the derivation process, as well as the comparison of the magnitude among the sub-terms and the rest of the terms in the momentum equation, becomes easier.

$$\mathrm{S}_w^{(1)} = \underbrace{-\frac{1}{D}\frac{\partial S_{\alpha\beta}}{\partial x_\beta}}_{(1)} \underbrace{-\frac{1}{D}\frac{\partial \zeta}{\partial x_\beta}\frac{\partial S_{\alpha\beta}}{\partial z}}_{(2)} \underbrace{-\frac{z}{D^2}\frac{\partial D}{\partial x_\beta}\frac{\partial S_{\alpha\beta}}{\partial z}}_{(3)} \underbrace{+\frac{\zeta}{D^2}\frac{\partial D}{\partial x_\beta}\frac{\partial S_{\alpha\beta}}{\partial z}}_{(4)} \tag{4.10.26}$$

The four terms in equation 4.10.26 are transformed in non-dimensional form as follows:

$$(1): \qquad -\frac{1}{D}\frac{\partial S_{\alpha\beta}}{\partial x_\beta} = -\frac{1}{f\mathrm{U_r}}\frac{1}{\mathrm{Z_r}}\frac{f^2\mathrm{U_r}^2\mathrm{X_r}^2}{g\mathrm{X_r}}\frac{1}{\check{D}}\frac{\partial \check{S}_{\alpha\beta}}{\partial x_\beta} = -\frac{\mathbb{F}_\mathrm{r}^2}{\mathbb{R}_\mathrm{o}}\frac{1}{\check{D}}\frac{\partial \check{S}_{\alpha\beta}}{\partial \check{x}_\beta} \tag{4.10.27}$$

$$(2): \qquad -\frac{1}{D}\frac{\partial \zeta}{\partial x_\beta}\frac{\partial S_{\alpha\beta}}{\partial z} = -\frac{1}{f\mathrm{U_r}}\frac{1}{\mathrm{Z_r}}\frac{f\mathrm{U_r}\mathrm{X_r}}{g\mathrm{X_r}}\frac{f^2\mathrm{U_r}^2\mathrm{X_r}^2}{g\mathrm{Z_r}}\frac{1}{\check{D}}\frac{\partial \check{\zeta}}{\partial \check{x}_\beta}\frac{\partial \check{S}_{\alpha\beta}}{\partial \check{z}} = -\Big(\frac{\mathbb{F}_\mathrm{r}^2}{\mathbb{R}_\mathrm{o}}\Big)^2\frac{1}{\check{D}}\frac{\partial \check{\zeta}}{\partial \check{x}_\beta}\frac{\partial \check{S}_{\alpha\beta}}{\partial \check{z}} \tag{4.10.28}$$

$$(3): \qquad -\frac{z}{D^2}\frac{\partial D}{\partial x_\beta}\frac{\partial S_{\alpha\beta}}{\partial z} = -\frac{\mathbb{F}_\mathrm{r}^2}{\mathbb{R}_\mathrm{o}}\frac{\check{z}}{\check{D}}\frac{\partial \check{D}}{\partial \check{x}_\beta}\frac{\partial \check{S}_{\alpha\beta}}{\partial \check{z}} \tag{4.10.29}$$

$$(4): \qquad \frac{\zeta}{D^2}\frac{\partial D}{\partial x_\beta}\frac{\partial S_{\alpha\beta}}{\partial z} = \Big(\frac{\mathbb{F}_\mathrm{r}^2}{\mathbb{R}_\mathrm{o}}\Big)^2\frac{\check{\zeta}}{\check{D}}\frac{\partial \check{D}}{\partial \check{x}_\beta}\frac{\partial \check{S}_{\alpha\beta}}{\partial \check{z}} \tag{4.10.30}$$

Working on the remaining wave terms as described above, substituting the resulting expressions in the momentum equation 4.10.11 and dropping the check accents, the final form of the 3D non-dimensional momentum equation is given by:

$$\frac{\partial u_\alpha}{\partial t} + \mathbb{R}_\mathrm{o}\left\{\frac{\partial (u_\alpha u_\beta)}{\partial x_\beta} + \frac{\partial [u_\alpha (w - \mathrm{w_{st}})]}{\partial z}\right\} = -\epsilon_{\alpha 3\beta}\frac{f_3}{f}(u_\beta + \mathrm{u_{st\beta}})$$

$$-\frac{\partial p_\mathrm{atm}}{\partial x_\alpha} - \frac{\partial \zeta}{\partial x_\alpha} - \frac{\mathbb{R}_\mathrm{o}}{\mathbb{F}_\mathrm{rd}^2}\int_z^\zeta \frac{\partial \rho}{\partial x_\alpha}\,dz' + \mathbb{E}_\mathrm{kh}\frac{\partial}{\partial x_\beta}\Big[\mathcal{A}_\mathrm{h}\frac{\partial u_\alpha}{\partial x_\beta}\Big] + \underbrace{\mathbb{E}_\mathrm{kv}\frac{\partial}{\partial z}\Big[\mathcal{A}_\mathrm{v}\frac{\partial u_\alpha}{\partial z}\Big]}_{(1)}$$

$$+\mathbb{R}_\mathrm{o}\left\{\mathrm{u_{st\beta}}\Big(\frac{\partial u_\beta}{\partial x_\alpha} - \frac{\partial u_\alpha}{\partial x_\beta}\Big) - \mathrm{w_{st}}\frac{\partial u_\alpha}{\partial z}\right\} + \mathbb{R}_\mathrm{o}\frac{\mathring{\sigma}\,|\mathbf{u_{st}}|}{\sinh 2kD}\frac{\partial D}{\partial x_\alpha} - \mathbb{R}_\mathrm{o}\,\mathrm{u_{st\beta}}\frac{\partial (u_\beta - \hat{u}_{A\beta})}{\partial x_\alpha}$$

$$-\frac{\mathbb{F}_\mathrm{r}^2}{\mathbb{R}_\mathrm{o}}\frac{1}{D}\frac{\partial S_{\alpha\beta}}{\partial x_\beta} - \underbrace{\Big(\frac{\mathbb{F}_\mathrm{r}^2}{\mathbb{R}_\mathrm{o}}\Big)^2\left\{\frac{1}{D}\left[\frac{\partial \zeta}{\partial x_\beta} + \frac{\frac{\mathbb{R}_\mathrm{o}}{\mathbb{F}_\mathrm{r}^2}z - \zeta}{D}\frac{\partial D}{\partial x_\beta}\right]\frac{\partial S_{\alpha\beta}}{\partial z}\right\}}_{(2)} \tag{4.10.31}$$

and the final form of the 2D non-dimensional momentum equation is:

$$\frac{\partial (DU_\alpha)}{\partial x_\alpha} + \mathbb{R}_\mathrm{o}\frac{\partial (DU_\alpha U_\beta)}{\partial x_\beta} = -\epsilon_{\alpha 3\beta}\frac{f_3}{f}(U_\beta + \mathrm{U_{st\beta}}) - D\frac{\partial p_\mathrm{atm}}{\partial x_\alpha} - D\frac{\partial \zeta}{\partial x_\alpha} - \frac{D^2}{2}\frac{\mathbb{R}_\mathrm{o}}{\mathbb{F}_\mathrm{r}^2}\frac{\partial \rho}{\partial x_\alpha}$$

$$+\mathbb{E}_\mathrm{kh}\frac{\partial}{\partial x_\beta}\Big[\mathcal{A}_\mathrm{h}\frac{\partial (DU_\alpha)}{\partial x_\beta}\Big] - \frac{\mathbb{F}_\mathrm{r}^2}{\mathbb{R}_\mathrm{o}}\frac{\partial R_{\alpha\beta}}{\partial x_\beta} + \tau_{sx_\alpha} - \tau_{bx_\alpha}$$

$$+\mathbb{R}_\mathrm{o}\,D\,\mathrm{U_{st\beta}}\Big(\frac{\partial \hat{u}_{A\beta}}{\partial x_\alpha} - \frac{\partial \hat{u}_{A\alpha}}{\partial x_\beta}\Big) + \mathbb{R}_\mathrm{o}\frac{\mathring{\sigma}\,D\,|\mathbf{U_{st}}|}{\sinh 2kD}\frac{\partial D}{\partial x_\alpha} \tag{4.10.32}$$

Scalar:

In equation 4.10.16, only the non-dimensional representation of the Stokes terms need to be determined, since all the other terms have already been evaluated in Section 2.1.5. Following the same procedure as in the derivation of the momentum equation, using the scalings previously defined for the scalar (Section B.2.4), dividing the resulting terms by $f\,(\Phi_r - \Phi_o)$ and dropping the check accents, the non-dimensional equation for the scalar transport under the action of currents and waves becomes:

$$\frac{\partial \Phi}{\partial t} + \mathbb{R}_{\mathrm{D}}\left[\frac{\partial (u_\alpha \Phi)}{\partial x_\alpha} + \frac{\partial [(w - \mathrm{w_{st}})\Phi]}{\partial z}\right] = \frac{\mathbb{E}_{\mathbb{k}\mathrm{h}}}{\mathbb{S}_{\mathbb{c}\mathrm{h}}}\frac{\partial}{\partial x_\alpha}\left[\mathcal{B}_{\mathrm{h}}\frac{\partial \Phi}{\partial x_\alpha}\right] + \frac{\mathbb{E}_{\mathbb{k}\mathrm{v}}}{\mathbb{S}_{\mathbb{c}\mathrm{v}}}\frac{\partial}{\partial \mathrm{z}}\left[\mathcal{B}_{\mathrm{v}}\frac{\partial \Phi}{\partial \mathrm{z}}\right] - \mathbb{R}_{\mathrm{D}}\left[\mathrm{u_{st\alpha}}\frac{\partial \Phi}{\partial x_\alpha} - \mathrm{w_{st}}\frac{\partial \Phi}{\partial \mathrm{z}}\right] \tag{4.10.33}$$

The complete set of dimensional and the non-dimensional equations in (x, y, z), (x, y, σ) and curvilinear coordinates is given in Appendix C.

CHAPTER 5

INCORPORATION OF THE WAVE-CURRENT INTERACTIONS INTO THE HYDRODYNAMIC MODEL

5.1 Introduction

The equations derived in Chapter 4 require the use of a 3D wave model, such that all the relevant wave terms appearing in the equations of motion are evaluated. In the absence of a functional, fully tested 3D wave model, common sense dictates the use of existing 2D wave prediction models to accompany the wave enhanced hydrodynamic calculations proposed in the present research.

Modern wave models, predict the wave fields based on spectral representations of their governing equations. The wave induced equations of motion presented in Chapter 4, were derived assuming monochromatic surface waves, therefore, direct use of the wave model output parameters in the hydrodynamic calculations is not possible unless the wave terms appearing in the equations of motion are extended to use the spectral representations of the required wave parameters. This issue is the focal point of the discussion presented in Section 5.2.

Furthermore, the wave models do not utilize the full spectrum in their calculations, but rather the portion of the wave spectrum centered about its spectral peak, which is usually a user defined input parameter. The common practice is to assume that the total wave energy is well approximated by only using the higher frequency portion of the spectrum where most, but not all, of the energy of the wind generated waves is contained. Mathematically, the total spectral wave energy calculated by a wave model given by the following equation:

$$\int_0^{\infty}\int_0^{2\pi} S(f,\,\theta)\,df\,d\theta \approx \int_{f_{min}}^{f_{max}}\int_0^{2\pi} S(f,\,\theta)\,df\,d\theta \tag{5.1.1}$$

where $S(f, \theta)$ represents the spectrum and the lower and upper frequencies are normally taken as $f_{min} \approx 0.04$ Hz and $f_{max} \approx 1.0$ Hz, respectively.

To account for the unresolved portions of the wave spectrum by the wave models and subsequently to more accurately calculate the total wave energy of the surface waves required in the hydrodynamic calculations, a formulation is proposed in Section 5.3 to estimate the total spectral wave energy using the wave model output parameters.

Evaluation of the remaining wave terms in the equations of motion requires calculation of all wave parameters at each vertical level, at each hydrodynamic calculation step and for the full specified spectrum range, imposing a significant computational burden on the overall calculations. In addition, wave model output parameters like the Stokes drift and the wave radiation stresses are 2D (vertically averaged) variables that need to be utilized, such that the full 3D wave effects can be incorporated into the hydrodynamic model calculations. In Sections 5.4, 5.5 and 5.6, it is proposed a detailed methodology developed during the present research for the incorporation of the full 3D wave effects into hydrodynamic models using the output of the existing 2D spectral wave models that does not require extensive computational resources.

5.2 Extension to the Spectral Waves

Since the development and evolution of the wave spectrum depends upon factors including the variable wind field, bottom bathymetric variability, movement of the bottom sediments, and non linear wave interactions (triad, quadratic, pedantic, ...), it is clear that neither a standard equilibrium spectrum like *JONSWAP* and its variations, nor an approximation such as the one in equation 5.1.1 are sufficient to accurately describe the wave-current interactions. Wave models (*SWAN*, *WAVEWATCH*, *WAM*) make no assumptions on the shape of the wave spectrum, while refined near shore wave models like SWAN also include descriptions of the non linear wave interactions. This Chapter presents a method to re-modulate the wave energy so that all the filtered waves can be included in the hydrodynamic calculations by using the model calculated spectral parameters (functions of x, y, z, f, θ).

All the equations up to this point have been derived assuming monochromatic waves. Coupling with a spectral wave model requires that these equations be extended to include the effect of spectral waves. To this end, the vertical coordinate $\tilde{s}$ defined in Section 4.5, equation 4.5.3, using the linear

wave theory, is redefined here for random waves by letting $\tilde{s}$ to be the sum of the contributions from each wave train as done in Komen et al. [1996]:

$$\tilde{s} = \sum \alpha_n(x,t)e^{i\psi_n} + \text{higher order terms} \tag{5.2.1}$$

Equation 5.2.1 simply expands $\tilde{s}$ into a series of the small parameter $\epsilon_1 = k_0\alpha_0$, where $k_0\alpha_0$ is the maximum wave slope and the higher order terms are neglected. Re-writing equation 5.2.1 to conform with Mellor's equations gives:

$$\tilde{s} = \sum_k F_{SS}(k)\mathcal{A}_k^{\pm}e^{i\psi_k} \tag{5.2.2}$$

where $\mathcal{A}_k^{\pm}$ is the complex amplitude, which is a slow function of k and ψ_k is the wave phase function defined as:

$$\psi_k = \vec{k}\cdot\vec{x} \pm \omega t + O(\epsilon_2) \tag{5.2.3}$$

ϵ_2 is yet another small parameter describing the horizontal variations of the medium the waves traverse (e.g., bottom slope). Any other first order quantity ϕ_k associated with $\tilde{s}$ and k is simply the sum of two complex components ϕ_k^+ and ϕ_k^-. The change of the vertical coordinate performed by Mellor allows the first order wave quantities in ϵ_1 and zeroth order in ϵ_2 and consequently $\tilde{s}$, to be written as superpositions of linear wave components (equation 5.2.2). To the lowest order, the wave spectrum is written as (Ardhuin and Jenkins [2006a]):

$$\mathcal{E}(k) = \lim_{\Delta k\to 0}\frac{2\mathcal{A}_k^+\mathcal{A}_k^-}{\Delta k} \tag{5.2.4}$$

Herbers and Burton [1997] using higher order spectral statistics, evaluated the wave terms of higher order in ϵ_1 and ϵ_2, thus allowing the calculation of the longer wave effects (triad interactions) in the near-shore region, that might improve wave calculations by the wave models. It is so noted here, that the higher order terms in ϵ_1 andϵ_2 are related to the wind forcing, the wave dissipation near the surface, the bottom friction, the wave spreading and the non linear wave-wave interactions.

5.3 Re-modulation of the Wave Energy

The total wave energy E is given by (Komen et al. [1996], LeBlond and Mysak [1979]):

$$E = \frac{1}{2}\rho g\overline{\tilde{\zeta}^2} \approx \rho g\frac{H_{mo}^2}{8} \tag{5.3.1}$$

where $\overline{\tilde{\zeta}^2}$ is the free surface variance and H_{mo}^2 is the spectral significant wave height. In terms of the wave spectrum E is written as:

$$E = \rho g \int_0^{\infty} \int_0^{2\pi} \mathcal{E}(\omega, \theta) d\omega d\theta \tag{5.3.2}$$

The usual practice here is to split $\mathcal{E}(\omega, \theta)$ into two components, that is a 1D frequency (or wavenumber) spectrum and a 1D directional spectrum. Using Donelan's theory (Donelan et al. [1985], Donelan and Pierson, Jr. [1987]), equation 5.3.2 is written as:

$$E = \rho g \int_0^{\infty} S(\omega) d\omega \int_0^{2\pi} \frac{2}{\pi} \cos^2(\theta - \bar{\theta}) d\theta \tag{5.3.3}$$

where $\bar{\theta}$ is the mean angle of wave propagation that is independent of the frequency. From the above equation it is seen that when $|\theta - \bar{\theta}| > \pi/2$, the energy is nullified. Therefore, equation 5.3.3 becomes:

$$E = 2\rho g \int_0^{\infty} S(\omega) d\omega \tag{5.3.4}$$

where $S(\omega)$ is the one sided frequency spectrum of the waves. Comparison of equations 5.3.4 and 5.3.1 yields that:

$$\int_0^{\infty} S(\omega) d\omega = \frac{H_{mo}^2}{16} \tag{5.3.5}$$

For later use the moments of the variance spectrum are defined here as (Doering and Donelan [1993]):

$$m_n = \int_0^{\infty} \omega^n S(\omega) d\omega = \int_0^{\infty} f^n S(f) df \tag{5.3.6}$$

where $\omega = 2\pi f$ and m_n is the n-th moment of the spectrum. Another spectral parameter defined here for later use is the spectral width parameter ν_s:

$$\nu_s = \left(\frac{m_0 m_2}{m_1^2} - 1 \right)^{1/2} \tag{5.3.7}$$

A slightly different definition of ν_s is used in *SWAN*:

$$\nu_s = \frac{\left| \int_0^{\infty} S(\omega) e^{i\omega\tau} d\omega \right|}{\mathcal{E}_T}; \qquad \tau = T_{mo2} = 2\pi \left(\frac{m_0}{m_2} \right)^{1/2} \tag{5.3.8}$$

and $\mathcal{E}_T$ is the total spectral energy.

It was mentioned earlier that the evolution of the wave spectrum depends upon a variety of physical parameters and it is greatly affected by non linear wave-wave interactions. The common practice is to use the fetch limited *JONSWAP* spectrum (Komen et al. [1996]), which is a deep water wave spectrum, to describe the spectral characteristics of the waves in both shallow and deep waters. Application of *JONSWAP* in shallow waters becomes possible by adjusting its peak enhancement parameter (γ). Additional adjustments to the peak enhancement parameter γ are suggested in Bouws et al. [1985, 1987] and Lavrenov [2003] to account for the effects of the long period waves on the shape and evolution of the spectrum.

In the analysis that follows, a generalized version of a *JONSWAP* type spectrum is used as follows:

$$S(\omega) = \alpha \cdot g^2 \frac{1}{\omega^m} e^{-\beta\left(\frac{\omega}{\omega_p}\right)^{-n}} \cdot \gamma^{\Gamma}$$

$$\Gamma = e^{-\frac{(\omega-\omega_p)^2}{2\sigma^2\omega_p}} = e^{-\frac{\left(\frac{\omega}{\omega_p}-1\right)^2}{2\sigma^2}} \tag{5.3.9}$$

where ω_p is the peak frequency of the spectrum, that is the frequency where the spectrum assumes its maximum value and $m, n, \beta, \alpha, \gamma$ are the spectral parameters allowed to take any value or expression, depending upon the wave characteristics at a location (x, y) and at a time "t" as calculated by the wave model.

At $\omega_p = \omega_p$ the following should be true:

$$\left.\frac{dS(\omega)}{d\omega}\right|_{\omega=\omega_p} = 0 \tag{5.3.10}$$

To transform $S(\omega)$ to wavenumber (k) or frequency (f) space, the following expressions are used:

$$S(k) = S(\omega)\frac{\omega}{2k} = S(f)\frac{f}{2k} \tag{5.3.11}$$

together with the deep water dispersion equation:

$$\omega^2 = (2\pi f)^2 = gk \tag{5.3.12}$$

which describes how the spectrum developed by the wind forcing disperses according to linear wave theory (Hanson and Phillips [2001]). Use of equations 5.3.11 and 5.3.12 is currently a common practice. Using equation 5.3.11, the wave spectrum (equations 5.3.9) in wavenumber space are

written as:

$$S(k) = S\left(\frac{k}{k_p}\right) = S(\phi) = \frac{\alpha g^{-\frac{m-5}{2}}}{2k_p^{\frac{m+1}{2}}} f(\phi) \tag{5.3.13}$$

$$f(\phi) = \phi^{-\frac{m+1}{2}} e^{g(\phi)} \tag{5.3.14}$$

$$g(\phi) = -\beta\phi^{\frac{n}{2}} + (\ln\gamma)\, e^{-\frac{(\sqrt{\phi}-1)^2}{2\sigma^2}} \tag{5.3.15}$$

where k_p is the peak wavenumber.

The objective is to find a simplified expression for $S(k)$ and subsequently for $S(f)$, so that the spectral energy for different bands of the spectrum can be easily evaluated. An approach similar to the one described in Onorato et al. [2003]) is used. First, $S(k)$ or $f(\phi)$ is expanded in a Taylor series up to the second order about the spectral peak $k = k_p$ or $\phi = 1$. To use the Taylor series expansion, the functions $f(\phi)$, $g(\phi)$ and their first and second derivatives are evaluated at $\phi = 1$ as follows:

$$g(1) = -\beta + \ln\gamma; \qquad e^{g(1)} = \gamma e^{-\beta} \tag{5.3.16}$$

$$g'(1) = \frac{\beta n}{2} \tag{5.3.17}$$

$$g''(1) = -\frac{\beta n(n+2)\sigma^2 + \ln\gamma}{4\sigma^2} \tag{5.3.18}$$

and the corresponding expressions for $f(1)$, $f'(1)$ and $f''(1)$ are evaluated as:

$$f(1) = e^{g(1)} = \gamma e^{-\beta} \tag{5.3.19}$$

$$f'(1) = \Big[-\frac{m+1}{2} + \frac{\beta n}{2} \Big] \gamma e^{-\beta} \tag{5.3.20}$$

$$f''(1) = \left\{ \frac{\beta^2 n^2}{4} - \frac{\beta n(m+1)}{2} + \frac{(m+1)(m+3)}{4} - \frac{\beta n(n+2)\sigma^2 + \ln\gamma}{4\sigma^2} \right\} \gamma e^{-\beta} \tag{5.3.21}$$

Since equation 5.3.10 gives $f'(1) = 0$, then β is evaluated from equation 5.3.20 as:

$$\beta = \frac{m+1}{n} \tag{5.3.22}$$

Therefore:

$$f''(1) = -\frac{n(m+1)\sigma^2 + \ln\gamma}{4\sigma^2}\,\gamma e^{-\beta} \tag{5.3.23}$$

The Taylor series expansion of $f(\phi)$ is:

$$f(\phi) = f(1) + (\phi - 1)f'(1) + \frac{(\phi-1)^2}{2} f''(1) \tag{5.3.24}$$

(with $f'(1) = 0$). Using equations 5.3.19 and 5.3.23, equation 5.3.24 becomes:

$$f(\phi) = \gamma e^{-\beta}\left\{1 - \frac{1}{p^2}(\phi-1)^2\right\}; \qquad p = \left[\frac{8\sigma^2}{n(m+1)\sigma^2 + \ln\gamma}\right]^{1/2} \tag{5.3.25}$$

Now, $f(\phi)$ is placed in the following form:

$$f(\phi) = \frac{1}{a(\phi-1)^2 + b(\phi-1) + c} \tag{5.3.26}$$

Expanding equation 5.3.26 in a Taylor series and comparing the resulting equation to equation 5.3.24, it is obtained that:

$$c = \frac{1}{\gamma e^{-\beta}}; \quad b = 0; \quad a = \frac{\gamma e^{-\beta}}{p^2} \tag{5.3.27}$$

Therefore, equation 5.3.26 becomes:

$$f(\phi) = \frac{p^2\gamma e^{-\beta}}{(\phi-1)^2 + p^2} \tag{5.3.28}$$

and the spectrum $S(\phi)$ (equation 5.3.13) becomes:

$$S(\phi) = \frac{\alpha g^{-\frac{m-5}{2}}}{2k_p^{\frac{m+1}{2}}} \cdot \frac{p^2\gamma e^{-\beta}}{(\phi-1)^2 + p^2} \tag{5.3.29}$$

The total wave energy is given by equation 5.3.4, therefore, the integration of equation 5.3.29 yields:

$$\int S(k)\,dk = k_p \int S(\phi)\,d\phi = \frac{\alpha\gamma p g^{-\frac{m-5}{2}}}{2e^{\beta}k_p^{\frac{m-1}{2}}} \int \frac{p}{(\phi-1)^2 + p^2}\,d(\phi-1) =$$

$$\frac{\alpha\gamma p g^{-\frac{m-5}{2}}}{2e^{\beta}k_p^{\frac{m-1}{2}}} \arctan\frac{\frac{k}{k_p} - 1}{p} \tag{5.3.30}$$

where the integral in equation 5.3.30 is evaluated according to equation 3.3.16 in Abramowitz and Stegun [1972]:

$$\int \frac{p}{(\phi-1)^2 + p^2}\,d\phi = \arctan\frac{\phi - 1}{p} \tag{5.3.31}$$

Using equations 5.3.30 and 5.3.4 the wave energy equation can be written as:

$$E = 2\rho g \int S(k)\,dk = 2\rho g \frac{\alpha\gamma p g^{-\frac{m-5}{2}}}{2e^{\beta} k_p^{\frac{m-1}{2}}} \arctan \frac{\frac{k}{k_p} - 1}{p} =$$

$$2\rho g \frac{H_{mo}^2}{16} \frac{1}{\pi} \arctan \frac{\frac{k}{k_p} - 1}{p} \tag{5.3.32}$$

with:

$$H_{mo} = 4\left[\pi \frac{\alpha\gamma p g^{-\frac{m-5}{2}}}{2e^{\beta} k_p^{\frac{m-1}{2}}}\right]^{1/2} \tag{5.3.33}$$

where β and p are given by equations 5.3.22 and 5.3.25, respectively.

Next equations 5.3.32 and 5.3.33 are written in frequency (f) space using $(2\pi f)^2 = gk$:

$$E\Big|_1^2 = \rho g \frac{H_{mo}^2}{8}\Big[\frac{1}{\pi} \arctan G(f)\Big]_{f_1}^{f_2} \tag{5.3.34}$$

with:

$$G(f) = \frac{(\frac{f}{f_p})^2 - 1}{p}\ ; \quad H_{mo} = 4\left[\pi \frac{\alpha\gamma p g^2}{2e^{\beta}(2\pi) f_p^{m-1}}\right]^{1/2} \tag{5.3.35}$$

Equation 5.3.34 gives the spectral energy contained between frequencies f_1 and f_2. To ensure that E is equal to $\rho g \frac{H_{mo}^2}{8}$ when the integration is performed over the whole spectrum, equation 5.3.34 is slightly modified as:

$$E\Big|_1^2 = \beta_* \rho g \frac{H_{mo}^2}{8}\Big[\frac{1}{\pi} \arctan G(f)\Big]_{f_1}^{f_2} \tag{5.3.36}$$

where β_* is a constant to be determined.

The limits of $\arctan G(f)$ for $f \to 0$ and $f \to \infty$ are:

$$\lim_{f\to 0}\{\arctan G(f)\} = -\arctan(\frac{1}{p}) \quad \text{and} \quad \lim_{f\to\infty}\{\arctan G(f)\} = \frac{\pi}{2} \tag{5.3.37}$$

Performing the integration from zero to infinity, equation 5.3.36 gives:

$$E_T = \rho g \frac{H_{mo}^2}{8} = E\Big|_0^{\infty} = \beta_* \rho g \frac{H_{mo}^2}{8} \frac{1}{\pi}\Big[\frac{\pi}{2} + \arctan(\frac{1}{p})\Big] \tag{5.3.38}$$

From equation 5.3.38 the coefficient β_* is calculated as:

$$\beta_* = \frac{\pi}{\frac{\pi}{2} + \arctan(\frac{1}{p})} \tag{5.3.39}$$

and equation 5.3.36 can be written as:

$$E\Big|_1^2 = \rho g \frac{H_{mo}^2}{8} \frac{\arctan G(f_2) - \arctan G(f_1)}{\frac{\pi}{2} + \arctan(\frac{1}{p})} \tag{5.3.40}$$

and this is the final equation that calculates the wave energy contained between frequencies f_1 and f_2 with $(f_1 < f_2)$.

Now, as mentioned earlier the wave model assumes that all (or most) of the energy is contained between a f_{max} and a f_{min} frequency. f_{max} and f_{min} are both user inputs and are usually defined according to the problem being solved and the expected (guessed) frequency range. The total wave energy that the model calculates is then:

$$E_T \approx E\Big|_{f_{min}}^{f_{max}} \tag{5.3.41}$$

Because all the wave terms are functions of the total energy of the wave spectrum, the above, model calculated, wave energy needs to be re-modulated to include the portion of the wave energy of the Reynolds filtered waves that is not accounted for. The wave energy of the Reynolds filtered waves, according to the Nyquist sampling theorem (Bedford [1994, page 68] and Stull [1988, page 306]), is contained between the frequencies:

$$(f_{min},\, f_{max}) = (f_R = \frac{1}{2\Delta t}, \infty) \tag{5.3.42}$$

By applying equation 5.3.41 twice: the first time for the model frequencies (f_{min}, f_{max}); and the second time for the frequencies defined by equation 5.3.42, the following two expressions are obtained:

$$E_M = E\Big|_{f_{min}}^{f_{max}} = \rho g \frac{H_{mo}^2}{8} \frac{\arctan G(f_{max}) - \arctan G(f_{min})}{\frac{\pi}{2} + \arctan(\frac{1}{p})} \tag{5.3.43}$$

and:

$$E_R = E\Big|_{f_R}^{\infty} = \rho g \frac{H_{mo}^2}{8} \frac{\frac{\pi}{2} - \arctan G(f_R)}{\frac{\pi}{2} + \arctan(\frac{1}{p})} \tag{5.3.44}$$

Dividing equation 5.3.44 by equation 5.3.43 the factor β_ε becomes:

$$\beta_\varepsilon = \frac{E_R}{E_M} = \frac{\frac{\pi}{2} - \arctan G(f_R)}{\arctan G(f_{max}) - \arctan G(f_{min})} \tag{5.3.45}$$

where $G(f_R)$ as defined by equation 5.3.35.

Now, in the wave induced equations of motion all the wave terms are functions of the wave energy and specifically the wave energy of the resolved waves E_R. The wave model output gives the wave energy E_M between the specified frequencies (f_{min}, f_{max}), therefore, the E_R is estimated using 5.3.45 as follows:

$$E_R = \frac{E_R}{E_M} E_M \Longrightarrow E_R = \beta_\varepsilon E_M \tag{5.3.46}$$

and equation 5.3.46 is the re-modulation of the wave energy.

All the required parameters for the calculation of β_ε are computed by the wave model (these are standard calculations). That is, $f_p(\omega_p)$ and p are spectral parameters that are computed in the wave model. The parameter "p", as stated in Onorato et al. [2003], corresponds to the half-width at half-maximum of the spectrum and can be estimated (Priestley [1994], page 514) as:

$$p = \frac{1}{2}\nu_s \tag{5.3.47}$$

where the spectrum width is calculated either by equation 5.3.7 or 5.3.8. Note that p and ν_s are dimensionless. The practical application of equations 5.3.46 and 5.3.45 implies that the re-modulation of the wave energy is performed at every point of the solution domain at every time step and can be either incorporated into the wave model or in the hydrodynamic model.

The variation of β_ε for various values of f_p and p, and for $\Delta t = 0\,\text{s}$ to $1200\,\text{s}$ is shown in Figure 5.1. From the plots, it is clear that $\beta_\varepsilon > 1$ for $f_R = 1/2\Delta t \leq f_{min}$, while for $f_R > f_{max}$, β_ε gradually goes to zero (as $\Delta t \to 0$). As f_p is pushed towards the two ends f_{min} or f_{max} β_ε increases drastically, that is β_ε is controlled by f_p. The development of longer waves from the interaction of the gravity waves pushes f_p towards the lower frequencies thus increasing the value of β_ε. In any case β_ε is not identically 1 and the re-modulation of the wave energy should be considered in the hydrodynamic calculations.

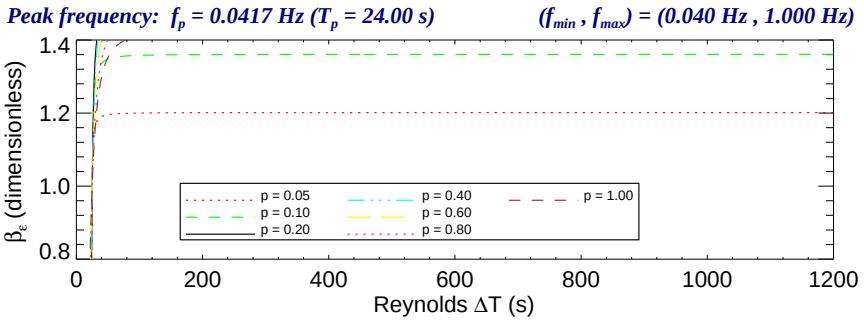

(a)

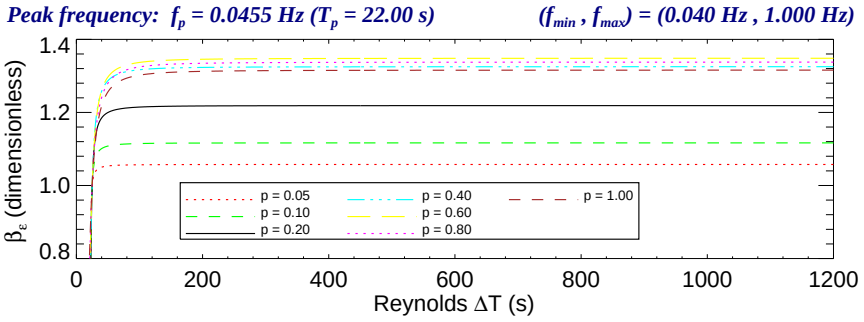

(b)

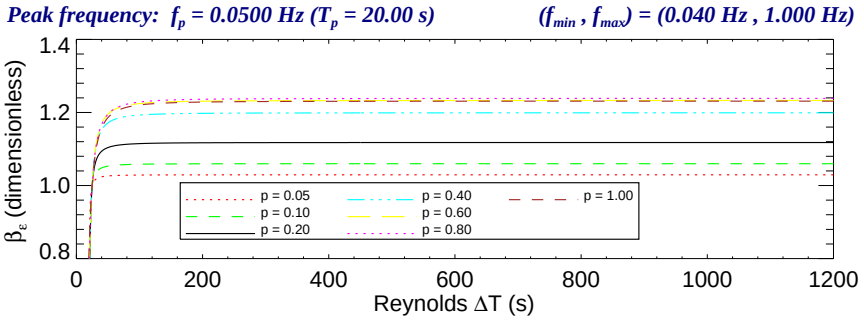

(c)

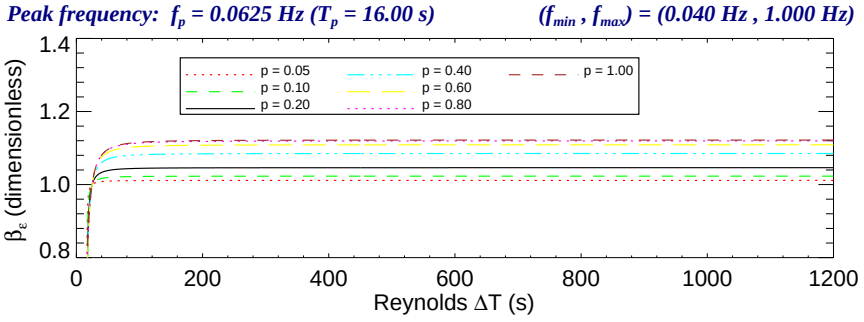

(d)

Figure 5.1 Variation of the wave energy re-modulation coefficient as a function of the Reynolds averaging interval. (Continued)

Figure 5.1 Continued.

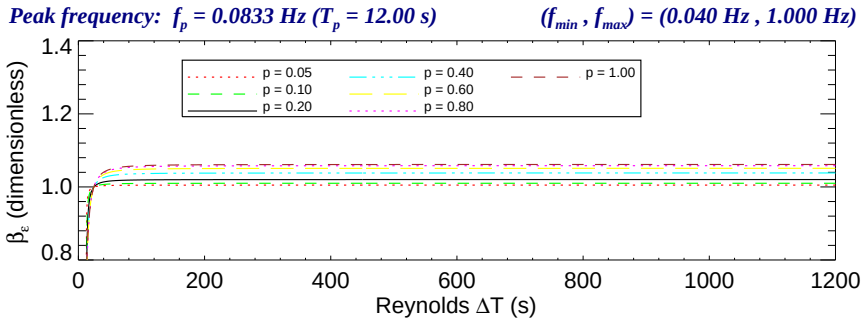

(e)

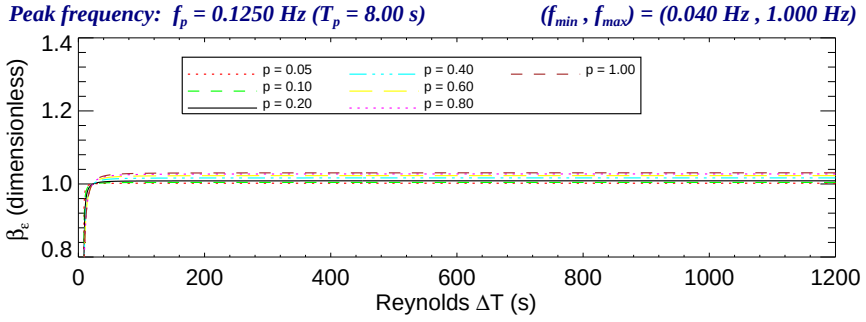

(f)

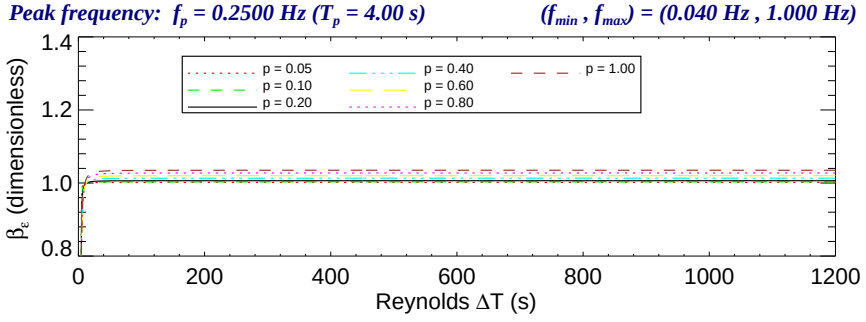

(g)

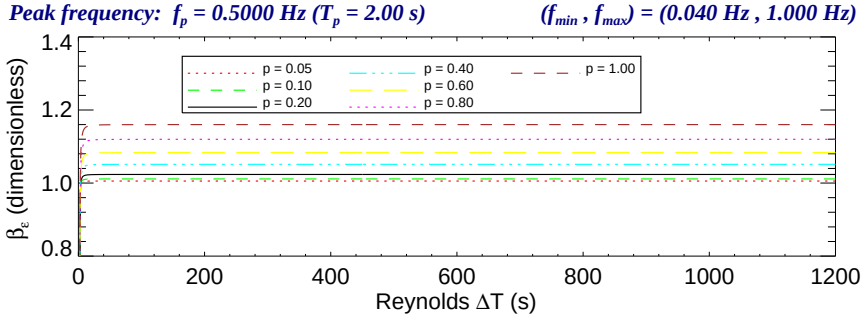

(h)

5.4 Vertical Structure of the Radiation Stress

Let $S_{\alpha\beta}(\vec{x},\sigma;\ k,\theta)$ be the symmetric stress tensor defining the 3D representation of the radiation stress for uni-directional monochromatic waves in σ coordinates, $R_{\alpha\beta}(\vec{x};\ k,\theta)$ be its vertically averaged counterpart and $\tilde{S}_{\alpha\beta}(\vec{x},\sigma;\ k,\theta)$, $\tilde{R}_{\alpha\beta}(\vec{x};\ k,\theta)$ be their corresponding spectral representations.

According to Longuet-Higgins and Stewart [1964], Phillips [1977], LeBlond and Mysak [1978] and Mei [1983], $R_{\alpha\beta}$ is calculated by the following expression:

$$R_{\alpha\beta} = E\left[\frac{k_\alpha k_\beta}{k^2}\frac{c_g}{c} + \delta_{\alpha\beta}(\frac{c_g}{c} - \frac{1}{2})\right]; \qquad \delta_{\alpha\beta} = \begin{cases} 0 & \text{for: } \alpha \neq \beta \\ 1 & \text{for: } \alpha = \beta \end{cases} \tag{5.4.1}$$

where the dummy indexes $\alpha,\beta = (1,2)$ are used to represent the horizontal coordinates: $(x_1, x_2) = (x, y)$ and a repeated dummy index denotes summation over that index. E (N/m) is the total wave energy per unit area and $\delta_{\alpha\beta}$ is the Kronecker delta. The remaining variables in equation 5.4.1 are as defined in Section 4.5.

The vertically averaged radiation stress is defined as:

$$R_{\alpha\beta} = \frac{1}{D}\int_{-h}^{\zeta} S_{\alpha\beta}\, dz = \int_{-1}^{0} S_{\alpha\beta}\, d\sigma\ ; \qquad D = h + \zeta \tag{5.4.2}$$

with the vertical σ transformation defined as: $\sigma = (z - \zeta)/D$. Mellor [2003, 2005], Xia et al. [2004] and others give expressions for the 3D radiation stress $S_{\alpha\beta}$ derived from the conventional equations of motion by considering linear wave theory. The formulation presented in Mellor [2003, 2005], relates $S_{\alpha\beta}$ to the total wave energy E and to the mean depth of the water column D by the following expression:

$$S_{\alpha\beta} = kDE\left[\frac{k_\alpha k_\beta}{k^2}F_{CS}F_{CC} + \delta_{\alpha\beta}\left(F_{CS}F_{CC} - F_{SS}F_{CS}\right)\right] \tag{5.4.3}$$

where $S_{\alpha\beta}$ has units of force per unit width. For a detailed derivation of equation 5.4.3 from the phase averaged 3D equations of motion, the reader is referred to Mellor [2003, 2005].

Equations 5.4.1 and 5.4.3 are considered as implicitly multiplied by ρ_o to conform with equation 5.4.4. In this sense their present definitions are slightly different from the definitions given by equations 4.1.2 and 4.7.6, respectively.

The vertically averaged radiation stress is a wave output parameter of the spectral wave models. However, the calculated $\tilde{R}_{\alpha\beta}$ by the spectral wave models, takes into consideration the whole range

of the wave frequencies and directions. $\tilde{R}_{\alpha\beta}$ is related to $R_{\alpha\beta}$ by the following relationship (Booij et al. [2004]):

$$\tilde{R}_{\alpha\beta} = \rho_o g \int_0^{2\pi}\int_0^{\infty} \mathring{\mathcal{E}}(\mathring{\sigma},\theta)\Big[\frac{k_\alpha k_\beta}{k^2}\frac{c_g}{c} + \delta_{\alpha\beta}(\frac{c_g}{c}-\frac{1}{2})\Big] d\mathring{\sigma}\, d\theta = \rho_o g \int_0^{2\pi}\int_0^{\infty} \mathring{\mathcal{E}}(\mathring{\sigma},\theta)\frac{R_{\alpha\beta}}{E} d\mathring{\sigma}\, d\theta \tag{5.4.4}$$

where the symbol $\mathring{\mathcal{E}}(\mathring{\sigma},\theta)\,(\mathrm{m}^2\mathrm{s})$ represents the wave energy density spectrum. Utilizing the definition of the total wave energy E in terms of the total spectral energy $\mathcal{E}_T$ (Komen et al. [1996], Mei [1983], LeBlond and Mysak [1978]):

$$E = \rho_o g\, \mathcal{E}_T = \rho_o g \int_0^{2\pi}\int_0^{\infty} \mathring{\mathcal{E}}(\mathring{\sigma},\theta)\, d\mathring{\sigma}\, d\theta \tag{5.4.5}$$

it can be seen that $\tilde{R}_{\alpha\beta}$ in equation 5.4.4 is simply the weighted average of $R_{\alpha\beta}$ over the complete spectral space range $(\mathring{\sigma},\theta)$, and thus:

$$\tilde{R}_{\alpha\beta} = \frac{1}{\mathcal{E}_T}\int_0^{2\pi}\int_0^{\infty} \mathring{\mathcal{E}}(\mathring{\sigma},\theta)\, R_{\alpha\beta}\, d\mathring{\sigma}\, d\theta = \overline{R_{\alpha\beta}(x,y,k,\theta)}^{(\mathring{\sigma},\theta)} \tag{5.4.6}$$

Extension to the three-dimensional case follows after the above arguments. Using equation 5.4.3, the expression for the 3D spectral wave radiation stress $\tilde{S}_{\alpha\beta}$ is derived as follows:

$$\tilde{S}_{\alpha\beta} = \rho_o g \int_0^{2\pi}\int_0^{\infty} \mathring{\mathcal{E}}(\mathring{\sigma},\theta)\, kD\Big[\frac{k_\alpha k_\beta}{k^2} F_{CS}F_{CC} + \delta_{\alpha\beta}\,(F_{CS}F_{CC} - F_{SS}F_{CS})\Big] d\mathring{\sigma}\, d\theta =$$

$$\rho_o g \int_0^{2\pi}\int_0^{\infty} \mathring{\mathcal{E}}(\mathring{\sigma},\theta)\frac{S_{\alpha\beta}}{E} d\mathring{\sigma}\, d\theta = \frac{1}{\mathcal{E}_T}\int_0^{2\pi}\int_0^{\infty} \mathring{\mathcal{E}}(\mathring{\sigma},\theta)\, S_{\alpha\beta}\, d\mathring{\sigma}\, d\theta = \overline{S_{\alpha\beta}(x,y,\sigma,k,\theta)}^{(\mathring{\sigma},\theta)} \tag{5.4.7}$$

At this point, it is convenient to introduce a tensor notation using upper case letters as indexes, to denote that no summation over the repeated indexes takes place for the tensor product $A_{\mathrm{AB}}\, B_{\mathrm{AB}}$. This tensor notation will be followed whenever situations requiring the use of upper case indices arise. Let $A_{\alpha\beta}(\tilde{k}D,\sigma)$ be an arbitrary vertical distribution function, such that the expression $\tilde{S}_{\mathrm{AB}} - A_{\mathrm{AB}}(\tilde{k}D,\sigma)\,\tilde{R}_{\mathrm{AB}}$ can be expanded in a Taylor series about the point $(\tilde{k},\tilde{\theta})$:

$$\tilde{S}_{\mathrm{AB}} - A_{\mathrm{AB}}\,\tilde{R}_{\mathrm{AB}} = \tilde{S}_{\mathrm{AB}}(\tilde{k},\tilde{\theta},\sigma) - A_{\mathrm{AB}}(\tilde{k}D,\sigma)\,\tilde{R}_{\mathrm{AB}}(\tilde{k},\tilde{\theta}) +$$

$$\frac{\partial}{\partial\theta}(\tilde{S}_{\mathrm{AB}} - A_{\mathrm{AB}}\,\tilde{R}_{\mathrm{AB}})\Big|_{\theta=\tilde{\theta}}\Delta\theta + \frac{\partial}{\partial k}(\tilde{S}_{\mathrm{AB}} - A_{\mathrm{AB}}\,\tilde{R}_{\mathrm{AB}})\Big|_{k=\tilde{k}}\Delta k + O(\Delta\theta^2,\Delta k^2) \tag{5.4.8}$$

As seen from the above equation, it is possible to find a function A_{AB} such that all the terms of the form: $\frac{\partial^{m+n}}{\partial\theta^m \partial k^n}(\tilde{S}_{AB} - A_{AB}\,\tilde{R}_{AB})$ either vanish or become very small. Assuming that such a function has been found, then all the terms on the r.h.s of equation 5.4.8 can be neglected as long as the function satisfies the equation: $\tilde{S}_{AB}(\tilde{k},\tilde{\theta},\sigma) = A_{AB}(\tilde{k}D,\sigma)\,R_{AB}(\tilde{k},\tilde{\theta})$. For such a case, the spectral averaging of equation 5.4.8 in combination with equations 5.4.6 and 5.4.7 gives:

$$\overline{(\tilde{S}_{AB} - A_{AB}\,\tilde{R}_{AB})}^{(\mathring{\sigma},\theta)} = \overline{\tilde{S}}^{(\mathring{\sigma},\theta)}_{AB} - A_{AB}\,\overline{\tilde{R}}^{(\mathring{\sigma},\theta)}_{AB} = S_{AB}(\tilde{k},\tilde{\theta},\sigma) - A_{AB}(\tilde{k}D,\sigma)\,R_{AB}(\tilde{k},\tilde{\theta}) = 0 \qquad (5.4.9)$$

Using the expressions for $S_{AB}(\tilde{k},\tilde{\theta},\sigma)$ and $R_{AB}(\tilde{k},\tilde{\theta})$ from equations 5.4.3 and 5.4.1, respectively, the last of equations 5.4.9 determines $A_{AB}(\tilde{k}D,\sigma)$, while the second equation determines the spectrally averaged radiation stress S_{AB}. The spectrally averaged wavenumber $\tilde{k}$ and wave direction $\tilde{\theta}$ are defined as (Booij et al. [2004], The WAMDI Group [1988]):

$$\tilde{k} = \left[\frac{1}{\mathcal{E}_T}\int_0^{2\pi}\int_0^{\infty}\frac{1}{\sqrt{k}}\,\mathring{\mathcal{E}}(\mathring{\sigma},\theta)\,d\mathring{\sigma}\,d\theta\right]^{-2} ; \qquad \tilde{\theta} = \arctan\left[\frac{\int_0^{2\pi}\int_0^{\infty}\mathring{\mathcal{E}}(\mathring{\sigma},\theta)\sin\theta\,d\mathring{\sigma}\,d\theta}{\int_0^{2\pi}\int_0^{\infty}\mathring{\mathcal{E}}(\mathring{\sigma},\theta)\cos\theta\,d\mathring{\sigma}\,d\theta}\right] \qquad (5.4.10)$$

Following the arguments presented in this Section, equation 4.1.4, written in terms of the radiation stress for monochromatic and uni-directional waves, can be extended to the spectral waves by simply replacing $R_{\alpha\beta}$ with $\tilde{R}_{\alpha\beta}$.

5.5 Vertical Shape Function of the 3D Radiation Stress

The objective of this Section is to determine a vertical distribution function $A(\tilde{k}D,\sigma)$, such that the 3D radiation stresses $S_{\alpha\beta}$ can be estimated from the wave model calculated $\tilde{R}_{\alpha\beta}$. This function should have a simple representation, possibly some kind of polynomial expansion that can be easily integrable or differentiable, and should satisfy the following two conditions:

$$S_{\alpha\beta} = A(\tilde{k}D,\sigma)\,R_{\alpha\beta} ; \qquad \text{with} \qquad \int_{-1}^{0} A(\tilde{k}D,\sigma)\,d\sigma = 1 \qquad (5.5.1)$$

The choice for A to be a function of the spectrally averaged wavenumber $\tilde{k}$ comes as a result of the arguments presented in Section 5.4. For the case of the monochromatic waves considered here, it can be shown from the first of equations 5.4.10 that $\tilde{k}$ is equal to k. Close inspection of the functions F_{CS}, F_{CC} and F_{SS} (equations 4.5.9a, 4.5.9b) reveals that as $kD \to 0$ then, $kDF_{CS} \to 1$,

$F_{CC} \to 1$ and $F_{SS} \to 1+\sigma$; while as $kD \to \infty$ all three functions asymptotically approach $e^{kD\sigma}$ (Mellor [2003]). The asymptotic behavior of these functions merely suggests the following representation for $A(kD,\sigma)$:

$$A(kD,\sigma) = A(x,\sigma) = \Big(\sum_{m=0}^{M} f_m(x)\,\sigma^m\Big)\,e^{2x\sigma} \tag{5.5.2}$$

where, $x = kD$ and $f_m(x)$ are polynomials of x defined as:

$$f_m(x) = \sum_{n=0}^{N} a_n^m x^n = a_0^m + a_1^m x + a_2^m x^2 + \cdots + a_n^m x^n \tag{5.5.3}$$

The constants a_n^m as well as the degrees M and N of the σ and x polynomials, respectively, still need to be determined. Exactly the same results can be obtained using power series expansions for all the terms involved in the first of equations 5.5.1. Since $|\sigma| \le 1$, the higher order σ terms ($M > 2$) in equation 5.5.2 can be truncated and $f_0(x)$ is determined using the vertical averaging property of A.

A more precise and elegant approach is presented here that supports the previous discussion. The wavenumber tensor appearing in equations 5.4.1 and 5.4.3 is defined as:

$$\frac{k_\alpha\,k_\beta}{k^2} = \begin{pmatrix} \dfrac{k_1^2}{k^2} & \dfrac{k_1\,k_2}{k^2} \\[2ex] \dfrac{k_1\,k_2}{k^2} & \dfrac{k_2^2}{k^2} \end{pmatrix} = \begin{pmatrix} \sin^2\theta & \sin\theta\cos\theta \\[2ex] \sin\theta\cos\theta & \cos^2\theta \end{pmatrix} \tag{5.5.4}$$

where, θ is the direction of the propagating waves measured clockwise from the true North.

Case $\delta_{\alpha\beta} = 0$ $(\alpha \neq \beta)$:

The combination of equations 5.4.1, 5.4.3, 4.5.9a, 4.5.9b, 5.5.2 and the first of equations 5.5.1 yields:

$$x\,F_{CS}\,F_{CC} = \Big(\sum_{m=0}^{M} f_m(x)\,\sigma^m\Big)\,e^{2x\sigma}\,\frac{c_g}{c} \Rightarrow$$

$$\underbrace{\cosh 2x(1+\sigma)+1}_{2 \text{ for } x\to 0} = \Big(\sum_{m=0}^{M} f_m(x)\,\sigma^m\Big)\,e^{2x\sigma}\Big[\underbrace{\frac{\sinh 2x}{2x}+1}_{2 \text{ for } x\to 0}\Big] \tag{5.5.5}$$

As now $x \to \infty$, the term $e^{2x\sigma}$ ($\sigma < 0$) vanishes (except at the free surface) along with the whole equation. To determine the coefficients a_n^m, the limits of both sides of equation 5.5.5 are taken as

$x \to 0$, yielding the following equations:

$$\lim_{x\to 0} f_0(x) = 1\ ; \qquad \lim_{x\to 0} f_m(x) = 0 \quad (m = 1, M) \tag{5.5.6}$$

Equating the coefficients of the same powers of x in both sides of equations 5.5.6 gives:

$$a_0^0 = 1 \qquad \text{and} \qquad a_0^m = 0 \quad (m = 1, M) \tag{5.5.7}$$

The second of equations 5.5.7 suggests that the polynomials $f_m(x)$ can be represented as: $f_m(x) = x(a_1^m + a_2^m\, x + \cdots + a_n^m\, x^{n-1})$ $(m \geq 1)$. From the definition of A (equation 5.5.2) it is seen that A attains its maximum value at the free surface ($\sigma = 0$), while at the bottom ($\sigma = -1$) approaches zero as $x \to \infty$. Rearranging equation 5.5.5 and taking the limits of both sides as $x \to \infty$ it is found that:

$$\lim_{x\to\infty} A(x,\sigma) = \lim_{x\to\infty} \frac{2x\,(\cosh 2x(1+\sigma) + 1)}{\sinh 2x + 2x} = 1 + 2x \qquad (\sigma = 0) \tag{5.5.8}$$

Equation 5.5.8 suggests that the polynomials $f_m(x)$ are at most of the first order. Combining the results from equations 5.5.7 and 5.5.8, the distribution function assumes the form:

$$A(x,\sigma) = \left(f_0(x) + b_1\, x\sigma + b_2\, x\sigma^2 + \cdots + b_m\, x\sigma^m\right) e^{2x\sigma} \tag{5.5.9}$$

The function $f_0(x)$ was intentionally kept in equation 5.5.9 so it can serve as the placeholder of all the truncated terms from the original expression for A and will eventually be determined using the vertical averaging property of A. After using equation 5.5.9, equation 5.5.5 is written as:

$$\cosh 2x(1+\sigma) + 1 = \left(f_0(x) + b_1\, x\sigma + b_2\, x\sigma^2 + \cdots + b_m\, x\sigma^m\right) e^{2x\sigma}\left[\frac{\sinh 2x}{2x} + 1\right] \tag{5.5.10}$$

Differentiation of equation 5.5.10 with respect to σ and after the division of both sides by $2x$ gives:

$$\sinh 2x(1+\sigma) = \left(\frac{b_1}{2} + b_2\,\sigma + \frac{3b_3}{2}\,\sigma^2 + \cdots + \frac{m\,b_m}{2}\,\sigma^{m-1}\right) e^{2x\sigma}\left[\frac{\sinh 2x}{2x} + 1\right] +$$

$$\left(f_0(x) + b_1\, x\sigma + b_2\, x\sigma^2 + \cdots + b_m\, x\sigma^m\right) e^{2x\sigma}\left[\frac{\sinh 2x}{2x} + 1\right] \tag{5.5.11}$$

Taking the limits of both sides as $x \to 0$ of equation 5.5.11 gives:

$$\frac{b_1}{2} + b_2\,\sigma + \frac{3b_3}{2}\,\sigma^2 + \cdots + \frac{m\,b_m}{2}\,\sigma^{m-1} \equiv -1 \tag{5.5.12}$$

and by equating the coefficients of the same powers of σ in both sides of equation 5.5.12 the values the coefficients b_m are:

$$b_1 = -2 \qquad \text{and} \qquad b_2 = b_3 = \cdots = b_{m-1} = b_m = 0 \tag{5.5.13}$$

Substitution of the values of the coefficients b_m into equation 5.5.9 yields:

$$A(x,\sigma) = [\, f_0(x) + f_1(x)\,\sigma]\, e^{2x\sigma}\ ; \qquad f_1(x) = -2x \tag{5.5.14}$$

and integration of equation 5.5.14 by using the vertical averaging property of $A(x,\sigma)$ (the second of equations 5.5.1), gives that:

$$f_0(x) = \frac{2x}{1-e^{-2x}} - f_1(x)\,\frac{(2x+1)e^{-2x}-1}{2x(1-e^{-2x})} \tag{5.5.15}$$

From equation 5.5.15, it can be shown using L'Hospital's rule that $\lim\limits_{x\to 0} f_0(x) = 1$, which satisfies the first of equations 5.5.6 as it should.

Case $\delta_{\alpha\beta} = 1$ $(\alpha = \beta)$:

Again, the objective here is to find the distribution function $A(x,\sigma)$ with the same properties as before. Using equations 5.4.1, 5.4.3 and the first of equations 5.5.1 and after substituting all the variables involved with their mathematical definitions, the following equation is derived:

$$\Big[\frac{k_\alpha^2}{k^2}+1\Big]\Big[\,\cosh 2x(1+\sigma)+1\Big] - \underbrace{\frac{\sinh 2x(1+\sigma)\,\cosh x}{\sinh 2x}}_{2\,(1+\sigma)\ \text{for}\ x\to 0} =$$

$$\Big(\sum_{m=0}^{M} f_m(x)\,\sigma^m\Big)\, e^{2x\sigma}\Big[\frac{k_\alpha^2}{k^2}\Big\{\frac{\sinh 2x}{2x}+1\Big\}+1\Big] \tag{5.5.16}$$

Since the polynomials $f_m(x)$ cannot be functions of the wave direction θ, equation 5.5.16 needs first to be averaged over the interval $[0, 2\pi]$ (range of the wave directions). Using the equations 5.5.4, the resulting integrals of the wavenumber terms are evaluated as follows:

$$\frac{1}{2\pi}\int_0^{2\pi}\frac{k_1^2}{k^2}\,d\theta = \frac{1}{2\pi}\int_0^{2\pi}\frac{k_2^2}{k^2}\,d\theta = \frac{1}{2} \tag{5.5.17}$$

and equation 5.5.16 becomes:

$$3\Big[\,\cosh 2x(1+\sigma)+1\Big] - \frac{2\sinh 2x(1+\sigma)\,\cosh x}{\sinh 2x} =$$

$$\Big(\sum_{m=0}^{M} f_m(x)\,\sigma^m\Big)\, e^{2x\sigma}\Big[\frac{\sinh 2x}{2x}+3\Big] \tag{5.5.18}$$

Taking the limits of both sides of equation 5.5.18 as $x \to 0$ yields:

$$\lim_{x\to 0} f_0(x) = \frac{1}{2}\ ; \qquad \lim_{x\to 0} \sum_{m=1}^{M} f_m(x)\,\sigma^m = -\sigma \tag{5.5.19}$$

and equating the coefficients of the same powers of x and σ in both sides of equations 5.5.19 the coefficients a_m are evaluated as follows:

$$a_0^0 = \frac{1}{2}\ , \qquad a_0^1 = -1\ , \qquad \text{and} \qquad a_0^m = 0 \quad (m = 2, M) \tag{5.5.20}$$

The last of equations 5.5.20 suggests that the polynomials $f_m(x)$ can be represented as: $f_m(x) = x(a_1^m + a_2^m\, x + \cdots + a_n^m\, x^{n-1})$ $(m \geq 2)$. Rearranging equation 5.5.18 and taking the limits of both sides as $x \to \infty$ gives that:

$$\lim_{x\to\infty} A(x,\sigma) = 2 + 2x \qquad (\sigma = 0) \tag{5.5.21}$$

Equation 5.5.21 suggests that the polynomials $f_m(x)$ are again at most first order. Combining the results from equations 5.5.20 and 5.5.21, the distribution function assumes the form:

$$A(x,\sigma) = \Big(f_0(x) + b_1\,\sigma + b_2\, x\sigma^2 + \cdots + b_m\, x\sigma^m\Big)\, e^{2x\sigma} \tag{5.5.22}$$

Substitution of equation 5.5.22 into equation 5.5.18 the differentiation of the resulting equation with respect to σ gives:

$$\underbrace{6x\sinh 2x(1+\sigma)}_{0 \text{ for } x\to 0} - \underbrace{\frac{4x\cosh 2x(1+\sigma)\sinh 2x}{\sinh 2x}}_{4 \text{ for } x\to 0} =$$

$$\Big(b_1 + 2\,b_2\, x\sigma + 3\,b_3\, x\sigma^2 + \cdots + m\,b_m\, x\sigma^{m-1}\Big)\, e^{2x\sigma}\Big[\frac{\sinh 2x}{2x} + 3\Big] +$$

$$2x\Big(f_0(x) + b_1\,\sigma + b_2\, x\sigma^2 + \cdots + b_m\, x\sigma^m\Big)\, e^{2x\sigma}\Big[\frac{\sinh 2x}{2x} + 3\Big] \tag{5.5.23}$$

The coefficient b_1 is determined by taking the limits of both sides of equation 5.5.23 as $x \to 0$: $-4 = 4b_1 \Rightarrow b_1 = -1$, thus recovering the second of equations 5.5.20 as expected. Differentiating equation 5.5.23 with respect to σ, dividing the resulting equation by $2x$ and taking the limits as $x \to 0$, determines the coefficients $b_2, b_3, \cdots, b_m$ as previously outlined:

$$b_2 = 2 \qquad \text{and} \qquad b_3 = b_4 = \cdots = b_{m-1} = b_m = 0 \tag{5.5.24}$$

Substitution of the values of the coefficients b_m into equation 5.5.22 yields:

$$A(x,\sigma) = [\,f_0(x) + f_1(x)\,\sigma + f_2(x)\,\sigma^2]\,e^{2x\sigma}\ , \qquad f_1(x) = -1\ , \qquad f_2(x) = 2x \tag{5.5.25}$$

Vertically integrating the first of equations 5.5.25 the following expression is derived for $f_0(x)$:

$$f_0(x) = \frac{2x}{1-e^{-2x}} - f_1(x)\,\frac{(2x+1)e^{-2x}-1}{2x(1-e^{-2x})} + f_2(x)\,\frac{(2x^2+2x+1)e^{-2x}-1}{2x^2(1-e^{-2x})} \tag{5.5.26}$$

From equation 5.5.26, it can be shown using L'Hospital's rule that $\lim_{x\to 0} f_0(x) = 1/2$, which satisfies the first of equations 5.5.19. Summarizing the results, first the vertical distribution function is represented as the 2D symmetric tensor $A_{\alpha\beta}(x,\sigma) = \begin{pmatrix} A_{11} & A_{12} \\ A_{21} & A_{22} \end{pmatrix}$, such that:

$$A_{11} = A_{22} = A = \left[A_0(x) + A_1(x)\,\sigma + A_2(x)\,\sigma^2\right] e^{2x\sigma}, \quad A_1(x) = -1, \quad A_2(x) = 2x \tag{5.5.27}$$

$$A_0(x) = \frac{2x}{1-e^{-2x}} - A_1(x)\,\frac{(2x+1)e^{-2x}-1}{2x(1-e^{-2x})} + A_2(x)\,\frac{(2x^2+2x+1)e^{-2x}-1}{2x^2(1-e^{-2x})} \tag{5.5.28}$$

$$A_{12} = A_{21} = B = \left[B_0(x) + B_1(x)\,\sigma + B_2(x)\,\sigma^2\right] e^{2x\sigma}, \quad B_1(x) = -2x, \quad B_2(x) = 0 \tag{5.5.29}$$

$$B_0(x) = \frac{2x}{1-e^{-2x}} - B_1(x)\,\frac{(2x+1)e^{-2x}-1}{2x(1-e^{-2x})} + B_2(x)\,\frac{(2x^2+2x+1)e^{-2x}-1}{2x^2(1-e^{-2x})} \tag{5.5.30}$$

Next, the radiation stress tensor is represented as: $S_{\mathrm{AB}} = A_{\mathrm{AB}}\,R_{\mathrm{AB}}$ with $\mathrm{A,B} = (1,2)$. The expressions for the normal and cross components of the wave radiation stresses subsequently can be written in terms of the distribution functions A and B given by the equations 5.5.27 and 5.5.29, respectively.

The important limiting cases for the stresses are given next:

normal radiation stresses: $S_{\mathrm{AB}} = A_{\mathrm{AB}}\,R_{\mathrm{AB}} = A\,R_{\mathrm{AB}}$; $\mathrm{A = B} = (1,2)$

$$\lim_{x\to 0} S_{\mathrm{AB}} = \begin{cases} \dfrac{1}{2}\,R_{\mathrm{AB}} & (\sigma = 0) \\ \dfrac{3}{2}\,R_{\mathrm{AB}} & (\sigma = -1) \end{cases} \qquad \text{and} \qquad \lim_{x\to\infty} S_{\mathrm{AB}} = \begin{cases} 2x\,R_{\mathrm{AB}} & (\sigma = 0) \\ 0 & (\sigma \neq 0) \end{cases} \tag{5.5.31}$$

cross radiation stresses: $S_{\mathrm{AB}} = A_{\mathrm{AB}}\,R_{\mathrm{AB}} = B\,R_{\mathrm{AB}}$; $\mathrm{A \neq B} = (1,2)$

$$\lim_{x\to 0} S_{\mathrm{AB}} = \begin{cases} R_{\mathrm{AB}} & (\sigma = 0) \\ R_{\mathrm{AB}} & (\sigma = -1) \end{cases} \qquad \text{and} \qquad \lim_{x\to\infty} S_{\mathrm{AB}} = \begin{cases} 2x\,R_{\mathrm{AB}} & (\sigma = 0) \\ 0 & (\sigma \neq 0) \end{cases} \tag{5.5.32}$$

The significance of the first of the limiting cases in equations 5.5.31 is that for shallow waters the normal radiation stresses increase with depth, while the corresponding shear radiation stresses (equations 5.5.32) approach to a constant value. This behavior of the stresses is seen more clearly in Figure 5.2. In deeper waters, both the normal and the shear radiation stresses attain a maximum value at the free surface (asymptotically equal to $2kD$) while they rapidly approach zero with increasing depth (Figures 5.2), establishing the minimal effect that they have on the bottom physics.

The equations for the 3D stresses given here have a simpler representation than those given by Mellor [2003], and are more suitable for modeling purposes (for example, an accuracy improvement will probably only require the adjustment of the functions $A_i(x)$ and $B_i(x)$ in equations 5.5.27 and 5.5.29). The results in this Section are consistent with the vertical structure of the wave radiation stresses reported in the literature (e.g., Xia et al. [2004], Mellor [2003]). Since $e^{2kD\sigma} \to 1$ for $kD \to 0$, in shallow waters the waves exhibit their full 3D nature. In deeper waters as $kD \to \infty$, $e^{2kD\sigma} \to 0$ everywhere in the vertical direction, except at the free surface where $e^{2kD\sigma} \to 1$. Therefore, in deep waters the 3D velocity structure is only slightly affected by the waves and only by association with the 2D currents and the surface 3D velocities.

5.6 Implementation of the Radiation Stress in the Hydrodynamic Model

The results presented in Section 5.5 are valid for uni-directional and monochromatic waves. The extension to a spectrum of waves follows the arguments presented in Sections 5.2 and 5.4 by simply replacing $R_{\alpha\beta}$ with $\tilde{R}_{\alpha\beta}$, therefore, the relation between the 3D and the vertically averaged radiation stress is written as:

$$\tilde{S}_{\mathrm{AB}} = A_{\mathrm{AB}}(x,\sigma)\,\tilde{R}_{\mathrm{AB}}\,, \qquad x = \tilde{k}D\,; \qquad \mathrm{A,B} = (1,2) \tag{5.6.1}$$

Since all the wave variables introduced in this Chapter are functions of both the spatial and the spectral spaces, the notation $F(\mathring{\sigma},\theta)$ for a wave variable F is used here with the understanding that $F(\mathring{\sigma},\theta) \to F(x,y,\mathring{\sigma},\theta)$. The spectral averaging of equation 4.1.4 gives:

$$\mathcal{M}_\alpha = -\frac{1}{\rho_o}\,\overline{\frac{\partial R_{\alpha\beta}}{\partial x_\beta}}^{(\mathring{\sigma},\theta)} = -\frac{1}{\rho_o}\,\frac{\partial \overline{R}_{\alpha\beta}^{(\mathring{\sigma},\theta)}}{\partial x_\beta} = -\frac{1}{\rho_o}\,\frac{\partial \tilde{R}_{\alpha\beta}}{\partial x_\beta} \tag{5.6.2}$$

$\mathcal{M}_\alpha$ is the momentum per unit mass of the water that collectively represents all the non-wave terms of the external momentum equation. Since $\mathcal{M}_\alpha$ has no wave components attached to it, the spectral averaging of this term is simply $\mathcal{M}_\alpha$. The wave radiation stress term in equation 5.6.2 was

derived by invoking equation 5.4.6. The other wave terms present in the equations (e.g., equations 4.10.10, 4.10.24, etc.), are treated exactly the same way producing similar results.

The derivation of the complete, spectrally averaged, equations of motion and scalar transport is a straight forward process and follows the same procedure as described in the derivation of equation 5.4.6, therefore, there is no need for it to be presented here.

Section 5.3 presented a methodology to account for the un-resolved portions of the wave spectrum by the spectral wave models. In the same Section the re-modulation of the wave energy appearing in the wave terms of the equations of motion is suggested by multiplying the total spectral wave energy calculated in the wave model by the factor β_ε (equation 5.3.45). Let $F = F(\mathring{\sigma}, \theta) = F(k, \theta)$ be a wave variable and $\tilde{F}$ its integral representation over the wave spectrum:

$$\tilde{F} = \int_0^{2\pi} \int_0^{\infty} \mathring{\mathcal{E}}(\mathring{\sigma}, \theta)\, F\, d\mathring{\sigma}\, d\theta \tag{5.6.3}$$

Application of the first mean value theorem for integrals (equation B.47) for $\xi = (\widetilde{\mathring{\sigma}}, \tilde{\theta})$ gives:

$$\tilde{F} = \int_0^{2\pi} \int_0^{\infty} \mathring{\mathcal{E}}(\mathring{\sigma}, \theta)\, F\, d\mathring{\sigma}\, d\theta \approx F(\widetilde{\mathring{\sigma}}, \tilde{\theta}) \int_0^{2\pi} \int_0^{\infty} \mathring{\mathcal{E}}(\mathring{\sigma}, \theta)\, d\mathring{\sigma}\, d\theta \approx \mathcal{E}_M F(\widetilde{\mathring{\sigma}}, \tilde{\theta}) = \frac{\mathcal{E}_R}{\beta_\varepsilon} F(\widetilde{\mathring{\sigma}}, \tilde{\theta}) \tag{5.6.4}$$

where in the above equation, $\mathcal{E}_M$ is the wave model calculated total spectral wave energy, $\mathcal{E}_R$ is the total energy contained in the wave spectrum and $\tilde{F}$ is the wave variable as incorporated into the hydrodynamic equations of motion. To account for the complete spectral wave energy, equation 5.6.4 suggests that all the wave variables in the hydrodynamic equations need to simply be multiplied by β_ε. This option is available in M^2COPS (user choice).

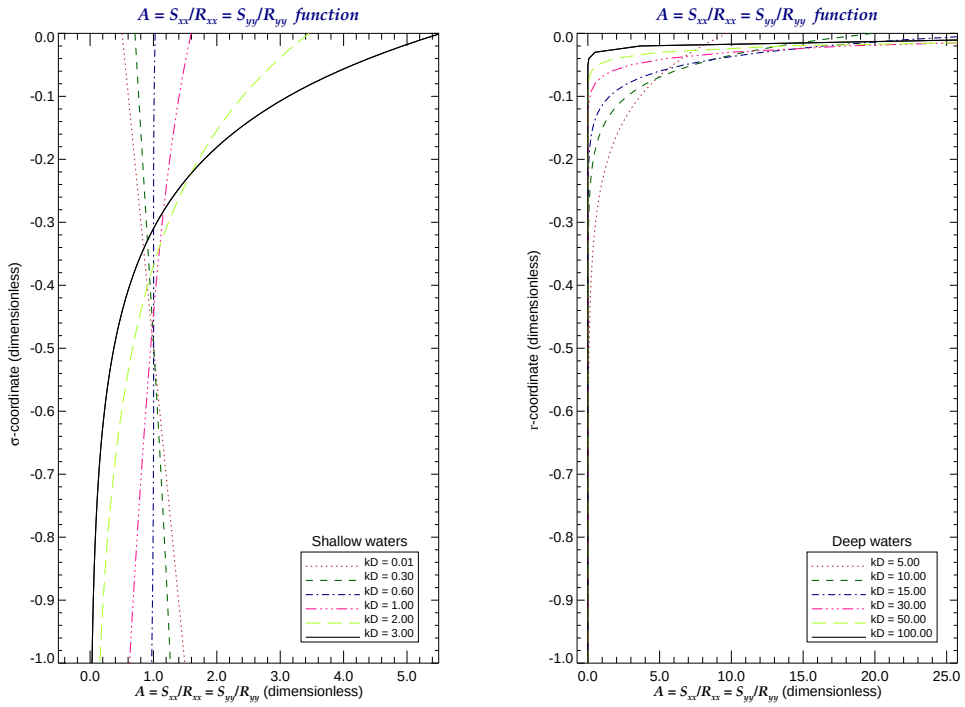

(a) Normal components of the radiation stresses.

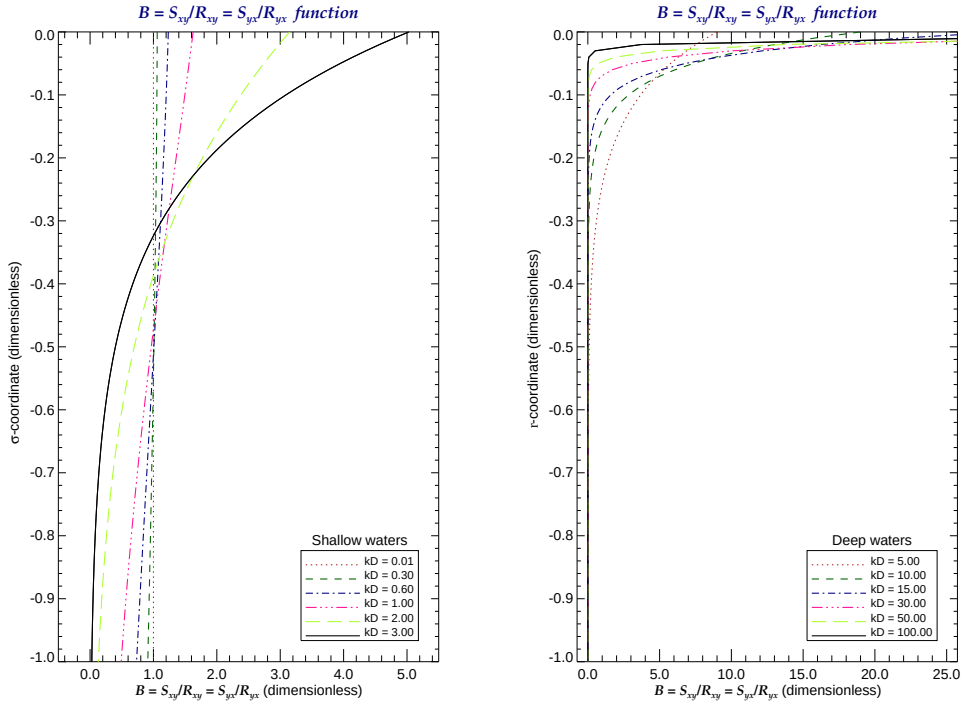

(b) Shearing or cross components of the radiation stresses.

Figure 5.2 Plots of the vertical distribution functions for the 3D wave radiation stresses.

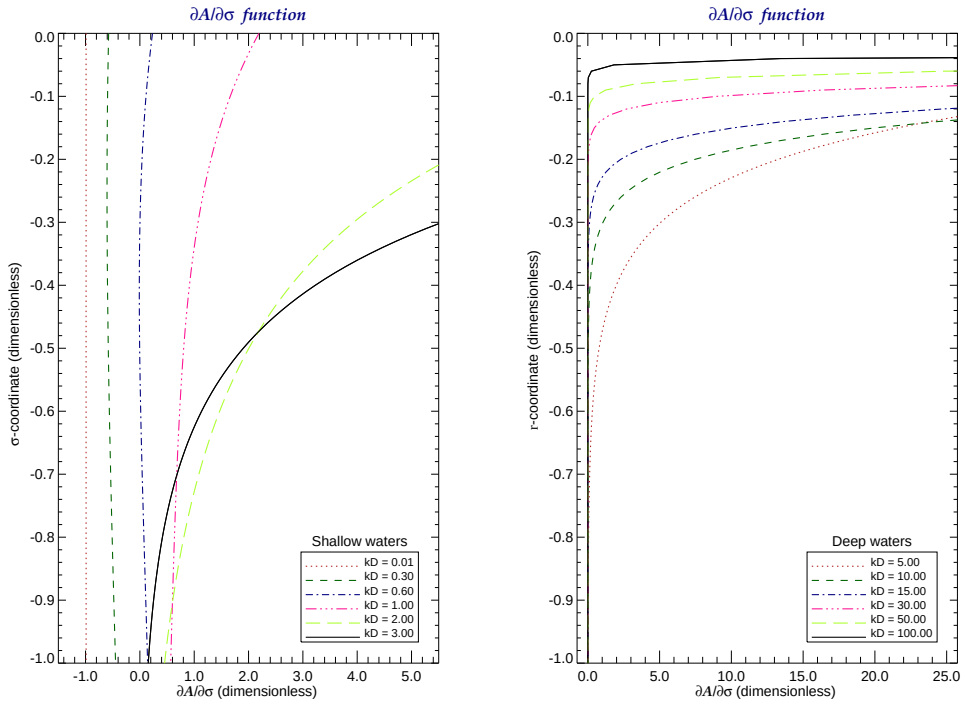

(a) Function for the normal components of the radiation stresses.

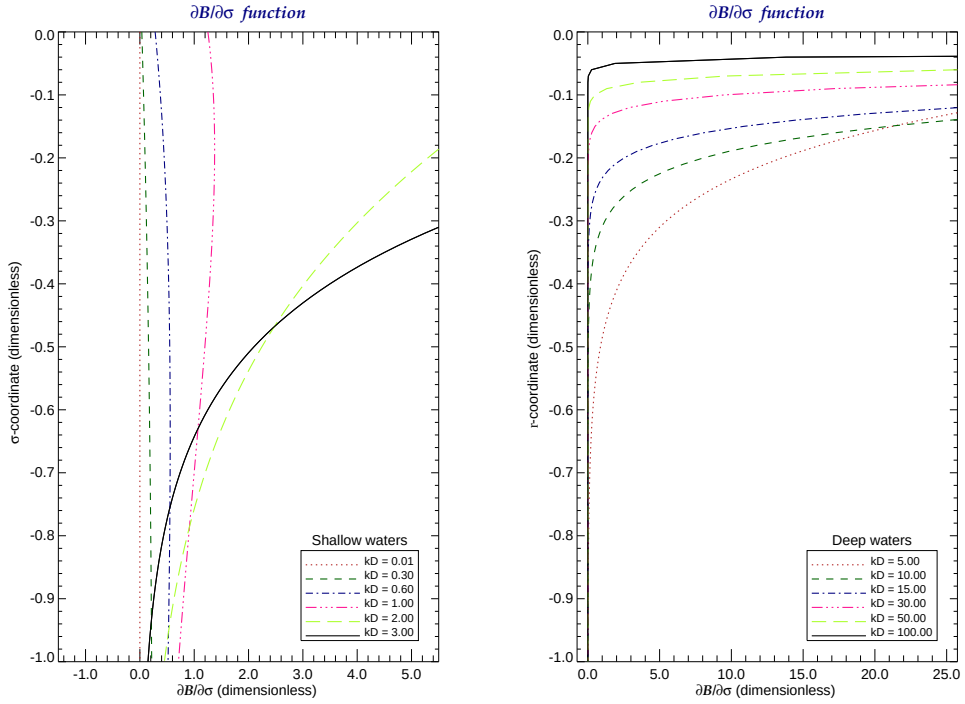

(b) Function for the cross components of the radiation stresses.

Figure 5.3 Plots of the vertical variation of the 3D wave radiation stress distribution functions.

CHAPTER 6

WAVE-CURRENT BOTTOM BOUNDARY LAYER MODEL

6.1 Introduction

Bottom boundary layers (*BBL*s) are thin fluid regions next to the "solid" bottom boundary, which are very important in coastal engineering practice. The fluid physics in these regions affects the fluid motions away from the bottom, as well as the entrainment and transport of the bottom sediments. The presence of wind-driven surface waves additionally produces a thin oscillatory wave boundary layer (*WBL*), where the flow is rotational and the bottom friction is significantly enhanced by the oscillatory nature of the wave motion. The *WBL* is nested within the current boundary layer (*CBL*). The region resulting from the interaction of the waves and the currents is known as the wave-current bottom boundary layer (*WCBBL*). Figure 6.1 illustrates a conceptual representation of the two layers along with the corresponding vertical profiles for the flow velocity and the sediment concentration (source: Glenn [1987]).

Typically the thickness of the *WCBBL* ranges from 2 cm to 20 cm Glenn [1987]. The small scale of the *WCBBL* causes the bottom shear stresses associated with the waves to be much greater than the shear stresses associated with the currents. The increased bottom friction by the waves is a function of both the wave and the current induced flow velocities, and expresses the highly non-linear interaction between the waves and the currents. Since, the flow motions away from the bottom and the entrainment of the sediments depend upon the bottom shear stresses, the accurate description of the flow field and the sediment transport requires the accurate description of the near-bottom flow field and its impact on the water column dynamics.

Various bottom boundary layer models (*BBLM*s) have been proposed by different researchers to be used either as stand-alone modeling tools or as modules coupled with general hydrodynamic/sediment models. These *BBL* models assume logarithmic near-bottom velocity profiles and

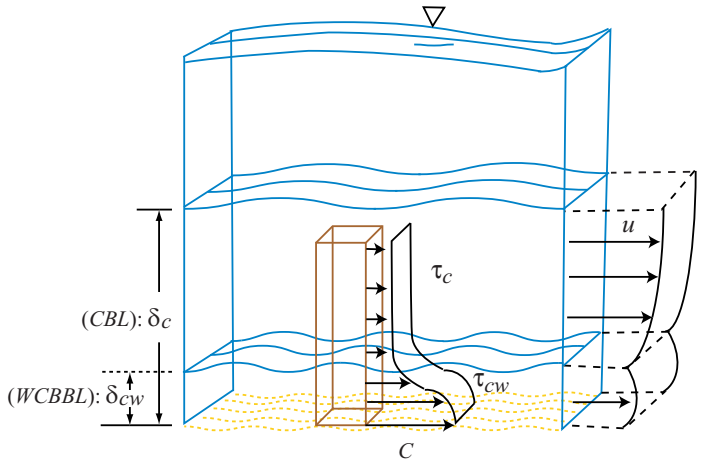

Figure 6.1 Definition of a wave-current bottom boundary layer.

are usually distinguished by the turbulence closure model they are using. The more advanced or second generation *BBLM* formulations use higher order, time dependent turbulence closure models (e.g., κ-ϵ two equation model), while others use eddy viscosity models (e.g., linear, parabolic) that are less computationally demanding.

Mellor [2002], made the interesting argument that the inclusion of an additional turbulence production term in the turbulence closure model can effectively simulate the effects of a wave-current boundary layer model. The possibility of replacing the complete *WCBBL* formulation by an elegant, simple and computationally efficient formulation, is very challenging and needs to be explored.

Puleo et al. [2004] compared six *BBLM* formulations (eddy viscosity: laminar, linear and parabolic, and turbulence closure: κ one equation, κ-ϵ two equation and κ-ω two equation), and concluded that the linear eddy viscosity models perform equally well to the higher order turbulence closure models.

Supported by the above arguments, the linear eddy viscosity *BBLM* by Glenn [1987] and Glenn and Grant [1987] (henceforth; *GG87*) is used as a basis for the development of the M^2*COPS* bottom boundary layer model (M^2*BBL*) that approximates the near-bottom flow field under the combined action of the waves and the currents. The *GG87* model determines the vertical distribution of the velocity and sediment concentration and it is an enhanced version of the previous models by Grant and Madsen [1979, 1982] (henceforth; *GM79* and *GM82*, respectively) and Grant and Madsen [1986] (henceforth; *GM86*), which include the effects of the sediment stratification due to the presence of

the near-bottom concentration gradients. Two drawbacks of the *GG87* model are the assumption that the stratification effects inside the *WCBBL* are negligible and the discontinuity of the eddy diffusivities at the top of the *WCBBL*. These drawbacks possibly compromise an accurate prediction of suspended sediment loads and add considerable computing burdens.

More recent research efforts rectify these deficiencies of the model by accounting for suspended sediment induced stratification and by separating the *WCBBL* in an upper and a lower portion, and requiring continuity of the eddy diffusivities at the top of the boundary layer. Such an approach was adopted by Styles and Glenn [2000, 2002] that separated the overall *BBL* into a 3-layer region (the current portion of the *BBL* layer plus an upper and a lower portion in the *WCBBL*).

Although the Styles and Glenn model represents better the physical processes in the bottom layer, it is still computationally more expensive than the original *GG87* model. Another point that is somewhat troubling is the sensitivity of the Styles and Glenn model to the height $z_1 = \alpha \mathbf{k} u_* / \omega$ of the lower layer in the *WCBBL* (see Figure 6 in Styles and Glenn [2000]), where ω is the wave angular frequency and α is a constant to be determined. The sensitivity of the model to the values of the constant α makes calibration necessary to ensure that a proper value for this parameter is being used. Due to *CPU* time considerations, especially whenever the implementation requires an increased number of sediment classes, as well as to uncertainty in the estimation of the constant α, the Styles and Glenn model is not used in M^2*COPS*.

The modifications/enhancements and corrections to the original *GG87* model during the course of the present study are addressed in the Sections that follow.

6.2 Model Physics and Dynamics

The *WCBBL* model describes the effects of the wind driven surface wave oscillations on the bottom boundary layer. The presence of the surface waves introduces an oscillatory wave boundary layer at the bottom nested within the current boundary layer (*CBL*), with a length scale much smaller than the length scale of the *CBL* that has a thickness limited by either the water depth or the Ekman layer height $\delta_E = \mathbf{k} u_* / f$. The near-bottom flow field is resolved in the *WCBBL* model by approximating the vertical structure of the wave/current velocities and the sediment concentration over a movable sediment bed under the non-linear interaction of the currents and waves. Furthermore, the model enhances the previous *WCBBL* models (*GM79*, *GM82* and *GM86*) by considering

the effects of the ripple formation/degradation and the sediment induced stratification. These are crucial parameters affecting the bottom shear stresses and the resulting vertical structures of the predicted variables.

The model equations are derived assuming slow varying, low frequency currents interacting with short-period high frequency surface waves. The current is mathematically described by the temporally averaged flow velocities, having time scales much greater than the time scales of the waves. The wave velocities are derived from the phase averaged equations of motion, assuming that the flow variables can be partitioned in three components: an average, a periodic and a turbulent component.

The near-bottom velocity profile is assumed to be logarithmic and associated with the turbulent diffusion of the momentum. Above the *WCBBL*, the turbulent diffusion is associated with the enhanced by the waves currents while in the *WCBBL* the turbulent diffusion is associated with the combined effects of the currents and the waves. The increased turbulent momentum diffusion in the *WCBBL* reduces the current velocities, resulting in wave velocities that dominate in this region. Therefore, the observed significant increase of the bottom shear stresses is attributed to the waves. The effect of the increased bottom stresses is also felt in the region above the *WCBBL*, where the shear stresses due to the current are also enhanced.

The shear stresses in the rough turbulent flow of the *WCBBL* depend upon the bottom physical roughness, while the enhanced currents above the *WCBBL* are related to an enhanced bottom roughness (apparent roughness), which is a function of the bottom physical roughness and characteristics of the *WCBBL*. The issue that two different physical processes (currents and waves) are using a common physical bottom roughness was addressed in a series of papers by Mathisen and Madsen [1996a,b, 1999]. The authors, during an experimental study at the Ralph M. Parsons Laboratory at the Massachusetts Institute of Technology, concluded that a single bottom physical roughness height can be used to characterize pure currents, pure waves and eventually both currents and waves in combined wave-current induced flows. Since the single physical roughness assumption is considered as being verified, the results of Mathisen and Madsen are adopted here as well.

In the present study, the *WCBBL* model is coupled with and driven by the spectral wave models, thus invalidating the assumption of monochromatic waves used in the *GG87* model. This issue was addressed in the third of the previously mentioned series of papers (Mathisen and Madsen [1999])

that presented the results of experiments designed to verify the use of a common bottom physical roughness for waves (spectral and monochromatic) and currents over a rough sediment bottom. The spectral waves in the experiment were simulated using a discrete wave spectrum of five components, while the currents were generated in a 20 m long wave flume with a fixed rippled bottom. The authors matched the *GM86* predicted velocity profiles with the measured velocity profiles for both spectral waves and currents, provided that the modified boundary layer thickness δ_{cw} is used instead of the δ_w defined in *GG87*. The analytical expression for δ_{cw} is taken from Madsen and Salles [1999] and will be discussed in the following Sections. The results of the above work have been adopted in the M^2*COPS* version of the *WCBBL* model that implements this modified boundary layer thickness in place of the definition given in *GG87*.

The traveling surface waves introduce additional momentum on the water column that is transported by the currents as an added radiation stress term in the momentum equations. As seen from Figures 5.2 and 5.3 for shallow waters, these radiation stress terms are not nil near the bottom but can be rather large thus affecting both the near-bottom currents and the sediments being transported. As it will be shown shortly, the effect of the radiation stresses is felt through an increase of the bottom shear stresses that enhances both the near-bottom currents and the entrained bottom sediments. In deeper waters (Figures 5.2 and 5.3) the bottom radiation stresses are almost nil, as they rapidly decay with water depth and have a minimal effect in the near-bottom region.

Most of the entrainment of the bottom sediments takes place in the near-shore zone, where they are picked up by the currents to be transported off-shore. It is, therefore, apparent that the radiation stress terms need to be included in the *WCBBL* model as well, thus completing the full implementation of the radiation stresses into M^2*COPS*. To be consistent with the rest of the hydrodynamic model, the atmospheric pressure forcing is not neglected in the present *WCBBL* formulation, but rather the bottom pressure gradients are retained in the *WCBBL* momentum equations.

6.3 Boundary Layer Equations

The equations governing the near bottom flow and sediment transport are derived in this Section using the 3D Reynolds averaged continuity, momentum and scalar transport equations. The sediment volumetric concentration is assumed to be small, less than 0.003 ($\sim 8\,\mathrm{kg/m^3} = 8000\,\mathrm{mg/L}$), such that there is no interaction among the sediment particles (Lumley [1976]). In anticipation of solutions for rough turbulent flows, the second order molecular viscous and diffusion terms appearing

in the momentum and scalar transport equations, respectively, are neglected. The equations derived in this Section for the bottom shear stresses include both the effects due to wave growth (radiation stresses) and to wave interactions with the bottom sediments. They also include the contributions of surface barotropic variations during the passage of storms over the calculation domain.

Definition of the coordinate systems used in the derivation of the bottom boundary layer equations and their relation to each other is shown in Figure 6.2 and in equations 6.3.1.

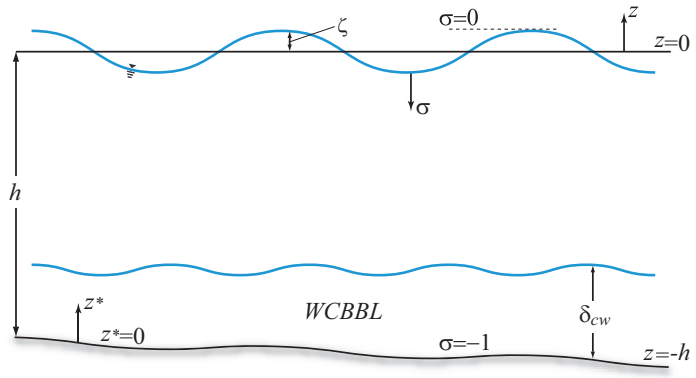

Figure 6.2 Definition of the coordinate system for the bottom boundary layer.

$$D = h + \zeta \; ; \quad \sigma = \frac{z - \zeta}{D} \; ; \quad z^* = (1 + \sigma) D = z + h \; : \begin{cases} z = \zeta & \rightarrow \quad z^* = D \; ; \quad \sigma = 0 \\ z = -h & \rightarrow \quad z^* = 0 \; ; \quad \sigma = -1 \end{cases} \tag{6.3.1}$$

The boundary layer equations are derived from the full equations 4.10.31 and 4.10.33 using the following scaling arguments: *(a)* the average variables are slow varying, quasi-steady ($\partial/\partial t \approx 0$ during Δt) and horizontally homogeneous, *(b)* the convective acceleration terms are neglected, assuming that the current and the wave velocities are much smaller than the wave phase speed, and *(c)* the horizontal gradients of the Reynolds stresses can be neglected compared to the vertical gradients. The last assumption is based on the observation that the length scale δ_{cw} of the boundary layer is much less than the horizontal length scales so that, $\partial/\partial x$; $\partial^2/\partial x^2 \sim O(1)$ and $\partial/\partial z \sim O(\delta_{cw}^{-1})$; $\partial^2/\partial z^2 \sim O(\delta_{cw}^{-2})$.

Regarding the sediment transport equation, the horizontal sediment particle velocities are assumed equal to the flow velocities, while the vertical velocity is replaced by $w - w_{sn}$ where, w_{sn} is

the settling velocity corresponding to the "n-th" sediment particle size. For the derivation of the sediment transport equation, it is also assumed that there is no interaction between the scalar quantity C_n and the waves (Mellor [2003]).

Applying the boundary layer approximation $\mathrm{Z_r} \ll \mathrm{X_r}$, for $\mathbb{R}_\mathrm{o} \ll 1$ equation 4.10.31 gives:

$$\frac{\partial u_\alpha}{\partial t} = -\epsilon_{\alpha 3\beta}\frac{f_3}{f}(u_\beta + \mathrm{u_{st\beta}}) - \frac{\partial p_{\mathrm{atm}}}{\partial x_\alpha} - \frac{\partial \zeta}{\partial x_\alpha} + \mathbb{E}_{\mathrm{lv}}\frac{\partial}{\partial z}\left[\mathcal{A}_\mathrm{v}\frac{\partial(u_\alpha + \mathrm{u_{st\alpha}})}{\partial z}\right]$$

$$-\frac{\mathbb{F}_\mathrm{r}^2}{\mathbb{R}_\mathrm{o}}\frac{1}{D}\frac{\partial S_{\alpha\beta}}{\partial x_\beta} - \left(\frac{\mathbb{F}_\mathrm{r}^2}{\mathbb{R}_\mathrm{o}}\right)^2\left\{\frac{1}{D}\left[\frac{\partial \zeta}{\partial x_\beta} + \frac{\left(\frac{\mathbb{R}_\mathrm{o}}{\mathbb{F}_\mathrm{r}^2}\right)z - \zeta}{D}\frac{\partial D}{\partial x_\beta}\right]\frac{\partial S_{\alpha\beta}}{\partial z}\right\} \tag{6.3.2}$$

The calculations that follow assume that not only the current velocity is quasi-steady but the Coriolis effects are minimal within the boundary layer as well. Therefore equation 6.3.2 is reduced to:

$$0 = \underbrace{-\frac{\partial p_{\mathrm{atm}}}{\partial x_\alpha} - \frac{\partial \zeta}{\partial x_\alpha}}_{(1)} + \underbrace{\mathbb{E}_{\mathrm{lv}}\frac{\partial}{\partial z}\left[\mathcal{A}_\mathrm{v}\frac{\partial(u_\alpha + \mathrm{u_{st\alpha}})}{\partial z}\right]}_{(2)}$$

$$\underbrace{-\frac{\mathbb{F}_\mathrm{r}^2}{\mathbb{R}_\mathrm{o}}\frac{1}{D}\frac{\partial S_{\alpha\beta}}{\partial x_\beta}}_{(3)} \underbrace{-\left(\frac{\mathbb{F}_\mathrm{r}^2}{\mathbb{R}_\mathrm{o}}\right)^2\left\{\frac{1}{D}\left[\frac{\partial \zeta}{\partial x_\beta} + \frac{(\frac{\mathbb{R}_\mathrm{o}}{\mathbb{F}_\mathrm{r}^2})z - \zeta}{D}\frac{\partial D}{\partial x_\beta}\right]\frac{\partial S_{\alpha\beta}}{\partial z}\right\}}_{(4)} \tag{6.3.3}$$

where terms (1) are the barotropic terms that are retained in equation 6.3.3 to account for the significant variations in the atmospheric pressure during storm events, as done in the hydrodynamic model.

Term (2) represents the vertical gradient of the Reynolds turbulent fluxes that have been enhanced to account for the dissipation of the wave energy due to viscous wave energy losses near the free surface and the energy losses in the water column caused by the interactions of the waves with the mean flow. The energy lost by the waves in the water column is gained by the mean flow field as a wave induced turbulent kinetic energy and it is parametrized as in term (2) of equation 6.3.3.

A close inspection of equation 6.3.3 shows that $\mathbb{E}_{\mathrm{lv}}$ is of order $O(\mathrm{Z_r^{-2}})$, while $\frac{\mathbb{F}_\mathrm{r}^2}{\mathbb{R}_\mathrm{o}} \approx O(\mathrm{Z_r^{-1}})$ and $\left(\frac{\mathbb{F}_\mathrm{r}^2}{\mathbb{R}_\mathrm{o}}\right)^2 \approx O(\mathrm{Z_r^{-2}})$. It is, therefore, clear that the main wave induced momentum contributions to the Reynolds fluxes come from term (4), while term (3) is a first order $O(\mathrm{Z_r})$ contributor to term (2). Term (4) represents the vertical momentum flux due to $S_{\alpha\beta}$ through the horizontal "z" planes.

This portion of the wave induced momentum flux becomes apparent when the equation is written in "z" coordinates, while in "σ" coordinates this vertical flux is lumped into the corresponding term (3). In the subsequent calculations all terms in equation 6.3.3 are retained. The dimensional form of equation 6.3.3 is:

$$\frac{\partial}{\partial z}\left\{\mathcal{A}_{\mathrm{v}}\frac{\partial(u_\alpha+\mathrm{u}_{\mathrm{st}\alpha})}{\partial z}\right\}=\frac{1}{\rho_{\mathrm{o}}}\frac{\partial p_{\mathrm{atm}}}{\partial x_\alpha}+g\frac{\partial \zeta}{\partial x_\alpha}+\frac{1}{D}\frac{\partial S_{\alpha\beta}}{\partial x_\beta}+\frac{1}{D}\left\{\frac{\partial \zeta}{\partial x_\beta}+\frac{z-\zeta}{D}\frac{\partial D}{\partial x_\beta}\right\}\frac{\partial S_{\alpha\beta}}{\partial z} \tag{6.3.4}$$

and the corresponding form of the equation in "σ" coordinates is

$$\frac{\partial}{\partial \sigma}\left\{\mathcal{A}_{\mathrm{v}}\frac{\partial(u_\alpha+\mathrm{u}_{\mathrm{st}\alpha})}{\partial \sigma}\right\}=\frac{D^2}{\rho_{\mathrm{o}}}\frac{\partial p_{\mathrm{atm}}}{\partial x_\alpha}+gD^2\frac{\partial \zeta}{\partial x_\alpha}+D\frac{\partial S_{\alpha\beta}}{\partial x_\beta} \tag{6.3.5}$$

which has a much simpler form than equation 6.3.4. Consequently, calculations that follow are performed in "σ" coordinates using equation 6.3.5.

Using the non-dimensional equation for the scalar transport derived in equation 4.10.33 and replacing Φ by C_n which represents the mean sediment concentration for sediment class size n, and $w-\mathrm{w}_{\mathrm{st}}$ by $w-\mathrm{w}_{\mathrm{st}}-w_{sn}$ where w_{sn} represents the particle settling velocity and w_{st} the Stokes vertical pseudo velocity, the following is obtained:

$$\frac{\partial C_n}{\partial t}+\mathbb{R}_{\mathrm{o}}\left[\frac{\partial(u_\alpha C_n)}{\partial x_\alpha}+\frac{\partial[(w-\mathrm{w}_{\mathrm{st}})C_n]}{\partial z}\right]-\mathbb{R}_{\mathrm{op}}\frac{\partial(w_{sn}C_n)}{\partial z}=$$

$$\frac{\mathbb{E}_{\mathrm{kh}}}{\mathbb{S}_{\mathrm{ch}}}\frac{\partial}{\partial x_\alpha}\left[\mathcal{D}_{\mathrm{h}}\frac{\partial C_n}{\partial x_\alpha}\right]+\frac{\mathbb{E}_{\mathrm{kv}}}{\mathbb{S}_{\mathrm{cv}}}\frac{\partial}{\partial z}\left[\mathcal{D}_{\mathrm{v}}\frac{\partial C_n}{\partial z}\right]-\mathbb{R}_{\mathrm{o}}\left[\mathrm{u}_{\mathrm{st}\alpha}\frac{\partial C_n}{\partial x_\alpha}+\mathrm{w}_{\mathrm{st}}\frac{\partial C_n}{\partial z}\right] \tag{6.3.6}$$

Assuming a small $\mathbb{R}_{\mathrm{o}}$, a quasi-steady variation of the mean sediment concentration C_n and applying the boundary layer approximation, equation 6.3.6 reduces to:

$$-\mathbb{R}_{\mathrm{op}}\frac{\partial(w_{sn}C_n)}{\partial z}=\frac{\mathbb{E}_{\mathrm{kv}}}{\mathbb{S}_{\mathrm{cv}}}\frac{\partial}{\partial z}\left[\mathcal{D}_{\mathrm{v}}\frac{\partial C_n}{\partial z}\right] \tag{6.3.7}$$

Here $\mathbb{R}_{\mathrm{op}}$ is the particle Rossby number defined as: $\mathbb{R}_{\mathrm{op}}=\dfrac{w_{sn}}{f\mathrm{Z}_{\mathrm{r}}}$. Equation 6.3.7 in dimensional form is written as:

$$-\frac{\partial(w_{sn}C_n)}{\partial z}=\frac{\partial}{\partial z}\left[\mathcal{D}_{\mathrm{v}}\frac{\partial C_n}{\partial z}\right] \tag{6.3.8}$$

and in "σ" coordinates:

$$-\frac{\partial(w_{sn}C_n)}{\partial \sigma}=\frac{1}{D}\frac{\partial}{\partial \sigma}\left[\mathcal{D}_{\mathrm{v}}\frac{\partial C_n}{\partial \sigma}\right] \tag{6.3.9}$$

6.4 Parametrization of the Reynolds Stresses

The Reynolds stresses and turbulent sediment fluxes that appear in equations 6.3.2 and 6.3.6 are related to the mean flow variables via the eddy viscosity concept (Chapter 7). The usual eddy viscosity formulations are enhanced, as described in Glenn [1987], Glenn and Grant [1987] to include the effects of sediment stratification. By analogy to the stable thermal stratification approach in the atmospheric boundary layer (*ABL*), the vertical Reynolds turbulent stresses and mass fluxes are parametrized using the following equations:

$$-\overline{w'u'} = \mathcal{A}_v \frac{\partial u}{\partial z} \; ; \qquad -\overline{w'v'} = \mathcal{A}_v \frac{\partial v}{\partial z} \; ; \qquad -\overline{w'C_n'} = \mathcal{D}_v \frac{\partial C_n}{\partial z} \tag{6.4.1}$$

here $\mathcal{A}_v$ (m^2/s) is the eddy viscosity and $\mathcal{D}_v$ (m^2/s) is the eddy mass diffusivity, which are related to their neutral counterparts $\mathcal{A}_{nv}$ and $\mathcal{D}_{nv}$, respectively, by the following expressions (Glenn and Grant [1987]):

$$\mathcal{A}_v = \frac{\mathcal{A}_{nv}}{1 + \beta \dfrac{z^*}{L}} \qquad \text{and} \qquad \mathcal{D}_v = \frac{\mathcal{D}_{nv}}{\gamma + \beta \dfrac{z^*}{L}} \tag{6.4.2}$$

where the coefficients β and γ, given in Businger et al. [1971], are equal to: $\beta = 4.7$ and $\gamma = 0.74$.

The parameter L is the well known Monin-Obukhov length, which is a function of the vertical coordinate and the term z^*/L is the so called stability parameter. The neutral eddy viscosities/diffusivities are assumed to be a linear functions of the depth, thus:

$$\mathcal{A}_{nv} = \mathcal{D}_{nv} = \mathbf{k} u_* z^* \qquad \text{with:} \qquad u_*^2 = \frac{\tau_b}{\rho_o} \tag{6.4.3}$$

The symbols τ_b and u_* represent the shear stress and the shear velocity at the bottom boundary and $\mathbf{k} = 0.4$ is the von Kármán's constant.

6.5 Solution for the Current

Because of the different definitions used for $\mathcal{A}_v$ outside and inside the *WCBBL*, at the top of the *WCBBL* equation 6.3.5 has two solutions. The continuity of the solution at $\sigma = -1 + \delta_{cw}/D$ requires that the following conditions hold:

$$u_\alpha^+ + u_{st\alpha}^+ = u_\alpha^- + u_{st\alpha}^- \; ; \qquad \mathcal{A}_v^+ \frac{\partial (u_\alpha^+ + u_{st\alpha}^+)}{\partial \sigma} = \mathcal{A}_v^- \frac{\partial (u_\alpha^- + u_{st\alpha}^-)}{\partial \sigma} \tag{6.5.1}$$

where: u_α^+, $u_{st\alpha}^+$ and $\mathcal{A}_v^+$ are the Eulerian velocity, the Stokes drift and the turbulent diffusion coefficient, respectively, outside the *WCBBL*. The corresponding variables inside the *WCBBL* are denoted as u_α^-, $u_{st\alpha}^-$ and $\mathcal{A}_v^-$.

Inside the *WCBBL* ($\sigma \leq -1 + \delta_{cw}/D$) the integration of equation 6.3.5 gives:

$$\mathcal{A}_v \frac{\partial(u_\alpha + u_{st\alpha})}{\partial\sigma} = C_1 + (1 + \sigma - \frac{z_o}{D})\left\{\frac{D^2}{\rho_o}\frac{\partial p_{atm}}{\partial x_\alpha} + gD^2\frac{\partial\zeta}{\partial x_\alpha}\right\} + D\int_{-1+\frac{z_o}{D}}^{\sigma}\frac{\partial S_{\alpha\beta}}{\partial x_\beta}d\sigma \tag{6.5.2}$$

where C_1 is the constant of integration of the term in the l.h.s of equation 6.5.2 and z_o is the bottom roughness. Integration of equation 6.3.5 for the region outside the *WCBBL* ($\sigma \geq -1 + \delta_{cw}/D$) gives:

$$\mathcal{A}_v \frac{\partial(u_\alpha + u_{st\alpha})}{\partial\sigma} = C_2 + (1 + \sigma - \frac{\delta_{cw}}{D})\left\{\frac{D^2}{\rho_o}\frac{\partial p_{atm}}{\partial x_\alpha} + gD^2\frac{\partial\zeta}{\partial x_\alpha}\right\} + D\int_{-1+\frac{\delta_{cw}}{D}}^{\sigma}\frac{\partial S_{\alpha\beta}}{\partial x_\beta}d\sigma \tag{6.5.3}$$

The constant of integration C_2 can be determined as a function of C_1 by using the condition expressed by the second of equations 6.5.1 at $\sigma = -1 + \delta_{cw}/D$:

$$C_2 = C_1 + \left(\frac{\delta_{cw} - z_o}{D}\right)\left\{\frac{D^2}{\rho_o}\frac{\partial p_{atm}}{\partial x_\alpha} + gD^2\frac{\partial\zeta}{\partial x_\alpha}\right\} + D\int_{-1+\frac{z_o}{D}}^{-1+\frac{\delta_{cw}}{D}}\frac{\partial S_{\alpha\beta}}{\partial x_\beta}d\sigma \tag{6.5.4}$$

Considering the slight variations of $S_{\alpha\beta}$ within the *WCBBL* (Figure 5.3), the last term in equation 6.5.4 can be approximated as follows:

$$D\int_{-1+\frac{z_o}{D}}^{-1+\frac{\delta_{cw}}{D}}\frac{\partial S_{\alpha\beta}}{\partial x_\beta}d\sigma \approx (\delta_{cw} - z_o)\left.\frac{\partial S_{\alpha\beta}}{\partial x_\beta}\right|_{\sigma=-1} \tag{6.5.5}$$

and, finally, equation 6.5.4 takes the form:

$$C_2 = C_1 + \left(\delta_{cw} - z_o\right)\left\{\underbrace{\frac{D}{\rho_o}\frac{\partial p_{atm}}{\partial x_\alpha} + gD\frac{\partial\zeta}{\partial x_\alpha}}_{(1)} + \underbrace{\left.\frac{\partial S_{\alpha\beta}}{\partial x_\beta}\right|_{\sigma=-1}}_{(2)}\right\} \tag{6.5.6}$$

Term (1) in equation 6.5.6 represents the barotropic effects on the bottom shear stress, while term (2) represents the enhancement of the bottom shear stresses due to the wave growth. Furthermore, term (2) has no relation to wave induced turbulence in the *WCBBL* by the interactions of waves with the bottom sediments.

It is noted that:

$$C_1 = \mathcal{A}_v\left.\frac{\partial(u_\alpha + u_{st\alpha})}{\partial\sigma}\right|_{\sigma=-1} = \mathcal{A}_v\left.\frac{\partial u_\alpha}{\partial\sigma}\right|_{\sigma=-1} \quad \text{since} \quad \mathcal{A}_v\left.\frac{\partial u_{st\alpha}}{\partial\sigma}\right|_{\sigma=-1} = 0 \tag{6.5.7}$$

with the definition:

$$\mathcal{A}_v \frac{\partial u_\alpha}{\partial \sigma}\bigg|_{\sigma=-1} = D\frac{\tau_{b\alpha}}{\rho_o} \tag{6.5.8}$$

where $\tau_{b\alpha}$ is the α-th component of the bottom shear stress due to currents only. Because of equation 6.5.8, equation 6.5.6 is written as:

$$C_2 = D\left\{\frac{\tau_{b\alpha}}{\rho_o} + \frac{\delta_{cw} - z_o}{D}\left(\frac{D}{\rho_o}\frac{\partial p_{atm}}{\partial x_\alpha} + gD\frac{\partial \zeta}{\partial x_\alpha} + \frac{\partial S_{\alpha\beta}}{\partial x_\beta}\bigg|_{\sigma=-1}\right)\right\} \tag{6.5.9}$$

with a conceptual representation:

$$C_2 = D\tilde{\tau}_{bc\alpha} = D\left(\tau_{bc\alpha} + \tau_{bp\alpha} + \tau_{bs\alpha}\right) \qquad (\sigma \text{ coordinates}) \tag{6.5.10}$$

such that:

$$|\tilde{\tau}_{bc}|^2 = (\tau_{bc\alpha} + \tau_{bp\alpha} + \tau_{bs\alpha})(\tau_{bc\alpha} + \tau_{bp\alpha} + \tau_{bs\alpha}) \tag{6.5.11a}$$

$$\tau_{bc\alpha} = \frac{\tau_{b\alpha}}{\rho_o} \tag{6.5.11b}$$

$$\tau_{bp\alpha} = \frac{\delta_{cw} - z_o}{D}\left(\frac{D}{\rho_o}\frac{\partial p_{atm}}{\partial x_\alpha} + gD\frac{\partial \zeta}{\partial x_\alpha}\right) \tag{6.5.11c}$$

$$\tau_{bs\alpha} = \frac{\delta_{cw} - z_o}{D}\frac{\partial S_{\alpha\beta}}{\partial x_\beta}\bigg|_{\sigma=-1} \tag{6.5.11d}$$

Here $\tau_{bc\alpha}$ is the kinematic stress term describing the portion of the bottom shear stress due to currents only, $\tau_{bp\alpha}$ is the kinematic stress term describing the portion of the bottom shear stress due to the surface barotropic variations and $\tau_{bs\alpha}$ is the kinematic stress term describing the portion of the bottom shear stress due to the wave induced momentum by the wind generated surface waves.

Again, this last term represents only the effects due to the wave growth that introduce an extra momentum flux into the system and it is not related to the turbulence production by the interactions between the waves and the bottom sediments that take place in the *WCBBL*. With the information supplied so far, the two equations that describe the vertical distribution of the Lagrangian velocity $u_\alpha + u_{st\alpha}$ are:

$$\mathcal{A}_v \frac{\partial(u_\alpha + u_{st\alpha})}{\partial \sigma} = C_2 + (1 + \sigma - \frac{\delta_{cw}}{D})\left\{\frac{D^2}{\rho_o}\frac{\partial p_{atm}}{\partial x_\alpha} + gD^2\frac{\partial \zeta}{\partial x_\alpha}\right\} + D\int_{-1+\frac{\delta_{cw}}{D}}^{\sigma}\frac{\partial S_{\alpha\beta}}{\partial x_\beta}d\sigma; \tag{6.5.12}$$

$$(\sigma \le -1 + \frac{\delta_{cw}}{D})$$

and:

$$\mathcal{A}_v \frac{\partial(u_\alpha + u_{st\alpha})}{\partial\sigma} = C_2 + (1 + \sigma - \frac{\delta_{cw}}{D})\left\{\frac{D^2}{\rho_o}\frac{\partial p_{atm}}{\partial x_\alpha} + gD^2\frac{\partial\zeta}{\partial x_\alpha}\right\} + D\int_{-1+\frac{\delta_{cw}}{D}}^{\sigma}\frac{\partial S_{\alpha\beta}}{\partial x_\beta}\,d\sigma; \qquad (6.5.13)$$

$$(\sigma \geq -1 + \frac{\delta_{cw}}{D})$$

From equations 6.5.12 and 6.5.13 it is clear that the formulation of the two equations is identical. Differences arise in: *(a)* the range of σ, and *(b)* the $\mathcal{A}_v$, which is defined slightly differently in the two regions of the *WCBBL*. C_2 in equation 6.5.13 is the shear stress that the Lagrangian current above the *WCBBL* feels. It is also the current shear stress that is enhanced by the production of turbulence due to wave-sediment interactions within the *WCBBL*.

6.5.1 Velocity Distribution

Assuming that the diffusion coefficient $\mathcal{A}_v$ varies linearly with respect to the vertical coordinate, a close inspection of equation 6.5.12 shows that the terms to the right of term C_2 can be lumped into $\mathcal{A}_v$ by slightly redefining $\mathcal{A}_v$. This approach reduces equation 6.5.12 to:

$$\mathcal{A}_v \frac{\partial(u_\alpha + u_{st\alpha})}{\partial\sigma} = C_2\ ; \quad (\sigma \leq -1 + \frac{\delta_{cw}}{D}) \qquad (6.5.14)$$

and recasts *WCBBL* region as a constant stress region. This re-formulation implies a modification in the value of z_o (as it is done in Glenn and Grant [1987]), as well as the re-definition of the bottom shear stresses. Another approach is to use an effective or displacement height z_e, as it is done for the wave induced surface stresses. From equation 6.5.14:

$$\lim_{\sigma+1\to\frac{z_o}{D}}\left[\mathcal{A}_v\frac{\partial(u_\alpha + u_{st\alpha})}{\partial\sigma}\right] \approx \lim_{\sigma+1\to\frac{\delta_{cw}}{D}}\left[\mathcal{A}_v\frac{\partial(u_\alpha + u_{st\alpha})}{\partial\sigma}\right] = \mathcal{A}_v\frac{\partial(u_\alpha + u_{st\alpha})}{\partial\sigma}\bigg|_{\sigma=-1} = C_2 \qquad (6.5.15)$$

The second of equations 6.5.15 satisfies the condition described by the second of equations 6.5.1, while the first and the last equations in 6.5.15 define the bottom shear stresses as they are affected by the barometric and wave growth effects. As has been shown (equations 6.5.12 and 6.5.13) the same vertical distribution for $\mathcal{A}_v\,\partial(u_\alpha + u_{st\alpha})/\partial\sigma$ is valid for the regions inside and outside the *WCBBL*, as long as the logarithmic layer assumption holds (usually confined by the extent of the bottom Ekman layer $\delta_E \approx 0.4(u_*/f)$, or in the case of shallow-water flows by the water depth).

The logarithmic portion of the *BBL* is defined as $\delta_l = 0.1\delta_E$, while the thickness of the constant stress layer for current only induced flows (δ_c) is defined in equation 6.6.15 and the thickness of the wave-current *WCBBL* (δ_{cw}) is defined in equation 6.7.14. Recasting equation 6.5.13 such that the second of equations 6.5.15 holds everywhere outside the *WCBBL* we have:

$$\mathcal{A}_\mathrm{v}\frac{\partial(u_\alpha + \mathrm{u_{st\alpha}})}{\partial\sigma} = C_2 \; ; \quad (\sigma \geq -1 + \frac{\delta_{cw}}{D}) \tag{6.5.16}$$

The differences between equations 6.5.12 and 6.5.14 and 6.5.13 and 6.5.16 have been absorbed in the definition of $\mathcal{A}_\mathrm{v}$ for the regions inside and outside the *WCBBL*. Finally, assuming that the bottom kinematic shear stress C_2 and the Lagrangian velocity $\mathcal{u}$ are co-directional, the two equations for $\mathcal{u}$ inside and outside the *WCBBL* are:

$$\mathcal{A}_\mathrm{v}\frac{\partial|\mathcal{u}_\mathbf{h}|}{\partial\sigma} = |C_2| \; ; \quad (\sigma \leq -1 + \frac{\delta_{cw}}{D}) \tag{6.5.17}$$

$$\mathcal{A}_\mathrm{v}\frac{\partial|\mathcal{u}_\mathbf{h}|}{\partial\sigma} = |C_2| \; ; \quad (\sigma \geq -1 + \frac{\delta_{cw}}{D}) \tag{6.5.18}$$

where $\mathcal{A}_\mathrm{v}$ is defined differently inside and outside the *WCBBL*, $\mathcal{u}_\mathbf{h}$ is the horizontal vector of the Lagrangian velocity defined as $|\mathcal{u}_\mathbf{h}|^2 = \mathcal{u}^2 + \mathcal{v}^2$ and $|C_2|$ is the total bottom kinematic shear stress defined in σ coordinates as:

$$|C_2|^2 = D\,\tilde{\tau}_{bc\alpha}\tilde{\tau}_{bc\alpha} \tag{6.5.19}$$

with:

$$\tilde{\tau}_{bc\alpha} = \tau_{bc\alpha} + \frac{\delta_{cw} - z_\mathrm{o}}{D}\left[\frac{D}{\rho_\mathrm{o}}\frac{\partial p_\mathrm{atm}}{\partial x_\alpha} + gD\frac{\partial\zeta}{\partial x_\alpha}\right] + \frac{\delta_{cw} - z_\mathrm{o}}{D}\frac{\partial S_{\alpha\beta}}{\partial x_\beta}\bigg|_{\sigma=-1} \tag{6.5.20}$$

6.6 Bottom Roughness

The roughness height z_o introduced in equation 6.5.9 is actually an integration constant, defining the height where the current velocity appears to be equal to zero. The roughness height z_o as a function of the physical bottom roughness k_b is given by equation 2.8.1. Since C_2 is the kinematic total bottom shear stress, it can be written using the concept of the bottom friction velocity as:

$$|C_2| = Du_*^2 \qquad (\sigma \text{ coordinates}) \tag{6.6.1}$$

Assuming that $\mathcal{A}_\mathrm{v}$ varies linearly in the vertical direction, the following two expressions are considered here in σ coordinates:

$$\mathcal{A}_\mathrm{v} = \mathbf{k}u_*(1+\sigma)D \; ; \qquad \mathcal{A}_\mathrm{v} = \mathbf{k}u_*(1+\sigma+\sigma_e-\sigma_o)D \tag{6.6.2}$$

The second of equations 6.6.2 considers the concept of the effective roughness (z_e) as introduced by Janssen [2004] to account for the wave induced effects in the surface shear stresses. In z coordinates the above two equations are written as:

$$\mathcal{A}_v = \mathbf{k}u_*(z+h)\ ; \qquad \mathcal{A}_v = \mathbf{k}u_*(z+h+z_e-z_o) \tag{6.6.3}$$

Modifications to z_o

Introduction of equation 6.6.1 and the first of equations 6.6.2 into equation 6.5.17 and integration of the resulting equation produces:

$$|\boldsymbol{u}_\mathbf{h}| = \frac{u_*}{\mathbf{k}} \ln \frac{(1+\sigma)D}{z_o} \tag{6.6.4}$$

where $\mathbf{k} = 0.4$ is the von Karman's constant. Retaining the Stokes drift and in the absence of the barotropic and wave induced stress terms:

$$|\boldsymbol{u}_\mathbf{h}| = \frac{u_*}{\mathbf{k}} \ln \frac{(1+\sigma)D}{z_o}\ ; \qquad |\boldsymbol{u}_\mathbf{h}| = \frac{u'_*}{\mathbf{k}} \ln \frac{(1+\sigma)D}{z'_o} \tag{6.6.5}$$

where the first of equations 6.6.5 implies that $u(z_o) = 0$ and the second that $u(z'_o) = 0$. Matching the velocity $\boldsymbol{u}$ at the top of the constant stress layer ($\sigma = -1 + \delta_{cw}/D$) yields:

$$z'_o = z_o\Big(\frac{\delta_{cw}}{z_o}\Big)^{1-\epsilon_1}\ ; \qquad \epsilon_1 = \frac{u_*}{u'_*} \tag{6.6.6}$$

From equation 6.6.6 when $\epsilon_1 > 1 \Rightarrow z_o{}' < z_o$ and when $\epsilon_1 < 1 \Rightarrow z_o{}' > z_o$. As is the usual practice, z_o is expressed in terms of the physical bottom roughness k_b, therefore, z'_o can be expressed as a function of a modified physical bottom roughness k'_b. In this formulation and in the presence of pressure/radiation stress terms, all equations should use z'_o instead of z_o.

Effective roughness z_e

The diffusion coefficient in this case is assumed to follow the second of equations 6.6.2, where z_e is the effective roughness height according to Janssen. The Lagrangian velocity $\boldsymbol{u}$ still goes to zero at $z = z_o$ above the bottom instead of z'_o. Introducing equation 6.6.1 and the second of equations 6.6.2 into equation 6.5.17 we obtain:

$$\frac{\partial|\boldsymbol{u}_\mathbf{h}|}{\partial\sigma} = \frac{u'_*}{\mathbf{k}} \frac{1}{1+\sigma+\sigma_e-\sigma_o} \tag{6.6.7}$$

In equation 6.6.7 u_* has been replaced by u'_* to reflect the wave enhanced bottom shear stresses. Now, the integration of equation 6.6.7 gives:

$$\int_{-1+\frac{z_o}{D}}^{\sigma} \frac{\partial|\boldsymbol{u}_\mathbf{h}|}{\partial\sigma}\,d\sigma = \frac{u'_*}{\mathbf{k}} \int_{-1+\frac{z_o}{D}}^{\sigma} \frac{d\sigma}{1+\sigma+\sigma_e-\sigma_o} \Longrightarrow |\boldsymbol{u}_\mathbf{h}| = \frac{u'_*}{\mathbf{k}} \ln \frac{(1+\sigma)D+z_e-z_o}{z_e} \tag{6.6.8}$$

where z_e, z_o are distances above the bottom and $u(z_o) = 0$. Rearranging gives:

$$\frac{u'_*}{\mathbf{k}} \ln \frac{(1+\sigma)D + z_e - z_o}{z_e} = \frac{u_*}{\mathbf{k}} \ln \frac{(1+\sigma)D}{z_o} \Longrightarrow \frac{z_o}{z_e} \approx \frac{\ln \dfrac{(1+\sigma)D + z_e - z_o}{z_e}}{\ln \dfrac{(1+\sigma)D}{z_o}} = \frac{u_*}{u'_*} = \epsilon_1 \qquad (6.6.9)$$

Near the bottom, equation 6.6.9 reduces to:

$$z_e = \frac{z_o}{\epsilon_1} = \frac{z_o}{\left(\dfrac{\tau_{bc}}{\tilde{\tau}_{bc}}\right)^{1/2}} \qquad (6.6.10)$$

and z_e has a form similar to what the displacement height z_e assumes at the free surface (see equation 2.5.2) to account for the effects of the surface waves on the wind (Janssen [2004]). Through the calculation of the auxiliary effective roughness z_e (usually an iterative process since δ_{cw} is not known a priori), the additional wave terms are introduced in the bottom shear stresses (equations 6.6.8 and 6.6.9).

Relationship between z'_o and z_e

For the velocity at the top of the boundary layer the second of equations 6.6.5 gives:

$$u\Big|_{-1+\frac{\delta_{cw}}{D}} = \frac{u'_*}{\mathbf{k}} \ln \frac{\delta_{cw}}{z'_o} \qquad (6.6.11)$$

while equation 6.6.8 gives:

$$u\Big|_{-1+\frac{\delta_{cw}}{D}} = \frac{u'_*}{\mathbf{k}} \ln \frac{\delta_{cw} + z_e - z_o}{z_e} \qquad (6.6.12)$$

Equating the above two expressions:

$$z'_o = \frac{z_e \delta_{cw}}{\delta_{cw} + z_e - z_o} z_e \; ; \quad z_e = z'_o \frac{\delta_{cw} - z_o}{\delta_{cw} - z'_o} \qquad (6.6.13)$$

and 6.6.13 establishes the relationship between z'_o and z_e. It should be noted that $z'_o \le z_e$ since $z_e \ge z_o$. If atmospheric pressure variations are included, but waves are not considered in the model calculations, equation 6.5.20 assumes the form:

$$\tilde{\tau}_{bc\alpha} = \tau_{bc\alpha} + \frac{\delta_c - z_o}{D}\Big[\frac{D}{\rho_o}\frac{\partial p_{atm}}{\partial x_\alpha} + gD\frac{\partial \zeta}{\partial x_\alpha}\Big] \; ; \qquad \alpha = (1,2) \qquad (6.6.14)$$

where δ_c in this case is defined as the thickness of the bottom constant stress layer (Bedford and Abdelrhman [1987]):

$$\delta_c = 0.2\, C_D^{1/2} \frac{u_*}{f} \qquad (6.6.15)$$

and C_D is calculated in reference to a height z_r above the bottom where the flow velocity is known (usually at the half grid spacing above the bottom). If C_D is defined as a function of z_e and $u_* = u'_*$ then an iterative approach should be used to determine the final value of δ_c.

6.7 *WCBBL* Induced Turbulence

Thus far, only the effects due to the wave growth and the surface barometric changes have been included in the formulations. To facilitate the effects of the wave interactions with the bottom sediments within the *WCBBL*, as well as the sediment stratification effects, the turbulent diffusion coefficient $\mathcal{A}_v$ is formulated, by considering the effective roughness approach, as follows:

$$\mathcal{A}_v = \frac{\mathbf{k}\, u_{*cw}\Big[(1+\sigma)D + z_e - z_o\Big]}{1 + \beta\,\dfrac{(1+\sigma)D + z_e - z_o}{L_{cw}}}\ ; \qquad (\sigma \le -1 + \frac{\delta_{cw}}{D}) \tag{6.7.1}$$

$$\mathcal{A}_v = \frac{\mathbf{k}\, u_{*c}\Big[(1+\sigma)D + z_{ec} - z_o\Big]}{1 + \beta\,\dfrac{(1+\sigma)D + z_{ec} - z_o}{L_c}}\ ; \qquad (\sigma \ge -1 + \frac{\delta_{cw}}{D}) \tag{6.7.2}$$

where the wave enhanced bottom friction velocity u'_*, is replaced by u_{*c} the current enhanced bottom friction velocity, that in the absence of the *WCBBL* effects is the friction velocity the "current" feels throughout the water column.

Furthermore, in anticipation that z_e will be modified by the wave induced turbulence in *WCBBL*, the displacement length, z_{ec}, is introduced in equation 6.7.2 and replaces z_e. The friction velocity u_{*cw} reflects the maximum of the instantaneous bottom shear stress τ_{bcw} experienced within the *WCBBL* and L_c, L_{cw} are the Monin-Obukhov lengths for the two regions. Outside the *WCBBL* u_{*cw} is nil. This formulation modifies u_{*c} to reflect the additional effects within the *WCBBL*. Substitution of the expressions 6.7.1 and 6.7.2 into equations 6.5.17 and 6.5.18 with $|C_2| = Du_{*c}^2$ gives:

$$\frac{\partial |\boldsymbol{u}_\mathbf{h}|}{\partial \sigma} = \frac{Du_{*c}^2}{\mathbf{k}\, u_{*cw}} \left\{ \frac{1}{(1+\sigma)D + z_e - z_o} + \frac{\beta}{L_{cw}} \right\}\ ; \qquad (\sigma \le -1 + \frac{\delta_{cw}}{D}) \tag{6.7.3}$$

$$\frac{\partial |\boldsymbol{u}_\mathbf{h}|}{\partial \sigma} = \frac{Du_{*c}^2}{\mathbf{k}\, u_{*c}} \left\{ \frac{1}{(1+\sigma)D + z_{ec} - z_o} + \frac{\beta}{L_c} \right\}\ ; \qquad (\sigma \ge -1 + \frac{\delta_{cw}}{D}) \tag{6.7.4}$$

and the integration of the above equations yields:

$$|\boldsymbol{u}_\mathbf{h}| = \frac{u_{*c}^2}{\mathbf{k}\, u_{*cw}} \left\{ \ln \frac{(1+\sigma)D + z_e - z_o}{z_e} + \beta D \int_{-1+\frac{z_o}{D}}^{\sigma} \frac{1}{L_{cw}}\, d\sigma \right\}\ ; \quad (\sigma \le -1 + \frac{\delta_{cw}}{D}) \tag{6.7.5}$$

$$|\boldsymbol{u}_\mathbf{h}| = \frac{u_{*c}}{\mathbf{k}} \left\{ \ln \frac{(1+\sigma)D + z_e - z_o}{z_{ec}} + \beta D \int_{-1+\frac{z_o}{D}}^{\sigma} \frac{1}{L_c}\, d\sigma \right\}\ ; \quad (\sigma \ge -1 + \frac{\delta_{cw}}{D}) \tag{6.7.6}$$

The parameter z_{ec} is the enhanced value of z_e due to the wave effects within the *WCBBL*. It reflects the bottom shear stresses that the current above the *WCBBL* actually feels. The above formulations for z_e and z_{ec} are consistent in the sense that $u|_{z=z_o} = 0$.

Following the conclusions in Glenn and Grant [1987] that the sediment stratification effects within the *WCBBL* are negligible ($1/L_{cw} \approx 0$), and then matching the velocity u at $\sigma = -1 + \delta_{cw}/D$ (top of the *WCBBL*) given by equations 6.7.5 and 6.7.6, equation 6.7.7 is obtained:

$$\left.\begin{aligned} z_{ec} &= (\delta_{cw} - z_o)\frac{A}{1-A} \\ A &= \left(\frac{\delta_{cw} + z_e - z_o}{z_o}\right)^{-\epsilon_2} ; \qquad \epsilon_2 = \frac{u_{*c}}{u_{*cw}} \end{aligned}\right\} \tag{6.7.7}$$

The relationship between z_{ec} and z_{oc} in the Glenn and Grant's approach is given by:

$$\left.\begin{aligned} z_{oc} = \delta_{cw}\left(\frac{\delta_{cw} + z_e - z_o}{z_o}\right)^{-\epsilon_2} &= z_o'\left(\frac{\delta_{cw} + z_e - z_o}{z_e}\right)^{1-\epsilon_2} \\ \epsilon_2 &= \frac{u_{*c}}{u_{*cw}} \end{aligned}\right\} \tag{6.7.8}$$

The maximum bottom friction velocity in the *WCBBL* due to waves is given by (Styles and Glenn [2000] and Mellor [2002]) as:

$$u_{*wm}^2 = \frac{1}{2} f_{cw} U_{wb}^2 \tag{6.7.9}$$

where f_{cw} is the friction coefficient and U_{wb} is the maximum (within a wave cycle) bottom orbital velocity. For monochromatic waves, linear wave theory gives the following expression for the maximum bottom wave orbital velocity U_{wb}, as related to the bottom wave excursion amplitude A_{wb}:

$$U_{wb} = A_{wb}\omega \qquad \text{with} \qquad A_{wb} = \frac{a}{\sinh kD} \tag{6.7.10}$$

here, ω is the wave radian frequency and a is the surface wave amplitude. The wave bottom orbital velocity and the excursion amplitude of the spectral waves are given by equations 3.4.8. Comparison of equations 6.7.10 and 3.4.8 yields the expression:

$$U_{wb} = A_{wb}\tilde{\tilde{\sigma}} \tag{6.7.11}$$

which is the same expression as the one suggested in Madsen et al. [1988], Mathisen and Madsen [1999] and used in Styles and Glenn [2002] in their calculation of the bottom roughness. Equation

6.7.11 slightly modifies the expression in *GG87* by replacing the wave angular frequency with the spectrally averaged Doppler shifted frequency (equation 3.4.6). In the wave models used here, U_{wb} represents the root mean square of the maximum values of the near-bottom orbital velocity.

To avoid the unnecessary iterations of the *GG87* model and to account for the spectral waves (Mathisen and Madsen [1999]), the following expressions for f_{cw} are used (Mellor [2002]):

$$f_{cw} = 0.23\left(\frac{A_{wb}}{k_b}\right)^{-0.62} ; \qquad \frac{A_{wb}}{k_b} \leq 12.5 \tag{6.7.12}$$

$$f_{cw} = 0.13\left(\frac{A_{wb}}{k_b}\right)^{-0.40} ; \qquad \frac{A_{wb}}{k_b} > 12.5 \tag{6.7.13}$$

The *WCBBL* thickness is defined in the *GG87* model as:

$$\delta_{cw} = A\,\frac{\mathbf{k}u_{*cw}}{\omega} \tag{6.7.14}$$

where the value of the constant $A = 2$. Grant and Madsen [1979] state that the value of the constant A ranges between 1 and 2, but it can be taken equal to 2 as it is done in the *GG87* model. Madsen and Salles [1999] in an effort to calculate the *WCBBL* thickness more precisely, derived the following alternative analytical expression for A:

$$A = \exp\left[2.96\left(\frac{A_{wb}}{k_b}\right)^{-0.071} - 1.45\right] \tag{6.7.15}$$

Using equation 6.7.15, the value $A = 2$ is obtained for $A_{wb}/k_b = 100$. Mathisen and Madsen [1996b] showed that using the analytical expression for A instead of a constant value into equation 6.7.14, improved the results of the *GM86* model for monochromatic waves significantly. Mathisen and Madsen [1999] considered the same formulation for the constant A in considering spectral waves and showed equally good comparisons between the model predicted and the measured data. Consequently, Mathisen and Madsen's recommendation is that equation 6.7.15 be used for the determination of δ_{cw} in both monochromatic and spectral waves. Adopting the above recommendation, M^2COPS uses equation 6.7.15 in its calculations as well.

The friction velocity due to the wave-current interactions at the bottom of the *WCBBL* is computed by:

$$u_{*cw}^2 = C_R\, u_{*wm}^2 \tag{6.7.16}$$

$$C_R = \left\{1 + 2\left(\frac{u_{*c}}{u_{*wm}}\right)^2 \cos\phi + \left(\frac{u_{*c}}{u_{*wm}}\right)^4\right\}^{1/2} \tag{6.7.17}$$

where $\phi\,(0 \le \phi \le 90°)$ is the angle between the current and the wave, with the x-axis aligned to the wave direction at the bottom. Substituting equation 6.7.16 into equation 6.7.17 and using $\epsilon_2 = \epsilon = \dfrac{u_{*c}}{u_{*cw}}$ the following expression for C_R is derived:

$$(\epsilon^4 - 1)\, C_R^2 + 2\, C_R\, \epsilon^2 \cos\phi + 1 = 0 \tag{6.7.18}$$

Equation 6.7.18 has the solution:

$$C_R = \frac{\epsilon^2 \cos\phi + \sqrt{1 - \epsilon^4 \sin^2\phi}}{1 - \epsilon^4} = \frac{\epsilon^2 \cos\phi + \sqrt{(1 - \epsilon^4) + (\epsilon^2 \cos\phi)^2}}{1 - \epsilon^4}\ ; \qquad \epsilon < 1 \tag{6.7.19}$$

where only the root of 6.7.18 that gives a positive C_R value is used. In M^2COPS the angle ϕ is calculated using:

$$\sin\phi = \frac{|U_{wby}\tilde{\tau}_{bcx} - U_{wbx}\tilde{\tau}_{bcy}|}{U_{wb}|\tilde{\tau}_{bc}|}\ ; \qquad 0 \le \phi \le \frac{\pi}{2} \tag{6.7.20}$$

where $\tilde{\tau}_{bcx}$ and $\tilde{\tau}_{bcy}$ are given by equation 6.5.20 and $|\tilde{\tau}_{bc}| = [(\tilde{\tau}_{bcx})^2 + (\tilde{\tau}_{bcy})^2]$.

The two components of the bottom wave orbital velocity are defined as:

$$U_{wb\alpha} = U_{wb}\,\frac{k_\alpha}{k} \tag{6.7.21}$$

where in M^2COPS the spectrally averaged wavenumber components $k_\alpha = \tilde{k}_\alpha$ (a wave model output) are used.

6.8 Effects on Bottom Sediment Concentration Distributions

The solution of equation 6.3.9 requires the specification of two boundary conditions. The first is applied at the top of the *BBL*, where the sediment concentration flux is specified, and the second at the bottom of the *BBL*, where the sediment concentration at a reference height is specified. Integration of equation 6.3.9 gives:

$$\mathcal{D}_v \frac{\partial C_n}{\partial \sigma} + D\, w_{sn}\, C_n = C_1\ ; \qquad (\sigma \ge -1 + \frac{\delta_{cw}}{D}) \tag{6.8.1a}$$

where the constant of integration C_1 is evaluated at the top of the overall *BBL* (Figure 6.1).

The continuity of the sediment concentration flux at the top of the *BBL* gives (Boudreau and Jørgensen [2001]):

$$C_1 = \mathcal{D}_v^- \frac{\partial C_n^-}{\partial \sigma} + D\, w_{sn}^-\, C_n^- = \mathcal{D}_v^+ \frac{\partial C_n^+}{\partial \sigma} + D\, w_{sn}^+\, C_n^+ \tag{6.8.1b}$$

The variables w_{sn}^{-}, C_n^{-} and $\mathcal{D}_{\mathrm{v}}^{-}$ represent the settling velocity, the concentration and the mass diffusivity, respectively, just below the top of the *BBL* for the sediment particle class n. The corresponding variables for the region just above the top of the *BBL* are denoted by w_{sn}^{+}, C_n^{+} and $\mathcal{D}_{\mathrm{v}}^{+}$, respectively. In shallow waters the height δ_c of the bottom boundary layer is usually limited by the water depth, therefore, in the case that the atmospheric sediment inputs are nil, the last of equations 6.8.1b reduces to: $\mathcal{D}_{\mathrm{v}}^{+}\,\partial C_n^{+}/\partial\sigma + D\,w_{sn}^{+}\,C_n^{+} = 0$, that is $C_1 = 0$, and equation 6.8.1a becomes:

$$\mathcal{D}_{\mathrm{v}}\frac{\partial C_n}{\partial\sigma} + Dw_{sn}C_n = 0\ ; \qquad (\sigma \geq -1 + \frac{\delta_{cw}}{D}) \tag{6.8.2}$$

In deep waters the height of the *BBL* is less than the water depth (limited though by the Ekman layer height δ_E), but significantly exceeds the height of the *WCBBL*. Because the sediment concentrations are low at the top of the *BBL*, the zero sediment flux boundary condition used for the derivation of equation 6.8.2 can be adopted in this case as well, without degrading the model's accuracy significantly (Boudreau and Jørgensen [2001]).

With the appropriate expression for the mass diffusivity, equation 6.8.2 is valid both inside and outside the *WCBBL* (Glenn and Grant [1987]), that is:

$$\mathcal{D}_{\mathrm{v}}\frac{\partial C_n}{\partial\sigma} + Dw_{sn}C_n = 0\ ; \qquad (\sigma \leq -1 + \frac{\delta_{cw}}{D}) \tag{6.8.3}$$

The turbulent mass diffusivity $\mathcal{D}_{\mathrm{v}}$ in terms of z_{e}, z_{ec} is defined in the two regions of the *WCBBL* as:

$$\mathcal{D}_{\mathrm{v}} = \frac{\mathbf{k}\,u_{*cw}\Big[z + z_{\mathrm{e}} - z_{\mathrm{o}}\Big]}{\gamma + \beta\,\dfrac{z + z_{\mathrm{e}} - z_{\mathrm{o}}}{L_{cw}}} = \frac{\mathbf{k}\,u_{*cw}\Big[(1+\sigma)D + z_{\mathrm{e}} - z_{\mathrm{o}}\Big]}{\gamma + \beta\,\dfrac{(1+\sigma)D + z_{\mathrm{e}} - z_{\mathrm{o}}}{L_{cw}}}\ ; \qquad (\sigma \leq -1 + \frac{\delta_{cw}}{D}) \tag{6.8.4}$$

$$\mathcal{D}_{\mathrm{v}} = \frac{\mathbf{k}\,u_{*c}\Big[z + z_{ec} - z_{\mathrm{o}}\Big]}{\gamma + \beta\,\dfrac{z + z_{ec} - z_{\mathrm{o}}}{L_{c}}} = \frac{\mathbf{k}\,u_{*c}\Big[(1+\sigma)D + z_{ec} - z_{\mathrm{o}}\Big]}{\gamma + \beta\,\dfrac{(1+\sigma)D + z_{ec} - z_{\mathrm{o}}}{L_{c}}}\ ; \qquad (\sigma \geq -1 + \frac{\delta_{cw}}{D}) \tag{6.8.5}$$

Substituting the appropriate expressions for $\mathcal{D}_{\mathrm{v}}$ into equations 6.8.2 and 6.8.3 yields:

$$\frac{\partial C_n}{\partial\sigma} = -D\,\frac{w_{sn}\,C_n}{\mathbf{k}\,u_{*cw}}\cdot\left\{\frac{\gamma}{(1+\sigma)D + z_{\mathrm{e}} - z_{\mathrm{o}}} + \frac{\beta}{L_{cw}}\right\}\ ; \qquad (\sigma \leq -1 + \frac{\delta_{cw}}{D}) \tag{6.8.6}$$

$$\frac{\partial C_n}{\partial\sigma} = -D\,\frac{w_{sn}\,C_n}{\mathbf{k}\,u_{*c}}\cdot\left\{\frac{\gamma}{(1+\sigma)D + z_{ec} - z_{\mathrm{o}}} + \frac{\beta}{L_{c}}\right\}\ ; \qquad (\sigma \geq -1 + \frac{\delta_{cw}}{D}) \tag{6.8.7}$$

where the concentration is known at $z = z_o$, that is $C_{no} = C_n(z_o)$ = reference concentration. Integration of equations 6.8.6 and 6.8.7 gives:

$$C_n = C_{no}\left\{\frac{(1+\sigma)D + z_e - z_o}{z_e}\right\}^{-\frac{\gamma\, w_{sn}}{\mathbf{k}\, u_{*cw}}} \cdot \exp\left[-\frac{D\beta\, w_{sn}}{\mathbf{k}\, u_{*cw}} \int_{-1+\frac{z_o}{D}}^{\sigma} \frac{d\sigma}{L_{cw}}\right]; \quad (\sigma \le -1 + \frac{\delta_{cw}}{D}) \tag{6.8.8}$$

$$C_n = C_n(\delta_{cw})\left\{\frac{(1+\sigma)D + z_{ec} - z_o}{z_{ec}}\right\}^{-\frac{\gamma\, w_{sn}}{\mathbf{k}\, u_{*cw}}} \cdot \exp\left[-\frac{D\beta\, w_{sn}}{\mathbf{k}\, u_{*c}} \int_{-1+\frac{z_o}{D}}^{\sigma} \frac{d\sigma}{L_c}\right]; \quad (\sigma \ge -1 + \frac{\delta_{cw}}{D}) \tag{6.8.9}$$

where $C_{no} = C_n(z_o)$ is the sediment concentration at $\sigma = -1 + z_o/D$ and $C_n(\delta_{cw})$ is the concentration at the top of the *WCBBL* ($\sigma = -1 + \delta_{cw}/D$). To determine the relationship between $C_n(\delta_{cw})$ and $C_n(z_o)$, equation 6.8.8 is applied at $\sigma = -1 + \delta_{cw}/D$ and taking into consideration that $1/L_{cw} \approx 0$ (Glenn and Grant [1987]), then:

$$C_n(\delta_{cw}) = C_{no}\left\{\frac{\delta_{cw} + z_e - z_o}{z_e}\right\}^{-\frac{\gamma\, w_{sn}}{\mathbf{k}\, u_{*cw}}} \tag{6.8.10}$$

For a particular sediment class, the suspended load is defined as:

$$\boldsymbol{S_{sn}} = |\boldsymbol{u_h}|\, C_n \tag{6.8.11}$$

where $|\boldsymbol{u_h}|$ is the total flow velocity at level σ (or z) and $C_n = C_n(\sigma)$ is the corresponding sediment concentration. Equation 6.8.11 is evaluated at each vertical level (as defined in the hydrodynamic model) and it can be a source term in the sediment transport equation representing the shoreline erosion. When $\sigma \le -1 + \delta_{cw}/D$, equations 6.7.5 and 6.8.8 are used in the calculation of $\boldsymbol{S_{sn}}$. When $\sigma \ge -1 + \delta_{cw}/D$, equations 6.7.6 and 6.8.9 are used instead.

6.8.1 Definition of the Stability Parameter

The stratification correction terms appearing in equations 6.7.6 and 6.8.9 do not have a known analytical representation and they are usually evaluated iteratively. However, a simplification of the equations is possible, if it can be shown that the sediment stratification or strong vertical gradients within the *WCBBL* are negligible. The *WCBBL* is a highly energetic region of the near-bottom flow field where mixing is strong relative to the background stratification, especially at its lower portion. The almost uniform vertical concentration gradients limit the stratification effects in this region. Glenn and Grant [1987], using scaling arguments and typical values for the variables, determined

that the stratification correction term $\beta z^*/L$ is small (less than $O(1)$) relative to the vertical turbulent momentum fluxes in the *WCBBL*. It is noted here that this statement is more likely to be true near the bottom and invalid near the top of the *WCBBL*.

The system of equations described so far is not considered "closed" until an expression for the stratification correction factor is determined. Following Glenn and Grant, the stability parameter $1/L_{cw}$ within the *WCBBL* is set equal to zero and stratification is assumed negligible inside *WCBBL*. Following Glenn and Grant [1987] and Styles and Glenn [2000], the stability parameter outside the *WCBBL* is related to the sediment concentration as follows:

$$\frac{z + z_{ec} - z_o}{L_c} = -\frac{\mathcal{D}_{nv}}{u_{*c}^4} \sum_{n=1}^{N} g\,(S_{pn} - 1)\mathcal{D}_v \frac{\partial C_n}{\partial z} \tag{6.8.12}$$

$$\frac{(1+\sigma)D + z_{ec} - z_o}{L_c} = -\frac{\mathcal{D}_{nv}}{u_{*c}^4} \sum_{n=1}^{N} \frac{1}{D} g\,(S_{pn} - 1)\mathcal{D}_v \frac{\partial C_n}{\partial \sigma} \tag{6.8.13}$$

where the neutral mass diffusivity ($\mathcal{D}_{nv}$), defined in equation 6.4.3, is modified here to include the effective roughness concept: $\mathcal{D}_{nv} = \mathbf{k}\, u_{*c}\,(z + z_{ec} - z_o) = \mathbf{k}\, u_{*c}\,[(1+\sigma)D + z_{ec} - z_o]$. Using equation 6.8.2 and equation 6.8.13, the expression for $1/L_c$, valid in both coordinate systems, is:

$$\frac{1}{L_c} = \frac{g\,\mathbf{k}}{u_{*c}^3} \sum_{n=1}^{N} (S_{pn} - 1)\, w_{sn}\, C_n \tag{6.8.14}$$

Equation 6.8.14 defines the required vertical profile of the stability parameter $1/L_c$ for sediment stratification and it must be determined iteratively.

6.9 Solution Procedure

Calculation of the *BBL* variables is complex and the following pseudo-code is applicable to each case:

Case (1): Currents only

The bottom shear stresses are readily calculated from equations 2.1.19 and 2.1.20 where the reference elevation z_r is taken to be at the first grid point above the bottom where the flow velocity is known (for the staggered grid used in M^2COPS, this is the half grid point above the bottom).

Case (2): Currents plus barotropic effects

(a) Calculate $\tau_{bc\alpha}$, $\alpha = (1, 2)$ using equations 2.1.19 and 2.1.20

(b) Calculate $u_* = \tau_{bc}^{1/2}$; $\tau_{bc}^2 = \tau_{bc\alpha}\tau_{bc\alpha}$, $\alpha = (1,2)$ using equation 6.5.11b

(c) Calculate the thickness of the boundary layer as: $\delta_{cw} = \delta_c$, using equation 6.6.15

(d) Calculate $\tilde{\tau}_{bc\alpha} = \tau_{bc\alpha} + \tau_{bp\alpha}$, $\alpha = (1,2)$ using equations 6.5.11b and 6.5.11c

(e) Calculate z_e from equation 6.6.10; $\tilde{\tau}_{bc}^2 = \tilde{\tau}_{bc\alpha}\tilde{\tau}_{bc\alpha}$, $\alpha = (1,2)$

(f) Calculate the new value of C_D using: $C_D = \mathbf{k}^2[\ln(z_r + z_e - z_o)/z_e]^{-2}$

(g) Calculate the updated value of $u_* = \tilde{\tau}_{bc}^{1/2}$. Repeat steps *(c)* through *(g)* until $u_*^{new} \approx u_*^{old}$ (within some tolerance)

(h) The bottom boundary conditions become: $\tilde{\tau}_{bcx} = C_D|\boldsymbol{u}_\mathbf{h}|u_\alpha$

Case (3): Currents and waves, no sediment stratification

(a) Calculate or obtain from the wave model output all relevant wave parameters:

(1) Obtain the wave bottom orbital velocity U_{wb}

(2) Obtain the spectrally averaged variables: $\tilde{\tilde{\sigma}}$, $\tilde{k}$, $\tilde{k}_\alpha$, $\alpha = (1,2)$

(3) Calculate $A_{wb} = U_{wb}/\tilde{\tilde{\sigma}}$

(4) Calculate the bottom radiation stress gradients $(\partial S_{\alpha\beta}/\partial x_\beta)|_{\sigma=-1}$ from the wave model supplied radiation stress $R_{\alpha\beta}$

(b) Calculate f_{cw} using equations 6.7.12 and 6.7.13

(c) Calculate the maximum bottom wave friction velocity u_{*wm} from equation 6.7.9

(d) Determine the initial value of u_{*c} from equations 2.1.19 and 2.1.20

(e) Calculate the angle ϕ using equation 6.7.20

(f) Calculate C_R using equation 6.7.17

(g) Calculate u_{*cw}^2 using equation 6.7.16

(h) Calculate $\delta_{cw} = \delta_{cw}$ using equation 6.7.14

(i) Calculate z_e as in case *(2)* and z_{ec} from equation 6.7.7

(j) Calculate the updated value of u_{*c} from equation 6.5.20. Repeat steps *(e)* through *(j)* until: $u_{*c}^{new} \approx u_{*c}^{old}$ (within some tolerance). The result gives the wave induced bottom shear stresses which is exported to hydrodynamic model.

Case (4): Currents and waves with sediment stratification

This case is only used when the calculation of the vertical distribution of the suspended load source terms $\boldsymbol{S_{sn}}$ is desired. First perform the calculations for the unstratified field (complete case *(3)*) to determine all relevant parameters and then:

(a) From equation 6.8.9 and with $\frac{1}{L_c} \approx 0$ calculate the initial unstratified concentration profile

(b) Use equation 6.8.14 to calculate the vertical profile for $\frac{1}{L_c}$

(c) Calculate C_n for each sediment class using equation 6.8.9

(d) Repeat steps *(b)* and *(c)* until $L_c^{new} \approx L_c^{old}$ at each vertical level (within some tolerance)

(e) Use the calculated profile for $\frac{1}{L_c}$ and calculate the velocity profile using equation 6.7.6

(f) Calculate $\boldsymbol{S_{sn}}$ for each sediment class at each vertical level using equation 6.8.11

(g) Export the results to sediment model.

CHAPTER 7

TURBULENCE CLOSURE

The solution of the derived turbulent Navier-Stokes and scalar transport equations requires the determination of the horizontal and vertical viscosities/diffusivities so that the system of the equations can be closed. One way to approach this problem is by solving these equations in the length scale of the large eddies and by resolving the subgrid turbulence using appropriate turbulence closure models. The higher order correlations of the turbulent fluctuating terms are simulated in the turbulence closure models by using mean flow properties to close the time averaged transport equations.

M^2COPS follows the above approach and uses a two equation κ-ϵ turbulence closure model that solves the two differential equations of κ (turbulent kinetic energy per unit mass) and ϵ (dissipation rate of the turbulent kinetic energy) to determine the turbulent viscosities and diffusivities. The κ-ϵ model, parametrized via empirical constants and equations, has been widely used for more than two decades in successfully predicting the turbulent flows in the case of: *(a)* 2D and 3D weakly swirling and recirculating flows, *(b)* conduit and channel flows, and *(c)* boundary layer flows near plain wall. It is known though that the κ-ϵ model has not been equally successful in predicting: *(a)* strongly swirling and buoyant flows, *(b)* boundary layer flows near curved walls, and *(c)* low $\mathbb{R}_e$ number flows.

7.1 Governing Equations of the Turbulence Transport

The transport of the turbulent kinetic energy per unit mass $\kappa = 0.5\ \overline{u_i' u_i'}$ and its viscous dissipation rate $\epsilon = \nu\,\overline{(\partial u_i'/\partial x_j + \partial u_j'/\partial x_i)(\partial u_i'/\partial x_j)}$ (summation over the repeated indices $i, j = (1, 3)$) are modeled using the eddy viscosity/diffusivity concept (ASCE Task Committee on Turbulence Models in Hydraulic Computation [1988a,b], Rodi [1994]). The turbulent transport terms resulting from

the temporal averaging of the Navier-Stokes and scalar transport equations are related to the eddy viscosities/diffusivities and the mean flow variables as follows (Cheng and Smith [1990]):

$$\frac{\partial \overline{u'u'}}{\partial x} + \frac{\partial \overline{u'v'}}{\partial y} + \frac{\partial \overline{u'w'}}{\partial z} = -\frac{\partial}{\partial x}\left[\mathcal{A}_h \frac{\partial u}{\partial x}\right] - \frac{\partial}{\partial y}\left[\mathcal{A}_h \frac{\partial u}{\partial y}\right] - \frac{\partial}{\partial z}\left[\mathcal{A}_v \frac{\partial u}{\partial z}\right] \tag{7.1.1}$$

$$\frac{\partial \overline{u'v'}}{\partial x} + \frac{\partial \overline{v'v'}}{\partial y} + \frac{\partial \overline{v'w'}}{\partial z} = -\frac{\partial}{\partial x}\left[\mathcal{A}_h \frac{\partial v}{\partial x}\right] - \frac{\partial}{\partial y}\left[\mathcal{A}_h \frac{\partial v}{\partial y}\right] - \frac{\partial}{\partial z}\left[\mathcal{A}_v \frac{\partial v}{\partial z}\right] \tag{7.1.2}$$

$$\frac{\partial \overline{u'\Phi'}}{\partial x} + \frac{\partial \overline{v'\Phi'}}{\partial y} + \frac{\partial \overline{v'\Phi'}}{\partial z} = -\frac{\partial}{\partial x}\left[\mathcal{B}_h \frac{\partial \Phi}{\partial x}\right] - \frac{\partial}{\partial y}\left[\mathcal{B}_h \frac{\partial \Phi}{\partial y}\right] - \frac{\partial}{\partial z}\left[\mathcal{B}_v \frac{\partial \Phi}{\partial z}\right] \tag{7.1.3}$$

In the case of homogeneous turbulence the vertical coefficients $\mathcal{A}_v$ and $\mathcal{B}_v$ are defined in terms of $\boldsymbol{\kappa}$ and $\boldsymbol{\epsilon}$, by the following empirical equations (Rodi [1994]):

$$\mathcal{A}_v = c_\mu \frac{\boldsymbol{\kappa}^2}{\boldsymbol{\epsilon}} \qquad \text{and} \qquad \mathcal{B}_v = \frac{\mathcal{A}_v}{\mathbb{P}_{rt}} \tag{7.1.4}$$

where $\mathbb{P}_{rt}$ is the turbulent Prandtl number. For completely unstratified flows the vertical eddy viscosities and diffusivities are equal. The one dimensional transport equations for $\boldsymbol{\kappa}$ and $\boldsymbol{\epsilon}$ as presented in Burchard and Baumert [1995], Chapman et al. [1996] are:

$\boldsymbol{\kappa}$-equation:
$$\frac{\partial \boldsymbol{\kappa}}{\partial t} = \frac{\partial}{\partial z}\left[\frac{\mathcal{A}_v}{\sigma_{\boldsymbol{\kappa}}} \frac{\partial \boldsymbol{\kappa}}{\partial z}\right] + P + G - \boldsymbol{\epsilon} \tag{7.1.5}$$

$\boldsymbol{\epsilon}$-equation:
$$\frac{\partial \boldsymbol{\epsilon}}{\partial t} = \frac{\partial}{\partial z}\left[\frac{\mathcal{A}_v}{\sigma_{\boldsymbol{\epsilon}}} \frac{\partial \boldsymbol{\epsilon}}{\partial z}\right] + c_{\epsilon 1} \frac{\boldsymbol{\epsilon}}{\boldsymbol{\kappa}} (P + c_{\epsilon 3} G) - c_{\epsilon 2} \frac{\boldsymbol{\epsilon}^2}{\boldsymbol{\kappa}} \tag{7.1.6}$$

where P represents the production of turbulence due to the interaction of the turbulent stresses with the vertical gradients of the horizontal mean flow velocities and G represents the buoyancy production of turbulence. These two terms are defined as (Burchard and Baumert [1995], Chapman et al. [1996]):

$$P = -\overline{u'_\alpha w'} \frac{\partial u_a}{\partial z} = -\overline{u'w'} \frac{\partial u}{\partial z} - \overline{v'w'} \frac{\partial v}{\partial z} = \mathcal{A}_v \left[\left(\frac{\partial u}{\partial z}\right)^2 + \left(\frac{\partial v}{\partial z}\right)^2\right]; \quad G = \frac{\mathcal{A}_v}{\mathbb{P}_{rt}} \frac{g}{\rho_o} \frac{\partial \rho}{\partial z} \tag{7.1.7}$$

The values of the constants c_μ, $c_{\epsilon 1}$, $c_{\epsilon 2}$, and $c_{\epsilon 3}$ are not model tunable and have been determined from numerous experimental applications (Rodi [1994]). The constant $c_{\epsilon 3}$, which multiplies the buoyancy production term, does not have a universal value, but rather depends upon the flow conditions. For unstable-stratified conditions ($G > 0$) is taken close to 1, while for stable-stratified

flows ($G < 0$) is taken close to 0. In M^2COPS these constants are used as defined in Burchard and Baumert [1995]:

$$\sigma_{\boldsymbol{\kappa}} = 1.0\,, \quad \sigma_{\boldsymbol{\epsilon}} = 1.3\,, \quad c_\mu = 0.09\,, \quad c_{\epsilon 1} = 1.44\,, \quad c_{\epsilon 2} = 1.92 \quad \text{and} \quad c_{\epsilon 3} = 0 \tag{7.1.8}$$

Writing the equation of the *TKE* using the triple decomposition of the variables (Section B.1.2), as it is done in Reynolds and Hussain [1972] and Finnigan and Einaudi [1981], the term for the shear production of the *TKE* can be approximated as:

$$P = P_c + P_w = -\overline{u_i' u_j'}\,\frac{\partial \overline{u}_i}{\partial x_j} - \overline{\widehat{u_i' u_j'}\,\frac{\partial \tilde{u}_i}{\partial x_j}} = -\overline{u_\alpha' w'}\,\frac{\partial u_\alpha}{\partial z} - \overline{\widehat{u_\alpha' w'}\left(\frac{\partial \tilde{u}_\alpha}{\partial z} + \frac{\partial \tilde{w}}{\partial x_\alpha}\right)}^{L} \tag{7.1.9}$$

It has been shown in Ardhuin and Jenkins [2006b], that

$$\overline{\frac{\partial \tilde{u}_\alpha}{\partial z}}^{L} = \overline{\frac{\partial \tilde{w}}{\partial x_\alpha}}^{L} = \frac{1}{2}\frac{\partial \mathrm{u_{st}}_\alpha}{\partial z} \tag{7.1.10}$$

therefore, equation 7.1.9 becomes:

$$P = -\overline{u_\alpha' w'}\,\frac{\partial u_\alpha}{\partial z} - \overline{u_\alpha' w'}\,\frac{\partial \mathrm{u_{st}}_\alpha}{\partial z} = -\overline{u_\alpha' w'}\,\frac{\partial \mathcal{U}_\alpha}{\partial z} \tag{7.1.11}$$

The wave enhanced production term P given by the above equation is now used in place of the first of equations 7.1.7 in the $\boldsymbol{\kappa}$-$\boldsymbol{\epsilon}$ model equations 7.1.5 and 7.1.6. The inclusion of the Stokes shear production terms in the turbulence model accounts for the additional production of the *TKE* by the Langmuir cells (Kantha and Clayson [2004], Carniel et al. [2005]). The complete form of P is:

$$P = -\overline{u_\alpha' w'}\,\frac{\partial \mathcal{U}_\alpha}{\partial z} = \mathcal{A}_\mathrm{v}\frac{\partial u_\alpha}{\partial z}\frac{\partial \mathcal{U}_\alpha}{\partial z} \tag{7.1.12}$$

7.1.1 Boundary Conditions

The boundary conditions for equations 7.1.5 and 7.1.6 are parametrized using the surface and bottom shear stresses (Section 2.1.3). Assuming local equilibrium for the turbulence (that is, the turbulence production equals the dissipation of turbulence), the boundary conditions for $\boldsymbol{\kappa}$ and $\boldsymbol{\epsilon}$ are Dirichlet type conditions defined by the following equations (Chapman et al. [1996]):

$$\boldsymbol{\kappa}|_\zeta = \frac{u_*^2|_\zeta}{\sqrt{c_\mu}} = \frac{\tau_s/\rho_\mathrm{o}}{\sqrt{c_\mu}} \qquad \text{and} \qquad \boldsymbol{\kappa}|_{-h} = \frac{u_*^2|_{-h}}{\sqrt{c_\mu}} = \frac{\tau_b/\rho_\mathrm{o}}{\sqrt{c_\mu}} \tag{7.1.13}$$

$$\boldsymbol{\epsilon}|_\zeta = \frac{u_*^3|_\zeta}{\mathbf{k}(\Delta z/2)} = \frac{(\tau_s/\rho_\mathrm{o})^{3/2}}{\mathbf{k}(\Delta z/2)} \qquad \text{and} \qquad \boldsymbol{\epsilon}|_{-h} = \frac{u_*^3|_{-h}}{\mathbf{k}(\Delta z/2)} = \frac{(\tau_b/\rho_\mathrm{o})^{3/2}}{\mathbf{k}(\Delta z/2)} \tag{7.1.14}$$

7.2 Turbulent Prandtl Number

The turbulent Prandtl number $\mathbb{P}_r$ is crucial in the calculations performed by the κ-ϵ model, since an incorrect definition of this number can easily yield physically unacceptable results from the turbulence model and, subsequently, erroneous results from the hydrodynamic model. Matters become even more complicated when multiple constituents are modeled.

The original *CH3D* model code uses the following definition of the turbulent Prandtl number, as described in Bloss et al. [1988]:

$$\mathbb{P}_{rt} = \left(1 + 3\,\mathbb{R}_{ig}\right)^2 \tag{7.2.1}$$

therefore, the combination of equations 7.2.1 and the second of equations 7.1.4 yields:

$$\mathcal{B}_v = \frac{\mathcal{A}_v}{\left(1 + 3\,\mathbb{R}_{ig}\right)^2} \tag{7.2.2}$$

where $\mathbb{R}_{ig}$ is the gradient Richardson's number defined as:

$$\mathbb{R}_{ig} = -\frac{g}{\rho_o}\,\frac{\dfrac{\partial \rho}{\partial z}}{\left(\dfrac{\partial u}{\partial z}\right)^2 + \left(\dfrac{\partial v}{\partial z}\right)^2} \tag{7.2.3}$$

The Richardson's number accounts for the effects of stratification due to resulting vertical density gradients influenced by the temperature and salinity changes in the flow field. From equation 7.2.2, it is clear that as $\mathbb{R}_{ig}$ increases, $\mathcal{B}_v$ rapidly goes to zero, therefore, implicitly this definition of $\mathbb{P}_{rt}$ introduces an artificial laminarization of the flow field. A common modeling practice is to define the critical gradient Richardson number ($\mathbb{R}_{igc} \approx 0.2 - 0.25$) beyond which the turbulent diffusivities are set equal to zero (for $\mathbb{R}_{ig} \geq \mathbb{R}_{ic}$). Thus, only the molecular effects become active for this $\mathbb{R}_{ig}$ range.

Oceanic measurements of $\mathbb{R}_{ig}$ (Large et al. [1994] and Large and Gent [1999]) show that the $\mathbb{R}_{ig}$ values are usually within the range: $0.4 \leq \mathbb{R}_{ig} \leq 1.0$ rarely falling as low as $0.2 - 0.25$. If this is the case, then equation 7.2.2 gives very low values for $\mathcal{B}_v$ ($\mathcal{B}_v = 0.16\,\mathcal{A}_v$ for $\mathbb{R}_{ig} = 0.5$ and $\mathcal{B}_v = 0.06\,\mathcal{A}_v$ for $\mathbb{R}_{ig} = 1.0$), that is, the flow is treated as laminar (turbulence is suppressed by stratification). Close to zero ($\mathbb{R}_{ig} \ll 0.1$) equation 7.2.2 asymptotically reaches its full active turbulence status, assuming a well mixed flow field with: $\mathcal{B}_v \approx \mathcal{A}_v$. Furthermore, this formulation predicts unrealistically low values for the flux Richardson number $\mathbb{R}_{if}$ as well, implying that a well mixed flow regime always exists in the calculations (Figure 7.1b).

The expected values of $\mathbb{R}_{if}$ in oceanic environments are less than 0.25 ($\mathbb{R}_{if} \leq 0.2$), (Thorpe [2005]), a finding that is also reported in Shih et al. [2005], Pardyjak et al. [2002] and implicitly in Large et al. [1994]. The above values for $\mathbb{R}_{if}$ imply that $\mathbb{R}_{ig} > 0.4$ (Thorpe [2005]). Therefore, as stated in Zilitinkevich et al. [2008], the concept of a critical $\mathbb{R}_{ic}$ number beyond which turbulence is completely suppressed is not valid, an argument that has also been verified by recent observations (Zilitinkevich and Esau [2007], Grachev et al. [2007], Peters and Baumert [2007]).

Due to its erratic behavior, the formulation of Bloss et al. was criticized in Abraham [1990] as being applicable only in well mixed environments, where the locally produced turbulence is dissipated at the rate at which it is produced, thus limiting its applicability in more general flow fields. Indeed, Bloss et al. applied their proposed $\mathbb{P}_{rt}$ formulation only in estuaries with low density gradients (Bloss et al. [1988, 1990], Lang et al. [1989]).

Nunes Vaz and Simpson [1994] evaluated seven different parametrizations for the vertical mixing coefficients for momentum and mass, among others the formulations of Munk and Anderson [1948], Pacanowski and Philander [1981], Bloss et al. [1988] and Mellor and Yamada [1982]. The authors found that in stably stratified estuarine flows all the parametrizations produced poor results by under-predicting stratification, although the schemes by Mellor and Yamada and Pacanowski and Philander produced the best quantitative fits to the measured data.

The latest research efforts and analyses of observational data reveal that turbulence and mixing do exist at $\mathbb{R}_{ig} > \mathbb{R}_{ic} = 0.2 - 0.25$ and well beyond $\mathbb{R}_{ig} > 1$ (Ivey et al. [2008], Shih et al. [2005], Pardyjak et al. [2002], van Haren and Howarth [2004], Esau and Grachev [2007] and possibly others). Consequently, the standard understanding that turbulence is suppressed beyond the critical Richardson number (0.2-0.25) is not a valid argument. Zilitinkevich et al. [2008] suggests that to separate the stratified flow regime it is better to replace the terms "turbulent high energetic" and "laminar" based on the definition of the $\mathbb{R}_{ic}$ number by the terms "strong mixing" and "weak mixing" (the latest being the region where molecular effects become the controlling factor), based on the definition of an intermediate regime, as proposed by Shih et al. [2005] where $\mathbb{R}_{if} \approx 0.2$.

The above discussion shows the difficulties in the parametrization of $\mathbb{P}_{rt}$, which is not a function of the $\mathbb{R}_{ig}$ only, but as $\mathbb{R}_{ig}$ increases, it becomes a function of the Reynolds number as well (Shih et al. [2005]). The objective of this Section is to define an appropriate parametrization for $\mathbb{P}_{rt}$ to be used in M^2COPS. To this end the following empirical, semi-empirical or theoretical schemes have been investigated:

(a) Munk and Anderson [1948] (henceforth *MA*):

$$\mathbb{P}_{\mathrm{rt}} = \frac{\left(1 + \frac{10}{3}\,\mathbb{R}_{\mathrm{ig}}\right)^{3/2}}{\left(1 + 10\,\mathbb{R}_{\mathrm{ig}}\right)^{1/2}} \tag{7.2.4}$$

(b) Pacanowski and Philander [1981] (henceforth *PP*):

$$\mathbb{P}_{\mathrm{rt}} = \frac{\left(1 + 5\,\mathbb{R}_{\mathrm{ig}}\right) + 10^{-2}\left(1 + 5\,\mathbb{R}_{\mathrm{ig}}\right)^{3}}{1 + 10^{-2}\left(1 + 5\,\mathbb{R}_{\mathrm{ig}}\right)^{2} + 10^{-3}\left(1 + 5\,\mathbb{R}_{\mathrm{ig}}\right)^{3}} \tag{7.2.5}$$

(c) Bloss et al. [1988] (henceforth *BL*):

$$\mathbb{P}_{\mathrm{rt}} = \left(1 + 3\,\mathbb{R}_{\mathrm{ig}}\right)^{2} \tag{7.2.6}$$

(d) Mellor and Yamada [1982] (henceforth *MY*):

$$\mathbb{P}_{\mathrm{rt}} = \frac{1}{0.725}\,\frac{\mathbb{R}_{\mathrm{ig}}}{\mathbb{R}_{\mathrm{ig}} + 0.186 - \left(\mathbb{R}_{\mathrm{ig}}^{2} - 0.316\mathbb{R}_{\mathrm{ig}} + 0.0346\right)^{1/2}} \tag{7.2.7}$$

(e) Nakanishi [2001] (henceforth *NK*):

$$\mathbb{P}_{\mathrm{rt}} = \frac{1}{0.774}\,\frac{\mathbb{R}_{\mathrm{ig}}}{\mathbb{R}_{\mathrm{ig}} + 0.220 - \left(\mathbb{R}_{\mathrm{ig}}^{2} - 0.328\mathbb{R}_{\mathrm{ig}} + 0.0484\right)^{1/2}} \tag{7.2.8}$$

(f) Schumann and Gerz [1995] (henceforth *SG*):

$$\mathbb{P}_{\mathrm{rt}} = \mathbb{P}_{\mathrm{rn}} \cdot \exp\left(-\frac{\mathbb{R}_{\mathrm{ig}}}{0.25\,\mathbb{P}_{\mathrm{rn}}}\right) + \frac{\mathbb{R}_{\mathrm{ig}}}{0.25} \tag{7.2.9}$$

(g) Zilitinkevich and Esau [2007] (henceforth *ZL*):

$$\mathbb{P}_{\mathrm{rt}} = \frac{1}{1.25}\,\frac{\left(1 + 19\,\mathbb{R}_{\mathrm{ig}}\right)^{2.7}}{\left(1 + 36\,\mathbb{R}_{\mathrm{ig}}\right)^{1.7}} \tag{7.2.10}$$

(h) Linear Zilitinkevich et al. [2008] (henceforth *ZLL*):

$$\mathbb{P}_{\mathrm{rt}} = 0.8 + 5\,\mathbb{R}_{\mathrm{i}} \tag{7.2.11}$$

where $\mathbb{P}_{\mathrm{rt}} = \mathcal{A}_{\mathrm{v}}/\mathcal{B}_{\mathrm{v}} = \mathbb{R}_{\mathrm{ig}}/\mathbb{R}_{\mathrm{if}}$, $\mathcal{A}_{\mathrm{v}}$ is the vertical eddy viscosity, $\mathcal{B}_{\mathrm{v}}$ is the vertical eddy diffusivity, $\mathbb{R}_{\mathrm{ig}}$ is the gradient Richardson number and $\mathbb{R}_{\mathrm{if}}$ is the flux Richardson number defined as:

$$\mathbb{R}_{\mathrm{if}} = -\frac{g}{\rho_{\mathrm{o}}}\,\frac{\overline{\rho' w'}}{\overline{u' w'}\,\dfrac{\partial u}{\partial z} + \overline{v' w'}\,\dfrac{\partial v}{\partial z}} \tag{7.2.12}$$

All the above parametrizations were obtained by assuming locally stationary and homogeneous turbulence or an asymptotic approximation of the theoretical equations for steady homogeneous turbulence (e.g., Zilitinkevich and Esau). Equations 7.2.1 to 7.2.11 are plotted in 7.1 and 7.2.

From Figure 7.1b, it can be seen that both *BL* and *PP* equations give unrealistic results. The *PP* solution predicts infinite $\mathbb{R}_{if}$ for large $\mathbb{R}_{ig}$ and thus contradicts the assumption of local equilibrium of the turbulence ($\mathbb{R}_{if} < 1$). The *BL* parametrization predicts very low $\mathbb{R}_{if}$ numbers at any range of $\mathbb{R}_{ig}$ values. Therefore, both parametrizations have not been considered as good candidates for use in *M*^{2}*COPS*.

The *MA* equation also predicts unreasonably high values for $\mathbb{R}_{if}$ ($\mathbb{R}_{ig} \to 0.52$ for large values of $\mathbb{R}_{i}$) and in combination with the conclusions of Nunes Vaz and Simpson, it has been abandoned as well. The equation of Nakanishi [2001] is actually a modified version of the *MY* equation where the values of the coefficients were improved using *LES* calculations, therefore, both *NK* and *MY* are viewed as a unified approach. Both predict reasonable $\mathbb{R}_{if}$ values $\mathbb{R}_{ig} \to 0.25$ (*MY*) and $\mathbb{R}_{ig} \to 0.3$ (*NK*) for large $\mathbb{R}_{ig}$ values, generally within the acceptable ranges for $\mathbb{R}_{if}$.

As seen from Figures 7.1a and 7.1b, *SG* gives results identical to the ones produced by the *MY* type equations, except for the slight differences that appear in the region $10^{-2} < \mathbb{R}_{ig} < 0.293$. The value $\mathbb{R}_{ic} = 0.293$ is a critical value for the gradient Richardson number predicted by the *MY* parametrization. All three parametrizations are possible candidates for the *M*^{2}*COPS* parametrization of the $\boldsymbol{\kappa}$-$\boldsymbol{\epsilon}$ model, bearing in mind the conclusions of Nunes Vaz and Simpson [1994] that *MY* performs rather poorly in stably stratified flow environments.

From Figure 7.2a, it is clear that all equations agree in the region where $\mathbb{R}_{ig} < 0.1$. The differences are pronounced in the region $0.1 \leq \mathbb{R}_{ig} \leq 1$, which is considered as the crucial range for $\mathbb{R}_{ig}$ in oceanographic modeling (Large et al. [1994]). In this region the *ZL* type equations seem to give more reasonable results and not so sharp gradients in the profile (Figure 7.2a) for $\mathbb{R}_{if}$, while for large values of $\mathbb{R}_{ig}$ the *ZL* type equations are bounded by: $\mathbb{R}_{ig} \leq 0.2$. The linear approximation *ZLL* equation gives almost the same results as the *ZL* equation, except the very slight differences shown for the region where $0.1 \leq \mathbb{R}_{ig} \leq 1.0$ (Figure 7.2b).

As $\mathbb{R}_{ig} \to 0$, all the equations predict a neutral Prandtl number of about $\mathbb{P}_{rn} \approx 0.8$. *MY* gives $\mathbb{P}_{rn} = 0.75$, *NK* gives $\mathbb{P}_{rn} = 0.74 \approx 0.75$ the *ZL* and the *ZLL* equations give $\mathbb{P}_{rn} = 0.8$. These values for $\mathbb{P}_{rn}$ contradict the common assumption that $\mathbb{P}_{rn} \approx 1.0$. However, experimental values for the $\mathbb{P}_{rn}$

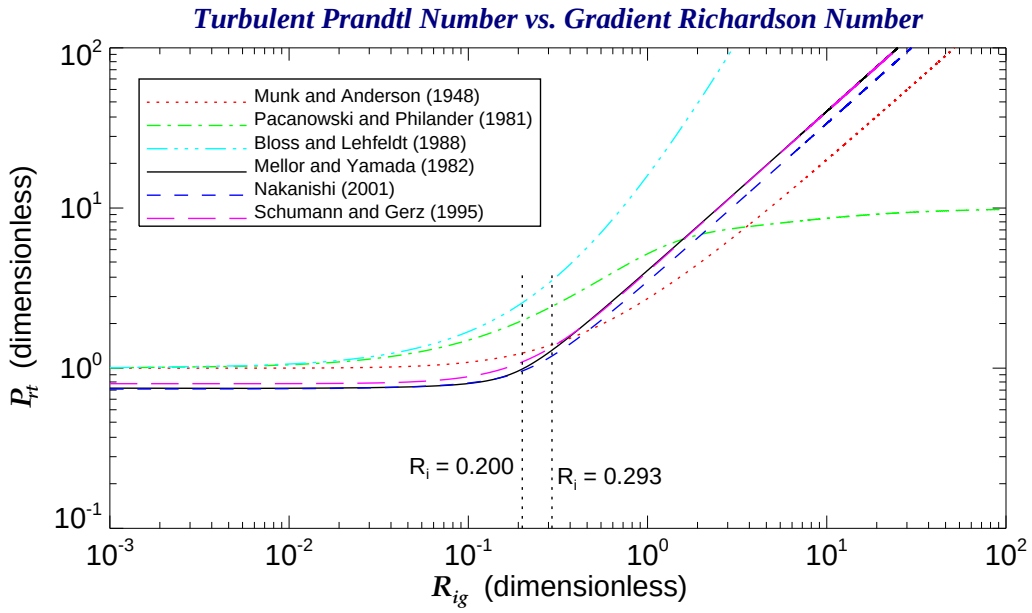

(a) Variation of the turbulent Prandtl number as a function of the gradient Richardson's number.

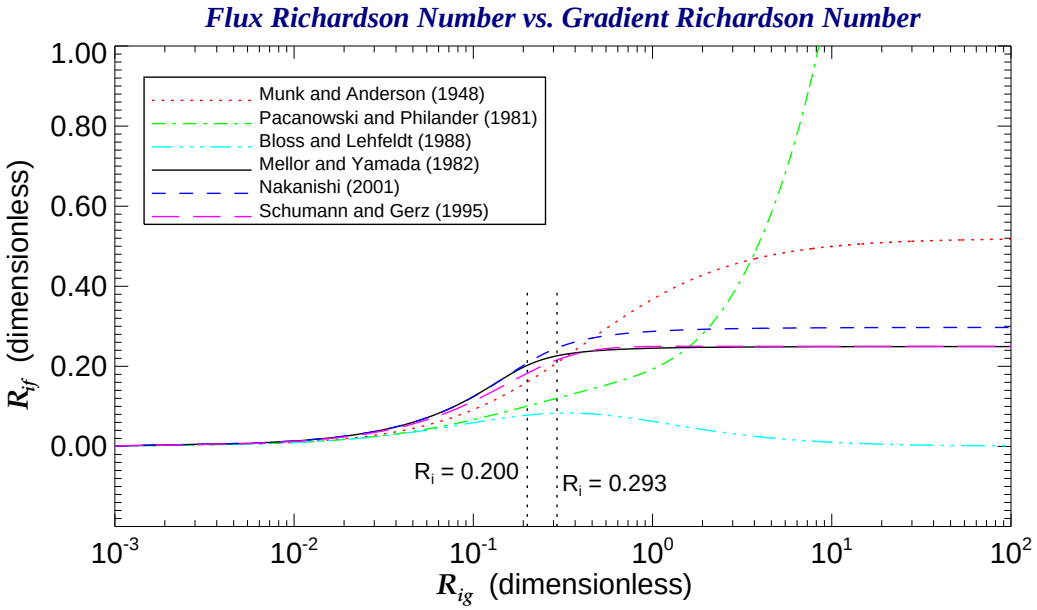

(b) Variation of the flux Richardson's number in relation to the gradient Richardson's number.

Figure 7.1 Plots of the turbulent Prandtl and the gradient Richardson's numbers using the equations of *(a)* Munk and Anderson (1948), *(b)* Pacanowski and Philander (1981), *(c)* Bloss and Lehfeldt (1988), *(d)* Mellor and Yamada (1982), *(e)* Nakanishi (2001) and *(f)* Schumann and Gertz (1995).

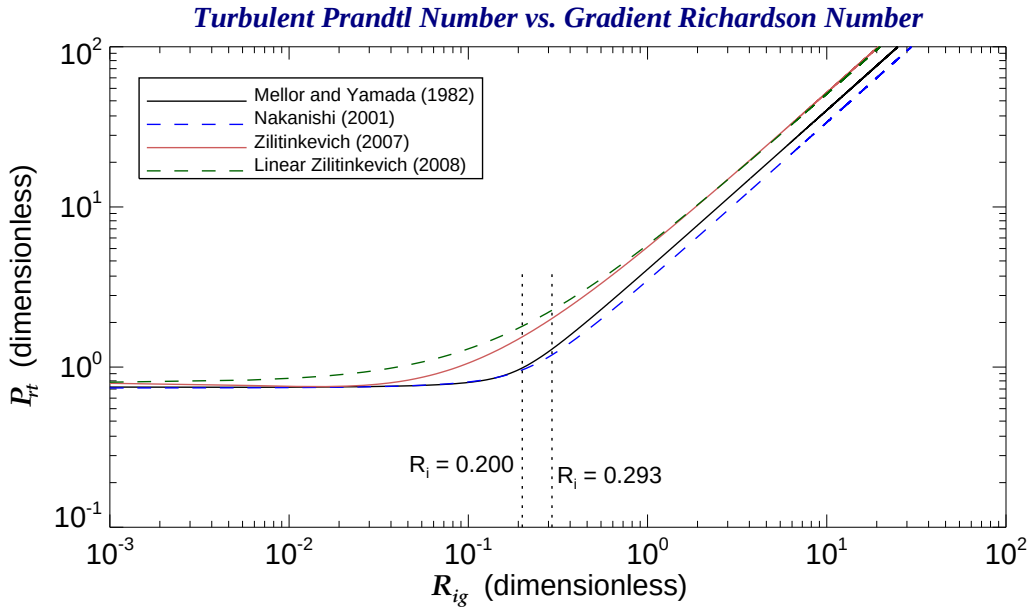

(a) Variation of the turbulent Prandtl number as a function of the gradient Richardson's number.

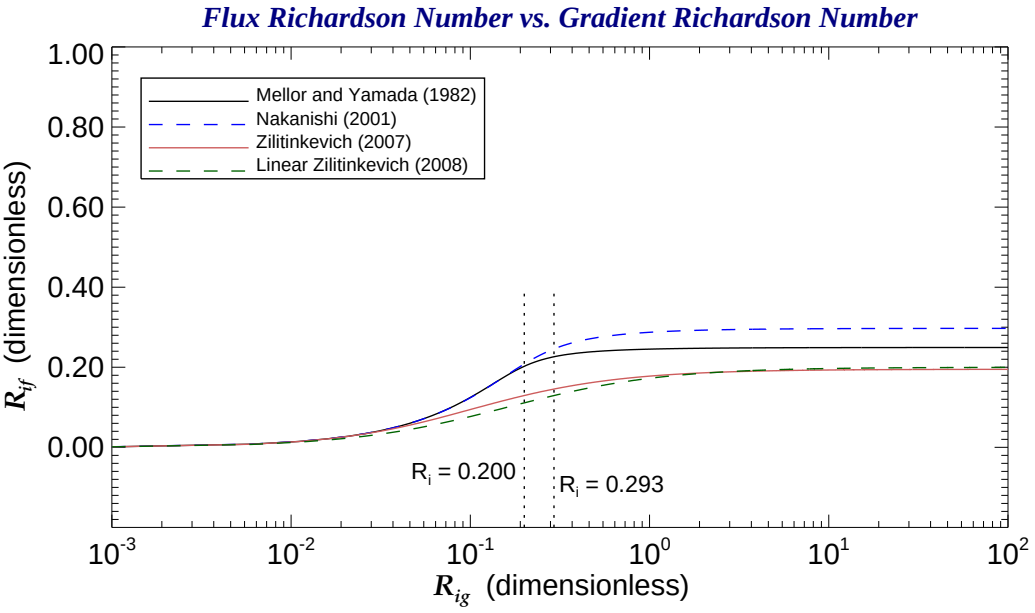

(b) Variation of the flux Richardson's number in relation to the gradient Richardson's number.

Figure 7.2 Comparative plots of the turbulent Prandtl and the gradient Richardson's numbers using the equations of *(a)* Mellor and Yamada (1982), *(b)* Nakanishi (2001), *(c)* Zilitinkevich (2007), *(d)* Zilitinkevich (linear) (2008).

reported in the literature are: 0.7-1.0 (Schumann and Gerz [1995]), $\mathbb{P}_{rt} = 0.7 - 0.9$ as $\mathbb{R}_{ig} \rightarrow 0$ and $\mathbb{P}_{rn} \approx 0.85$ (Shih et al. [2005]), 0.5-1.0 (Burchard [2002]), 0.6-1.0 (Grachev et al. [2007]), and $\mathbb{P}_{rn} \approx 0.85$ (Churchill [2002]). In view of the above findings the value adopted for the neutral Prandtl number in *M*^{2}*COPS* is $\mathbb{P}_{rn} = 0.8$.

The theory of Zilitinkevich et al. [2007] predicts a value of $\mathbb{P}_{rn} = 0.8$, while it predicts $\mathbb{R}_{if} \approx 0.2$ as $\mathbb{R}_{ig} \rightarrow \infty$, both values fully consistent with the observational findings discussed above. The results of this theory were compared against a significant amount of observational and *LES* produced datasets from independent sources, and exhibited very good agreement between the theoretical and observational results (Esau and Grachev [2007], Zilitinkevich et al. [2008, 2007]). Since the theory of Zilitinkevich and Esau predicts results very close to the experimental findings and also satisfies the conditions for $\mathbb{R}_{if}$ and $\mathbb{P}_{rn}$, it is the one adopted by *M*^{2}*COPS* for the $\mathbb{P}_{rt}$ parametrization in the κ-ϵ turbulence model.

The novel theory of Zilitinkevich and Esau [2007] and Zilitinkevich et al. [2008] uses a stress /flux approach (ASCE Task Committee on Turbulence Models in Hydraulic Computation [1988a,b]) that examines the budget of the turbulent kinetic energy (*TKE*) and the turbulent potential energy (*TPE*). Their equations are written in terms of the total turbulent energy (*TTE*, main energy budget) and the *TPE* (function of the potential temperature) instead of the classical approach that uses the *TKE* budget only. The expression for the $\mathbb{R}_{if}$, for the case of steady homogeneous turbulence, based on their theory is equation 7.2.10 and an approximation to this expression is the linear equation 7.2.11. Since the differences between the two equations are small (Figures 7.2a and 7.2b), the linear approximation *ZLL* has been chosen over the initial *ZL* to be used in *M*^{2}*COPS* to reduce the extensive computational load.

7.3 Stratification

Density stratification effects are incorporated in *M*^{2}*COPS* by: *(a)* the calculation of the density ρ as a function of the temperature (T), the salinity (S), the pressure (p) and the sediment concentration (C), and *(b)* the use of an augmented version of the standard κ-ϵ model in which certain terms and coefficients are defined in terms of the gradient Richardson number.

In the absence of sediment calculations, the water density is calculated as $\rho_w = \rho_w(T, S, p)$ using the equation of state. In the presence of sediment in the water, the mixture density ρ_m is

calculated using equation 2.7.3 (Zhou and McCorquodale [1992]). The form of equation 2.7.3 is valid for non-adhesive, quartz type sediments, that is, all sediment classes assume the same specific gravity. If sediments are modeled as having different properties, then equation 2.7.3 should be re-cast as:

$$\rho_m = \rho_w + \sum_{i=1}^{n_s} C_i \left(1 - \frac{1}{S_{pi} - 1}\right) \tag{7.3.1}$$

where n_s is the total number of sediment classes, C_i is the sediment concentration of the "i-th" sediment class with a specific gravity of S_{pi} and ρ_w is the water density calculated by the equation of state.

The κ-ϵ turbulence model used in *M*^{2}*COPS* is an augmented version of the standard version of the model, such that the buoyancy production or destruction term G, is calculated using the second of equations 7.1.7 and the turbulent Prandtl number is a function of the local gradient Richardson number defined as:

$$\mathbb{R}_{ig} = -\frac{g}{\rho_o} \frac{\left(\frac{\partial \rho}{\partial z}\right)}{\frac{\partial u}{\partial z}\cdot\frac{\partial u}{\partial z} + \frac{\partial v}{\partial z}\cdot\frac{\partial v}{\partial z}} \tag{7.3.2}$$

In the absence of waves, equation 7.3.2, is the same as equation 7.2.3 however, in view of the results of the present work, shear production of turbulence P will be adjusted to also include the wave effects. The eddy diffusivities ($\mathcal{B}_v$) are calculated from the eddy viscosities ($\mathcal{A}_v$) using a Richardson number type expression, as described by the second of the equations 7.1.4. In *M*^{2}*COPS* equation 7.1.4 is used only for the temperature and salinity calculations. In the case of sediment calculations, the mass diffusivities ($\mathcal{D}_v$) are calculated using the empirical formulations of van Rijn (van Rijn [1984a,b, 2007b,c]), as discussed in Section 2.8.4.

The formulation of the κ-ϵ model in *M*^{2}*COPS* uses the ϵ equation 7.1.6 with its coefficients defined as in equation 7.1.8. While the coefficients $c_{\epsilon 1}$, $c_{\epsilon 2}$ and σ_ϵ are well established empirical constants, the $c_{\epsilon 3}$ coefficient, as mentioned in Section 7.1, does not have a universally accepted constant value. Furthermore, $c_{\epsilon 3}$ is not a constant, but rather a function of the local conditions affected by the shear production, the buoyancy production/destruction and the mean flow characteristics. The $c_{\epsilon 3}$ term and other issues related to ocean turbulence modeling are currently being addressed within the framework of the Global Ocean Turbulence Model (*GOTM*, http://www.gotm.net/). *GOTM* is in active development and testing, but specifics like the $c_{\epsilon 3}$ issue are still remain unresolved.

Burchard and Baumert [1995], Burchard [2002], Baumert et al. [2000] and Peters and Baumert [2007], using the usual assumption of the local equilibrium of turbulence (stationarity and homogeneity), derived a value for $c_{\epsilon 3} = -1.4$. In Burchard and Baumert [1995], the authors derived this value from the condition that for the κ-ϵ model to reach steady state, the condition $c_{\epsilon 3} < 0$ be satisfied. Using the best fit approach, between modeled and measured data, it was concluded that the value $c_{\epsilon 3} = -1.4$ should be used in the standard κ-ϵ model. This result contradicts the accepted values $0 \leq c_{\epsilon 3} \leq -1.4$ (Rodi [1994], ASCE Task Committee on Turbulence Models in Hydraulic Computation [1988a,b]) used routinely in the κ-ϵ turbulence models today.

Following the suggestions of Burchard [2002], Peters and Baumert [2007] and Burchard [2001], van Rijn [2007b] examined the effects of sediment stratification using a value of $c_{\epsilon 3} = -1.4$. He found that by using this value for $c_{\epsilon 3}$ in the ϵ equation, the calculated results for the flow velocity and concentration profiles exhibit better agreement with the measured data. Van Rijn suggests the use of $c_{\epsilon 3} = -1.4$ in the κ-ϵ turbulence model to account for the sediment stratification effects. Setting aside the limited data set used for the comparisons, Figures 13a and 13b in van Rijn [2007b] show a good agreement for the concentration profile within the limits of the bottom boundary layer (~ 10 cm) and a fair to poor agreement in the region above the bottom boundary layer. The velocity profile in Figure 13b shows a fair to poor agreement with the measured data throughout the water column (with the best agreement reported at locations away from the bottom).

To further complicate matters, Baumert et al. [2000] states that standard κ-ϵ models augmented to account for stratification effects and using a value of $c_{\epsilon 3} < 0$, perform reasonably well only in the case of $\mathbb{R}_{ig} \ll 0.25$ (weak stable stratification). As the $\mathbb{R}_{ig}$ increases, the κ-ϵ model results (with $c_{\epsilon 3} < 0$) exhibit strong deviations from the measured data. In the same paper, they suggest the use of yet another value for $c_{\epsilon 3}$, that is: $c_{\epsilon 3} \approx 1/c_{\epsilon 1}$.

The work of Burchard and Baumert [1995], Baumert and Peters [2000] presents an advanced version of the κ-ϵ model that uses stress/flux algebraic formulations (see also ASCE Task Committee on Turbulence Models in Hydraulic Computation [1988a,b]) to derive an expression for $c_{\epsilon 3}$. This latest effort is the one actually implemented in *GOTM* and it is fully documented in Burchard [2002], but although it sounds promising, it is still in the development stage. In this advanced version of the κ-ϵ model, the G term is basically defined as the product of a functional form of $c_{\epsilon 3}$ with the buoyancy gradient. The function $c_{\epsilon 3}$ is related to the local conditions via $\mathbb{R}_{ig}$ representations, similar

to the representations that define the turbulent Prandtl number. The essence of all the above efforts in defining $c_{\epsilon 3}$ (and also the turbulent Prandtl number) is the concept of a critical $\mathbb{R}_{ic}$ above of which turbulence is completely suppressed by buoyancy.

Large et al. [1994] and Large and Gent [1999] in their analysis of the mixing processes at the boundaries and the interior of the ocean state that according to oceanic field measurements, the $\mathbb{R}_{ig}$ values rarely fall as low as the critical $\mathbb{R}_{ic}$ value; most often being in the range of 0.4-1.0. It is also shown in Ivey et al. [2008] that mixing in the ocean is still present beyond the $\mathbb{R}_{ic}$ value, as turbulent fluxes sustained by winds, waves and the local topography.

The brief analysis/discussion presented so far is not directed towards the incorporation of a new turbulence model in M^2COPS, but it is rather intended for the identification of possible error sources due to problematic turbulence formulations in the $\boldsymbol{\kappa}$-$\boldsymbol{\epsilon}$ model used. The inconclusive results about the $c_{\epsilon 3}$ issue presented in the literature prohibits the use of any suggested $c_{\epsilon 3}$ formulations, until universally accepted values are in place. In M^2COPS only stably stratified flows are modeled as usually done in marine hydrodynamic calculations, thus a value of $c_{\epsilon 3} = 0$ is used. For stably stratified calculations $G < 0$ it is assumed that $\partial\rho/\partial z < 0$, that is the fluid density increases with depth. There will be limited regions where $G > 0$, especially in the presence of sediments. In those regions the flow is treated as neutrally stratified and the turbulent Prandtl number assumes its neutral value.

7.3.1 Relative Effects of Stratification

As described in the previous Section, the calculations in a density stratified flow field are affected by the same scalars, temperature (T), salinity (S), pressure (p) and sediment concentration (C) that contribute to the evolution of the density field. The relevant contribution of each scalar to the stratification can be determined by using the equation of state in combination with equation 2.7.3. Equation 2.7.3 gives:

$$-\frac{1}{\rho_o}\frac{\partial \rho_m}{\partial z} = -\frac{1}{\rho_o}\frac{\partial \rho}{\partial z} - \frac{1}{\rho_o}\left(1 - \frac{1}{S_p - 1}\right)\frac{\partial C}{\partial z} \tag{7.3.3}$$

where in the absence of sediments: $\rho_m = \rho$. The term $\partial\rho/\partial z$ (< 0) is calculated from the equation of state, when $\rho = \rho(T, S, p)$:

$$-\frac{1}{\rho_o}\frac{\partial \rho}{\partial z} = -\frac{1}{\rho_o}\frac{\partial \rho}{\partial T}\frac{\partial T}{\partial z} - \frac{1}{\rho_o}\frac{\partial \rho}{\partial S}\frac{\partial S}{\partial z} - \frac{1}{\rho_o}\frac{\partial \rho}{\partial p}\frac{\partial p}{\partial z} \tag{7.3.4}$$

with:

$$\alpha = -\frac{1}{\rho_o}\left(\frac{\partial \rho}{\partial T}\right)_{S,p} ; \qquad \beta = \frac{1}{\rho_o}\left(\frac{\partial \rho}{\partial S}\right)_{T,p} ; \qquad K = -\frac{1}{\rho_o}\left(\frac{\partial \rho}{\partial p}\right)_{T,S} \tag{7.3.5}$$

where α is the thermal expansion coefficient, β is the salinity contraction coefficient and K is the isothermal compressibility coefficient (bulk modulus). Defining the scalar (Φ) related buoyancy frequency as:

$$N_\Phi^2 = -\frac{g}{\rho_o}\frac{\partial \rho}{\partial \Phi}\frac{\partial \Phi}{\partial z} \tag{7.3.6}$$

The combination of equations 7.3.3 and 7.3.4 gives:

$$N_\rho^2 = N_T^2 + N_S^2 + N_p^2 + N_C^2 \tag{7.3.7}$$

where:

$$N_\rho^2 = -\frac{g}{\rho_o}\frac{\partial \rho}{\partial z} ; \; N_T^2 = \alpha g \frac{\partial T}{\partial z} ; \; N_S^2 = -\beta g \frac{\partial S}{\partial z} ; \; N_p^2 = -Kg\frac{\partial p}{\partial z} ; \; N_C^2 = -\frac{g}{\rho_o}\left(1 - \frac{1}{S_p - 1}\right)\frac{\partial C}{\partial z} \tag{7.3.8}$$

and in terms of the gradient Richardson's number:

$$\mathbb{R}_{ig\rho} = \mathbb{R}_{igT} + \mathbb{R}_{igS} + \mathbb{R}_{igp} + \mathbb{R}_{igC} \tag{7.3.9}$$

Equations 7.3.7 or 7.3.9, break the vertical buoyancy profile in its four contributing components, thus helping in the identification of regions where stratification is controlled by one or another component or from a combination of individual contributions.

7.4 Oscillatory Surface Boundary Layer

The surface boundary layer is a thin (compared to the water depth) region below the free surface with a similar vertical structure as the bottom boundary layer. In the presence of surface waves, three regions comprise the wave affected surface region (Benilov and Ly [2002], Craig and Banner [1994]): *(a)* a wave-turbulent viscous layer where the production of turbulent energy due to the wave breaking exceeds the mean shear production, *(b)* a wave-turbulent diffusion layer where the wave motion effects are small, but still the turbulent diffusion exceeds the mean shear production, and *(c)* a logarithmic turbulent layer where the laws of wall turbulence are valid and the turbulent characteristics are controlled by the wave breaking and the dynamics in the overlying wave-turbulent layers. The above three layers comprise the upper part of the surface Ekman layer, a region defined as the constant stress layer. In this region, it is assumed that the mean current exhibits quasi-steady

characteristics that complement the constant stress law, thus allowing an analysis similar to the one for the wave-current bottom boundary layer.

The boundary layer equation 6.3.5 is valid for the area immediately below the free surface and strictly speaking is evaluated at the bottom of the viscous surface layer (Ardhuin et al. [2008b]). To determine the constant surface stress that the mean flow feels, equation 6.3.5 is integrated in the interval (z_{os}, δ_s), where z_{os} is the roughness height for the water side at the free surface and δ_s is the distance from the free surface to approximately the beginning of the surface turbulent logarithmic sublayer. Both parameters z_{os} and δ_s do not have established analytical expressions and are usually determined empirically, thus introducing additional uncertainty in the model calculations. Later in this Section a method of determining z_{os} is presented, but the calculation of δ_s is not well defined. Scaling arguments (Benilov and Ly [2002], Shen et al. [2000], Soloviev and Lukas [2003], Craig and Banner [1994], Wüest and Lorke [2003]) classify δ_s as a length of $O(10\,\mathrm{cm})$. In the subsequent derivations δ_s is regarded as the thickness of the surface thin layer where viscous and turbulent diffusion effects are important.

Integrating equation 6.3.5 over the vertical distance δ_s we obtain:

$$\underbrace{\mathcal{A}_v \frac{\partial \mathcal{U}_\alpha}{\partial \sigma}}_{(1)} = \underbrace{\mathcal{A}_v \frac{\partial \mathcal{U}_\alpha}{\partial \sigma}\bigg|_{\sigma=-z_{os}/D\approx 0}}_{(2)} \underbrace{- \int_{-\delta_s/D}^{-z_{os}/D} \left(\frac{D^2}{\rho_o} \frac{\partial p_{atm}}{\partial x_\alpha} + gD^2 \frac{\partial \zeta}{\partial x_\alpha} \right) d\sigma}_{(3)} \underbrace{- D \int_{-\delta_s/D}^{-z_{os}/D} \frac{\partial S_{\alpha\beta}}{\partial x_\beta} d\sigma}_{(4)} \tag{7.4.1}$$

where term (1) is evaluated at the distance δ_s below the free surface, term (2) is evaluated almost at the free surface, while the remaining terms represent the integral effects in the interval (z_{os}, δ_s), of their respective parameters. The individual terms in the r.h.s of equation 7.4.1 are evaluated as follows:

$$(2): \qquad \mathcal{A}_v \frac{\partial \mathcal{U}_\alpha}{\partial \sigma}\bigg|_{\sigma\approx 0} = \underbrace{\mathcal{A}_v \frac{\partial u_\alpha}{\partial \sigma}\bigg|_{\sigma=-z_{os}/D\approx 0}}_{\text{Eulerian part}} + \underbrace{\mathcal{A}_v \frac{\partial u_{st\alpha}}{\partial \sigma}\bigg|_{\sigma=-z_{os}/D\approx 0}}_{\text{Stokes part}} \tag{7.4.2a}$$

The Stokes part in equation 7.4.2a is actually the term $\nu_w \, \partial u_{st\alpha}/\partial\sigma\big|_{\sigma\approx 0}$ (ν_w is the water viscosity) that represents the viscous wave energy dissipation and has been lumped into the Reynolds flux term $\mathcal{A}_v \, \partial \mathcal{U}_\alpha/\partial\sigma$. Therefore:

$$\mathcal{A}_v \frac{\partial u_{st\alpha}}{\partial \sigma}\bigg|_{\sigma\approx 0} \approx \nu_w \frac{\partial u_{st\alpha}}{\partial \sigma}\bigg|_{\sigma\approx 0} = \nu_w (2kD)^2 U_{st\alpha} \frac{\sinh 2kD(1+\sigma)}{\sinh 2kD}\bigg|_{\sigma\approx 0} = \nu_w (2kD)^2 U_{st\alpha} \tag{7.4.2b}$$

The Eulerian part in equation 7.4.2a is:

$$\mathcal{A}_{\nu}\frac{\partial u_{\alpha}}{\partial \sigma}\bigg|_{\sigma\approx 0} = D\frac{\tau_{ca}}{\rho_{o}} = Du_{*\alpha}^{2} \tag{7.4.2c}$$

where u_{*} represents the friction velocity at the water side of the free surface interface. Putting all these together, term (2) is written as:

$$(2): \qquad \mathcal{A}_{\nu}\frac{\partial u_{\alpha}}{\partial \sigma}\bigg|_{\sigma\approx 0} = D\frac{\tau_{ca}}{\rho_{o}} + \nu_{w}\,(2kD)^{2}\,U_{st\alpha} \tag{7.4.2d}$$

$$(3): \qquad \int_{-\delta_{s}/D}^{-z_{os}/D}\Big(\frac{D^{2}}{\rho_{o}}\frac{\partial p_{atm}}{\partial x_{\alpha}} + gD^{2}\frac{\partial \zeta}{\partial x_{\alpha}}\Big)d\sigma = \Big(\frac{D^{2}}{\rho_{o}}\frac{\partial p_{atm}}{\partial x_{\alpha}} + gD^{2}\frac{\partial \zeta}{\partial x_{\alpha}}\Big)\int_{-\delta_{s}/D}^{-z_{os}/D}d\sigma$$

$$= (\delta_{s} - z_{os})\Big(\frac{D}{\rho_{o}}\frac{\partial p_{atm}}{\partial x_{\alpha}} + gD\frac{\partial \zeta}{\partial x_{\alpha}}\Big) \tag{7.4.3}$$

and term (4) is evaluated as:

$$(4): \qquad D\int_{-\delta_{s}/D}^{-z_{os}/D}\frac{\partial S_{\alpha\beta}}{\partial x_{\beta}}\,d\sigma \approx (\delta_{s} - z_{os})\;\frac{\partial S_{\alpha\beta}}{\partial x_{\beta}}\bigg|_{\sigma\approx 0} \tag{7.4.4}$$

The combination of equations 7.4.1, 7.4.2d, 7.4.3 and 7.4.4 gives:

$$\mathcal{A}_{\nu}\frac{\partial u_{\alpha}}{\partial \sigma} = \underbrace{D\frac{\tau_{ca}}{\rho_{o}}}_{(1)} + \underbrace{\Big\{\nu_{w}\,(2kD)^{2}\,U_{st\alpha} - (\delta_{s} - z_{os})\;\frac{\partial S_{\alpha\beta}}{\partial x_{\beta}}\bigg|_{\sigma\approx 0}\Big\}}_{(2)}$$

$$\underbrace{-\Big\{(\delta_{s} - z_{os})\Big(\frac{D}{\rho_{o}}\frac{\partial p_{atm}}{\partial x_{\alpha}} + gD\frac{\partial \zeta}{\partial x_{\alpha}}\Big)\Big\}}_{(3)} \tag{7.4.5}$$

where the r.h.s of equation 7.4.5 represents the wave induced constant total shear stress that also accounts for the possible variations of the atmospheric pressure. In equation 7.4.5, term (1) represents the direct wind input into the mean current that is calculated using the drag law, term (2) represents the wind input to the waves for the maintenance of their growth, and term (3) represents the contributions of the surface barometric terms. Assuming that near the surface, winds, currents and waves are co-linear and co-directional, sharing the direction of the generating winds, equation 7.4.5 can be written in terms of the total Lagrangian velocity as:

$$\mathcal{A}_{\nu}\frac{\partial \mathcal{U}}{\partial \sigma} = \underbrace{D\frac{\tau_{ca}}{\rho_{o}}}_{(1)} + \underbrace{\Big\{\nu_{w}\,(2kD)^{2}\,U_{st} - (\delta_{s} - z_{os})S_{R}\Big\}}_{(2)} - \underbrace{(\delta_{s} - z_{os})P_{B}}_{(3)} \tag{7.4.6}$$

where U_{st} is the vertically averaged Stokes drift velocity and:

$$S_R = S_R|_{\sigma\approx 0} = \left[\left(\frac{\partial S_{xx}}{\partial x} + \frac{\partial S_{xy}}{\partial y}\right)^2 + \left(\frac{\partial S_{yx}}{\partial x} + \frac{\partial S_{yy}}{\partial y}\right)^2\right]^{1/2} \tag{7.4.7a}$$

$$P_B = \left[\left(\frac{D}{\rho_o}\frac{\partial p_{atm}}{\partial x} + gD\frac{\partial \zeta}{\partial x}\right)^2 + \left(\frac{D}{\rho_o}\frac{\partial p_{atm}}{\partial y} + gD\frac{\partial \zeta}{\partial y}\right)^2\right]^{1/2} \tag{7.4.7b}$$

Assuming small spatial variations of P_A and ζ and taking into consideration the smallness of the term $(\delta_s - z_{os})$, the term $(\delta_s - z_{os})P_B$ in equation 7.4.6 can be neglected. Consistency requires that the similar terms in the bottom boundary layer formulation to be neglected as well. It is noted here that the atmospheric pressure gradients are still retained in the momentum equations. Using the definition of the kinematic stress (stress divided by the fluid density), equation 7.4.6 can conceptually be written as:

$$\tau_{tot} = \tau_c + \tau_w \tag{7.4.8}$$

where τ_{tot} is the total shear stress at the free surface, τ_c represents term (1) in equation 7.4.6 and τ_w represents term (2). The stress τ_{tot} is the shear stress that the mean flow feels near the free surface (a similar situation as with the bottom stresses) and it is the stress used for the definition of the boundary conditions in the momentum equations for a wave induced mean flow field. The wave induced stress τ_w is a complicated construct (equation 7.4.6), but it is evaluated using the expression derived by Janssen [2004] (see also Janssen [2008]):

$$\vec{\tau}_w = \rho_w \int_0^{2\pi}\int_0^{\infty} \beta \frac{\rho_{air}}{\rho_w}\left(\frac{u_\#}{c_p}\right)^2 \max\left[0,\ \cos(\theta - \theta_W)\right]^2 \mathcal{E}(\mathring{\sigma},\ \theta)\,\mathring{\sigma}^2\,\frac{\vec{k}}{k}\,d\mathring{\sigma}\,d\theta_W \tag{7.4.9}$$

where ρ_{air} and ρ_w are the densities of the air and the water, respectively, β is the Miles constant (Miles [1957]), $u_\#$ is the friction velocity at the air side of the free surface and c_p is the wave phase speed.

7.4.1 Wave Breaking

Waves break and they more often do so in shallow waters due to the bottom topography variations. In deep waters waves also break, a phenomenon known as white capping, and in both cases the breaking waves inject turbulent kinetic energy into the mean flow. As noted in Craig [2005], breaking waves act as a source of turbulent kinetic energy at the free surface and the phenomenon is

modeled by modifying of the turbulence closure model (Craig [2005], Mellor and Blumberg [2004], Craig and Banner [1994], Craig [1996], Benilov and Ly [2002], Jones and Monismith [2008]).

The modifications of the κ-ϵ turbulence model, used in M^2COPS, to account for the effects of wave breaking follow the work of Craig and Banner [1994] and Craig [1996], as outlined in Burchard [2001]. In M^2COPS, the κ-ϵ model uses surface boundary conditions for κ and ϵ as defined by the first of equations 7.1.13 and the first of equations 7.1.14 respectively. The friction velocity u_* already accounts for the effects due to the wave growth and it is calculated from the total surface shear stress (equation 7.4.8). Burchard [2001] used the results of Craig and Banner [1994] and Craig [1996] to calculate the steady state solutions for κ and ϵ as follows:

$$\kappa = \frac{u_*^2}{\sqrt{c_\mu}} \left[1 + \gamma\, \alpha_{\mathrm{cb}}\, c_\mu^{1/4} \left(\frac{3\sigma_\kappa}{2} \right)^{1/2} \left(\frac{z' + z_{\mathrm{os}}}{z_{\mathrm{os}}} \right)^{-m} \right]^{2/3} \tag{7.4.10}$$

$$\epsilon = \frac{u_*^3}{\mathbf{k}\,(z' + z_{\mathrm{os}})} \left[1 + \gamma\, \alpha_{\mathrm{cb}}\, c_\mu^{1/4} \left(\frac{3\sigma_\kappa}{2} \right)^{1/2} \left(\frac{z' + z_{\mathrm{os}}}{z_{\mathrm{os}}} \right)^{-m} \right] \tag{7.4.11}$$

$$m^2 = \frac{3}{2} \frac{c_\mu^{1/2}\, \sigma_\kappa}{\mathbf{k}^2} \tag{7.4.12}$$

where $\mathbf{k} = 0.41$ is the von Kármán constant and c_μ, σ_κ are the usual κ-ϵ model parameters. The coefficient γ in equations 7.4.10 and 7.4.11 is assigned a value of 0, if wave breaking is not modeled and a value of 1 otherwise. The elevation $z' + z_{os}$ below the free surface is assigned the value: $z' + z_{\mathrm{os}} = \Delta z/2$, as in equation 7.1.14, while the roughness height z_{os} is calculated by the Charnock type equation (Mellor and Blumberg [2004]):

$$z_{os} = \max\left(\frac{0.14\nu}{u_\#},\, \alpha_{\mathrm{ch}}\, \frac{u_\#^2}{g} \right); \quad \alpha_{\mathrm{ch}} = 0.45\, \frac{u_\#}{c_p} \tag{7.4.13}$$

where $u_\# = (\tau/\rho_{\mathrm{air}})^{1/2}$ and c_p is the wave phase speed. The coefficient α_{cb} in equations 7.4.10 and 7.4.11 is calculated (Mellor and Blumberg [2004]) as a curve fit of the observation data in Terray et al. [1996]:

$$\alpha_{\mathrm{cb}} = 15\, \frac{c_p}{u_\#}\, \exp\left[-\left(0.04\, \frac{c_p}{u_\#} \right)^4 \right] \tag{7.4.14}$$

In Burchard [2001], is stated that in addition to the above modifications, the term $c_{\epsilon 3}$ needs to be modified as well, otherwise the κ-ϵ model will produce inaccurate results related to the wave breaking. The analytical expression for $c_{\epsilon 3}$ is difficult to be derived in the presence of both wave breaking and shear production and the suggestion in Burchard [2001] is to use the linear fit for $c_{\epsilon 3}$

shown in his Figure 1. For $P/\epsilon = 0$, $\sigma_\epsilon = 1.111$, and for $P/\epsilon = 1$ it is $\sigma_\epsilon = 2.4$, therefore, the linear fit gives:

$$\sigma_\epsilon = 1.289\,\frac{P}{\epsilon} + 1.111 \tag{7.4.15}$$

where:

$$\frac{\epsilon}{P} = 1 + \gamma\,\alpha_{\mathrm{cb}}\,c_\mu^{1/4}\left(\frac{3\sigma_\kappa}{2}\right)^{1/2}\left(\frac{z' + z_{\mathrm{os}}}{z_{\mathrm{os}}}\right)^{-m} \tag{7.4.16}$$

7.5 Alternative Representation of the *WCBBL*

As discussed in Chapter 6 the effects of the waves near the bed can be divided into: *(a)* effects due to the wave growth expressed in the form of the bottom wave radiation stresses, and *(b)* effects due to the interaction of the waves with the bottom sediments in the region within the wave-current bottom boundary layer. If these effects are not resolved within the hydrodynamic model, then a wave-current bottom boundary layer model should be used to describe them. The *WCBBL* model calculates z_{o}, z_{e} and z_{ec} and exports these parameters in the hydrodynamic model for the calculation of the wave enhanced bottom shear stresses. This approach requires the calculation of the thickness of the *WCBBL* and the matching of the flow velocities above and inside the *WCBBL* at $z = \delta_{cw}$.

Mellor [2002] proposed an alternative approach that actually resolves these effects within the hydrodynamic model by introducing an additional production term in the turbulence model that possibly eliminates a significant overhead in the calculations performed by the *WCBBL* model. It should be noted here that this approach takes care of only the effects due to the wave-bottom interaction in the *WCBBL* and not the effects due to the wave growth (radiation stresses).

The effects due to the wave growth are easily included, as they can be lumped into the bottom shear stresses, as long as δ_{cw} is known and subsequently introduced into the hydrodynamic and turbulence model through their respective bottom boundary conditions. The thickness δ_{cw} is calculated using equations 6.7.14 and 6.7.15 as before, and the wave induced shear stresses at the bottom are calculated using equations 6.7.16 and 6.7.17.

The bottom physical roughness k_{b} is still calculated using the methods presented in Section 2.8.1, while the current induced bottom shear stress is calculated using the drag law:

$$u_* = |\boldsymbol{u}_{\mathbf{h}}|_r \frac{\mathbf{k}}{\ln\left(\frac{z_r}{z_{\mathrm{o}}}\right)}\,; \qquad \mathrm{r} = \text{reference location} \tag{7.5.1}$$

Finally, the angle between the "current" and the "wave" is calculated using equation 6.7.20. Therefore, all the parameters required for the calculation of the enhanced bottom shear stresses due to the wave growth are known and the calculation steps are outlined in Chapter 6.

The remaining part includes the effects due to the wave-bottom interactions that introduce additional turbulence into the main flow. Here is used the approach described in Mellor [2002], which is based upon a turbulence production term P_{wb} defined as:

$$\left(\frac{P_{wb}}{A_{wb}^2}\right)^{1/3} = \tilde{\tilde{\sigma}}\, F_\phi\, F_{z'} \tag{7.5.2a}$$

$$P_{wb} = \tilde{\tilde{\sigma}}^3 A_{wb}^2\, F_\phi^3\, F_{z'}^3 \tag{7.5.2b}$$

$$F_\phi = 1.22 + 0.22\, \cos 2\phi \tag{7.5.3}$$

$$F_{z'} \geq 0\ ; \quad F_{z'} = \alpha_0 + \alpha_1 \ln\left(\frac{z'}{A_{wb}}\right) + \alpha_2 \ln^2\left(\frac{z'}{A_{wb}}\right) \tag{7.5.4}$$

$$\alpha_0 = -0.0488 - 0.0102\, A_{z_o} \tag{7.5.5a}$$

$$\alpha_1 = 0.02917 - 0.00253\, A_{z_o} \tag{7.5.5b}$$

$$\alpha_2 = 0.01703 + 0.00273\, A_{z_o} \tag{7.5.5c}$$

$$A_{z_o} = 1.125\left[\log_{10}\left(\frac{z_o}{A_{wb}}\right) + 5\right] + 0.125\left[\log_{10}\left(\frac{z_o}{A_{wb}}\right) + 5\right]^4 \tag{7.5.5d}$$

where z' represents the vertical z coordinate referenced relative to the bottom ($z' = 0$ at the bottom), A_{wb} is the bottom wave excursion amplitude (a wave model output parameter) and z_o is the bottom roughness height determined by the methods described earlier. To be consistent with the M^2COPS coordinate system ($z = 0$ at the mean water level), $z' = 0$ is replaced in equations 7.5.2a through 7.5.6 by $z' \rightarrow z + h$ while, in σ coordinates z' is replaced by: $z' \rightarrow (1 + \sigma)D$.

It is noted that the expressions 7.5.2a, 7.5.3 and 7.5.4 were derived under "wave" only conditions. The overall goal is to replace the *WCBBL* model in the hydrodynamic model by a simple

modification of the turbulence model. The suggestion is that the shear production term in the turbulence model be modified as:

$$P = \mathcal{A}_v \frac{\partial u_\alpha}{\partial z}\frac{\partial u_\alpha}{\partial z} + P_{wb} \tag{7.5.6}$$

Representing P_{wb} as: $\mathcal{A}_v^* (\partial u_\alpha/\partial z)(\partial u_\alpha/\partial z)$, the terms in the r.h.s in equation 7.5.6 can be combined together through the modified eddy viscosity $\mathcal{A}_v' = \mathcal{A}_v + \mathcal{A}_v^*$, where $\mathcal{A}_v^*$ is used to model the wave-bottom interactions in the *WCBBL* and the final modified eddy viscosity $\mathcal{A}_v'$ is used to represent all the shear turbulence production in the water column. Using equation 7.5.2b P_{wb} can be written as:

$$P_{wb} = \mathcal{A}_v^* \frac{\partial u_\alpha}{\partial z}\frac{\partial u_\alpha}{\partial z} = \tilde{\tilde{\sigma}}^3 A_{wb}^2 F_\phi^3 F_{z'}^3 \tag{7.5.7}$$

and assuming that near the bottom the direction of the current is independent of the depth, equation 7.5.7 gives:

$$\mathcal{A}_v^* \frac{\partial |\boldsymbol{u}_\mathbf{h}|}{\partial z}\frac{\partial |\boldsymbol{u}_\mathbf{h}|}{\partial z} = \tilde{\tilde{\sigma}}^3 A_{wb}^2 F_\phi^3 F_{z'}^3 \tag{7.5.8}$$

Evaluation of 7.5.8 near the bottom, with $\lim_{z\to z_o} \mathcal{A}_v^* (\partial |\boldsymbol{u}_\mathbf{h}|/\partial z) = u_{*cw}^2$ equation 7.5.8 gives:

$$u_{*cw}^2 \frac{\partial |\boldsymbol{u}_\mathbf{h}|}{\partial z} = \tilde{\tilde{\sigma}}^3 A_{wb}^2 F_\phi^3 F_{z'}^3 \tag{7.5.9a}$$

and integration of 7.5.9a gives:

$$u_{*cw}^2 \int_{z_o}^{z} \partial |\boldsymbol{u}_\mathbf{h}| = \tilde{\tilde{\sigma}}^3 A_{wb}^2 F_\phi^3 \int_{z_o}^{z} F_{z'}^3\, dz\,; \quad |\boldsymbol{u}_\mathbf{h}|_{z=z_o} = 0 \quad \Longrightarrow \quad u_{*cw}^2 |\boldsymbol{u}_\mathbf{h}| = \tilde{\tilde{\sigma}}^3 A_{wb}^2 F_\phi^3 \int_{z_o}^{z} F_{z'}^3\, dz \tag{7.5.9b}$$

As in *WCBBL* model, near the bottom, we apply equation 6.7.5 (without stratification), therefore:

$$|\boldsymbol{u}_\mathbf{h}| = \frac{u_{*c}^2}{\mathbf{k}\, u_{*cw}} \ln\left(\frac{z'}{z_o}\right) \quad \Longrightarrow \quad u_{*cw} = \frac{u_{*c}^2}{\mathbf{k}\, |\boldsymbol{u}_\mathbf{h}|} \ln\left(\frac{z'}{z_o}\right) \tag{7.5.9c}$$

Combination of equations 7.5.9b and 7.5.9c yields:

$$u_{*c}^2 = \frac{\mathbf{k}\, |\boldsymbol{u}_\mathbf{h}|^{1/2}}{\ln(z'/z_o)}\, \tilde{\tilde{\sigma}}^{3/2} A_{wb}\, F_\phi^{3/2} \Big[\int_{z_o}^{z} F_{z'}^3\, dz\Big]^{1/2} \tag{7.5.10}$$

where $\tilde{\tilde{\sigma}}$, A_{wb} are wave model output parameters, $z' = z_r$ is defined as the location where the flow velocity is matched and $|u|$ is the flow velocity at $z' = z_r$. Usually z_r is taken as the half grid point above the bottom. Equation 7.5.10 defines a modified bottom friction velocity enhanced by the wave-bottom interactions within the *WCBBL*. Combination of equations 7.5.9c and 7.5.10 produces:

$$u_{*cw} = |\boldsymbol{u}_\mathbf{h}|^{-1/2}\, \tilde{\tilde{\sigma}}^{3/2} A_{wb}\, F_\phi^{3/2} \Big[\int_{z_o}^{z} F_{z'}^3\, dz\Big]^{1/2} \tag{7.5.11}$$

and this equation gives the contribution of the *WCBBL* produced turbulence in the bottom friction velocity. Equation 7.5.10 is used as a boundary condition in both the turbulence model and in the hydrodynamic model. To include the effects due to the wave growth and/or barometric variations, equation 7.5.10 should be modified such that: $z'/z_o \rightarrow (z' + z_e - z_o)/z_e$, where z_e is calculated as in Chapter 6. In principle, the integral in equations 7.5.10 and 7.5.11 should be evaluated in the interval (z_o, δ_{cw}), where δ_{cw} is the thickness of the *WCBBL*. The flow velocity is still matched at the top of the *WCBBL* and it is approximated as the velocity at $z' = z_r$.

Now, let $I_{z'}$ represent the integral term in equation 7.5.11. First, $I_{z'}$ should be evaluated numerically, since the exact integration produces a very complicated term. Second, δ_{cw} should be determined by an iterative process after $I_{z'}$ is evaluated at $z' = \delta_{cw}$. This process is very complicated however, an approximate value for $I_{z'}$ $(z' = \delta_{cw})$ can be calculated from the equation given in (Mellor [2002]) for the wave energy dissipation $\mathcal{D}_b$ due to the bottom sediments in the *WCBBL*:

$$\mathcal{D}_b = \tilde{\tilde{\sigma}}\, U_{wb}^2 \int_{z_o}^{\delta_{cw}} F_z^3\, dz \approx 0.029 \cdot 2^{\log_{10}(z_o/A_{wb})} \tag{7.5.12}$$

Using the value $I_{z'}$ $(z' = \delta_{cw})$ from equation 7.5.12, u_{*c} and u_{*cw} can be easily computed from equations 7.5.10 and 7.5.11, respectively. The thickness δ_{cw} of the *WCBBL* is still determined iteratively, as described in Section 6.9 using equation 6.7.14.

While Mellor's approach introduces a degree of complexity in the calculations similar to the *WCBBL* model described in Chapter 6, it has the advantage of not requiring the exact matching of the flow velocities at the top of the *WCBBL*. This is a very important consequence since the commonly used practice in the application of the *WCBBL* formulation is to match the flow velocities at the half grid point above the bottom. Depending upon the total depth of the flow field, the vertical grid size and the vertical coordinate transformation used, the half grid point might be further away from the top of the *WCBBL* (in deeper waters), or it might be within the *WCBBL* (in shallower water). Despite the fact that the functions F_ϕ and F_z still do not have a universally accepted form, Mellor's *WCBBL* approach is implemented in *M*^{2}*COPS* as an option so that this alternative *WCBBL* formulation can be closer investigated. Upon successful evaluation, it is expected to replace the currently used *WCBBL* model.

CHAPTER 8

FIELD DATA

The development of the newly enhanced prediction system, as well as the analysis of the model results requires that three levels of data need to be considered: *(a)* input data for the model forcing and the free surface boundary conditions, *(b)* data to be used for the internal model calculations during the initial and intermediate computational stages (e.g., initialization of the wave field parameters, suspended and bottom sediment calculations, heat flux calculations), and *(c)* data for the validation of the model results during specified skill tests.

8.1 Meteorological Data

The principal source of the meteorological data is the Marine Observation System (*MAROBS*, http://coastwatch.glerl.noaa.gov/marobs/). The dataset used here was obtained from the Great Lakes Forecasting System *MAROBS* database and consists of more than a decade of archived data. Eleven years (1991 to 2001) of meteorological records were used to examine long term or recurring patterns in the weather data and to extract long term mean values of parameters such as the barometric pressure.

The *MAROBS* data contain values for: *(a)* the wind (speed and direction), *(b)* the ambient air and dew point temperatures and cloud cover (used for the calculation of the surface heat fluxes), and *(c)* the barometric pressure (directly incorporated into the model calculations). Details for the format of the data and the location of the various weather stations can be found at http://coastwatch.glerl.noaa.gov/marobs/, while the more specific technical information can be found in the Federal Meteorological Handbook No. 1 (FMH 1 [2005]).

The *MAROBS* data are reported at stations scattered all over the Great Lakes (as shown in Figure 8.1 for Lake Michigan), with a reporting frequency up to five times per hour. The data can

be acquired every hour, as hourly averaged values, and subsequently be decoded to produce the field of the meteorological parameters. During this stage, the data are adjusted (where applicable) to: *(a)* include the effects of the stability of the *ABL* and account for the transition from land to water, and *(b)* a common reference height of 10 m above the mean water level.

Data gaps, due to the fact that not all the weather stations report data continuously, are filled using a simple linear interpolation in time with a variable interpolation window width of up to three days. The next step requires the production of model compatible, gridded meteorological fields therefore, the data are spatially interpolated on the $2x2$ km Lake Michigan grid to produce these fields. Here the natural neighbor interpolation technique (Watson [1992]), as implemented in the natural neighbor algorithms by Sambridge et al. [1995] (see Section 10.5.1), is used to create the spatial interpolation.

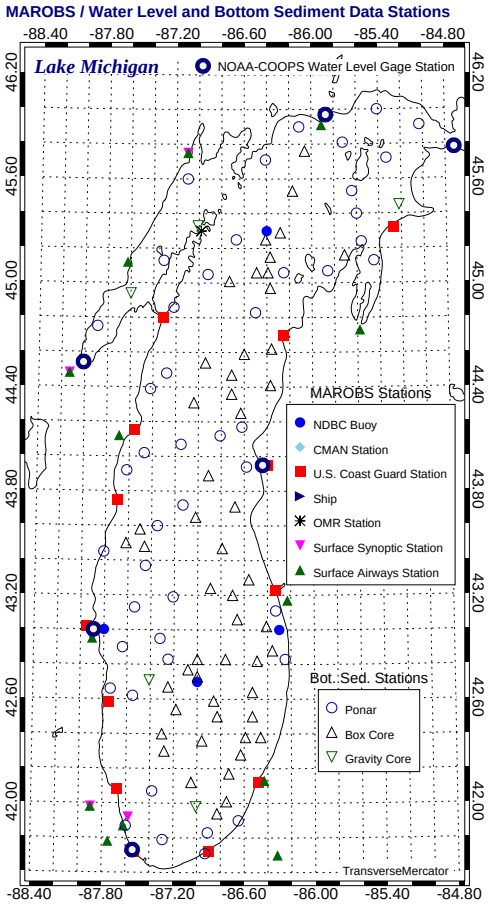

Figure 8.1 *MAROBS, NOAA-COOPS* stations and bottom sediment sampling locations.

8.1.1 Wind Field

The *MAROBS* wind observations are reported as wind speed and direction pairs where the wind speed is in knots (1 kn = 0.514444 m/s) and the wind direction is defined as the direction (measured clockwise from the true North) the wind is blowing from. The wind speeds considered here range from calm (0 – 1 m/s) to violent storms (30 m/s), according to the Beaufort scale shown in Table 8.1 (WMO-No. 702 [1998]), although a minimum wind speed of 0.01 m/s is imposed to the data.

Beaufort number	Descriptive term	Equivalent wind speed	Intervals	
		m/s	m/s	kn
0	Calm	0.8	0–1	0–2
1	Light air	2.0	2	3–5
2	Light breeze	3.6	3–4	6–8
3	Gentle breeze	5.6	5–6	9–12
4	Moderate breeze	7.8	7–9	13–16
5	Fresh breeze	10.2	9–11	17–21
6	Strong breeze	12.6	12–14	22–26
7	Near gale	15.1	14–16	27–31
8	Gale	17.8	17–19	32–37
9	Strong gale	20.8	19–22	38–43
10	Storm	24.2	23–26	44–50
11	Violent storm	28.0	26–30	51–57
12	Hurricane		31–	58–

Table 8.1 Beaufort wind scale.

The wind observations are modified to account for the land to water transition (wind speeds are generally lower over land), as referenced in Schwab and Morton [1984], Liu and Schwab [1987] and CEM II [2006], using the following equations (Schwab [1978]):

$$U_W = U_L \cdot \left(1.2 + \frac{1.85}{U_L}\right) \cdot \left[1.0 - \frac{\Delta T}{|\Delta T|}\left(\frac{|\Delta T|}{1920}\right)^{1/3}\right] \tag{8.1.1}$$

$$\Delta\theta = (1.25 - 1.5\,\Delta T) - U_W \cdot (0.38 - 0.03\,\Delta T) \tag{8.1.2}$$

where U_L and U_W represent the over-land and over-water wind speeds (m/s), respectively, $\Delta T = T_{air} - T_w$ is the air-water temperature difference (^{O}C) and $\Delta\theta$ is the angle between the over-land and the over-water winds (deg, measured clockwise).

The measurements are further adjusted to a common reference height of 10 m above the mean water level, according to the profile methods described in Section 2.5.1, equation 2.5.18 (*ABL* stability effects are included). The corrected wind observations are then spatially interpolated to produce the 2*x*2 km Lake Michigan hourly wind fields.

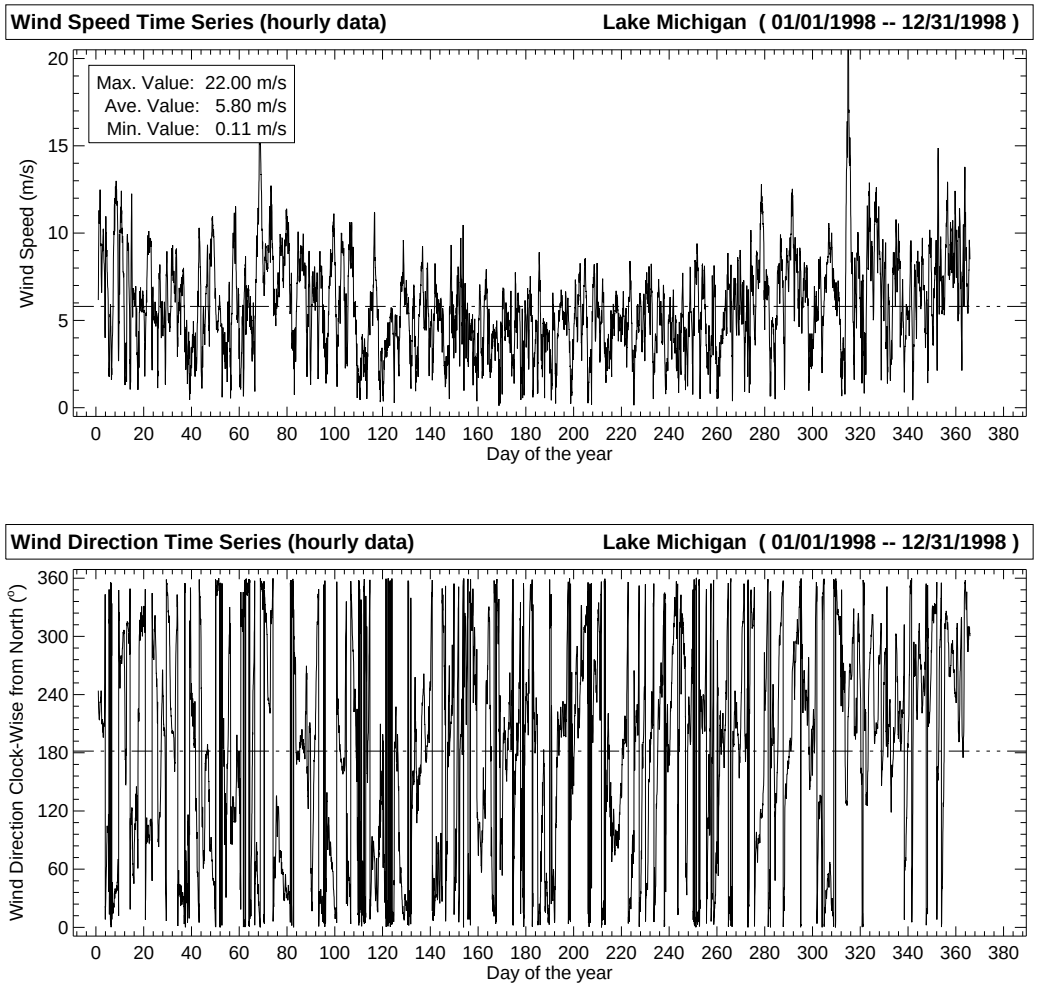

Figure 8.2 Time series of the hourly averaged wind speed and direction (1998).

The plots in Figure 8.2, show time series of lake-wide averaged hourly wind speeds and directions. From these plots, based on the meteorological definition for the seasons of the year, one can identify for analysis: *(a)* two Winter storm events (01/07-01/10 and 12/22-12/25, 1998), *(b)* two Spring storm events (03/08-03/11 and 04/08-04/09), *(c)* two Summer storm events (05/31-06/03 and 07/03-07/06), and *(d)* two Autumn storm events (10/04-10/07, and 11/08-11/11).

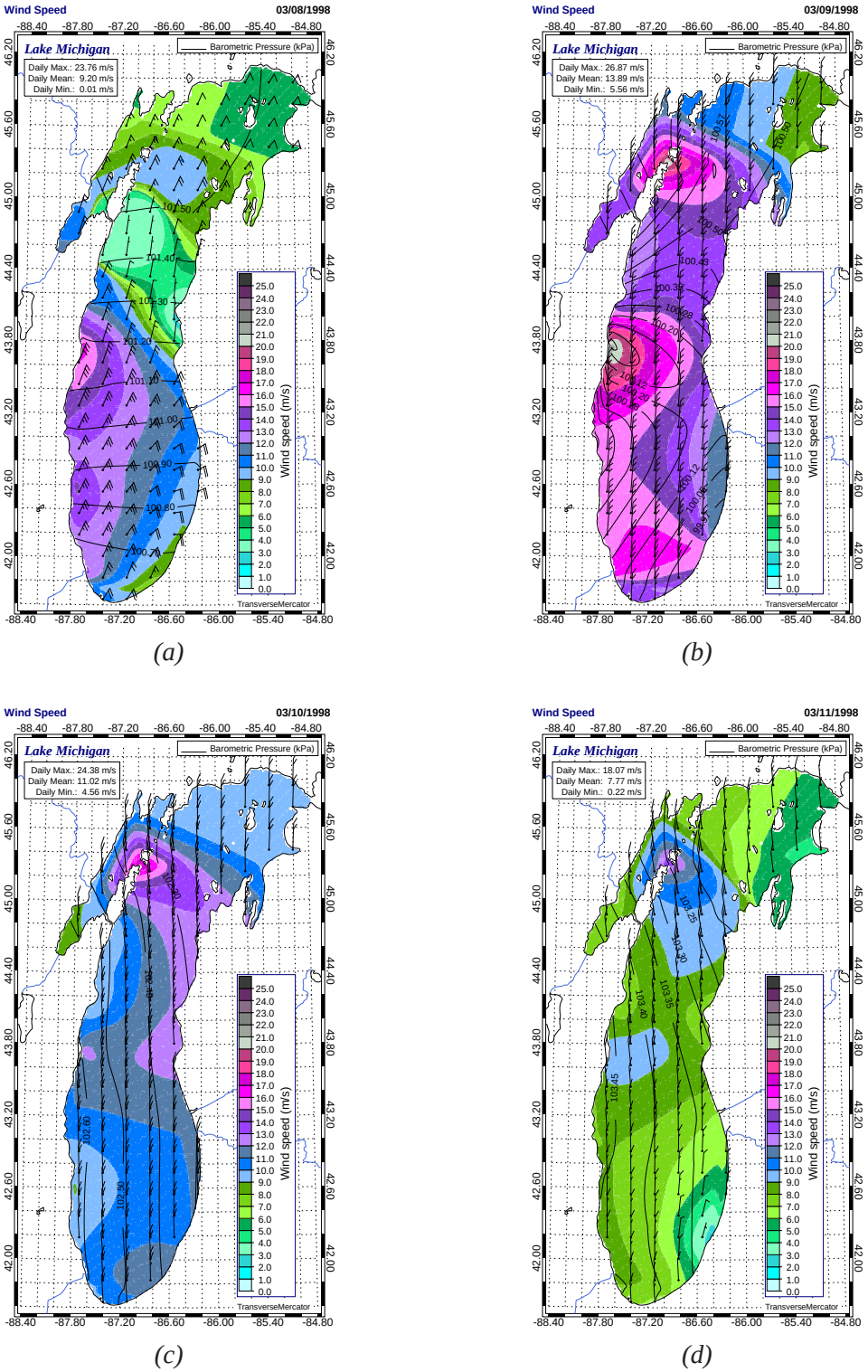

Figure 8.3 Mean daily wind speed distribution during the March 8-11, 1998 storm event in Lake Michigan.

The storm chosen to be examined in the present study is the early Spring storm ((03/08-03/11), which is associated with the appearance of the Spring plume. The wind distribution maps (Figure 8.3) show the direction the intensity of the wind and their changes during the storm event. On March 8th and 9th the wind direction as indicated by the wind barbs is southwestward due to the Northeastern blowing winds. The direction changes southward on March 10th and 11th and the winds become Northerly. The storm initially covers the southern area of the lake and gradually advances to cover the whole lake, while the intensity of the winds increases from around 12 m/s to around 17 m/s (that is, from Strong Breeze to Gale in the Beaufort scale). Affected from the storm areas in the Lake are all those confined between the Manitowoc and Lake counties, that is the South-Western shores. Most heavily affected is Sheboygan County where the wind intensity on March 9th reaches $20 - 21$ m/s (Storm in the Beaufort scale).

8.1.2 Air and Dew Point Temperatures

The importance of the air-water temperature differences in the calculation of the surface drag coefficients and the heat fluxes has been demonstrated in Sections 2.5.1 and 2.6, respectively. The temperatures are reported in the *MAROBS* dataset in ^{o}C and they are filtered to include temperature values between $-40\,^{o}$C and $40\,^{o}$C.

Since, the dew point temperature observations are only available from land stations, the temperatures are corrected according to the methods described in Philips and Irbe [1978] as referenced in Beletsky and Schwab [2001]. The over-water dew point temperatures are estimated from the over-land values (assuming neutral *ABL* stability) by the following empirical equation:

$$T_{dw} = -1.31 + 0.7\,T_{dl} + 0.35\,T_{w} \tag{8.1.3}$$

where T_{dw} and T_{dl} are the dew point temperatures over water and over land respectively (^{o}C) and T_{w} is the lake-wide averaged water surface temperature (^{o}C). The air temperatures reported from the land stations are similarly adjusted using the following empirical formula (Beletsky and Schwab [2001]):

$$T_{air} = 0.4\,T_{airl} + 0.6\,T_{w} \tag{8.1.4}$$

The results of the interpolated, lake-wide averaged, air and dew point temperatures are given in Figure 8.4. The yearly averaged air and dew point temperatures for 1998, are about $10\,^{o}$C and $6\,^{o}$C respectively with the highest values observed during the month of July.

Figures 8.5 and 8.6, present the air and dew point temperature maps for Lake Michigan for the March 8-11 storm event. In these maps, the effect of the storm is clearly shown as colder air masses are being transported by the wind over the lake, resulting to the gradual drop of the air temperatures.

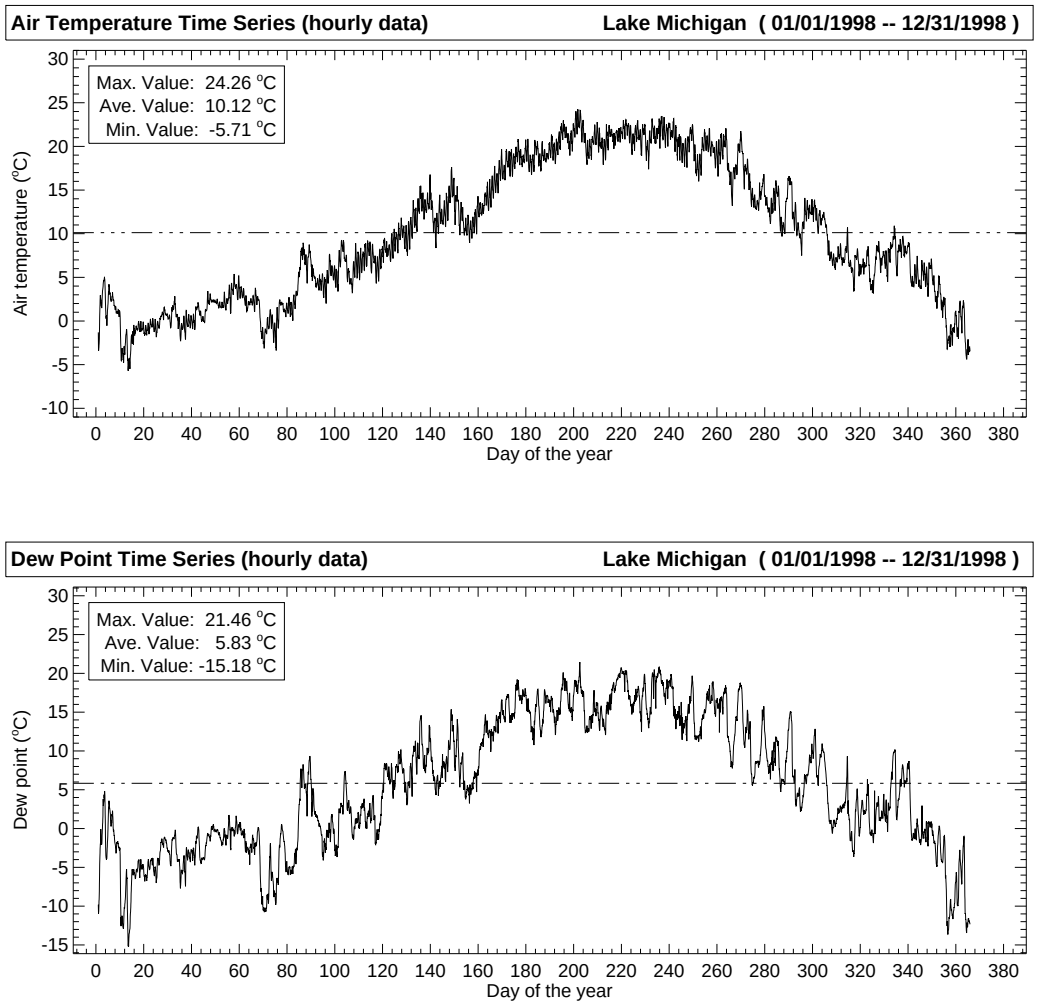

Figure 8.4 Time series of the hourly averaged air and dew point temperatures (1998).

During Winter, ice is formed in Lake Michigan, and the first waters to be affected are Green Bay and Bay de Noc, followed by the Straits of Mackinac and the shallow waters North of the Beaver Island. The hydrodynamic model can be run only under ice-free conditions and since there is no ice model currently implemented in M^2COPS special attention needs to be given in the definition of the ice-free simulation period.

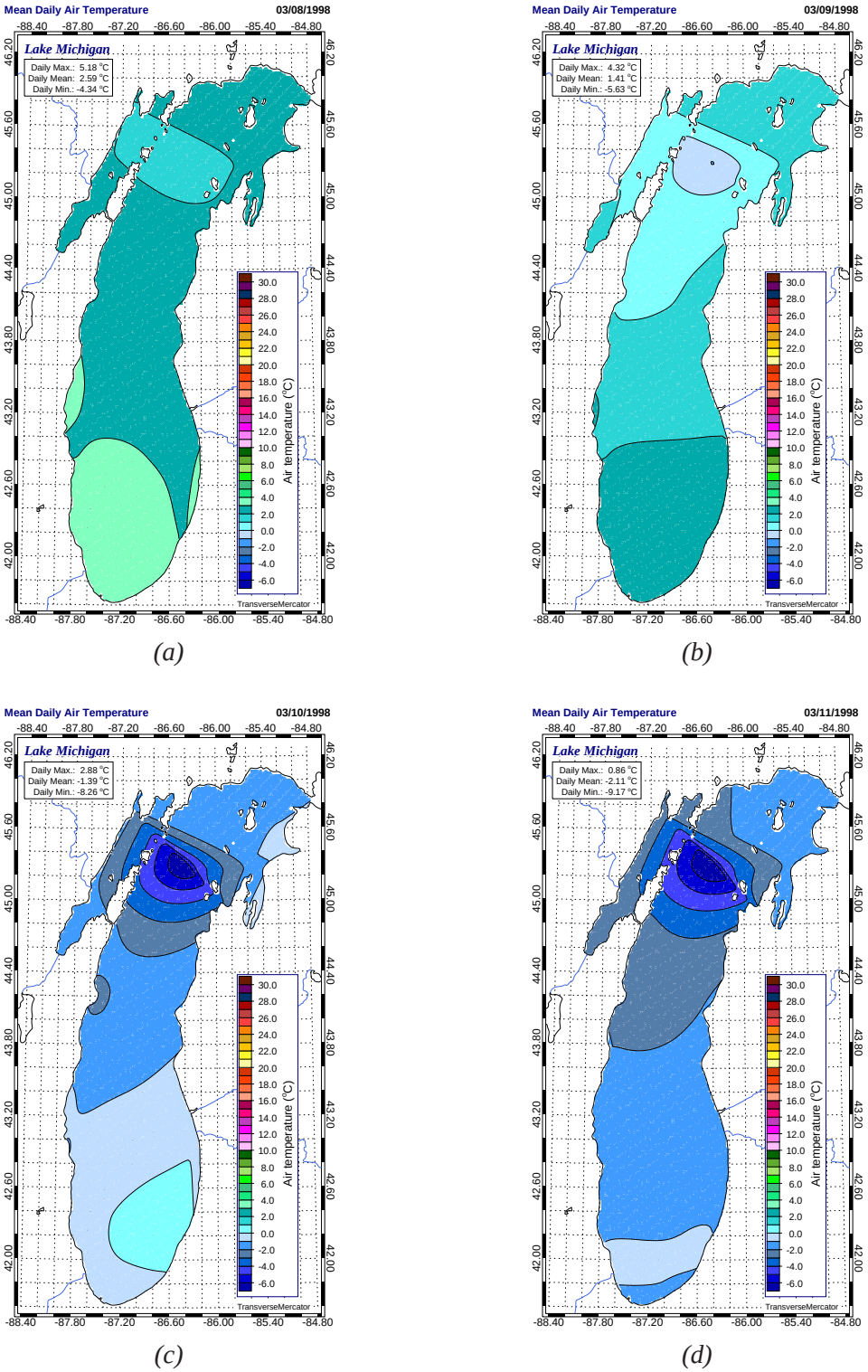

Figure 8.5 Mean daily temperature distribution during the March 8-11, 1998 storm event in Lake Michigan.

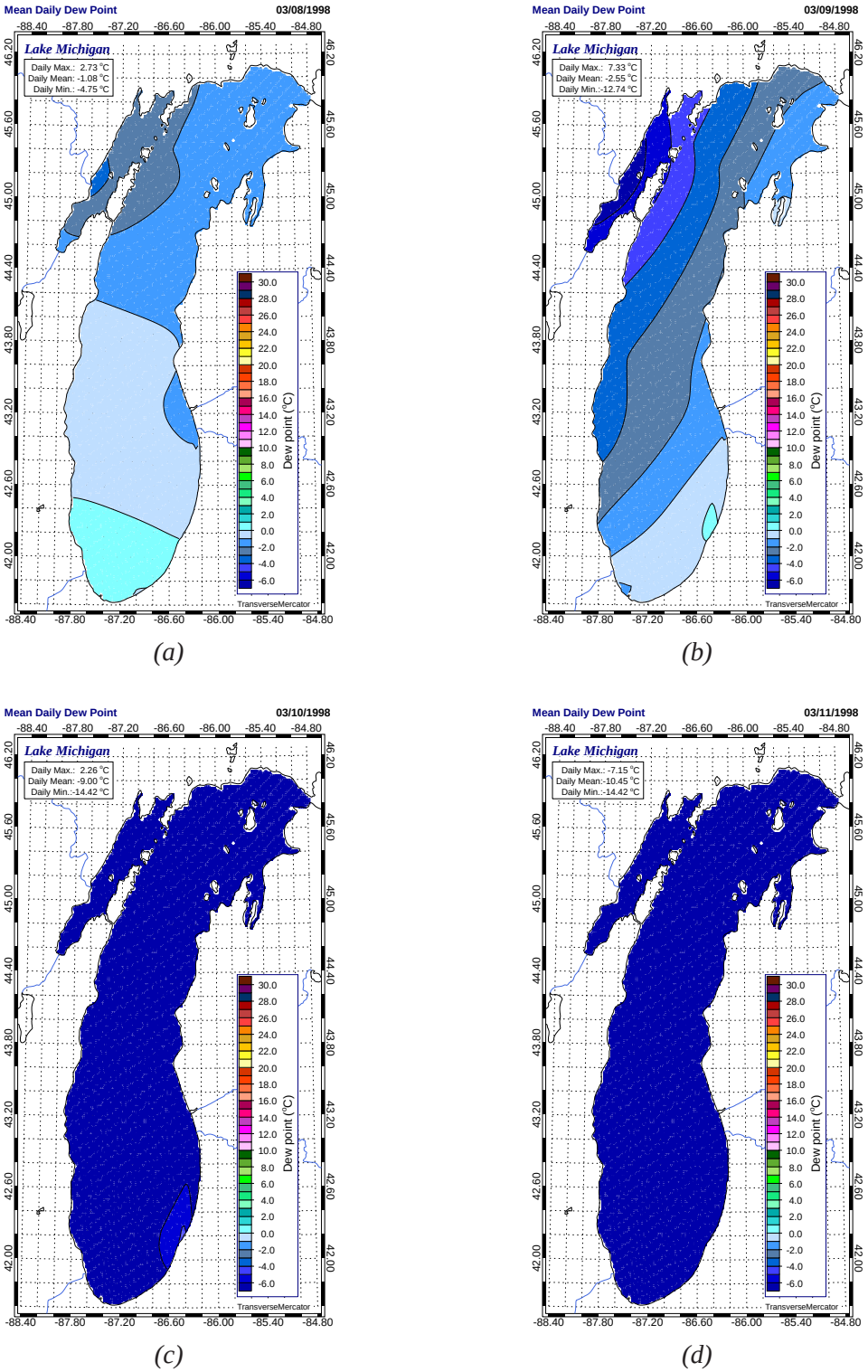

Figure 8.6 Mean daily dew point temperature distribution during the March 8-11, 1998 storm event in Lake Michigan.

Ice maps for Lake Michigan were obtained from *GLERL/NOAA* (http://www.glerl.noaa.gov/data/pgs/ice.html). From these ice maps, it was clear that year 1998 was an almost ice-free year for Lake Michigan, therefore, the ice-free model simulations may start as early as January 1, 1998 in contrast to other years that simulations have to be postponed until the end of Winter.

8.1.3 Barometric Pressure

The barometric pressure is reported in the *MAROBS* data in tenths of a *mbar* , transformed in kPa to meet the model's requirements (1 mb = 0.1 kPa). Over-land to over-water transition corrections are not applied to the pressure observations and only the adjustment to the common height over the mean water level is considered.

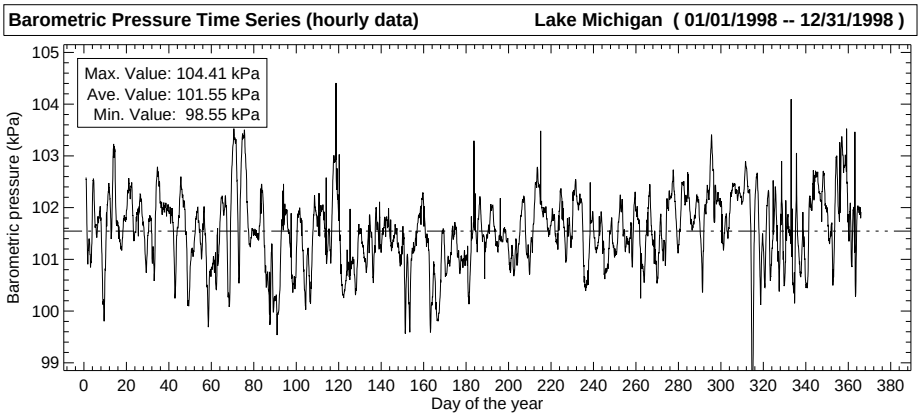

Figure 8.7 Time series of the hourly averaged barometric pressure (1998).

The time series of the lake-wide averaged barometric pressure for 1998 (Figure 8.7) show significant fluctuations, as high as 2 kPa, from the mean values. The March 8-11 storm event pressure maps (Figure 8.8) show the drop in the barometric pressure before the storm and its gradual increase afterwards.

More careful examination of the pressure data revealed that temporal pressure deviations from the yearly mean (101.50 kPa) are as high as ~ 8 kPa for specific regions within the lake (e.g., at the Mackinaw City, *NOAA-COOPS* water elevation station, Figure 8.14). Spatial atmospheric pressure differences of about 6 – 9 kPa are not uncommon over the water, especially during storm events.

Converting a pressure difference of 1 kPa to an equivalent height of water, yields an equivalent water level fluctuation of about 10 cm. It is apparent that the presence of horizontal atmospheric

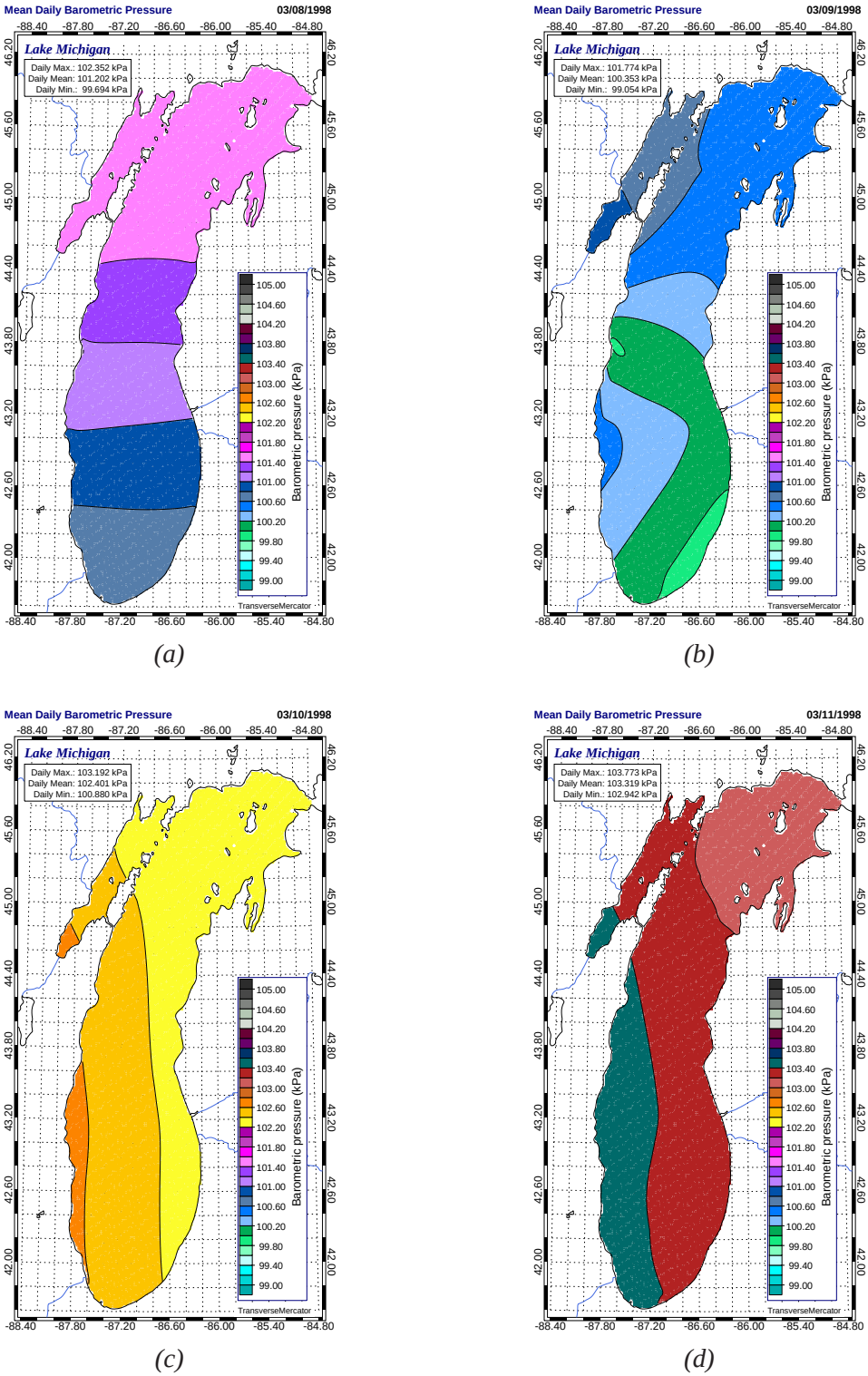

Figure 8.8 Mean daily barometric pressure distribution during the March 8-11, 1998 storm event in Lake Michigan.

pressure gradients might affect the model calculations if they are significant. In the current implementation of M^2COPS it was decided, due to the above reasoning, that the atmospheric pressure forcing is to be included by appropriately modifying the governing equations (see Section 2.1.2).

In order to be consistent with the local Lake Michigan environment, the local standard barometric pressure was recalculated from the pressure observations using the available data from eleven years (1991-2001). The standard barometric pressure is defined as the mean of the observations (in our case the lake-wide mean of the observations) and it was calculated to be equal to 101.654 kPa. This value of the atmospheric pressure is the standard value used here in all the model related calculations.

8.1.4 Cloud Cover

The cloud cover (FMH 1 [2005]) is reported as the percent of the sky covered by the clouds. A value of 0 defines a clear sky, while a value of 1 corresponds to a sky that is 100 % covered by the clouds. The principal use of the cloud cover data is for the estimation of the shortwave (Section 2.6.1) and the longwave (Section 2.6.4) radiation terms in the surface heat balance equation. As seen from Figure 8.9, the winter sky coverage by the clouds almost reaches 100 % while clearer skies are observed during Spring and Summer, so that the radiative heating of the deeper waters is more pronounced during the spring/summer months. The calculated yearly mean cloud cover for 1998 is $\sim$ 56 %. In the cloud cover maps for the March 8-11, 1998 storm event (Figure 8.10), it can be seen that during 03/09/1998 the lake is almost covered by clouds and after that the clouds gradually clear.

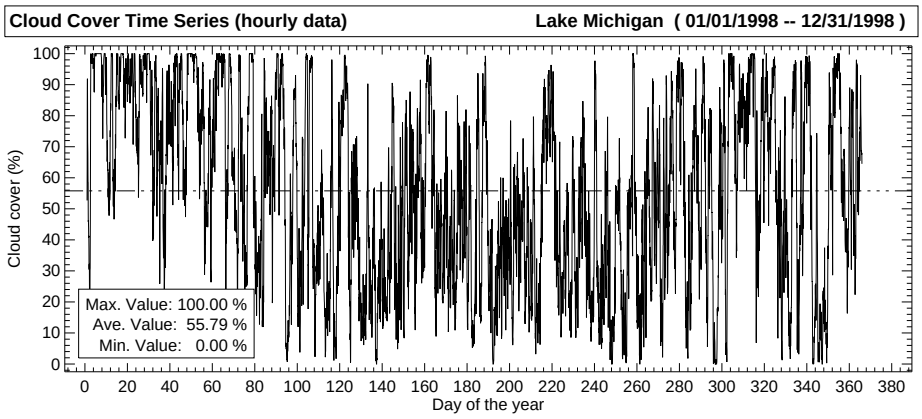

Figure 8.9 Time series of the hourly averaged cloud cover (1998).

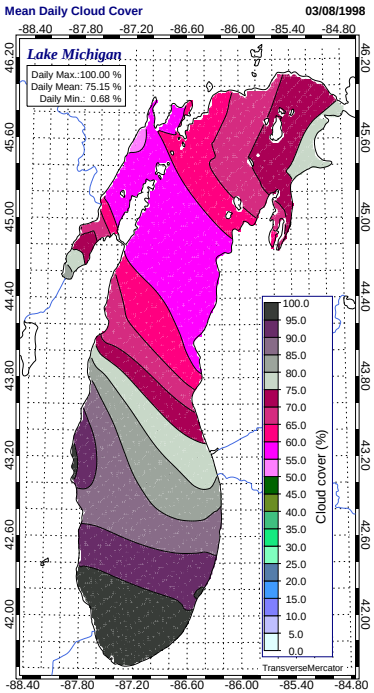

(a)

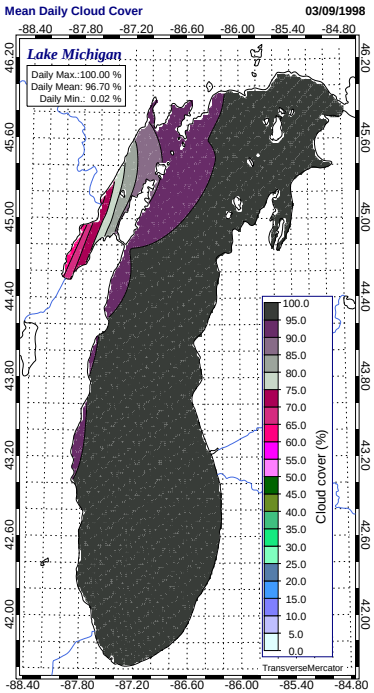

(b)

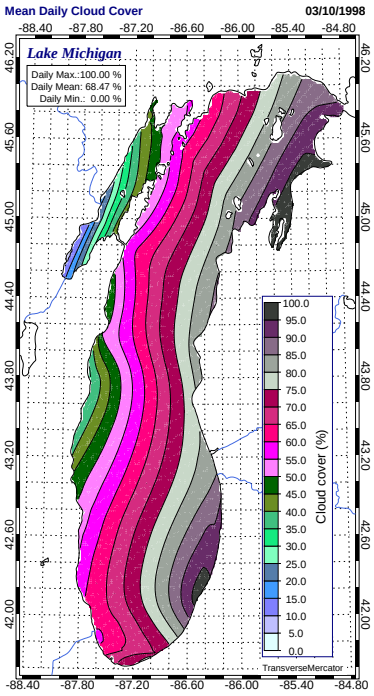

(c)

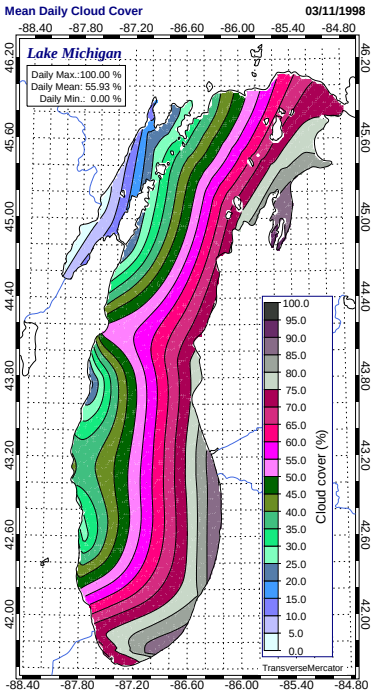

(d)

Figure 8.10 Mean daily cloud cover distribution during the March 8-11, 1998 storm event in Lake Michigan.

8.2 Water Elevation Data

The water levels in the lakes are affected by factors like precipitation, runoff from the lake basin, riverine inflows, diversions of water into the lake, evaporation, outflows at the lake outlets and losses to groundwater. Most of these factors, exhibit highly variable temporal behaviors, since they depend upon the local weather patterns and the nature of the various uses of the surrounding land. The result of the above factors is that the water levels in the lakes attain minima (usually during Winter) and maxima (usually during Summer) with fluctuations about their mean values.

The water elevation status of the Lake at the time of the plume was examined using the *NOAA* gage elevation data set for the year 1998, as well as historical data that covered the ten year period from 1990 to 2001. Comparison of calculated lake-wide averaged water elevations for 1998 (Figure 8.12) to yearly averaged historical water elevation data for Lake Michigan obtained from *GLERL/NOAA* at http://www.glerl.noaa.gov/data/now/wlevels/ indicates that the year 1998 with a mean water elevation of 176.73 m, approximately 23 cm above the long term mean elevation reported in Figure 8.11, can be regarded as a year of high water. During high water years higher waves are created and they cause higher erosion activity.

The oscillatory motion behavior of the Lake and its effect on the water elevation was also examined through inspection of the water elevation time series power spectra. The 1998 power spectra are given in Figure 8.13. Distinct spectral peaks are identified at periods of 12.42 h, 12.0 h, 8.8 h, $\sim$ 5.2 h and $\sim$ 3.2 h. The spectral peaks at 12.42 h, 12.0 h and 8.8 h were found to be consistently present in all the power spectra that were were examined (years 1996-2001). Spectral peaks with periods of 12.42 h and 12.0 h are associated with semidiurnal (lunar and solar) tides in the lake, a fact also exploited in As-Salek and Schwab [2004] and Sawicki [1999]. Furthermore, Sawicki establishes the claim that the semidiurnal tides in the Great Lakes have amplitudes in the order of 5 cm. Spectral peaks with periods of 9 h or less are associated with the presence of seiches (free oscillation modes) in Lake Michigan, generated by the blowing winds (As-Salek and Schwab [2004]).

Examination of the power spectra of the water elevations at the individual *NOAA-COOPS* gage stations confirmed the 12.42 h, 12.0 h and 8.8 h peaks in all cases, except at the Ludington, MI gage station. The $\sim$ 5.2 h and $\sim$ 3.2 h spectral peaks were observed at the spectral plots of all gage stations and every year in the period 1996-2001.

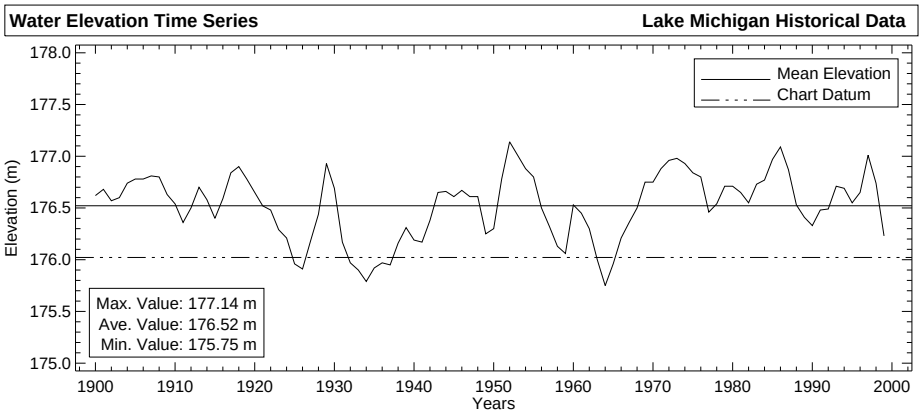

Figure 8.11 Historical water levels for Lake Michigan (source: http://www.glerl.noaa.gov/data/now/wlevels/).

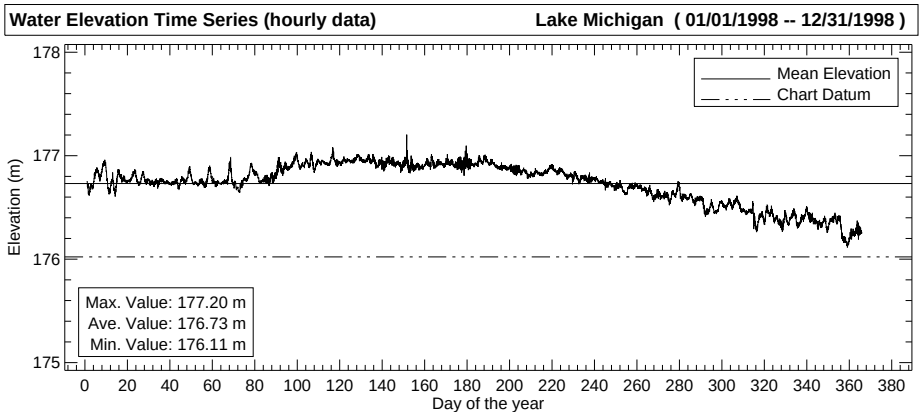

Figure 8.12 Time series of the hourly averaged, interpolated water elevations (1998).

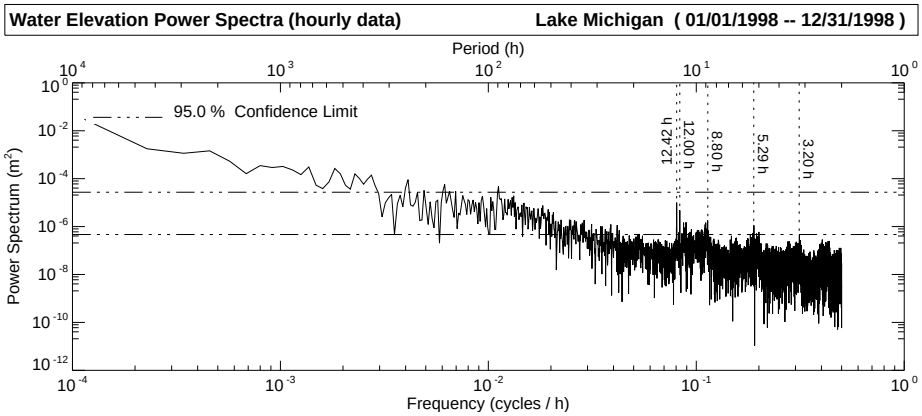

Figure 8.13 Power spectra of the hourly averaged, interpolated water elevations (1998).

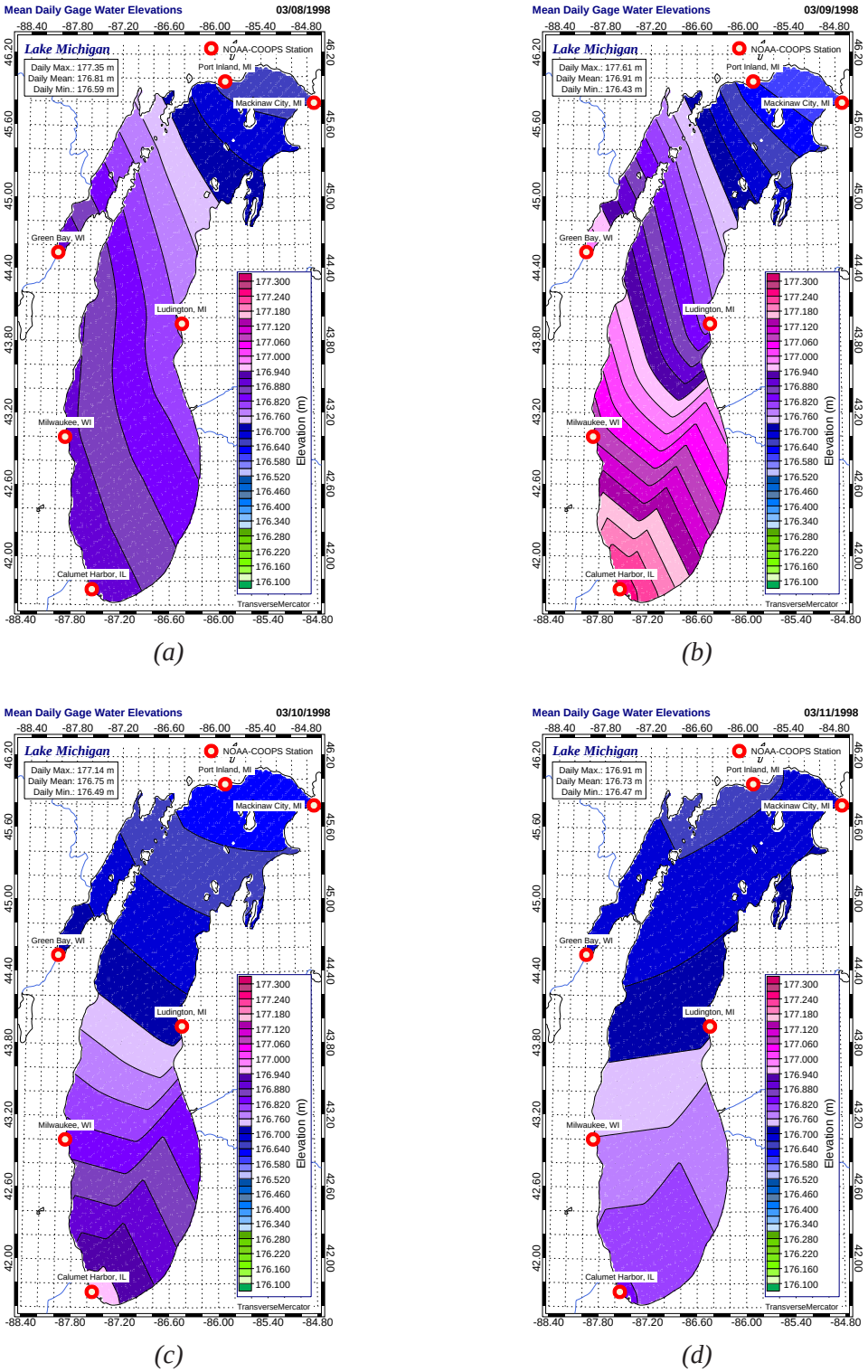

Figure 8.14 Mean daily interpolated water elevation distribution during the March 8-11, 1998 storm event in Lake Michigan.

Finally, the *GLERL/NOAA* gage elevation data set for 1998 was used to produce water elevation data on the $2x2$ km Lake Michigan grid by interpolation. Figure 8.14 presents selected water elevation maps for the storm event March 8-11, 1998 created by the interpolated water elevation data. The surge generated by the Northerly winds blowing over Lake Michigan during the storm, is clearly indicated in the maps by the initial water accumulation at the Southern part of the lake (03/09/1998) and its release towards the end of the storm (03/11/1998).

8.3 Suspended Particle Data

Suspended particles in Lake Michigan can be organic or inorganic in nature, the result of shoreline erosion, bottom sediment resuspension or biological activity and calcite formation in the water body. The present study is interested only in the fate of suspended particles that originate from the entrainment of the bottom sediments. To this end, the separation of the particles into inorganic and organic is not consider necessary, but the separation into particles originating from the bottom and particles added in the water column due to biological or chemical activities is important for the comparisons between the model calculated fractions, fluxes and concentrations of the suspended solids and the available measured ones.

8.3.1 Total Suspended Particulate Matter

A considerable amount of suspended particle data were collected the years 1997 to 2001 during the *EEGLE* program for the Southern part of Lake Michigan. The suspended particle data can be separated into the total suspended mass, the phytoplankton mass expressed as chlorophyll-a, and the zooplankton mass. Measurements of suspended particle mass include: *(a)* collection of water samples at various locations and depths that were further analyzed to give total suspended mass, chlorophyll-a concentrations and particle size fractions, *(b)* collection of data on light scattering and fluorescence by various instruments moored with *CTD* (conductivity, temperature, depth) profilers that were further related to total mass and chlorophyll-a concentrations, *(c)* collection of continuous data on zooplankton concentrations, and *(d)* collection of settling suspended particles onto sediment traps.

Data from 1998, the year selected for the preliminary model test, are being used in the present study. The focus of the suspended particle data collection operations during 1998 is the Spring plume and the pre-plume and the post-plume periods. Regression analysis was used to examine

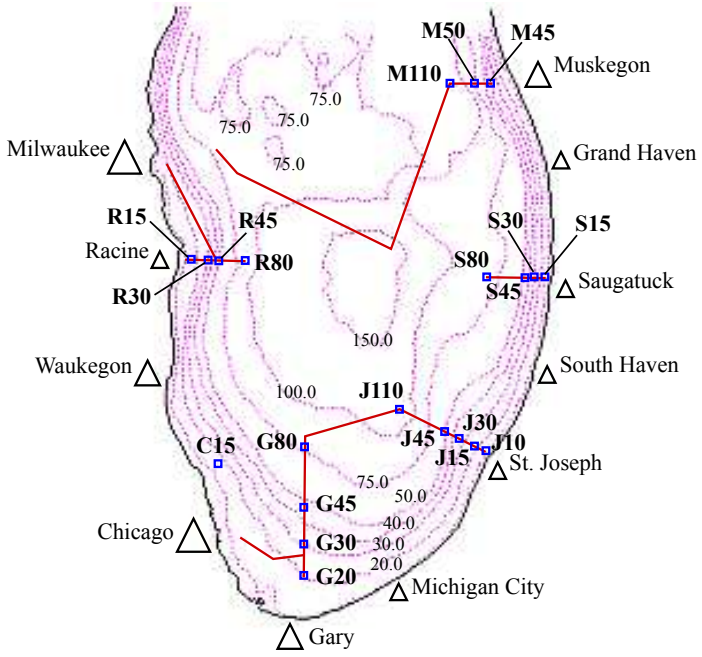

Figure 8.15 *EEGLE* survey January 28 to February 5, 1998 (source: http://www.glerl.noaa.gov/eegle/cruises/cruises_1998.html).

the statistical significance between: *(a)* the total suspended mass (*TSM*) and chlorophyll-a, *(b)* the total suspended mass and the particulate organic carbon (*POC*), and *(c)* the chlorophyll-a and the particulate organic carbon. Water samples were collected during the January 28th to 31st and the May 20th to 23rd deployments (pre-plume and post-plume periods) at various stations along the four transects shown in Figure 8.15. The samples were analyzed for *TSM*, *POC*, and chlorophyll-a among other parameters. Only data at stations with depth less than 15 m have been considered for the regression analysis and the results are shown in Figures D.21 and D.22 (appendix D).

During the pre-plume winter period the regression of the *TSM* versus the phytoplankton biomass expressed as chlorophyll-a, shows a weak negative relation with $R^2 = 0.23$. The *TSM* versus the *POC* regression shows no relation between the two parameters ($R^2 = 0.0002$). The *POC* with the phytoplankton biomass shows a weak positive relation with $R^2 = 0.23$.

During the post-plume period the regression of the *TSM* versus the phytoplankton biomass, expressed as chlorophyll-a, shows an improved relationship between *TSM* and chlorophyll-a with $R^2 = 0.34$. The *TSM* regression versus the *POC* shows an also improved relation between the two parameters with $R^2 = 0.34$. The *POC* regression with the phytoplankton biomass shows a significant

positive relationship between *POC* and phytoplankton biomass, expressed as chlorophyll-a, with $R^2 = 0.73$.

The behavior of these three parameters during the pre-plume period can be explained by the dominance of suspended material of terrestrial origin over phytoplankton. This behavior changed during the post-plume period pointing to a larger contribution of the phytoplankton biomass to the total suspended mass.

Calcite formation and precipitation in the lake, a process known as whiting, happens from mid to late summer. Since suspended particle mass concentrations do not include this constituent during the study period, the phenomenon will not be examined any further in the present study.

Description of the Particle Size Fractions, Solids Concentrations and Water Samples

Water samples were collected from January 28 to February 4, 1998 on the four transects at the Southern part of Lake Michigan. The transects start near the cities of Racine (R), Gary (G), St. Joseph (J) and Saugatuck (S), and are directed off-shore (Figure 8.15). Stations were made at the intersections of the transects with the 15 m, 30 m and 45 m bathymetry contours. Water samples were collected from three depths at the 15 m depth locations, from four depths at the 30 m depth locations and from five depths at the 45 m depth locations. At all stations there is always one sample 1 m below the water surface and another sample 1 m above the bottom of the lake.

The concentrations of the total suspended solids were calculated from the volume of the samples and the weight of the solids remaining on Whatman 44 mm GFF filters. The weight was determined gravimetrically with a 0.01 mg precision. The particle sizes of the suspended solids were determined by a Spectrex Laser Particle Counter. The operation, the limitations of the instruments and the analysis process are described by Winkelman et al. [1999] and in the Spectrex Corporation [2003] manual. Sediment data at each station are the result of three scanning trials per water sample.

A total of 48 samples were collected in 8 L Niskin bottles (height = 50 cm, diameter = 14 cm), they were analyzed and the results were reported as the average mass fraction of the three trials for each particle size bin. The particle bin size consists of two 16 size range groups. The first group includes bin ranges $1 - 16\,\mu$m (bin size = $1\,\mu$m), and the second group includes bin ranges $17 - 100\,\mu$m (bin size = $5\,\mu$m). This particle size range includes clay size particles, silt size particles and partially very fine sand size particles ($1\,\mu\text{m} < \text{clay} \leq 4\,\mu\text{m}$, $4\,\mu\text{m} < \text{silt} \leq 62.5\,\mu\text{m}$ and $62.5\,\mu\text{m} < \text{very fine sand} \leq 125\,\mu\text{m}$) according to the Wentworth sediment classification scale.

The suspended sediment solids data are presented in plots of *(a)* the mass fractions versus the 32 (16 + 16) particle sizes for each location and depth, *(b)* the mass fractions of the clay, silt and very fine sand particle size ranges versus the water depth at each transect and *(c)* the suspended solids concentration profiles.

The graphs show a clear dominance of the silt size particles everywhere in the Southern part of the lake and an increased total suspended solids concentration on the Southwestern part of the lake (Racine transect).

Total Suspended Particle and Phytoplankton Concentration Profiles

CTD attenuation and fluorescence data as 1 m depth increment profiles were collected at various transects around the Southern part of Lake Michigan. The majority of the data were collected at depths less than 45 m (shallower waters). The collection dates are January 28 to February 5, March 9 to March 19 and April 24 to April 28. The attenuation coefficient was measured by transmissometers moored with the *CTD* profilers. The equipment measures the loss of light of a monochromatic light beam as it travels through a water column due to both absorption by the water and scattering by the suspended solids and reports an attenuation coefficient (corrected for absorption) that is related to the suspended solid concentrations. Regression equations between the attenuation coefficient (A) and the suspended solids concentrations (*SSC*) have been developed by Andrew Winkelman (*GLERL/NOAA*), which for the year 1998 the regression equation is written as:

$$SSC\,(\mathrm{mg/L}) = 1.58 \cdot A\,(\mathrm{m}^{-1}) - 0.24\,, \qquad R^2 = 0.84 \tag{8.3.1}$$

while, for other years the equations are reported in the *PPS* Light Attenuance / *TSM* metadata file (http://www.glerl.noaa.gov/eegle/data/objects/obj_17.TSM.2.html).

Fluorescence emitted by chloroplyll-a, which is one of phytoplankton pigments, was measured by fluorometers also moored with the *CTD* profilers. Regression equations between the fluorescence (F) and chlorophyll-a (Chl-a) for Lake Michigan, have been developed by James Liebig (*GLERL/NOAA*). The regression equations for the year 1998 are:

Jan/Feb:
$$Chl-a\,(\mu\mathrm{g/L}) = 0.030\left[10^{F\,(\mathrm{volts})} - 10^{0.486}\right] + 0.137\,, \quad R^2 = 0.698 \tag{8.3.2}$$

March:
$$Chl-a\,(\mu\mathrm{g/L}) = 0.077\left[10^{F\,(\mathrm{volts})} - 10^{0.486}\right] - 0.772\,, \quad R^2 = 0.753 \tag{8.3.3}$$

while regressions for other years and seasons are reported at the previously mentioned *EEGLE* website (*PPS* fluorescence / chlorophyll metadata file).

Chlorophyll-a mass concentrations can be expressed as phytoplankton mass concentrations whenever the mass fraction of chlorophyll-a to the total mass of the living phytoplankton organism is known. The chlorophyll-a content of a phytoplankton cell depends on the phytoplankton species (Tolstoy [1979]), the nutritional status (chlorophyll-a content is higher under nutrient abundance), and the season of the year (chlorophyll-a content is higher during the winter months (Nicholls [1976])). For Lake Michigan a relationship between chlorophyll-a and phytoplankton biomass has not been developed (Brian J. Eadie, *GLERL/NOAA*, personal communication).

An estimate of the phytoplankton biomass for the present study has consequently been based upon previous studies and specifically on the research of Tolstoy [1979] on the chlorophyll-a content of various phytoplankton species in four Swedish Lakes in the period 1965 to 1974. The chlorophyll-a to phytoplankton volume ratio reported ranges vary from 0.3 – 0.6 % for *Bacillariophyceae* and *Cyanophycaae*, to 0.5 – 0.7 % for *Cryprophyceae*. Other researchers referenced by Tolstoy also report similar ratio values, ranging from 0.3 – 2.0 % on samples of single phytoplankton species and on samples of mixed species taken at various lakes around the world. The percentage of chlorophyll-a to phytoplankton volume ratio can also be expressed in μg of Chl-a per mm^3 of phytoplankton biovolume or by assuming a specific gravity of 1 ($\rho = 1000\,kg/m^3$) for the phytoplankton (Makarewicz et al. [1994]), which can be expressed in μg of Chl-a per mg of phytoplankton biomass.

In Lake Michigan the Sub-Phylum *Bacillariophyceae* / *Diatomaceae* prevails in the phytoplankton population (49.1 – 85.6 % of the total phytoplankton biomass), especially during the spring bloom (Makarewicz et al. [1994], Scavia and Fahnenstiel [1987]). Table 8.2 *(a)* has been prepared by converting the measured chlorophyll-a concentrations during the Spring and the Summer of the years 1998-2000 to phytoplankton volume using the range of chlorophyll-a to phytoplankton volume ratios reported by Tolstoy [1979] for the *Bacillariophyceae*. Table 8.2 *(b)* lists the measured average biomass for the Spring and Summer period of the years 1983-1992 in Lake Michigan (Makarewicz et al. [1994]). By comparison, the chlorophyll-a to phytoplankton volume ratio that gives phytoplankton biomass values closer to the ten year record is $r = 0.3$ % or 3 μg of Chl-a per mg of phytoplankton biomass, and this is the value to be used in the present study.

	(a)				(b)	
Year	$r = 0.3\,\%$	$r = 0.4\,\%$	$r = 0.5\,\%$	$r = 0.6\,\%$	Year	Biomass (mg/L)
	Biomass (mg/L)					
1998	0.330	0.247	0.198	0.165	1983	0.391
1999	0.358	0.268	0.215	0.179	1984	0.610
2000	0.530	0.397	0.318	0.265	1985	0.530
					1986	1.190
					1987	0.267
					1988	0.391
					1989	0.410
					1990	0.470
					1991	0.427
					1992	0.633

Table 8.2 Estimated and measured averaged phytoplankton biomass during the Spring and the Summer.

Zooplankton Concentration Profiles

Zooplankton measurements during the period of interest were collected from January 29 to February 3 and from March 16 to March 18 at transects that started near the cities of Racine (R), Gary (G), St. Joseph (J), Saugatuck (S), and Muskegon (M) and moved off-shore. The size and the number of zooplankton particles were measured with a Focal Technologies Mini-Optical Plankton Counter mounted on an Endeco/YSI Type 493 V-fin. The instrument works by sending a laser beam and transmits the cross-sectional area of each particle passing through the beam. The wet zooplankton biomass is decided from the particle geometry and its specific gravity (Herman [2000]). The system with the instrument moved both horizontally (at 2.5 m/s speed) and vertically (surface to bottom and back again) collecting data in a wavy mode. The water depth was decided by a depth sounder and the location by a differential *GPS*. During the period of model simulations, however, zooplankton biomass measurements are not available, consequently, total suspended mass cannot be corrected for the zooplankton biomass in the lake.

8.4 Sediment Trap Data and Mass Fluxes

Sediment traps are instruments that intercept settling particles and collect time integrated sediment samples. They come in a variety of shapes; cylinders, flat plates, domed cylinders, funnels, and they are manufactured from a variety of materials, glass, plexiglass, *PVC*, polyethylene. In

quantitative studies the use of the material collected by the sediment trap to calculate the total mass fluxes and the various constituents mass fluxes presents some serious problems.

One issue arises from the definition of the flux. Mass fluxes are considered to be the product of the concentration of the particles and their settling velocity, as this is decided by the local turbulent field and the settling velocities of the particles. Since the flux is a vector quantity, at some instance the flux may have a downward direction and at some other instance an upward one. Such temporal changes of the fluxes cannot be captured by the sediment traps. From the total mass M_t collected in the trap, the trap collection area A_t and the duration of the sampling period t_s, the "settling flux" is calculated as $F_s = M_t/(A_t \cdot t_s)$ (Eadie et al. [1984], Ittekkot et al. [1996]). Sample collection intervals range from a couple of days to many months providing "settling fluxes" that should be better characterized as collection rates.

Another issue associated with the sediment traps is their collection efficiency. Laboratory tests on the efficiency of the sediment traps shows that the parameters affecting the collection efficiency are the geometric shape of the traps, the density and the size distribution of the suspended sediments, known as the snowfence effect, and the current velocity and flow direction. Best collection efficiencies were shown by axially symmetric traps especially the cylindrical ones. Even with such trap designs the snowfence effect remains a problem causing smaller particles to be carried over and away from the trap while larger particles to be carried up toward the edge of the trap and drop inside it, thus leading to an under- or an over-estimation of the overall collection rate and of the collection rates of the individual sediment grain sizes (Gardner [1980], Hung and Chung [1998]).

Field experiments with sediment traps have shown that cylindrical traps have good performance in environments with current velocities less than 10 cm/s (Eadie [1997], Bale [1998]), especially when their aspect ratio (length to diameter ratio) is greater than two. In higher magnitude current environments, the possibility for loss of collected material from resuspension requires taller sediment traps. Studies within the region of the nepheloid layer of Lake Michigan that employed plexiglass cylindrical sediment traps with aspect ratios of 5:1 and 8:1 showed about 90 % efficiency (Eadie et al. [1984, 2000a,b]). Further studies in Grand Traverse Bay, Lake Michigan on mass fluxes collected by duplicate cylindrical traps with 10 cm and 20 cm diameters and an aspect ratio 5:1 showed smaller capture efficiencies by the 20 cm diameter traps. The efficiency of the higher diameter traps was improved and inter-calibration of the two trap sizes that were used was achieved when the aspect ratio of the 20 cm traps was increased to 8:1 (Eadie et al. [2000a]).

The sediment trap design used during the *EEGLE* project was based on the results of the above experiments and studies with sediment traps. The program used three sizes of cylindrical traps with diameters 5, 10 and 20 cm. The length to width ratios that were used are 5:1 for the smaller diameter traps and 8:1 for the 20 cm traps. The traps are designed such that the bottom of them leads to a funnel that directs the particles into a polyethylene bottle where they are collected (Eadie et al. [1991]). Both simple traps with variable range of exposure (from a few days to many months) and sequencing traps that have the ability to rotate and empty the particles in a new bottle in defined pre-programmed time intervals were used. The usual exposure time interval for the sequencing traps was 9 days, they carried 23 bottles and they had the ability to collect settling particles for a total of six months uninterrupted.

After collection, the trap samples were screened to separate larger particles (in some cases greater than 500 μm and in others greater than 335 μm), dried, and the weight of the particles that passed the sieves and of the particles retained on them determined with a precision of less than 1 % (Moored Arrays Workgroup [1997]). Some of the samples were further screened to separate the finer particles (less than 64 μm) that were then examined for carbon, nitrogen and other chemical ingredients. The composition of the trap samples consisted of inorganic particles, diatoms and other phytoplankton species, zooplankton, zooplankton fragments and fecal pellets, fish eggs and unidentified organic debris (Evans et al. [1998]). Zooplankton usually is screened out with the 350 μm screens since most species are greater than 0.3 mm.

Phytoplankton content may be estimated from the organic carbon in the screened samples and the phytoplankton flux may be subtracted from the total mass. The ratio of carbon to chlorophyll-a in phytoplankton cells depends on the growth stage of the phytoplankton and the nutrient availability in the water. Antia et al. 1963 (as referenced by Parsons et al. [1984]) studied an algal bloom event of phytoplankton of the Sub-Phylum *Bacillariophyceae* / *Diatomaceae* for 12 days. The carbon to chlorophyll-a ratios ranged between 23 to 79 with the smallest ratios representing the fast growing initial phase and the highest ratios the final nutrient-limiting stage. The average ratio over the duration of the bloom event is 47.5 and the median ratio is 49. Similar average C:Chl-a ratios have been reported by Faugeras et al. [2003], who used a C:Chl-a = 55 for their phytoplankton modeling and Bernal et al., 1989, as referenced by Graco et al. [2006], who used a C:Chl-a = 42.5 to transform Chl-a fluxes in carbon fluxes. Using the chlorophyll-a to phytoplankton ratio from above and a ratio

of wet biomass to dry biomass equal to 5, it has been calculated that 0.75 mg of carbon correspond to 1 mg of dry phytoplankton. The trap locations, their diameters and their deployment schedules for the year 1998 are presented in Table 8.3.

All the available trap data for 1998 are presented as bar plots (Figures D.23 through D.26, appendix D) of mass fluxes at each station and depth versus the collection time interval. The graphs show a sudden increase in the mass flux of about 800 $g/m^2/d$ in the time period between March 4 and March 13 for traps T-15 and T-20 that are located at the Southwestern and the Southern part of Lake Michigan correspondingly. An increase in the mass flux of this size is not evident either in the deep water area represented by trap T-12 nor in the Southeastern part of the lake represented by traps T-24, T-27 and T-28 at any time. A small gradual increase of only $5 - 8\ g/m^2/d$ is noted at stations T-24, T-27 and T-28 that started on the March 4 and March 13 time period but it reached its highest value during the March 22 and March 31 time period with a delay of 9 days. Immediately after the plume, the graphs show a reduction of the mass flux to about 100 $g/m^2/d$ for the Southwestern traps and to 2.5 $g/m^2/d$ for the Southeastern traps.

Duplicate traps were set at the stations T-12 (deep water) and T-24 (South region near Gary) to examine the performance of the 20 cm (8:1 aspect ratio) and the 5 cm (5:1 aspect ratio) diameter. From the available data for 1998 the following comparisons took place in the present study: *(a)* between the 20 cm (8:1 aspect ratio) and the 5 cm (5:1 aspect ratio) diameter duplicate traps at T-12 that gave a slope of -0.5423 with $R^2 = 0.0366$ ($n = 5$); *(b)* between the 20 cm (8:1 aspect ratio) and the 5 cm (5:1 aspect ratio) diameter duplicate traps at T-24 that gave a slope of 0.8986 with $R^2 = 0.1445$ ($n = 11$); *(c)* between the 20 cm (8:1 aspect ratio) at T-24 and its duplicate 20 cm (8:1 aspect ratio) diameter at T-24A that gave a slope of 0.941 with $R^2 = 0.4259$ ($n = 11$); and *(d)* between the 20 cm (8:1 aspect ratio) at T-24A and its duplicate 5 cm (5:1 aspect ratio) diameter at T-24 that gave a slope of 1.047 with $R^2 = 0.408$ ($n = 11$).

The 5 cm diameter and the 20 cm diameter traps give quite different sediment fluxes and the question that arises here is which one of the sediment traps used during the *EEGLE* project gives more reliable sediment fluxes estimates. Literature review suggests examination of the trap aspect ratio and Reynolds number. Traps with smaller Reynolds numbers, that is with smaller diameters under similar environmental conditions, have a higher collection efficiency and traps with smaller aspect ratios, other factors kept constant, have a smaller collection efficiency. In four out of five

Station	Latitude (°)	Longitude (°)	Station Depth (m)	Trap Depth (m)	Date In	Date Out	Days		Trap Diameter (cm)
T12	42.73	-87.00	160	30	12/31/97	05/15/98	Every	9	20
T12	42.73	-87.00	160	30	12/31/97	02/14/98	Every	9	5 (duplicate)
T12	42.73	-87.00	160	30	05/15/98	06/09/98	Total	25	10
T12	42.73	-87.00	160	30	06/11/98	10/09/98	Every	30	20
T12	42.73	-87.00	160	30	10/09/98	12/20/98	Every	12	20
T12	42.73	-87.00	160	155	12/31/97	05/15/98	Every	9	20
T12	42.73	-87.00	160	155	05/15/98	06/09/98	Total	25	10
T12	42.73	-87.00	160	155	06/11/98	10/09/98	Every	30	20
T12	42.73	-87.00	160	155	10/09/98	12/20/98	Every	12	20
T15	42.77	-87.70	22	12	12/31/97	05/15/98	Every	9	5
T20	41.81	-87.25	25	12	12/31/97	05/15/98	Every	9	5
T20	41.81	-87.25	25	12	10/09/98	12/20/98	Every	12	10
T24	42.28	-86.64	56	30	12/31/97	04/09/98	Every	9	20
T24A	42.29	-86.64	56	30	12/31/97	05/15/98	Every	9	20 (duplicate)
T24	42.28	-86.64	56	30	12/31/97	05/15/98	Every	9	5 (duplicate)
T24	42.28	-86.64	56	30	05/17/98	06/10/98	Total	24	10
T24	42.28	-86.64	56	30	06/11/98	07/29/98	Every	12	20
T24	42.28	-86.64	56	51	06/11/98	08/10/98	Every	12	20
T27	43.05	-86.65	100	30	12/31/97	05/18/98	Every	9	20
T27	43.05	-86.65	100	30	05/18/98	06/09/98	Total	22	10
T27	43.05	-86.65	100	30	06/11/98	10/09/98	Every	30	20
T27	43.05	-86.65	100	30	10/09/98	11/14/98	Every	12	20
T27	43.05	-86.65	100	95	11/05/97	05/18/98	Total	194	10
T28	43.22	-86.59	110	30	05/18/98	06/09/98	Total	22	10
T28	43.22	-86.59	110	30	06/11/98	10/09/98	Every	30	20
T28	43.22	-86.59	110	30	10/09/98	12/20/98	Every	12	20
T29	44.49	-86.69	260	30	09/09/98	10/09/98	Total	30	20
T29	44.49	-86.69	260	30	10/09/98	12/08/98	Every	12	20
T30	42.39	-86.53	54	49	10/09/98	11/02/98	Every	12	10
T31	42.28	-86.59	44	39	10/09/98	01/01/99	Every	12	10
T33	42.16	-86.70	67	62	10/09/98	01/01/99	Every	12	10

Table 8.3 Sediment trap locations and schedules for the year 1998.

cases at station T-12 (deep water) the 5 cm diameter traps (5:1 aspect ratio) presented higher sediment fluxes, but this was true only in half of the cases at station T-24. The above investigation is obviously inconclusive and an independent means of calculating the sediment flux is not available.

Based on the reported performance issues of the sediment traps, measured data by this method cannot be used for the evaluation of the sediment model, however, they can be used in a qualitative initial understanding of the Michigan plume behavior. In this case it is better to rely on data from the 20 cm diameter traps that exhibit a better overall performance (personal communication with B. J. Eadie (*GLERL/NOAA*)), especially during periods of high sediment concentrations when the 5 cm diameter traps performance is questionable (Moored Arrays Workgroup [1997]).

8.5 Bottom Sediments

The second important source for the suspended sediment load is the bottom of the lake. The bottom has been designed, in modeling terms, to act as a continuous pool of sediments that under critical local flow conditions may entrain to become part of the sediments already in suspension. The amount of the sediments that actually entrain, directly depends upon their particle sizes and the corresponding mass fractions.

Bottom sediment grain size distribution data were collected for the Lake Michigan Mass Balance (*LMMB*) and the Environmental Mapping and Assessment (*EMAP*) studies conducted by the *EPA*. During the *LMMB* study two cruises were deployed, the first in August to September, 1995 and the second in May, 1996. Samples were taken at 74 locations with the methods of box coring, ponar, and gravity coring. During the *EMAP* study samples were collected in July and October, 1994 at 35 locations with the ponar method. In both cases, the grain size analysis was performed on sub-samples taken from the upper 1 cm of the coring samples (Eadie and Lozano [1999]).

The *LMMB* dataset reports the measured mass fraction distributions for grain sizes ranging from 2 μm to sizes greater than 1000 μm. The *EMAP* data set contains the measured mass fraction distributions for grain sizes ranging from about 0.08 μm to sizes greater than 2000 μm. The data collected from the two studies were further combined and linearly interpolated as necessary, to produce a final dataset. In the combined dataset, the data are reported for grain sizes $\leq 4\,\mu$m (cumulative), 4 μm to 60 μm (in 4 μm increments), and $> 60\,\mu$m (cumulative).

To meet the requirements of the present study, the reported data in the above three datasets were further: *(a)* linearly interpolated to produce four clay size ranges ($0 - 4\,\mu$m) of 1 μm increments,

14 silt size ranges (4 – 60 μm) of 4 μm increments and six sand size ranges (> 60 μm): 60 – 70 μm, 75 – 100 μm, 150 – 300 μm, 300 – 500 μm, 1000 – 2000 μm, and *(b)* spatially interpolated using Watson's natural neighbor interpolation method to produce the size distributions for any missing station data. The results of the interpolation are given in Table 8.5 at the end of this Chapter and represent the complete data set of the Lake Michigan bottom sediments to be used in the present study. The data were prepared in accordance to the Wentworth's scale (CEM III [2006]), which classifies the sediments as clay (0 – 4 μm), silt (4 – 60 μm), and sand (60 – 2000 μm). For each sediment size range an equivalent particle diameter was assigned to be equal to the diameter corresponding to the midpoint of each size range.

8.5.1 Spatial Distribution of the Sediment Classes

The initialization of the bottom sediment model requires that the mass fractions and the corresponding grain sizes to be known a priori at every grid point of the calculation domain. The gridded bottom sediment data, therefore, are obtained from the data in Table 8.5 using again the natural neighbor interpolation approach. After the completion of the spatial interpolation, the size distribution (24 grain sizes) at each grid point is known and the summation of the mass fractions of all grain size ranges within each sediment class will give the spatial distribution of the clay, silt and sand sediment classes on the 2*x*2 km Lake Michigan grid. The results of this interpolation are shown as 2D maps in Figures 8.16 *(a,b,c)*.

Figures 8.16 *(a-c)* show a clear dominance of the sandy material, covering almost half the bottom of Lake Michigan with mass fractions above 50 %. The highest bottom sand mass fractions (> 99 %) are noticed at the Southern part of the lake near the Cook and the Lake counties, and at the Northern part near the Marinette, Menominee and Delta counties. Another area with high bottom sand mass fractions (> 95 %) starts at Milwaukee County and extends to about 40 km off-shore.

Figure 8.16 *(c)* shows that the contribution of the clay sediment is limited to a maximum of 2 %, mostly deposited on the Eastern and Central areas of both the Southern and the Northern parts of the lake. Figure 8.16 *(b)* indicates the Eastern and Central areas of both the Southern and the Northern part of the lake as the deposition areas of the silt size sediment as well. In the case of the silt size sediment the highest bottom mass fractions can be observed at the deeper water areas of the South Chippewa Basin in the Central part of the lake and of the Ludington Basin in the Eastern part of the lake. In these areas the bottom silt mass fractions reach up to 95 %, with sand mass fractions not exceeding 6 %.

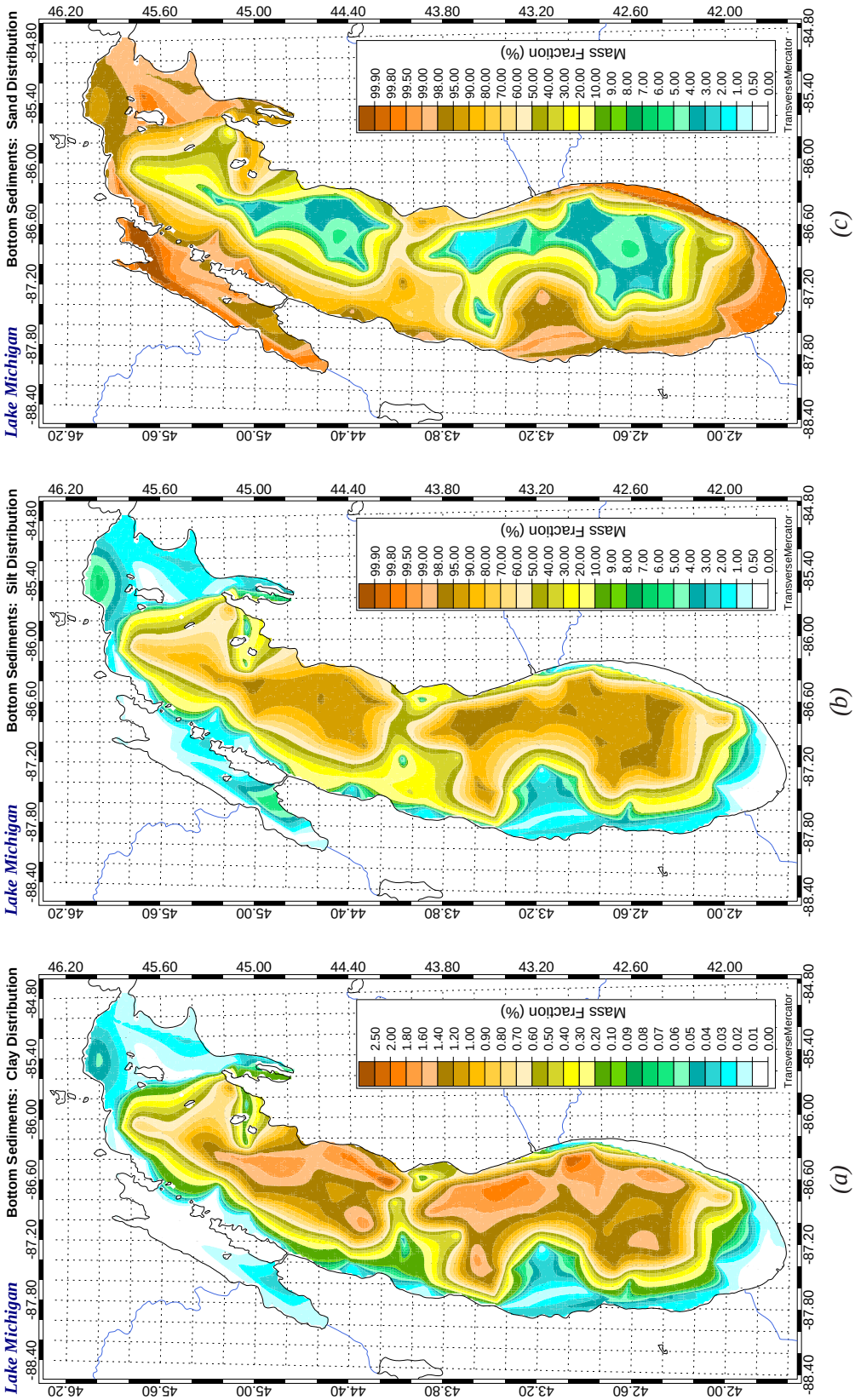

Figure 8.16 Spatial distribution of the bottom sediments of Lake Michigan.

8.5.2 Spatial Distribution of the Sediment Sizes

Four typical diameters were chosen to represent the spatial distribution of the sediment sizes in Lake Michigan, that is, the d_{10}, d_{90}, d_{50} and the mass fraction weighted diameter d_W. The d_{10} and the d_{90} diameters are defined as the particle diameters for which 10 % and 90 %, by weight, of the sediments have smaller diameters, respectively. The d_{50} is defined as the median diameter and the d_W is the grain diameter used as an input to the sediment model, and it is reported here to be compared to the other sediment sizes.

As described in CEM III [2006], plotting the cumulative percent coarse value (F) versus the sediment diameter (d), produces a nearly Gaussian distribution for well sorted sediments, that will appear as a nearly straight line on a log-log plot, described by the equation:

$$\log F = A \log d + B \; ; \qquad d = 10^{\Lambda} \; ; \qquad \Lambda = \frac{\log F - B}{A} \tag{8.5.1}$$

Since at each grid point the sediment size distribution is known, the coefficients A and B are determined by fitting a straight line to the data as described by the first of the equations 8.5.1. The d_{10}, d_{90} and d_{50} diameters are determined from the second of equations 8.5.1 by setting F to be equal to 10 %, 90 % and 50 %, respectively. The mass fraction weighted, average diameter d_W is calculated using the following expression:

$$d_W = \frac{\sum_{i=1}^{N} \beta_i \, d_i}{\sum_{i=1}^{N} \beta_i} \; ; \qquad \sum_{i=1}^{N} \beta_i = 100\,\% \tag{8.5.2}$$

where β_i is the mass fraction of the "i-th" diameter d_i.

The spatial distributions of the four sediment sizes are shown in Figures 8.17,and show that the coarser material is found in the Northern and Southern edges of the lake, while the finer material is mainly found in the lower, middle and the upper basins of the lake. Figure 8.17 *(d)* represents the nearly actual state of the bottom sediments as opposed to Figure 8.17 *(c)*, which represents the central tendency of the size distribution.

8.6 Salinity

The interest on salinity in the present study is a more accurate calculation of the water density. The measurements of salinity in Lake Michigan, during the *EEGLE* project, took place from March

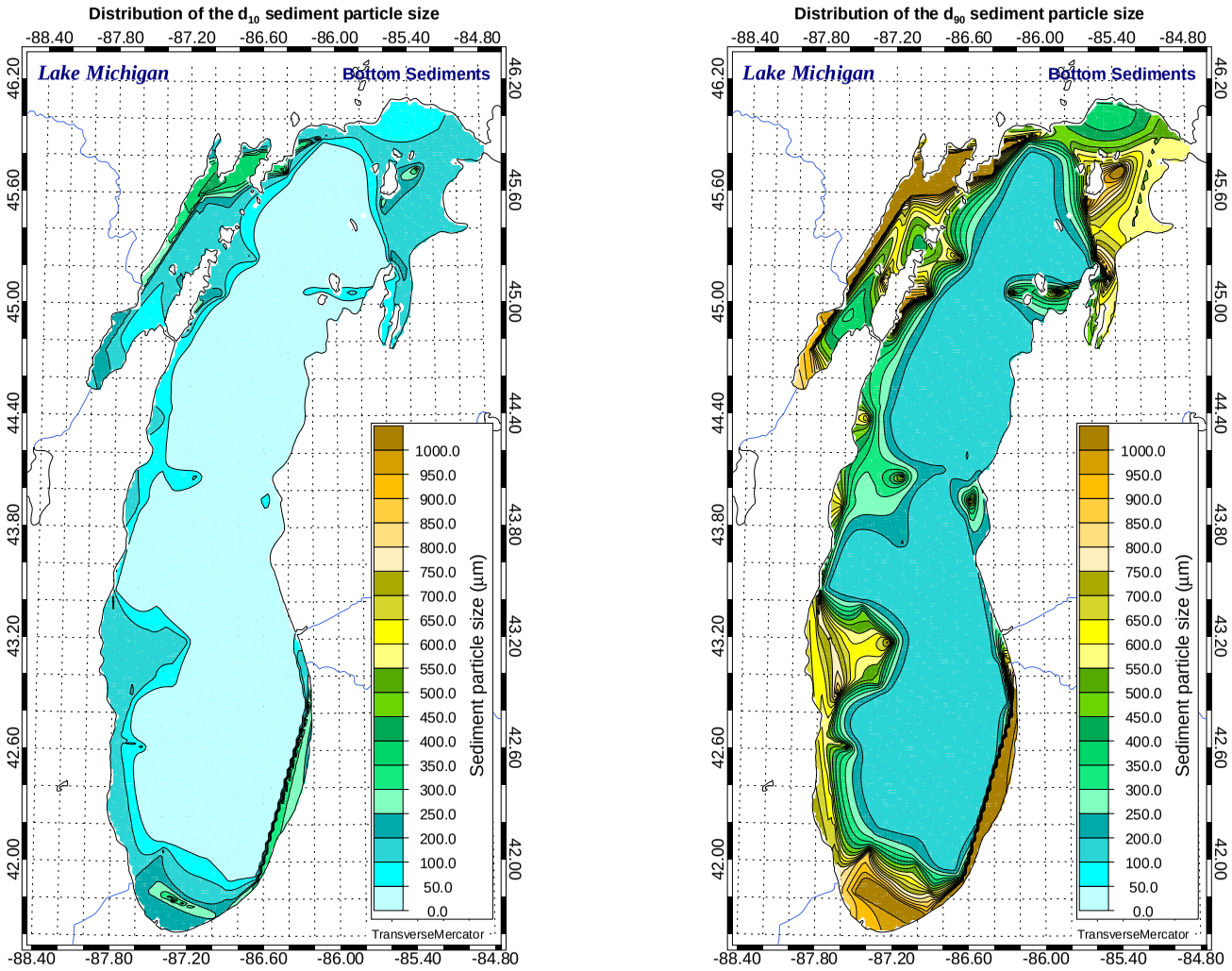

Figure 8.17 Spatial distribution of selected particle size classes for the bottom sediments of Lake Michigan. (Continued)

Figure 8.17 Continued.

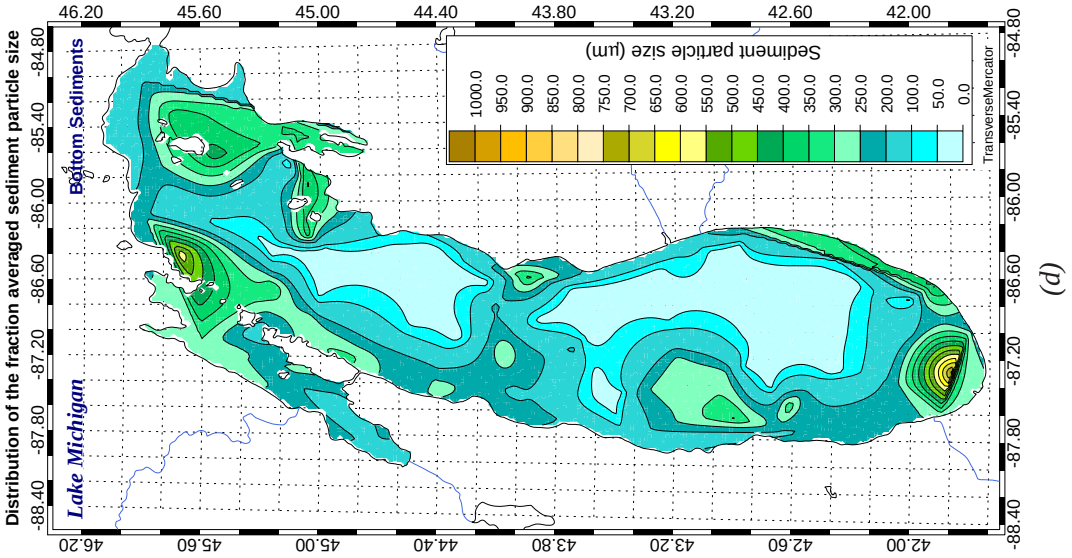

(d)

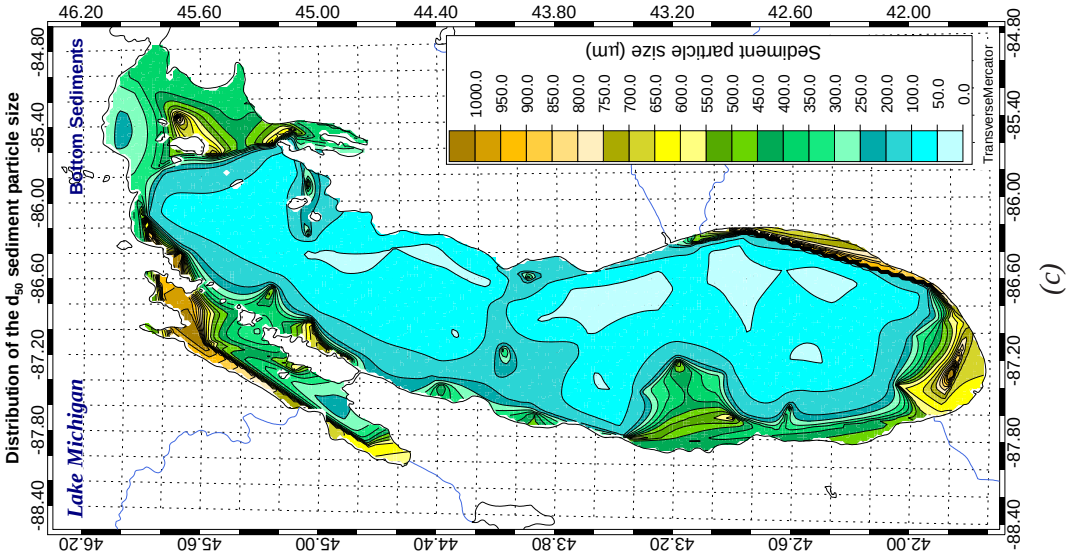

(c)

11 to March 10 in 1999, at the Racine, Chicago and Saint Joseph transects and again from March 22 to March 30, April 25 to May 5 and May 17 to May 20 in 2000, at the Milwaukee transects. Stations were made at the intersections of the Racine, Chicago and Saint Joseph transects with the 20 m, 30 m, 45 m and 80 m bathymetry contours and at the intersections of the Milwaukee transect with the 10 m, 20 m, and 30 m bathymetry contours. Conductivity measurements were taken at 1 m vertical intervals from the water surface to the lake bottom and salinities were calculated.

Year	Deployment period	Salinity (psu) max.	mean	min.	std. dev.
1999	03/10-03/12	0.17190	0.13711	0.13240	0.00618
	Average:	0.17190	0.13711	0.13240	0.00618
2000	03/22-03/30	0.13390	0.13272	0.13210	0.00032
	04/25-05/05	0.14920	0.13303	0.13150	0.00217
	05/17-05/26	0.18170	0.13403	0.13170	0.00451
	Average:	0.15493	0.13326	0.13177	0.00233
1999-2000	Average:	0.16342	0.13519	0.13209	0.00426

Table 8.4 Lake Michigan salinity levels measured during the *EEGLE* project.

Vertical profiles of the salinity show a uniform distribution from top to bottom in all cases. The one exception is the salinity profile at the station of the Saint Joseph transect with the 20 m bathymetry contour, where the salinity increases with the depth and presents higher values than the ones at other stations. This behavior might be explained by the mixing of higher temperature and halogen content municipal/industrial effluents into the near-shore waters at this location. The mean salinity of the data reported for each individual year and for the two year period along with the observed maximum and minimum salinity values during each deployment are shown in Table 8.4.

From the reported salinity data an overall mean value equal to 0.13519 psu was calculated (Table 8.4). Since, the *EEGLE* data salinity profiles exhibit almost constant and uniform distributions in Lake Michigan, no additional salinity related calculations are required and a constant value for the salinity equal to the calculated mean salinity value is assigned in M^2COPS. Use of this value for the salinity instead of a commonly used for fresh waters salinity value of zero is expected to increase the water density by $\sim 0.1\,\mathrm{kg/m^3}$ ($\sim 0.01\,\%$).

8.7 Data for Model Evaluations

Extensive wave, current and temperature datasets are available for year 1998. Most of the data were collected during the *EEGLE* project, while the rest of the data were collected on a regular basis from the *NOAA* meteorological stations. Only a selected sub-set of these data is used here for model evaluations during specified time periods.

Wave data are available at the National Data Buoy Center (*NDBC*) buoys 45002 (at the Northern basin of Lake Michigan, lat: 45.30^{o}, lon: 86.40^{o}) and 45007 (at the Southern basin of Lake Michigan, lat: 42.67^{o}, lon: 87.02^{o}). These data are presented in the form of hourly averaged significant wave heights and periods.

Additional wave data for 1998 collected during the *EEGLE* project consisted of tripod deployment data collected towards the end of the year. Three tripod deployments are available: *(a)* Benton Harbor (lat: 42.135^{o}, lon: 86.493^{o}, starting day: 10/14/1998); *(b)* Michigan City (lat: 41.735^{o}, lon: 86.907^{o}, starting day: 10/14/1998); and *(c)* Milwaukee (lat: 42.958^{o}, lon: 87.813^{o}, starting day: 10/26/1998). The data are reported as "instantaneous" wave heights and periods.

The current data were obtained during the *EEGLE* project from Acoustic Doppler Current Profiler (*ADCP*) moorings (11/02/97 to 06/12/98), Smart Acoustic Current Meter (*SACM*) moorings (06/15/98 to 04/26/99) and from Vector Averaging Current Meter (*VACM*) moorings (10/06/97 to 06/02/99). Both the *SACM* and the *VACM* data report the values of the horizontal currents as Eastward and Northward components at various locations in Lake Michigan.

The temperature data accompanying both the wave and the flow velocity data can be used in the model evaluations as well, for depth averaged temperature comparisons. The additional temperature data taken at the transects shown in Figure 8.15, as *CTD* (Conductivity-Temperature-Depth) casts are used for direct comparisons between the model results and the data for the vertical temperature distributions at these locations.

Stat #	Lat (°)	Lon (°)	Sediment particle size range (μm)											
			0-1	1-2	2-3	3-4	4-8	8-12	12-16	16-20	20-24	24-28	28-32	32-36
1	41.713	-86.933	0.0045	0.0033	0.0023	0.0019	0.0250	0.0160	0.0480	0.0430	0.0230	0.0080	0.0110	0.0150
2	41.790	-87.293	0.0018	0.0018	0.0013	0.0011	0.0120	0.0080	0.0260	0.0210	0.0100	0.0010	0.0030	0.0070
3	41.833	-86.906	0.0053	0.0036	0.0028	0.0023	0.0681	0.0641	0.0651	0.0581	0.0541	0.0531	0.0561	0.0591
4	41.872	-87.598	0.0018	0.0021	0.0016	0.0016	0.0190	0.0270	0.0960	0.0870	0.0480	0.0170	0.0090	0.0020
6	41.899	-86.649	0.0016	0.0021	0.0019	0.0014	0.0140	0.0080	0.0280	0.0270	0.0200	0.0130	0.0090	0.0050
7	41.943	-86.829	0.1276	0.0860	0.0738	0.0602	1.8222	1.9803	2.1637	2.1819	2.1981	2.1698	2.1171	2.0654
8	41.984	-87.014	0.0600	0.0260	0.0229	0.0202	0.3746	1.4483	0.6831	0.2364	0.1322	0.1322	0.3786	0.6240
9	42.014	-86.750	0.3566	0.2394	0.2133	0.1780	7.7221	9.2798	10.4006	10.9650	11.5023	10.6196	8.9564	7.2933
10	42.066	-87.380	0.0040	0.0050	0.0041	0.0039	0.0390	0.0320	0.1050	0.0980	0.0560	0.0250	0.0140	0.0040
11	42.122	-87.054	0.0916	0.0528	0.0458	0.0431	2.2007	2.6375	2.9342	3.1235	3.3097	3.3527	3.3148	3.2759
13	42.175	-86.734	0.3212	0.1316	0.1221	0.1235	4.8533	5.8875	5.7377	5.4312	5.2332	4.7217	4.2222	3.7307
15	42.285	-86.633	0.5992	0.3704	0.3000	0.2761	11.1913	14.8234	15.3452	12.9658	10.5962	8.7584	7.2087	5.6620
17	42.303	-87.283	0.2986	0.2703	0.2214	0.2095	7.8853	7.9834	8.2776	8.6375	8.9802	8.4019	7.3192	6.2355
18	42.359	-86.956	0.4343	0.3074	0.2491	0.2330	10.0082	12.3865	12.8284	11.5958	10.3591	9.0095	7.5969	6.1823
19	42.382	-86.464	0.2832	0.2573	0.1873	0.1573	5.4624	5.7341	7.6491	8.3404	8.4873	7.7350	5.9659	4.2127
21	42.402	-87.296	0.3997	0.3834	0.3076	0.2902	10.7429	13.7459	14.0540	11.9762	9.9074	8.3261	7.0140	5.7020
22	42.385	-86.591	0.6020	0.4330	0.3334	0.2970	12.3691	17.0916	17.3315	13.5941	9.8884	7.6751	6.2842	4.8953
24	42.503	-86.529	0.6708	0.5101	0.3799	0.3308	13.2108	16.3851	16.0406	12.4200	8.8339	6.8573	5.7715	4.6827
25	42.496	-86.829	0.3832	0.2913	0.2258	0.2063	9.1883	12.3933	13.2811	12.1496	11.0130	9.5838	7.9958	6.4059
26	42.544	-87.179	0.4676	0.4416	0.3426	0.3179	11.4818	13.8893	14.2201	12.5474	10.8757	9.2318	7.6007	5.9717
27	42.587	-86.856	0.3441	0.2825	0.2144	0.1942	8.7252	11.6423	12.3794	11.2527	10.1220	8.8708	7.5554	6.2379
28	42.619	-87.554	0.0067	0.0085	0.0066	0.0062	0.0670	0.0560	0.1750	0.1670	0.1020	0.0510	0.0310	0.0140
29	42.643	-86.532	0.5103	0.3930	0.2874	0.2494	11.0911	13.3170	13.4108	11.5947	9.7836	8.3136	7.0260	5.7405
30	42.660	-87.738	0.0158	0.0165	0.0133	0.0135	0.3448	0.2896	0.2726	0.2666	0.2606	0.2536	0.2465	0.2385
31	42.670	-87.251	0.3707	0.3906	0.2957	0.2723	10.2869	12.5804	13.0381	11.8066	10.5721	9.1730	7.6833	6.1955
32	42.713	-87.409	0.3272	0.3847	0.2898	0.2682	9.8151	11.9761	12.5256	11.5595	10.5864	9.2915	7.8169	6.3432
33	42.733	-86.999	0.3576	0.3399	0.2536	0.2289	9.5015	12.3690	13.0814	11.8894	10.6935	9.2997	7.7991	6.2984
34	42.773	-87.081	0.3298	0.3304	0.2467	0.2234	8.4694	11.7481	12.7421	11.5787	10.4144	9.1017	7.7078	6.3149
36	42.818	-86.486	0.5829	0.4663	0.3306	0.2827	13.4976	15.8835	15.2595	12.1723	9.1089	7.2667	6.0990	4.9294
37	42.828	-86.759	0.5155	0.4666	0.3396	0.2979	12.5157	13.5855	13.0934	11.2178	9.3522	7.9218	6.7295	5.5382
38	42.834	-87.250	0.3795	0.4183	0.3130	0.2855	10.3753	11.6018	11.8805	11.1524	10.4133	9.2267	7.7935	6.3612
39	42.834	-86.999	0.3984	0.3937	0.2923	0.2619	10.9737	15.0395	15.3681	12.5301	9.7110	7.8887	6.6161	5.3434
40	42.835	-86.246	0.0033	0.0015	0.0011	0.0010	0.0130	0.0220	0.0130	0.0060	0.0020	0.0000	0.0000	0.0000
41	42.879	-86.357	0.6856	0.4912	0.3455	0.2931	13.9120	15.7452	15.0355	12.1173	9.2228	7.4113	6.1957	4.9811
43	42.895	-87.641	0.0023	0.0032	0.0023	0.0021	0.0240	0.0230	0.0700	0.0700	0.0510	0.0320	0.0220	0.0120
44	42.953	-87.315	0.0253	0.0291	0.0219	0.0199	0.6512	0.7323	0.7353	0.6462	0.5580	0.4999	0.4578	0.4148
46	43.016	-86.407	0.8101	0.6949	0.4765	0.3993	21.4281	13.4339	9.1866	8.8154	8.4344	7.5490	6.3853	5.2225
48	43.059	-86.662	0.4075	0.3909	0.2826	0.2416	10.0936	12.3115	12.9190	11.9839	11.0397	9.6574	8.0351	6.4117
50	43.112	-86.329	0.0039	0.0036	0.0024	0.0020	0.0450	0.0440	0.0780	0.0830	0.0740	0.0650	0.0490	0.0310

Table 8.5 Calculated sediment size distributions (mass fraction %) at the *EMAP/LMMB* Lake Michigan stations. (Continued)

Table 8.5 Continued.

Stat #	Lat (°)	Lon (°)	Sediment particle size range (μm)											
			0-1	1-2	2-3	3-4	4-8	8-12	12-16	16-20	20-24	24-28	28-32	32-36
51	43.130	-87.544	0.0081	0.0097	0.0074	0.0069	0.1993	0.2113	0.2073	0.1813	0.1552	0.1412	0.1362	0.1312
52	43.186	-87.215	0.0016	0.0018	0.0014	0.0012	0.0430	0.0430	0.0380	0.0310	0.0240	0.0200	0.0160	0.0110
53	43.199	-86.701	0.5269	0.5332	0.3943	0.3350	15.0735	11.3406	9.2690	8.8567	8.4384	7.6728	6.7161	5.7584
54	43.241	-86.889	0.4294	0.4556	0.3456	0.2972	10.6304	11.8526	12.0253	10.9799	9.9314	8.7192	7.4151	6.1110
55	43.294	-86.559	0.5444	0.5481	0.4049	0.3383	15.1190	15.1764	13.8809	11.6037	9.3394	7.7134	6.4387	5.1630
57	43.366	-87.446	0.0228	0.0256	0.0204	0.0184	0.6392	0.8696	0.8706	0.6632	0.4609	0.3747	0.3527	0.3306
58	43.480	-87.455	0.3653	0.4033	0.3279	0.2916	10.3122	12.9392	13.5154	12.1382	10.7580	9.2673	7.7160	6.1656
60	43.447	-87.809	0.0019	0.0019	0.0016	0.0016	0.0180	0.0110	0.0230	0.0250	0.0230	0.0200	0.0110	0.0040
61	43.474	-86.785	0.5118	0.5488	0.4351	0.3652	13.6011	15.3999	14.9665	12.4411	9.9306	8.1240	6.7053	5.2866
62	43.500	-87.617	0.3143	0.3368	0.2784	0.2560	8.4988	10.1009	10.6434	10.0295	9.4086	8.4525	7.3093	6.1660
63	43.583	-87.499	0.3934	0.4274	0.3539	0.3108	10.0074	10.8442	11.2071	10.7612	10.3023	9.2486	7.8650	6.4813
64	43.601	-87.346	0.4667	0.5138	0.4249	0.3647	12.7085	14.9784	14.9191	12.6236	10.3379	8.5501	7.0378	5.5236
65	43.653	-87.016	0.3662	0.4056	0.3387	0.2831	10.3893	12.2398	12.9653	12.4926	12.0010	10.5876	8.6657	6.7428
66	43.709	-86.682	0.4594	0.5088	0.4337	0.3571	12.5431	13.5673	13.6826	12.7036	11.7138	10.1302	8.2196	6.3090
67	43.715	-87.126	0.0671	0.0746	0.0631	0.0526	1.8935	2.2074	2.3567	2.3153	2.2730	2.1650	2.0196	1.8733
70	43.888	-86.913	0.4350	0.4957	0.4399	0.3601	13.0690	14.3591	13.9700	12.0384	10.1127	8.4949	7.0484	5.6029
71	43.918	-87.624	0.0033	0.0035	0.0029	0.0022	0.0280	0.0360	0.1190	0.1300	0.1100	0.0900	0.0640	0.0400
72	43.944	-86.579	0.0021	0.0025	0.0024	0.0019	0.0180	0.0100	0.0310	0.0270	0.0140	0.0040	0.0020	0.0000
73	44.017	-87.475	0.0379	0.0418	0.0361	0.0283	1.1180	1.3188	1.4166	1.4063	1.4022	1.6915	2.1444	2.5974
74	44.069	-87.146	0.0015	0.0017	0.0015	0.0013	0.0380	0.0410	0.0420	0.0400	0.0370	0.0340	0.0300	0.0270
75	44.124	-86.807	0.0751	0.0893	0.0811	0.0676	2.5330	3.4357	3.8717	3.8636	3.8514	3.6908	3.4479	3.2049
76	44.166	-86.624	0.6160	0.7575	0.6893	0.5830	17.1474	17.5626	16.2450	12.8762	9.5317	7.4257	6.0010	4.5763
78	44.254	-86.625	0.3227	0.4032	0.3638	0.3127	9.5209	13.1693	14.0777	12.2759	10.4801	8.9074	7.4582	6.0090
79	44.305	-87.041	0.4423	0.5204	0.4646	0.3978	11.1346	12.2759	12.8974	12.3825	11.8498	10.4322	8.5312	6.6283
80	44.358	-86.708	0.2793	0.3506	0.3116	0.2729	8.9218	11.1815	12.0950	11.6063	11.1036	9.8943	8.2962	6.6991
81	44.388	-87.423	0.0044	0.0050	0.0047	0.0039	0.0410	0.0470	0.1440	0.1470	0.1070	0.0700	0.0410	0.0140
82	44.413	-86.371	0.4140	0.5517	0.5011	0.4458	13.1481	14.2533	13.8536	11.8202	9.7948	8.2037	6.8481	5.4955
83	44.474	-86.705	0.2341	0.3006	0.2638	0.2368	8.7252	11.6423	12.3794	11.2527	10.1220	8.8708	7.5554	6.2379
84	44.481	-87.277	0.0420	0.0482	0.0429	0.0381	1.4530	2.0336	2.2555	2.1592	2.0640	1.9930	1.9363	1.8796
85	44.539	-86.937	0.3046	0.3766	0.3225	0.2921	9.3364	10.8412	11.5160	11.2081	10.8841	9.7763	8.2366	6.6969
86	44.588	-86.604	0.2679	0.3594	0.3151	0.2900	9.0779	10.4700	11.3601	11.5517	11.7174	10.6297	8.8484	7.0672
87	44.624	-86.355	0.3190	0.4500	0.4046	0.3724	12.1056	14.3227	14.0897	11.7443	9.4127	7.8079	6.6004	5.3938
89	44.747	-87.895	0.0031	0.0036	0.0033	0.0029	0.0300	0.0230	0.0690	0.0580	0.0240	0.0010	0.0000	0.0010
91	44.825	-86.498	0.3677	0.5365	0.4702	0.4566	13.4654	14.6944	13.9921	11.5044	9.0355	7.4127	6.2551	5.0985
92	44.857	-87.219	0.0008	0.0009	0.0007	0.0007	0.0070	0.0140	0.0420	0.0360	0.0170	0.0030	0.0020	0.0010
95	44.940	-87.602	0.0060	0.0061	0.0109	0.0121	0.1623	0.3917	1.2491	1.2621	0.9215	0.6341	0.4648	0.3065
97	44.975	-86.367	0.3146	0.4908	0.4381	0.4412	12.0150	13.2336	13.2049	11.8425	10.4790	9.0145	7.4973	5.9802
98	45.131	-85.454	0.0013	0.0022	0.0023	0.0023	0.0210	0.0150	0.0430	0.0460	0.0370	0.0280	0.0150	0.0040
99	45.007	-86.729	0.2460	0.3648	0.3071	0.3112	9.9676	12.0938	12.3336	10.9579	9.5833	8.3391	7.1641	5.9902

Table 8.5 Continued.

Stat #	Lat (°)	Lon (°)	Sediment particle size range (μm)											
			0-1	1-2	2-3	3-4	4-8	8-12	12-16	16-20	20-24	24-28	28-32	32-36
100	45.050	-86.923	0.0037	0.0053	0.0041	0.0038	0.0390	0.0250	0.0710	0.0630	0.0320	0.0080	0.0050	0.0020
101	45.061	-86.389	0.2969	0.4738	0.4250	0.4390	12.4193	14.1165	13.9211	12.0056	10.0971	8.5020	7.0816	5.6601
102	45.063	-86.252	0.0011	0.0017	0.0016	0.0016	0.0590	0.0710	0.0730	0.0670	0.0620	0.0540	0.0450	0.0370
103	45.062	-86.491	0.2856	0.4526	0.4019	0.4201	10.4228	12.4959	13.1724	12.2132	11.2461	9.8059	8.1058	6.4076
104	45.069	-85.857	0.0020	0.0033	0.0029	0.0028	0.0260	0.0200	0.0530	0.0490	0.0300	0.0170	0.0160	0.0160
106	45.134	-87.306	0.0014	0.0019	0.0017	0.0020	0.0190	0.0200	0.0590	0.0560	0.0340	0.0170	0.0120	0.0050
107	45.155	-86.367	0.2941	0.4803	0.4369	0.4587	11.6939	12.0253	11.8899	11.0470	10.1961	8.9859	7.5746	6.1654
108	45.163	-85.707	0.2017	0.3461	0.3249	0.3122	8.8567	11.7595	12.6099	11.5031	10.3943	9.1051	7.7188	6.3305
109	45.248	-86.669	0.0005	0.0008	0.0008	0.0009	0.0110	0.0150	0.0440	0.0420	0.0290	0.0170	0.0090	0.0020
110	45.251	-86.409	0.2474	0.4097	0.3789	0.4063	10.8532	14.4468	14.9414	12.6361	10.3417	8.5876	7.1315	5.6754
111	45.242	-85.556	0.0018	0.0032	0.0031	0.0028	0.0260	0.0190	0.0570	0.0490	0.0210	0.0030	0.0060	0.0110
112	45.294	-86.284	0.2364	0.3858	0.3596	0.3723	10.2462	11.8535	12.0538	10.9162	9.7755	8.5717	7.3328	6.0950
113	45.327	-87.009	0.0017	0.0018	0.0018	0.0017	0.0290	0.0761	0.2792	0.3383	0.3353	0.3313	0.3232	0.3112
115	45.396	-85.595	0.0005	0.0009	0.0008	0.0008	0.0630	0.1050	0.1200	0.1190	0.1180	0.1100	0.1010	0.0900
117	45.446	-85.222	0.0068	0.0105	0.0082	0.0085	0.1011	0.1452	0.4886	0.4826	0.3284	0.2023	0.1442	0.0911
120	45.529	-86.171	0.1407	0.2108	0.2010	0.1948	6.6483	9.4392	10.2698	9.4544	8.6380	7.8063	6.9645	6.1237
121	45.534	-85.636	0.0011	0.0019	0.0019	0.0021	0.0190	0.0150	0.0440	0.0440	0.0320	0.0210	0.0140	0.0080
123	45.603	-87.097	0.0008	0.0008	0.0008	0.0006	0.0080	0.0070	0.0150	0.0130	0.0050	0.0000	0.0000	0.0000
124	45.710	-86.409	0.0014	0.0020	0.0019	0.0017	0.0170	0.0110	0.0260	0.0220	0.0090	0.0010	0.0000	0.0000
125	45.723	-85.331	0.0007	0.0006	0.0007	0.0009	0.0070	0.0060	0.0140	0.0120	0.0060	0.0000	0.0000	0.0010
126	45.761	-86.064	0.1664	0.2252	0.2170	0.2082	6.4181	8.2437	8.6547	7.7959	6.9392	6.3243	5.8388	5.3554
127	45.812	-85.718	0.0032	0.0043	0.0046	0.0048	0.0610	0.0870	0.2761	0.2511	0.1320	0.0430	0.0220	0.0070
129	45.900	-86.105	0.0009	0.0011	0.0010	0.0010	0.0130	0.0110	0.0270	0.0230	0.0090	0.0010	0.0000	0.0000
130	45.909	-85.025	0.0035	0.0055	0.0055	0.0055	0.0571	0.0541	0.1652	0.1862	0.1672	0.1602	0.1752	0.1902
131	46.001	-85.410	0.0098	0.0118	0.0183	0.0152	0.2313	0.4425	1.5087	1.3925	0.7779	0.3053	0.1612	0.0430

Table 8.5 Continued.

Stat #	Lat (°)	Lon (°)	Sediment particle size range (μm)											
			36-40	40-44	44-48	48-52	52-56	56-60	60-70	75-150	150-300	300-500	500-1000	1000-2000
1	41.713	-86.933	0.0200	0.0260	0.0290	0.0260	0.0220	0.0290	1.3936	39.8763	55.9190	1.8654	0.5596	0.0329
2	41.790	-87.293	0.0090	0.0140	0.0160	0.0130	0.0090	0.0080	0.2328	0.6985	6.2649	13.1543	64.0040	15.4825
3	41.833	-86.906	0.0631	0.0651	0.0701	0.0891	0.1122	0.1352	0.7984	36.9778	46.2184	9.3529	4.4106	1.2155
4	41.872	-87.598	0.0080	0.0190	0.0250	0.0240	0.0230	0.0200	0.6901	22.1376	55.3383	17.3294	3.2277	0.8459
6	41.899	-86.649	0.0030	0.0020	0.0020	0.0030	0.0050	0.0080	0.5826	14.4687	36.7274	25.8624	16.6913	5.5134
7	41.943	-86.829	2.0127	1.9610	1.9083	1.8546	1.7999	1.7462	0.2900	23.2351	29.2125	11.7024	5.6160	1.6153
8	41.984	-87.014	0.6240	0.5278	0.5218	0.7242	0.9145	0.6851	0.0000	42.7528	34.5069	10.8621	3.1791	0.5630
9	42.014	-86.750	5.6291	3.9650	2.4134	1.9554	1.7776	1.5979	0.0134	1.4151	1.9709	0.9689	0.4419	0.1250
10	42.066	-87.380	0.0100	0.0210	0.0320	0.0420	0.0500	0.0510	1.7212	22.2377	54.6269	16.8605	3.7942	0.1633
11	42.122	-87.054	3.2371	3.2002	3.1532	3.0171	2.8585	2.6999	0.2644	19.8924	25.2318	9.5437	2.2826	0.2370
13	42.175	-86.734	3.1789	2.6010	2.0734	1.9035	1.8081	1.5387	0.0000	16.8684	20.5763	7.6895	1.2461	0.0000
15	42.285	-86.633	4.1143	2.5656	1.1288	0.7803	0.7080	0.6377	0.0476	0.6237	0.8666	0.3645	0.0643	0.0017
17	42.303	-87.283	5.1517	4.0690	3.0510	2.6881	2.4899	2.2928	0.1575	3.4191	7.2020	3.6656	0.9792	0.1137
18	42.359	-86.956	4.7687	3.3551	2.0354	1.6475	1.4986	1.3456	0.0531	1.2127	1.7906	0.8756	0.2063	0.0206
19	42.382	-86.464	3.3376	2.8071	2.1538	1.6003	1.1708	0.9370	1.7643	9.2885	14.7889	6.5901	1.0897	0.0000
21	42.402	-87.296	4.3879	3.0748	1.8505	1.4925	1.3569	1.2204	0.0401	0.7503	1.6901	0.9823	0.2709	0.0340
22	42.385	-86.591	3.5054	2.1145	0.8253	0.5262	0.4778	0.4294	0.0411	0.4081	0.5855	0.2471	0.0437	0.0013
24	42.503	-86.529	3.5959	2.5091	1.4946	1.2016	1.0917	0.9819	0.0942	0.9258	1.3881	0.5291	0.0908	0.0036
25	42.496	-86.829	4.8169	3.2279	1.7488	1.3513	1.2264	1.1036	0.0569	1.0447	1.4438	0.6918	0.1552	0.0153
26	42.544	-87.179	4.3416	2.7115	1.1983	0.8299	0.7556	0.6784	0.0242	0.4743	0.8942	0.5398	0.1448	0.0192
27	42.587	-86.856	4.9204	3.6050	2.3728	1.9822	1.8055	1.6298	0.0911	1.8155	2.4356	1.2078	0.2813	0.0320
28	42.619	-87.554	0.0210	0.0390	0.0440	0.0250	0.0060	0.0060	0.9297	9.3509	41.9848	34.6684	10.6579	1.5765
29	42.643	-86.532	4.4540	3.1684	1.9667	1.6077	1.4631	1.3154	0.1002	1.4565	1.9364	0.6843	0.1213	0.0087
30	42.660	-87.738	0.2305	0.2235	0.2165	0.2295	0.2455	0.2616	0.3165	48.6666	36.3401	8.5737	1.9056	0.5585
31	42.670	-87.251	4.7067	3.2179	1.8308	1.4439	1.3113	1.1807	0.0385	0.7382	1.5362	1.0123	0.2780	0.0405
32	42.713	-87.409	4.8706	3.3959	2.0222	1.6245	1.4767	1.3268	0.0385	0.5824	1.7664	1.2878	0.3678	0.0564
33	42.733	-86.999	4.7967	3.2971	1.8973	1.5047	1.3678	1.2289	0.0462	1.1051	1.5219	0.8724	0.2197	0.0302
34	42.773	-87.081	4.9211	3.5272	2.2266	1.8308	1.6654	1.5021	0.0568	1.3994	2.0464	1.2481	0.3226	0.0463
36	42.818	-86.486	3.7598	2.5922	1.5019	1.1934	1.0853	0.9752	0.0494	1.2344	1.2605	0.3935	0.0681	0.0070
37	42.828	-86.759	4.3469	3.1556	2.0410	1.6923	1.5379	1.3826	0.0576	1.5725	1.6452	0.7935	0.1783	0.0230
38	42.834	-87.250	4.9270	3.4937	2.1564	1.7569	1.5971	1.4353	0.0419	1.0304	1.7882	1.1989	0.3236	0.0495
39	42.834	-86.999	4.0698	2.7972	1.6112	1.2776	1.1601	1.0436	0.0362	0.9848	1.2542	0.7382	0.1840	0.0260
40	42.835	-86.246	0.0000	0.0000	0.0000	0.0000	0.0000	0.0000	0.0000	15.6118	74.0690	9.9175	0.2964	0.0423
41	42.879	-86.357	3.7665	2.5519	1.4195	1.1107	1.0077	0.9067	0.0338	1.1444	1.2987	0.2857	0.0345	0.0032
43	42.895	-87.641	0.0180	0.0300	0.0340	0.0220	0.0090	0.0080	0.7078	3.3765	47.6766	36.0852	9.9785	1.7404
44	42.953	-87.315	0.3737	0.3306	0.2905	0.2825	0.2825	0.2805	0.7773	22.9893	36.9003	24.9508	6.6947	1.0555
46	43.016	-86.407	4.0588	2.8960	1.8103	1.4845	1.3513	1.2200	0.0418	2.3899	1.4436	0.3967	0.0624	0.0087
48	43.059	-86.662	4.7904	3.1670	1.6572	1.2598	1.1443	1.0288	0.0320	1.3636	1.0907	0.5615	0.1154	0.0147
50	43.112	-86.329	0.0280	0.0290	0.0320	0.0380	0.0450	0.0470	0.7604	68.7307	23.8071	5.2411	0.6434	0.1170

Table 8.5 Continued.

Stat #	Lat (°)	Lon (°)	Sediment particle size range (μm)											
			36-40	40-44	44-48	48-52	52-56	56-60	60-70	75-150	150-300	300-500	500-1000	1000-2000
51	43.130	-87.544	0.1242	0.1192	0.1142	0.1262	0.1432	0.1592	0.5584	27.9460	37.7801	23.9544	6.4688	1.1112
52	43.186	-87.215	0.0090	0.0040	0.0000	0.0000	0.0000	0.0000	0.7644	31.2760	36.8401	24.1437	5.8732	0.8575
53	43.199	-86.701	4.8027	3.8449	2.9412	2.5720	2.3358	2.1006	0.0526	2.6895	2.1269	1.3215	0.2655	0.0320
54	43.241	-86.889	4.8049	3.5018	2.2816	1.8982	1.7255	1.5517	0.0397	1.8131	1.7374	1.1723	0.2500	0.0312
55	43.294	-86.559	3.8884	2.6137	1.4261	1.1054	1.0045	0.9026	0.0174	1.2792	0.8300	0.5515	0.1002	0.0106
57	43.366	-87.446	0.3096	0.2865	0.2675	0.2655	0.2685	0.2715	0.6371	33.2885	34.2462	19.9585	4.8371	0.7148
58	43.480	-87.455	4.6152	3.0639	1.6210	1.2389	1.1245	1.0120	0.0241	1.1664	1.1381	0.6310	0.1457	0.0192
60	43.447	-87.809	0.0020	0.0020	0.0050	0.0070	0.0110	0.0080	0.0000	75.8488	21.6517	1.1768	0.8123	0.3333
61	43.474	-86.785	3.8690	2.4503	1.1324	0.8056	0.7325	0.6595	0.0112	0.6591	0.6854	0.5630	0.1057	0.0102
62	43.500	-87.617	5.0228	3.8796	2.8068	2.4294	2.2271	2.0248	0.0679	4.6136	3.3097	1.4218	0.3508	0.0513
63	43.583	-87.499	5.0987	3.7150	2.4214	2.0125	1.8275	1.6446	0.0457	1.9997	1.8595	0.9387	0.2097	0.0243
64	43.601	-87.346	4.0103	2.4971	1.0925	0.7527	0.6845	0.6144	0.0168	0.6317	0.7162	0.4339	0.0912	0.0096
65	43.653	-87.016	4.8200	2.8982	1.1160	0.7027	0.6383	0.5739	0.0118	0.4586	0.6588	0.5344	0.1008	0.0087
66	43.709	-86.682	4.3993	2.4887	0.7199	0.3358	0.3053	0.2748	0.0030	0.1688	0.2963	0.3204	0.0555	0.0039
67	43.715	-87.126	1.7300	1.5836	1.4453	1.3686	1.3091	1.2495	0.5670	19.0669	28.4594	21.4450	4.0766	0.3379
70	43.888	-86.913	4.1564	2.7098	1.3643	1.0188	0.9247	0.8317	0.0128	0.3772	1.0124	0.9823	0.1724	0.0113
71	43.918	-87.624	0.0420	0.0550	0.0580	0.0370	0.0170	0.0260	2.1014	31.7472	46.2317	15.6599	3.3006	0.0950
72	43.944	-86.579	0.0000	0.0000	0.0010	0.0020	0.0050	0.0040	0.0000	0.2611	36.9614	53.1300	8.9656	0.5549
73	44.017	-87.475	3.0494	3.5023	3.9028	3.7978	3.5621	3.3284	1.0024	17.0936	30.9193	13.8173	2.6691	0.1162
74	44.069	-87.146	0.0230	0.0190	0.0170	0.0150	0.0150	0.0160	0.7154	15.4238	44.3185	33.1121	5.7037	0.3264
75	44.124	-86.807	2.9620	2.7190	2.4842	2.3369	2.2108	2.0858	0.1077	3.1482	23.3416	25.9789	4.1692	0.2436
76	44.166	-86.624	3.1525	1.7288	0.4093	0.1335	0.1208	0.1082	0.0002	0.0080	0.1274	0.1699	0.0282	0.0016
78	44.254	-86.625	4.5598	3.1096	1.7600	1.3845	1.2590	1.1315	0.0030	0.1012	1.3287	1.7581	0.2889	0.0150
79	44.305	-87.041	4.7263	2.8233	1.0595	0.6540	0.5949	0.5347	0.0046	0.1586	0.7439	0.6468	0.0914	0.0051
80	44.358	-86.708	5.1000	3.5030	2.0128	1.5951	1.4492	1.3032	0.0046	0.1767	1.5943	1.9345	0.2996	0.0150
81	44.388	-87.423	0.0090	0.0140	0.0150	0.0130	0.0100	0.0100	0.4296	17.6607	54.0744	22.7662	4.1237	0.2455
82	44.413	-86.371	4.1409	2.7864	1.5268	1.1844	1.0766	0.9667	0.0050	0.0833	1.0085	1.5927	0.2867	0.0121
83	44.474	-86.705	4.9204	3.6050	2.3728	1.9822	1.8055	1.6298	0.0078	0.2811	2.3176	2.8147	0.4228	0.0193
84	44.481	-87.277	1.8218	1.7641	1.7083	1.6546	1.6009	1.5492	0.2076	8.9790	36.1022	25.8119	2.7008	0.1541
85	44.539	-86.937	5.1571	3.6184	2.1826	1.7627	1.6007	1.4398	0.0067	0.3395	1.9390	1.9170	0.2343	0.0108
86	44.588	-86.604	5.2869	3.5066	1.8491	1.4100	1.2813	1.1526	0.0057	0.1476	1.3381	1.7780	0.2780	0.0112
87	44.624	-86.355	4.1882	2.9806	1.8537	1.5162	1.3768	1.2374	0.0074	0.0812	1.2555	2.0855	0.3804	0.0139
89	44.747	-87.895	0.0170	0.0380	0.0510	0.0440	0.0350	0.0350	1.2002	45.9076	42.8293	8.7459	0.6668	0.2111
91	44.825	-86.498	3.9409	2.7843	1.7051	1.3887	1.2677	1.1457	0.0105	0.1776	1.5945	2.3116	0.3724	0.0119
92	44.857	-87.219	0.0000	0.0000	0.0000	0.0000	0.0000	0.0000	0.0000	2.9245	40.0872	56.4199	0.4434	0.0000
95	44.940	-87.602	0.2474	0.2244	0.1933	0.1412	0.0912	0.1302	6.4350	60.7816	20.8427	4.4798	0.8352	0.1708
97	44.975	-86.367	4.4631	2.9460	1.5340	1.1631	1.0560	0.9509	0.0088	0.0809	0.9472	1.6106	0.2796	0.0080
98	45.131	-85.454	0.0100	0.0230	0.0300	0.0250	0.0200	0.0170	0.7473	1.7323	34.2949	53.7238	9.1030	0.0566
99	45.007	-86.729	4.8172	3.6423	2.5416	2.1603	1.9626	1.7659	0.0144	0.3947	2.2395	2.4757	0.3192	0.0078

Table 8.5 Continued.

Stat #	Lat (°)	Lon (°)	Sediment particle size range (μm)											
			36-40	40-44	44-48	48-52	52-56	56-60	60-70	75-150	150-300	300-500	500-1000	1000-2000
100	45.050	-86.923	0.0260	0.0610	0.0800	0.0590	0.0380	0.0240	0.2049	13.7060	48.2302	32.9330	4.3396	0.0362
101	45.061	-86.389	4.2396	2.8181	1.4969	1.1447	1.0396	0.9354	0.0092	0.0750	0.9201	1.5895	0.2852	0.0085
102	45.063	-86.252	0.0280	0.0190	0.0120	0.0090	0.0090	0.0070	0.3173	1.6749	28.5359	56.9436	11.6174	0.3528
103	45.062	-86.491	4.7075	3.0084	1.4293	1.0336	0.9383	0.8451	0.0084	0.0908	0.8989	1.3859	0.2175	0.0062
104	45.069	-85.857	0.0140	0.0110	0.0110	0.0120	0.0140	0.0120	0.3352	0.5202	22.1593	62.2819	14.0678	0.3237
106	45.134	-87.306	0.0100	0.0170	0.0230	0.0250	0.0260	0.0260	0.8232	23.8298	50.3159	20.8113	3.1722	0.6915
107	45.155	-86.367	4.7552	3.3449	2.0293	1.6431	1.4928	1.3416	0.0138	0.0765	1.2264	2.3205	0.4910	0.0168
108	45.163	-85.707	4.9442	3.5569	2.2607	1.8631	1.6918	1.5215	0.0212	0.1129	1.4062	2.5656	0.5800	0.0129
109	45.248	-86.669	0.0030	0.0070	0.0100	0.0090	0.0090	0.0090	0.4330	1.1691	35.7644	56.8399	5.4231	0.1515
110	45.251	-86.409	4.2193	2.7632	1.4094	1.0578	0.9615	0.8641	0.0090	0.0319	0.7451	1.4931	0.3749	0.0150
111	45.242	-85.556	0.0140	0.0170	0.0170	0.0140	0.0110	0.0100	0.5303	5.6751	42.4106	41.6998	9.1388	0.2595
112	45.294	-86.284	4.8552	3.6174	2.4576	2.0711	1.8818	1.6925	0.0160	0.0482	1.2826	2.9027	0.9370	0.0392
113	45.327	-87.009	0.2332	0.1271	0.0490	0.0310	0.0170	0.0430	2.8910	65.0224	26.2903	2.6458	0.6066	0.0129
115	45.396	-85.595	0.0810	0.0700	0.0600	0.0540	0.0490	0.0450	0.8260	3.5113	30.4991	49.8524	13.8538	0.2690
117	45.446	-85.222	0.0851	0.0961	0.1021	0.0911	0.0831	0.1141	8.2612	9.8315	41.3573	31.8501	5.5644	0.5462
120	45.529	-86.171	5.2808	4.4400	3.6409	3.2565	2.9759	2.6973	0.0273	0.3643	2.8898	5.2465	2.9469	0.1421
121	45.534	-85.636	0.0090	0.0130	0.0140	0.0110	0.0070	0.0080	0.5464	1.5834	21.3317	57.6169	18.3991	0.2565
123	45.603	-87.097	0.0010	0.0020	0.0030	0.0040	0.0040	0.0030	0.0000	2.2910	62.7167	33.1828	1.7001	0.0415
124	45.710	-86.409	0.0050	0.0130	0.0160	0.0110	0.0040	0.0010	0.0000	0.2287	4.7266	43.5956	48.6162	2.6900
125	45.723	-85.331	0.0000	0.0000	0.0000	0.0000	0.0000	0.0010	0.2892	0.2376	30.1937	56.9579	11.6209	0.6508
126	45.761	-86.064	4.8689	4.3865	3.9163	3.6083	3.3401	3.0729	0.0745	2.2925	9.4009	5.3677	3.1147	0.1696
127	45.812	-85.718	0.0280	0.0660	0.0880	0.0750	0.0630	0.0570	1.7718	40.2046	33.3257	17.1449	5.4197	0.8599
129	45.900	-86.105	0.0010	0.0020	0.0030	0.0020	0.0010	0.0030	0.1875	13.6374	76.8446	8.3137	0.7814	0.1354
130	45.909	-85.025	0.1552	0.1001	0.0621	0.0611	0.0641	0.0891	4.2062	61.6954	17.9050	10.5981	3.5835	0.3050
131	46.001	-85.410	0.1712	0.3954	0.5156	0.3924	0.2613	0.1992	3.1777	75.9138	10.1569	3.0022	0.7408	0.1560

CHAPTER 9

SHORELINE EROSION

Sediments enter Lake Michigan via river and runoff loading and shoreline erosion by the wind and the waves. A study on the US Great Lakes Shoreline Erosion Loadings (Monteith and Sonzogni [1976]) shows that the sediment contribution from the rivers is about 5.5 % while the sediment contribution from runoff and aeolian erosion is much less, even with the increased erosion of the dunes by the wind on the east side and the upper peninsula of Lake Michigan (Monteith and Sonzogni [1976]). This points to material eroded from the shoreline due to wave action as the major external sediment loading source for Lake Michigan. The shoreline of Lake Michigan is about 2160 km and the amount of sediments that are being eroded from it and transported under water has been estimated to be, on average, $8.375 \cdot 10^6$ m^3 annually (Monteith and Sonzogni [1976]).

9.1 Lake Michigan Beach Classification

In 1986 the U.S. Army Corps of Engineers, Detroit District (Stewart [1994, 1997]) started an effort to re-classify the various reaches within each county along the Lake Michigan shoreline according to their erodibility characteristics and to compute the measured recession rates data for the lake. It may be worth mentioning here that this new classification is based on an improved and more detailed version of the 1975 US Army Corps of Engineers shoreline classification that initially included only ten shoreline types (Monteith and Sonzogni [1976]). Recession and erosion rates, based on the new shoreline classification, although expected to be more accurate are not available at the present time. The 17 new shoreline types from the above study, along with the calculated percentages of each shoreline type for Lake Michigan during the present study, are presented in Table 9.1 and graphically presented in Figure 9.1.

Classification #	Classification Type	Total (%)	SL* Total (%)	SL* Reaches (%)
1	High Bluff (> 15 m)	2.85	6.08	92.29
2	High Bluff (> 15 m) with Beach	13.00	25.83	85.90
3	Low Bluff (< 15 m)	4.15	2.01	21.05
4	Low Bluff (< 15 m) with Beach	1.90	4.40	100.00
5	Sandy/Silt Banks	0.63	1.48	100.00
6	Clay Banks	0.00	0.00	0.00
7	Sandy Beach/ Dunes	49.35	34.25	30.00
8	Coarse Beaches	0.58	0.18	13.67
9	Baymouth-Barrier Beaches	8.70	11.77	58.44
10	Bedrock (Resistant)	2.84	0.00	0.00
11	Bedrock (Non-Resistant)	5.57	0.00	0.00
12	Low Riverine/Coastal Plain	0.00	0.00	0.00
13	Open Shoreline Wetlands	0.47	0.00	0.00
14	Semi-Protected Wetlands	0.00	0.00	0.00
15	Composites	0.00	0.00	0.00
16	Artificial	6.32	13.70	93.75
17	Unclassified	3.64	0.30	3.56

(*) Southern Lake

Table 9.1 Lake Michigan shoreline classification.

From the above new classification scheme (Table 9.1), a file with Lake Michigan shoreline type data was prepared during the *EEGLE/NOAA* project (http://www.glerl.noaa.gov/eegle/resources/#reg_met) by assigning the number that corresponds to the shoreline type of each shoreline segment to the first grid point nearest to the shoreline as based upon a 2*x*2 km grid. Analysis of the shoreline data show that Sheboygan County (location shown on Figure 9.2, to give an example), consists of 8 % high bluffs, 16 % high bluffs with beach, 4 % low bluffs, 4 % low bluffs with beach, 12 % sandy/silty banks, 48 % sandy beaches/dunes and 8 % baymouth barrier beaches. Distribution of the shoreline types within each of the other counties can be decided in a similar way.

Table 9.1 shows the distributions of the various shore types along the whole lake shoreline and along the Southern part (SL) of the lake shoreline. The last column indicates the percent of reaches of a specific soil type that exist at the Southern part of the lake. For example, 55.53 km of the whole lake shoreline is classified as high bluffs and 51.25 km of the Southern part of the lake is classified as high bluffs. This shows that 92.29 % of the total high bluff reaches are positioned in the Southern part of the lake.

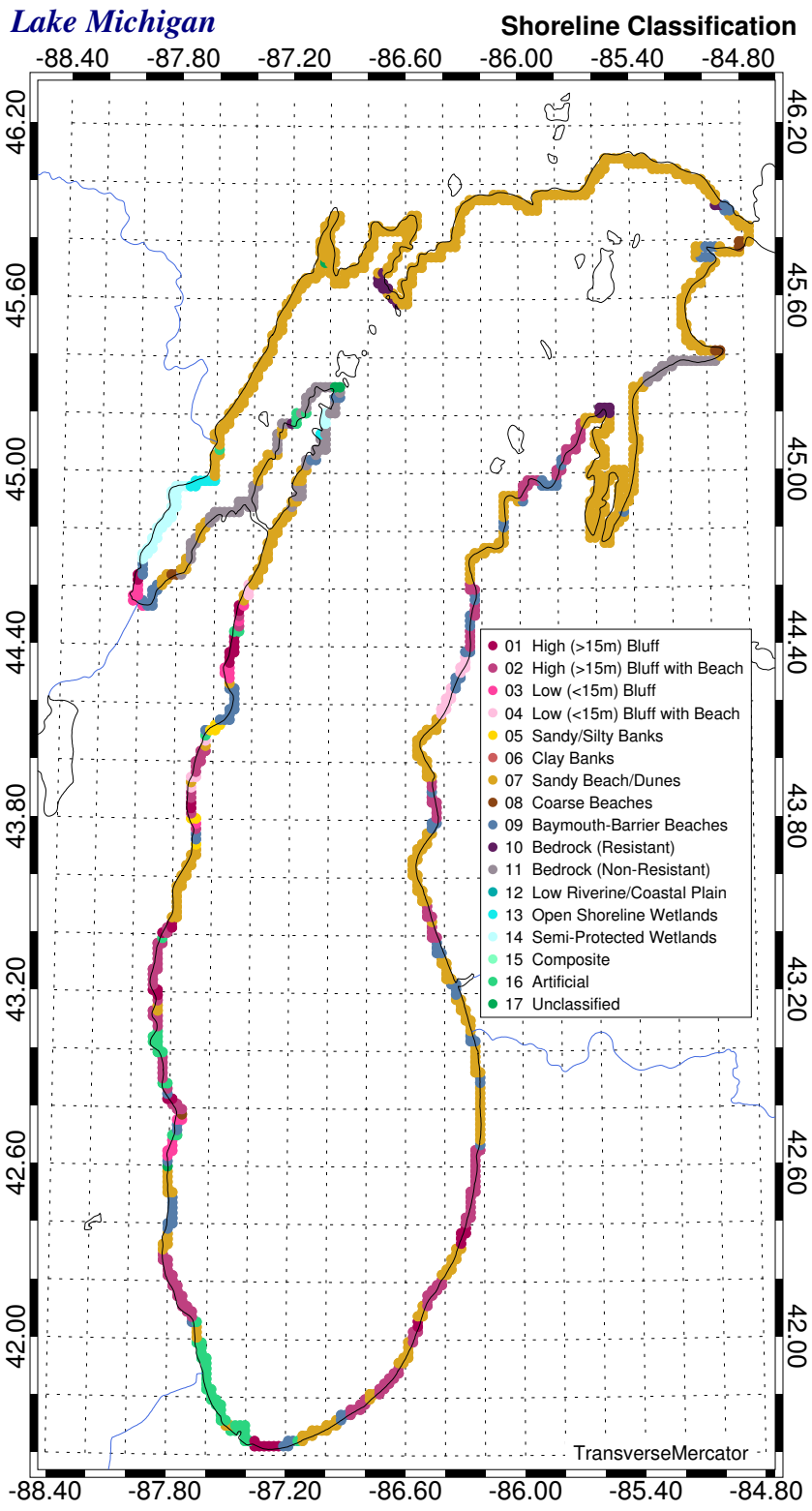

Figure 9.1 Lake Michigan shoreline classification.

9.2 Lake Michigan Shoreline Erosion

The work of Armstrong et al. [1976], as cited by Monteith and Sonzogni [1976], is the main source of all the available information that exists on the erosion rates of the Great Lakes to date, and is used in the present study. The erosion rates in the above study were calculated for each reach within a county from measured or estimated recession rates and then summed to reflect the total erosion rate for the county. Erosion rates from measured recession rates consisted 77 % of the cases, while the rest were estimated by analysis of recession rates from areas with similar erosion characteristics, soil consistency, and exposure to waves.

The measured recession rates were derived from field measurements or aerial photos and they are included in a report by the University of Michigan (Armstrong et al. [1976]). The report incorporated most of the known studies on the shoreline erosion of the Great Lakes that took place until the mid 1970's. Taking into account the estimated recession rates, the calculated overall quality of the potential erosion rates have been characterized as "only fair". Maximum confidence is placed on the erosion rates of the Berrien, Van Buren, Allegan and Ottawa Counties where 96 %, were calculated from measured recession rates (Monteith and Sonzogni [1976]). According to Stewart [1994], the recession rates presented by Armstrong et al. [1976] do not indicate the actual time period over which the recession rates were calculated. Most current works on the shoreline erosion of the Great Lakes accept the data collected by Armstrong et al. [1976] and add information on recession rates from more recent studies at regions where recession rate gaps existed (Stewart [1994]).

The average, maximum and minimum annual bluff erosion rates are calculated using the following rectangular prism method:

$$E_c = B \cdot L \cdot R \tag{9.2.1}$$

where E_c (m^3/yr) is the erosion rate for a given shoreline reach (average, maximum or minimum), B (m) is the bluff height for the reach, L (m) is the shoreline length and R (m/yr) is the recession rate (average, maximum or minimum). In other words, the volume of the sediment removed from the bluff is equated to the volume of an equivalent rectangular prism with height equal the bluff height, length equal to the length of the bluff toe along the shoreline and width equal to the distance of the bluff recession within the observed time period, that is, the recession rate. Reaches characterized as non-erodible and beach fills are assigned a zero recession rate.

Since the recession rate is a parameter that varies continuously with the ever changing characteristics of each reach, the water levels and the weather patterns, the above authors reported their results as an average, a maximum and a minimum erosion rate, expressed as the volume of material eroded from each county along the shoreline of the lake annually. Wherever measured maximum, average and minimum recession rates were available, they were used for the calculation of the corresponding erosion rates. For reaches lacking measured recession rates, the maximum recession rates were estimated as being equal to 1.8 the value of the estimated average value and the minimum recession rates were estimated as being equal to 0.4 times the estimated average value. The average, maximum and minimum erosion rates per county per year and the calculated average, maximum and minimum erosion rates per km of shoreline per year are listed in Table 9.2 and their graphical representation is given in Figure 9.2.

From Table 9.2, Leelanau with $1.44 \cdot 10^6$ m^3/yr, is the county that contributes the highest sediment load annually, followed by Allegan with $8.27 \cdot 10^5$ m^3/yr and Ozaukee with $5.90 \cdot 10^5$ m^3/yr. However, the contribution of eroded material per kilometer of shoreline is highest at Allegan County with $2.11 \cdot 10^4$ m^3/yr $\cdot$ km, followed by Ozaukee with $1.43 \cdot 10^4$ m^3/yr $\cdot$ km and Porter with $1.35 \cdot 10^4$ m^3/yr $\cdot$ km. The Southern part of the lake with 823 km shoreline, defined by the border of Kewaunee County with Door County on the Western lake side and by the border of Benzie County with Leelanau County on the Eastern side, contributes $6.215 \cdot 10^6$ m^3 of eroded soil annually on average, or 74 % of the total lake erosion loadings, while the Northern part of the lake with 1336 km shoreline contributes $2.159 \cdot 10^6$ m^3 of eroded soil annually on average or 26 % of the total loadings.

9.3 The Soil Types of Lake Michigan

Clay, silt and sand mass fractions per county, measured or estimated, are given in Table 9.3. Measured data (Table 9.3, table footnote 1) exist for only 11 counties, mostly at the Southwestern part of the lake, and were obtained from *GLERL/NOAA*. The data are expressed in kg/yr $\cdot$ km of eroded clayey, loamy and sandy soils. The fractions of the clay, silt and sand particle size classes are inferred from the soil texture using the *USDA* soil textural triangle.

The soil types for counties without measured data were decided from the geological map and the soil descriptions in Veach [1953] (Table 9.3, table footnote 2), and the Web Soil Survey maps and soil descriptions (Table 9.3, table footnote 3). From the soil types present at each sub-reach of the shoreline, the fractions of the clay, silt and sand particle size classes are inferred using the *USDA* soil

State	County	Shore (km)	max Erosion[1] (10^3 m^3/yr)	ave Erosion[2] (10^3 m^3/yr)	min Erosion[3] (10^3 m^3/yr)	max Erosion (10^3 m^3/yr · km)	ave Erosion (10^3 m^3/yr · km)	min Erosion (10^3 m^3/yr · km)
Wisconsin	Marinette	28.2	7.0	4.0	0.0	0.248	0.142	0.000
Wisconsin	Oconto	43.6	10.0	3.0	0.0	0.229	0.069	0.000
Wisconsin	Brown	57.4	13.0	4.0	0.0	0.226	0.070	0.000
Wisconsin	Door	262.5	52.0	18.0	5.0	0.198	0.069	0.019
Wisconsin	Kewaunee	45.8	163.0	138.0	57.0	3.560	3.010	1.240
Wisconsin	Manitowoc	55.9	212.0	148.0	53.0	3.790	2.650	0.948
Wisconsin	Sheboygan	42.1	99.0	76.0	58.0	2.350	1.810	1.380
Wisconsin	Ozaukee	41.3	705.0	590.0	519.0	17.100	14.300	12.600
Wisconsin	Milwaukee	43.7	474.0	367.0	258.0	10.900	8.410	5.910
Wisconsin	Racine	22.2	251.0	172.0	95.0	11.300	7.740	4.280
Wisconsin	Kenosha	19.8	101.0	84.0	66.0	5.100	4.240	3.330
Illinois	Lake	42.3	443.0	286.0	129.0	10.500	6.750	3.050
Illinois	Cook	61.5	137.0	86.0	34.0	2.230	1.400	0.552
Indiana	Lake	35.0	43.0	29.0	21.0	1.230	0.829	0.600
Indiana	Porter	26.1	479.0	352.0	269.0	18.300	13.500	10.300
Indiana	La Porte	10.7	68.0	52.0	44.0	6.380	4.880	4.130
Michigan	Berrien	67.7	785.0	556.0	147.0	11.600	8.220	2.170
Michigan	Van Buren	20.9	534.0	248.0	41.0	25.600	11.900	1.970
Michigan	Allegan	39.3	1320.0	827.0	427.0	33.500	21.100	10.900
Michigan	Ottawa	39.3	1040.0	481.0	80.0	26.300	12.200	2.030
Michigan	Muskegon	42.5	887.0	379.0	37.0	20.900	8.910	0.870
Michigan	Oceana	42.4	808.0	337.0	37.0	19.100	7.950	0.873
Michigan	Mason	45.5	955.0	346.0	1.0	21.000	7.600	0.022
Michigan	Manistee	40.8	604.0	298.0	75.0	14.800	7.300	1.840
Michigan	Benzie	39.1	827.0	363.0	20.0	21.200	9.290	0.512
Michigan	Leelanau	157.4	3160.0	1440.0	304.0	20.100	9.150	1.930
Michigan	Grand Traverse	87.7	364.0	209.0	2.0	4.150	2.380	0.023
Michigan	Antrim	41.2	29.0	16.0	1.0	0.704	0.388	0.024
Michigan	Charlevoix	35.3	52.0	13.0	1.0	1.470	0.368	0.028
Michigan	Emmet	106.9	259.0	152.0	66.0	2.420	1.420	0.618
Michigan	Mackinac	117.8	310.0	154.0	48.0	2.630	1.310	0.407
Michigan	Schoolcraft	72.9	32.0	20.0	9.0	0.439	0.274	0.123
Michigan	Delta	263.0	172.0	113.0	73.0	0.654	0.430	0.278
Michigan	Menominee	62.1	23.0	13.0	5.0	0.370	0.209	0.081

(1, 2, 3) Calculated using the highest, average and lowest reccession rates for all reaches within each county respectively.

Table 9.2 Estimated shoreline erosion rates from the counties along the Lake Michigan shoreline.

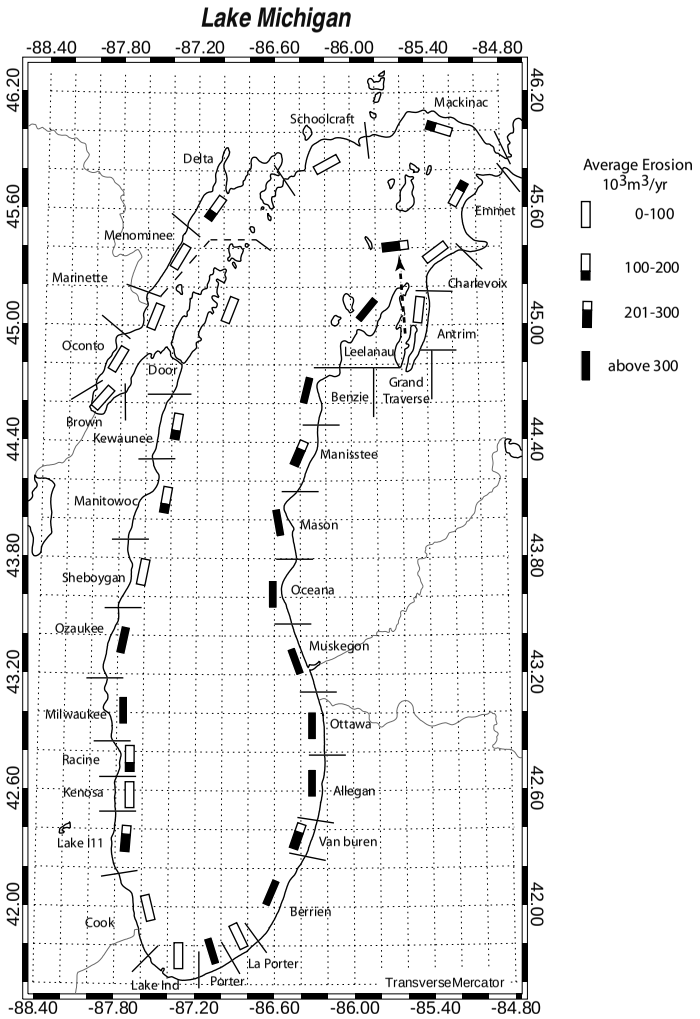

(a) (source: Monteith and Sonzogni [1976])

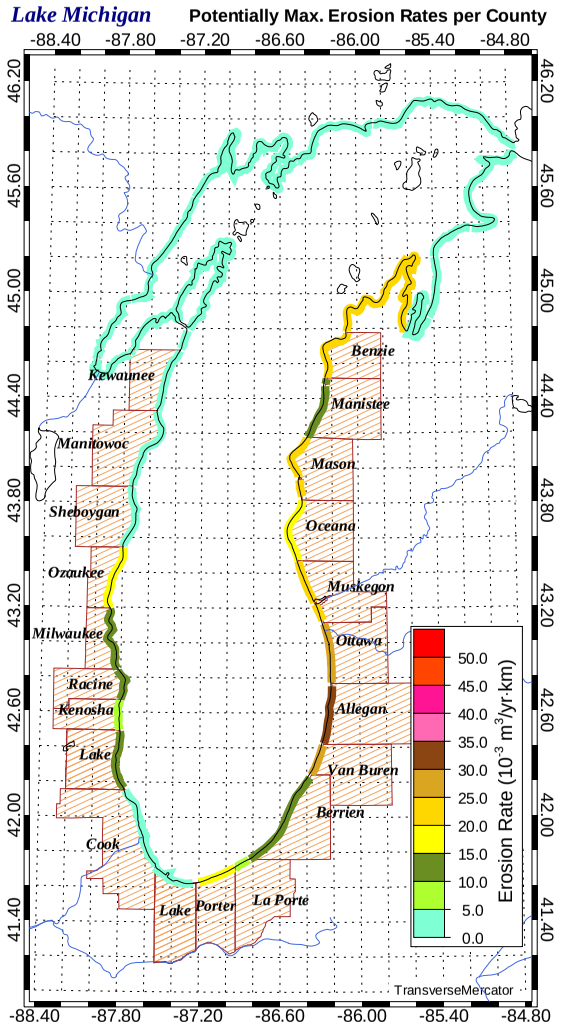

(b)

Figure 9.2 County and shoreline erosion rates. (Continued)

Figure 9.2 Continued.

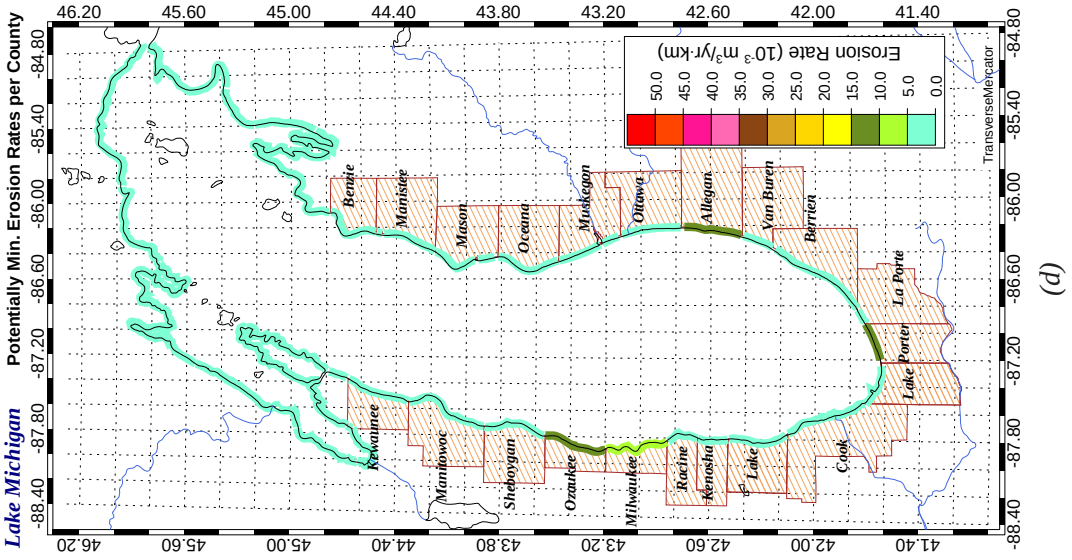

(d)

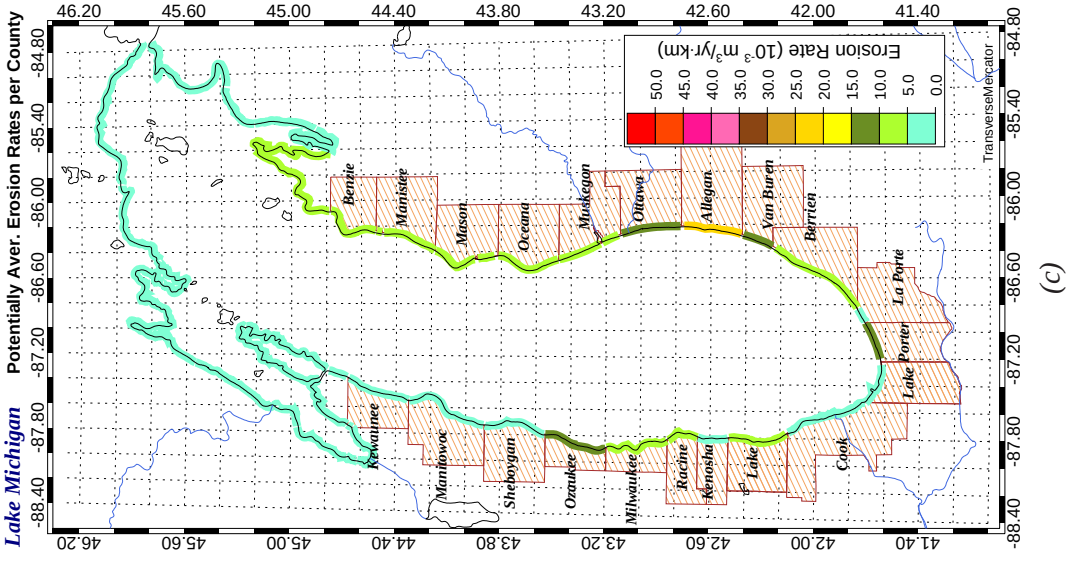

(c)

County Name	Source	Clay (%)	Silt (%)	Sand (%)
Marinette	(1)	28	36	36
Oconto	(3)	7	9	84
Brown	(2)	18	17	65
Kewaunee	(1)	10	45	45
Door	(3)	10	35	55
Manitowoc	(1)	10	25	65
Sheboygan	(1)	14	43	43
Ozaukee	(1)	10	41	49
Milwaukee	(1)	30	35	35
Racine	(1)	7	25	68
Kenosha	(3)	8	19	73
Lake I11	(1)	9	42	49
Cook	(1)	6	15	79
Lake Ind.	(3)	6	9	85
Porter	(3)	5	5	90
LaPorte	(3)	5	5	90
Berrien	(2)	9	13	78
Van Buren	(2)	6	6	88
Allegan	(2)	16	27	57
Ottawa	(2)	7	10	83
Muskegon	(2)	7	9	84
Oceana	(1)	5	7	78
Mason	(2)	15	8	77
Manistee	(2)	15	14	70
Benzie	(2)	10	14	76
Leelanau	(2)	14	14	72
Grand Traverse	(2)	16	27	57
Antrim	(2)	6	6	88
Charlevoix	(2)	6	11	84
Emmet	(2)	10	15	75
Mackinac	(2)	17	15	68
Schoolcraft	(2)	5	5	90
Delta	(1)	7	19	74
Menominee	(2)	20	10	70

(1) D. Schwab, *GLERL/NOAA* personal communication
(2) Inferred from the geological map and soil descriptions in Veach [1953]
(3) Inferred from Web Soil Survey maps and soil descriptions, http://websoilsurvey.nrcs.usda.gov/app/

Table 9.3 Particle size fractions of the eroded material along the Lake Michigan shoreline.

textural triangle. The fractions of each size class are calculated as the sum of the weighted fractions of all the reaches, with the weight for each reach set equal to the ratio between the shoreline length of the reach and the total erodible shoreline length of the county. Rocky non-erodible shoreline types have not been considered in the calculations.

From Table 9.3 it is evident that the majority of the eroded material from the Lake Michigan shoreline is sand, followed by silt and clay. It can be calculated that $6.018 \cdot 10^6$ m^3 of the material that enters the lake on a year with average erosion activity is sand, $1.591 \cdot 10^6$ m^3 is silt and only $7.65 \cdot 10^5$ m^3 is clay. These percentage amounts of eroded material per particle size class correspond to 72 % sand, 19 % silt, and 9 % clay. Monteith and Sonzogni also reported that Lake Michigan has the highest percentage of sandy soils among the Great Lakes.

9.4 Beach Erosion Models

Most of the developed beach erosion models are empirical or semi-empirical models that focus on the changes of the beach profiles (Fox and Davis, Jr. [1973], Wright et al. [1985], Masselink and Short [1993], Leont'ev [1996], Larson and Kraus [1994], Ostrowski [2003]). Modeling of the beach profile changes usually deal with the underwater erosion of the sandy surf zone (Figure 9.3) caused by monochromatic waves and the transport and re-distribution of the sand longshore or crossshore under the effect of the wave enhanced currents. The beaches under examination are treated as closed systems with lengths determined by the beach extent (scale of one to a few kilometers) and widths equal to the distance between a moving berm and an also moving first bar (Figure 9.3).

Beach profile changes as a result of random wave action have been studied by Sato and Mitsunobu [1991] and have been modeled in Larson [1996] by superimposing the action of the individual waves within a wave spectrum (Larson [1996]). Fewer models have been developed that focus on establishing relationships between the intensity of the wave generated forces and the erosion rates of various shoreline types (Wright [1970], Sunamura [1977], Trenhaile [2000]).

The existing beach models work reasonably well when they are applied to small spatial scales and focus on specific problems, such as the longshore transport of sediments and the displacement of the shoreline position (Rosati et al. [1991], Hanson [1989]) or the fate of the beach fills (Larson and Kraus [1991]) or the effect of various coastal structures on beach erosion and the corresponding profile evolution (Leont'ev [1996, 1999], Gonzalez et al. [1999]). Use of any of these models to predict the shoreline erosion in Lake Michigan, however is not practical. The shoreline types of Lake Michigan vary from high bluffs to silty banks and from barrier beaches to beaches with dunes. Prediction of short term shoreline erosion (a few days, a few months or a year) for the whole of Lake Michigan under the effect of the incident waves and the local shoreline characteristics must

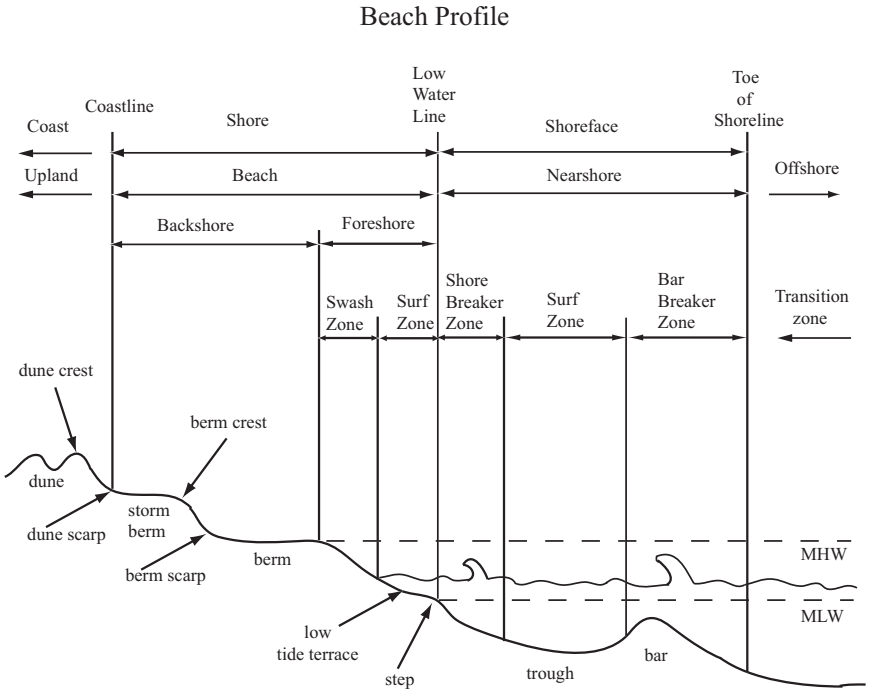

Figure 9.3 Conceptual diagram of a beach profile (source: CEM III [2006]).

rely heavily on empirical formulations with various coefficients requiring calibrations. To avoid the complexity and the uncertainties of such a modeling undertaking, it was decided to introduce the eroded from the shoreline sediments into the water column through an appropriate formulation of the lateral erosion term $\boldsymbol{S_{si}}$ (equation 2.7.4), based on concepts and parameters readily available from the sediment and the wave models. The suggested formulation does not have predictive capabilities of either the shoreline erosion or the beach evolution. It is rather an effort of reasonably describing in lumped fashion the spatial and temporal variations in the sediment mass entering the water column by relating the observed yearly erosion rates to the action of the waves, as explained in the following Section.

9.5 Correlation between Beach Erosion and Incoming Waves

Table 9.2 reports the shoreline erosion as an estimated average, maximum and minimum rate. Monteith and Sonzogni [1976], suggest that during years of high water level, the maximum erosion rates should be used. Indeed, a study of the recession rates in Lake Michigan during high water elevation (years 1970 and 1980) showed an increased erosion activity on the lake shoreline (Stewart

[1997]). Based on the above studies the maximum erosion rates have been selected in the formulation of the shoreline erosion for the dissertation simulation year 1998; a year recognized from gage data analysis as a year of high water elevation.

Erosion rates from the shoreline of each county around Lake Michigan are reported as the volume of eroded material per year. To be expressed in mass of eroded material entering the water column per year and per kilometer of shoreline, the erosion rates are first multiplied by the density of the sediments (ρ_s, same as the sediment density used by the sediment model) and then they are divided by the total shoreline length of each county, to produce the erosion loadings for that county.

The county shoreline lengths were determined using the geospatial data file (*ESRI* shapefile) for the continental U.S political boundaries (freely downloadable, upon registration, from http://data.geocomm.com/catalog/US/group21.html). The shoreline length consists of a number of segments (identifiable by their midpoints), each of which is assigned a uniform erosion loading such that the sum of all these loadings multiplied by their corresponding shoreline segment length is equal to the total erosion rate for that county.

Since the model requires that the erosion loadings should be set at a grid point of the calculation domain, the natural neighbor interpolation method was used to determine the erosion loadings at all the "wet" grid points adjacent to the shoreline. The interpolation helps to smooth out overlapping effects at the borders of the counties, as well as the effects from shoreline irregularities, and existing structures.

The number of the "wet" grid points corresponding to each county in general is not equal to the number of the shoreline segments. Since both represent the same shoreline length, the grid point loadings need to be multiplied by the factor:

$$f = \frac{\text{Number of segments}}{\text{Number of grid points}} \tag{9.5.1}$$

to produce the adjusted grid point erosion loadings. Finally, the loadings are further slightly adjusted by evenly distributing the very small residual introduced from the interpolation smoothing, such that the sum of all grid point loadings is exactly equal to the sum of all shoreline erosion loadings.

For all practical purposes, the above approach simply assigns the erosion rates at the grid points where they can be picked up by the model calculations such that the shoreline sediments are either transported as suspended load or become part of the bottom sediments depending upon the local flow conditions.

The shoreline erosion by the mechanical action of the near-shore breaking waves has long been recognized as the chief mechanism of beach evolution and profile changes. Various researchers have correlated the beach erosion to the action of the waves (e.g., Trenhaile [2000], Larson [1996], Dally [1990], Wright [1987] and others). The same approach is followed here, e.g., to correlate the waves to the spatial erosion loadings and to produce temporal distributions of these loadings.

The point shoreline erosion loading $\epsilon_s(x, y, t)$ in kg/m · s, is linearly related to the total wave energy flux per unit wavelength, also called the wave power $\mathcal{P}(x, y, t)$ in N/s, through a coefficient $\overline{m}(x, y)$ in s^2/m^2, that expresses the soil removed from the shoreline when it is acted upon by a unit wave power as follows:

$$E_s = \sum_{n=1}^{N} \overline{\epsilon_s}_b^{\Delta t} \Delta t \; ; \qquad \overline{\epsilon_s}_b^{\Delta t} = \overline{m} \cdot \overline{\mathcal{P}}_b^{\Delta t} ; \qquad \overline{\mathcal{P}}_b^{\Delta t} = \frac{1}{t_2 - t_1} \int_{t_1}^{t_2} \mathcal{P}\, dt = \frac{1}{\Delta t} \int_{0}^{\Delta t} \mathcal{P}\, dt \tag{9.5.2}$$

where, $E_s(x, y)$ is the total mass of the eroded sediments (kg/m), Δt (s) is the time step used in the model calculations, $\overline{\epsilon_s}_b^{\Delta t}$ is the temporal average of the point erosion loading, $\overline{\mathcal{P}}_b^{\Delta t}$ is the temporal average of the total wave power, $\overline{m}$ is the average value of the coefficient m for the total length of records considered and N is the total number of records. For a time period equal to one year, the coefficient $\overline{m}$ is calculated as:

$$\overline{m} = \frac{E_s}{\sum\limits_{n=1}^{N} \overline{\mathcal{P}}_b^{\Delta t}} \qquad \text{with:} \qquad N = \frac{1\,\text{yr}}{\Delta t(\text{yr})} \tag{9.5.3}$$

where E_s is already known from the previous spatial calculations of the point shoreline erosion loadings. The two horizontal components of the wave power $\mathcal{P}_x$ and $\mathcal{P}_y$ are calculated from the wave model at each model time step, with the wave power $\mathcal{P} = \sqrt{\mathcal{P}_x^2 + \mathcal{P}_y^2}$ calculated using the following equations:

$$\mathcal{P}_x = \rho_o g \int_0^{2\pi} \int_0^{\infty} cx\, \mathring{\mathcal{E}}(\mathring{\sigma}, \theta)\, d\mathring{\sigma}\, d\theta \; ; \quad \mathcal{P}_y = \rho_o g \int_0^{2\pi} \int_0^{\infty} cy\, \mathring{\mathcal{E}}(\mathring{\sigma}, \theta)\, d\mathring{\sigma}\, d\theta \tag{9.5.4}$$

From equation 9.5.3 a coefficient $\overline{m}$ at each grid point adjacent to the shoreline can be decided by running the wave model for the simulation period (year 1998) and subsequently incorporating the calculated $\overline{m}$ values into M^2COPS, so that the erosion loadings at each time step can be determined from the wave power.

At this point, the concept of the "virtual bedload rate" is introduced, which is equal to the above calculated grid point erosion loading. The sediments of the "virtual bedload" at the location were they are introduced, do not physically interact at all with the bottom sediments, but rather, depending upon the local flow conditions and the wave characteristics, are possibly entrained to become part of the suspended load. At each model time step the fraction of the "virtual bedload" that is not entrained becomes part of the bedload to complete the mass balance for the "virtual bedload rate".

In practice some or all of the "virtual bedload" sediments entrains when the local shear stresses exceed their critical limits and remains at the bottom as part of the local bedload in any other case. Physically, this is the same behavior that a shoreline exhibits under the action of the weather patterns and the wave conditions. The details of how much of the sediments are eroded at each time step are explained in the next Section.

9.6 Incorporation of the Shoreline Erosion into M^2COPS

The suggested method for the inclusion of the shoreline loadings into the model is to vertically distribute the sediments as point sources (equation 2.7.4) at the shoreline grid nodes instead of imposing concentration profiles that prescribe a fixed solution of the transport equation at all the neighboring to the shoreline "wet" grid points. This approach allows the model to transport the shoreline sediments the same way it treats the suspended and the bottom sediments.

The shoreline sediments are divided in three particle size classes (clay, silt and sand), and their mass fractions are estimated as reported in Table 9.3. Therefore, the "virtual" bedload flux can be written as:

$$\overline{\epsilon_{sb}}^{\Delta t} = \sum_{i=1}^{3} \beta_i \, \overline{\epsilon_{sbi}}^{\Delta t}; \qquad \sum_{i=1}^{3} \beta_i = 1 \tag{9.6.1}$$

where, β_i represents the mass fraction of the "i-th" particle size and $\epsilon_{sbi}^{\Delta t}$ is the bedload flux corresponding to that particle size.

Starting with the suspended sediment concentration mass balance equation in a finite volume and assuming a streamline type, steady state and uniform flow, the differential equation of Rouse's distribution of the suspended sediments in the vertical direction takes the form (Vanoni [1977]):

$$\mathcal{D}_v \frac{dC}{dz} + w_s C = 0 \,, \quad C < 0.001 \,; \qquad \mathcal{D}_v \approx \mathcal{A}_v = \frac{\tau}{\rho_o} \left[\frac{du}{dz} \right]^{-1} \tag{9.6.2}$$

where C is the volumetric sediment concentration. The second of equations 9.6.2 assumes that the vertical mass diffusivity is approximately equal to the turbulent momentum diffusivity, which exhibits the vertical distribution shown. It is also assumed that, the shear stress is a linear function of the vertical coordinate according to:

$$\tau = \tau_b \left(1 - \frac{z+h}{D}\right) = \rho_o \, u_*^2 \left(1 - \frac{z+h}{D}\right) \qquad \text{with:} \qquad \frac{du}{dz} = \frac{u_*}{\mathbf{k}} \frac{1}{z+h} \tag{9.6.3}$$

where, equations 9.6.3 conform to the model's coordinate system (Figure 2.1). Integration of the first of equations 9.6.2 and of the second of equations 9.6.3 in the interval $[-h+\alpha, \zeta]$ and substitution of all the relevant terms, yields:

$$u(z) = u_\alpha + \frac{u_*}{\mathbf{k}} \ln\left(\frac{z+h}{\alpha}\right); \qquad C(z) = C_\alpha \left[\frac{\alpha}{D-\alpha} \frac{\zeta - z}{D-(\zeta - z)}\right]^{w_s/\mathbf{k}\,u_*} \tag{9.6.4}$$

and in σ-coordinates:

$$u(\sigma) = u_\alpha + \frac{u_*}{\mathbf{k}} \ln\left[\frac{D}{\alpha}(1+\sigma)\right]; \qquad C(\sigma) = C_\alpha \left[-\frac{\alpha}{D-\alpha} \frac{\sigma}{1+\sigma}\right]^{w_s/\mathbf{k}\,u_*} \tag{9.6.5}$$

where all the variables in equations 9.6.2 through 9.6.5 are defined in Chapter 2. All the parameters in equation 9.6.5, except the z-coordinate, are invariant under any vertical coordinate transformation, since a steady, uniform flow is assumed for this derivation of the concentration profile.

Combining equations 2.8.17a and 2.8.27, the near bottom dimensionless concentration for the "i-th" particle size sediment class is calculated as follows:

$$C_{\alpha_i} = 0.283 \frac{\overline{\epsilon_s}_{bi}^{\Delta t} \, T_i^{-0.6}}{\rho_s \, \alpha \sqrt{(S_p - 1)\, g \, d_{s_i}}} \qquad \text{with:} \qquad \overline{\epsilon_s}_{bi}^{\Delta t} = \rho_s \, C_{\alpha_i} \, u_{\alpha_i} \, \alpha \tag{9.6.6}$$

Equations 9.6.6 define the concentration and velocity at the reference height α above the mean bed surface. Therefore, the vertical distribution of the source terms $\boldsymbol{S}_{s_i}$ is calculated using equations 9.6.4 or 9.6.5 as follows:

$$\boldsymbol{S}_{s_i} = u_i(z)\, C_i(z) = u_i(\sigma)\, C_i(\sigma)\,, \qquad i = 1, 3 \tag{9.6.7}$$

Using actual data from Lake Michigan, $\overline{\epsilon_s}_b^{\Delta t} = 0.00404\,\text{kg/m}\cdot\text{s}$ (maximum shoreline erosion loading), where $d_s = 2\,\mu\text{m}, 26\,\mu\text{m}, 106\,\mu\text{m}$ (average particle diameters of the three sediment classes). Equation 9.6.7 is plotted for various water depths, shear velocities and reference heights as shown in Figures 9.4, *(a)* through *(f)*.

From these plots, it is apparent that a value of $\alpha = 0.10\,\mathrm{m}$ gives the most reasonable results since, the profiles seem to converge around this value of α. Smaller values of α seem to overestimate the source terms $\boldsymbol{S}_{s_i}$. Similar conclusions have been obtained by van Rijn [1984b], who suggests that the use of reference heights very close to the bed should be avoided because they introduce large errors.

The amount of the "virtual bedload" subject to entrainment is given by $\overline{\epsilon}_{sbi}^{\Delta t}\, T_i^{-0.6}$ consequently the amount that remains at the bottom is given by $(\overline{\epsilon}_{sbi}^{\Delta t})_R = \overline{\epsilon}_{sbi}^{\Delta t}(1 - T_i^{-0.6})$. To complete the mass balance for the "virtual bedload" at each model time step, equation 2.7.9 is written as follows:

$$\rho_s\,(1-\mathrm{p})\frac{\partial(\beta_i\,E_\mathrm{m})}{\partial t} + \frac{\partial q_{\mathrm{b}_i x}}{\partial x} + \frac{\partial q_{\mathrm{b}_i y}}{\partial y} = -\boldsymbol{S}_{\boldsymbol{e}_i} + \boldsymbol{S}_{\boldsymbol{d}_i} + \boldsymbol{S}_{\boldsymbol{f}_i} + \frac{(\overline{\epsilon}_{sbi}^{\Delta t})_R}{\alpha} \tag{9.6.8}$$

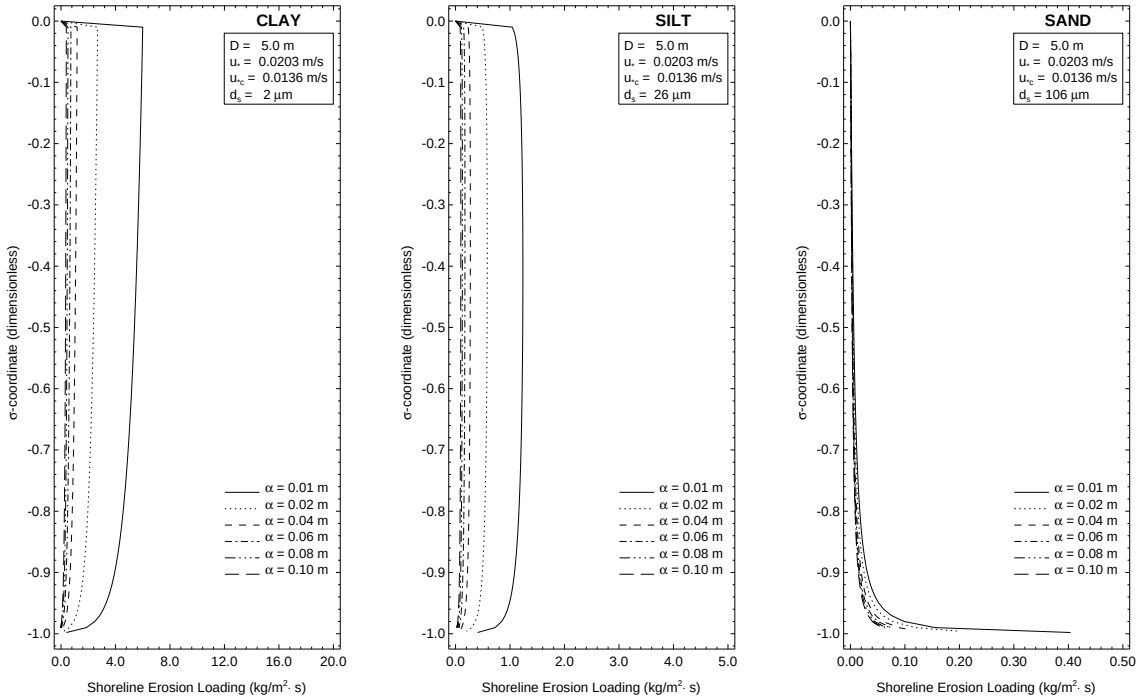

(a)

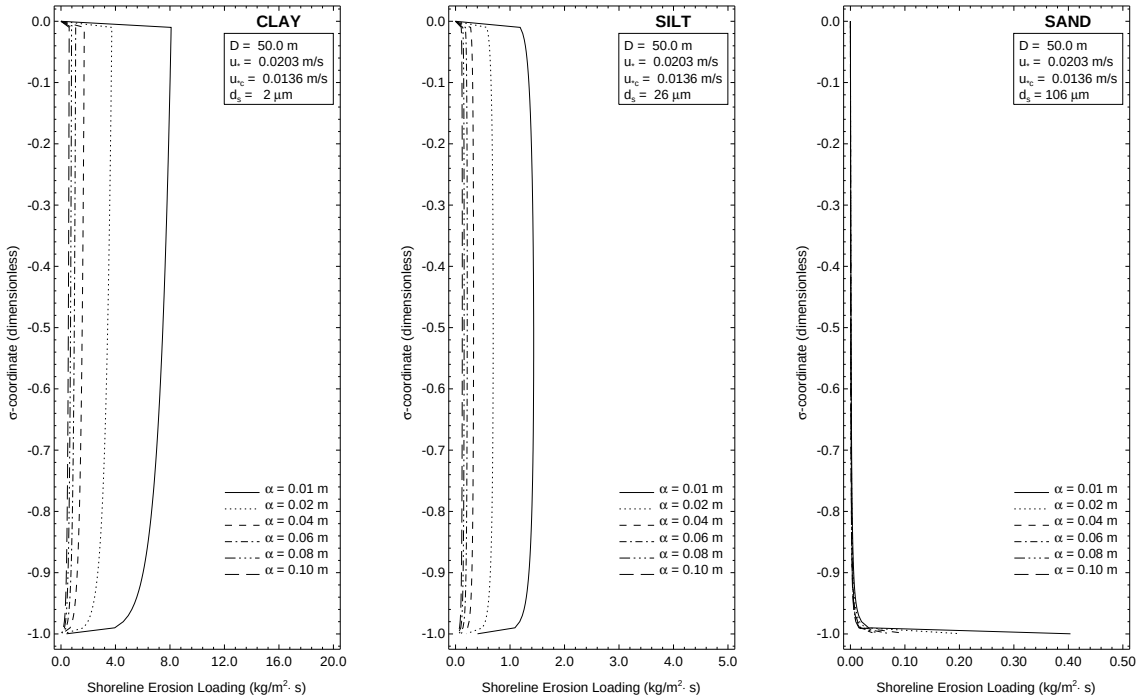

(b)

Figure 9.4 Suggested vertical distribution of the shoreline erosion loadings. (Continued)

Figure 9.4 Continued.

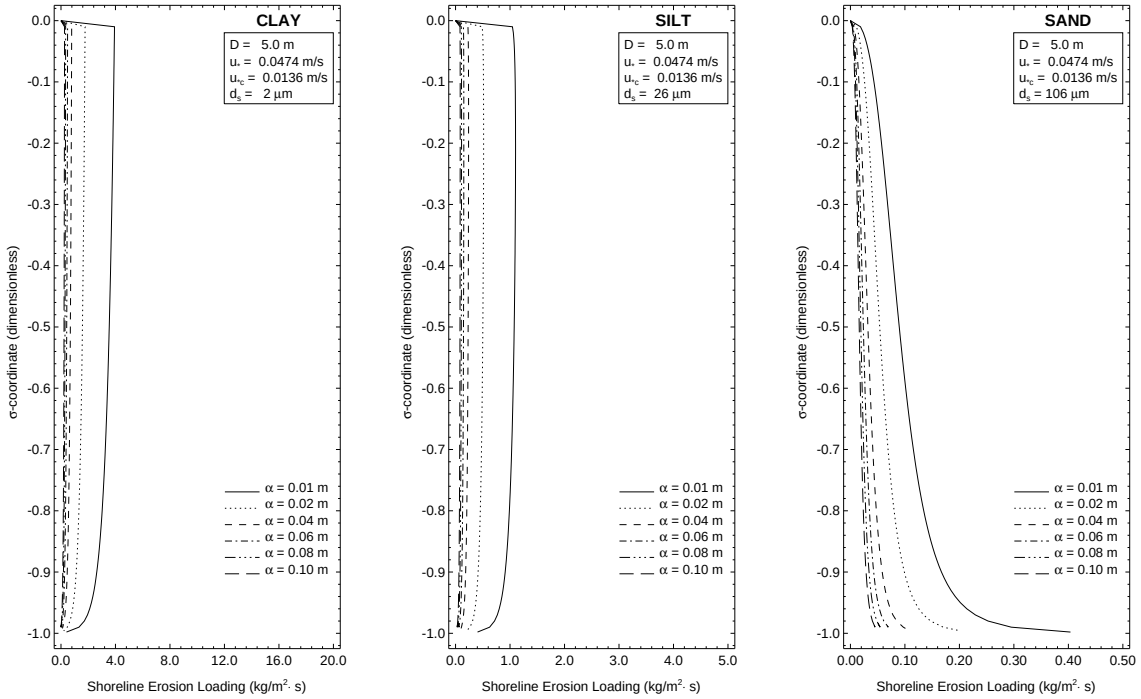

(c)

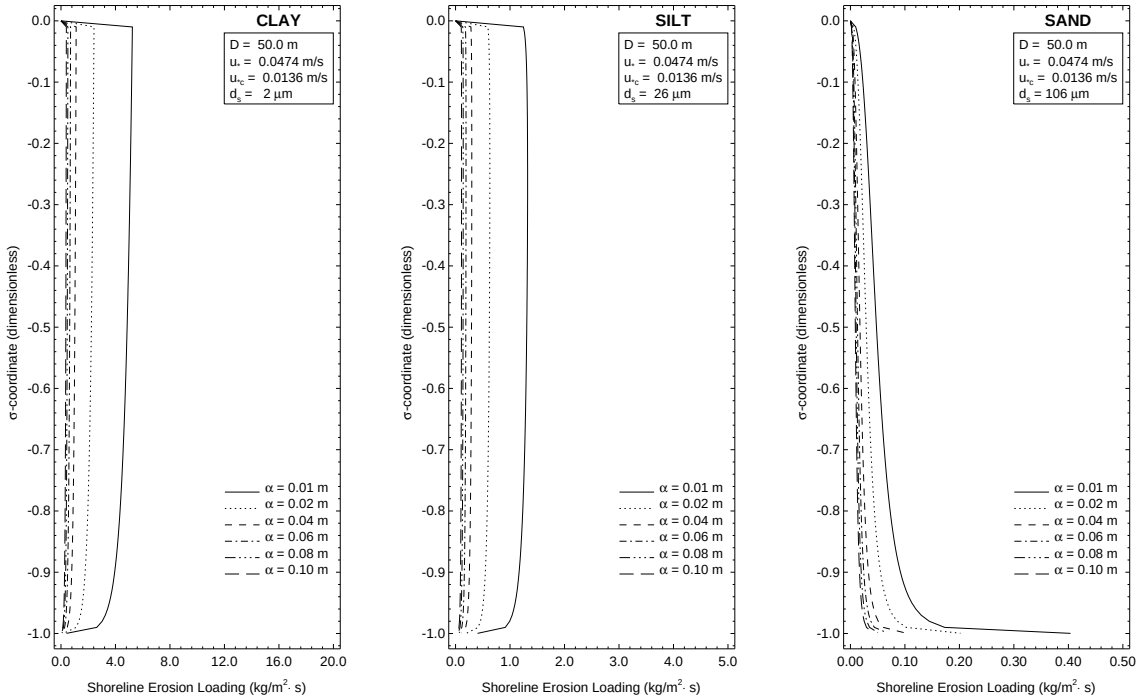

(d)

Figure 9.4 Continued.

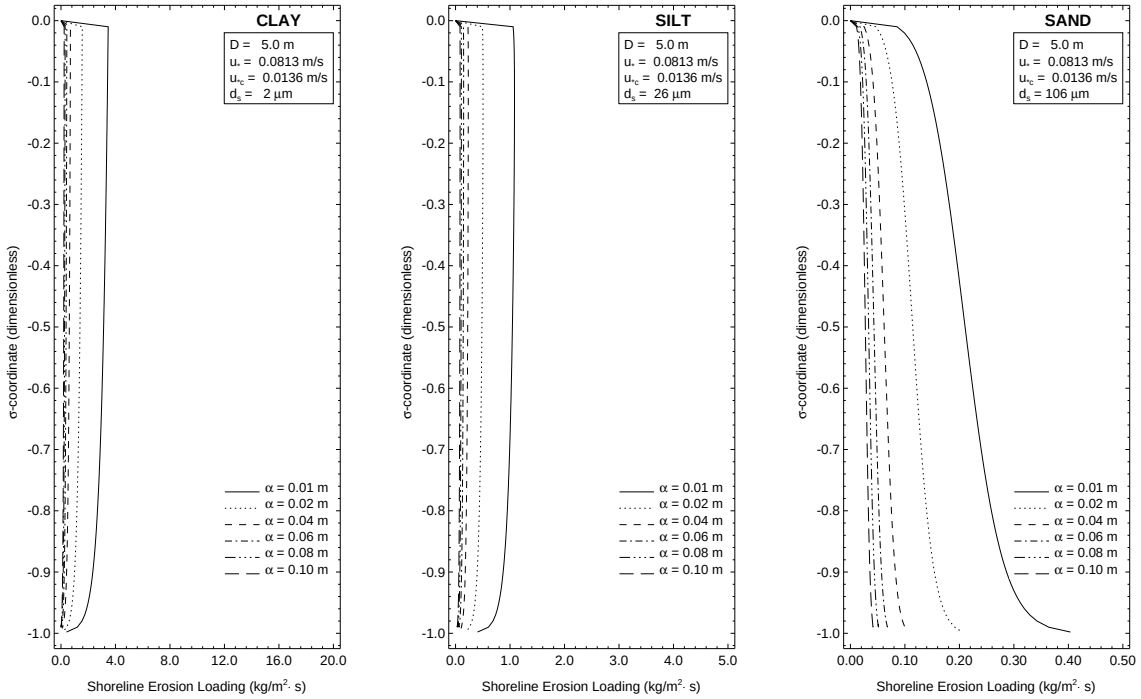

(e)

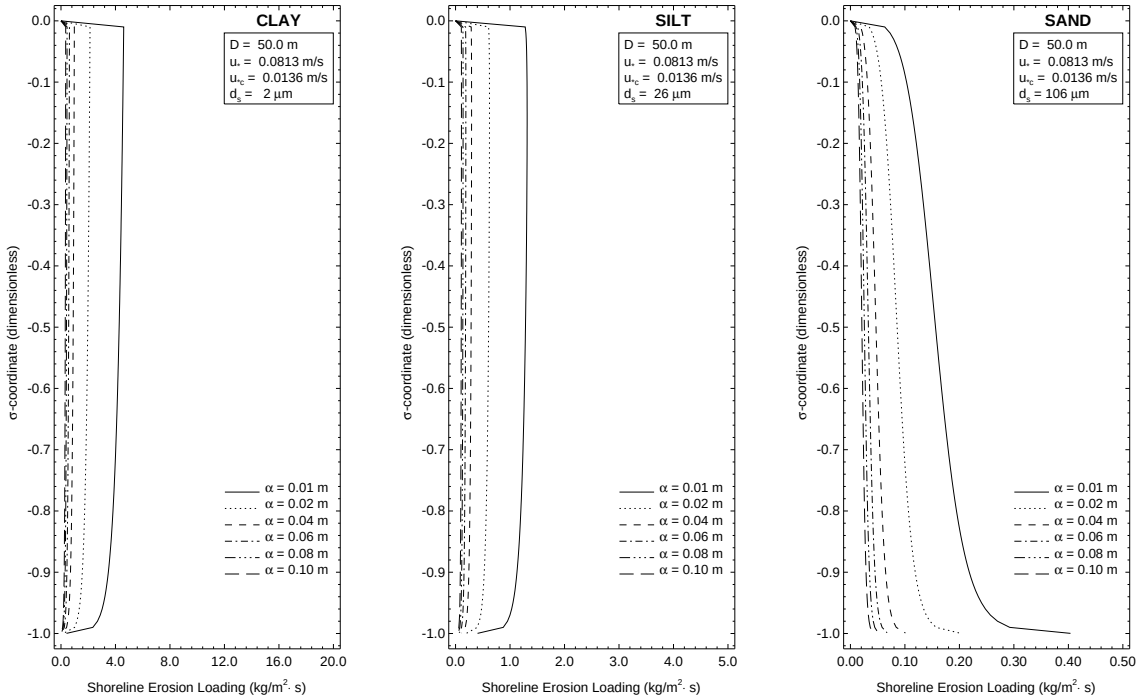

(f)

CHAPTER 10

MODEL APPLICATION AND IMPLEMENTATION TECHNOLOGY

This Chapter summarizes the grid technology, particle tracking, model coupling strategy, and computational constructs for M^2COPS.

10.1 The Lake Michigan Computational Domain

The implementation of the model in Lake Michigan and the hydrodynamic model calculations take place on a rectilinear horizontal $2x2$ km Cartesian coordinate grid and on a σ-stretched vertical coordinate grid. The horizontal y-axis is aligned with the greater axis of the lake (oriented South to North) and the x-axis is aligned with the smaller axis (oriented West to East). The above grid for Lake Michigan has been derived from a 9 arc-second grid defined on a Lambert conformal conic map projection and has been created by the cooperation of the National Geophysical Data Center (*NGDC*) with the *GLERL/NOAA* Laboratory.

The basic wave computational domain is defined as an irregular orthogonal Cartesian mesh derived from an irregular orthogonal mesh in geographical coordinates. The wave grid in geographical coordinates considers two different grid point spacings, one for the longitudinal and one for the latitudinal direction, respectively. The geographic grid spacings have been derived such that the resulting Cartesian grid cells are close in size and alignment to the hydrodynamic grid cells.

10.1.1 Details of the Horizontal Hydrodynamic Model Grid

The Lambert conformal conic map projection used in Lake Michigan is based on the "two standard parallels" method, as described in Snyder [1987], to minimize distortions introduced by its large latitudinal extent. The equations for the transformations from geographic to Cartesian space

and the corresponding inverse equations are given as (Snyder [1987]):

$$x = \rho \ \sin\theta \tag{10.1.1}$$

$$y = \rho_0 - \rho \ \cos\theta \tag{10.1.2}$$

$$\rho = R\ F\ \ \tan^{-n}\left(\frac{\phi}{2} + \frac{\pi}{4}\right) \tag{10.1.3}$$

$$\rho_0 = R\ F\ \ \tan^{-n}\left(\frac{\phi_0}{2} + \frac{\pi}{4}\right) \tag{10.1.4}$$

$$F = \frac{1}{n}\ \cos\phi_1\ \ \tan^{n}\left(\frac{\phi_1}{2} + \frac{\pi}{4}\right) \tag{10.1.5}$$

$$\theta = n\ (\lambda - \lambda_0) \tag{10.1.6}$$

$$n = \frac{\ln(\cos\phi_1/\cos\phi_2)}{\ln\left[\tan(\phi_2/2 + \pi/4)/\tan(\phi_1/2 + \pi/4)\right]} \tag{10.1.7}$$

while, the inverse equations for the sphere are written as follows:

$$\phi = 2\arctan\left(R\,F/\rho\right)^{1/n} - \frac{\pi}{2} \tag{10.1.8}$$

$$\lambda = \frac{\theta}{n} + \lambda_0 \tag{10.1.9}$$

$$\rho = \text{sign}(n)\left[x^2 + (\rho_0 - y)^2\right]^{1/2} \tag{10.1.10}$$

$$\theta = \arctan\left[x/(\rho_0 - y)\right] \tag{10.1.11}$$

where (λ, ϕ) are the longitude and latitude, respectively, (λ_0, ϕ_0) are the longitude and latitude for the origin of the Cartesian coordinates, λ_0 is the central meridian, (ϕ_1, ϕ_2) are the two standard parallels and R is the radius of the earth which, is taken equal to 6366197.724 m. Using chain rule differentiation equations 10.1.1 and 10.1.2 give:

$$dx = (n\rho\cos\theta)\,d\lambda - \frac{n\rho\sin\theta}{\sin\left(\phi + \frac{\pi}{2}\right)}\,d\phi \tag{10.1.12}$$

$$dy = (n\rho\sin\theta)\,d\lambda + \frac{n\rho\cos\theta}{\sin\left(\phi + \frac{\pi}{2}\right)}\,d\phi \tag{10.1.13}$$

and the inverse equations are:

$$d\lambda = \frac{\cos\theta}{n\ \rho}\,dx + \frac{\sin\theta}{n\ \rho}\,dy \tag{10.1.14}$$

$$d\phi = -\frac{\sin\theta}{n\ \rho}\sin(\phi + \frac{\pi}{2})\,dx + \frac{\cos\theta}{n\ \rho}\sin(\phi + \frac{\pi}{2})\,dy \tag{10.1.15}$$

The two standard parallels have been chosen at latitudes 43^{o} N and 45^{o} N, while the central meridian is at longitude 86.5^{o} W. The origin of the grid has been set at latitude 41.5976372^{o} N and longitude 87.9898071^{o} W. Derivation of the projected coordinates (x, y) from the known geographical coordinates (*lat*, *lon*) has been made using the two standard parallels formula.

The horizontal grid yields 131 grid points on the x-direction and 251 points on the y-direction. The total number of surface grid points is 32881, 14459 of which are the "wet" or water points and 18422 are the land points.

10.1.2 Details of the Vertical Hydrodynamic Model Grid

The vertical grid is based on the so called "σ stretching" that transforms the vertical physical domain into a rectangular computational domain with an upper boundary $\sigma = 0$ at the free surface and a lower boundary $\sigma = -1$ at the lake bottom. The vertical σ-coordinates allow for a better resolution of the bottom boundary layer with fewer number of layers compared to the ones needed by a Cartesian vertical grid to achieve a similar resolution.

The vertical coordinate system used for the model implementation in Lake Michigan consists of 20 σ levels or 19 layers. Starting from the free surface the top 10 layers use a uniform vertical spacing with $\Delta\sigma = 0.0227$. From the 11th layer until the 15th layer, spacings increase linearly and from the 16th layer till the bottom they decrease again linearly for a better resolution near the lake bottom (Table 10.1). The maximum physical spacing is 37.183 m and it is found at the central part of the lake while the minimum physical spacing is 0.068 m.

10.1.3 Details of the Wave Computational Domain

The two wave models used in the prediction system can be configured to run either using spherical or Cartesian coordinates. Furthermore, M^2SWAN accepts curvilinear coordinates, a feature that makes this model more compatible with M^2HYD. The Cartesian coordinates in M^2WAM are described by the definition of a uniform rectangular grid in geographical coordinates where the grid spacing $\Delta x = \Delta y = 2000$ m is defined at the equator such that: $\Delta\lambda = \Delta\phi = (360x2000)/40000000 = 0.018^{o}$.

Level number	σ	Layer number	$\Delta\sigma$	Physical spacing (based on model depths) max. depth 273.0 m	min. depth 3.0 m	aver. depth 84.44 m
1	0.0000					
2	−0.0227	1	0.0227	6.197	0.068	1.917
3	−0.0454	2	0.0227	6.197	0.068	1.917
4	−0.0681	3	0.0227	6.197	0.068	1.917
5	−0.0908	4	0.0227	6.197	0.068	1.917
6	−0.1135	5	0.0227	6.197	0.068	1.917
7	−0.1362	6	0.0227	6.197	0.068	1.917
8	−0.1589	7	0.0227	6.197	0.068	1.917
9	−0.1816	8	0.0227	6.197	0.068	1.917
10	−0.2043	9	0.0227	6.197	0.068	1.917
11	−0.2270	10	0.0227	6.197	0.068	1.917
12	−0.2724	11	0.0454	12.394	0.136	3.834
13	−0.3405	12	0.0681	18.591	0.204	5.750
14	−0.4313	13	0.0908	24.788	0.272	7.667
15	−0.5448	14	0.1135	30.986	0.341	9.584
16	−0.6810	15	0.1362	37.183	0.409	11.501
17	−0.7945	16	0.1135	30.986	0.341	9.584
18	−0.8853	17	0.0908	24.788	0.272	7.667
19	−0.9534	18	0.0681	18.591	0.204	5.750
20	−1.0000	19	0.0466	12.722	0.140	3.935

Table 10.1 Definition of the σ layers used in Lake Michigan.

The above definition introduces significant distortion into the resulting rectangular grid because of the latitudinal extent of Lake Michigan. Therefore, M^2WAM has been modified to accept a non-uniform Cartesian mesh, such that $\Delta\lambda \neq \Delta\phi$. The value of $\Delta\lambda$ is calculated from the longitudes of the hydrodynamic grid points and an average value of $\Delta\lambda = 0.0259^{\,o}$ is used.

The origin of the wave computational mesh is set at $\lambda_0 = 88.0940^{\,o}$W and $\phi_0 = 41.6044^{\,o}$N. Starting from this point, each grid point location is calculated as: $\lambda_i = \lambda_{i-1} + \Delta\lambda$ $(i = 1, 131)$ and $\phi_j = \phi_{j-1} + \Delta\phi$ $(j = 1, 251)$. While the resulting grid is orthogonal with constant cell sizes in geographical space, the transformation of the coordinates in Cartesian space produces a slightly curvilinear grid, as shown by the equations 10.1.1 and 10.1.2. In other words, the wave and the hydrodynamic computational domains do not coincide.

Though both grids are aligned together, the slightly different cell sizes introduce differences in the longitudinal direction with a maximum value of ~ 200 m (in the Southernmost part of the lake). To remedy this problem, two approaches can be used: *(a)* redefine the hydrodynamic computational

domain to be the same as the wave computational domain, and *(b)* simply interpolate the required parameters that are being exchanged between the models. Using the first approach, both M^2HYD and M^2SWAN should be run using curvilinear coordinates, while M^2WAM uses the above defined Cartesian mesh. This approach is elegant, however, it introduces significant computational load by calculating the metrics of the transformations during the course of the various interpolations performed within the models.

The second approach requires interpolation of the fields being exchanged between the models. All the models have been adapted to output the data in user defined grids, where the required interpolations are performed in all the models using the Natural Neighbor interpolation described in 10.5.1. This interpolation method is an improvement to the simple bi-linear interpolation scheme used in the wave models.

10.2 Grid Refinement and Nesting

The accurate description of the near-shore sediment transport dynamics requires, if possible, the accurate forecasting of the near-shore wave field. The near-shore region is defined as the area where the bathymetric effects on both the wave and the current fields become dominant. For the case at hand, that is, the prediction of the evolution of the Lake Michigan Spring plume, the accurate prediction of the near-shore wave parameters ensures a better or a more accurate representation of the magnitudes of the shoreline and the bottom erosion rates, therefore, a better representation of the plume. Both erosion rates are input to the sediment model and are defined at locations (grid points) where they can be picked up by the model for their subsequent transport under the action of the currents and the waves.

The accuracy of the near-shore wave calculations depends on: *(a)* the quality of the input of the boundary and the initial conditions, *(b)* the existence of shallow water related physics in the wave model (e.g., depth induced wave breaking), and *(c)* the resolution of the computational grid. Usually finer grid calculations are used as a means to obtain better shallow water wave predictions.

M^2SWAN is specifically designed for coastal wave predictions, while M^2WAM is more of a global model extensively used for deep water or ocean wave calculations. Both models use the same basic physics: *(a)* wave propagation in both space and time, *(b)* depth induced shoaling and refraction, *(c)* current induced shoaling and refraction, *(d)* whitecapping, *(e)* bottom friction, and *(f)*

quadruplet wave-wave interactions. In addition to the above, M^2SWAN incorporates depth induced wave breaking and triad wave-wave interactions, making this model to be more suitable for near-shore wave calculations.

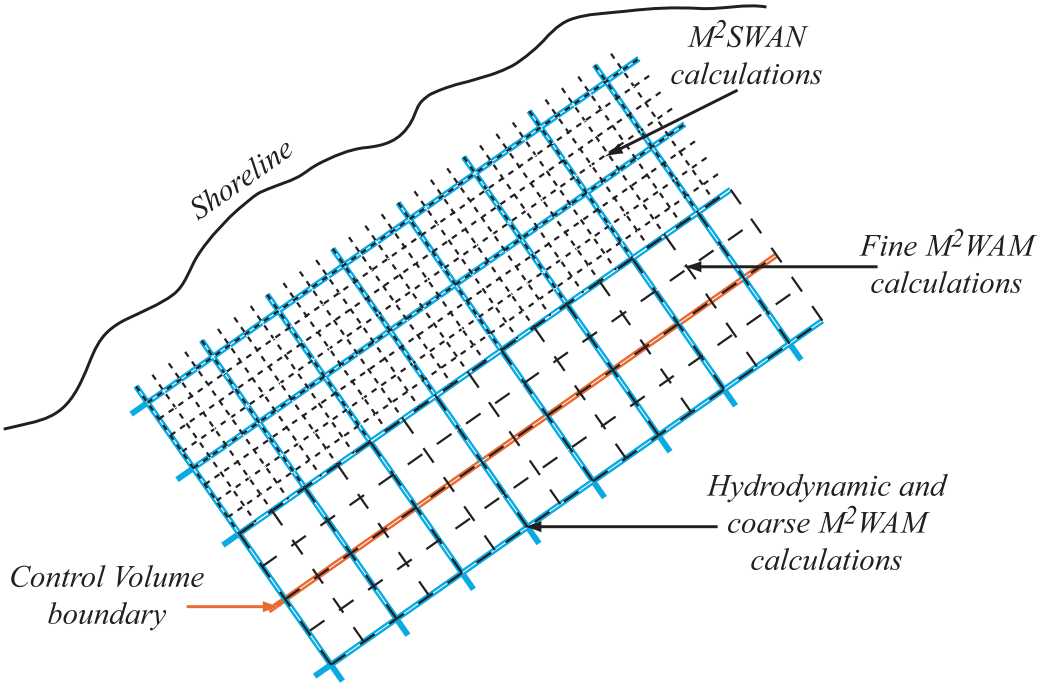

Figure 10.1 Suggested near-shore 3-level nested computational grid.

The description of the characteristics and limitations of the two wave models and the required accuracy of the prediction of the near-shore wave field imply that a more refined computational grid is needed near the shore. The region of interest (*ROI*) in the near-shore computations is defined by the near-shore control volumes and it is the region where M^2SWAN is applied. To avoid errors caused by numerical diffusion (see Section 3.5) M^2SWAN should be run with a grid resolution of ~ 1000 m or less. The transition from the ~ 2000 m resolution of the coarse wave computational grid to the ~ 1000 m resolution is achieved by incorporating an intermediate M^2WAM nest. As described in Wornom et al. [2001], this approach gives superior results than running M^2SWAN in the ~ 1000 m resolution and coupling it directly to the ~ 2000 m M^2WAM domain. After the fine M^2WAM nest, M^2SWAN assumes the computations using a resolution of ~ 500 m. The proposed double nesting is shown in Figure 10.1 and is implemented here.

10.3 Definition of the Eulerian Particle Tracking (M^2EPT)

Eulerian particle tracking is the modeling method that quantifies the distribution pathways of any scalar quantity that can be treated as a particulate matter. The method shares the same Eulerian framework as the underlying computational models and can be applied to a variety of substances that can be identified by principal characteristics such as density and particle size. Examples of such substances are sediments, phytoplankton, zooplankton, oil-spills and even water. This technique has been fully explained in Bedford et al. [1999] and Velissariou et al. [1999] and is only summarized here.

The particle tracking framework requires the complete identification of the source or sources of origin (location and area of extent) of the modeled scalar quantity. The sources of origin can extend to occupy areas as large as the whole computational domain or as small as the neighborhood of a single point. Within each source area, multiple substances can be identified based on their principal characteristics. With more than one source of origin and more than one substance or component identified within the domain, a multi-source, multi-component Eulerian particle tracking framework is established. Figure 10.2 shows the definition of various sources of origin for a single scalar quantity within the computational domain.

Let us assume that for the multi-source, single component formulation shown in Figure 10.2 the modeled substance is sediment. We further assume that the extended sources E_1 and E_2 supply sediments found both at the bottom and in suspension. The point sources P_1 and P_2 only supply sediments found at the bottom. The boundary point sources C_1 supply the sediments eroded from the boundary (shoreline) under the action of various physical elements on the boundary. The sediment model calculates the sediment distribution in the domain for each sediment particle size, therefore, to identify the origin of the sediments we just need to assign different particle sizes for each source.

For all practical purposes, the sources should be located at areas or points where the sediment supply can be picked up by the sediment model (e.g., at grid point locations). Sources P_1, P_2 and C_1 are exactly located at model grid points, while the extended sources E_1 and E_2 contain a number of grid point locations that supply the sediments. If the sediment particle size distribution is known or can be determined at all these grid points (one for the bottom and one for the suspended sediments) it is simply supplied to the sediment model. The sediment diameters (model input) are set equal to

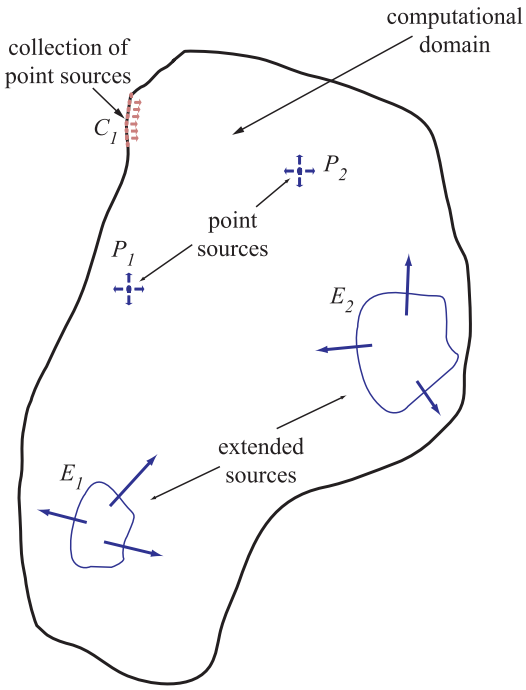

Figure 10.2 Representation of an Eulerian particle tracking system of sources.

the diameters corresponding to the midpoint of each sediment range found within the particle size distribution.

The sediment model is initialized with a zero sediment concentration everywhere in the domain. After the initialization period is over, the sediments from each source are tracked by looking up their diameter and their corresponding concentration ($C > 0$) everywhere in the domain. For the method to be successful, all the assigned sediment diameters should be different from each other. In case that two sediment diameters are indistinguishable, one can slightly be perturbed such that the settling velocity of the particular sediment size remains virtually the same.

In the case of limited availability of sediment data, it will be necessary to slightly perturb the sediment diameters as discussed above to apply the method successfully. The final question is: "What is the limit in the number of particle diameters that can be used?" The answer is that depends upon the available computer resources and the amount of available storage. Considering only the three main sediment size classes, that is, sand, silt and clay, the number of the particle diameters decreases drastically, while the number of the sources considered can at the same time be increased to achieve a better resolution.

10.3.1 Particle Tracking Formulation

As explained previously the spring plume is directly related to the general near-shore advective and diffusive transport mechanisms that control the long-shore and cross-shore transport of the suspended mass. To study the transport processes at the near-shore regions, the entrainment and settling of the sediments from the lake bottom at near-shore and off-shore locations and the re-distribution of the entrained sediments must be resolved in the model of Lake Michigan.

According to this modeling system, the lake shoreline is divided in a number of segments with each one identified as a separate source of sediments. Furthermore, the lake bottom is divided in areas of various sizes that consist of additional sediment sources (Section 10.3.3). Each source is represented using three sediment size classes (sand, silt, and clay), but the sediment particle diameters for these classes vary among the sources. This is necessary to be able to "track" the different particle sizes in their journey from a sediment source to a depositional area, to examine the sediment transport patterns, to identify deposition areas and to quantify the sediment load transported from each source and sediment size to each deposition area.

10.3.2 Definition of the Control Volumes

For a closer study of the sediment transport during the spring plume event, the lake is divided into a number of control volumes (Figure 10.4) the bottom area of which corresponds to the sediment sources described in Section 10.3.3. Due to computational considerations, only a limited number of such control volumes can be established. In the present implementation, the lake and the lake shore are divided into 17 control volumes, which are considered as a heavy computational load.

Six of the control volumes ($CV8$-$CV13$) have been established at the near-shore area of the Southern part of the lake to study the along-shore and cross-shore movement of the sediments, as well as the entrainment and the deposition rates of the sediments within these control volumes. Three of the near-shore control volumes are set on the Western part of the lake and three on the Eastern part of the lake.

Figure 10.3 shows a near-shore control volume segment and the definitions of the various net sediment fluxes in that control volume, where q_s is the sediment flux due to the net shoreline erosion rate, q_x, q_y are the net bedload fluxes in the x and y directions, respectively, S_z is the net sediment entrainment flux and S_x, S_y are the net horizontal suspended sediment fluxes in the x and y directions, respectively.

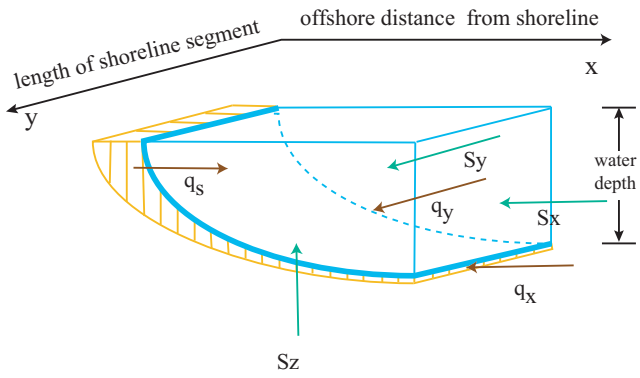

Figure 10.3 Conceptual diagram of a beach profile.

The width of the near-shore control volumes (off-shore distance from the shoreline) shown in Figure 10.4 *(b)* is between 15 and 25 km (depending on the shoreline irregularities) to capture the plume, the width of which has been estimated to be between 10 km to 16 km. The length of the shoreline included in each control volume varies from 104.5 km to 167.8 km (average shoreline length 137 km). In the definition of the control volumes besides the size, some consideration was also given to the erosion loadings, the soil texture, the shore types and the shoreline exposure to the waves. Since erosion loadings and soil texture information are given for counties rather than sub regions within each county, the control volumes have been set so that they include the undivided shoreline of each county.

Three control volumes have been set at the off-shore part of the lake, two of which cover the Southernmost area of the lake (*CV*16-*CV*17) and one the area between the Two Rivers Ridge and the Door-Leelanau Ridge (*CV*15), to study the entrainment and deposition rates of the sediments at the off-shore regions, as well as to identify sediment deposition areas within these control volumes. The Northern part of the lake does not affect the evolution and transport of the Spring plume and in the present study it has been set as one control volume (*CV*14) that includes both the near-shore and the off-shore regions.

Finally, seven more control volumes (*CV*1-*CV*7) have been named at the shoreline (foreshore and backshore regions), where sediments from the beaches, the bluffs and the lake banks are eroded and enter the near-shore region or sediments from the near-shore region are accreted under the action of the waves. The bottom area of the control volumes on the lake shore are defined by the grid points immediately neighboring to the shoreline definition.

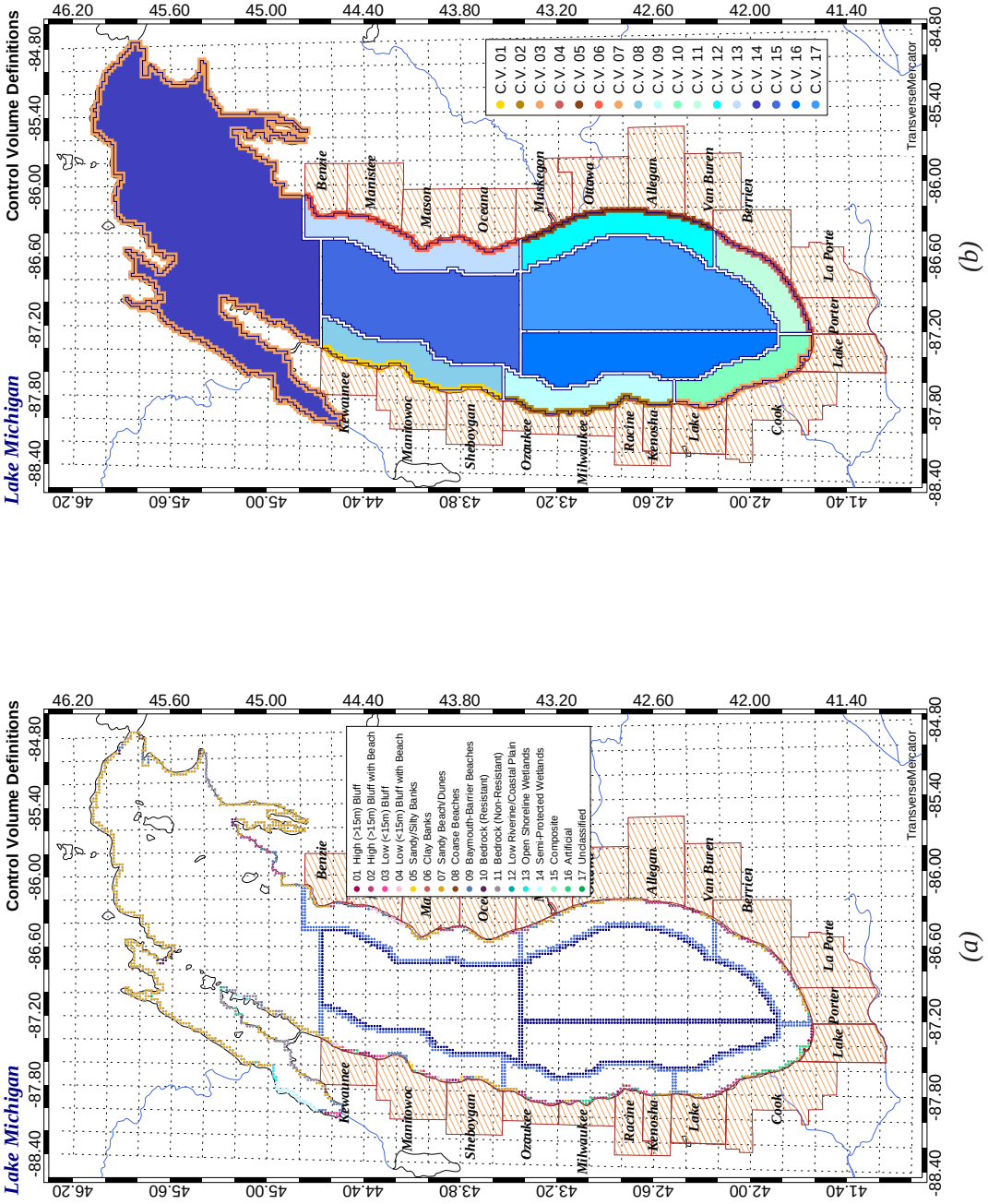

Figure 10.4 Definition of the Lake Michigan control volumes.

10.3.3 Computational Definition of the Control Volumes

Starting with the shoreline definition obtained from *GLERL* (David Schwab, personal communication) a region of interest (*ROI*) can be defined by setting all the points that lie inside the shoreline definition as foreground points and all the points that lie outside the shoreline definition as background points. Shrinking the *ROI* gradually by one grid point each time a new *ROI* is constructed. The difference between the new and the old *ROI* gives a segment parallel to the shoreline definition. This process is repeated until the required width of this segment is obtained. The whole procedure was performed using the *IDL* (Interactive Data Language) scripting language (http://www.ittvis.com/).

The core procedures (subroutines) for the code that calculate the *ROI* boundary are part of the publicly available Coyote's library of the Fanning Consulting (http://www.dfanning.com/). This code was substantially modified and enriched by personally developed *IDL* code to produce the required results. Irregularities of the domain (e.g., islands) and of the shoreline (e.g., sharp edges), limits the ability of the code to be run automatically, therefore, the user intervention to remove unwanted points so that a smooth *ROI* outline can be obtained is necessary.

After the completion of the procedure two files are generated, the first containing the grid points (i, j) of the outline of each control volume going counterclockwise (starting from the top), and the other contains all the grid points (including the boundary that defines the area of the control volume). The first file is used to outline the control volumes, as shown in Figure 10.4a, and to calculate property fluxes through the faces of the control volumes. The second file is used to define the average bottom sediment properties for each control volume using the bottom sediment particle size distribution. The grid points defined in the later file are also used by the sediment model to differentiate sediment sources with different properties.

10.3.4 Definition of the Sediment Sizes and Fractions

The particle tracking method described in Section 10.3.1 requires tagging of the sediment particles in such a way that the various sediment sources / control volumes can be safely identified. Tagging of the sediments is done here by assigning three sediment diameters (one for the clay, one for the silt and one for the sand size classes) to each control volume. Since 17 control volumes are defined in Section 10.3.2 the total number of sediment diameters required is 51.

In Sections 8.5 and 8.5.1 the procedure followed to create the gridded sediment data is described. The gridded sediment data give the distribution of 24 grain sizes (4 from the clay, 14 from the silt and 6 from the sand size class) at each grid point. To calculate a representative diameter for each size class and for each control volume, using the gridded sediment data, the following approach is used: *(a)* calculate the average mass fraction for each grain size within a control volume as: $\overline{\beta}_j = \frac{1}{N}\sum_{i=1}^{N}\beta_i$ $(j = 1, 24)$ where, N is the total number of the grid points in the control volume, β_i is the mass fraction of the particular grain size at the "i-th" grid point and $\overline{\beta}_j$ is the control volume averaged mass fraction of the particular grain size (repeat for all 24 grain sizes), *(b)* slightly adjust (if necessary) the averaged mass fractions such that $\sum_{j=1}^{24}\overline{\beta}_j = 1$ and *(c)* calculate an average diameter for each size class using the following expression:

$$\overline{d}_s^{C\forall} = \frac{\sum_{s=1}^{N_s}\overline{\beta}_s D_s}{\sum_{s=1}^{N_s}\overline{\beta}_s} \tag{10.3.1}$$

The process is repeated for all the control volumes. The selected diameters per control volume and sediment size class are shown in Table 10.2.

Control Volume	Clay (m)	Silt (m)	Sand (m)
$C\forall 1$	0.0000019115	0.0000309215	0.0002295079
$C\forall 2$	0.0000019132	0.0000285939	0.0001875699
$C\forall 3$	0.0000018872	0.0000284318	0.0002488595
$C\forall 4$	0.0000017533	0.0000257123	0.0003167730
$C\forall 5$	0.0000018267	0.0000206898	0.0002531482
$C\forall 6$	0.0000019877	0.0000206072	0.0003212457
$C\forall 7$	0.0000020642	0.0000234938	0.0002644130
$C\forall 8$	0.0000019111	0.0000279773	0.0002511235
$C\forall 9$	0.0000019000	0.0000247554	0.0002217254
$C\forall 10$	0.0000018687	0.0000264239	0.0002946005
$C\forall 11$	0.0000016793	0.0000249549	0.0003385879
$C\forall 12$	0.0000017400	0.0000209555	0.0002447994
$C\forall 13$	0.0000019670	0.0000205854	0.0003430683
$C\forall 14$	0.0000020885	0.0000234153	0.0003052565
$C\forall 15$	0.0000019292	0.0000225324	0.0002931433
$C\forall 16$	0.0000018574	0.0000231655	0.0002962815
$C\forall 17$	0.0000017660	0.0000222718	0.0002712074

Table 10.2 Sediment particle diameters (m) defined for the Control Volumes of Lake Michigan.

The final mass fraction for the sediment represented by each average diameter at the near-shore and off-shore volume is the one calculated in step (b) above. The mass fractions for the on-shore control volumes are assigned according to the mass fractions per size class that have been estimated for each county around the lake, and are shown in Table 9.3.

10.4 Model Coupling

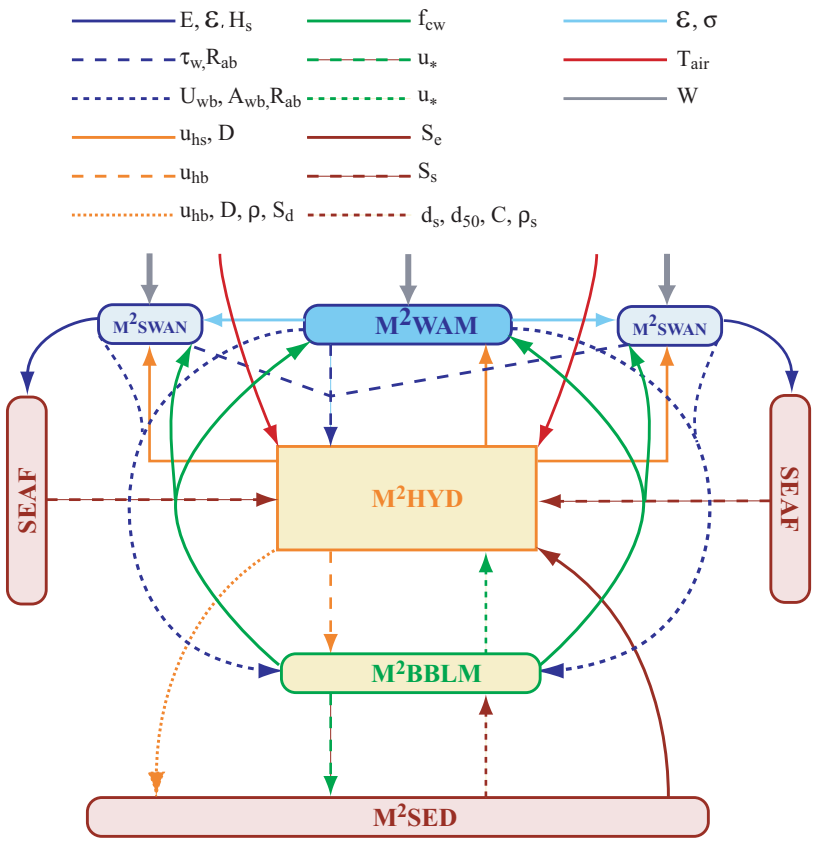

Figure 10.5 Schematic representation of the model coupling.

Figure 10.5 shows the exchange of the variables defined as follows that takes place among the various coupled model components: *(a)* hydrodynamic variables: W is the wind speed, T_{air} is the air temperature, D is the total water depth, U is the vertically averaged mean flow velocity, $\hat{u}_A$ is the Doppler velocity, $\boldsymbol{u}_{\mathbf{h}s}$ and $\boldsymbol{u}_{\mathbf{h}b}$ are the velocity vectors representing the horizontal flow velocity components at the free surface and the bottom, respectively, u_* is the friction velocity at the bottom and f_{cw} is the combined wave-current bottom friction factor; *(b)* wave variables: E and $\mathcal{E}$ are the total

and spectral wave energy, respectively, $\tilde{\omega}$ and $\widetilde{\mathring{\sigma}}$ are the spectrally averaged radial and intrinsic wave frequencies, respectively, $\tilde{k}$ and $\tilde{\theta}$ are the spectrally averaged wave number and direction, H_s is the significant wave height, U_{wb} is the maximum near bottom wave orbital velocity, A_{wb} is the bottom wave excursion amplitude, τ_w is the surface wave induced shear stress, $R_{\alpha\beta}$ is the wave radiation stress tensor and u_{st} is the Stokes drift; and *(c)* sediment variables: C is the volumetric concentration of the suspended sediments, ρ_s and ρ are the sediment and mixture densities respectively, d_s is the sediment particle diameter, d_{50} is the median diameter, $\boldsymbol{S_d}$ is the depositional flux of the suspended sediments near the bottom, $\boldsymbol{S_e}$ is the entrainment flux of the bottom sediments and $\boldsymbol{S_s}$ is the erosion flux of the shore sediments.

The various models and sub-models used in *M2COPS* are coupled either directly within the main hydrodynamic code or indirectly using the parallel Message Passing Interface (*MPI*) described in Section 10.5.2. The hydrodynamic, sediment and bottom boundary layer models are coupled directly so that the parameter exchange mechanisms are hardcoded into the main hydrodynamic and sediment models. The default exchange frequency among the directly coupled models is every time step. The user, however, has the options to start the sediment calculations at a time different than the hydrodynamic start time or to control the exchange frequency. Since all calculations performed in *M2COPS* are highly tied together when the full spectrum of physics is used (hydrodynamic, sediment), use of the default exchange frequency (that is every time step) is preferable and computationally more correct.

The wave models are considered external to the hydrodynamic model and to each other and as such are coupled using the Message Passing Interface (*MPI*). The requirement here is that all the codes implement all the necessary calls to exchange the needed data and that the resulting code is executed in computer platforms with parallel capabilities (cluster or multi-processor systems). Simplifications to the above procedure can be achieved by using available coupling software that is already extensively tested and adoptable in different computer environments (e.g., the *OASIS* software at: https://prismtrac.cerfacs.fr/wiki/ and the Model Coupling Toolkit at: http://www-unix.mcs.anl.gov/mct/).

The *M2COPS* framework is constructed with the use of the *MPI*, which is highly tied with *MPICH* (http://www-unix.mcs.anl.gov/mpi/) and *OpenMPI* (http://www.open-mpi.org/) projects. *OpenMPI* has the additional capability to allow coupled models to run sequentially. The latter is

important in the case that coupled model components need to be switched off and on or when the models need to be run in sequential mode.

10.5 Implementation Technology

Solving large scale problems requires the use of complex modeling systems that generate extraordinary amounts of output data the analysis of which requires special handling. Therefore, an important objective is to identify the necessary technology, methodology and resources required to execute the model, to store and retrieve the usually huge data outputs produced by the model computations, to manipulate and analyze the data sets and finally to visualize the results. The various aspects of the technological requirements as implemented in M^2COPS are outlined in the following Sections. Their use though is not strictly limited to the current modeling system but can rather be incorporated in any modeling framework.

10.5.1 Natural Neighbor Interpolation

In M^2COPS and its application to the Lake Michigan turbidity plume, Natural Neighbor interpolation is used as the basic interpolation technique. Natural Neighbor is employed to create the gridded meteorological and sediment input files and to compare the model output data to measured water elevation, velocity, wave and sediment data. This method has been successfully used for the interpolation of scattered or arbitrarily distributed meteorological and geophysical data for many years. Some properties of the Natural Neighbor interpolation are that: *(a)* the original observed or measured variable values (F_i) are recovered exactly at the sampling points; and *(b)* the interpolated function has continuous derivatives, except at the sampling points (Sambridge et al. [1995]).

The method is applied here by constructing Delaunay triangles and their dual Voronoi cells (known in 2D spaces as Thiesen polygons) for the given data set using the Watson triangulation algorithm. The Natural Neighbor code used in M^2COPS was obtained from Dr. M. Sambridge (personal communication) and his contribution is gratefully acknowledged. Natural neighbors of any sampling point are considered: *(a)* the sampling points in the neighboring Voronoi cells, and *(b)* the sampling points to which it is connected by the sides of the Delaunay triangles. Each sampling point has only one Voronoi cell (known as first order Voronoi cell) associated with it.

The two dimensional horizontal domain of Lake Michigan is partitioned by assigning each grid point (x, y) to the nearest sampling point or observation station (S) such that:

$$\text{Voronoi Cell} = \{(x,y) : |S_i - (x,y)| \leq |S_j - (x,y)| \quad \text{for all } j \neq i\} \tag{10.5.1}$$

Each grid point also has only one Voronoi cell (known as second order Voronoi cell) associated with it. The Natural Neighbor interpolation on the given grid is local and influenced only by its natural neighbor Voronoi cells. The interpolated values $F(x,y)$ are calculated from the observed values F_i using the following equation:

$$F(x,y) = \sum_{i=1}^{N} w_i(x,y) F_i \tag{10.5.2}$$

where $i = (1,N)$ represents the index of the neighboring sampling points or observation stations, $w_i(x,y)$ represents the weight functions and F_i is the observed value at the neighboring Voronoi cell "i". Full details of the method can be found in Sibson [1981], Watson [1992] and Sambridge et al. [1995].

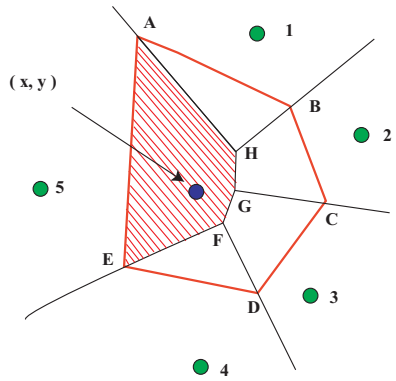

(x, y) : grid point
(1-5) : neighboring sampling points
ABCDE: second order Voronoi cell for grid point (x, y)
AHGFE: overlapping area between first order Voronoi cell for neighboring sampling point 5 and second order Voronoi cell for grid point (x, y).

Figure 10.6 Definition of the Natural Neighbor interpolation weight functions.

The weight functions are defined as the area of overlap between the second and the first order Voronoi cells (see Figure 10.6). Mathematically, the weight functions are defined as:

$$w_i(x,y) = \frac{A_i(x,y)}{A(x,y)} \tag{10.5.3}$$

Using the above definition of the weight functions equation 10.5.2 is written as:

$$F(x,y) = \sum_{i=1}^{N} \frac{A_i(x,y)}{A(x,y)} F_i \tag{10.5.4}$$

where $A_i(x,y)$ is the overlapped area of the first order Voronoi cell "i" and the second order Voronoi cell for the grid point (x, y) and $A(x,y)$ is the total area of the second order Voronoi cell for the grid point (x, y). The definition of the weights implies that $\sum_{i=1}^{N} w_i(x,y) = 1$.

The Natural Neighbor interpolation method produces smooth interpolated fields. Physically, the smoothness of the interpolated data set is necessary to avoid sharp gradients, however, the accuracy of the final gridded surfaces is not related to the degree of smoothness of the interpolated field, but rather to the correct determination of the weight functions.

10.5.2 *MPI* Implementation

As previously described, the model components are parallelized using the Message Passing Interface (*MPI*) where information exchanged among the model components (coupling) is achieved through *MPI* calls. Initially M^2*COPS* used the *MPICH* libraries (http://www-unix.mcs.anl.gov/mpi/, that have currently been replaced by the *OpenMPI* libraries (http://www.open-mpi.org/). *OpenMPI* is a continual effort on *MPI* development, which is fully compatible with the *MPICH* and the *MPI* standards, and it is actively supported. Specific portions of the M^2*COPS* parallel code were adopted from the *GLFS* developed code (Welsh et al. [2000]). The parallel M^2*COPS* code is currently run on quad-core Intel Systems with the possible use of up to 16 processor cores. The code can be also used also in sequential mode by running each model component individually.

The parallel M^2*COPS* is still under development and a future objective is the use of a coupler toolkit for the model couplings, such that additional model components can be easily added. One such solution for model couplings and communication among the different processes that needs to be further investigated is the use of the Model Coupling Toolkit (*MCT* at http://www-unix.mcs.anl.gov/mct/). *MCT* allows both parallel and sequential model runs by using *MPI* and emulated *MPI* interfaces, respectively.

10.5.3 Programming Language Interfacing

The availability of the high performance compilers and vectorization techniques requires the use of modern programming languages as well. The M^2*HYD* , M^2*SED* , M^2*BBL* and M^2*WAM* submodels use *Fortran 77* as their core programming language, but certain portions of the M^2*COPS*

system have been extended to use *Fortran 90*. The *M*^{2}*SWAN* model is completely written in *Fortran 90/95*. While it is not the principal objective of the current work to translate and test the *Fortran 77* code to *Fortran 90* code, it is suggested that all new model components be written in *Fortran 90* towards a full implementation of the latest *Fortran* standards. Furthermore, the needs of the *CPU* speed utilization and the "on demand loading" of resources is achieved by the use of modern computing languages.

The *IDL* (Interactive Data Language) software used for the analysis and visualization needs of *M*^{2}*COPS* has implemented facilities for calling *Fortran* and *C* functions and subroutines, while the *Fortran* and *C* programs can call needed *IDL* procedures. *IDL* has a sophisticated Advanced Programming Interface (*API*) in *C* that can be used to develop specialized calls from other languages.

Various model components in *M*^{2}*COPS* are written in *C* programming language (e.g., natural neighbor interpolation and various utilities) which need to be accessed from *Fortran* as well. Consistency requires that specific *Fortran* and *C* utilities of *M*^{2}*COPS* should be accessible by the graphics and analysis packages as well. *Fortran 77* and even *Fortran 90/95* have very limited capabilities for the development of a re-usable interface among the various languages and it usually requires extensive programming effort. In *M*^{2}*COPS* the interfacing among *Fortran*, *C* and *IDL* is achieved by the use of a package called *CFortran* (http://www-zeus.desy.de/~burow/cfortran/). *CFortran* is not a regular software package, but rather just a header file that contains directives compatible with the majority of the computer platforms, and can be used to construct the necessary calls for the various computing languages. The resulting code is compiled in a library subsequently used in the final linking of the model executable code with the the *IDL*, *Fortran*, and *C* libraries of the system. *IDL* uses the dynamic counterpart of the above created library. This procedure, as implemented in *M*^{2}*COPS*, produces facilities that are common to all modeling components, thus ensuring the consistency in the data analysis and manipulation.

10.6 Visualization and Computer Resources

A multi-component modeling system that utilizes additional software packages and is designed to perform scheduled runs (either continuous or discrete) requires use of some sort of automation software, since continuous user intervention is impractical. *M*^{2}*COPS* extensively uses "glue" scripts to automate the various aspects of its runs. Model runs, data storage and extraction, data analysis

and visualization are all controlled by *C* shell scripts (*UNIX*) that have been developed side by side with the M^2COPS development efforts.

The data analysis and visualization needs of M^2COPS are fulfilled using the Interactive Data Language (*IDL* at http://www.ittvis.com/ProductServices/IDL.aspx) which has numerous facilities for data analysis and visualization. Individual facilities have also been developed as part of M^2COPS. Other tools required for the production of the final products (e.g., image manipulation, animations, data format handling) are either part of a standard *UNIX/LINUX* operating system or are usually available as an open-source software package. The documents related to M^2COPS (including the present document) are generated using *LATEX* in both *Postscript* and *PDF* formats.

The memory and storage requirements for the full M^2COPS simulations are mainly controlled from the presence of the 4-dimensional arrays in the sediment and wave models. A reasonable estimate, based on personal experience with these models, for the memory requirements is ~ 2 GB. The most computationally expensive model is the sediment model. Depending upon the number of the sediment particle sizes used, the memory requirements easily reach ~ 2 GB and use of refined requirements can easily reach even higher levels.

M^2COPS currently runs on four computers with 8 GB *RAM* each. This is sufficient for a full Lake Michigan simulation. Considering the Lake Michigan $2x2$ km computational grid as a basis of a large scale simulation, the output requirements for a full 3D model simulation per week is estimated to be ~ 1.5 GB to ~ 2 GB. Therefore, a full Lake Michigan simulation for one year using 51 sediment classes, 3D velocity and temperature fields rises the storage requirements to ~ 7 TB. Data analysis and visualization will introduce an additional ~ 1 TB to ~ 2 TB storage requirement that brings the storage requirements to a total of ~ 10 TB.

If the data are to be archived, a compression /decompression scheme should be used. Depending upon the data type the usual compression rates are between 75 % to 95 %. An alternative and more efficient approach is to write and read the model data in *CDF* (http://cdf.gsfc.nasa.gov/) or *HDF5* (http://www.hdfgroup.org/) format that compress the data on the fly. However, using either method the storage requirements and data handling at the end are still expensive.

Modern computers are very fast and subsequently the numerical models are executed fast as well. The time for a weekly model run depends upon the model components used and the detail in the computations and can take as little as $10 - 20$ min and as high as $2 - 3$ days per simulation week.

A compression/decompression approach of a ~ 2 GB stored file can take as long as $10 - 15$ min at a time and needs to be further multiplied by the number of the variables being retrieved. This makes the whole approach a very time consuming process. Since most numerical models, including *M*^{2}*COPS*, are equipped with restart facilities to facilitate long term runs, the model restart files can be utilized to overcome the requirements related to storage and compression of the data. Personal experience shows that the long term model simulation data can be discarded after the generation of the final products and only the model restart files at specified days (e.g., once per week) need to be retained. This approach, in combination with the use of the *CDF*/*HDF* format reduces the storage requirements to a bare minimum without losing the capability of retrieving/regenerating the data for any specified date within the simulation period. The above approach has been tested in many previous model simulations and is certainly adopted in *M*^{2}*COPS*.

CHAPTER 11

M^2COPS PRELIMINARY TEST RESULTS AND CONCLUSIONS

11.1 Initial Model Application and Testing

The developed prediction system and its associated code components need to be applied and tested under different conditions and varying flow domains so that code bugs can be isolated and model behavior can be tested. The model output may include the following physical variables: *(a)* currents, *(b)* temperatures, *(c)* sediment concentrations, *(d)* free surface elevations, *(e)* surface wave parameters (height, period, energy and direction), *(f)* vertically integrated currents, *(g)* vertically integrated sediment concentrations, and *(h)* bottom characteristics (bedload fluxes, bottom evolution and sediment grain size distributions). Derived physical parameters may include: *(a)* horizontal and vertical momentum and mass fluxes at selected locations, *(b)* control volume fluxes, *(c)* numerical collection rates at selected locations, *(d)* total suspended sediment mass (local and global), and *(e)* temporal histories of the above parameters.

Although the individual model components of the *SMF* have been thoroughly tested and evaluated, the improvements and additions to individual model components as well as the new comprehensive model approach still need evaluation and verification. Switching on and off the different model components shows the relative importance of each model component with respect to each other and to the problem being modeled.

In the present initial model evaluation its behavior with and without the effect of the waves is examined in the physical domain of Lake Michigan and specifically during the Spring plume event of 1998.

11.2 Boundary and Initial Conditions and Model Forcing for the Preliminary Tests.

The lake domain in the present application is considered closed without inflows from the basin rivers or outflow to Huron Lake. Daily lake stage elevation adjustments are determined as the average of the hourly water elevation data at 6 gage stations around the Lake shoreline (stations numbers: 9087023 at Ludington, MI, 9087044 at Calumet Harbor, IL, 9087057 at Milwaukee, WI, 9075080 at Mackinow, MI, 9087079 Green Bay, WI, 9087096 at Port Inland, MI).

The boundary conditions for the hydrodynamic and sediment models mathematically are defined as:

free surface:
$$\mathcal{A}_{\mathrm{v}}\left[\frac{\partial u}{\partial z},\frac{\partial v}{\partial z}\right]=\left[\frac{\tau_{sx}}{\rho_{\mathrm{o}}},\frac{\tau_{sy}}{\rho_{\mathrm{o}}}\right],\quad \mathcal{K}_{\mathrm{v}}\left.\frac{\partial T}{\partial z}\right|_{\zeta}=\frac{\mathcal{H}_{\mathrm{N}}}{\rho_{\mathrm{o}}\,c_p}\quad\text{and}\quad\frac{\partial S}{\partial z}=0 \tag{11.2.1}$$

bottom:
$$\mathcal{A}_{\mathrm{v}}\left[\frac{\partial u}{\partial z},\frac{\partial v}{\partial z}\right]=\left[\frac{\tau_{bx}}{\rho_{\mathrm{o}}},\frac{\tau_{by}}{\rho_{\mathrm{o}}}\right],\quad\frac{\partial T}{\partial z}=\frac{\partial S}{\partial z}=0\quad\text{and}\quad w=0 \tag{11.2.2}$$

The wave boundary conditions are set as: $\mathcal{N}(x,y,\mathring{\sigma},\theta,t)\big|_{Land}=0$, that is, the land boundary absorbs all incoming waves.

For the "cold" model start all the fields in the water column (velocities, temperature, sediments) are initialized by setting them equal to zero. The initial conditions for the bottom sediments of Lake Michigan are set according to the data presented in Figures 8.16 *(a-c)* and details of how the bottom sediment data were obtained are given in Section 8.5. The wave models may assume one of the following two initial conditions: *(a)* no waves at all; and *(b)* some very young sea state. Here, the wave field is set to zero (that is, no waves exist at $t = 0$). The above set up for the initial conditions of the hydrodynamic and wave model requires that the model run for some time to allow the initial conditions to propagate through the computational domain and the model to reach a state of statistical equilibrium. This procedure in modeling practice is known as spin up. In the present wind driven 3D model application, one week spin up period is adequate for the model to reach equilibrium and the results to become realistic.

Forcing of the model during the spin up (February 22nd to February 28th, 1998) and the actual simulation period (March 1st to March 31st, 1998) requires meteorological data (air temperature, cloud cover and dew point), wind speed and direction, and temperature data. Details of how these data where obtained and processed are found in Section 8.1.

11.3 Statistical Tests

Only parametric statistical tests are used in the initial evaluation of the developed model prediction ability that include the mean (m) of the differences between the calculated and the measured or observed data sets, the *range* of variability, the standard deviation (σ) and the root mean square error (*RMSE*).

The mean of the differences between the modeled and measured data provides a gross overall measure of the model performance and is calculated as:

$$m = \frac{\sum_{i=1}^{n} \left(O_i - M_i\right)}{n} \tag{11.3.1}$$

where n is the total number of observation or modeled points, M_i are the modeled and O_i are the observed values of each evaluated variable. The smaller the mean difference the better the agreement between the model and the observed values, with a value of zero denoting absolute agreement.

The standard deviation (s) is a measure of the distance of the difference between the calculated and observed data from the mean difference. Small standard deviations indicate that the differences are closer to the mean. The standard deviation is calculated as:

$$s = \sqrt{\frac{\sum_{i=1}^{n} \left[\left(O_i - M_i\right) - m\right]^2}{n}} \tag{11.3.2}$$

The root mean square error (*RMSE*) is another test of the overall model performance that measures how close the modeled value of a variable is to the observed value. Mathematically, the test is defined as:

$$RMSE = \sqrt{\frac{\sum_{i=1}^{n} \left(O_i - M_i\right)^2}{n}} \tag{11.3.3}$$

The differences between the modeled and observed data are squared so that more weight is given to larger errors. All the above tests give information on the size, but not of the nature of the error, which make them adequate measures for the preliminary model evaluation. However, deeper analysis may require specific tests that can reveal the nature of the errors and help with in future model improvements.

11.4 Preliminary Test Results and Discussion

Water Level Simulations Without Waves

A comparison between observed and modeled without the effect of the waves water elevation data take place here. Modeled water elevations have been interpolated to the location of the water elevation gage stations using the Natural Neighbor method. The mean of each data set is calculated and subtracted from the water elevation data in this data set to produce two new data sets one for the observed and another for the modeled water level fluctuations about their corresponding means. Then, time series of hourly modeled water fluctuations are compared to hourly water fluctuations observed at six gage stations around the lake. A summary of the evaluation statistics and the maximum positive and negative deviations from the zero mean level denoted as max and min are shown in Table 11.1. Graphical representation of the time series is shown in Figures 11.1 to 11.6.

Location	max (cm)	min (cm)	s (cm)	RMSE (cm)
Mackinaw, MI	21.18	−32.66	6.75	8.28
Ludington, MI	14.83	−14.35	3.69	3.81
Calumet, IL	39.21	−18.91	5.84	6.26
Milwaukee, WI	24.20	−18.63	3.96	4.87
Green Bay, WI	29.57	−48.92	13.02	13.37
Port Inland, MI	15.60	−35.18	5.51	6.56

Table 11.1 Evaluation of water level fluctuations; effect of waves not included

From Figures 11.1 to 11.6 it is apparent that the model predicts well for all the significant set-up and draw-downs of the water surfaces. Although specifically designed tests need to be applied to accurately decide whether the modeled and observed water fluctuations are in phase, the visual agreement seems encouraging. The magnitude of the differences expressed by the standard deviation and the *RMSE* is variable around the Lake. The best agreement is found at Ludington and the worst at Green Bay with standard deviations 3.69 cm and 13.02 cm and *RMSE* 3.81 cm and 13.37 cm, respectively. Actual water differences range from 14.83 cm to 48.92 cm. Because the differences are calculated by subtracting the model from the observed fluctuations, the model shows a general tendency to underestimate the observed water elevations.

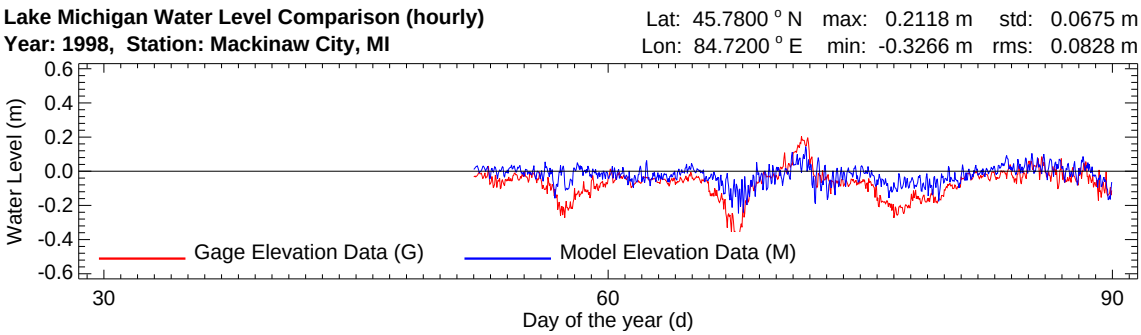

Figure 11.1 Water fluctuation time series at the Mackinaw, MI gage station.

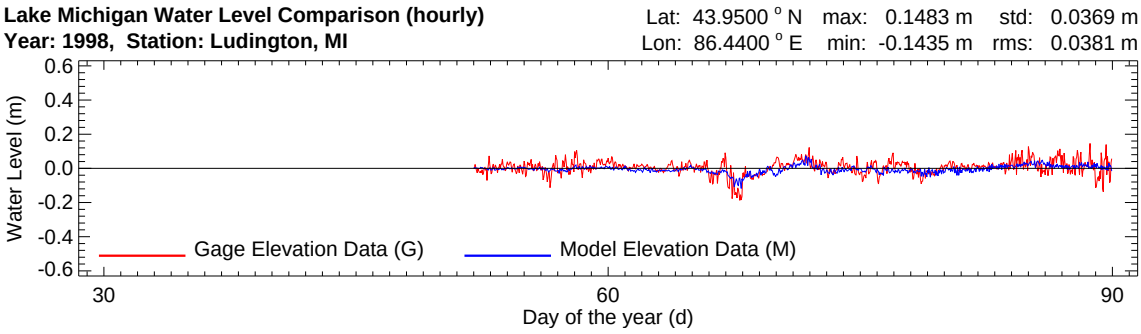

Figure 11.2 Water fluctuation time series at the Ludington, MI gage station

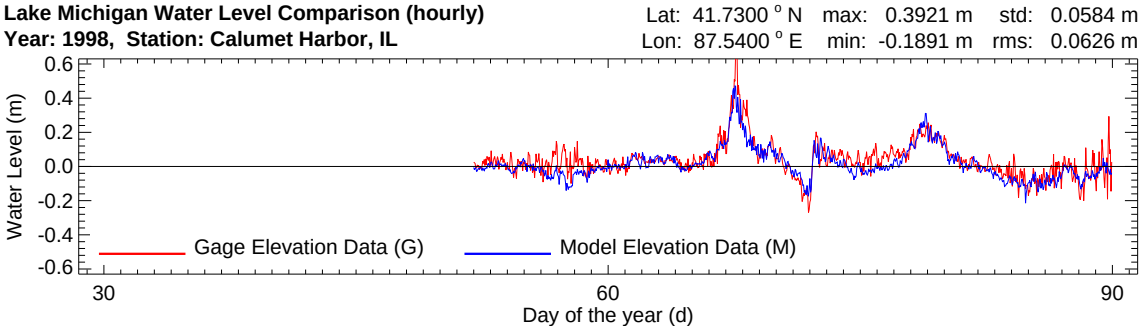

Figure 11.3 Water fluctuation time series at the Calumet, IL gage station

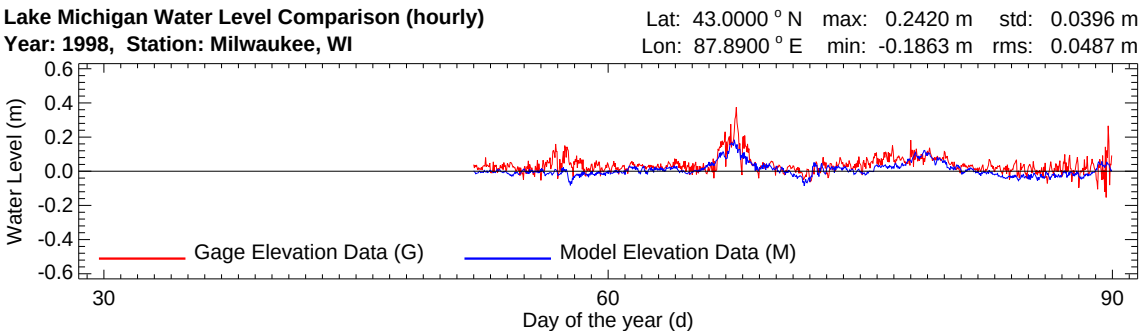

Figure 11.4 Water fluctuation time series at the Milwaukee, WI gage station

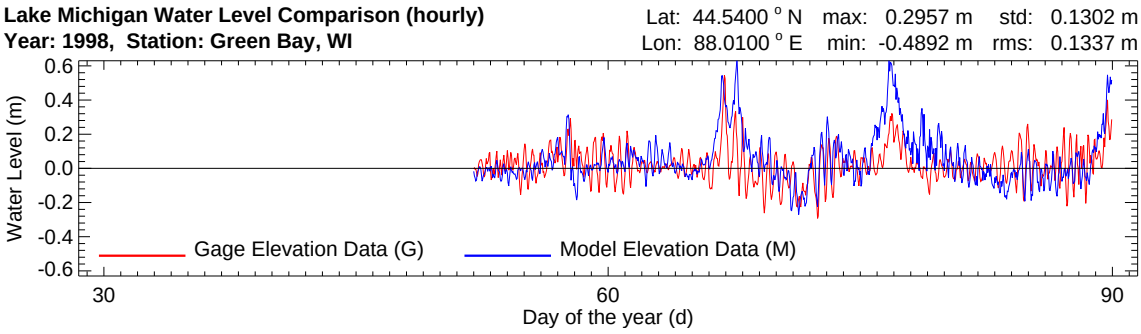

Figure 11.5 Water fluctuation time series at the Green Bay, WI gage station

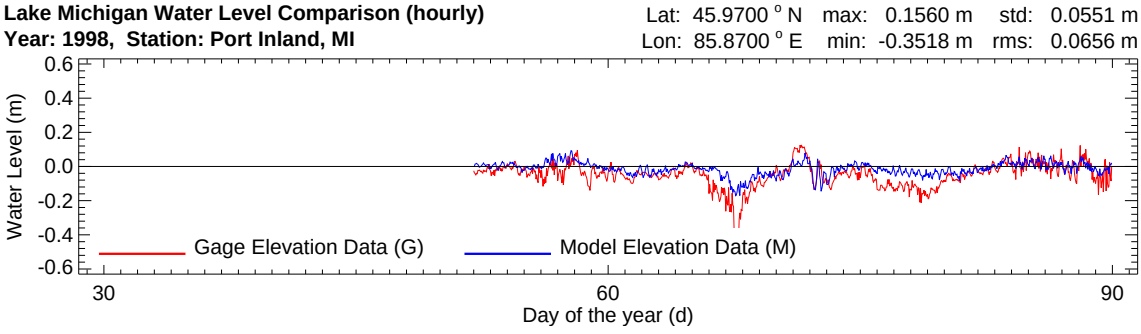

Figure 11.6 Water fluctuation time series at the Port Inland, MI gage station

Water Level Simulations; Wave effects included

The comparison between modeled and observed water elevation data is repeated to examine this time the barotropic response of the model when the wave effect is included. Time series of hourly modeled water fluctuations are compared to hourly water fluctuations at the same 6 gage stations around the lake. A summary of the evaluation statistics and the maximum positive and negative deviations from the zero mean level, denoted as max and min, are shown in Table 11.2. Graphical representation of the time series is shown in Fiqures 11.7 to 11.12.

Location	max (cm)	min (cm)	s (cm)	RMSE (cm)
Mackinaw, MI	20.26	−34.97	6.85	8.44
Ludington, MI	13.92	−14.33	3.71	3.82
Calumet, IL	39.33	−17.49	5.79	6.28
Milwaukee, WI	24.91	−18.09	3.97	4.91
Green Bay, WI	32.98	−36.80	11.07	11.18
Port Inland, MI	14.10	−34.24	5.49	6.57

Table 11.2 Evaluation of water level fluctuations; effect of waves included.

From Figures 11.7 to 11.12 and Table 11.2 it is obvious that water level simulations with the wave effects included improved the magnitude differences at all the stations around the lake. The biggest improvement is noticed at the Green Bay area where maximum water fluctuation difference dropped from 48.92 cm to 36.8 cm. Overall improvements are approximately between $1 - 8$ cm.

11.5 Conclusions

The main objective of this dissertation has been the development of a coastal prediction system that includes the 3D effect of the waves on water circulation and sediment transport. The momentum and scalar equations have been re-derived to incorporate the extra momentum produced by the waves, known as radiation stress, not only on 2D fields but on 3D fields as well. The need to consider the 3D radiation stresses when studying the interactions between waves and currents has been recognized and a few efforts have been made towards this direction in the recent years. This dissertation has taken into consideration all the known previous studies on this subject and has developed a full theoretical background for the incorporation of the 3D radiation stresses. The developed theoretical background has become part of the coastal prediction system presented as a whole for the first time here.

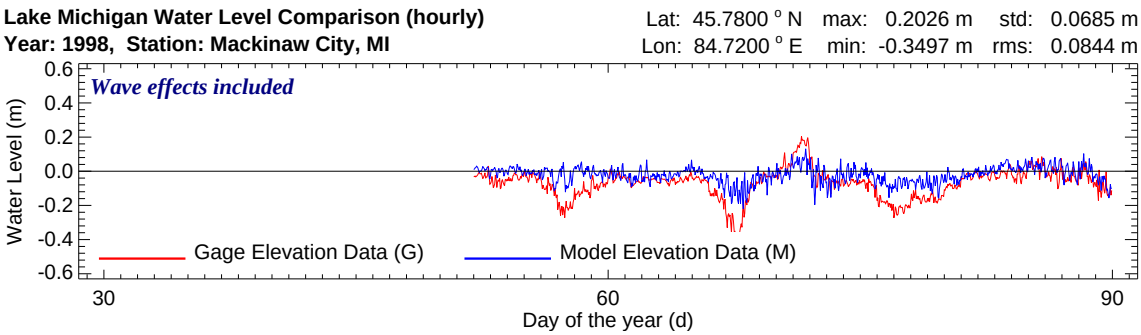

Figure 11.7 Water fluctuation time series at the Mackinaw, MI gage station; waves included.

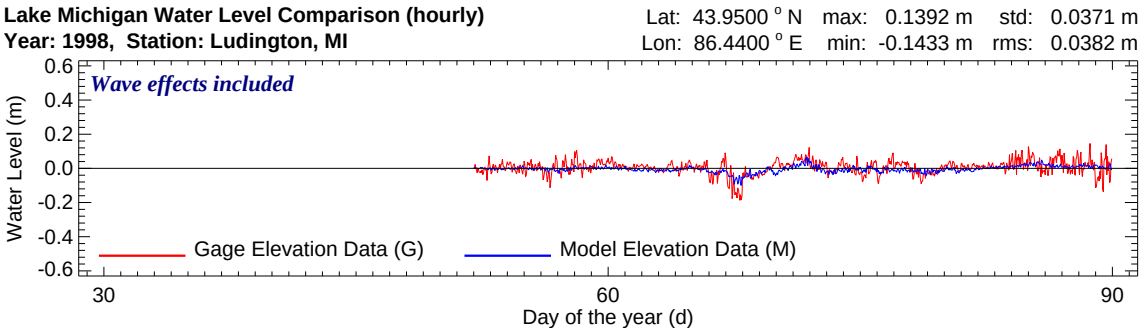

Figure 11.8 Water fluctuation time series at the Ludington, MI gage station; waves included.

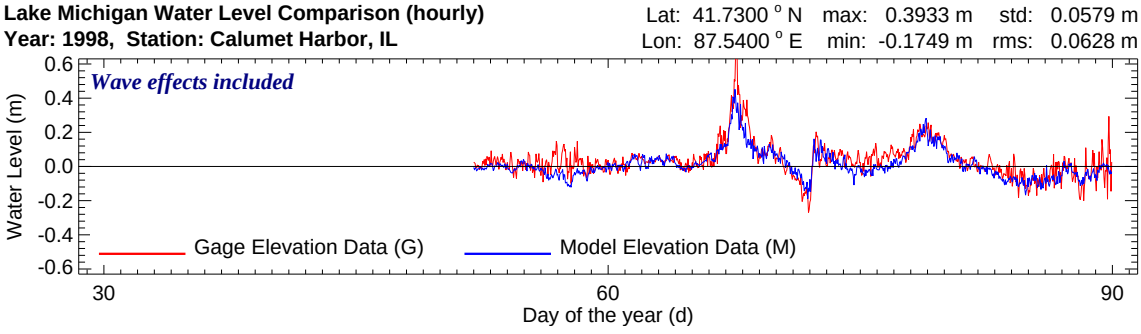

Figure 11.9 Water fluctuation time series at the Calumet, IL gage station; waves included.

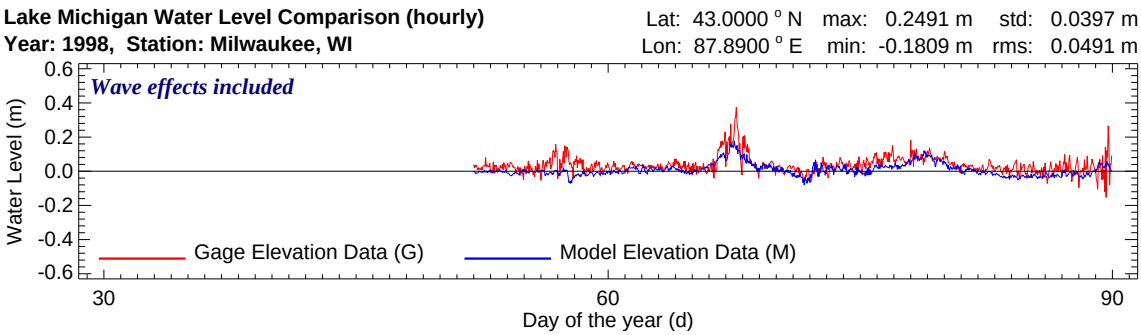

Figure 11.10 Water fluctuation time series at the Milwaukee, WI gage station; waves included.

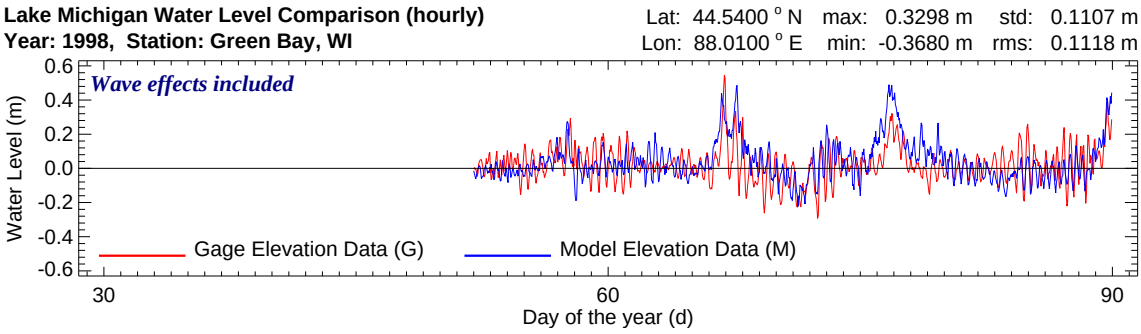

Figure 11.11 Water fluctuation time series at the Green Bay, WI gage station; waves included.

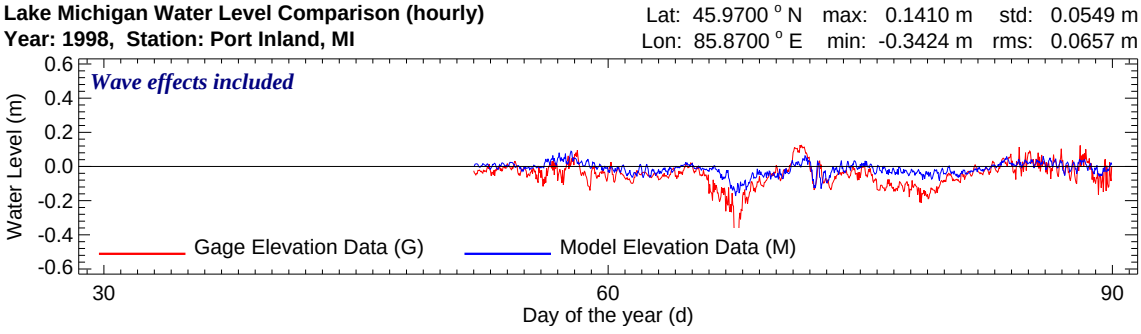

Figure 11.12 Water fluctuation time series at the Port Inland, MI gage station; waves included.

In addition to the incorporation of the 3D radiation stresses, many features of the models that consist the basis for the *M*^{2}*COPS* coastal prediction system have been replaced or modified to reflect the latest advancements in the hydrodynamic and sediment fields. Such modifications include use of the *UNESCO* equation of state; re-formulation of the surface drag coefficients for heat and momentum to account for the effect of the Atmospheric Boundary Layer stability in both the hydrodynamic and wave models; use of variable barometric pressure along the solution domain; re-formulation of the bottom roughness height, the Shields critical stress and the skin friction coefficients in the sediment models; and re-formulation of the bottom boundary layer and turbulence model to account for the radiation stresses.

The *M*^{2}*COPS* coupled wave, current and sediment transport coastal prediction system is applicable in lake and coastal ocean environments and it is expected to aid specifically in the modeling and analysis of flood surges, near-shore current systems, coastal and rip currents and surf zone waves. Techniques required to make modeling efforts using *M*^{2}*COPS* easily adaptable to future applications and identification of programming and code organizational issues required for the efficient incorporation of the new research advancements into the model have also been discussed.

The system has been applied in the Lake Michigan domain during the Spring plume of 1998. A detailed analysis of measurements taken during the *EEGLE* project has been presented, accompanied by a methodology capable of examining the genesis, evolution and disappearance of the Spring sediment plume. The proposed methodology includes an Eulerian Particle Tracking formulation and a conceptual and computational set up of control volumes at the shore and the bottom of the lake. A complete database for the texture of the eroded material from each shoreline segment and lake county has been developed by collecting existing data and by inferring data from various sources. A relationship between the chlorophyll-a content and the phytoplankton biomass has been established for Lake Michigan to allow the exclusion of suspended mass due to biological activity from the total suspended particulate matter measurements. The developed methodology is based on the ability of the sediment model to accept an unlimited number of sediment particle sizes.

The present preliminary evaluation of the system, although limited to water elevations, shows the improvement from the inclusion of the effect of the waves. Future work is needed to evaluate the performance of the other system components and to examine the effect of the added features and modifications on the prediction ability of the system.

APPENDIX A

NOTATION

Symbol	Units	Definition
A, A		
$\mathcal{A}_h$, $\mathcal{A}_v$	$m^2 \cdot s^{-1}$	Horizontal and vertical eddy viscosities (turbulent eddy diffusion coefficients)
α	dimensionless	Water surface albedo
B, B		
β	dimensionless	Fraction of the sediment size class currently in the active layer
β_s	dimensionless	Fraction of the sediment size class currently in the active stratum
C, Ψ		
C, C_o, C_r	dimensionless	Dimensionless sediment concentration of the particular sediment size class and its reference definitions
C_D	dimensionless	Drag coefficient
C_M, C_{NM}	dimensionless	Wind surface, drag and neutral drag coefficients
c_p	$J \cdot kg \cdot {}^oC$	Specific heat of the water
c_p^a	$J \cdot kg \cdot {}^oC$	Specific heat of the air
C_H	dimensionless	Aerodynamic bulk heat transfer coefficient
D, Δ		
$\mathcal{D}_h$, $\mathcal{D}_v$	$m^2 \cdot s^{-1}$	Horizontal and vertical mass diffusivities (turbulent mass diffusion coefficients)
d_s	m	Diameter of a sediment size class
δ	radians	Sun's declination angle (angular postion of the sun at solar noon with respect to the plane of equator)

Symbol	Units	Definition
E, E		
E_{m}	m	Active layer thickness
η		Horizontal coordinate in the Curvilinear coordinate system (mapping of the y direction)
$\boldsymbol{\epsilon}$	$\mathrm{m}^2\cdot\mathrm{s}^{-3}$	Dissipation rate of the turbulent kinetic energy
$\boldsymbol{\varepsilon}$	dimensionless	Emittance of the water surface: $\boldsymbol{\varepsilon} = 0.98$
$\mathbb{E}_{\mathbb{k}}$, $\mathbb{E}_{\mathbb{k}\mathrm{h}}$, $\mathbb{E}_{\mathbb{k}\mathrm{v}}$	dimensionless	Ekman number and the horizontal and vertical Ekman numbers respectively
F, Φ		
Φ, Φ_{o}, Φ_{r}		General modeled scalar quantity and its reference definitions
$\mathbb{F}_{\mathrm{r}}$, $\mathbb{F}_{\mathrm{rd}}$	dimensionless	Froude number and densimetric Froude number respectively
G, Γ		
g	$\mathrm{m}\cdot\mathrm{s}^{-1}$	Gravitational acceleration
γ_s	$\mathrm{N}\cdot\mathrm{m}^{-3}$	Specific weight of the sediments
γ_s	$\mathrm{N}\cdot\mathrm{m}^{-3}$	Specific weight of the water (also represents the specific weight of the mixture of the water and the suspended sediments (all size classes)
γ_{air}	$\mathrm{N}\cdot\mathrm{m}^{-3}$	Specific gravity of the air
γ_{o}, γ_{r}	$\mathrm{N}\cdot\mathrm{m}^{-3}$	Reference water specific gravities
γ_w	$\mathrm{N}\cdot\mathrm{m}^{-3}$	Specific gravity of the pure water
H, H		
h	m	Mean water depth (from bathymetry)
D	m	Total water depth ($D = h + \zeta$)
$\mathcal{H}$	$\mathrm{W}\cdot\mathrm{m}^{-2}$	Heat flux at the water surface
$\mathcal{H}_{\mathrm{N}}$	$\mathrm{W}\cdot\mathrm{m}^{-2}$	Net heat flux
$\mathcal{H}_{\mathrm{S}}$	$\mathrm{W}\cdot\mathrm{m}^{-2}$	Sensible heat flux
$\mathcal{H}_{\mathrm{L}}$	$\mathrm{W}\cdot\mathrm{m}^{-2}$	Latent heat flux
$\mathcal{H}_{\mathrm{LR}}$	$\mathrm{W}\cdot\mathrm{m}^{-2}$	Longwave radiation heat flux
$\mathcal{H}_{\mathrm{SR}}$	$\mathrm{W}\cdot\mathrm{m}^{-2}$	Shortwave radiation heat flux
$\mathcal{H}_{\mathrm{CSR}}$	$\mathrm{W}\cdot\mathrm{m}^{-2}$	Clear sky shortwave radiation heat flux
h_q	dimensionless	Specific humidity of the air

Symbol	Units	Definition
h_q^a	dimensionless	Specific humidity of the air at the instrument height (usually 10 m above the surface
h_q^w	dimensionless	Specific humidity of the air at the water surface

I, I

I	$W{\cdot}m^{-2}$	Incident shortwave radiation
$\mathbf{I}_o$	$W{\cdot}m^{-2}$	Average solar constant taken equal to: $1373\,W/m^2$

J, Ξ

ξ		Horizontal coordinate in the Curvilinear coordinate system (mapping of the *x* direction)

K, K

$\mathcal{K}_h, \mathcal{K}_v$	$m^2{\cdot}s^{-1}$	Horizontal and vertical eddy diffusivities (turbulent eddy diffusion coefficients)
$\boldsymbol{\kappa}$	$m^2{\cdot}s^{-2}$	Turbulent kinetic energy per unit mass
k		von Kármán's constant (equal to 0.4)
K	$W{\cdot}m^{-2}.{}^oC$	Bulk heat transfer coefficient

L, Λ

l	m	Surface mixing layer height

M, M

μ	$N{\cdot}s{\cdot}m^{-2}$	Dynamic viscosity of the water
μ_{air}	$N{\cdot}s{\cdot}m^{-2}$	Dynamic viscosity of the air
μ_o, μ_r	$N{\cdot}s{\cdot}m^{-2}$	Reference dynamic viscosities of the water
μ_w	$N{\cdot}s{\cdot}m^{-2}$	Dynamic viscosity of the pure water

N, N

n_s	dimensionless	Total number of the sediment size classes
ν	$m^2{\cdot}s^{-1}$	Kinematic viscosity of the water
ν_{air}	$m^2{\cdot}s^{-1}$	Kinematic viscosity of the air
ν_o, ν_r	$m^2{\cdot}s^{-1}$	Reference kinematic viscosities of the water
ν_w	$m^2{\cdot}s^{-1}$	Kinematic viscosity of the pure water

P, Π

p	dimensionless	Porosity of the bottom material (constant)

Symbol	Units	Definition
p	$N{\cdot}m^{-2}$	Pressure (gage or absolute) of the water
p_{atm}	$N{\cdot}m^{-2}$	Pressure (gage or absolute) of the moist air above the water
p_d	$N{\cdot}m^{-2}$	Pressure of the dry air
p_o, p_r	$N{\cdot}m^{-2}$	Reference Pressures of the water
p_s	$N{\cdot}m^{-2}$	Saturation vapor pressure of the moist air (absolute)
p_v	$N{\cdot}m^{-2}$	Vapor pressure of the moist air (absolute)
$\mathbb{P}_r$, $\mathbb{P}_{rt}$	dimensionless	Prandtl and turbulent Prandtl numbers respectively

Q

Q_b	$mg{\cdot}m^{-2}$	Vertically integrated (in respect to E_m) sediment mass per unit horizontal area of the particular size class currently at the bottom
q_{bi}, q_{bix}, q_{biy}	$mg{\cdot}m^{-1}{\cdot}s^{-1}$	Vertically integrated (in respect to E_m) sediment mass flux per unit horizontal area of the particular size class currently at the bottom, and its two components
q_L	$J{\cdot}kg^{-1}$	Latent heat of vaporization of the water
q_{L0}	$J{\cdot}kg^{-1}$	Latent heat of vaporization at $0\,^{o}C$ taken as: $2500297.8\,J/kg$

R, P

ρ	$mg{\cdot}L^{-1}$	Density of the water (also represents the density of the mixture of the water and the suspended sediments (all size classes)
ρ_s	$mg{\cdot}L^{-1}$	Density of the sediments
$\mathbb{R}_e$, $\mathbb{R}_{ep}$	dimensionless	Reynolds number and particle Reynolds number respectively
$\mathbb{R}_i$	dimensionless	Richardson's number
$\mathbb{R}_o$	dimensionless	Rossby number
ρ_{air}	$kg{\cdot}m^{-3}$	Density of the air
ρ_o, ρ_r	$kg{\cdot}m^{-3}$	Reference water densities
ρ_w	$kg{\cdot}m^{-3}$	Density of the pure water

S, Σ

$\mathbb{S}_c$, $\mathbb{S}_{ct}$	dimensionless	Schmidt and turbulent Schmidt numbers
$\mathbb{S}_{hp}$	dimensionless	Particle Sherwood number

Symbol	Units	Definition
$\boldsymbol{S_e}$	$mg{\cdot}m^{-2}{\cdot}s^{-1}$	Source sediment term representing the entrainment or resuspension flux of the bottom sediments. This term is only evaluated near the bottom and it is zero everywhere else in the water column
$\boldsymbol{S_d}$	$mg{\cdot}m^{-2}{\cdot}s^{-1}$	Sink sediment term representing the settling flux of the suspended sediments into the bottom. This term is only evaluated near the bottom and it is zero everywhere else in the water column
$\boldsymbol{S_f}$	$mg{\cdot}m^{-2}{\cdot}s^{-1}$	Source sediment term representing the exchange of particles between the active layer and the active stratum (specific to a particular size class)
S_p	dimensionless	Specific gravity
σ		Vertical coordinate in the Curvilinear coordinate system (mapping of the *z* direction)
$\boldsymbol{S_\Phi}$		General source/sink term of a modeled scalar
S	psu	Salinity (practical salinity) of the water
S_o, S_r	psu	Reference salinities of the water
$\boldsymbol{\sigma}_{SB}$	$W{\cdot}m^{-2}{\cdot}K^{-4}$	Stefan-Boltzmann's constant that equals to: $5.673 \cdot 10^{-8}\,W/m^2{\cdot}K^4$

T, T

t	s	Time
τ	$N{\cdot}m^{-2}$	Shear stress
τ_s, τ_{sx}, τ_{sy}	$N{\cdot}m^{-2}$	Surface shear stress and its two components
τ_b, τ_{bx}, τ_{by}	$N{\cdot}m^{-2}$	Bottom shear stress and its two components
T	^oC	Temperature of the water
T_{air}	^oC	Temperature of the air
T_d	^oC	Dewpoint temperature
T_e	^oC	Equilibrium temperature
T_o, T_r	^oC	Reference temperatures
T_w	^oC	Temperature at the free surface of the water

U, Θ

u	$m{\cdot}s^{-1}$	Flow velocity in the x-direction
U	$m{\cdot}s^{-1}$	Vertically integrated flow velocity in the x-direction
U_{bx}, U_{by}	$m{\cdot}s^{-1}$	Vertically integrated average horizontal velocities in the x- and y-directions respectively of the moving sediment size classes currently at the bottom

Symbol	Units	Definition
θ	dimensionless	Factor to reflect the availability of the particular sediment size class in the active layer control volume (0 or 1)
ϑ	dimensionless	Stability height (function of the Monin-Obukhov stability length)
u_*	$m{\cdot}s^{-1}$	Shear velocity
θ	^oC	Potential temperature of the water
θ_{air}	^oC	Potential temperature of the air
θ_e	^oC	Equilibrium potential temperature
θ_o, θ_r	^oC	Reference potential temperatures
θ_w	^oC	Potential Temperature at the free surface of the water
θ_h	radians	Hour angle (angular displacement of the sun from the local meridian)
V, Ω		
v	$m{\cdot}s^{-1}$	Flow velocity in the y-direction
V	$m{\cdot}s^{-1}$	Vertically integrated flow velocity in the y-direction
W		
w_s	$m{\cdot}s^{-1}$	Settling velocity for the particular sentiment size class
w	$m{\cdot}s^{-1}$	Flow velocity in the z-direction
W, W_x, W_y	$m{\cdot}s^{-1}$	Wind speed and its two horizontal components respectively
X, X		
x	m	Horizontal coordinate (x direction) in the Cartesian coordinate system
Y, ϒ		
y	m	Horizontal coordinate (y direction) in the Cartesian coordinate system
Z, Z		
z_b	m	Bed surface elevation
z	m	Vertical coordinate (z direction) in the Cartesian coordinate system
ζ	m	Water surface fluctuation
z_o	m	Roughness height
Z	radians	Solar zenith angle

APPENDIX B

MATHEMATICAL DEFINITIONS

B.1 Averaging Operations

Turbulent flows are defined as unsteady swirling fluid motions that strongly affect the distribution of mass, momentum and scalar quantities in the flow field. The highly random nature of the turbulent flows, makes the exact calculation of the flow parameters nearly impossible, a problem that is remedied by separating the flow in mean and turbulent components. Filtering out the fine scale turbulence effects introduces additional terms in the equations of motion and transport that are usually evaluated using an appropriate turbulence closure model. In the presence of the wind generated higher frequency surface waves, matters become even more complicated as the waves impose additional oscillatory type motions on the flow field that need to be resolved as well. In the next short Sections are introduced the basic principles of the averaging procedure in the presence and in the absence of surface waves.

B.1.1 Reynolds Averaging

The separation of the flow in mean (temporally averaged) and turbulent components is performed by considering a decomposition of a flow variable α, into a temporally averaged component $\bar{\alpha}$ and a turbulent component α' such that Stanišić [1988]:

$$\alpha = \bar{\alpha} + \alpha' \; ; \qquad \bar{\alpha} = \frac{1}{\Delta t}\int_{t}^{t+\Delta t} \alpha \, dt \tag{B.1}$$

where, the following Reynolds averaging rules are defined:

$$\overline{\alpha'} = 0 \; ; \;\; \overline{\bar{\alpha}\beta} = \bar{\alpha}\bar{\beta} \; ; \;\; \overline{\bar{\alpha}\beta'} = \bar{\alpha}\,\overline{\beta'} = 0 \; ; \;\; \overline{\alpha\beta} = \bar{\alpha}\bar{\beta} + \overline{\alpha'\beta'} \; ; \;\; \overline{\frac{\partial \alpha}{\partial \xi}} = \frac{\partial \bar{\alpha}}{\partial \xi} \; ; \; \overline{\int \alpha \, d\xi} = \int \bar{\alpha} \, d\xi \tag{B.2}$$

B.1.2 Extended Reynolds Averaging

Since the wave dynamics are represented by wave phase averaged equations and the hydrodynamics are represented by temporally averaged equations, there will be a gap in the time domain when the wave and the turbulence dynamics are coupled. Therefore, during the coupling process either, the hydrodynamic equations need to be phase averaged or the relevant wave terms used in the model coupling need to be temporally averaged.

The analysis of the interaction between the waves and the turbulence is performed by considering a decomposition of a flow variable α, into a temporally averaged component $\bar{\alpha}$, a wave component $\tilde{\alpha}$ and a turbulent component α' (Reynolds and Hussain [1972], Finnigan et al. [1984], Thais and Magnaudet [1995]) such that:

$$\alpha = \bar{\alpha} + \tilde{\alpha} + \alpha' \tag{B.3}$$

In this decomposition, the time and length scales of the wave component are assumed to be smaller than the corresponding scales of $\bar{\alpha}$. As also noted in Finnigan et al. [1984], there is a correspondence between the wave and turbulence time scales, mainly due to the fact that the wave frequencies often coincide with the energy containing frequencies of the turbulence. Therefore, the separation of the wave and the turbulence fields must be done, as shown in equation B.3, in time and not in length scales. To accompany the definition of this triple decomposition, they are introduced here two wave phase averaging operations:

(a) a *phase-conditioned averaging*, denoted by the use of the symbol $\widehat{(\cdot)}$, that separates the organized contributions to the variable α (that is, $\bar{\alpha}$ and $\tilde{\alpha}$) from the random contributions (background turbulence) defined by the following equation:

$$\hat{\alpha} = \bar{\alpha} + \tilde{\alpha} = \lim_{N\to\infty} \left\{ \frac{1}{N} \sum_{m=1}^{N} \alpha(t + mT_{\mathrm{r}}) \right\} \tag{B.4}$$

where, $\hat{\alpha}$ is the phase averaged component of the variable α, with the wave phase defined as: $\psi = k_\alpha x_\alpha - \omega t$ (summation over a, $a = 1, 2$) and T_{r} is a reference wave period. The above mentioned triple decomposition and the accompanying phase-conditioned averaging operation, is described in detail in the series of publications by Hussain and Reynolds [1970, 1972] and Reynolds and Hussain [1972], and it has been used to separate the background turbulence from the organized flow motions from field and laboratory wave data (see Hussain and Reynolds [1972], Finnigan and Einaudi [1981], Finnigan et al. [1984], Einaudi and Finnigan [1993]).

This phase-conditioned averaging procedure, defines the average of all realizations of the values of the variable α at a particular phase ψ and its application on the Navier-Stokes equations, allows the derivation of the equations of the wave velocities. In the absence of waves ($\tilde{\alpha} = 0$), the rules for the averaging of any flow variable are described by the Reynolds averaging procedure presented in Section B.1.1. To account for the wave-turbulence interaction, Hussain and Reynolds [1970] and Finnigan et al. [1984] presented an extension to the usual Reynolds averaging, by introducing a set of additional rules summarized as follows:

$$\hat{\alpha'} = \bar{\tilde{\alpha}} = 0 \; ; \quad \widehat{\tilde{\alpha}\beta} = \tilde{\alpha}\hat{\beta} \; ; \quad \widehat{\bar{\alpha}\beta} = \bar{\alpha}\hat{b} \; ; \quad \widehat{\bar{\alpha}} = \bar{\hat{\alpha}} = \bar{\alpha} \; ; \quad \overline{\tilde{\alpha}\beta'} = \overline{\tilde{\alpha}\widehat{\beta'}} = 0 \tag{B.5}$$

where, the last of the above equations implies that the background turbulence and the mean wave motions are uncorrelated.

(b) a *phase averaging*, denoted by the symbol $\overline{(\cdot)}^{\psi}$, that is used for the separation of the interactions between the waves and the mean flow (Mellor [2003] and Ardhuin and Jenkins [2006a]), and it is defined as follows:

$$\overline{\alpha}^{\psi} = \frac{1}{2\pi}\int_{0}^{2\pi} \alpha \, d\psi \tag{B.6}$$

where, the phase averages of the odd powers of $\sin\psi$, $\cos\psi$ and the products of $\sin\psi$ and $\cos\psi$ are zero (e.g., $\overline{\tilde{u}}^{\psi} = 0$).

B.2 Boundary Fitted Transformations

Most modern three-dimensional hydrodynamic numerical models for free surface flows (lakes, estuaries, coastal areas, etc.) are designed to better resolve the complex geometries in the horizontal directions and to adequately follow the bottom topography. This is accomplished by using: *(a)* general boundary-fitted coordinate systems horizontally (curvilinear coordinate systems with coordinate lines coinciding with all boundary segments), and *(b)* σ-coordinate transformations (stretched σ-grids) vertically.

B.2.1 Horizontal Curvilinear Transformation

The transformation of the horizontal solution domain requires the transformation of both the coordinates and the equations being solved where, the transformation of the Cartesian physical domain with the curvilinear coordinates as independent variables, maps the boundary segments in

the physical domain to vertical or horizontal lines in the transformed domain. In the subsequent analysis it is defined the symbol x_i to reflect the Cartesian coordinates (x, y, z), and the symbol ξ_i to reflect the curvilinear coordinates (ξ, η, z), therefore:

$$\begin{aligned} x_i &= x_i(\xi_1, \xi_2, \xi_3); \qquad & \xi_i &= \xi_i(x_1, x_2, x_3) \\ (x_1, x_2, x_3) &= (x, y, z); \qquad & (\xi_1, \xi_2, \xi_3) &= (\xi, \eta, z) \end{aligned} \tag{B.7}$$

Since the coordinates x_i and ξ_i are independent among themselves, the following expressions are valid:

$$\frac{\partial x_i}{\partial x_j} = \frac{\partial \xi_i}{\partial \xi_j} = \delta^i_j; \qquad \delta^i_j = \begin{cases} 1 & \text{if} \quad i = j \\ 0 & \text{if} \quad i \neq j \end{cases} \qquad \text{(Kronecker's delta)} \tag{B.8}$$

The partial derivative of any scalar variable f that is a function of x_i and therefore of ξ_i, $f = f(x_1, x_2, \cdots, x_n) = f(\xi_1, \xi_2, \cdots, \xi_n)$, can be written using the chain rule for the differentiation of a composite function as:

$$\frac{\partial f}{\partial x_i} = \frac{\partial \xi_j}{\partial x_i}\frac{\partial f}{\partial \xi_j} = \frac{\partial \xi_1}{\partial x_i}\frac{\partial f}{\partial \xi_1} + \frac{\partial \xi_2}{\partial x_i}\frac{\partial f}{\partial \xi_2} + \cdots + \frac{\partial \xi_n}{\partial x_i}\frac{\partial f}{\partial \xi_n} \tag{B.9}$$

$$\frac{\partial f}{\partial \xi_i} = \frac{\partial x_j}{\partial \xi_i}\frac{\partial f}{\partial x_j} = \frac{\partial x_1}{\partial \xi_i}\frac{\partial f}{\partial x_1} + \frac{\partial x_2}{\partial \xi_i}\frac{\partial f}{\partial x_2} + \cdots + \frac{\partial x_n}{\partial \xi_i}\frac{\partial f}{\partial x_n} \tag{B.10}$$

Designating the notation that a partial derivative of a function is represented by a variable subscript ($f_a = \partial f / \partial a$), the application of the above equations for the case of the two-dimensional coordinate transformation $(x, y) \rightarrow (\xi, \eta)$ yields:

$$\begin{pmatrix} f_\xi & f_\eta \\ f_x & f_y \end{pmatrix} = \begin{pmatrix} x_\xi f_x + y_\xi f_y & x_\eta f_x + y_\eta f_y \\ \xi_x f_\xi + \eta_x f_\eta & \xi_y f_\xi + \eta_y f_\eta \end{pmatrix} \tag{B.11}$$

Since now the coordinates (x, y) and (ξ, η) are related by (Thompson et al. [1985]):

$$\begin{pmatrix} \xi_x & \xi_y \\ \eta_x & \eta_y \end{pmatrix} = \frac{1}{\mathcal{J}} \begin{pmatrix} y_\eta & -x_\eta \\ -y_\xi & x_\xi \end{pmatrix} \qquad \text{and} \qquad \begin{pmatrix} x_\xi & y_\xi \\ x_\eta & y_\eta \end{pmatrix} = \mathcal{J} \begin{pmatrix} \eta_y & -\eta_x \\ -\xi_y & \xi_x \end{pmatrix} \tag{B.12}$$

where $\mathcal{J}$ is the Jacobian of the transformation: $\mathcal{J} = x_\xi y_\eta - x_\eta y_\xi$. For the function f, using the equations B.10 and B.12, it can be easily derived that the following equations are true:

$$f_x = \frac{1}{\mathcal{J}}\left[(f y_\eta)_\xi - (f y_\xi)_\eta\right] \qquad \text{and} \qquad f_y = \frac{1}{\mathcal{J}}\left[-(f x_\eta)_\xi + (f x_\xi)_\eta\right] \tag{B.13}$$

where the metric tensor of the transformation is defined as follows:

$$g_{ij} = \begin{pmatrix} x_\xi^2 + y_\xi^2 & x_\xi x_\eta + y_\xi y_\eta \\ x_\eta x_\xi + y_\eta y_\xi & x_\eta^2 + y_\eta^2 \end{pmatrix} = \begin{pmatrix} g_{11} & g_{12} \\ g_{21} & g_{22} \end{pmatrix} \tag{B.14}$$

and its inverse is:

$$g^{ij} = \begin{pmatrix} x_\eta^2 + y_\eta^2 & -x_\xi x_\eta + y_\xi y_\eta \\ -x_\eta x_\xi + y_\eta y_\xi & x_\xi^2 + y_\xi^2 \end{pmatrix} = \begin{pmatrix} g^{11} & g^{12} \\ g^{21} & g^{22} \end{pmatrix} \tag{B.15}$$

with $\det(g_{ij}) = \det(g^{ij}) = \mathcal{J}^2$. In addition to the coordinate and equation transformation, the flow velocities are also transformed so that their components are contravariant that is, normal to the (ξ,η) coordinate lines. This transformation follows the rule: $u_i = \dfrac{\partial x_i}{\partial \xi_j} u^j$ and therefore, the two horizontal physical velocities (u, v) are given in terms of their contravariant counterparts ($\breve{u}$, $\breve{v}$) by the following equations (Chapman et al. [1996]):

$$u = x_\xi \breve{u} + x_\eta \breve{v} \qquad \text{and} \qquad v = y_\xi \breve{u} + y_\eta \breve{v} \tag{B.16}$$

B.2.2 Vertical Stretched Transformation

The transformation of the vertical coordinate z to the σ coordinate (Figure 2.1) is defined as:

$$\sigma = \frac{z - \zeta(x,y,t)}{h(x,y) + \zeta(x,y,t)} = \frac{z - \zeta(x,y,t)}{D(x,y,t)} \tag{B.17}$$

h is the still water depth, ζ is the free water surface fluctuation and D is the total water depth. According to equation B.17, the coordinate σ takes the value 0 at the free surface ($z = \zeta$) and assumes the value -1 at the bottom ($z = -h$). The partial derivatives of σ in respect to (x, y, z, t) are easily obtained from equation B.17 as follows:

$$\frac{\partial \sigma}{\partial x} = -\frac{1}{D}\frac{\partial \zeta}{\partial x} - \frac{\sigma}{D}\frac{\partial D}{\partial x} = -\frac{1}{D}\left[\frac{\partial \zeta}{\partial x} + \sigma \frac{\partial D}{\partial x}\right] \tag{B.18}$$

$$\frac{\partial \sigma}{\partial y} = -\frac{1}{D}\frac{\partial \zeta}{\partial y} - \frac{\sigma}{D}\frac{\partial D}{\partial y} = -\frac{1}{D}\left[\frac{\partial \zeta}{\partial y} + \sigma \frac{\partial D}{\partial y}\right] \tag{B.19}$$

$$\frac{\partial \sigma}{\partial z} = \frac{1}{D} \tag{B.20}$$

$$\frac{\partial \sigma}{\partial t} = -\frac{1}{D}\frac{\partial \zeta}{\partial t} - \frac{\sigma}{D}\frac{\partial D}{\partial t} = -\frac{1+\sigma}{D}\frac{\partial D}{\partial t} = -\frac{1+\sigma}{D}\frac{\partial \zeta}{\partial t} \tag{B.21}$$

The operation of the partial differentiation of any field variable f in respect to the independent variables (x_1, x_2, x_3, x_4) = (x, y, z, t) is redefined using the chain rule for differentiation (equation B.9) for (ξ_1, ξ_2, ξ_3, ξ_4) = (x, y, σ, t), and the corresponding partial derivatives are replaced by the

following expressions:

$$\frac{\partial f}{\partial x} = \frac{\partial f^*}{\partial x^*} + \frac{\partial \sigma}{\partial x}\frac{\partial f^*}{\partial \sigma} = \frac{\partial f^*}{\partial x^*} - \frac{1}{D}\Big[\frac{\partial \zeta}{\partial x} + \sigma\frac{\partial D}{\partial x}\Big]\frac{\partial f^*}{\partial \sigma} \tag{B.22}$$

$$\frac{\partial f}{\partial y} = \frac{\partial f^*}{\partial y^*} + \frac{\partial \sigma}{\partial y}\frac{\partial f^*}{\partial \sigma} = \frac{\partial f^*}{\partial y^*} - \frac{1}{D}\Big[\frac{\partial \zeta}{\partial y} + \sigma\frac{\partial D}{\partial y}\Big]\frac{\partial f^*}{\partial \sigma} \tag{B.23}$$

$$\frac{\partial f}{\partial z} = \frac{\partial \sigma}{\partial z}\frac{\partial f^*}{\partial \sigma} = \frac{1}{D}\frac{\partial f^*}{\partial \sigma} \tag{B.24}$$

$$\frac{\partial f}{\partial t} = \frac{\partial f^*}{\partial t^*} + \frac{\partial \sigma}{\partial t}\frac{\partial f^*}{\partial \sigma} = \frac{\partial f^*}{\partial t^*} - \frac{1+\sigma}{D}\frac{\partial D}{\partial t}\frac{\partial f^*}{\partial \sigma} \tag{B.25}$$

Under the σ transformation the two horizontal velocities ($u = \frac{dx}{dt}$, $v = \frac{dy}{dt}$) are invariant but in the vertical direction a new velocity $\overset{\star}{\omega}$ is introduced:

$$\overset{\star}{\omega} = \frac{d\sigma}{dt} = \frac{\partial \sigma}{\partial t} + u\frac{\partial \sigma}{\partial x} + v\frac{\partial \sigma}{\partial y} + w\frac{\partial \sigma}{\partial z} \Rightarrow$$

$$D\overset{\star}{\omega} = w - (1+\sigma)\frac{\partial D}{\partial t} - u\Big[\frac{\partial \zeta}{\partial x} + \sigma\frac{\partial D}{\partial x}\Big] - v\Big[\frac{\partial \zeta}{\partial y} + \sigma\frac{\partial D}{\partial y}\Big] \tag{B.26}$$

B.2.3 Curvilinear Transformation of Symmetric Tensors

Let F_{ij} be a contravariant symmetric tensor in Cartesian coordinates and $\breve{F}_{pq}$ be its contravariant components in curvilinear coordinates. These two tensors obey the following transformation law:

$$F_{ij} = \frac{\partial x_i}{\partial \xi_p}\frac{\partial x_j}{\partial \xi_q}\breve{F}_{pq}\,; \quad i,j,p,q = 1,2 \tag{B.27}$$

where, x_i represent the Cartesian and ξ_i the curvilinear coordinates defined as $(x_1, x_2) = (x, y)$ and $(\xi_1, \xi_2) = (\xi, \eta)$ respectively. The components of F in terms of the components of $\breve{F}$ are derived using equation B.27:

$$F_{11} = F_{(xx)} = x_\xi^2\breve{F}_{(\xi\xi)} + 2x_\xi x_\eta\breve{F}_{(\xi\eta)} + x_\eta^2\breve{F}_{(\eta\eta)} \tag{B.28}$$

$$F_{22} = F_{(yy)} = y_\xi^2\breve{F}_{(\xi\xi)} + 2y_\xi y_\eta\breve{F}_{(\xi\eta)} + y_\eta^2\breve{F}_{(\eta\eta)} \tag{B.29}$$

$$F_{12} = F_{21} = F_{(xy)} = F_{(yx)} = x_\xi y_\xi\breve{F}_{(\xi\xi)} + (x_\xi y_\eta + x_\eta y_\xi)\breve{F}_{(\xi\eta)} + x_\eta y_\eta\breve{F}_{(\eta\eta)} \tag{B.30}$$

while, using the inverse transformation the components of $\breve{F}$ are written in terms of the components of F:

$$\breve{F}_{11} = \breve{F}_{(\xi\xi)} = \frac{y_\eta^2}{\mathcal{J}^2}F_{(xx)} - 2\frac{x_\eta y_\eta}{\mathcal{J}^2}F_{(xy)} + \frac{x_\eta^2}{\mathcal{J}^2}F_{(yy)} \tag{B.31}$$

$$\breve{F}_{22} = \breve{F}_{(\eta\eta)} = \frac{y_\xi^2}{\mathcal{J}^2} F_{(xx)} - 2\frac{x_\xi y_\xi}{\mathcal{J}^2} F_{(xy)} + \frac{x_\xi^2}{\mathcal{J}^2} F_{(yy)} \tag{B.32}$$

$$\breve{F}_{12} = \breve{F}_{21} = \breve{F}_{(\xi\eta)} = \breve{F}_{(\eta\xi)} = -\frac{y_\xi y_\eta}{\mathcal{J}^2} F_{(xx)} + \frac{x_\xi y_\eta + x_\eta y_\xi}{\mathcal{J}^2} F_{(xy)} - \frac{x_\xi x_\eta}{\mathcal{J}^2} F_{(yy)} \tag{B.33}$$

The notation $F_{(\cdot)}$ in the above equations is used to denote the spatial direction of F thus, avoiding the notation conflict when F_x is used to represent the partial derivative of F in respect to x. The divergence terms $\partial F_{ij}/\partial x_j$ are evaluated in curvilinear coordinates using equations B.13 after replacing all occurrences of F_{ij} by the corresponding expressions as given by the equations B.28, B.29 and B.30, resulting in the following equations:

$$\frac{\partial F_{(xx)}}{\partial x} + \frac{\partial F_{(xy)}}{\partial y} = \frac{1}{\mathcal{J}} \left\{ \left[\mathcal{J} \left(x_\xi \breve{F}_{(\xi\xi)} + x_\eta \breve{F}_{(\xi\eta)} \right) \right]_\xi + \left[\mathcal{J} \left(x_\xi \breve{F}_{(\xi\eta)} + x_\eta \breve{F}_{(\eta\eta)} \right) \right]_\eta \right\} \tag{B.34}$$

$$\frac{\partial F_{(xy)}}{\partial x} + \frac{\partial F_{(yy)}}{\partial y} = \frac{1}{\mathcal{J}} \left\{ \left[\mathcal{J} \left(y_\xi \breve{F}_{(\xi\xi)} + y_\eta \breve{F}_{(\xi\eta)} \right) \right]_\xi + \left[\mathcal{J} \left(y_\xi \breve{F}_{(\xi\eta)} + y_\eta \breve{F}_{(\eta\eta)} \right) \right]_\eta \right\} \tag{B.35}$$

B.2.4 Non-Dimensional Variables

The governing equations in *M*^{2}*COPS* are modeled using their non-dimensional form making it easier to compare the relative importance of one physical process to another. The non-dimensionalization of the governing equations is based upon the normalization of all dependent and independent variables in respect to reference constant values, presumably the largest values encountered in the problem being solved (Streeter et al. [1998]), and therefore, the newly created variables will have values ranging between -1 and 1. The equations are non-dimensionalized using the following variables: $\mathrm{X_r}$ and $\mathrm{Z_r}$ that are reference length scales for the horizontal and vertical directions respectively, $\mathrm{U_r}$ a reference flow velocity, ρ_r a reference water density, Φ_r a reference value of the modeled scalar quantity, and $\mathcal{B}_\mathrm{rh}$ and $\mathcal{B}_\mathrm{rv}$ are reference eddy viscosities/diffusivities for the horizontal and vertical directions respectively ($\mathcal{B}$ is conveniently replaced by $\mathcal{A}$ in the momentum equations and by $\mathcal{D}$ or $\mathcal{K}$ in the scalar equations). The dimensionless variables, denoted by the carats, are written using the following equations:

$$(\check{x}, \check{y}, \check{z}) = \frac{1}{\mathrm{X_r}} \left(x, y, z \frac{\mathrm{X_r}}{\mathrm{Z_r}}\right); \quad \check{\zeta} = \frac{g\zeta}{f \mathrm{U_r X_r}}; \quad (\check{h}, \check{D}) = \frac{1}{\mathrm{Z_r}} (h, D); \quad \check{t} = ft \tag{B.36}$$

$$(\check{u}, \check{v}, \check{w}) = \frac{1}{\mathrm{U_r}} \left(u, v, w \frac{\mathrm{X_r}}{\mathrm{Z_r}}\right); \qquad (\check{\tau}_x, \check{\tau}_y) = \frac{1}{\tau_\mathrm{r}} (\tau_x, \tau_y) = \frac{1}{\rho_\mathrm{o} f \mathrm{U_r Z_r}} (\tau_x, \tau_y) \tag{B.37}$$

$$(\check{u}_{st}, \check{v}_{st}, \check{w}_{st}) = \frac{1}{U_r}(u_{st}, v_{st}, w_{st}\frac{X_r}{Z_r}) \; ; \qquad (\check{\mathring{\sigma}}, \check{\omega}) = \frac{Z_r}{U_r}(\mathring{\sigma}, \omega) \; ; \qquad \check{E} = \frac{g}{f^2 U_r^2 X_r^2} E \tag{B.38}$$

$$\check{\Omega} = \frac{X_r}{U_r}\Omega \; ; \qquad \check{\rho} = \frac{\rho - \rho_o}{\rho_r - \rho_o} \; ; \qquad \check{p} = \frac{p}{\rho_o f U_r X_r} \; ; \qquad \check{p}_{atm} = \frac{p_{atm}}{\rho_o f U_r X_r} \tag{B.39}$$

$$\check{\Phi} = \frac{\Phi - \Phi_o}{\Phi_r - \Phi_o} \; ; \qquad \check{T} = \frac{T - T_o}{T_r - T_o} \; ; \qquad \check{S} = \frac{S - S_o}{S_r - S_o} \tag{B.40}$$

$$\begin{aligned} &\check{\mathcal{B}}_h = \frac{\mathcal{B}_h}{\mathcal{B}_{rh}} \; ; \qquad \check{\mathcal{B}}_v = \frac{\mathcal{B}_v}{\mathcal{B}_{rv}} \; ; \qquad \check{\mathcal{A}}_h = \frac{\mathcal{A}_h}{\mathcal{A}_{rh}} \; ; \qquad \check{\mathcal{A}}_v = \frac{\mathcal{A}_v}{\mathcal{A}_{rv}} \\ &\check{\mathcal{D}}_h = \frac{\mathcal{D}_h}{\mathcal{D}_{rh}} \; ; \qquad \check{\mathcal{D}}_v = \frac{\mathcal{D}_v}{\mathcal{D}_{rv}} \; ; \qquad \check{\mathcal{K}}_h = \frac{\mathcal{K}_h}{\mathcal{K}_{rh}} \; ; \qquad \check{\mathcal{K}}_v = \frac{\mathcal{K}_v}{\mathcal{K}_{rv}} \end{aligned} \tag{B.41}$$

Using the equations B.36 through B.41, dimensional analysis yields the following dimensionless numbers:

$$\mathbb{F}_r = \frac{U_r}{(gZ_r)^{1/2}} \; ; \qquad \mathbb{F}_{rd} = \frac{\mathbb{F}_r}{\sqrt{\frac{\rho_r - \rho_o}{\rho_o}}} = \frac{\rho_o^{1/2} U_r}{[g(\rho_r - \rho_o)Z_r]^{1/2}} \tag{B.42}$$

$$\mathbb{R}_o = \frac{U_r}{fX_r} \; ; \qquad \mathbb{E}_{kh} = \frac{\mathcal{A}_{rh}}{fX_r^2} \; ; \qquad \mathbb{E}_{kv} = \frac{\mathcal{A}_{rv}}{fZ_r^2} \tag{B.43}$$

$$\mathbb{S}_{ch} = \frac{\mathcal{A}_{rh}}{\mathcal{D}_{rh}} \; ; \qquad \mathbb{S}_{cv} = \frac{\mathcal{A}_{rv}}{\mathcal{D}_{rv}} \; ; \qquad \mathbb{P}_{rh} = \frac{\mathcal{A}_{rh}}{\mathcal{K}_{rh}} \; ; \qquad \mathbb{P}_{rv} = \frac{\mathcal{A}_{rv}}{\mathcal{K}_{rv}} \tag{B.44}$$

where $\mathbb{F}_r$ is the Froude number, $\mathbb{F}_{rd}$ is the densimetric Froude number, $\mathbb{R}_o$ is the Rossby number, $\mathbb{E}_{kh}$ and $\mathbb{E}_{kv}$ are the horizontal and vertical Ekman numbers, $\mathbb{S}_{ch}$ and $\mathbb{S}_{cv}$ are the horizontal and vertical Schmidt numbers, and $\mathbb{P}_{rh}$ and $\mathbb{P}_{rv}$ are the horizontal and vertical Prandtl numbers. Since $\partial\check{x}/\partial x = \partial\check{y}/\partial y = 1/X_r$, $\partial\check{z}/\partial z = 1/Z_r$ and $\partial\check{t}/\partial t = f$, all the partial derivatives are evaluated using the following equations:

$$\begin{aligned} &\frac{\partial^n}{\partial x^n} = \left(\frac{\partial\check{x}}{\partial x}\right)^n \cdot \frac{\partial^n}{\partial\check{x}^n} = \frac{1}{X_r^n}\frac{\partial^n}{\partial\check{x}^n} \; ; \qquad \frac{\partial^n}{\partial y^n} = \left(\frac{\partial\check{y}}{\partial y}\right)^n \cdot \frac{\partial^n}{\partial\check{y}^n} = \frac{1}{X_r^n}\frac{\partial^n}{\partial\check{y}^n} \\ &\frac{\partial^n}{\partial z^n} = \left(\frac{\partial\check{z}}{\partial z}\right)^n \cdot \frac{\partial^n}{\partial\check{z}^n} = \frac{1}{Z_r^n}\frac{\partial^n}{\partial\check{z}^n} \; ; \qquad \frac{\partial^n}{\partial t^n} = \left(\frac{\partial\check{t}}{\partial t}\right)^n \cdot \frac{\partial^n}{\partial\check{t}^n} = f^n\frac{\partial^n}{\partial\check{t}^n} \end{aligned} \tag{B.45}$$

B.3 Useful Calculus Theorems

(a) Leibnitz's rule for integrals (Pacanowski and Griffies [2000], page 49):

$$\frac{\partial}{\partial x}\int_{a(x)}^{b(x)} f(x,x')\,dx' = \int_{a(x)}^{b(x)} \frac{\partial f(x,x')}{\partial x}\,dx' + f(x,b(x))\frac{\partial b(x)}{\partial x} - f(x,a(x))\frac{\partial a(x)}{\partial x} \tag{B.46}$$

(b) First mean value theorem for integrals (Fulks [1978], page 161):

The theorem states that, given two continuous and integrable functions $f(x)$ and $g(x)$ on the interval $[a,b]$ such that: $g(x) \geq 0$ and $\int_a^b g(x)\,dx \geq 0$ or $g(x) \leq 0$ and $\int_a^b g(x)\,dx \leq 0$, the following expression is true:

$$\frac{1}{b-a}\int_a^b f(x)\,dx = f(\xi) = \frac{\int_a^b f(x)g(x)\,dx}{\int_a^b g(x)\,dx}\,; \qquad a \leq \xi \leq b \tag{B.47}$$

where, $f(\xi)$ is the weighted mean of the function $f(x)$ in respect to the weight function $g(x)$.

(c) Second mean value theorem for integrals (Fulks [1978], page 163):

The theorem states that, given two functions $f(x)$ and $g(x)$ such that $f(x)$ is monotone and $f'(x)$ is integrable and that $g(x)$ is continuous on the interval $[a,b]$ then, there is a $\xi \in [a,b]$ for which the following expression is true:

$$\int_a^b f(x)\,g(x)\,dx = f(a)\int_a^\xi g(x)\,dx + f(b)\int_\xi^b g(x)\,dx \tag{B.48}$$

APPENDIX C

COORDINATE TRANSFORMED EQUATIONS

The transformed equations of motion and scalar transport, in the (ξ, η, z) and the (ξ, η, σ) coordinate systems are presented here in both their dimensional and non-dimensional forms. The 3D equations were derived from equations 2.1.1, 2.1.10, 2.1.11 and 2.1.5, using the methods described in Sections B.2.1 and B.2.2. Following the usual practice, during the derivations all the higher order terms involving the gradients of D and ζ were neglected. The vertically averaged (external mode) equations were derived from equations 2.1.26b, 2.1.29b and 2.1.30b using a similar approach. The wave induced effects on the averaged flow field are introduced in the equations by the addition of *(a)* the various Stokes drift related terms and *(b)* the wave radiation terms. The final curvilinear forms of the equations are written in terms of their respective contravariant variables, denoted by the symbol $\breve{(\cdot)}$ while, the notations a_s and $a_{(s)}$ are used to represent the differentiation and the spatial representation of the variable a respectively. The various contravariant variables appearing in the subsequent equations are defined as follows:

Velocities:

$$u = u_{(x)} = \breve{u}_{(\xi)} = x_\xi \breve{u} + x_\eta \breve{v} \; ; \qquad v = u_{(y)} = \breve{u}_{(\eta)} = y_\xi \breve{u} + y_\eta \breve{v} \tag{C.1a}$$

$$\breve{u} = \frac{1}{\mathcal{J}}(y_\eta u - x_\eta v) \; ; \qquad \breve{v} = \frac{1}{\mathcal{J}}(-y_\xi u + x_\xi v) \tag{C.1b}$$

Doppler velocities:

$$u - \hat{u}_A = (\breve{u} - \breve{\hat{u}}_A)_{(\xi)} = x_\xi(\breve{u} - \breve{\hat{u}}_A) + x_\eta(\breve{v} - \breve{\hat{v}}_A)\ ;\ \ \breve{\hat{u}}_A = \frac{1}{D}\int_{-h}^{\zeta} \breve{u}\,\zeta_s(z)\,dz = \int_{-1}^{0} \breve{u}\,\zeta_s(\sigma)\,d\sigma \tag{C.2a}$$

$$v - \hat{v}_A = (\breve{u} - \breve{\hat{u}}_A)_{(\eta)} = y_\xi(\breve{u} - \breve{\hat{u}}_A) + y_\eta(\breve{v} - \breve{\hat{v}}_A)\ ;\quad \breve{\hat{v}}_A = \frac{1}{D}\int_{-h}^{\zeta} \breve{v}\,\zeta_s(z)\,dz = \int_{-1}^{0} \breve{v}\,\zeta_s(\sigma)\,d\sigma \tag{C.2b}$$

Stokes velocities:

$$\mathrm{u_{st}} = \mathrm{u_{st(x)}} = \breve{\mathrm{u}}_{\mathrm{st}(\xi)} = x_\xi \breve{\mathrm{u}}_{\mathrm{st}} + x_\eta \breve{\mathrm{v}}_{\mathrm{st}}\ ;\quad \mathrm{v_{st}} = \mathrm{u_{st(y)}} = \breve{\mathrm{u}}_{\mathrm{st}(\eta)} = y_\xi \breve{\mathrm{u}}_{\mathrm{st}} + y_\eta \breve{\mathrm{v}}_{\mathrm{st}} \tag{C.3a}$$

$$\breve{\mathrm{u}}_{\mathrm{st}} = \frac{1}{\mathcal{J}}(y_\eta \mathrm{u_{st}} - x_\eta \mathrm{v_{st}})\ ;\quad \breve{\mathrm{v}}_{\mathrm{st}} = \frac{1}{\mathcal{J}}(-y_\xi \mathrm{u_{st}} + x_\xi \mathrm{v_{st}}) \tag{C.3b}$$

$$|\mathbf{u_{st}}|^2 = \mathrm{u_{st}^2} + \mathrm{v_{st}^2} = g_{11}\breve{\mathrm{u}}_{\mathrm{st}}^2 + 2g_{12}\breve{\mathrm{u}}_{\mathrm{st}}\breve{\mathrm{v}}_{\mathrm{st}} + g_{22}\breve{\mathrm{v}}_{\mathrm{st}}^2 \tag{C.3c}$$

$$\breve{\mathrm{w}}_{\mathrm{st}}(z) = \frac{1}{\mathcal{J}}\left\{ \left[\mathcal{J}D\breve{\mathrm{U}}_{\mathrm{st}}(1 - f_2 f_3)\right]_\xi + \left[\mathcal{J}D\breve{\mathrm{V}}_{\mathrm{st}}(1 - f_2 f_3)\right]_\eta \right\} \tag{C.3d}$$

$$\breve{\mathrm{w}}_{\mathrm{st}}(\sigma) = \lambda_{(\xi)}\breve{\mathrm{u}}_{\mathrm{st}} + \lambda_{(\eta)}\breve{\mathrm{v}}_{\mathrm{st}} + \frac{1}{\mathcal{J}}\left\{ \left[\mathcal{J}D\breve{\mathrm{U}}_{\mathrm{st}}(1 - f_2 f_3)\right]_\xi + \left[\mathcal{J}D\breve{\mathrm{V}}_{\mathrm{st}}(1 - f_2 f_3)\right]_\eta \right\} \tag{C.3e}$$

σ vertical velocities:

$$D\breve{\Omega} = D\breve{\omega} - \breve{\mathrm{w}}_{\mathrm{st}}\ ; \qquad D\breve{\omega} = w - \lambda_{(\xi)}\breve{u} - \lambda_{(\eta)}\breve{v} + (1 + \sigma)\frac{\partial D}{\partial t} \tag{C.4}$$

Wave radiation stresses:

$$\breve{S}_{(\xi\xi)} = \frac{y_\eta^2}{\mathcal{J}^2}S_{(xx)} - 2\frac{x_\eta y_\eta}{\mathcal{J}^2}S_{(xy)} + \frac{x_\eta^2}{\mathcal{J}^2}S_{(yy)}\ ;\quad \breve{S}_{(\eta\eta)} = \frac{y_\xi^2}{\mathcal{J}^2}S_{(xx)} - 2\frac{x_\xi y_\xi}{\mathcal{J}^2}S_{(xy)} + \frac{x_\xi^2}{\mathcal{J}^2}S_{(yy)} \tag{C.5a}$$

$$\breve{S}_{(\xi\eta)} = \breve{S}_{(\eta\xi)} = -\frac{y_\xi y_\eta}{\mathcal{J}^2}S_{(xx)} + \frac{x_\xi y_\eta + x_\eta y_\xi}{\mathcal{J}^2}S_{(xy)} - \frac{x_\xi x_\eta}{\mathcal{J}^2}S_{(yy)} \tag{C.5b}$$

where:

$$\lambda_{(x)} = \frac{\partial \zeta}{\partial x} + \sigma\frac{\partial D}{\partial x}\ ; \qquad \lambda_{(y)} = \frac{\partial \zeta}{\partial y} + \sigma\frac{\partial D}{\partial y} \tag{C.6a}$$

$$\lambda_{(\xi)} = \frac{\partial \zeta}{\partial \xi} + \sigma\frac{\partial D}{\partial \xi}\ ; \qquad \lambda_{(\eta)} = \frac{\partial \zeta}{\partial \eta} + \sigma\frac{\partial D}{\partial \eta} \tag{C.6b}$$

$$\lambda_{(x)} = \frac{1}{\mathcal{J}}\big(y_\eta\lambda_{(\xi)} - y_\xi\lambda_{(\eta)}\big)\ ; \qquad \lambda_{(y)} = \frac{1}{\mathcal{J}}\big(-x_\eta\lambda_{(\xi)} + x_\xi\lambda_{(\eta)}\big) \tag{C.6c}$$

When the calculations are performed in the Cartesian instead of the curvilinear coordinate system (user's choice) the transformation is defined as: $(x, y, \sigma) \rightarrow (x, y, \sigma)$, and the modeled equations can readily be recovered from the transformed equations using the following expressions:

$$\left.\begin{array}{ll} x_\xi = y_\eta = 1; \quad x_\eta = y_\xi = 0; & \mathcal{J} = x_\xi\, y_\eta - x_\eta\, y_\xi = 1 \\ \breve{u} = u; \quad \breve{v} = v; & \breve{U} = U; \quad \breve{V} = V \\ g_{11} = g^{11} = g_{22} = g^{22} = 1; & g_{12} = g^{12} = g_{21} = g^{21} = 0 \end{array}\right\} \tag{C.7}$$

The leading coefficients β_i, γ_i and δ_i appearing in equations C.9 through C.18 are used to differentiate between the dimensional and the non-dimensional equations and are defined as:

dimensional equations			non-dimensional equations		
$\beta_1 = 1$	$\gamma_1 = 1$	$\delta_1 = 1$	$\beta_1 = \dfrac{\mathbb{R}_o{}^2}{\mathbb{F}_r{}^2}$	$\gamma_1 = \mathbb{R}_o$	$\delta_1 = \mathbb{R}_o$
$\beta_2 = 1$	$\gamma_2 = f$	$\delta_2 = 1$	$\beta_2 = \mathbb{R}_o$	$\gamma_2 = 1$	$\delta_2 = \dfrac{\mathbb{E}_{kh}}{\mathbb{S}_{ch}}$
	$\gamma_3 = \dfrac{1}{\rho_o}$	$\delta_3 = 1$		$\gamma_3 = 1$	$\delta_3 = \dfrac{\mathbb{E}_{kv}}{\mathbb{S}_{cv}}$
	$\gamma_4 = g$			$\gamma_4 = 1$	
	$\gamma_5 = \dfrac{g}{\rho_o}$			$\gamma_5 = \dfrac{\mathbb{R}_o{}^2}{\mathbb{F}_{rd2}}$	
	$\gamma_6 = 1$			$\gamma_6 = \mathbb{E}_{kh}$	
	$\gamma_7 = 1$			$\gamma_7 = \mathbb{E}_{kv}$	
	$\gamma_8 = \dfrac{1}{\rho_o}$			$\gamma_8 = 1$	
	$\gamma_9 = 1$			$\gamma_9 = \dfrac{\mathbb{F}_r{}^2}{\mathbb{R}_o{}^2}$	

Table C.1 Definition of the leading coefficients in the non-dimensional equations of motion.

Continuity (curvilinear-z coordinates)**:**

$$\frac{1}{\mathcal{J}}\left[\frac{\partial(\mathcal{J}\check{u})}{\partial\xi}+\frac{\partial(\mathcal{J}\check{v})}{\partial\eta}\right]+\frac{\partial(w-\check{w}_{st})}{\partial z}=0 \tag{C.8}$$

Continuity (curvilinear-σ coordinates)**:**

$$\left.\begin{aligned}\frac{\partial\zeta}{\partial t}+\beta_1\left\{\frac{1}{\mathcal{J}}\left[\frac{\partial(\mathcal{J}D\check{u})}{\partial\xi}+\frac{\partial(\mathcal{J}D\check{v})}{\partial\eta}\right]+\frac{\partial(D\overset{\star}{\Omega})}{\partial\sigma}\right\}=0\\ \\ \frac{\partial D}{\partial t}+\beta_2\left\{\frac{1}{\mathcal{J}}\left[\frac{\partial(\mathcal{J}D\check{u})}{\partial\xi}+\frac{\partial(\mathcal{J}D\check{v})}{\partial\eta}\right]+\frac{\partial(D\overset{\star}{\Omega})}{\partial\sigma}\right\}=0\end{aligned}\right\} \tag{C.9}$$

Vertically integrated continuity:

$$\left.\begin{aligned}\frac{\partial\zeta}{\partial t}+\beta_1\frac{1}{\mathcal{J}}\left[\frac{\partial(\mathcal{J}D\check{U})}{\partial\xi}+\frac{\partial(\mathcal{J}D\check{V})}{\partial\eta}\right]=0\\ \\ \frac{\partial D}{\partial t}+\beta_2\frac{1}{\mathcal{J}}\left[\frac{\partial(\mathcal{J}D\check{U})}{\partial\xi}+\frac{\partial(\mathcal{J}D\check{V})}{\partial\eta}\right]=0\end{aligned}\right\} \tag{C.10}$$

X-momentum (curvilinear-z coordinates)**:**

$$\frac{\partial \breve{u}}{\partial t}+\gamma_1\left\{\frac{y_\eta}{\mathcal{J}^2}\Big[\frac{\partial(\mathcal{J}\breve{u}\breve{u}_{(\xi)})}{\partial\xi}+\frac{\partial(\mathcal{J}\breve{v}\breve{u}_{(\xi)})}{\partial\eta}\Big]-\frac{x_\eta}{\mathcal{J}^2}\Big[\frac{\partial(\mathcal{J}\breve{u}\breve{u}_{(\eta)})}{\partial\xi}+\frac{\partial(\mathcal{J}\breve{v}\breve{u}_{(\eta)})}{\partial\eta}\Big]+\frac{\partial[(w-\breve{w}_{\rm st})\breve{u}]}{\partial z}\right\}=$$

$$\underbrace{+\frac{\gamma_2}{\mathcal{J}}\left(g_{12}\breve{u}+g_{22}\breve{v}\right)}_{\text{Coriolis terms}}\underbrace{-\frac{\gamma_3}{\mathcal{J}^2}\Big(g_{22}\frac{\partial p_{\rm atm}}{\partial\xi}-g_{12}\frac{\partial p_{\rm atm}}{\partial\eta}\Big)-\frac{\gamma_4}{\mathcal{J}^2}\Big(g_{22}\frac{\partial\zeta}{\partial\xi}-g_{12}\frac{\partial\zeta}{\partial\eta}\Big)}_{\text{Barotropic terms}}$$

$$\underbrace{-\frac{\gamma_5}{\mathcal{J}^2}\int_z^\zeta\Big(g_{22}\frac{\partial\rho}{\partial\xi}-g_{12}\frac{\partial\rho}{\partial\eta}\Big)dz'}_{\text{Baroclinic terms}}$$

$$+\gamma_6\frac{y_\eta}{\mathcal{J}^2}\left\{\left[\frac{\mathcal{A}_{\rm h}}{\mathcal{J}}\left(g_{22}[\breve{u}_{(\xi)}]_\xi-g_{12}[\breve{u}_{(\xi)}]_\eta\right)\right]_\xi+\left[\frac{\mathcal{A}_{\rm h}}{\mathcal{J}}\left(g_{11}[\breve{u}_{(\xi)}]_\eta-g_{12}[\breve{u}_{(\xi)}]_\xi\right)\right]_\eta\right\}$$

$$\underbrace{-\gamma_6\frac{x_\eta}{\mathcal{J}^2}\left\{\left[\frac{\mathcal{A}_{\rm h}}{\mathcal{J}}\left(g_{22}[\breve{u}_{(\eta)}]_\xi-g_{12}[\breve{u}_{(\eta)}]_\eta\right)\right]_\xi+\left[\frac{\mathcal{A}_{\rm h}}{\mathcal{J}}\left(g_{11}[\breve{u}_{(\eta)}]_\eta-g_{12}[\breve{u}_{(\eta)}]_\xi\right)\right]_\eta\right\}}_{\text{Horizontal diffusion terms}}$$

$$\underbrace{+\gamma_7\frac{\partial}{\partial z}\Big[\mathcal{A}_{\rm v}\frac{\partial\breve{u}}{\partial z}\Big]}_{\text{Vertical diffusion terms}}+\underbrace{\frac{\gamma_2}{\mathcal{J}}\left(g_{12}\breve{u}_{\rm st}+g_{22}\breve{v}_{\rm st}\right)}_{\text{(W) Stokes-Coriolis terms}}+\underbrace{\frac{\gamma_1}{\mathcal{J}^2}\frac{\mathring{\sigma}\,|\mathbf{u}_{\rm st}|}{\sinh 2kD}\Big(g_{22}\frac{\partial D}{\partial\xi}-g_{12}\frac{\partial D}{\partial\eta}\Big)}_{\text{(W) Stokes terms}}$$

$$\underbrace{+\gamma_1\left\{\frac{g_{12}\breve{u}_{\rm st}+g_{22}\breve{v}_{\rm st}}{\mathcal{J}^2}\Big[[g_{12}\breve{u}+g_{22}\breve{v}]_\xi-[g_{11}\breve{u}+g_{21}\breve{v}]_\eta\Big]-\breve{w}_{\rm st}\frac{\partial\breve{u}}{\partial z}\right\}}_{\text{(W) Stokes vorticity terms}}$$

$$\underbrace{-\gamma_1\frac{\breve{u}_{{\rm st}(\xi)}}{\mathcal{J}^2}\left\{g_{22}\left[(\breve{u}-\breve{\tilde{u}}_A)_{(\xi)}\right]_\xi-g_{12}\left[(\breve{u}-\breve{\tilde{u}}_A)_{(\xi)}\right]_\eta\right\}-\gamma_1\frac{\breve{u}_{{\rm st}(\eta)}}{\mathcal{J}^2}\left\{g_{22}\left[(\breve{u}-\breve{\tilde{u}}_A)_{(\eta)}\right]_\xi-g_{12}\left[(\breve{u}-\breve{\tilde{u}}_A)_{(\eta)}\right]_\eta\right\}}_{\text{(W) Stokes terms}}$$

$$-\frac{\gamma_9}{D}\frac{y_\eta}{\mathcal{J}^2}\left\{\left[\mathcal{J}(x_\xi \check{S}_{(\xi\xi)} + x_\eta \check{S}_{(\xi\eta)})\right]_\xi + \left[\mathcal{J}(x_\xi \check{S}_{(\xi\eta)} + x_\eta \check{S}_{(\eta\eta)})\right]_\eta\right\}$$

$$+\frac{\gamma_9}{D}\frac{x_\eta}{\mathcal{J}^2}\left\{\left[\mathcal{J}(y_\xi \check{S}_{(\xi\xi)} + y_\eta \check{S}_{(\xi\eta)})\right]_\xi + \left[\mathcal{J}(y_\xi \check{S}_{(\xi\eta)} + y_\eta \check{S}_{(\eta\eta)})\right]_\eta\right\}$$

$$\underbrace{-\frac{\gamma_9^2}{D}\left\{\lambda_{(\xi)}\frac{\partial \check{S}_{(\xi\xi)}}{\partial z} + \lambda_{(\eta)}\frac{\partial \check{S}_{(\xi\eta)}}{\partial z}\right\}}_{\text{(W) Radiation stress terms}} \tag{C.11}$$

Y-momentum (curvilinear-z coordinates)**:**

$$\frac{\partial \check{v}}{\partial t} + \gamma_1\left\{\frac{x_\xi}{\mathcal{J}^2}\left[\frac{\partial(\mathcal{J}\check{u}\check{u}_{(\eta)})}{\partial \xi} + \frac{\partial(\mathcal{J}\check{v}\check{u}_{(\eta)})}{\partial \eta}\right] - \frac{y_\xi}{\mathcal{J}^2}\left[\frac{\partial(\mathcal{J}\check{u}\check{u}_{(\xi)})}{\partial \xi} + \frac{\partial(\mathcal{J}\check{v}\check{u}_{(\xi)})}{\partial \eta}\right] + \frac{\partial[(w - \check{w}_{\text{st}})\check{v}]}{\partial z}\right\} =$$

$$\underbrace{-\frac{\gamma_2}{\mathcal{J}}(g_{11}\check{u} + g_{21}\check{v})}_{\text{Coriolis terms}} + \underbrace{\frac{\gamma_3}{\mathcal{J}^2}\left(g_{21}\frac{\partial p_{\text{atm}}}{\partial \xi} - g_{11}\frac{\partial p_{\text{atm}}}{\partial \eta}\right) + \frac{\gamma_4}{\mathcal{J}^2}\left(g_{21}\frac{\partial \zeta}{\partial \xi} - g_{11}\frac{\partial \zeta}{\partial \eta}\right)}_{\text{Barotropic terms}}$$

$$\underbrace{+\frac{\gamma_5}{\mathcal{J}^2}\int_z^\zeta\left(g_{21}\frac{\partial \rho}{\partial \xi} - g_{11}\frac{\partial \rho}{\partial \eta}\right)dz'}_{\text{Baroclinic terms}}$$

$$+\gamma_6\frac{x_\xi}{\mathcal{J}^2}\left\{\left[\frac{\mathcal{A}_{\text{h}}}{\mathcal{J}}\left(g_{22}[\check{u}_{(\eta)}]_\xi - g_{21}[\check{u}_{(\eta)}]_\eta\right)\right]_\xi + \left[\frac{\mathcal{A}_{\text{h}}}{\mathcal{J}}\left(g_{11}[\check{u}_{(\eta)}]_\eta - g_{21}[\check{u}_{(\eta)}]_\xi\right)\right]_\eta\right\}$$

$$\underbrace{-\gamma_6\frac{y_\xi}{\mathcal{J}^2}\left\{\left[\frac{\mathcal{A}_{\text{h}}}{\mathcal{J}}\left(g_{22}[\check{u}_{(\xi)}]_\xi - g_{21}[\check{u}_{(\xi)}]_\eta\right)\right]_\xi + \left[\frac{\mathcal{A}_{\text{h}}}{\mathcal{J}}\left(g_{11}[\check{u}_{(\xi)}]_\eta - g_{21}[\check{u}_{(\xi)}]_\xi\right)\right]_\eta\right\}}_{\text{Horizontal diffusion terms}}$$

$$+\underbrace{\gamma_7 \frac{\partial}{\partial z}\left[\mathcal{A}_v \frac{\partial \breve{v}}{\partial z}\right]}_{\text{Vertical diffusion terms}} - \underbrace{\frac{\gamma_2}{\mathcal{J}}\left(g_{11}\breve{u}_{st} + g_{21}\breve{v}_{st}\right)}_{\text{(W) Stokes-Coriolis terms}} - \underbrace{\frac{\gamma_1}{\mathcal{J}^2}\frac{\mathring{\sigma}\,|\mathbf{u_{st}}|}{\sinh 2kD}\left(g_{21}\frac{\partial D}{\partial \xi} - g_{11}\frac{\partial D}{\partial \eta}\right)}_{\text{(W) Stokes terms}}$$

$$\underbrace{-\gamma_1\left\{\frac{g_{11}\breve{u}_{st} + g_{21}\breve{v}_{st}}{\mathcal{J}^2}\left[\left[g_{12}\breve{u} + g_{22}\breve{v}\right]_\xi - \left[g_{11}\breve{u} + g_{21}\breve{v}\right]_\eta\right] - \breve{w}_{st}\frac{\partial \breve{v}}{\partial z}\right\}}_{\text{(W) Stokes vorticity terms}}$$

$$\underbrace{+\gamma_1\frac{\breve{u}_{st(\xi)}}{\mathcal{J}^2}\left\{g_{21}\left[(\breve{u} - \breve{\tilde{u}}_A)_{(\xi)}\right]_\xi - g_{11}\left[(\breve{u} - \breve{\tilde{u}}_A)_{(\xi)}\right]_\eta\right\} + \gamma_1\frac{\breve{u}_{st(\eta)}}{\mathcal{J}^2}\left\{g_{21}\left[(\breve{u} - \breve{\tilde{u}}_A)_{(\eta)}\right]_\xi - g_{11}\left[(\breve{u} - \breve{\tilde{u}}_A)_{(\eta)}\right]_\eta\right\}}_{\text{(W) Stokes terms}}$$

$$+\frac{\gamma_9}{D}\frac{y_\xi}{\mathcal{J}^2}\left\{\left[\mathcal{J}(x_\xi \breve{S}_{(\xi\xi)} + x_\eta \breve{S}_{(\xi\eta)})\right]_\xi + \left[\mathcal{J}(x_\xi \breve{S}_{(\xi\eta)} + x_\eta \breve{S}_{(\eta\eta)})\right]_\eta\right\}$$

$$-\frac{\gamma_9}{D}\frac{x_\xi}{\mathcal{J}^2}\left\{\left[\mathcal{J}(y_\xi \breve{S}_{(\xi\xi)} + y_\eta \breve{S}_{(\xi\eta)})\right]_\xi + \left[\mathcal{J}(y_\xi \breve{S}_{(\xi\eta)} + y_\eta \breve{S}_{(\eta\eta)})\right]_\eta\right\}$$

$$\underbrace{-\frac{\gamma_9^2}{D}\left\{\lambda_{(\xi)}\frac{\partial \breve{S}_{(\xi\eta)}}{\partial z} + \lambda_{(\eta)}\frac{\partial \breve{S}_{(\eta\eta)}}{\partial z}\right\}}_{\text{(W) Radiation stress terms}} \tag{C.12}$$

X-momentum (curvilinear-σ coordinates)**:**

$$\frac{\partial(D\breve{u})}{\partial t}+\gamma_1\left\{\frac{y_\eta}{\mathcal{J}^2}\Big[\frac{\partial(\mathcal{J}D\breve{u}\breve{u}_{(\xi)})}{\partial\xi}+\frac{\partial(\mathcal{J}D\breve{v}\breve{u}_{(\xi)})}{\partial\eta}\Big]-\frac{x_\eta}{\mathcal{J}^2}\Big[\frac{\partial(\mathcal{J}D\breve{u}\breve{u}_{(\eta)})}{\partial\xi}+\frac{\partial(\mathcal{J}D\breve{v}\breve{u}_{(\eta)})}{\partial\eta}\Big]+\frac{\partial(D\overset{\star}{\Omega}\breve{u})}{\partial\sigma}\right\}=$$

$$\underbrace{+\gamma_2\frac{D}{\mathcal{J}}\left(g_{12}\breve{u}+g_{22}\breve{v}\right)}_{\text{Coriolis terms}}\underbrace{-\gamma_3\frac{D}{\mathcal{J}^2}\Big(g_{22}\frac{\partial p_{\text{atm}}}{\partial\xi}-g_{12}\frac{\partial p_{\text{atm}}}{\partial\eta}\Big)-\gamma_4\frac{D}{\mathcal{J}^2}\Big(g_{22}\frac{\partial\zeta}{\partial\xi}-g_{12}\frac{\partial\zeta}{\partial\eta}\Big)}_{\text{Barotropic terms}}$$

$$\underbrace{-\gamma_5\frac{D}{\mathcal{J}^2}\left\{D\int_\sigma^0\Big(g_{22}\frac{\partial\rho}{\partial\xi}-g_{12}\frac{\partial\rho}{\partial\eta}\Big)d\sigma'+\Big(g_{22}\frac{\partial D}{\partial\xi}-g_{12}\frac{\partial D}{\partial\eta}\Big)\Big(\int_\sigma^0\rho\,d\sigma'+\sigma\rho\Big)\right\}}_{\text{Baroclinic terms}}$$

$$+\gamma_6\frac{y_\eta}{\mathcal{J}^2}\left\{\left[\frac{\mathcal{A}_{\text{h}}}{\mathcal{J}}\left(g_{22}[D\breve{u}_{(\xi)}]_\xi-g_{12}[D\breve{u}_{(\xi)}]_\eta\right)\right]_\xi+\left[\frac{\mathcal{A}_{\text{h}}}{\mathcal{J}}\left(g_{11}[D\breve{u}_{(\xi)}]_\eta-g_{12}[D\breve{u}_{(\xi)}]_\xi\right)\right]_\eta\right\}$$

$$\underbrace{-\gamma_6\frac{x_\eta}{\mathcal{J}^2}\left\{\left[\frac{\mathcal{A}_{\text{h}}}{\mathcal{J}}\left(g_{22}[D\breve{u}_{(\eta)}]_\xi-g_{12}[D\breve{u}_{(\eta)}]_\eta\right)\right]_\xi+\left[\frac{\mathcal{A}_{\text{h}}}{\mathcal{J}}\left(g_{11}[D\breve{u}_{(\eta)}]_\eta-g_{12}[D\breve{u}_{(\eta)}]_\xi\right)\right]_\eta\right\}}_{\text{Horizontal diffusion terms}}$$

$$\underbrace{+\gamma_7\frac{1}{D^2}\frac{\partial}{\partial\sigma}\Big[\mathcal{A}_{\text{v}}\frac{\partial(D\breve{u})}{\partial\sigma}\Big]}_{\text{Vertical diffusion terms}}+\underbrace{\gamma_2\frac{D}{\mathcal{J}}\left(g_{12}\breve{u}_{\text{st}}+g_{22}\breve{v}_{\text{st}}\right)}_{\text{(W) Stokes-Coriolis terms}}+\underbrace{\gamma_1\frac{1}{\mathcal{J}^2}\frac{\mathring{\sigma}\,D\,|\mathbf{u_{st}}|}{\sinh 2kD}\Big(g_{22}\frac{\partial D}{\partial\xi}-g_{12}\frac{\partial D}{\partial\eta}\Big)}_{\text{(W) Stokes terms}}$$

$$\underbrace{+\gamma_1\left\{\frac{g_{12}\breve{u}_{\text{st}}+g_{22}\breve{v}_{\text{st}}}{\mathcal{J}^2}\left[\,[D(g_{12}\breve{u}+g_{22}\breve{v})]_\xi-[D(g_{11}\breve{u}+g_{21}\breve{v})]_\eta\right.\right.}$$

$$\left.\left.-\frac{\partial}{\partial\sigma}\Big[(g_{21}\lambda_{(\xi)}-g_{11}\lambda_{(\eta)})\breve{u}+(g_{22}\lambda_{(\xi)}-g_{12}\lambda_{(\eta)})\breve{v}\Big]\right]-\breve{w}_{\text{st}}\frac{\partial\breve{u}}{\partial\sigma}\right\}$$

$$\text{(W) Stokes vorticity terms}$$

$$-\gamma_1 \frac{\breve{u}_{st(\xi)}}{\mathcal{J}^2}\left\{g_{22}\left[D(\breve{u}-\breve{\tilde{u}}_A)_{(\xi)}\right]_\xi - g_{12}\left[D(\breve{u}-\breve{\tilde{u}}_A)_{(\xi)}\right]_\eta - g_{22}\frac{\partial[\lambda_{(\xi)}(\breve{u}-\breve{\tilde{u}}_A)_{(\xi)}]}{\partial\sigma}\right.$$

$$\left.+g_{12}\frac{\partial[\lambda_{(\eta)}(\breve{u}-\breve{\tilde{u}}_A)_{(\xi)}]}{\partial\sigma}\right\}$$

$$\underbrace{-\gamma_1 \frac{\breve{u}_{st(\eta)}}{\mathcal{J}^2}\left\{g_{22}\left[D(\breve{u}-\breve{\tilde{u}}_A)_{(\eta)}\right]_\xi - g_{12}\left[D(\breve{u}-\breve{\tilde{u}}_A)_{(\eta)}\right]_\eta - g_{22}\frac{\partial[\lambda_{(\xi)}(\breve{u}-\breve{\tilde{u}}_A)_{(\eta)}]}{\partial\sigma}\right.}$$

$$\underbrace{\left.+g_{12}\frac{\partial[\lambda_{(\eta)}(\breve{u}-\breve{\tilde{u}}_A)_{(\eta)}]}{\partial\sigma}\right\}}$$

(W) Stokes terms

$$-\gamma_9 \frac{y_\eta}{\mathcal{J}^2}\left\{\left[\mathcal{J}(x_\xi \breve{S}_{(\xi\xi)} + x_\eta \breve{S}_{(\xi\eta)})\right]_\xi + \left[\mathcal{J}(x_\xi \breve{S}_{(\xi\eta)} + x_\eta \breve{S}_{(\eta\eta)})\right]_\eta\right\}$$

$$\underbrace{+\gamma_9 \frac{x_\eta}{\mathcal{J}^2}\left\{\left[\mathcal{J}(y_\xi \breve{S}_{(\xi\xi)} + y_\eta \breve{S}_{(\xi\eta)})\right]_\xi + \left[\mathcal{J}(y_\xi \breve{S}_{(\xi\eta)} + y_\eta \breve{S}_{(\eta\eta)})\right]_\eta\right\}} \tag{C.13}$$

(W) Radiation stress terms

Y-momentum (curvilinear-σ coordinates)**:**

$$\frac{\partial(D\breve{v})}{\partial t}+\gamma_1\left\{\frac{x_\xi}{\mathcal{J}^2}\Big[\frac{\partial(\mathcal{J}D\breve{u}\breve{u}_{(\eta)})}{\partial\xi}+\frac{\partial(\mathcal{J}D\breve{v}\breve{u}_{(\eta)})}{\partial\eta}\Big]-\frac{y_\xi}{\mathcal{J}^2}\Big[\frac{\partial(\mathcal{J}D\breve{u}\breve{u}_{(\xi)})}{\partial\xi}+\frac{\partial(\mathcal{J}D\breve{v}\breve{u}_{(\xi)})}{\partial\eta}\Big]+\frac{\partial(D\overset{\star}{\Omega}\breve{v})}{\partial\sigma}\right\}=$$

$$\underbrace{-\gamma_2\frac{D}{\mathcal{J}}\left(g_{11}\breve{u}+g_{21}\breve{v}\right)}_{\text{Coriolis terms}}+\underbrace{\gamma_3\frac{D}{\mathcal{J}^2}\Big(g_{21}\frac{\partial p_{\text{atm}}}{\partial\xi}-g_{11}\frac{\partial p_{\text{atm}}}{\partial\eta}\Big)+\gamma_4\frac{D}{\mathcal{J}^2}\Big(g_{21}\frac{\partial\zeta}{\partial\xi}-g_{11}\frac{\partial\zeta}{\partial\eta}\Big)}_{\text{Barotropic terms}}$$

$$\underbrace{+\gamma_5\frac{D}{\mathcal{J}^2}\left\{D\int_\sigma^0\Big(g_{21}\frac{\partial\rho}{\partial\xi}-g_{11}\frac{\partial\rho}{\partial\eta}\Big)d\sigma'+\Big(g_{21}\frac{\partial D}{\partial\xi}-g_{11}\frac{\partial D}{\partial\eta}\Big)\Big(\int_\sigma^0\rho\,d\sigma'+\sigma\rho\Big)\right\}}_{\text{Baroclinic terms}}$$

$$+\gamma_6\frac{x_\xi}{\mathcal{J}^2}\left\{\left[\frac{\mathcal{A}_{\text{h}}}{\mathcal{J}}\left(g_{22}[D\breve{u}_{(\eta)}]_\xi-g_{21}[D\breve{u}_{(\eta)}]_\eta\right)\right]_\xi+\left[\frac{\mathcal{A}_{\text{h}}}{\mathcal{J}}\left(g_{11}[D\breve{u}_{(\eta)}]_\eta-g_{21}[D\breve{u}_{(\eta)}]_\xi\right)\right]_\eta\right\}$$

$$\underbrace{-\gamma_6\frac{y_\xi}{\mathcal{J}^2}\left\{\left[\frac{\mathcal{A}_{\text{h}}}{\mathcal{J}}\left(g_{22}[D\breve{u}_{(\xi)}]_\xi-g_{21}[D\breve{u}_{(\xi)}]_\eta\right)\right]_\xi+\left[\frac{\mathcal{A}_{\text{h}}}{\mathcal{J}}\left(g_{11}[D\breve{u}_{(\xi)}]_\eta-g_{21}[D\breve{u}_{(\xi)}]_\xi\right)\right]_\eta\right\}}_{\text{Horizontal diffusion terms}}$$

$$\underbrace{+\gamma_7\frac{1}{D^2}\frac{\partial}{\partial\sigma}\Big[\mathcal{A}_{\text{v}}\frac{\partial(D\breve{v})}{\partial\sigma}\Big]}_{\text{Vertical diffusion terms}}\underbrace{-\gamma_2\frac{D}{\mathcal{J}}\left(g_{11}\breve{u}_{\text{st}}+g_{21}\breve{v}_{\text{st}}\right)}_{\text{(W) Stokes-Coriolis terms}}\underbrace{-\gamma_1\frac{1}{\mathcal{J}^2}\frac{\mathring{\sigma}\,D\,|\mathbf{u_{st}}|}{\sinh 2kD}\Big(g_{21}\frac{\partial D}{\partial\xi}-g_{11}\frac{\partial D}{\partial\eta}\Big)}_{\text{(W) Stokes terms}}$$

$$\underbrace{-\gamma_1\left\{\frac{g_{11}\breve{u}_{\text{st}}+g_{21}\breve{v}_{\text{st}}}{\mathcal{J}^2}\Big[\,[D(g_{12}\breve{u}+g_{22}\breve{v})]_\xi-[D(g_{11}\breve{u}+g_{21}\breve{v})]_\eta\right.}$$

$$\underbrace{\left.-\frac{\partial}{\partial\sigma}\Big[(g_{21}\lambda_{(\xi)}-g_{11}\lambda_{(\eta)})\breve{u}+(g_{22}\lambda_{(\xi)}-g_{12}\lambda_{(\eta)})\breve{v}\Big]\Big]-\breve{w}_{\text{st}}\frac{\partial\breve{v}}{\partial\sigma}\right\}}_{\text{(W) Stokes vorticity terms}}$$

$$+\gamma_1 \frac{\breve{u}_{st(\xi)}}{\mathcal{J}^2}\left\{ g_{21}\left[D(\breve{u}-\breve{\tilde{u}}_A)_{(\xi)}\right]_\xi - g_{11}\left[D(\breve{u}-\breve{\tilde{u}}_A)_{(\xi)}\right]_\eta - g_{21}\frac{\partial[\lambda_{(\xi)}(\breve{u}-\breve{\tilde{u}}_A)_{(\xi)}]}{\partial\sigma} \right.$$

$$\left. +g_{11}\frac{\partial[\lambda_{(\eta)}(\breve{u}-\breve{\tilde{u}}_A)_{(\xi)}]}{\partial\sigma} \right\}$$

$$\underbrace{+\gamma_1 \frac{\breve{u}_{st(\eta)}}{\mathcal{J}^2}\left\{ g_{21}\left[D(\breve{u}-\breve{\tilde{u}}_A)_{(\eta)}\right]_\xi - g_{11}\left[D(\breve{u}-\breve{\tilde{u}}_A)_{(\eta)}\right]_\eta - g_{21}\frac{\partial[\lambda_{(\xi)}(\breve{u}-\breve{\tilde{u}}_A)_{(\eta)}]}{\partial\sigma} \right.}$$

$$\underbrace{\left. +g_{11}\frac{\partial[\lambda_{(\eta)}(\breve{u}-\breve{\tilde{u}}_A)_{(\eta)}]}{\partial\sigma} \right\}}$$

(W) Stokes terms

$$+\gamma_9 \frac{y_\xi}{\mathcal{J}^2}\left\{ \left[\mathcal{J}(x_\xi \breve{S}_{(\xi\xi)} + x_\eta \breve{S}_{(\xi\eta)})\right]_\xi + \left[\mathcal{J}(x_\xi \breve{S}_{(\xi\eta)} + x_\eta \breve{S}_{(\eta\eta)})\right]_\eta \right\}$$

$$\underbrace{-\gamma_9 \frac{x_\xi}{\mathcal{J}^2}\left\{ \left[\mathcal{J}(y_\xi \breve{S}_{(\xi\xi)} + y_\eta \breve{S}_{(\xi\eta)})\right]_\xi + \left[\mathcal{J}(y_\xi \breve{S}_{(\xi\eta)} + y_\eta \breve{S}_{(\eta\eta)})\right]_\eta \right\}} \tag{C.14}$$

(W) Radiation stress terms

Vertically integrated x-momentum:

$$\frac{\partial(D\breve{U})}{\partial t}+\gamma_1\left\{\frac{y_\eta}{\mathcal{J}^2}\left[\frac{\partial(\mathcal{J}D\breve{U}\breve{U}_{(\xi)})}{\partial\xi}+\frac{\partial(\mathcal{J}D\breve{V}\breve{U}_{(\xi)})}{\partial\eta}\right]-\frac{x_\eta}{\mathcal{J}^2}\left[\frac{\partial(\mathcal{J}D\breve{U}\breve{U}_{(\eta)})}{\partial\xi}+\frac{\partial(\mathcal{J}D\breve{V}\breve{U}_{(\eta)}}{\partial\eta}\right]\right\}=$$

$$\underbrace{+\gamma_2\frac{D}{\mathcal{J}}\left(g_{12}\breve{U}+g_{22}\breve{V}\right)}_{\text{Coriolis terms}}\underbrace{-\gamma_3\frac{D}{\mathcal{J}^2}\left(g_{22}\frac{\partial p_{\text{atm}}}{\partial\xi}-g_{12}\frac{\partial p_{\text{atm}}}{\partial\eta}\right)-\gamma_4\frac{D}{\mathcal{J}^2}\left(g_{22}\frac{\partial\zeta}{\partial\xi}-g_{12}\frac{\partial\zeta}{\partial\eta}\right)}_{\text{Barotropic terms}}$$

$$\underbrace{-\gamma_5\frac{D^2}{2\mathcal{J}^2}\left(g_{22}\frac{\partial\rho}{\partial\xi}-g_{12}\frac{\partial\rho}{\partial\eta}\right)}_{\text{Baroclinic terms}}$$

$$+\gamma_6\frac{y_\eta}{\mathcal{J}^2}\left\{\left[\frac{\mathcal{A}_{\text{h}}}{\mathcal{J}}\left(g_{22}[D\breve{U}_{(\xi)}]_\xi-g_{12}[D\breve{U}_{(\xi)}]_\eta\right)\right]_\xi+\left[\frac{\mathcal{A}_{\text{h}}}{\mathcal{J}}\left(g_{11}[D\breve{U}_{(\xi)}]_\eta-g_{12}[D\breve{U}_{(\xi)}]_\xi\right)\right]_\eta\right\}$$

$$\underbrace{-\gamma_6\frac{x_\eta}{\mathcal{J}^2}\left\{\left[\frac{\mathcal{A}_{\text{h}}}{\mathcal{J}}\left(g_{22}[D\breve{U}_{(\eta)}]_\xi-g_{12}[D\breve{U}_{(\eta)}]_\eta\right)\right]_\xi+\left[\frac{\mathcal{A}_{\text{h}}}{\mathcal{J}}\left(g_{11}[D\breve{U}_{(\eta)}]_\eta-g_{12}[D\breve{U}_{(\eta)}]_\xi\right)\right]_\eta\right\}}_{\text{Horizontal diffusion terms}}$$

$$\underbrace{+\gamma_8\left(\breve{\tau}_{s(\xi)}-\breve{\tau}_{b(\xi)}\right)}_{\text{Shear stress terms}}\underbrace{+\gamma_2\frac{D}{\mathcal{J}}\left(g_{12}\breve{U}_{\text{st}}+g_{22}\breve{V}_{\text{st}}\right)}_{\text{(W) Stokes-Coriolis terms}}\underbrace{+\gamma_1\frac{1}{\mathcal{J}^2}\frac{\mathring{\sigma}\,D\,|\mathbf{U_{st}}|}{\sinh 2kD}\left(g_{22}\frac{\partial D}{\partial\xi}-g_{12}\frac{\partial D}{\partial\eta}\right)}_{\text{(W) Stokes terms}}$$

$$\underbrace{+\gamma_1\frac{D}{\mathcal{J}^2}(g_{12}\breve{U}_{\text{st}}+g_{22}\breve{V}_{\text{st}})\left\{[g_{12}\breve{\tilde{u}}_A+g_{22}\breve{\tilde{v}}_A]_\xi-[g_{11}\breve{\tilde{u}}_A+g_{21}\breve{\tilde{v}}_A]_\eta\right\}}_{\text{(W) Stokes vorticity terms}}$$

$$-\gamma_9\frac{y_\eta}{\mathcal{J}^2}\left\{\left[\mathcal{J}(x_\xi\breve{R}_{(\xi\xi)}+x_\eta\breve{R}_{(\xi\eta)})\right]_\xi+\left[\mathcal{J}(x_\xi\breve{R}_{(\xi\eta)}+x_\eta\breve{R}_{(\eta\eta)})\right]_\eta\right\}$$

$$\underbrace{+\gamma_9\frac{x_\eta}{\mathcal{J}^2}\left\{\left[\mathcal{J}(y_\xi\breve{R}_{(\xi\xi)}+y_\eta\breve{R}_{(\xi\eta)})\right]_\xi+\left[\mathcal{J}(y_\xi\breve{R}_{(\xi\eta)}+y_\eta\breve{R}_{(\eta\eta)})\right]_\eta\right\}}_{\text{(W) Radiation stress terms}} \tag{C.15}$$

Vertically integrated y-momentum:

$$\frac{\partial(D\breve{V})}{\partial t}+\gamma_1\left\{\frac{x_\xi}{\mathcal{J}^2}\left[\frac{\partial(\mathcal{J}D\breve{U}\breve{U}_{(\eta)})}{\partial\xi}+\frac{\partial(\mathcal{J}D\breve{V}\breve{U}_{(\eta)})}{\partial\eta}\right]-\frac{y_\xi}{\mathcal{J}^2}\left[\frac{\partial(\mathcal{J}D\breve{U}\breve{U}_{(\xi)})}{\partial\xi}+\frac{\partial(\mathcal{J}D\breve{V}\breve{U}_{(\xi)}}{\partial\eta}\right]\right\}=$$

$$\underbrace{-\gamma_2\frac{D}{\mathcal{J}}\left(g_{11}\breve{U}+g_{21}\breve{V}\right)}_{\text{Coriolis terms}}+\underbrace{\gamma_3\frac{D}{\mathcal{J}^2}\left(g_{21}\frac{\partial p_{\text{atm}}}{\partial\xi}-g_{11}\frac{\partial p_{\text{atm}}}{\partial\eta}\right)+\gamma_4\frac{D}{\mathcal{J}^2}\left(g_{21}\frac{\partial\zeta}{\partial\xi}-g_{11}\frac{\partial\zeta}{\partial\eta}\right)}_{\text{Barotropic terms}}$$

$$\underbrace{+\gamma_5\frac{D^2}{2\mathcal{J}^2}\left(g_{21}\frac{\partial\rho}{\partial\xi}-g_{11}\frac{\partial\rho}{\partial\eta}\right)}_{\text{Baroclinic terms}}$$

$$+\gamma_6\frac{x_\xi}{\mathcal{J}^2}\left\{\left[\frac{\mathcal{A}_{\text{h}}}{\mathcal{J}}\left(g_{22}[D\breve{U}_{(\eta)}]_\xi-g_{21}[D\breve{U}_{(\eta)}]_\eta\right)\right]_\xi+\left[\frac{\mathcal{A}_{\text{h}}}{\mathcal{J}}\left(g_{11}[D\breve{U}_{(\eta)}]_\eta-g_{21}[D\breve{U}_{(\eta)}]_\xi\right)\right]_\eta\right\}$$

$$\underbrace{-\gamma_6\frac{y_\xi}{\mathcal{J}^2}\left\{\left[\frac{\mathcal{A}_{\text{h}}}{\mathcal{J}}\left(g_{22}[D\breve{U}_{(\xi)}]_\xi-g_{21}[D\breve{U}_{(\xi)}]_\eta\right)\right]_\xi+\left[\frac{\mathcal{A}_{\text{h}}}{\mathcal{J}}\left(g_{11}[D\breve{U}_{(\xi)}]_\eta-g_{21}[D\breve{U}_{(\xi)}]_\xi\right)\right]_\eta\right\}}_{\text{Horizontal diffusion terms}}$$

$$\underbrace{+\gamma_8\left(\breve{\tau}_{s(\eta)}-\breve{\tau}_{b(\eta)}\right)}_{\text{Shear stress terms}}\underbrace{-\gamma_2\frac{D}{\mathcal{J}}\left(g_{11}\breve{U}_{\text{st}}+g_{21}\breve{V}_{\text{st}}\right)}_{\text{(W) Stokes-Coriolis terms}}\underbrace{-\gamma_1\frac{1}{\mathcal{J}^2}\frac{\mathring{\sigma}\,D\,|\mathbf{U_{st}}|}{\sinh 2kD}\left(g_{21}\frac{\partial D}{\partial\xi}-g_{11}\frac{\partial D}{\partial\eta}\right)}_{\text{(W) Stokes terms}}$$

$$\underbrace{-\gamma_1\frac{D}{\mathcal{J}^2}(g_{11}\breve{U}_{\text{st}}+g_{21}\breve{V}_{\text{st}})\left\{[g_{12}\breve{\tilde{u}}_A+g_{22}\breve{\tilde{v}}_A]_\xi-[g_{11}\breve{\tilde{u}}_A+g_{21}\breve{\tilde{v}}_A]_\eta\right\}}_{\text{(W) Stokes vorticity terms}}$$

$$+\gamma_9\frac{y_\xi}{\mathcal{J}^2}\left\{\left[\mathcal{J}(x_\xi\breve{R}_{(\xi\xi)}+x_\eta\breve{R}_{(\xi\eta)})\right]_\xi+\left[\mathcal{J}(x_\xi\breve{R}_{(\xi\eta)}+x_\eta\breve{R}_{(\eta\eta)})\right]_\eta\right\}$$

$$\underbrace{-\gamma_9\frac{x_\xi}{\mathcal{J}^2}\left\{\left[\mathcal{J}(y_\xi\breve{R}_{(\xi\xi)}+y_\eta\breve{R}_{(\xi\eta)})\right]_\xi+\left[\mathcal{J}(y_\xi\breve{R}_{(\xi\eta)}+y_\eta\breve{R}_{(\eta\eta)})\right]_\eta\right\}}_{\text{(W) Radiation stress terms}}\qquad\text{(C.16)}$$

Scalar (curvilinear-z coordinates)**:**

$$\frac{\partial \Phi}{\partial t}+\delta_1\left\{\frac{1}{\mathcal{J}}\Big[\frac{\partial(\mathcal{J}\check{u}\Phi)}{\partial \xi}+\frac{\partial(\mathcal{J}\check{v}\Phi)}{\partial \eta}\Big]+\frac{\partial[(w-\check{w}_{st})\Phi]}{\partial z}\right\}=$$

$$\underbrace{+\frac{\delta_2}{\mathcal{J}}\left\{\left[\frac{\mathcal{B}_h}{\mathcal{J}}\Big(g_{22}\frac{\partial \Phi}{\partial \xi}+g_{12}\frac{\partial \Phi}{\partial \eta}\Big)\right]_{\xi}+\left[\frac{\mathcal{B}_h}{\mathcal{J}}\Big(g_{11}\frac{\partial \Phi}{\partial \eta}+g_{12}\frac{\partial \Phi}{\partial \xi}\Big)\right]_{\eta}\right\}}_{\text{Horizontal diffusion terms}}$$

$$\underbrace{+\delta_3\frac{\partial}{\partial z}\Big[\mathcal{B}_v\frac{\partial \Phi}{\partial z}\Big]}_{\text{Vertical diffusion terms}}\underbrace{-\delta_1\left\{\check{u}_{st}\frac{\partial \Phi}{\partial \xi}+\check{v}_{st}\frac{\partial \Phi}{\partial \eta}+\check{w}_{st}\frac{\partial \Phi}{\partial z}\right\}}_{\text{Stokes driven advection terms}} \tag{C.17}$$

Scalar (curvilinear-σ coordinates)**:**

$$\frac{\partial(D\Phi)}{\partial t}+\delta_1\left\{\frac{1}{\mathcal{J}}\Big[\frac{\partial(\mathcal{J}D\check{u}\Phi)}{\partial \xi}+\frac{\partial(\mathcal{J}D\check{v}\Phi)}{\partial \eta}\Big]+\frac{\partial(D\overset{\star}{\Omega}\Phi)}{\partial \sigma}\right\}=$$

$$\underbrace{+\frac{\delta_2}{\mathcal{J}}\left\{\left[\mathcal{B}_h\frac{D}{\mathcal{J}}\Big(g_{22}\frac{\partial \Phi}{\partial \xi}+g_{12}\frac{\partial \Phi}{\partial \eta}\Big)\right]_{\xi}+\left[\mathcal{B}_h\frac{D}{\mathcal{J}}\Big(g_{11}\frac{\partial \Phi}{\partial \eta}+g_{12}\frac{\partial \Phi}{\partial \xi}\Big)\right]_{\eta}\right\}}_{\text{Horizontal diffusion terms}}$$

$$\underbrace{+\frac{\delta_3}{D}\frac{\partial}{\partial \sigma}\Big[\mathcal{B}_v\frac{\partial \Phi}{\partial \sigma}\Big]}_{\text{Vertical diffusion terms}}\underbrace{-\delta_1\left\{D\Big(\check{u}_{st}\frac{\partial \Phi}{\partial \xi}+\check{v}_{st}\frac{\partial \Phi}{\partial \eta}\Big)+\Big(\check{w}_{st}-\lambda_{(\xi)}\check{u}_{st}-\lambda_{(\eta)}\check{v}_{st}\Big)\frac{\partial \Phi}{\partial \sigma}\right\}}_{\text{Stokes driven advection terms}} \tag{C.18}$$

Turbulence model equations (curvilinear-z coordinates)**:**

$$\frac{\partial \boldsymbol{\kappa}}{\partial t} = \frac{\partial}{\partial z}\left[\frac{\mathcal{A}_{\mathrm{v}}}{\sigma_{\boldsymbol{\kappa}}}\frac{\partial \boldsymbol{\kappa}}{\partial z}\right] + (P + P_{wb}) + G - \boldsymbol{\epsilon} \tag{C.19a}$$

$$\frac{\partial \boldsymbol{\epsilon}}{\partial t} = \frac{\partial}{\partial z}\left[\frac{\mathcal{A}_{\mathrm{v}}}{\sigma_{\boldsymbol{\epsilon}}}\frac{\partial \boldsymbol{\epsilon}}{\partial z}\right] + c_{\epsilon 1}\Big[(P + P_{wb}) + c_{\epsilon 3}G\Big]\frac{\boldsymbol{\epsilon}}{\boldsymbol{\kappa}} - c_{\epsilon 2}\frac{\boldsymbol{\epsilon}^2}{\boldsymbol{\kappa}} \tag{C.19b}$$

$$P = \mathcal{A}_{\mathrm{v}}\, P_u\ ; \quad P_u = g_{11}\Big(\frac{\partial \breve{\mathrm{u}}}{\partial z}\cdot\frac{\partial \breve{u}}{\partial z}\Big) + g_{12}\Big(\frac{\partial \breve{\mathrm{u}}}{\partial z}\cdot\frac{\partial \breve{v}}{\partial z} + \frac{\partial \breve{v}}{\partial z}\cdot\frac{\partial \breve{u}}{\partial z}\Big) + g_{22}\Big(\frac{\partial \breve{v}}{\partial z}\cdot\frac{\partial \breve{v}}{\partial z}\Big) \tag{C.19c}$$

$$P_{wb} = 0\ ; \quad \mathcal{A}_{\mathrm{v}} = c_{\mu}\frac{\boldsymbol{\kappa}^2}{\boldsymbol{\epsilon}}\ ; \quad G = \frac{\mathcal{A}_{\mathrm{v}}}{\mathbb{P}_{\mathrm{rt}}}\frac{g}{\rho_{\mathrm{o}}}\frac{\partial \rho}{\partial z}\ ; \quad \mathbb{P}_{\mathrm{rt}} = 0.8 + 5\mathbb{R}_{\mathrm{i}}\ ; \quad \mathbb{R}_{\mathrm{i}} = -\frac{g}{\rho_{\mathrm{o}}}\cdot\frac{\dfrac{\partial \rho}{\partial z}}{P_u} \tag{C.19d}$$

Turbulence model equations (curvilinear-σ coordinates)**:**

$$\frac{\partial (D\boldsymbol{\kappa})}{\partial t} = \frac{1}{D}\frac{\partial}{\partial \sigma}\left[\frac{\mathcal{A}_{\mathrm{v}}}{\sigma_{\boldsymbol{\kappa}}}\frac{\partial \boldsymbol{\kappa}}{\partial \sigma}\right] + D\Big[(P + P_{wb}) + G - \boldsymbol{\epsilon}\Big] \tag{C.20a}$$

$$\frac{\partial (D\boldsymbol{\epsilon})}{\partial t} = \frac{1}{D}\frac{\partial}{\partial \sigma}\left[\frac{\mathcal{A}_{\mathrm{v}}}{\sigma_{\boldsymbol{\epsilon}}}\frac{\partial \boldsymbol{\epsilon}}{\partial \sigma}\right] + D\left\{c_{\epsilon 1}\Big[(P + P_{wb}) + c_{\epsilon 3}G\Big]\frac{\boldsymbol{\epsilon}}{\boldsymbol{\kappa}} - c_{\epsilon 2}\frac{\boldsymbol{\epsilon}^2}{\boldsymbol{\kappa}}\right\} \tag{C.20b}$$

$$P = \frac{\mathcal{A}_{\mathrm{v}}}{D^2}\, P_u\ ; \quad P_u = g_{11}\Big(\frac{\partial \breve{\mathrm{u}}}{\partial \sigma}\cdot\frac{\partial \breve{u}}{\partial \sigma}\Big) + g_{12}\Big(\frac{\partial \breve{\mathrm{u}}}{\partial \sigma}\cdot\frac{\partial \breve{v}}{\partial \sigma} + \frac{\partial \breve{v}}{\partial \sigma}\cdot\frac{\partial \breve{u}}{\partial \sigma}\Big) + g_{22}\Big(\frac{\partial \breve{v}}{\partial \sigma}\cdot\frac{\partial \breve{v}}{\partial \sigma}\Big) \tag{C.20c}$$

$$P_{wb} = 0\ ; \quad \mathcal{A}_{\mathrm{v}} = c_{\mu}\frac{\boldsymbol{\kappa}^2}{\boldsymbol{\epsilon}}\ ; \quad G = \frac{\mathcal{A}_{\mathrm{v}}}{D\,\mathbb{P}_{\mathrm{rt}}}\frac{g}{\rho_{\mathrm{o}}}\frac{\partial \rho}{\partial \sigma}\ ; \quad \mathbb{P}_{\mathrm{rt}} = 0.8 + 5\mathbb{R}_{\mathrm{i}}\ ; \quad \mathbb{R}_{\mathrm{i}} = -\frac{g}{\rho_{\mathrm{o}}}\cdot\frac{D\dfrac{\partial \rho}{\partial \sigma}}{P_u} \tag{C.20d}$$

where, the symbol $(\breve{\cdot})$ represents the contravariant velocities, (u, v) are the two horizontal components of the Eulerian velocity, and $(\mathcal{u}, \mathcal{v}) = (u + \mathrm{u_{st}}, v + \mathrm{v_{st}})$ are their Lagrangian counterparts.

APPENDIX D

SUMMARY OF THE LAKE MICHIGAN FIELD DATA

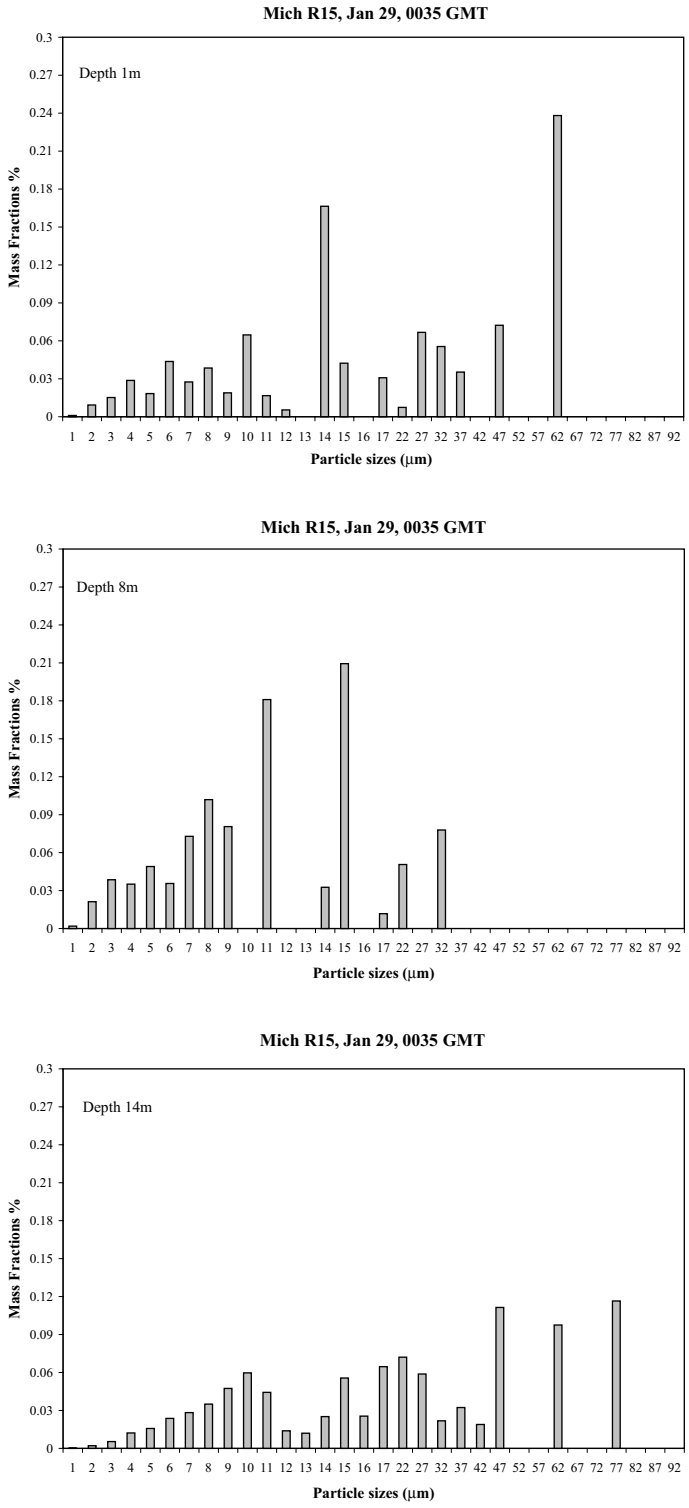

Figure D.1 Size distribution of the suspended solids at the Racine (R) transect (15 m contour depth).

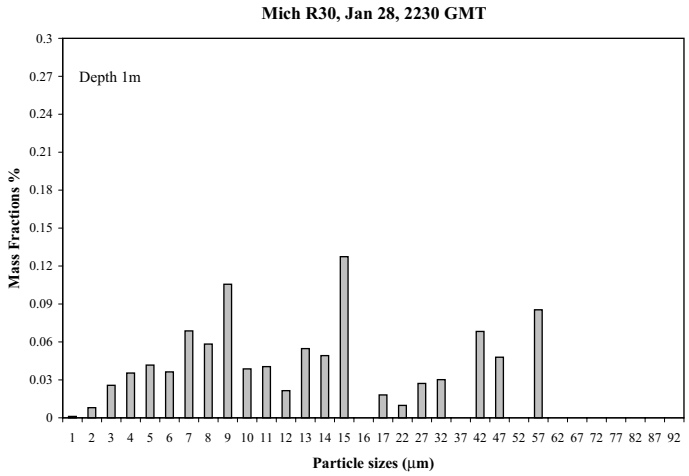

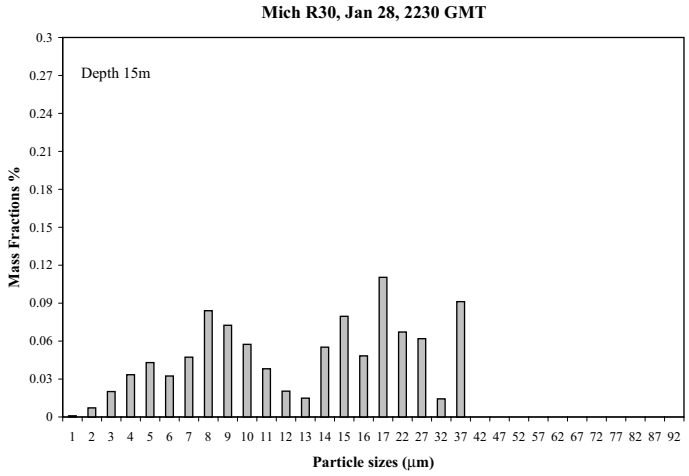

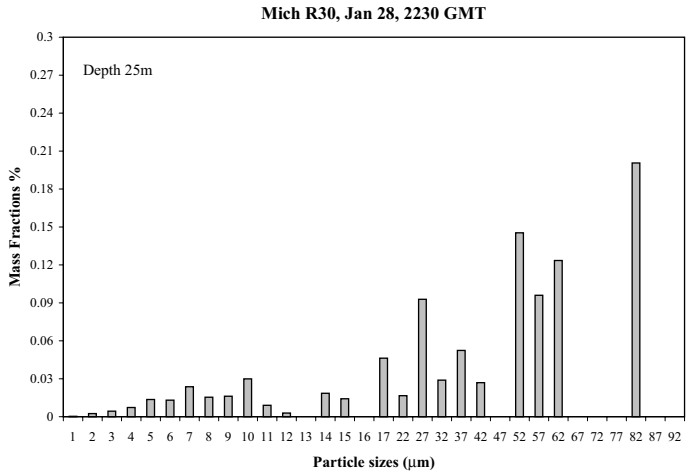

Figure D.2 Size distribution of the suspended solids at the Racine (R) transect (30 m contour depth). (Continued)

Figure D.2 Continued.

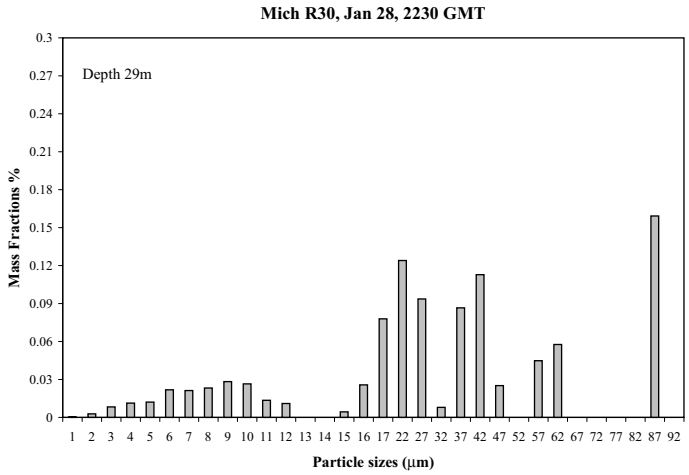

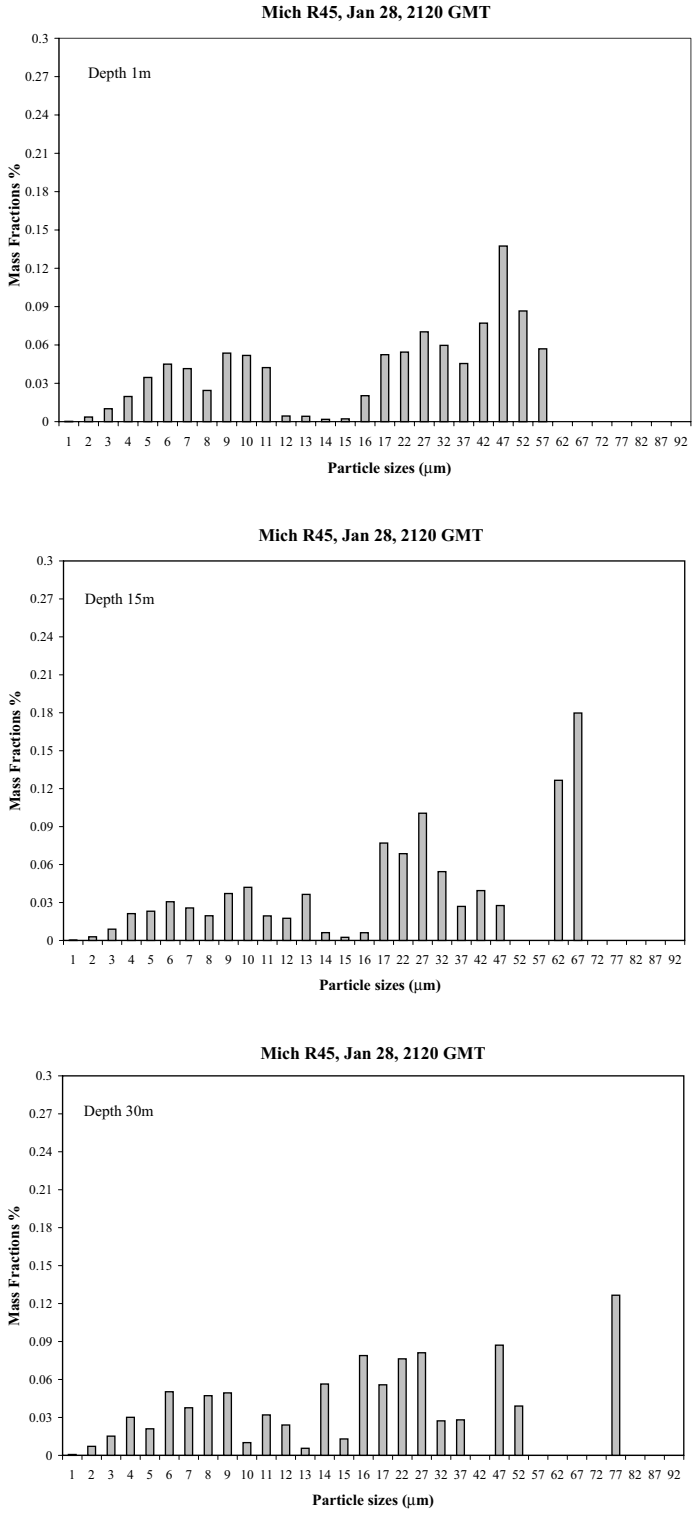

Figure D.3 Size distribution of the suspended solids at the Racine (R) transect (45 m contour depth). (Continued)

Figure D.3 Continued.

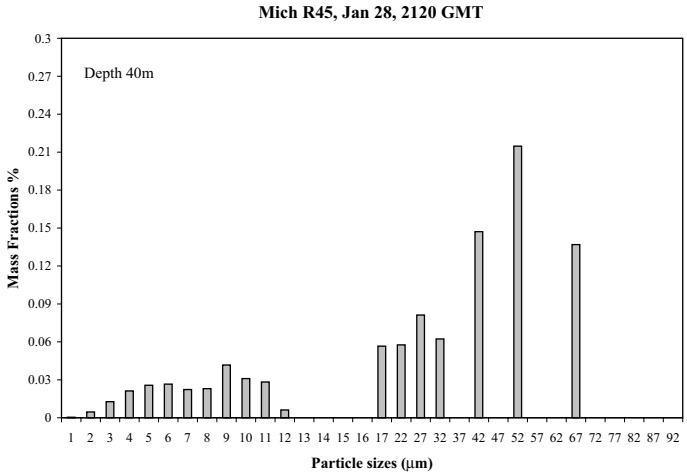

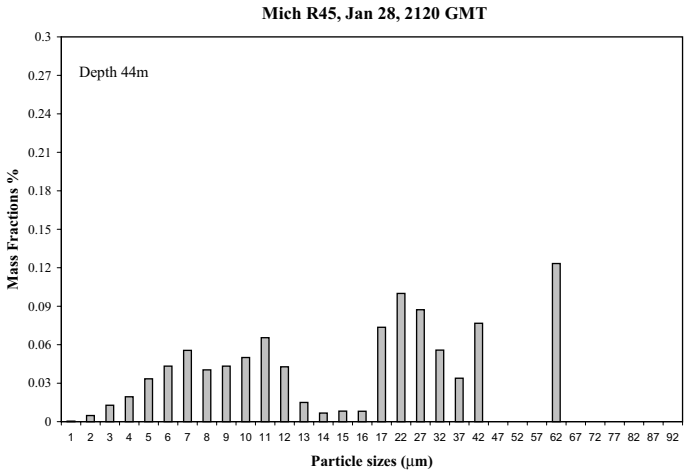

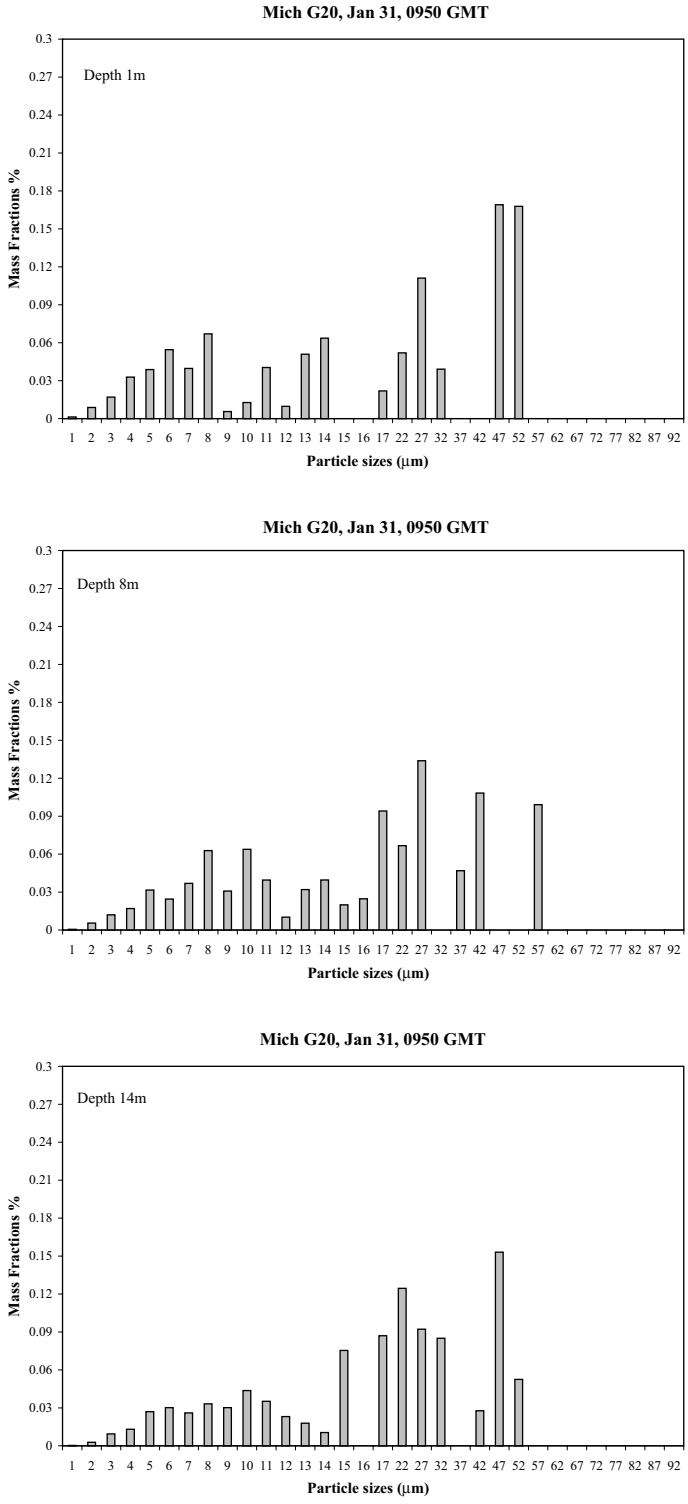

Figure D.4 Size distribution of the suspended solids at the Gary (G) transect (20 m contour depth).

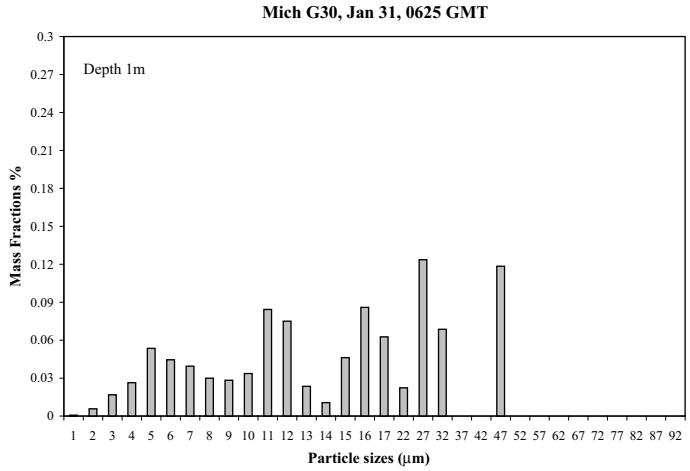

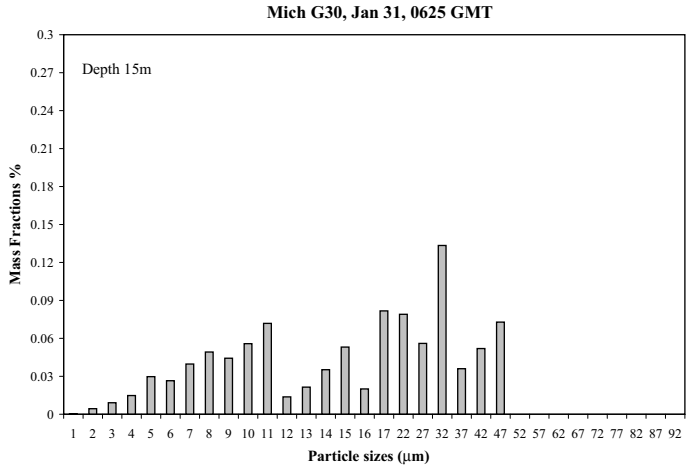

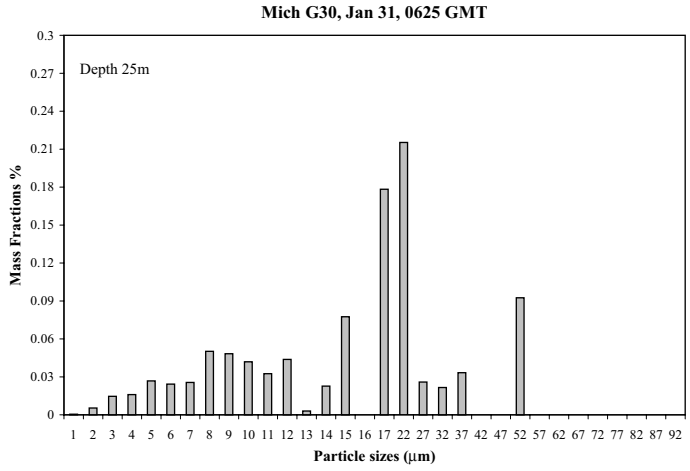

Figure D.5 Size distribution of the suspended solids at the Gary (G) transect (30 m contour depth). (Continued)

Figure D.5 Continued.

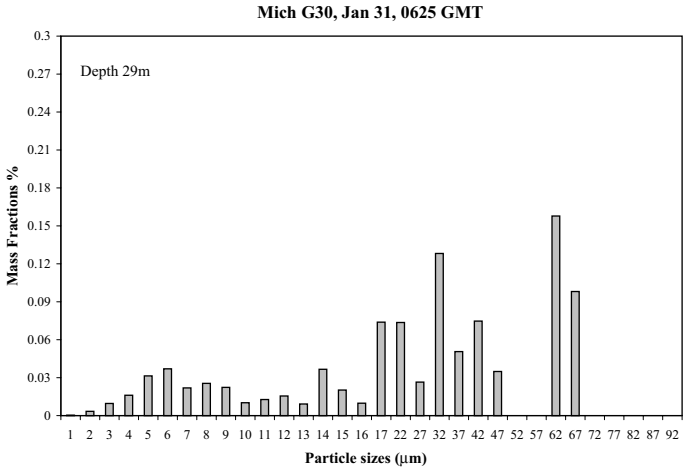

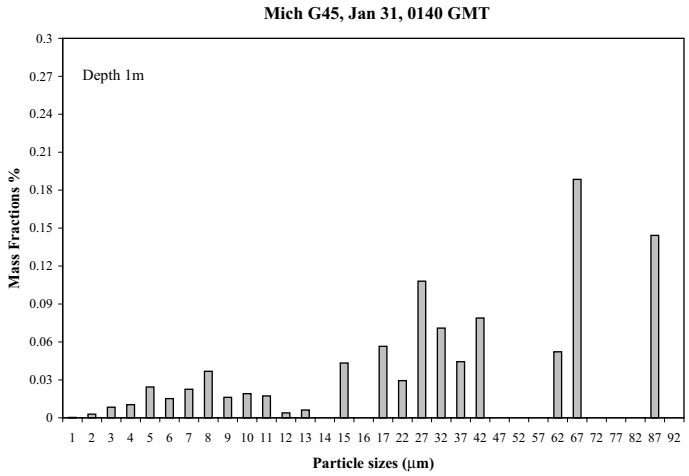

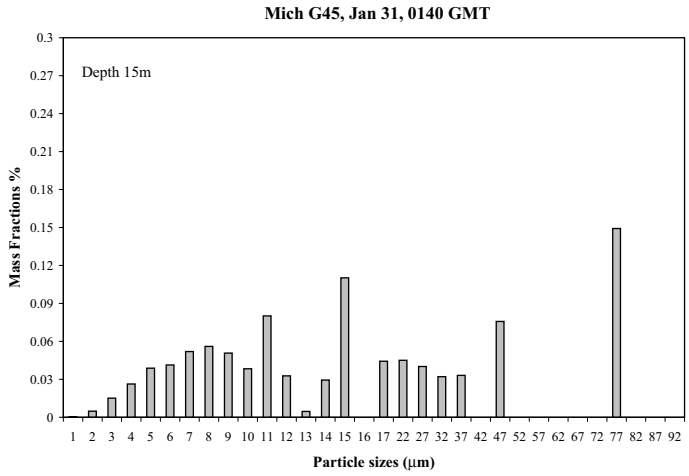

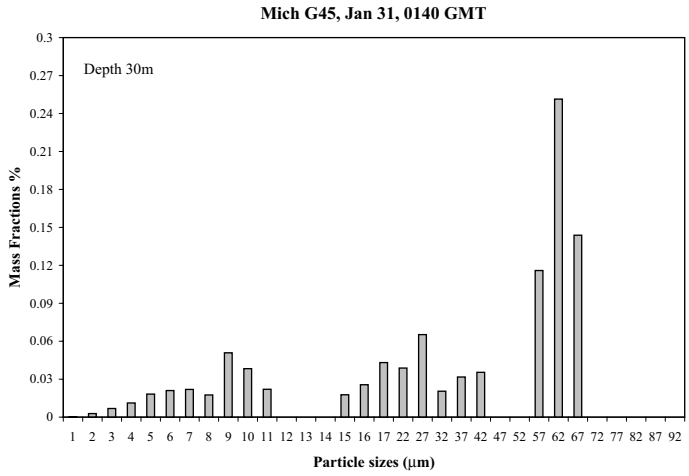

Figure D.6 Size distribution of the suspended solids at the Gary (G) transect (45 m contour depth). (Continued)

Figure D.6 Continued.

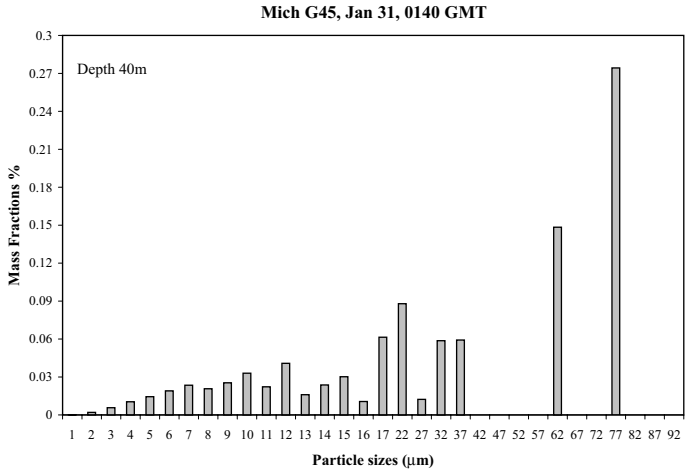

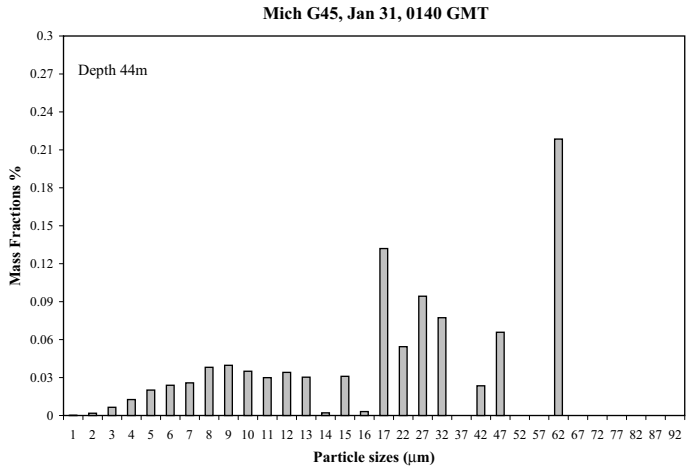

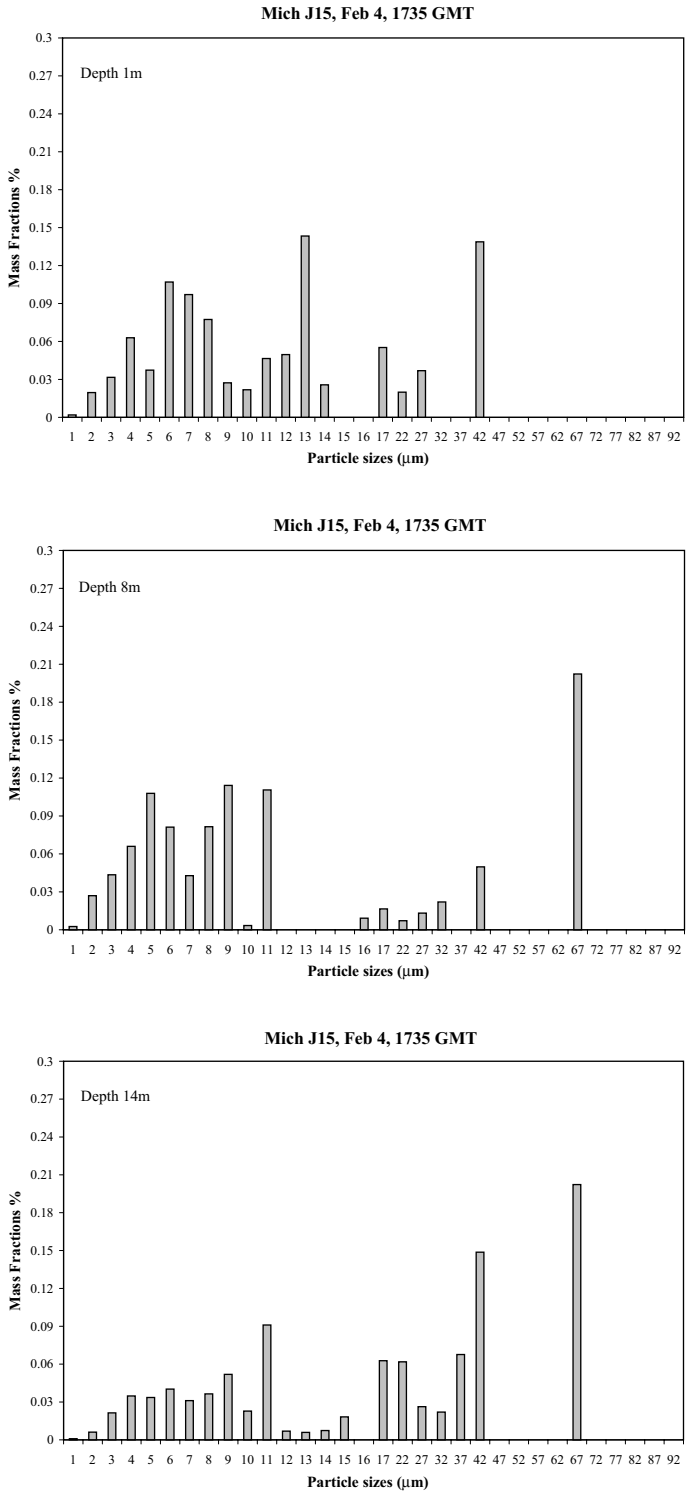

Figure D.7 Size distribution of the suspended solids at the St. Joseph (J) transect (15 m contour depth).

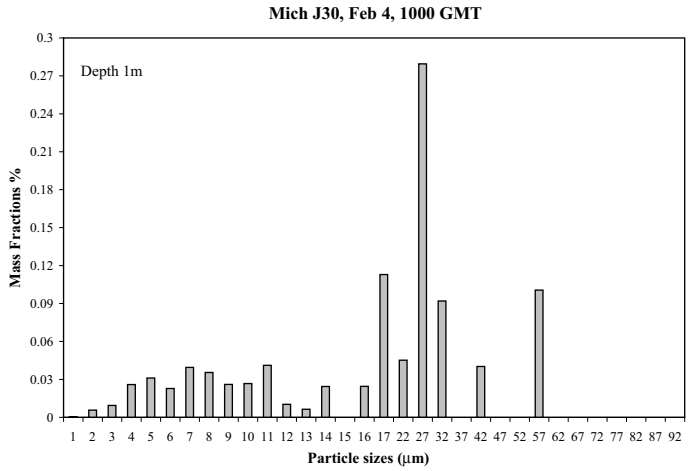

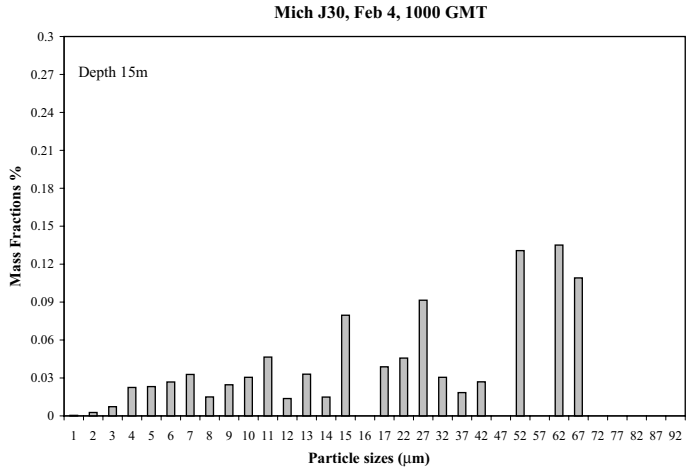

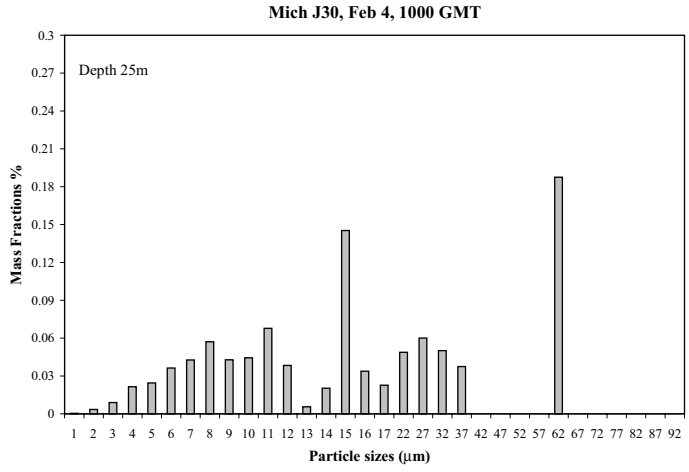

Figure D.8 Size distribution of the suspended solids at the St. Joseph (J) transect (30 m contour depth). (Continued)

Figure D.8 Continued.

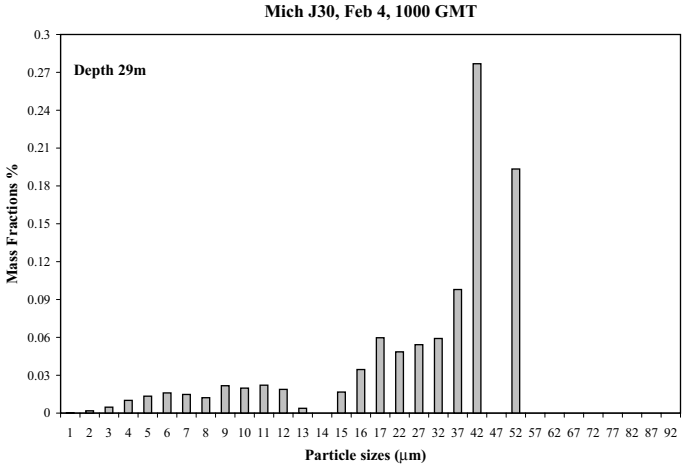

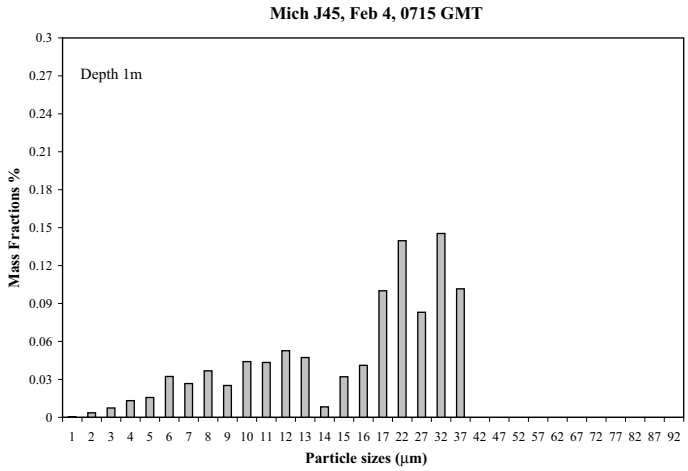

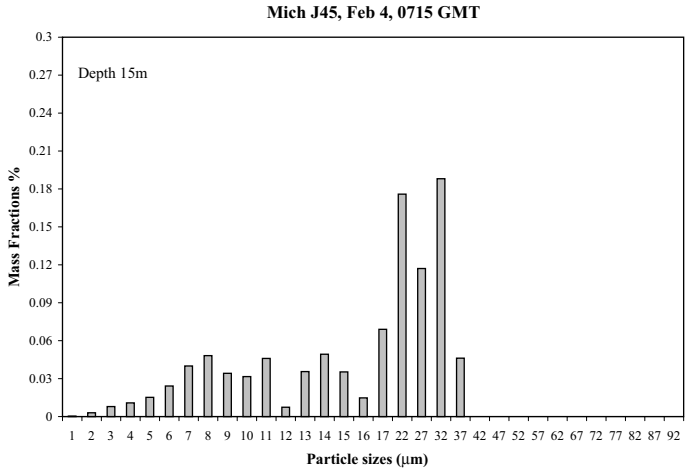

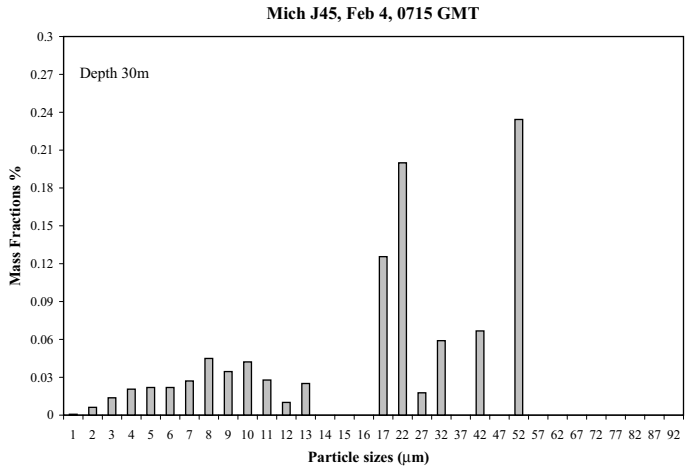

Figure D.9 Size distribution of the suspended solids at the St. Joseph (J) transect (45 m contour depth). (Continued)

Figure D.9 Continued.

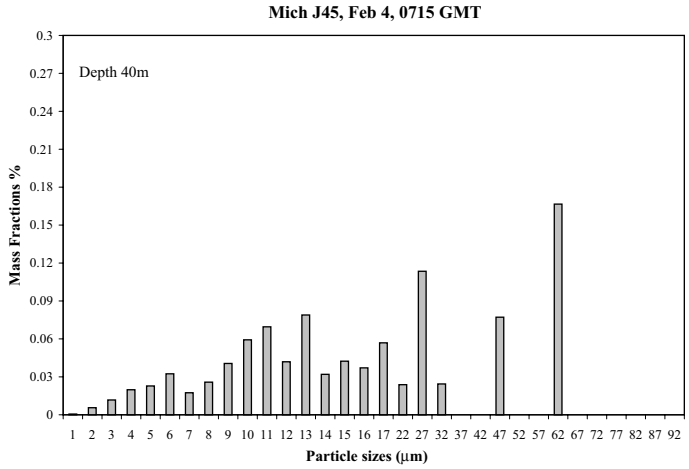

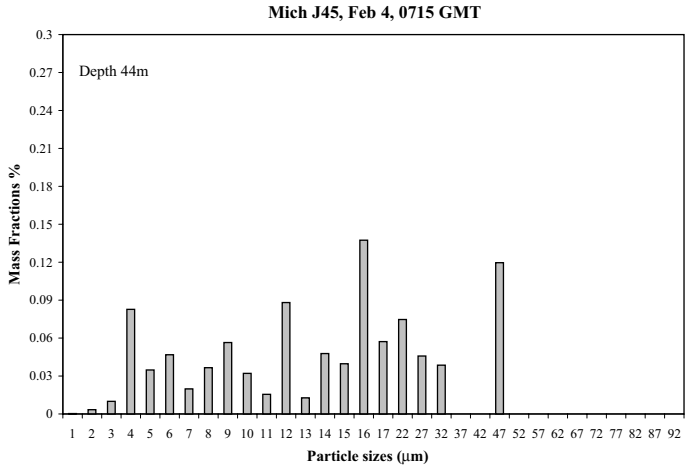

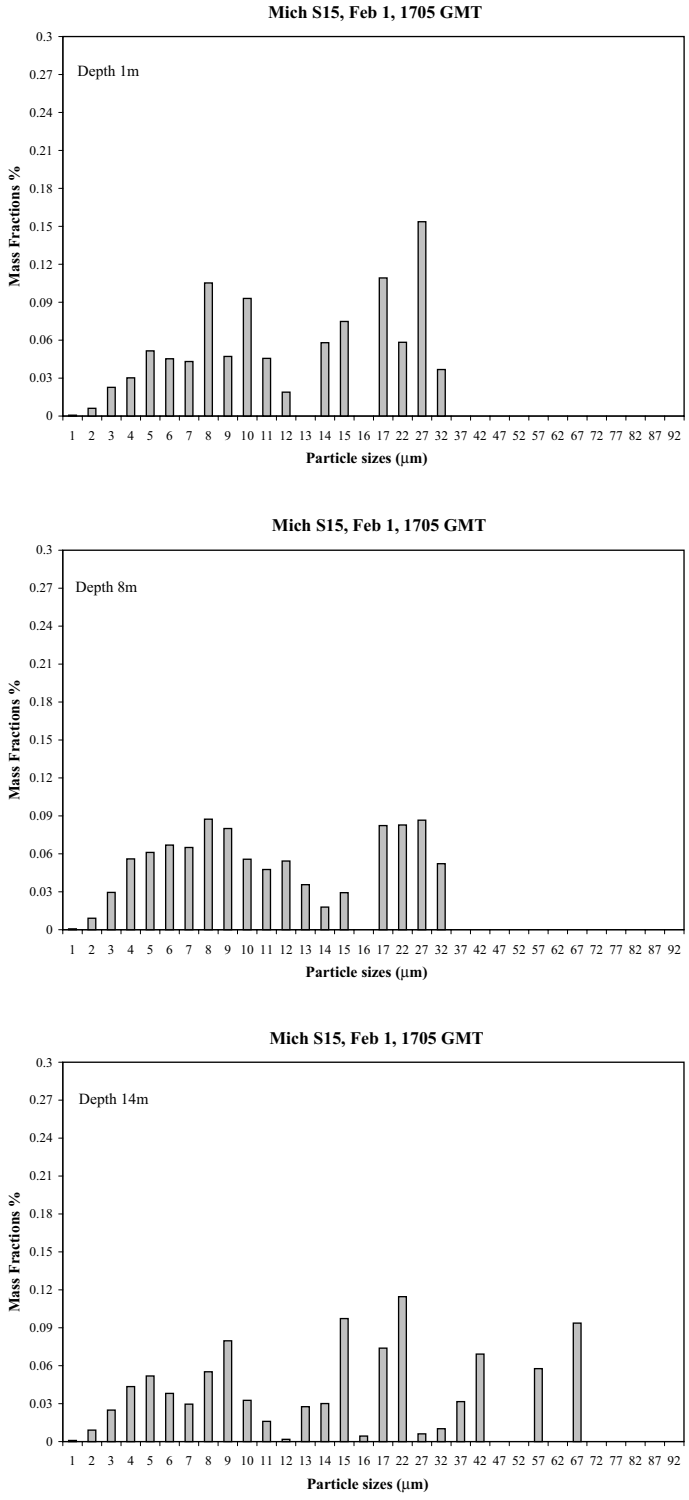

Figure D.10 Size distribution of the suspended solids at the Saugatuck (S) transect (15 m contour depth).

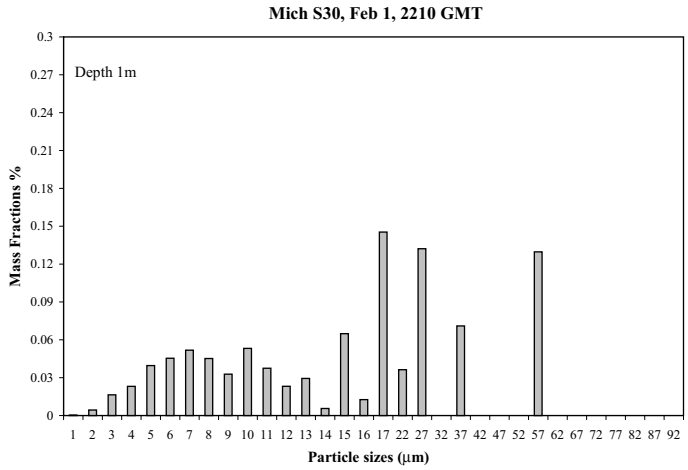

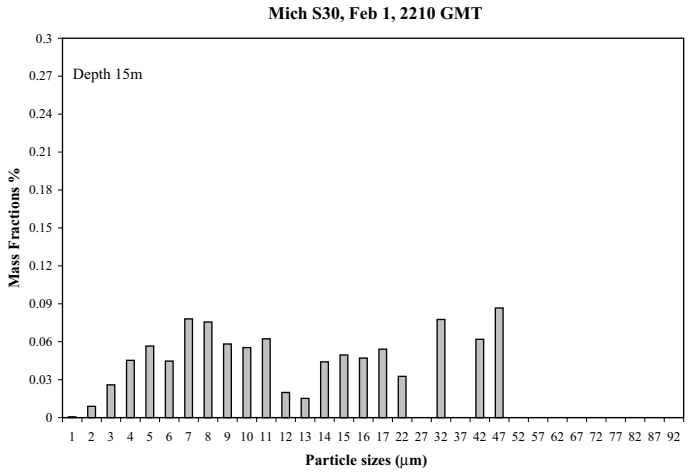

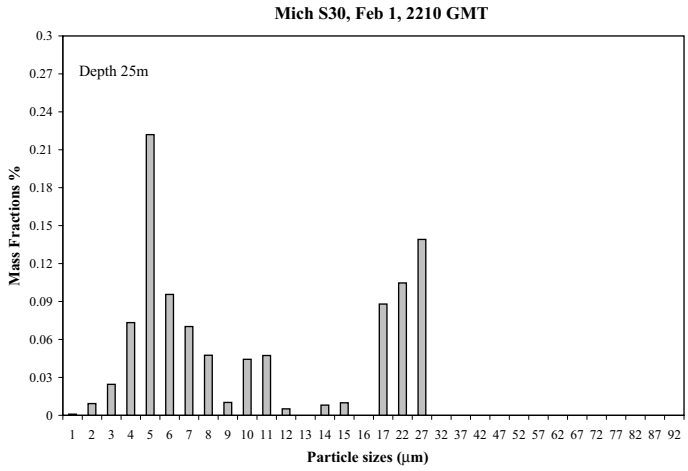

Figure D.11 Size distribution of the suspended solids at the Saugatuck (S) transect (30 m contour depth). (Continued)

Figure D.11 Continued.

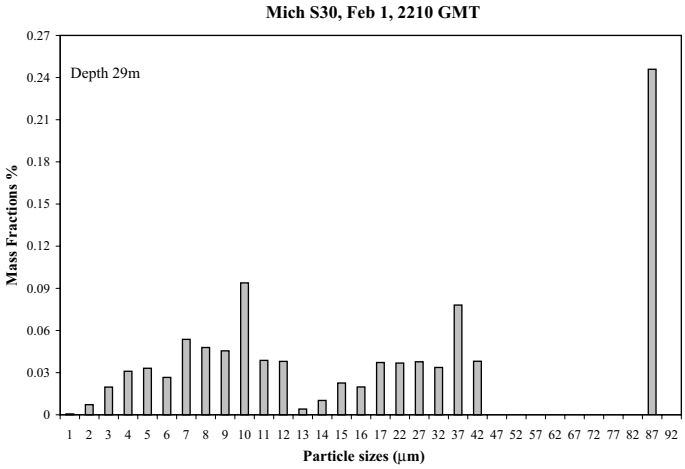

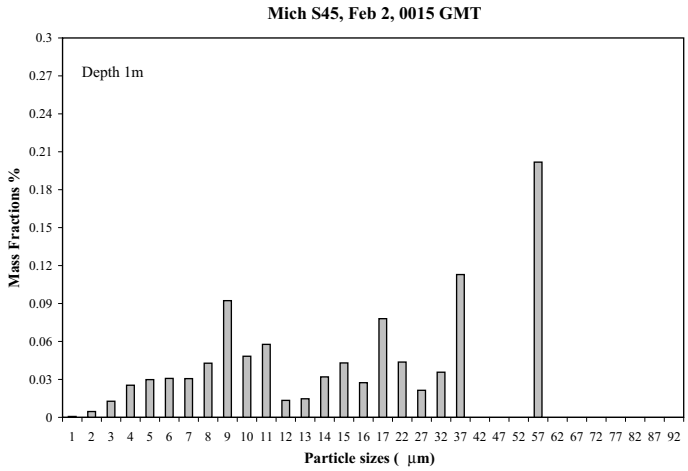

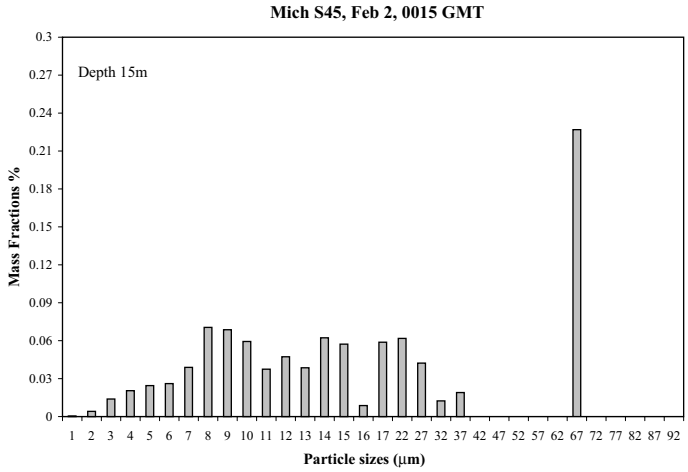

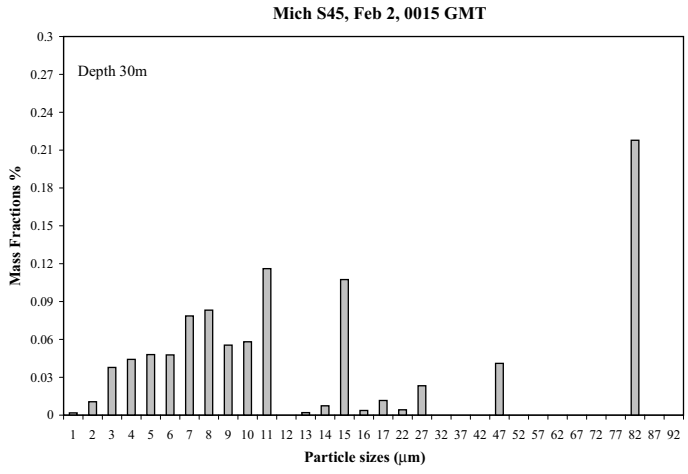

Figure D.12 Size distribution of the suspended solids at the Saugatuck (S) transect (45 m contour depth). (Continued)

Figure D.12 Continued.

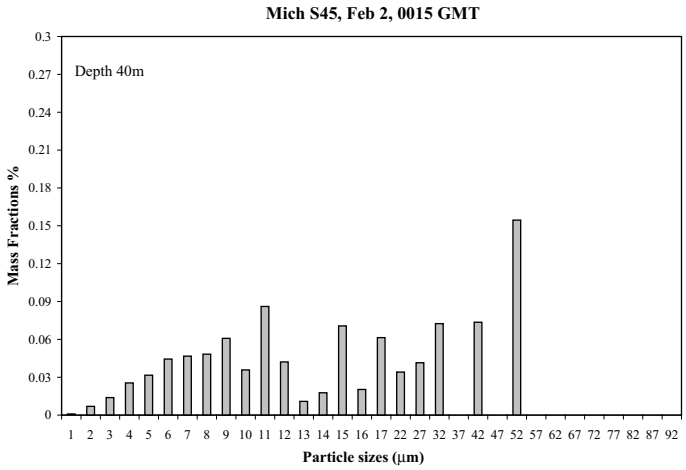

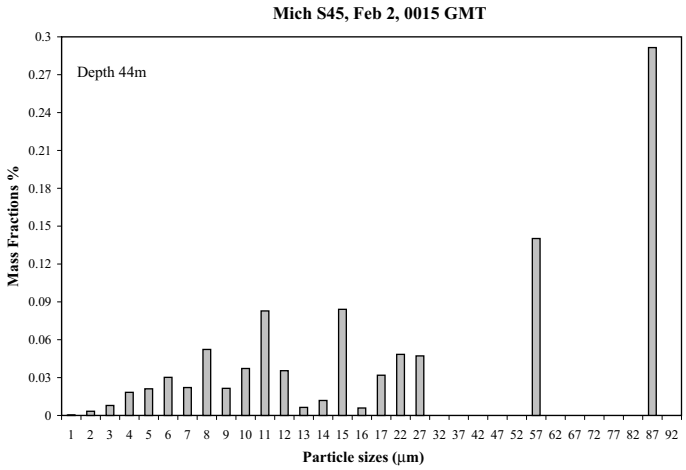

Transect R-15

Depth (m)	Clay %	Silt %	Sand %
1	5.42	94.85	0.00
8	9.68	90.32	0.00
14	1.99	86.36	11.65

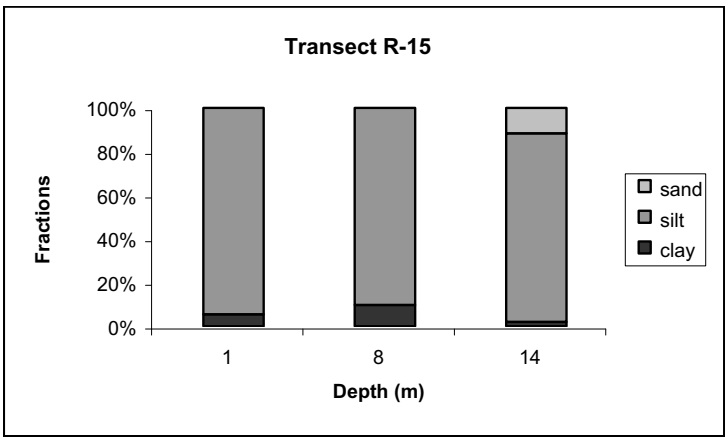

Transect R-30

Depth (m)	Clay %	Silt %	Sand %
1	7.02	92.95	0.00
15	6.16	93.81	0.00
25	1.45	78.53	20.06
29	2.27	8.18	15.92

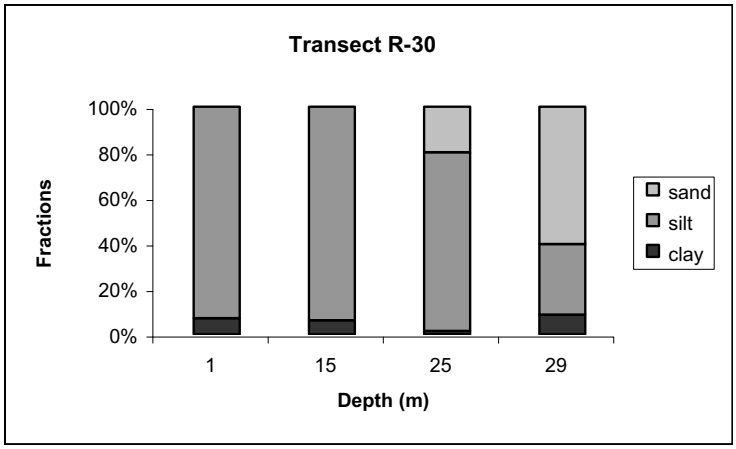

Transect R-45

Depth (m)	Clay %	Silt %	Sand %
1	3.36	96.65	0.00
15	3.32	78.72	17.98
30	5.31	82.02	12.66
40	3.89	82.43	13.69
44	3.74	96.29	0.00

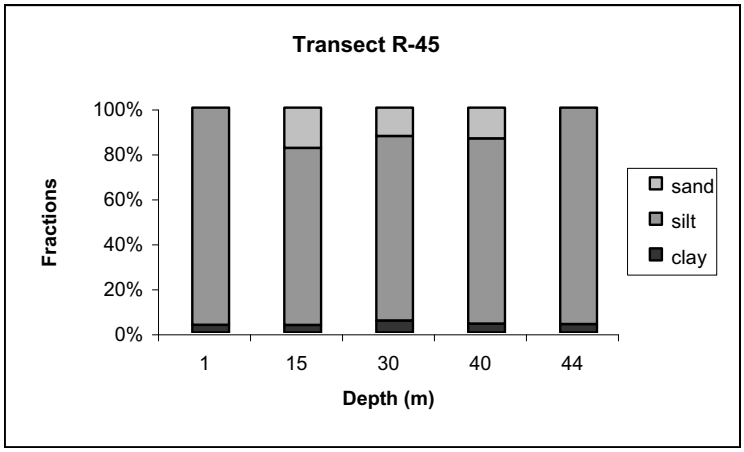

Figure D.13 Class size distribution of the suspended solids at the Racine (R) transect.

Transect G-15

Depth (m)	Clay %	Silt %	Sand %
1	5.99	94.39	0.00
8	3.51	96.52	0.00
14	2.56	97.44	0.00

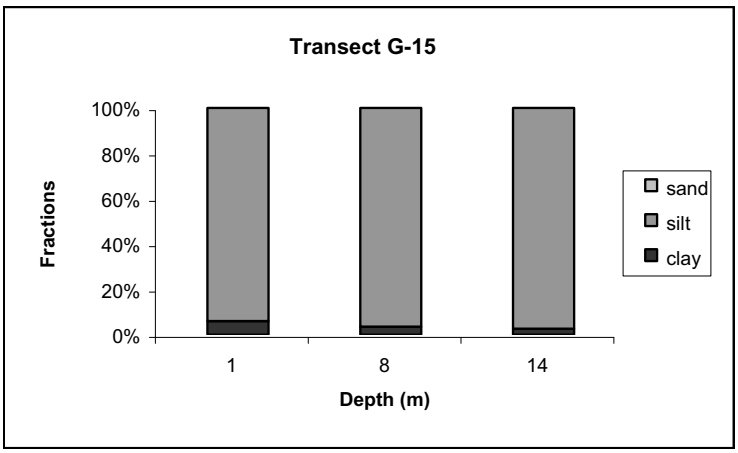

Transect G-30

Depth (m)	Clay %	Silt %	Sand %
1	4.96	95.02	0.00
15	2.87	97.12	0.00
25	3.65	96.35	0.00
29	2.94	87.25	9.81

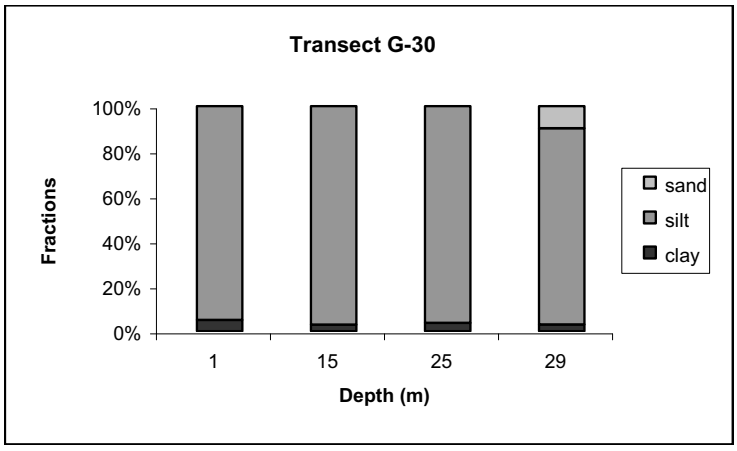

Transect G-45

Depth (m)	Clay %	Silt %	Sand %
1	2.20	64.53	33.27
15	4.65	80.43	14.92
30	2.11	83.50	14.38
40	1.83	70.74	27.43
44	2.10	97.89	0.00

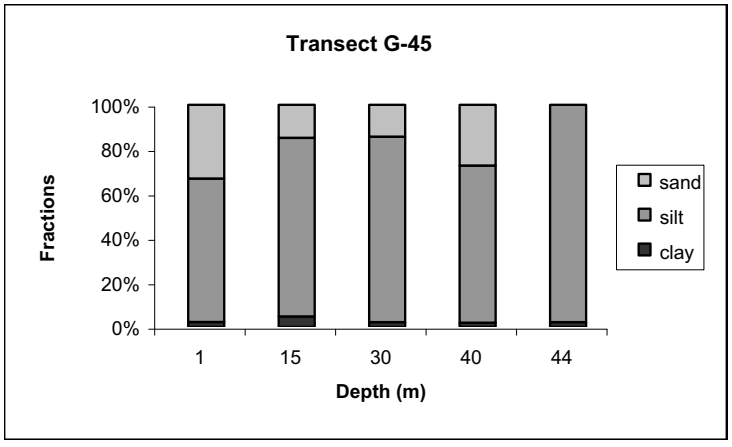

Figure D.14 Class size distribution of the suspended solids at the Gary (G) transect.

Transect J-15

Depth (m)	Clay %	Silt %	Sand %
1	0.116	0.8839	0
8	0.1391	0.6595	0.2023
14	0.0632	0.7345	0.2023

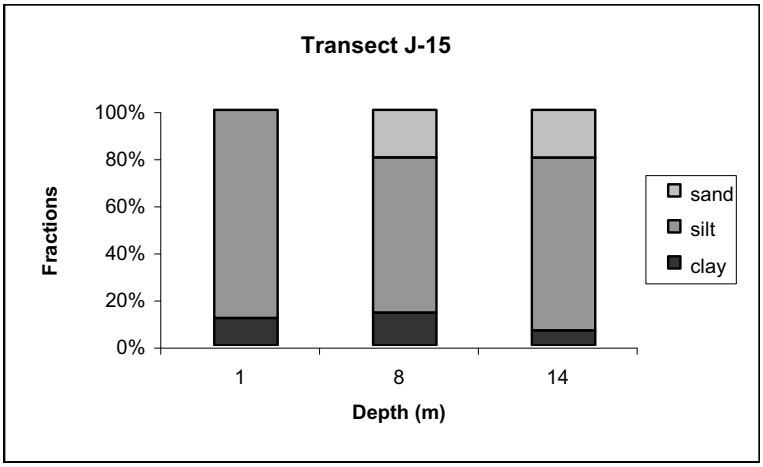

Transect J-30

Depth (m)	Clay %	Silt %	Sand %
1	0.0414	0.9587	0
15	0.0329	0.8582	0.1091
25	0.0344	0.9657	0
29	0.0168	0.9834	0

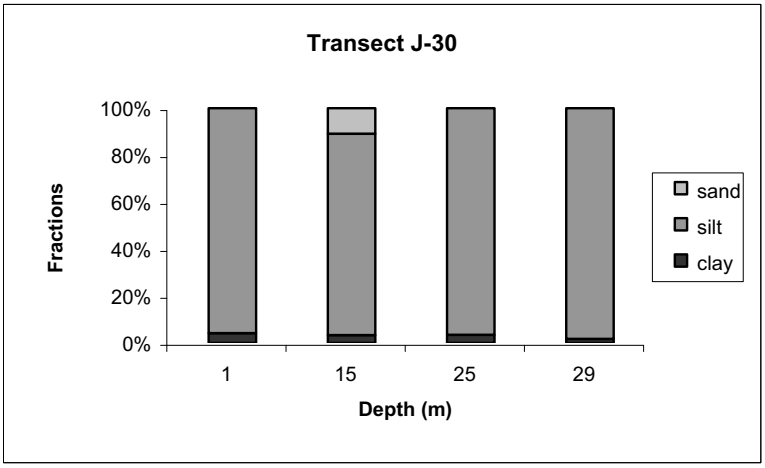

Transect J-45

Depth (m)	Clay %	Silt %	Sand %
1	0.0246	0.9756	0
15	0.022	0.9781	0
30	0.0412	0.9587	0
40	0.0377	0.9626	0
44	0.0964	0.9037	0

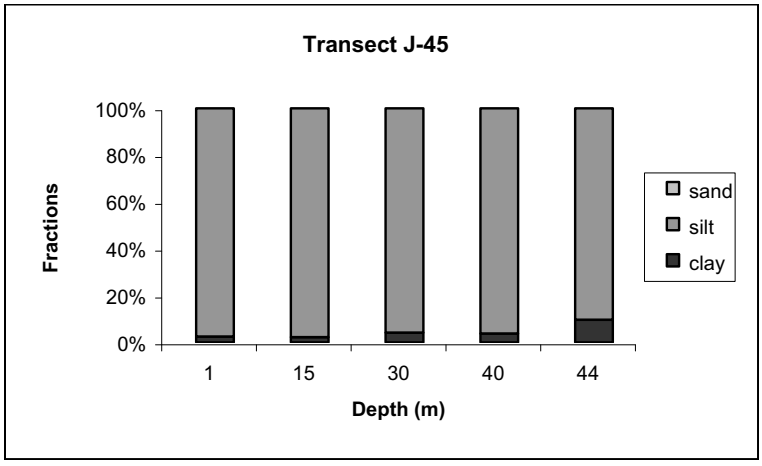

Figure D.15 Class size distribution of the suspended solids at the St. Joseph (J) transect.

Transect S-15

Depth (m)	Clay %	Silt %	Sand %
1	5.97	94.04	0.00
8	9.53	90.47	0.00
14	7.84	82.76	9.37

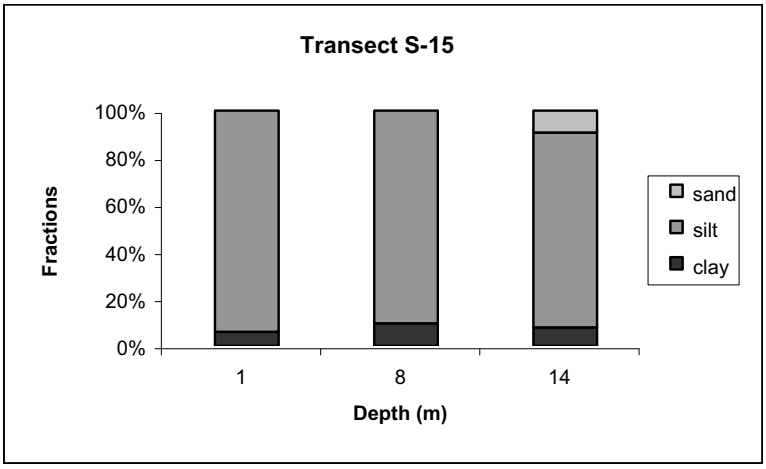

Transect S-30

Depth (m)	Clay %	Silt %	Sand %
1	4.42	95.58	0.00
15	8.07	91.96	0.00
25	1.08	89.2	0.00
29	5.85	69.57	24.59

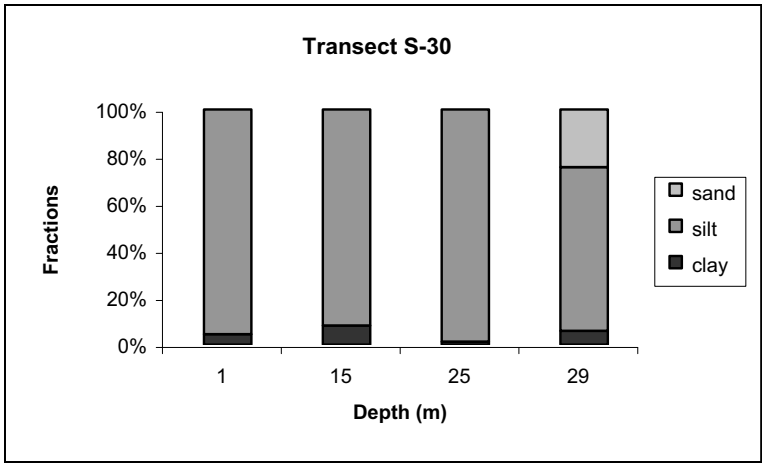

Transect S-45

Depth (m)	Clay %	Silt %	Sand %
1	4.34	95.63	0.00
15	3.89	73.41	22.69
30	9.44	68.78	21.78
40	4.72	95.3	0.00
44	2.98	67.87	29.15

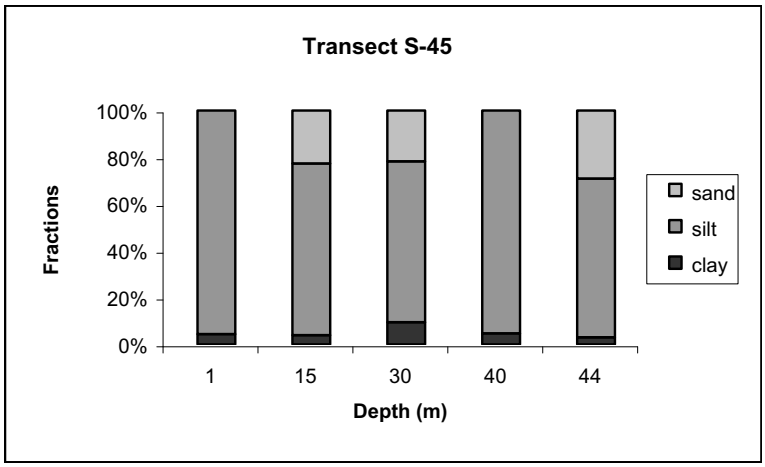

Figure D.16 Class size distribution of the suspended solids at the Saugatuck (S) transect.

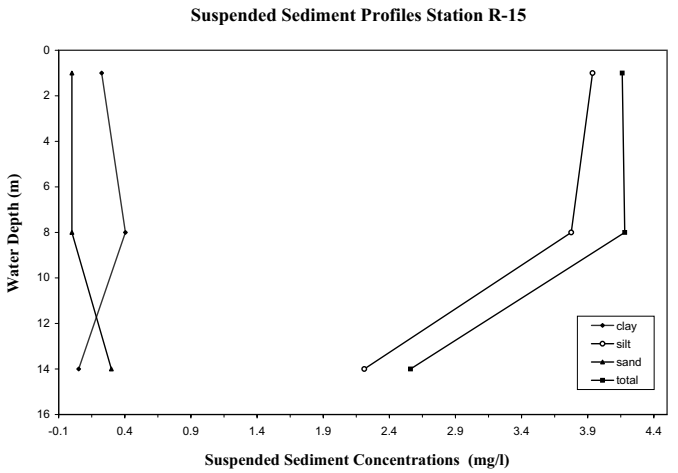

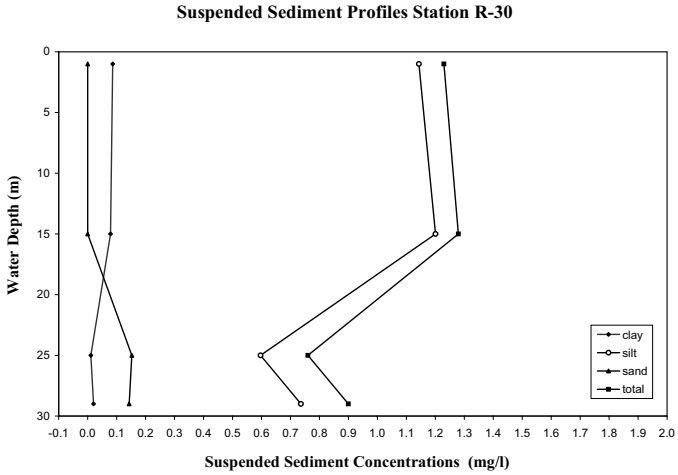

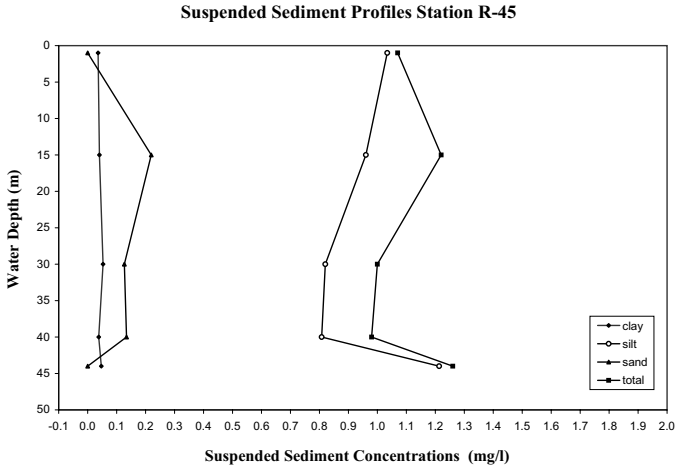

Figure D.17 Vertical distribution of the suspended solids at the Racine (R) transect.

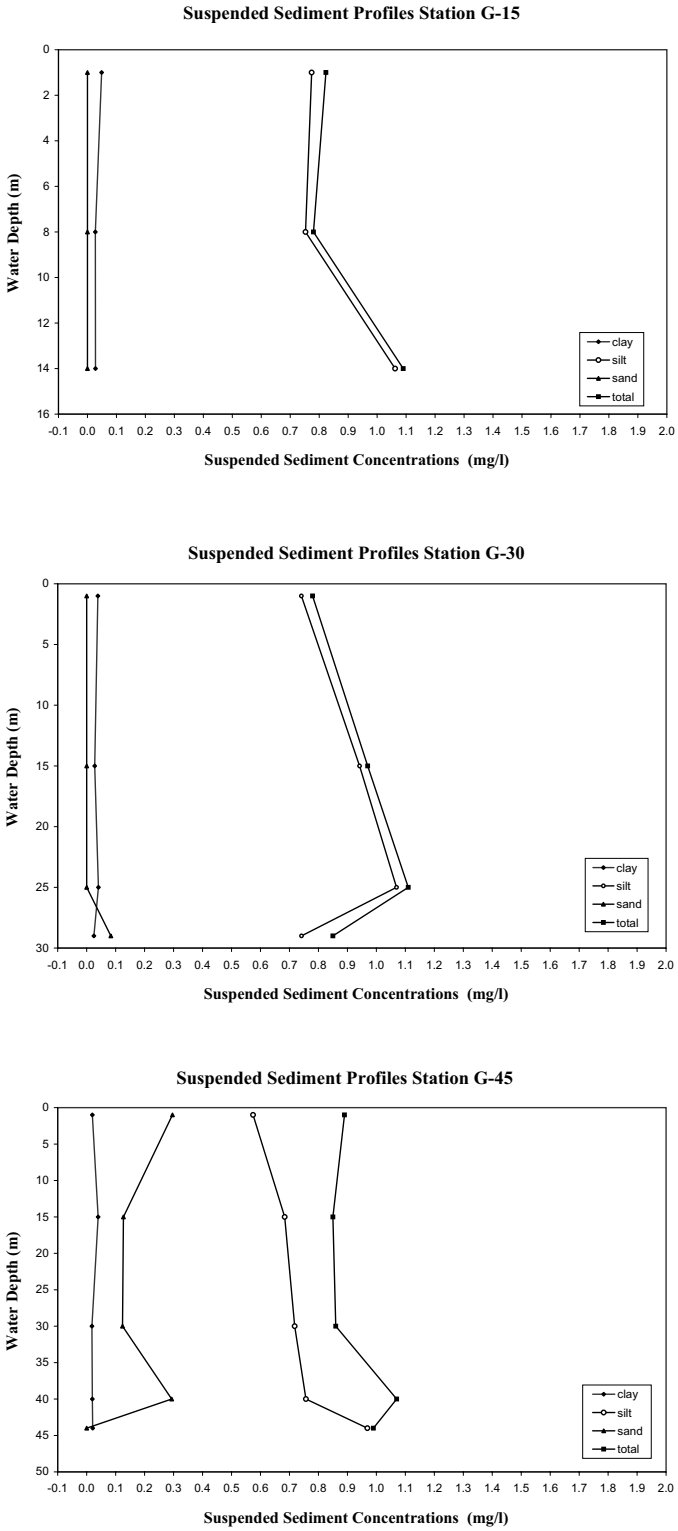

Figure D.18 Vertical distribution of the suspended solids at the Gary (G) transect.

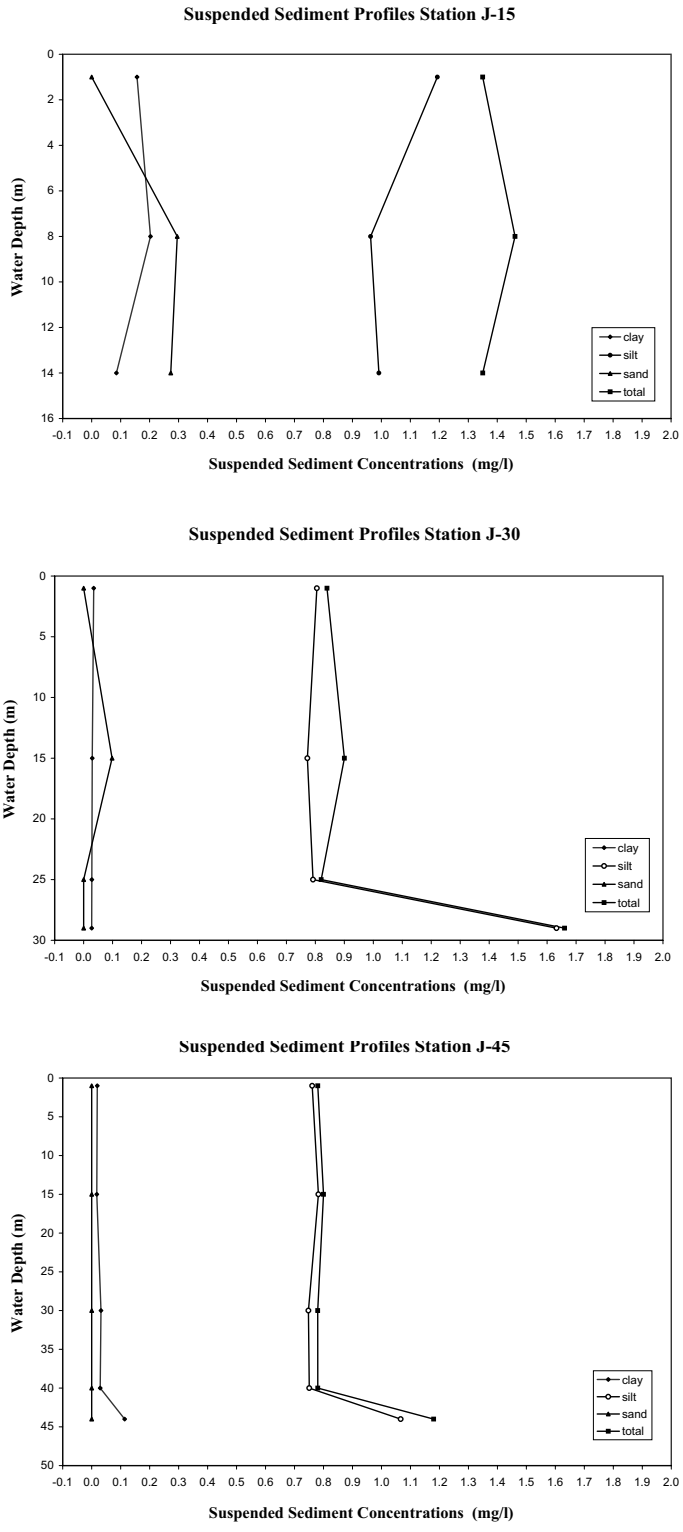

Figure D.19 Vertical distribution of the suspended solids at the St. Joseph (J) transect.

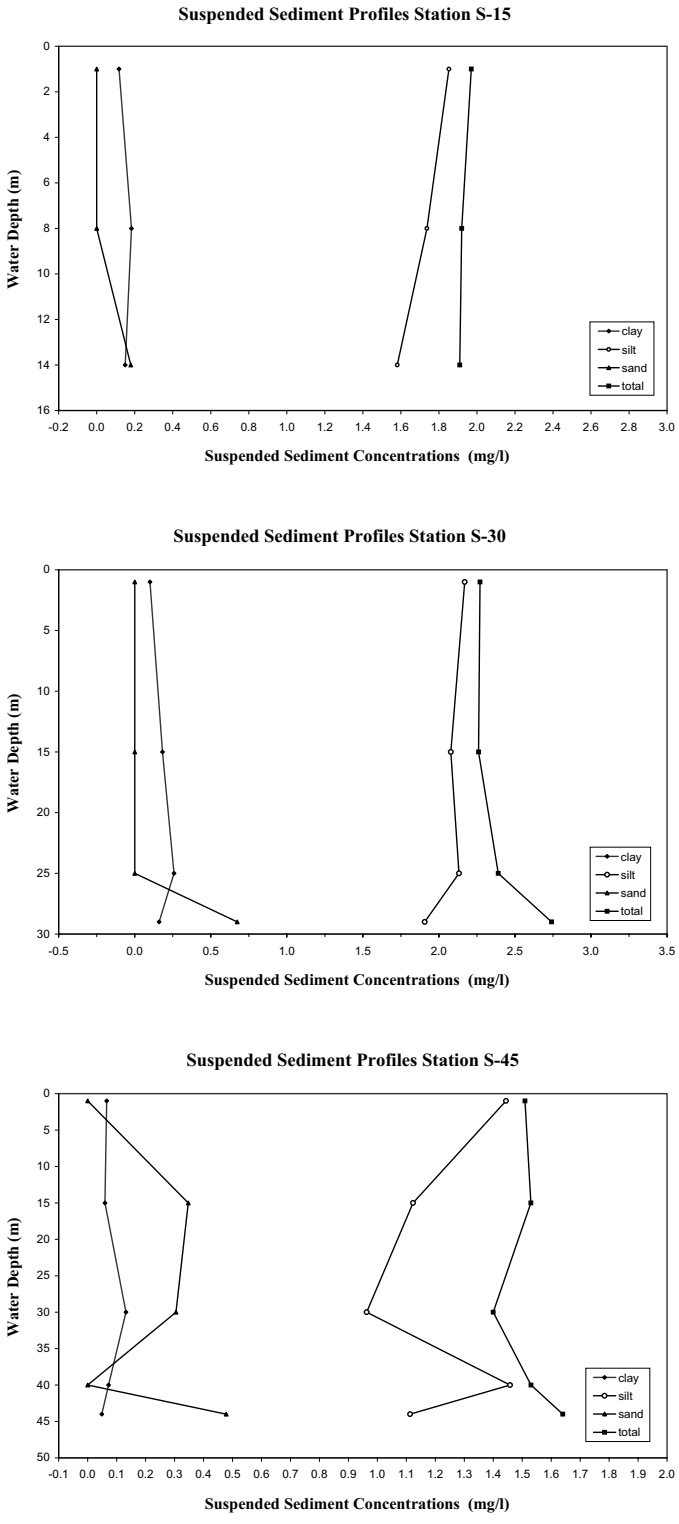

Figure D.20 Vertical distribution of the suspended solids at the Saugatuck (S) transect.

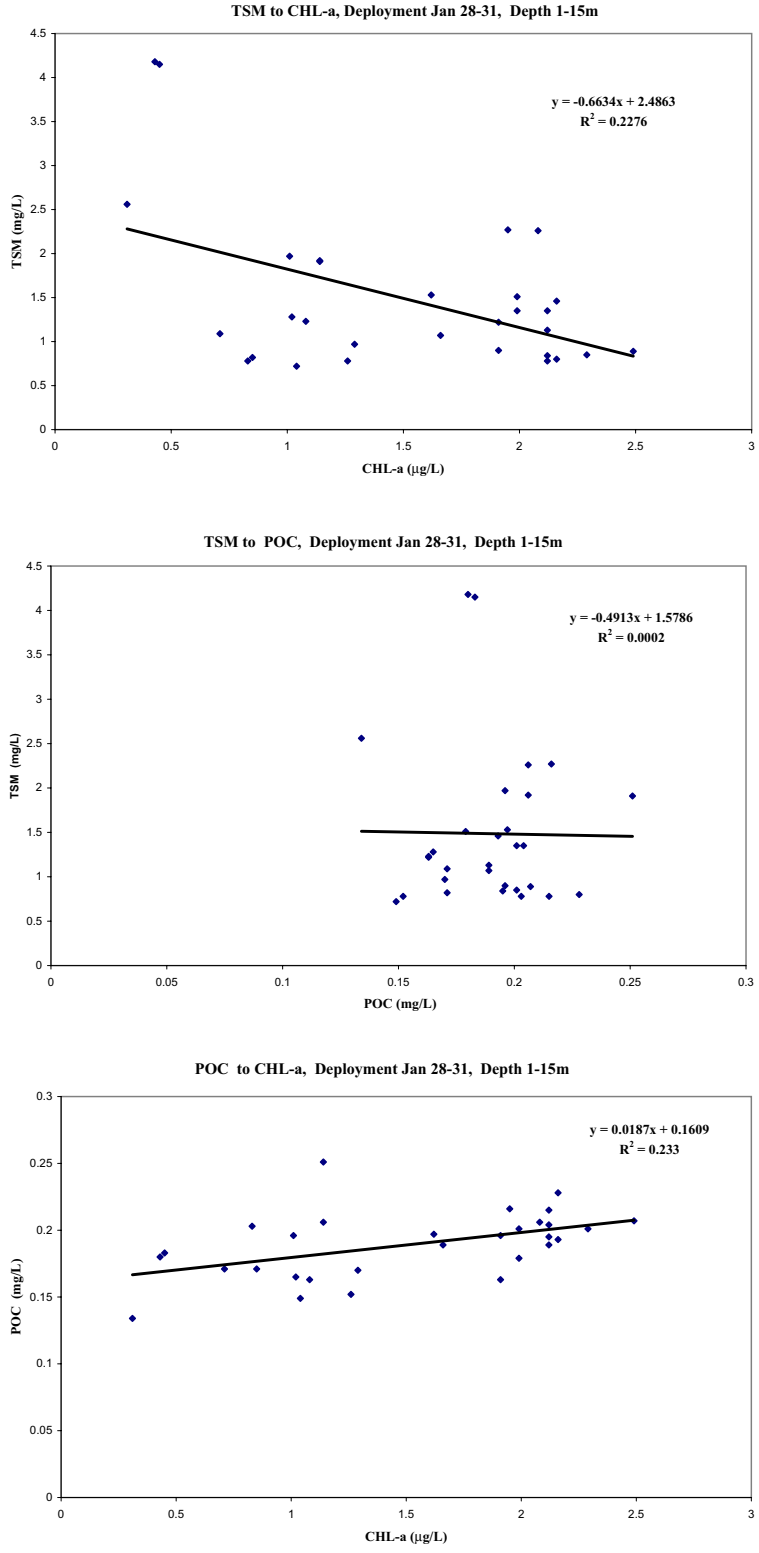

Figure D.21 Pre-plume correlations between the suspended solids parameters.

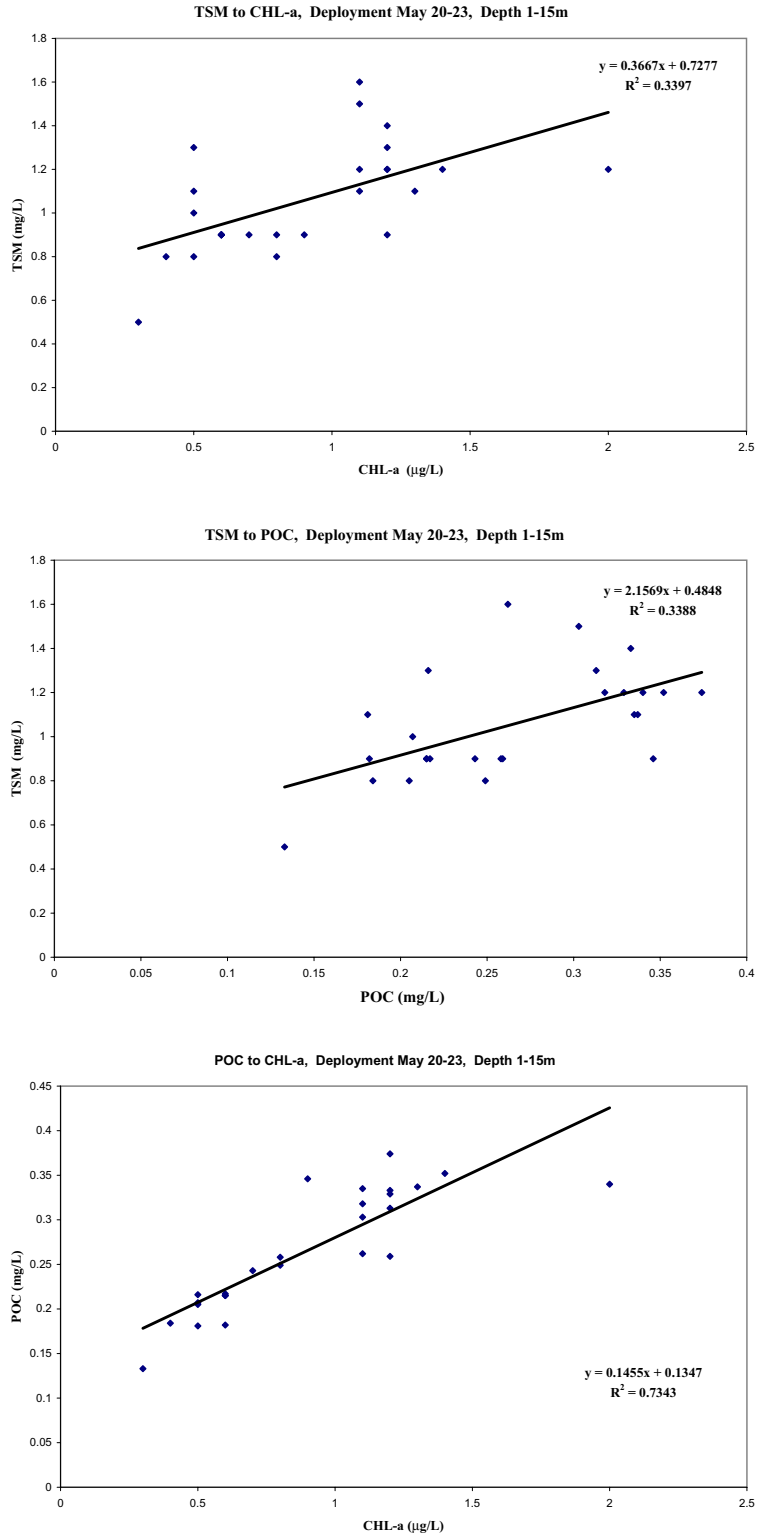

Figure D.22 Post-plume correlations between the suspended solids parameters.

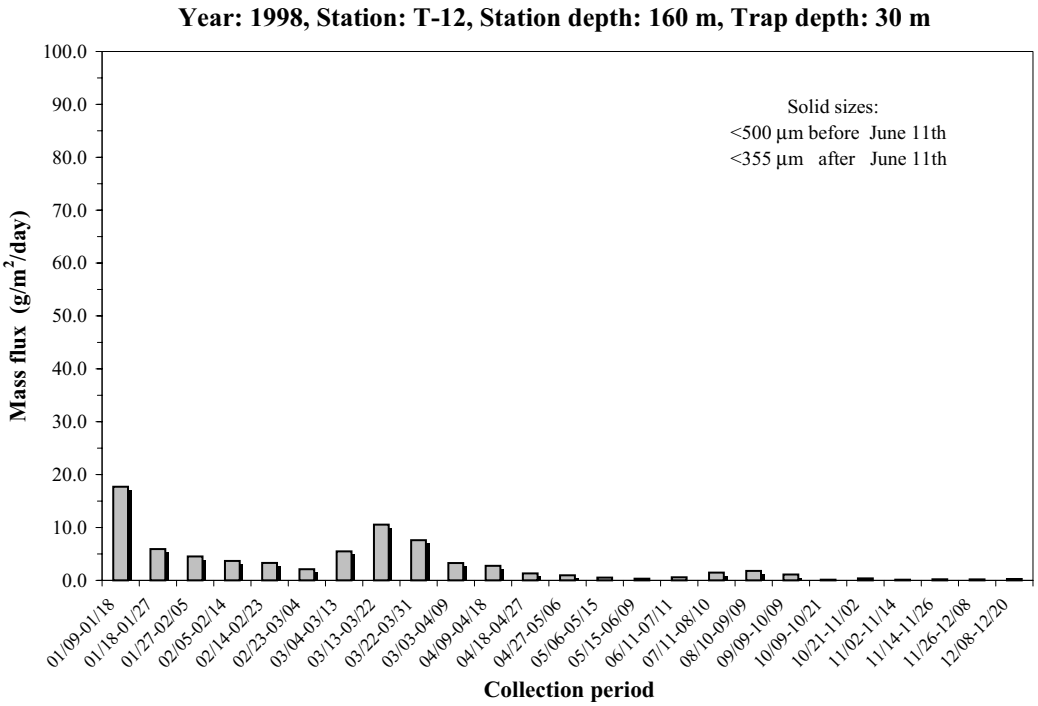

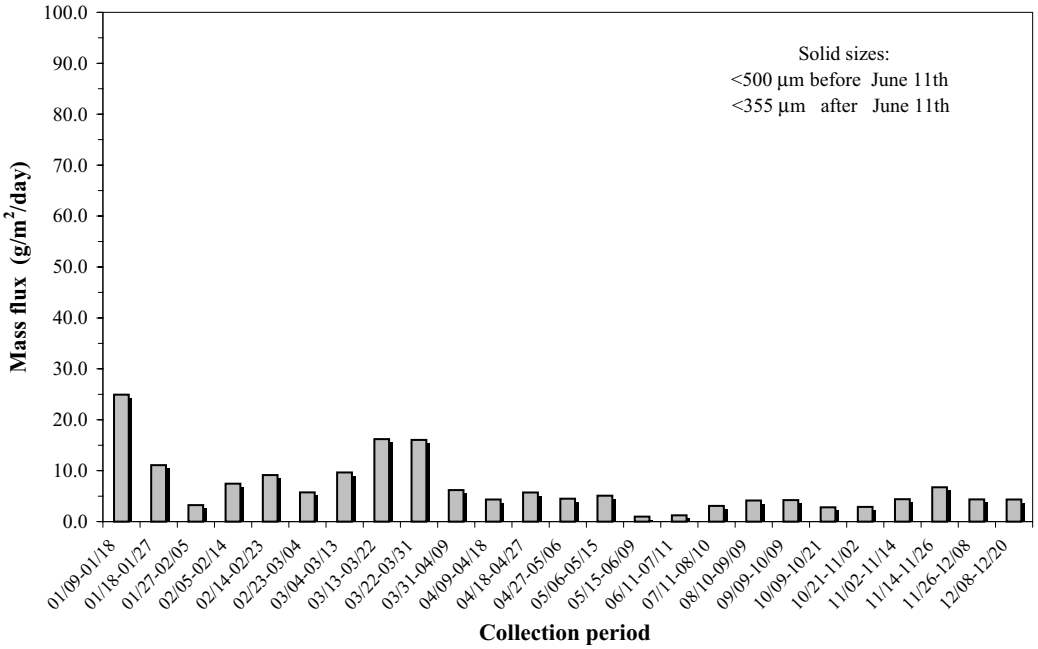

Figure D.23 Sediment trap data for the trap location T12.

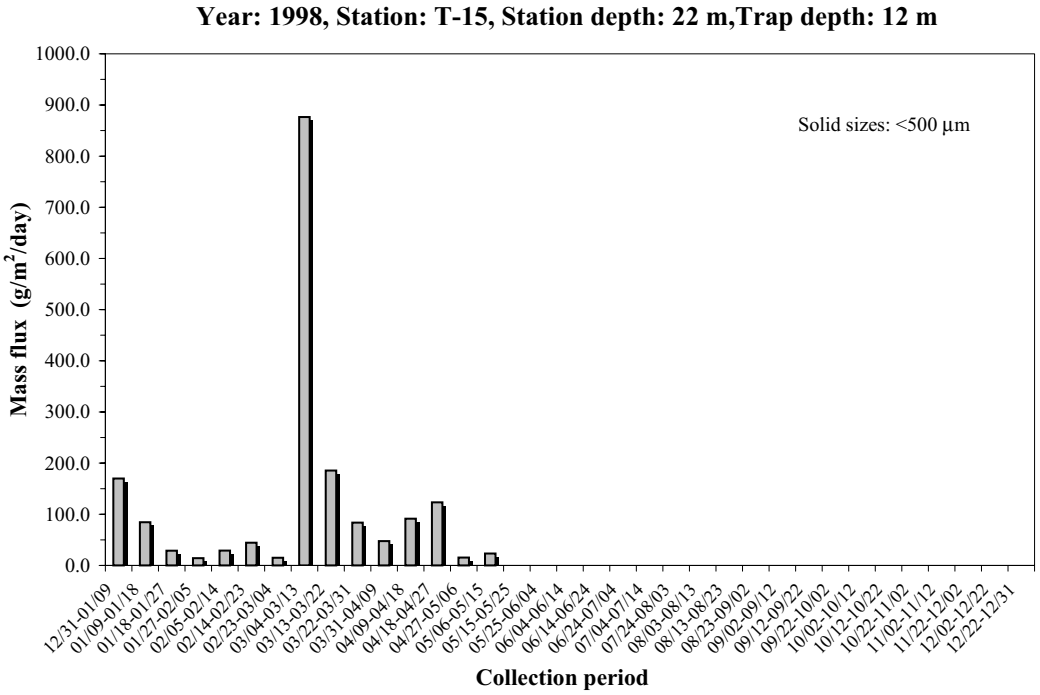

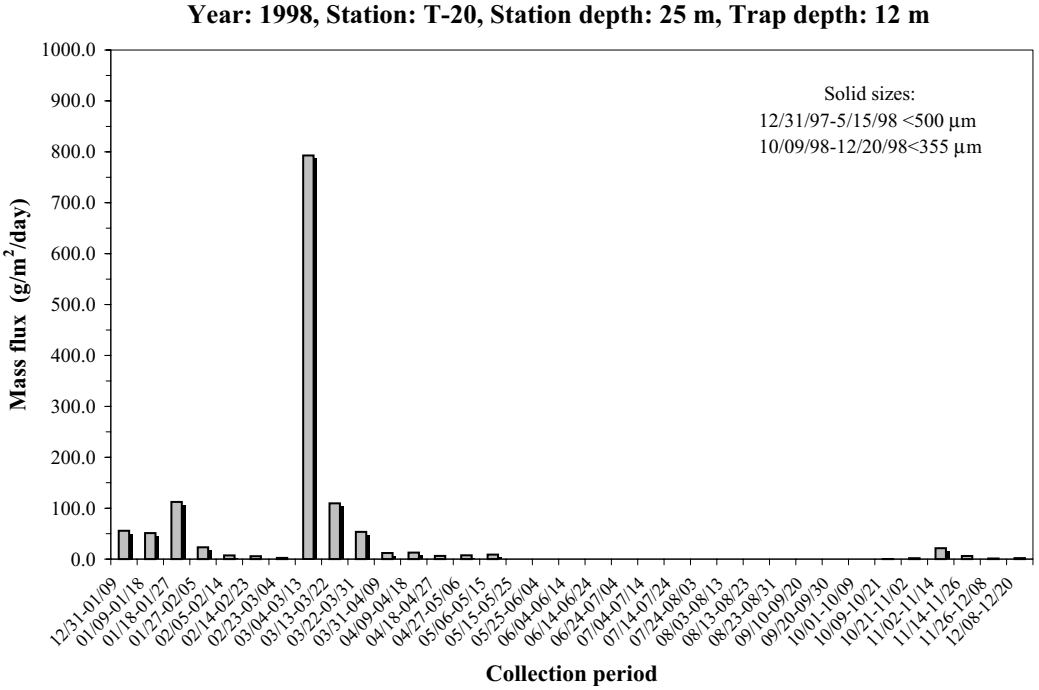

Figure D.24 Sediment trap data for the trap locations T15 and T20.

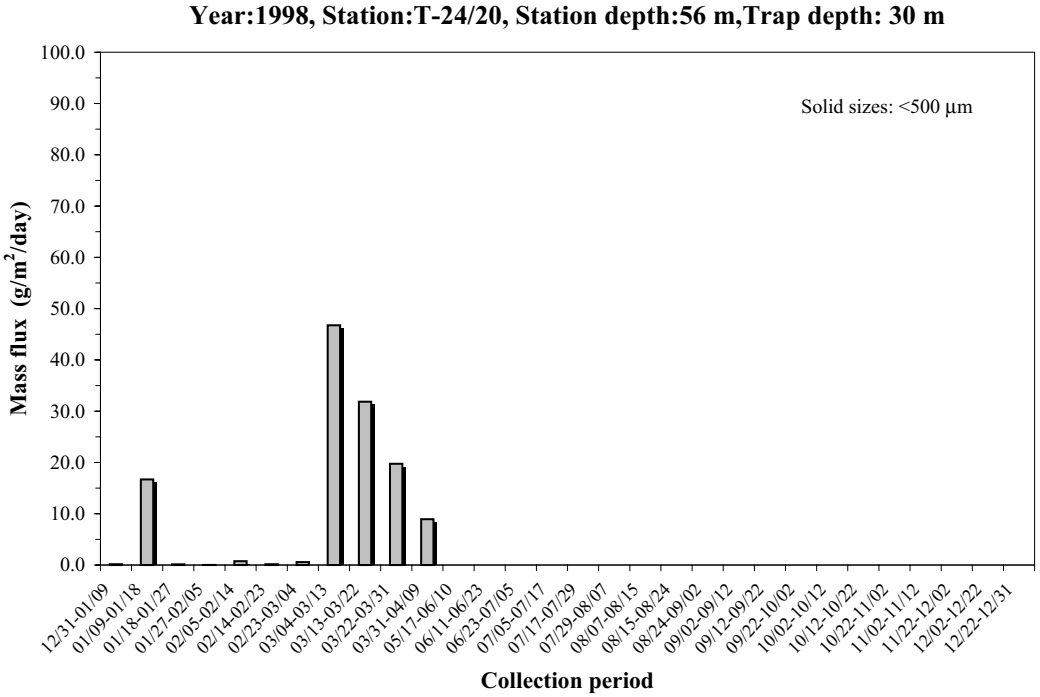

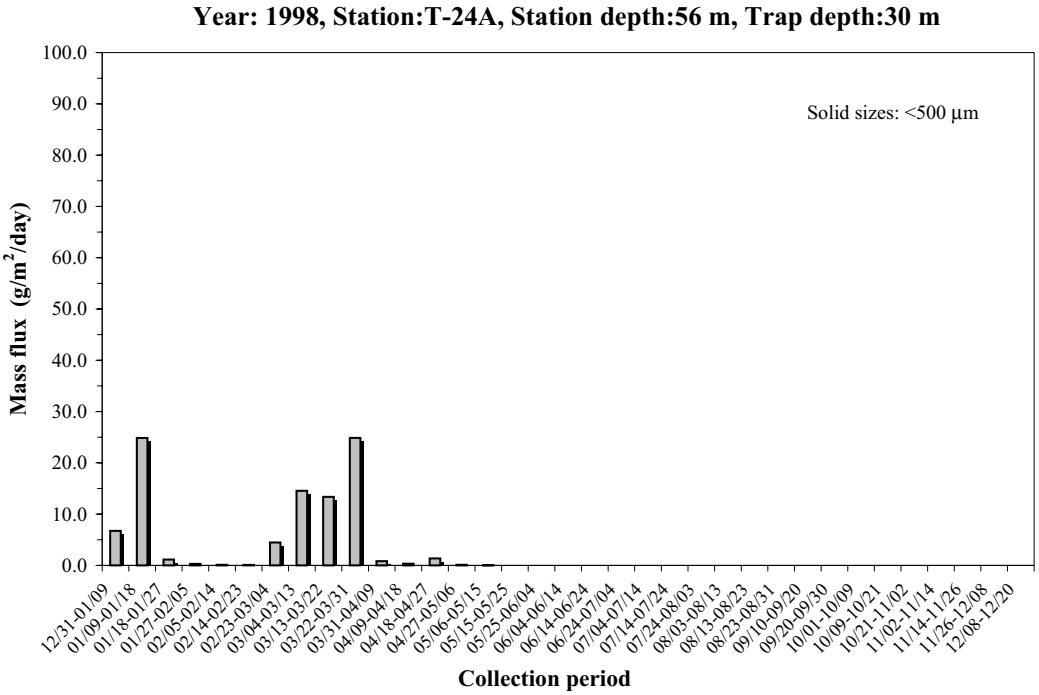

Figure D.25 Sediment trap data for the trap location T24.

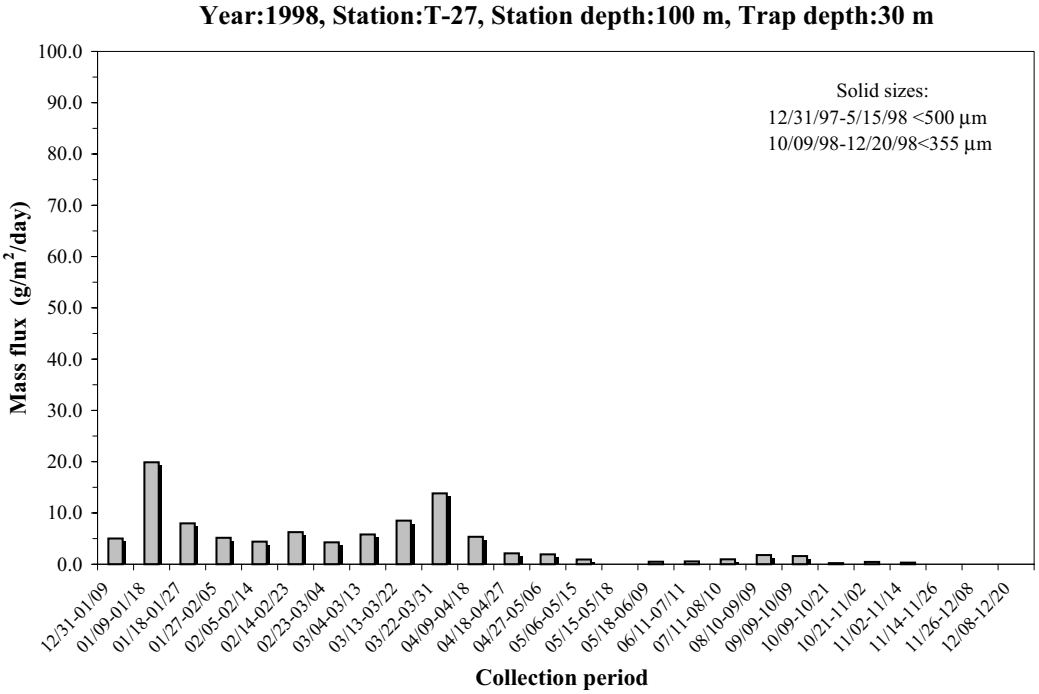

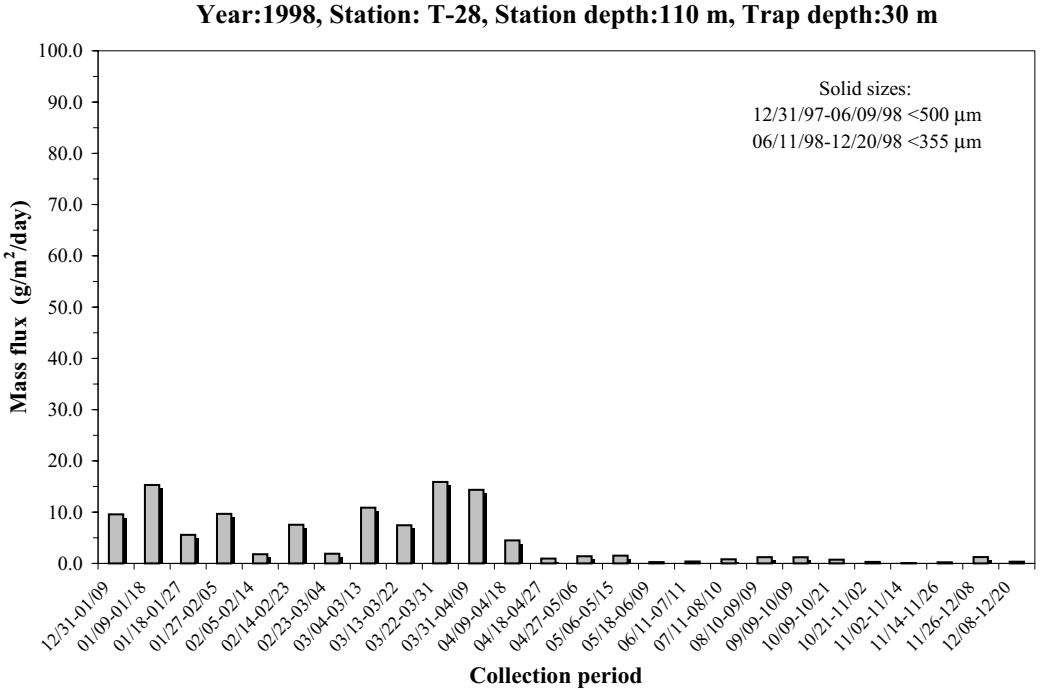

Figure D.26 Sediment trap data for the trap locations T27 and T28.

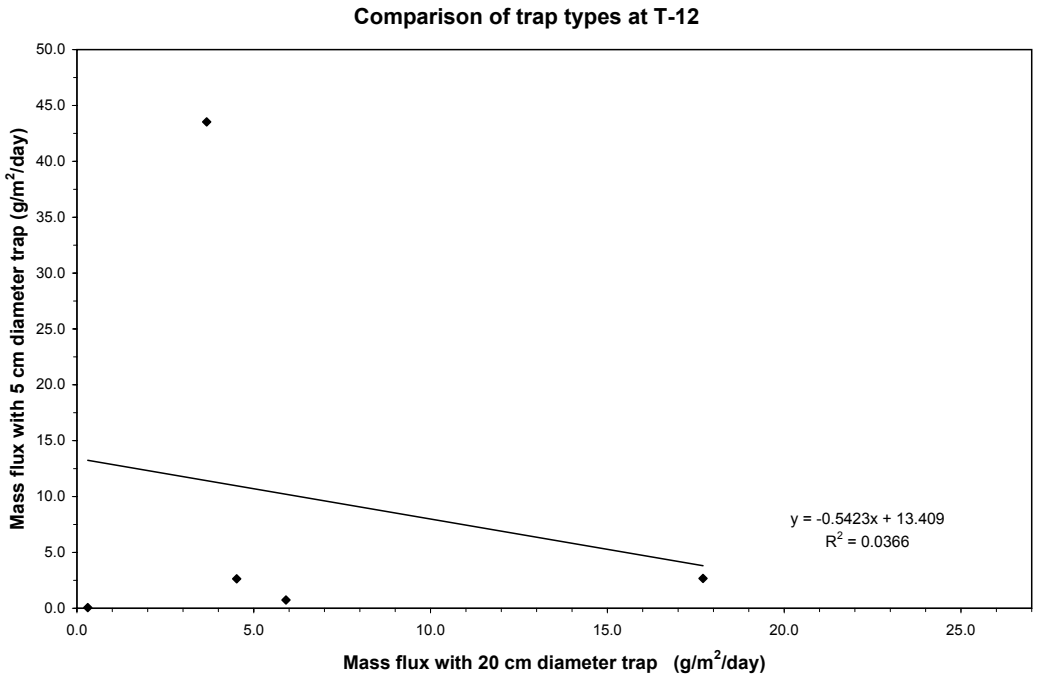

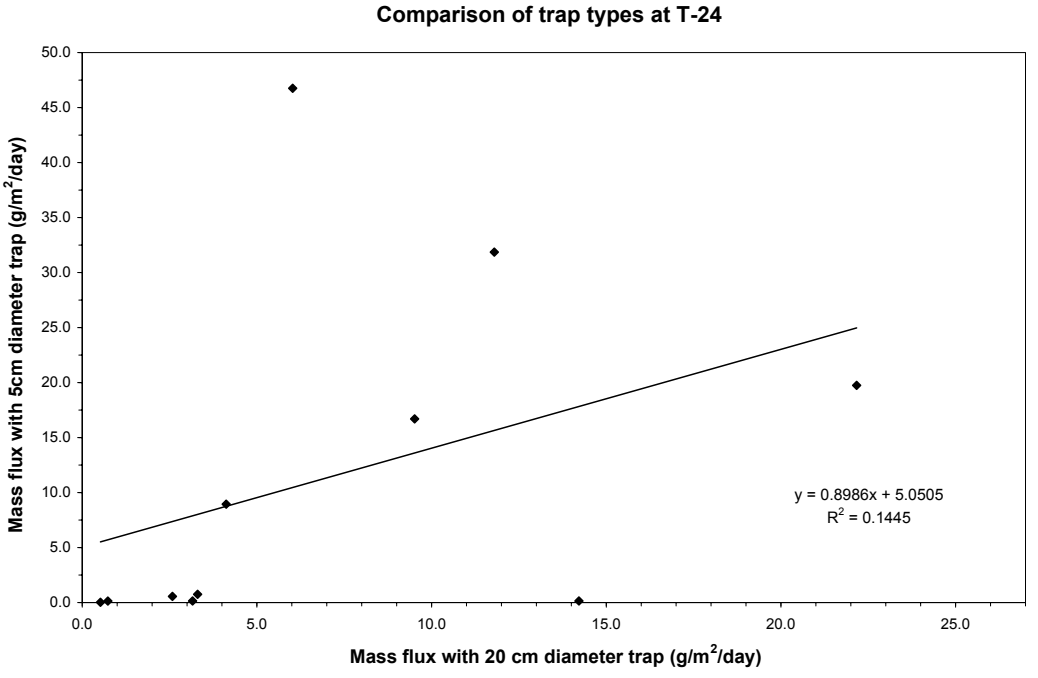

Figure D.27 Comparisons of the data between the 5 cm and the 20 cm diameter traps (trap locations T12 and T24).

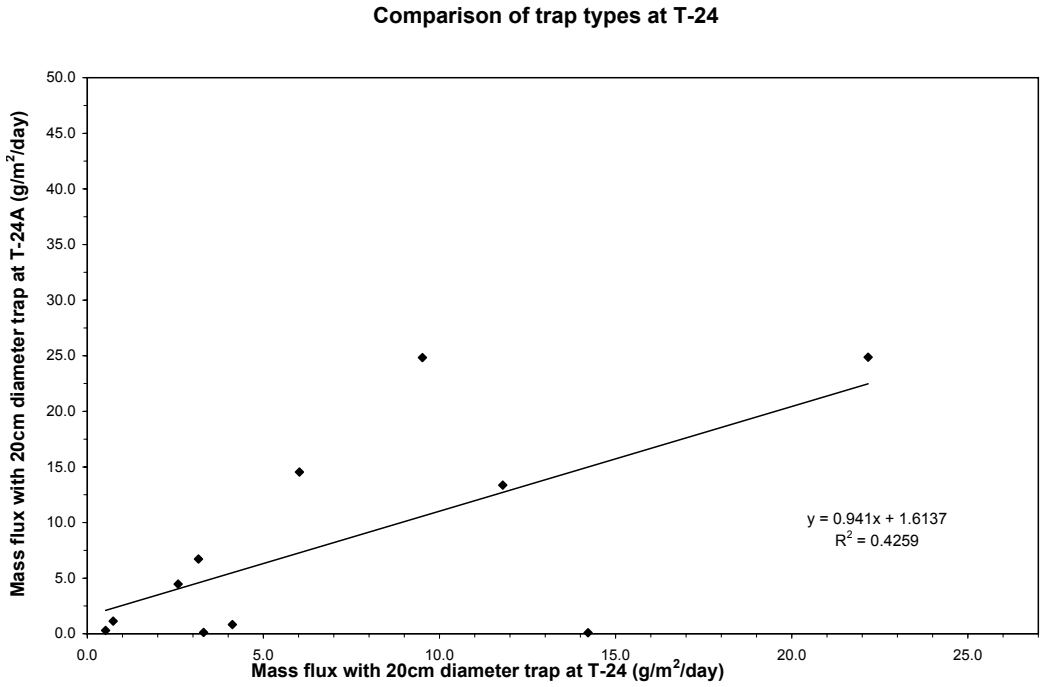

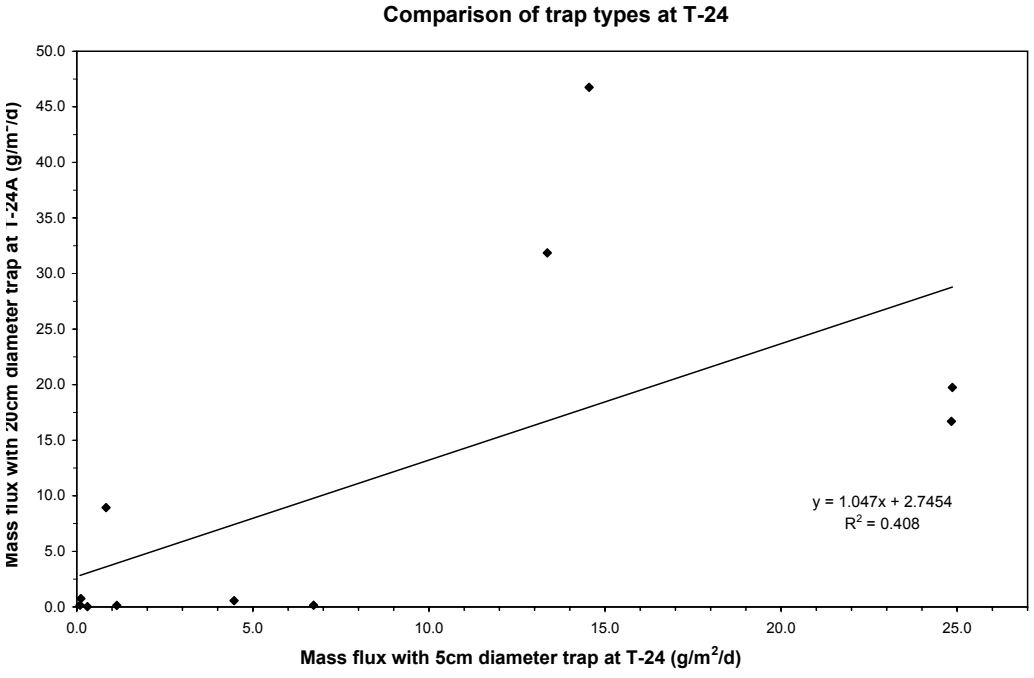

Figure D.28 Comparisons of the data between the 5 cm and the 20 cm diameter duplicate traps (trap locations T24 and T24A).

BIBLIOGRAPHY

1. G. Abraham. Discussion of "Modeling Turbulent Transport in Stratified Estuary" by Siegfried Bloss, Rainer Lehfeldt and John C. Patterson (September, 1988). *Journal of Hydraulic Engineering*, ASCE, 116(11):1428–1429, Sept. 1990.
2. M. Abramowitz and I. A. Stegun. *Handbook of Mathematical Functions with Formulas, Graphs and Mathematical Tables*. Dover Publications, Inc., New York, NY, 1972. Pages 1046, ISBN 0-486-61272-4.
3. A. K. M. Q. Ahsan and A. F. Blumberg. Three-Dimensional Hydrothermal Model of Onondaga Lake, New York. *Journal of Hydraulic Engineering*, ASCE, 125(9):912–923, Sept. 1999.
4. D. G. Andrews and M. E. McIntyre. An Exact Theory of Nonlinear Waves on a Lagrangian-Mean Flow. *Journal of Fluid Mechanics*, 89:609–646, Dec. 1978a.
5. D. G. Andrews and M. E. McIntyre. On Wave-Action and its Relatives. *Journal of Fluid Mechanics*, 89:647–664, Dec. 1978b.
6. J. A. P. Aranha and M. R. Martins. Low Frequency Wave Force Spectrum Influenced by Wave-Current Interaction. *Applied Ocean Research*, 23:147–157, 2001.
7. F. Ardhuin and A. D. Jenkins. A Practical Three Dimensional Formalism for the Ocean, Coupling Random Waves, Mean Flow, and Turbulence. *Under consideration for publication in the Journal of Fluid Mechanics (Rejected)*, June 2006a. URL: http://arxiv.org/abs/physics/0504097v1.
8. F. Ardhuin and A. D. Jenkins. On the Interaction of Surface Waves and Upper Ocean Turbulence. *Journal of Physical Oceanography*, 36:551–557, Mar. 2006b.
9. F. Ardhuin, A. D. Jenkins, and B. Chapron. Waves and Operational Oceanography: Toward a Coherent Description of the Upper Ocean. *EOS (Transactions of the American Geophysical Society)*, 86(4), Jan. 2005.
10. F. Ardhuin, A. D. Jenkins, and K. A. Belibassakis. Commentary on 'The Three-Dimensional Current and Surface Wave Equations'. *Journal of Physical Oceanography*, 38:1340–1350, June 2008a.
11. F. Ardhuin, N. Rascle, and K. A. Belibassakis. Explicit wave-averaged primitive equations using a Generalized Lagrangian Mean. *Ocean Modelling*, 20(1):35–60, 2008b.
12. J. A. As-Salek and D. J. Schwab. High-Frequency Water Level Fluctuations in Lake Michigan. *Journal of Waterway, Port, Coastal, and Ocean Engineering*, 130(1):45–53, 2004.
13. ASCE Task Committee on Turbulence Models in Hydraulic Computation. Turbulence Modeling of Surface Water Flow and Transport: Part I. *Journal of Hydraulic Engineering*, ASCE, 114(9): 970–991, 1988a.

14. ASCE Task Committee on Turbulence Models in Hydraulic Computation. Turbulence Modeling of Surface Water Flow and Transport: Part II. *Journal of Hydraulic Engineering*, ASCE, 114(9): 992–1014, 1988b.

15. A. J. Bale. Sediment Trap Performance in Tidal Waters: Comparison of Cylindrical and Conical Collectors. *Continental Shelf Research*, 18:1401–1418, 1998.

16. H. Baumert and H. Peters. Second-Moment Closures and Length Scales for Weakly Stratified Turbulent Shear Flows. *Journal of Geophysical Research*, 105(C3):6453–6468, Mar. 2000.

17. H. Baumert, G. Chapalain, H. Smaoui, J. P. McManus, H. Yagi, M. Regener, J. Sündermann, and B. Szilagy. Modelling and Numerical Simulation of Turbulence Waves and Suspended Sediments for Pre-Operational Use in Coastal Seas. *Coastal Engineering*, 41:63–93, 2000.

18. K. Bedford and M. Abdelrhman. Analytical and Experimental Studies of the Benthic Boundary Layer and Their Applicability to Near-Bottom Transport in Lake Erie. *Journal of Great Lakes Research*, 13(4):628–648, 1987.

19. K. W. Bedford. Diffusion, Dispersion and Sub-Grid Parameterization. In M. B. Abbott and W. A. Price, editors, *Coastal Estuarial and Harbour Engineer's Reference Book*, pages 61–81. E & FN SPON An Imprint of Chapman & Hall, Chapman & Hall Inc., One Penn Plaza, 41st Floor, New York, NY 10119, 1994. ISBN 0-419-15430-2.

20. K. W. Bedford, P. Velissariou, V. Velissariou, and Y. Guo. Integrated Analysis of the Impact of Unconfined Placement Activities in Near-Shore Sensitive Areas. Technical Report 3, US Army Corps of Engineers, Waterways Experiment Station, Vicksburg, MS, Sept. 1999.

21. D. Beletsky and D. J. Schwab. Modeling Circulation and Thermal Structure in Lake Michigan: Annual Cycle and Interannual Variability. *Journal of Geophysical Research*, 106(C9):19745–19771, 2001.

22. A. Y. Benilov and L. N. Ly. Modelling of Surface Waves Breaking Effects in the Ocean Upper Layer. *Mathematical and Computer Modelling*, 35:191–213, 2002.

23. S. Bloss, R. Lehfeldt, and J. C. Patterson. Modeling Turbulent Transport in Stratified Estuary. *Journal of Hydraulic Engineering*, ASCE, 114(9):1115–1133, Sept. 1988.

24. S. Bloss, R. Lehfeldt, and J. C. Patterson. Closure to "Modeling Turbulent Transport in Stratified Estuary" by Siegfried Bloss, Rainer Lehfeldt and John C. Patterson (September, 1988). *Journal of Hydraulic Engineering*, ASCE, 116(11):1430, Sept. 1990.

25. A. F. Blumberg and G. L. Mellor. A Description of a Three-Dimensional Coastal Ocean Circulation Model. In N. S. Heaps, editor, *Three-dimensional Coastal Ocean Models*, Coastal and Estuarine Sciences 4, pages 1–16. American Geophysical Union, 1987.

26. N. Booij, I. G. Haagsma, A. T. M. M. Kieftenburg, and L. H. Holthuijsen. *SWAN Cycle III Version 40.41: Implementation Manual*. Delft University of Technology, Department of Civil Engineering, P.O. Box 5048, 2600 GA Delft, The Netherlands, Oct. 2004. URL: http://www.fluidmechanics.tudelft.nl/.

27. B. P. Boudreau and B. B. Jørgensen, editors. *The Benthic Boundary Layer. Transport Processes and Biochemistry*. Oxford University Press, New York, NY, 2001. Pages 404, ISBN 0-19-511881-2.

28. E. Bouws, H. Günther, W. Rosenthal, and C. L. Vincent. Similarity of the Wind Wave Spectrum in Finite Depth Water. 1. Spectral Form. *Journal of Geophysical Research*, 90(C1):975–986, Jan. 1985.

29. E. Bouws, H. Günther, W. Rosenthal, and C. L. Vincent. Similarity of the Wind Wave Spectrum in Finite Depth Water. 1. Statistical Relations between Shape and Growth Stage Parameters. *Deutsche Hydrographische Zeitschrift*, 40(H1):1–24, Jan. 1987.

30. W. Brutsaert. *Evaporation Into the Atmosphere. Theory, History and Applications*. D. Reidel Publishing Company, P.O. Box 17, 3300 AA, Dordrecht, Holland, 1982. ISBN 90-277-1274-6.

31. K. Bryan and M. D. Cox. An Approximate Equation of State for Numerical Models of Ocean Circulation. *Journal of Physical Oceanography*, 2:510–514, 1972.

32. H. L. Bryden. New Polynomials for Thermal Expansion, Adiabatic Temperature Gradient and Potential Temperature of Sea Water. *Deep Sea Research*, 20:401–408, 1973.

33. H. Burchard. Simulating the Wave-Enhanced Layer Under Breaking Surface Waves With Two-Equation Turbulence Models. *Journal of Physical Oceanography*, 31:3133–3145, Nov. 2001.

34. H. Burchard. *Applied Turbulence Modelling in Marine Waters*. Lecture Notes in Earth Sciences. Springer-Verlag, Berlin, Germany, 2002. Pages 215, ISBN 3-540-43795-9.

35. H. Burchard and H. Baumert. On the Performance of a Mixed-Layer Model Based on the κ-ϵ Turbulence Closure. *Journal of Geophysical Research*, 100(C5):8523–8540, May 1995.

36. J. A. Businger, J. C. Wyngaard, Y. Izumi, and E. F. Brandley. Flux-Profile Relationships in the Atmospheric Surface Layer. *Journal of Atmospheric Sciences*, 28:181–189, Mar. 1971.

37. S. Carniel, M. Sclavo, L. H. Kantha, and C. A. Clayson. Langmuir Cells and Mixing in the Upper Ocean. *Il Nuovo Cimento*, 28(C):33–54, 2005.

38. CEM II. *Coastal Engineering Manual. Part II: Coastal Hydrodynamics*. U.S. Army Corps of Engineers, Washington, DC 20314-1000, June 2006. Pages 528, URL: http://chl.erdc.usace.army.mil/chl.aspx?p=s&a=ARTICLES;104.

39. CEM III. *Coastal Engineering Manual. Part III: Coastal Sediment Processes*. U.S. Army Corps of Engineers, Washington, DC 20314-1000, June 2006. Pages 472, URL: http://chl.erdc.usace.army.mil/chl.aspx?p=s&a=ARTICLES;104.

40. R. S. Chapman, B. H. Johnson, and S. R. Vemulakonda. User's Guide for the Sigma Stretched Version of CH3D-WES; A Three-Dimensional Numerical Hydrodynamic, and Temperature Model. Technical Report HL-96-21, U.S.Army Engineer Waterways Experiment Station, Vicksburg, MS, Nov. 1996.

41. H. Charnock. Wind Stress on a Water Surface. *Q. J. R. Meteorological Society*, 81:639–640, 1955.

42. R. T. Cheng and P. E. Smith. A Survey of Three-Dimensional Numerical Estuarine Models. *Estuarine and Coastal Modeling*, 1:1–15, 1990.

43. Y. P. Chu, K. W. Bedford, C. J. Merry, and J. S. Hobgood. Impact of GOES Data on Surface Heat Flux Predictions. In G. V. Cotroneo and R. R. Rumer, editors, *Hydraulic Engineering '94, Proceedings of the Conference*, pages 212–216, Buffalo, NY, 1994. ASCE.

44. S. W. Churchill. A Reinterpretation of the Turbulent Prandtl Number. *Industrial & Engineering Chemistry Research*, 41:6393–6401, 2002.

45. T. M. Cole and S. A. Wells. *CE-QUAL-W2: A Two-Dimensional Laterally Averaged, Hydrodynamic and Water Quality Model, Version 3.2*. U.S. Army Corps of Engineers, Washington, DC, 20314-1000, 2005.

46. P. Craig. Modeling Turbulence Generation by Breaking Waves. In H. Z. Baumert, J. H. Simpson, and J. Sündermann, editors, *Marine Turbulence - Theories, Observations and Models*, pages 273–276. Cambridge University Press, New York, NY, 2005. ISBN 0-521-83789-8.

47. P. D. Craig. Velocity Profiles and Surface Roughness Under Breaking Waves. *Journal of Geophysical Research*, 101(C1):1265–1277, 1996.

48. P. D. Craig and M. L. Banner. Modeling Wave-Enhanced Turbulence in the Ocean Surface Layer. *Journal of Physical Oceanography*, 24:2546–2558, Dec. 1994.

49. A. D. D. Craik. *Wave Interactions and Fluid Flows*. Cambridge Monographs on Mechanics and Applied Mathematics. Cambridge University Press, New York, NY, 1988. Pages 322, ISBN 0-521-36829-4.

50. A. D. D. Craik and S. Leibovich. A Rational Model for Langmuir Circulations. *Journal of Fluid Mechanics*, 73:401–426, Feb. 1976.

51. W. R. Dally. Random Breaking Waves: a Closed-Form Solution for Planar Beaches. *Coastal Engineering*, 14:233–263, 1990.

52. A. G. Davies and C. Villaret. Eulerian Drift Induced by Progressive Waves Above Rippled and Very Rough Beds. *Journal of Geophysical Research*, 104(C1):1465–1488, 1999.

53. U. K. Deiters and K. M. D. Reuck. Guidelines for Publication of Equations of State–I. Pure Fluids. *Pure & Applied Chemistry*, 69(6):1237–1249, 1997.

54. J. C. Doering and M. A. Donelan. The Joint Distribution of Heights and Periods of Shoaling Waves. *Journal of Geophysical Research*, 98(C7):12543–12555, July 1993.

55. M. A. Donelan and W. J. Pierson, Jr. Radar Scattering and Equilibrium Ranges in Wind-Generated Waves With Application to Scatterometry. *Journal of Geophysical Research*, 92(C5):4971–5029, May 1987.

56. M. A. Donelan, J. Hamilton, and W. H. Hui. Direction Spectra of Wind-Generated Waves. *Phil. Trans. R. Soc. Lond.*, A 315:509–562, 1985.

57. J. A. Duffie and W. A. Beckman. *Solar Engineering of Thermal Processes*. John Wiley & Sons, New York, 1980. ISBN 0-471-05066-0.

58. A. J. Dyer. A Review of Flux-Profile Relationships. *Boundary-Layer Meteorology*, 7:363–372, 1974.

59. B. Eadie, D. Schwab, V. Klump, and W. Gardner. The Impact of Episodic Events on the Nearshore-Offshore Transport and Transformation of Biogeochemically Important Materials in the Great Lakes. EEGLE: Episodic Events — Great Lakes Experiment. Program Summary, Sept. 2000b.

60. B. J. Eadie. Probing Particle Processes in Lake Michigan Using Sediment Traps. *Water, Air and Soil Pollution*, 99:133–139, 1997.

61. B. J. Eadie and S. Lozano. Grain Size Distribution of the Surface Sediments Collected During the Lake Michigan Mass Balance and Environmental Mapping and Assessment Programs. NOAA Technical Memorandum ERL GLERL-111, Great Lakes Environmental Research Laboratory, Ann Arbor, MI 48105, May 1999.

62. B. J. Eadie, R. L. Chambers, W. S. Gardner, and G. L. Bell. Sediment Trap Studies in Lake Michigan: Resuspension and Chemical Fluxes in the Southern Basin. *Journal of Great Lakes Research*, 10(3):307–321, 1984.

63. B. J. Eadie, G. L. Bell, and N. Hawley. Mass and Organic Carbon Fluxes, Resuspension, and Particle Settling Velocities. NOAA Technical Memorandum, Great Lakes Environmental Research Laboratory, Ann Arbor, MI 48105, July 1991.

64. B. J. Eadie, G. S. Miller, M. B. Lansing, and A. G. Winkelman. Settling Particle Fluxes and Current and Temperature Profiles in Grand Traverse Bay, Lake Michigan. NOAA Technical Memorandum ERL GLERL-116, Great Lakes Environmental Research Laboratory, Ann Arbor, MI 48105, Feb. 2000a.

65. C. Eckart. Properties of Water, Part II. The Equation of State of Water and Sea Water at Low Temperatures and Pressures. *American Journal of Science*, 256:225–240, 1958.

66. F. Einaudi and J. J. Finnigan. Wave-Turbulence Dynamics in the Stably-Stratified Boundary Layer. *Journal of the Atmospheric Sciences*, 50(13):1841–1864, July 1993.

67. S. Elgar, T. H. C. Herbers, V. Chandran, and R. T. Guza. Higher-Order Spectral Analysis of Nonlinear Ocean Surface Gravity Waves. *Journal of Geophysical Research*, 100(C3):4977–4983, Mar. 1995.

68. I. N. Esau and A. A. Grachev. Turbulent Prandtl Number in Stably Stratified Atmospheric Boundary Layer: Intercomparison between LES and SHEBA Data. *e-Windeng Journal*, pages 1–45, 2007. http://ejournal.windeng.net/, ISSN 1901-9181.

69. M. S. Evans, B. J. Eadie, and R. M. Glover. Sediment Trap Studies in Southern Lake Michigan: Fecal Pellet Express or the More Travelled Route. *Journal of Great Lakes Research*, 24(3):555–568, 1998.

70. B. Faugeras, M. Levy, L. Memery, J. Verron, J. Blum, and I. Charpentier. Can Biogeochemical Fluxes be Recovered From Nitrate and Chlorophyll data? A Case Study Assimilating Data in the Northwestern Mediterranean Sea at the JGOFS-DYFAMED Station. *J. Mar. Sys.*, 99(125):40–41, 2003.

71. F. Feddersen. Effect of Wave Directional Spread on the Radiation Stress: Comparing Theory and Observations. *Coastal Engineering*, 51:473–481, 2004.

72. R. Feistel. A New Extended Gibbs Thermodynamic Potential of Seawater. *Progress in Oceanography*, 58:43–114, 2003.

73. J. J. Finnigan and F. Einaudi. The Interaction Between an Internal Gravity Wave and the Planetary Boundary Layer. Part II: Effect of the Wave on the Turbulence Structure. *Quarterly Journal of the Royal Meteorological Society*, 107:807–832, 1981.

74. J. J. Finnigan, F. Einaudi, and D. Fuà. The Interaction Between an Internal Gravity Wave and Turbulence in the Stably-Stratified Nocturnal Boundary Layer. *Journal of the Atmospheric Sciences*, 41(16):2409–2436, Aug. 1984.

75. FMH 1. Federal Meteorological Handbook No. 1: Surface Weather Observations and Reports. Technical Report FCM-H1-2005, US Department of Commerce/National Oceanic and Atmospheric Administration, Washington, D.C., Sept. 2005.

76. N. P. Fofonoff and R. C. Millard. Algorithms for Computation of Fundamental Properties of Seawater. *Unesco Technical Papers in Marine Science 44*, 1983. Pages 54.

77. N. P. Fofonoff and R. C. Millard, Jr. Calculation of Physical Properties of Seawater. WHP Operations and Methods Manual. WOCE Reports 68/91, Woods Hole Oceanographic Institution, Woods Hole, Massachusetts, 02543, U.S.A, 1990. Unpublished Manuscript.

78. W. T. Fox and R. A. Davis, Jr. Simulation Model for Storm Cycles and Beach Erosion on Lake Michigan. *Geological Society of America Bulletin*, 84:1769–1790, 1973.

79. W. Fulks. *Advanced Calculus. An Introduction to Analysis*. John Wiley & Sons, Inc., New York, NY, 3rd edition, 1978. Pages 731, ISBN 0-471-02195-4.

80. W. D. Gardner. Sediment Trap Dynamics and Calibration: a Laboratory Evaluation. *Journal of Marine Research*, 38(1):17–39, 1980.

81. E. Garnier, B. Barnier, L. Siefridt, and K. Béranger. Investigating the 15 Years Air-Sea Flux Climatology From the ECMWF Re-Analysis Project as a Surface Boundary Condition for Ocean Models. *International Journal of Climatology*, 20:1653–1673, 2000.

82. C. Garrett and J. Smith. On the Interaction Between Long and Short Surface Waves. *Journal of Physical Oceanography*, 6:925–930, Nov. 1976.

83. S. M. Glenn. *A Continental Shelf Bottom Boundary Layer Model: The Effects of Waves, Currents and a Movable Bed*. PhD thesis, Woods Hole Oceanographic Institution, Woods Hole, Massachusetts, 02543, Feb. 1987.

84. S. M. Glenn and W. D. Grant. A Suspended Sediment Stratification Correction for Combined Wave and Current Flows. *Journal of Geophysical Research*, 92(C8):8244–8264, July 1987.

85. M. Gonzalez, R. Medina, and M. A. Losanda. Equilibrium Beach Profile Model for Perched Beaches. *Coastal Engineering*, 36:343–357, 1999.

86. A. A. Grachev, E. L. Andreas, C. W. Fairall, P. S. Guest, and P. O. G. Persson. On the Turbulent Prandtl Number in the Stable Atmospheric Boundary Layer. *Boundary-Layer Meteorology*, 125: 329–341, 2007.

87. M. Graco, D. Gutierrez, and L. Farias. Inter-Annual Variability of the Pelagic-Benthic Coupling in the Upwelling System off Central Chile. *Advances in Geosciences*, 6:127–132, 2006.

88. W. D. Grant and O. S. Madsen. Combined Wave and Current Interaction With a Rough Bottom. *Journal of Geophysical Research*, 84(C4):1797–1808, Apr. 1979.

89. W. D. Grant and O. S. Madsen. Movable Bed Roughness in Unsteady Oscillatory Flow. *Journal of Geophysical Research*, 87(C1):469–481, Jan. 1982.

90. W. D. Grant and O. S. Madsen. The Continental-Shelf Bottom Boundary Layer. *Annual Review of Fluid Mechanics*, 18:265–305, Jan. 1986.

91. J. Groeneweg and G. Klopman. Changes of the Mean Velocity Profiles in the Combined Wave-Current Motion Described in a GLM Formulation. *Journal of Fluid Mechanics*, 370:271–296, Sept. 1998.

92. H. Günther, S. Hasselmann, and P. A. E. M. Janssen. *Report No. 4: The WAM Model Cycle 4*. Max-Planck Instituut für Meteorologie, Hamburg, Germany, Oct. 1992. URL: http://www.mad.zmaw.de/fileadmin/extern/documents/reports/ReportNo.04.pdf.

93. S. K. Gupta, D. P. Kratz, P. W. Stackhouse, Jr., and A. C. Wilber. The Langley Parameterized Shortwave Algorithm (LPSA) for Surface Radiation Budget Studies. Technical report, National Aeronautics and Space Administration, Langley Research Center, Hampton, Virginia 23681-2199, Dec. 2001. NASA/TP-2001-211272.

94. H. Hanson. Genesis — A Generalized Shoreline Change Numerical Model. *Journal of Coastal Research*, 5(1):1–27, 1989.

95. J. L. Hanson and O. M. Phillips. Automated Analysis of Ocean Surface Directional Wave Spectra. *Journal of Atmospheric and Oceanic Technology*, 18:277–293, Feb. 2001.

96. T. H. C. Herbers and M. C. Burton. Nonlinear Shoaling of Directionally Spread Waves on a Beach. *Journal of Geophysical Research*, 102(C9):21101–21114, Sept. 1997.

97. A. Herman. Sampling Characteristics of Vertical Towed Plankton Nets and Intercomparison With an Optical Plankton Counter. *Journal of Plankton Research*, 2000. Under Review.

98. G. W. Hung and Y.-C. Chung. Particulate fluxes, ^{210}Pb and ^{210}Po Measured From Sediment Trap Samples in a Canyon off Northeastern Taiwan. *Continental Shelf Research*, 18:1475–1491, 1998.

99. A. K. M. F. Hussain and W. C. Reynolds. The Mechanics of an Organized Wave in Turbulent Shear Flow. *Journal of Fluid Mechanics*, 41:241–258, 1970.

100. A. K. M. F. Hussain and W. C. Reynolds. The Mechanics of an Organized Wave in Turbulent Shear Flow. Part 2. Experimental Results. *Journal of Fluid Mechanics*, 54:241–261, 1972.

101. V. Ittekkot, P. Schäfer, S. Honjo, and P. J. Depetris. *Particle Flux in the Ocean*. John Wiley & Sons, 1996. Pages 372, ISBN 0-471-96073-X.

102. A. Ivanoff. Oceanic Absorption of Solar Energy. In E. B. Kraus, editor, *Modelling and Prediction of the Upper Layers of the Ocean*, pages 47–71, Oxford 0X3 0BW, England, 1977. Pergamon Press. ISBN 0-08-020611-5.

103. G. N. Ivey, K. B. Winters, and J. R. Koseff. Density Stratification, Turbulence, but How Much Mixing? *Annual Review of Fluid Mechanics*, 40:169–184, 2008.

104. P. Janssen. *The Interaction of Ocean Waves and Wind*. Cambridge University Press, New York, NY, 2004. Pages 300, ISBN 0-521-46540-0.

105. P. A. E. M. Janssen. Quasi-Linear Theory of Wind-Wave Generation Applied to Wave Forecasting. *Journal of Physical Oceanography*, 21:1631–1642, 1991.

106. P. A. E. M. Janssen. Progress in Ocean Wave Forecasting. *Journal of Computational Physics*, 227: 3572–3594, 2008.

107. B. H. Johnson, K. W. Kim, Y. P. Sheng, and R. E. Heath. Development of a Three-Dimensional Hydrodynamic Model of Chesapeake Bay. *Estuarine and Coastal Modeling*, 1:162–171, 1990.

108. N. L. Jones and S. G. Monismith. The Influence of Whitecapping Waves on the Vertical Structure of Turbulence in a Shallow Estuarine Embayment. *Journal of Physical Oceanography*, 38:1563–1580, July 2008.

109. S. A. Josey, E. C. Kent, and P. K. Taylor. New Insights Into the Ocean Heat Budget Closure Problem from Analysis of the SOC Air-Sea Flux Climatology. *Journal of Climate*, 12:2856–2880, Sept. 1999.

110. L. H. Kantha and C. A. Clayson. On the Effect of Surface Gravity Waves on Mixing in the Oceanic Mixed Layer. *Ocean Modelling*, 6:101–124, 2004.

111. B. Kinsman. *Wind Waves. Their Generation and Propagation on the Ocean Surface*. Dover Publications, Inc., New York, NY, 1984. Pages 676, ISBN 0-486-64652-1.

112. J. T. Kirby and T.-M. Chen. Surface Waves on Vertically Sheared Flows: Approximate Dispersion Relations. *Journal of Geophysical Research*, 94(C1):1013–1027, Jan. 1989.

113. G. J. Komen, L. Cavaleri, M. Donelan, K. Hasselmann, S. Hasselmann, and P. A. E. M. Janssen. *Dynamics and Modelling of Ocean Waves*. Cambridge University Press, New York, NY, 1996. Pages 532, ISBN 0-521-57781-0.

114. D. Kruger, T. Ezer, A. M. Pence, and A. F. Blumberg. On the Computational Efficiency of Ocean Models: A High Performance Equation of State. *Submitted to: Journal of Atmospheric and Oceanic Technology*, 2005.

115. E. M. Lane, J. M. Restrepo, and J. C. McWilliams. Wave-Current Interaction: A Comparison of Radiation-Stress and Vortex-Force Representations. *Submitted in the Journal of Fluid Mechanics*, 2005.

116. G. Lang, R. Schubert, M. Markofsky, H.-U. Fanger, I. Grabemann, H. L. Krasemann, L. J. R. Neumann, and R. Riethmoller. Data Interpretation and Numerical Modeling of the Mud and Suspended Sediment Experiment 1985. *Journal of Geophysical Research*, 94(C10):14381–14393, Oct. 1989.

117. W. G. Large and P. R. Gent. Validation of Vertical Mixing in an Equatorial Ocean Model Using Large Eddy Simulations and Observations. *Journal of Physical Oceanography*, 29:449–464, Mar. 1999.

118. W. G. Large, J. C. McWilliams, and S. C. Doney. Oceanic Vertical Mixing: A Review ans a Model With a Nonlocal Boundary Layer Parameterization. *Reviews in Geophysics*, 32(4):363–403, Nov. 1994.

119. M. Larson. Model of Beach Profile Change Under Random Waves. *Journal of Waterway, Port, Coastal, and Ocean Engineering*, 122(4):172–181, 1996.

120. M. Larson and N. C. Kraus. Mathematical Modeling of the Fate of Beach fill. *Coastal Engineering*, 16:83–114, 1991.

121. M. Larson and N. C. Kraus. Temporal and Spatial Scales of Beach Profile Change, Duck, North Carolina. *Geology*, 117:75–94, 1994.

122. I. V. Lavrenov. *Wind-Waves in Ocean*. Springer-Verlag, New York, NY, 2003. Pages 376, ISBN 3-540-44015-1.

123. P. H. LeBlond and L. A. Mysak. *Waves in the Ocean*. Elsevier Oceanographic Series. Elsevier Scientific Publishing Company, 1978. Pages 602, ISBN 0-444-41926-8.

124. P. H. LeBlond and L. A. Mysak. Ocean Waves: A Survey of Some Recent Results. *Siam Review*, 21(3):289–328, July 1979.

125. B. Leonard. A Stable and Accurate Convection Modelling Procedure Based on Quadratic Upstream Interpolation. *Computer Methods in Applied Mechanics and Engineering*, 19:59–98, 1979.

126. I. O. Leont'ev. Numerical Modelling of Beach Erosion During Storm Event. *Coastal Engineering*, 29:187–200, 1996.

127. I. O. Leont'ev. Modelling of Morphological Changes due to Coastal Structures. *Coastal Engineering*, 38:143–166, 1999.

128. P. Lin and D. Zhang. The Depth-Dependent Radiation Stresses and Their Effect on Coastal Currents. In Cheng and Yeow, editors, *Hydrodynamics VI - Theory and Applications*, pages 247–253. Taylor & Francis Group, London, 2005. ISBN 04-1536-304-7.

129. R. K. Linsley, Jr., M. A. Kohler, and J. L. H. Paulhus. *Hydrology for Engineers*. McGraw Hill Book Company, New York, N.Y., 1982. Pages 508, ISBN 0-07-037956-4.

130. P. Liu and D. Schwab. A Comparison of Methods for Estimating u_* From Given u_z and Air-Sea Temperature Differences. *Journal of Geophysical Research*, 92(C6):6488–6494, 1987.

131. P. E. Long, Jr. GUST: A General Unified Similarity Theory for the Calculation of Turbulent Fluxes in Numerical Weather Prediction Models for Unstable Conditions. Office Note 302, U.S. Department of Commerce, NOAA, National Weather Service, National Meteorological Center, Jan. 1984. Pages 30, URL: http://www.ncep.noaa.gov/officenotes/.

132. P. E. Long, Jr. Derivation and Suggested Method of the Application of Simplified Relations for Surface Fluxes in the Medium Range Forecast Model: Unstable Case. Office Note 356, U.S. Department of Commerce, NOAA, National Weather Service, National Meteorological Center, Mar. 1990. Pages 53, URL: http://www.ncep.noaa.gov/officenotes/.

133. P. E. Long, Jr. and W. A. Shaffer. Some Physical and Numerical Aspects of Boundary Layer Modeling. NOAA Technical Memo NWS TDL-56 (COM75-10980), U.S. Department of Commerce,

NOAA, National Weather Service, National Meteorological Center, 1975. Pages 37.

134. M. S. Longuet-Higgins. Longshore Currents Generated by Obliquely Incident Sea Waves, 1. *Journal of Geophysical Research*, 75(33):6778–6789, Nov. 1970a.

135. M. S. Longuet-Higgins. Longshore Currents Generated by Obliquely Incident Sea Waves, 2. *Journal of Geophysical Research*, 75(33):6790–6801, Nov. 1970b.

136. M. S. Longuet-Higgins and R. W. Stewart. Radiation Stress in Water Waves; a Physical Discussion, With Applications. *Deep Sea Research*, 11:529–562, 1964.

137. J. L. Lumley. Two-Phase and non-Newtonian Flows. In P. Bradshaw, editor, *Topics in Applied Physics*, volume 12, chapter 7. Springer, 1976.

138. J. H. MacMahan, A. J. H. M. Reniers, E. B. Thornton, and T. P. Stanton. Surf Zone Eddies Coupled with Rip Current Morphology. *Journal of Geophysical Research*, 109(C07004):1–15, 2004a.

139. J. H. MacMahan, A. J. H. M. Reniers, E. B. Thornton, and T. P. Stanton. Infragravity Rip Current Pulsations. *Journal of Geophysical Research*, 109(C01033):1–9, 2004b.

140. O. S. Madsen. Spectral Wave-Current Bottom Boundary Layer Flows. In *Proceedings of the 24th International Conference on Coastal Engineering*, volume I, pages 384–398. American Society of Civil Engineers, New York, 1994.

141. O. S. Madsen and P. Salles. Eddy Viscosity Models for Wave Boundary Layers. In *Proceedings of the 26th International Conference on Coastal Engineering*, pages 2615–2627. American Society of Civil Engineers, New York, 1999.

142. O. S. Madsen, Y. K. Poon, and H. C. Graber. Spectral Wave Attenuation by Bottom Friction: Theory. In *21th International Conference in Coastal Engineering*, pages 492–504. ASCE, 1988. ISBN 0-87262-559-0.

143. J. C. Makarewicz, T. Lewis, and P. Bertram. Epilimnetic Phytoplankton and Zooplankton Biomass and Species Composition in Lake Michigan, 1983 to 1992. Technical report, U.S. Environmental Protection Agency, Great Lakes National Program Office, Oct. 1994.

144. F. Marin. Eddy Viscosity and Eulerian Drift Over Rippled Beds in Waves. *Coastal Engineering*, 50:139–159, 2004.

145. G. Masselink and A. D. Short. The Effect of Tide Range on Beach Morphodynamics and Morphology: A Conceptual Beach Model. *Journal of Coastal Research*, 9(3):785–800, 1993.

146. C. Mastenbroek, G. Burgers, and P. A. E. M. Janssen. The Dynamical Coupling of a Wave Model and a Storm Surge Model through the Atmospheric Boundary Layer. *Journal of Physical Oceanography*, 23:1856–1866, Aug. 1993.

147. P. P. Mathisen and O. S. Madsen. Waves and Currents Over a Fixed Rippled Bed: 1. Bottom Roughness Experienced by Waves in the Presence and Absence of Currents. *Journal of Geophysical Research*, 101(C7):16533–16542, 1996a.

148. P. P. Mathisen and O. S. Madsen. Waves and Currents Over a Fixed Rippled Bed: 2. Bottom and Apparent Roughness Experienced by Currents in the Presence of Waves. *Journal of Geophysical Research*, 101(C7):16543–16550, 1996b.

149. P. P. Mathisen and O. S. Madsen. Waves and Currents Over a Fixed Rippled Bed: 3. Bottom and Apparent Roughness for Spectral Waves. *Journal of Geophysical Research*, 104(C8):18447–18461, Aug. 1999.

150. M. J. McCormick and D. C. L. Lam. Lake Thermodynamics. In D. C. L. Lam and W. M. Schertzer, editors, *Potential Climate Change Effects on Great Lakes Hydrodynamics and Water Quality*, chapter 3, pages 1–20. American Society of Civil Engineers, 1801 Alexander Bell Drive, Reston, Virginia, 20191-4400, 1999. ISBN 0-7844-0413-5.

151. M. J. McCormick and G. A. Meadows. An Intercomparison of Four Mixed Layer Models in a Shallow Inland Sea. *Journal of Geophysical Research*, 93(C6):6774–6788, 1988.

152. T. J. McDougall and D. R. Jackett. Accurate and Computationally Efficient Algorithms for Potential Temperature and Density of Seawater. *Journal of Atmospheric and Oceanic Technology*, 20:730–741, 2003.

153. J. C. McWilliams, J. M. Restrepo, and E. M. Lane. An Asymptotic Theory for the Interaction of Waves and Currents in Coastal Waters. *Journal of Fluid Mechanics*, 511:135–178, July 2004.

154. C. C. Mei. *The Applied Dynamics of Ocean Surface Waves*. John Wiley & Sons, New York, N.Y., 1983. Pages 740, ISBN 0-471-06407-6.

155. G. Mellor. Oscillatory Bottom Boundary Layers. *Journal of Physical Oceanography*, 32:3075–3088, 2002.

156. G. Mellor and A. Blumberg. Wave Breaking and Ocean Surface Layer Thermal Response. *Journal of Physical Oceanography*, 34:693–698, Mar. 2004.

157. G. L. Mellor. Some Consequences of the Three-Dimensional Current and Surface Wave Equations. *Journal of Physical Oceanography*, 35(11):2291–2298, Nov. 2005.

158. G. L. Mellor. The Depth Dependent Current and Wave Interaction Equations; a Revision. *Journal of Physical Oceanography*, 38(11):2587–2596, Nov. 2008.

159. G. L. Mellor. *User's Guide for A Three-dimensional, Primitive Equation, Numerical Ocean Model*. Program in Atmospheric and Ocean Sciences, Princeton University, Princeton, NJ, 08544-0710, 1998.

160. G. L. Mellor. An Equation of State for Numerical Models of Oceans and Estuaries. *Journal of Atmospheric and Oceanic Technology*, 8:609–611, 1991.

161. G. L. Mellor. The Three-Dimensional Current and Surface Wave Equations. *Journal of Physical Oceanography*, 33:1978–1989, Sept. 2003.

162. G. L. Mellor and T. Yamada. Development of a Turbulence Closure Model for Geophysical Fluid Problems. *Reviews of Geophysics and Space Physics*, 20(4):851–875, 1982.

163. G. L. Mellor, M. A. Donelan, and L.-Y. Oey. A Surface Wave Model for Coupling with Numerical Ocean Circulation Models. *Journal of Atmospheric and Oceanic Technology*, 25(10):1785–1807, Oct. 2008.

164. J. J. Michalsky. The Astronomical Almanac's Algorithm for Approximate Solar Position (1950-2050). *Solar Energy*, 40(3):227–235, 1988.

165. J. W. Miles. On the Generation of Surface Waves by Shear Wind. *Journal of Fluid Mechanics*, 3: 185–204, 1957.

166. R. C. Millard. International Oceanographic Tables. *Unesco Technical Papers in Marine Science 40*, 1987. Pages 196.

167. S. Miller, P. Mupparapu, W. S. Brown, and F. L. Bub. Convex Air-Sea Heat Flux Calculations. Technical report, Ocean Process Analysis Laboratory, Institute for the Study of Earth, Oceans and Space. Department of Earth Sciences, University of New Hampshire, Sept. 1999. Technical Report UNH-OPAL-1999-004.

168. F. J. Millero. Seawater as a Multicomponent Electrolyte Solution. In E. D. Goldberg, editor, *The Sea. Ideas and Observations on Progress in the Study of the Sea*, volume 5, pages 3–80. John Wiley & Sons, New York, 1974.

169. O. Mohseni and H. G. Stefan. Stream Temperature/Air Temperature Relationship: A Physical Interpretation. *Journal of Hydrology*, 218:128–141, 1999.

170. T. J. Monteith and W. C. Sonzogni. U.S. Great Lakes Shoreline Erosion Loadings. Technical report, U.S. Environmental Protection Agency, Region 5, Library (PL-12J) 77 West Jackson Boulevard, 12th Floor, Chicago, IL 60604-3590, Dec. 1976.

171. I.-J. Moon. Impact of a Coupled Ocean Wave-Tide-Circulation System on Coastal Modeling. *Ocean Modelling*, 8:203–236, 2005.

172. Moored Arrays Workgroup. EEGLE Workshop. Miscellaneous report, GLERL/NOAA, Aug. 1997. www.glerl.noaa.gov/eegle/workshops/milwaukee97/reports/moored.html.

173. C. H. Mortimer. Discoveries and Testable Hypotheses Arising From Coastal Zone Color Scanner Imagery of Southern Lake Michigan. *Limnology and Oceanography*, 33:203–226, 1988.

174. W. H. Munk and E. R. Anderson. Notes on a Theory of the Thermocline. *Journal of Marine Research*, 7(3):276–295, 1948.

175. M. Nakanishi. Improvement of the Mellor-Yamada Turbulence Closure Model Based on Large-Eddy Simulation Data. *Boundary Layer Meteorology*, 99:349–378, 2001.

176. K. H. Nicholls. Nutrient-Phytoplankton Relationships in the Holland Marsh, Ontario. *Ecological Monographs*, 46(2):179–199, 1976.

177. R. A. Nunes Vaz and J. H. Simpson. Turbulence Closure Modeling of Estuarine Stratification. *Journal of Geophysical Research*, 99(C8):16143–16160, Aug. 1994.

178. M. Onorato, A. Osborne, R. Fedele, and M. Serio. Landau Damping and Coherent Structures in Narrow-Banded 1+1 Deep Water Gravity Waves. *Physical Review E*, 67(046305):1–6, 2003.

179. R. Ostrowski. A Quasi Phase-Resolving Model of Net Sand Transport and Short-Term Cross-Shore Profile Evolution. *Oceanologia*, 45(1):261–282, 2003.

180. P. Osuna and J. Monbaliu. Wave-Current Interaction in the Southern North Sea. *Journal of Marine Systems*, 52:65–87, 2004.

181. R. C. Pacanowski and S. M. Griffies. *MOM 3.0 Manual*. GFDL/NOAA Department of Commerce, Princeton Forrestal Campus, 201 Forrestal Road, Princeton, N.J. 08450, Mar. 2000. URL: http://www.gfdl.noaa.gov/~smg/MOM/MOM.html.

182. R. C. Pacanowski and S. G. H. Philander. Parameterization of Vertical Mixing in Numerical Models of Tropical Oceans. *Journal of Physical Oceanography*, 11:1443–1451, 1981.

183. G. W. Paltridge and C. M. R. Platt. *Radiative Processes in Meteorology and Climatology*. Elsevier Scientific Publishing Company, Amsterdam, 1976. ISBN 0-444-41444-4.

184. E. R. Pardyjak, P. Monti, and H. J. S. Fernando. Flux Richardson Number Measurements in Stable Atmospheric Shear Flows. *Journal of Fluid Mechanics*, 459:307–316, May 2002.

185. T. R. Parsons, M. Takahashi, and B. Hargrave. *Biological Oceanographic Processes*. Pergamon Press, 3rd edition, 1984. Pages 330, ISBN 0-08-030766-3.

186. C. A. Paulson. The Mathematical Representation of Wind Speed and Temperature Profiles in the Unstable Atmospheric Surface Layer. *Journal of Applied Meteorology*, 9:857–861, Dec. 1970.

187. H. Peters and H. Baumert. Validating a Turbulence Closure Against Estuarine Microstructure Measurements. *Ocean Modelling*, 19:183–203, 2007.

188. O. M. Phillips. On the Generation of Waves by Turbulent Wind. *Journal of Fluid Mechanics*, 2: 417–445, 1957.

189. O. M. Phillips. *The Dynamics of the Upper Ocean*. Monographs on Mechanics & Applied Mathematics. Cambridge University Press, New York, NY, 2nd edition, 1977. Pages 336, ISBN 0-521-21421-1.

190. W. J. Pierson and L. Moskowitz. A Proposed Spectral Form for Fully Developed Wind Seas Based on the Similarity Theory of S. A. Kitaigorodskii. *Journal of Geophysical Research*, 69(24):5181–5190, 1964.

191. M. B. Priestley. *Spectral Analysis and Time Series*. A Series of Monographs and Textbooks. Academic Press Inc., Academic Press Inc., San Diego, CA 92101, 1994. Pages 890, ISBN 0-12-564922-3.

192. J. A. Puleo, O. Mouraenko, and D. M. Hanes. One-Dimensional Wave Bottom Boundary Layer Model Comparison: Specific Eddy Viscosity and Turbulence Closure Models. *Journal of Waterway, Port, Coastal, and Ocean Engineering*, 130(6):322–325, 2004.

193. I. Reda and A. Andreas. Solar Position Algorithm for Solar Radiation Applications. Technical report, National Renewable Energy Laboratory, 1617 Cole Boulevard, Golden, Colorado 80401-3393, 2004. Technical Report NREL/TP-560-34302.

194. A. J. H. M. Reniers, A. R. V. Dongeren, J. A. Battjes, and E. B. Thornton. Linear Modeling of Infragravity Waves During Delilah. *Journal of Geophysical Research*, 107(C10):1–1–1–18, 2002.

195. A. J. H. M. Reniers, J. A. Roelvink, and E. B. Thornton. Morphodynamic Modeling of an Embayed Beach Under Wave Group Forcing. *Journal of Geophysical Research*, 109(C01030):1–22, 2004.

196. W. C. Reynolds and A. K. M. F. Hussain. The Mechanics of an Organized Wave in Turbulent Shear Flow. Part 3. Theoretical Models and Comparisons with Experiments. *Journal of Fluid Mechanics*,

54:263–288, 1972.

197. J. P. Riley and G. Skirrow, editors. *Chemical Oceanography*, volume 4, page 338. Academic Press, 2nd edition, 1974.

198. P. J. Roache. *Computational Fluid Dynamics*. Hermosa Publishers, Albuquerque, N.M, 1972. Pages 434, ISBN 0-913-47802-4.

199. W. Rodi. Elements of the Theory of Turbulence. In M. B. Abbott and W. A. Price, editors, *Coastal Estuarial and Harbour Engineer's Reference Book*, pages 45–59. E & FN SPON An Imprint of Chapman & Hall, Chapman & Hall Inc., One Penn Plaza, 41st Floor, New York, NY 10119, 1994. ISBN 0-419-15430-2.

200. W. E. Rogers and W. C. O'Reilly. Pacific Basin Wind-Wave Models: The Generation and Propagation of Low Frequency Energy. In B. L. Edge and J. M. Hemsley, editors, *Proceedings of the Fourth International Symposium Waves 2001*, volume 2, pages 934–943, San Francisco, California, 2002. ASCE. ISBN 0-7844-0604-9.

201. W. E. Rogers, J. M. Kaihatu, N. Booij, and L. Holthuijsen. Improving the Numerics of a Third-Generation Wave Action Model. NRL/FR/7320–99-9695, Naval Research Laboratory, U.S Navy, Washington, DC 20375-5320, Dec. 1999.

202. W. E. Rogers, J. M. Kaihatu, H. A. H. Petit, N. Booij, and L. H. Holthuijsen. Diffusion Reduction in an Arbitrary Scale Third Generation Wind Wave Model. *Ocean Engineering*, 29:1357–1390, 2002.

203. J. D. Rosati, K. J. Gingerich, N. C. Kraus, J. M. Smith, and R. Beach. Longshore Sand Transport Rate Distributions Measured in Lake Michigan. In *Coastal Sediments '91*, volume 1, pages 156–169. American Society of Civil Engineers, Committee on Coastal Engineering, 1991. ISBN 0-87262-808-6.

204. M. Sambridge, J. Braun, and H. McQueen. Geophysical Parameterization and Interpolation of Irregular Data Using Natural Neighbors. *Geophysical Journal International*, 122:837–857, 1995.

205. S. Sato and N. Mitsunobu. A Numerical Model of Beach Profile Change due to Random Waves. In *Coastal Sediments '91*, volume 1, pages 674–687. American Society of Civil Engineers, Committee on Coastal Engineering, 1991. ISBN 0-87262-808-6.

206. M. Sawicki. Myths about Gravity and Tides. *The Physics Teacher*, 37:438–441, 1999.

207. D. Scavia and G. L. Fahnenstiel. Dynamics of Lake Michigan Phytoplankton: Mechanisms Controlling Epilimnetic Communities. *Journal of Great Lakes Research*, 13(2):103–120, 1987.

208. U. Schumann and T. Gerz. Turbulent Mixing in Stably Stratified Shear Flows. *Journal of Applied Meteorology*, 34:33–47, Jan. 1995.

209. D. J. Schwab. Simulation and Forecasting of Lake Erie Storm Surges. *Monthly Weather Review*, 106:1476–1487, 1978.

210. D. J. Schwab and J. A. Morton. Estimation of Overlake Wind Speed From Overland Wind Speed: A Comparison of Three Methods. *Journal of Great Lakes Research*, 10(1):68–72, 1984.

211. L. Shen, G. S. Triantafyllou, and D. K. P. Yue. Turbulent Diffusion Near a Free Surface. *Journal of Fluid Mechanics*, 407:145–166, Mar. 2000.

212. Y. P. Sheng. Evolution of a Three-Dimensional Curvilinear-Grid Hydrodynamic Model for Estuaries, Lakes and Coastal Waters: CH3D. *Estuarine and Coastal Modeling*, 1:40–49, 1990.

213. Y. P. Sheng, H. K. Lee, and K. H. Wang. On Numerical Strategies of Estuarine and Coastal Modeling. *Estuarine and Coastal Modeling*, 1:291–301, 1990.

214. L. H. Shih, J. R. Koseff, G. N. Ivey, and J. H. Ferziger. Parameterization of Turbulent Fluxes and Scales Using Homogeneous Sheared Stably Stratified Turbulence Simulations. *Journal of Fluid Mechanics*, 525:193–214, Feb. 2005.

215. R. A. Sibson. *A brief Description of Natural Neighbor Interpolation, in Interpreting Multivariate Data*. John Wiley, New York, 1981.

216. J. A. Smith. Wave-Current Interactions in Finite Depth. *Journal of Physical Oceanography*, 36: 1403–1419, July 2006.

217. S. D. Smith and E. G. Banke. Variation of the Sea-Surface Drag Coefficient with Wind Speed. *Q. J. R. Meteorological Society*, 101:665–673, 1975.

218. J. P. Snyder. Map Projections - A Working Manual. Technical report, U.S. Geological Survey, Nov. 1987. U.S. Geological Survey Professional Paper 1395.

219. A. Soloviev and R. Lukas. Observation of Wave-Enhanced Turbulence in the Near-Surface Layer of the Ocean During TOGA COARE. *Deep Sea Research I*, 50:371–395, 2003.

220. R. Soulsby. *Dynamics of Marine Sands: A Manual for Practical Applications*. Thomas Telford Publications, London, 1997. Pages 249, ISBN 0-72-772584-X.

221. M. Spasojevic and M. Holly, Jr. Three Dimensional Numerical Simulation of Mobile-Bed Hydrodynamics. Technical Report HL-94-2, U. S. Army Engineer Waterways Experiment Station, Vicksburg, MS, 1994.

222. Spectrex Corporation. *Instruction Manual: Spectracount (LabView) for Windows, REV 1.0+, for Use with PC-2000 Laser Particle Counter*, 2003. URL: http://www.spectrex.com/.

223. SPM. *Shore Protection Manual. Volume I*. U.S. Army Corps of Engineers, Washington, DC 20314-1000, 4th edition, 1984.

224. M. M. Stanišić. *The Mathematical Theory of Turbulence*. Springer-Verlang, 175 Fifth Avenue, New York, NY 10010, 2nd edition, 1988. Pages 501, ISBN 0-387-96685-4.

225. G. S. Stelling and J. J. Leendertse. Approximation of Convective Processes by Cyclic AOI Methods. In *Proceedings of the Second International Conference on Estuarine and Coastal Modeling*, pages 771–782, Tampa, Florida, 1992. ASCE.

226. C. J. Stewart. United States Great Lakes Shoreline Recession Rate Data. Technical Report DACW39-93-M-6861 and DACW39-94-M-3972, US Army Corps of Engineers, Waterways Experiment Station, Coastal Engineering Research Center, 3909 Halls Ferry Road, Vicksburg, MS, USA, 39180-6199, May 1994.

227. C. J. Stewart. Recession Rate and Land Use Analyses. Lake Michigan Potential Damages Study. Technical Report DACW39-97-D-0007, US Army Corps of Engineers, Detroit District, Dec. 1997.

228. R. H. Stewart. *Introduction to Physical Oceanography*. Open Source Textbook, 2005. Pages 346, URL: http://oceanworld.tamu.edu/resources/ocng_textbook/contents.html.

229. V. L. Streeter, E. B. Wylie, and K. W. Bedford. *Fluid Mechanics*. McGraw Hill Companies, Inc, New York, NY, 9 edition, 1998. Pages 740, ISBN 0-07-062537-9.

230. R. B. Stull. *An Introduction to Boundary Layer Meteorology*. Atmospheric Sciences Library. Kluwer Academic Publishers, P.O. Box 17, 3300 AA Dordrecht, The Netherlands, 1988. Pages 666, ISBN 90-277-2769-4.

231. R. Styles and S. M. Glenn. Modeling Stratified Wave and Current Bottom Boundary Layers on the Continental Shelf. *Journal of Geophysical Research*, 105(C10):24119–24139, Oct. 2000.

232. R. Styles and S. M. Glenn. Modeling Bottom Roughness in the Presence of Wave-Generated Ripples. *Journal of Geophysical Research*, 107(C8):(24)1–15, 2002.

233. M. J. Suarez, W. J. Emery, and G. A. Wick. The Multi-Channel Infrared Sea Truth Radiometric Calibrator (MISTRC). *Journal of Atmospheric and Oceanic Technology*, 14:243–253, Apr. 1997.

234. T. Sunamura. A Relationship Between Wave-induced Cliff Erosion and Erosive Force of Wave. *The Journal of Geology*, 85:613–618, 1977.

235. E. A. Terray, M. A. Donelan, Y. C. Agrawal, W. M. Drennan, K. K. Kahma, A. J. Williams III, P. A. Hwang, and S. A. Kitaigorodskii. Estimates of Kinetic Energy Dissipation Under Breaking Waves. *Journal of Physical Oceanography*, 26:792–807, May 1996.

236. L. Thais and J. Magnaudet. A Triple Decomposition of the Fluctuating Motion Below Laboratory Wind Water Waves. *Journal of Geophysical Research*, 100(C1):741–755, Jan. 1995.

237. The WAMDI Group. The WAM model - a Third Generation Ocean Wave Prediction Model. *Journal of Physical Oceanography*, 18:1775–1810, 1988.

238. J. F. Thompson, Z. U. A. Warsi, and C. W. Mastin. *Numerical Grid Generation: Foundations and Applications*. Elsevier Science Publishing Co., Inc, P.O. Box 211, 1000 AE Amsterdam, The Netherlands, 1985. Pages 483, ISBN 0-444-00985-X.

239. S. A. Thorpe. *The Turbulent Ocean*. Cambridge University Press, New York, NY, 2005. Pages 439, ISBN 0-521-83543-7.

240. A. Tolstoy. Chlorophyll-a in Relation to Phytoplankton Volume in Some Swedish Lakes. *Archiv für Hydrobiologie*, 85(2):133–155, 1979.

241. A. S. Trenhaile. Modeling the Development of Wave-Cut Shore Platforms. *Marine Geology*, 116: 163–178, 2000.

242. Y. Uchiyama and J. C. McWilliams. Infragravity Waves in the Deep Ocean: Generation, Propagation, and Seismic Hum Excitation. *Journal of Geophysical Research*, 113(C07029):1–25, July 2008.

243. H. van Haren and M. J. Howarth. Enhanced Stability During Reduction of Stratification in the North Sea. *Continental Shelf Research*, 24:805–819, 2004.

244. L. C. van Rijn. Sediment Transport, Part I: Bed Load Transport. *Journal of Hydraulic Engineering*, ASCE, 110(10):1431–1456, 1984a.

245. L. C. van Rijn. Sediment Transport, Part II: Suspended Load Transport. *Journal of Hydraulic Engineering*, ASCE, 110(11):1613–1641, 1984b.

246. L. C. van Rijn. Unified View of Sediment Transport by Currents and Waves. I: Initiation of Motion, Bed Roughness, and Bed-Load Transport. *Journal of Hydraulic Engineering*, ASCE, 133(6):649–667, 2007a.

247. L. C. van Rijn. Unified View of Sediment Transport by Currents and Waves. II: Suspended Transport. *Journal of Hydraulic Engineering*, ASCE, 133(6):668–689, 2007b.

248. L. C. van Rijn. Unified View of Sediment Transport by Currents and Waves. III: Graded Beds. *Journal of Hydraulic Engineering*, ASCE, 133(7):761–775, 2007c.

249. V. A. Vanoni. *Sedimentation Engineering*. American Society of Civil Engineers, 345 East 47th St., New York, N.Y. 10017, 1977. ISBN 0-87262-001-8.

250. J. O. Veach. *Soils and Land of Michigan*. The Michigan State College Press, 1953.

251. J. Veeramony and I. A. Svendsen. The Flow in Surf-Zone Waves. *Coastal Engineering*, 39:93–122, 2000.

252. P. Velissariou, V. Velissariou, Y. Guo, and K. W. Bedford. A Multi-Size, Multi-Source Formulation for Determining Impacts of Sediments on Near-Shore Sensitive Sites. In M. L. Spaulding and H. L. Butler, editors, *Estuarine and Coastal Modeling. Proceedings of the Sixth International Conference*, pages 59–73, New Orleans, Louisiana, Nov. 1999. ASCE.

253. J. C. Warner, C. R. Sherwood, R. P. Signell, C. K. Harris, and H. G. Arango. Development of a Three-Dimensional, Regional, Coupled Wave, Current, and Sediment-Transport Model. *Computers Geosciences*, 34:1284–1306, 2008.

254. D. F. Watson. *Contouring - A Guide to the Analysis and Display of Spatial Data*. Computer Methods in the Geosciences. Pergamon, Washington, D.C., 1st edition, 1992. Pages 340, ISBN 0-08-040286-0.

255. D. J. S. Welsh, K. W. Bedford, R. Wang, and P. Sadayappan. A Parallel-Processing Coupled ave/Current/Sediment Transport Model. Technical Report ERDC MSRC/PET TR/00-20, US Army Corps of Engineers, Waterways Experiment Station, Vicksburg, MS, May 2000.

256. G. B. Whitham F. R. S. *Linear and Nonlinear Waves*. John Wiley & Sons, New York, N.Y., 1974. Pages 636, ISBN 0-471-94090-9.

257. A. G. Winkelman, E. R. Stabenau, and B. J. Eadie. Particle Size Distribution and Concentration of Total Suspended Matter in Southern Lake Michigan: January 28 - February 10, 1998. NOAA Technical Memorandum ERL GLERL-105, Great Lakes Environmental Research Laboratory, Ann Arbor, MI 48105, May 1999.

258. WMO-No. 702. Guide to Wave Analysis and Forecasting. Technical Report WMO-No. 702, World Meteorological Organization, 1998. Pages 159, ISBN 92-63-12702-6, URL: http://www.wmo.ch/web/aom/marprog/Publications/publications.htm.

259. S. F. Wornom, D. J. S. Welsh, and K. W. Bedford. On Coupling the SWAN and WAM Wave Models for Accurate Nearshore Wave Predictions. *Coastal Engineering Journal*, 43(3):161–201, 2001.

260. D. G. Wright. An Equation of State for Use in Ocean Models: Eckart's Formula Revisited. *Journal of Atmospheric and Oceanic Technology*, 14:735–741, 1997.

261. L. D. Wright. Shelf-Surfzone Coupling: Diabathic Shoreface Transport. In *Coastal Sediments '87*, volume 1, pages 25–40. American Society of Civil Engineers, Committee on Coastal Engineering, 1987. ISBN 0-87262-559-0.

262. L. D. Wright, A. D. Short, and M. O. Green. Short-term Changes in the Morphodynamic States of Beaches and Surf Zones: An Empirical Predictive Model. *Marine Geology*, 62:339–364, 1985.

263. L. W. Wright. Variation in the Level of the Cliff/Shore Platform Junction Along the South Coast of Great Britain. *Marine Geology*, 9:347–353, 1970.

264. J. Wu, E. M. Buchak, J. E. Edinger, and V. S. Kolluru. Simulation of Cooling-Water Discharges From Power Plants. *Journal of Environmental Management*, 61:77–92, 2001.

265. A. Wüest and A. Lorke. Small-Scale Hydrodynamics in Lakes. *Annual Review of Fluid Mechanics*, 35:373–412, 2003.

266. K. Wyrtki. The Average Annual Heat Balance of the North Pacific Ocean and Its Relation to Ocean Circulation. *Journal of Geophysical Research*, 70(18):4547–4559, 1965.

267. H. Xia, Z. Xia, and L. Zhu. Vertical Variation in Radiation Stress and Wave-Induced Current. *Coastal Engineering*, 51:309–321, 2004.

268. M. Y. Zhang and Y. S. Li. The Dynamic Coupling of a Third-Generation Wave Model and a 3D Hydrodynamic Model Through Boundary Layers. *Continental Shelf Research*, 17(10):1141–1170, 1997.

269. M. Y. Zhang and Y. S. Li. The Synchronous Coupling of a Third-Generation Wave Model and a Two-Dimensional Storm Surge Model. *Ocean Engineering*, 23(6):533–543, 1996.

270. S. Zhou and J. A. McCorquodale. Modeling of Rectangular Settling Tanks. *Journal of Hydraulic Engineering*, 118(10), 1992.

271. O. Zikanov and D. N. Slinn. Along-Slope Current Generation by Obliquely Incident Internal Waves. *Journal of Fluid Mechanics*, 445:235–261, 2001.

272. S. S. Zilitinkevich and I. N. Esau. Similarity Theory and Calculation of Turbulent Fluxes at the Surface for the Stably Stratified Atmospheric Boundary Layer. *Boundary-Layer Meteorology*, 125: 193–205, 2007.

273. S. S. Zilitinkevich, T. Elperin, N. Kleeorin, and I. Rogachevskii. Energy-and Flux-Budget (EFB) Turbulence Closure Model for Stably Stratified Flows. Part I: Steady-State, Homogeneous Regimes. *Boundary-Layer Meteorology*, 125:167–191, 2007.

274. S. S. Zilitinkevich, T. Elperin, N. Kleeorin, I. Rogachevskii, I. Esau, T. Mauritsen, and M. W. Miles. Turbulence Energetics in Stably Stratified Geophysical Flows: Strong and Weak Mixing Regimes. *Quarterly Journal of the Royal Meteorological Society*, 134:793–799, 2008.